SYNTHESIS AND CHARACTERISATION OF IRON OXIDE/SILICON OXIDE/ZINC OXIDE NANOCOMPOSITES FOR THE TREATMENT OF PETROLEUM REFINERY WASTEWATER

BY

SHABA, Elijah Yanda

PhD/SPS/2017/1015

DEPARTMENT OF CHEMISTRY

FEDERAL UNIVERSITY OF TECHNOLOGY, MINNA

MAY, 2023

SYNTHESIS AND CHARACTERISATION OF IRON OXIDE/SILICON OXIDE/ZINC OXIDE NANOCOMPOSITES FOR THE TREATMENT OF PETROLEUM REFINERY WASTEWATER

BY

SHABA, Elijah Yanda
PhD/SPS/2017/1015

A THESIS SUBMITTED TO THE POSTGRADUATE SCHOOL FEDERAL UNIVERSITY OF TECHNOLOGY, MINNA, NIGERIA IN PARTIAL FULFILLMENT OF THE REQUIREMENTS FOR THE AWARD OF THE DEGREE OF DOCTOR OF PHILOSOPHY (PhD) IN ANALYTICAL CHEMISTRY

MAY, 2023

CERTIFICATION

This thesis titled: '**SYNTHESIS AND CHARACTERISATION OF IRON OXIDE/SILICON OXIDE/ZINC OXIDE NANOCOMPOSITES FOR THE TREATMENT OF PETROLEUM REFINERY WASTEWATER''** by SHABA, Elijah Yanda (PhD/SPS/2017/1015) meets the regulations governing the award of the degree of Doctor of Philosophy (PhD) of the Federal University of Technology, Minna and is approved for its contribution to scientific knowledge and literary presentation.

Prof. J. O. JACOB   …………......………………
MAJOR SUPERVISOR   SIGNATURE AND DATE

PROF. M. A. T. SULEIMAN   ………......…………….....
CO-SUPERVISOR   SIGNATURE AND DATE

DR. J. O. TIJANI   ………......…………….....
CO-SUPERVISOR   SIGNATURE AND DATE

DR. L. A . FADIPE   ………..………………….
HEAD OF DEPARTMENT   SIGNATURE AND DATE

PROF. M. JIYA   ……...…………………
DEAN, SCHOOL OF PHYSICAL SCIENCES   SIGNATURE AND DATE

ENGR. PROF. O. K. ABUBAKRE   …………………………….
DEAN, POSTGRADUATE SCHOOL   SIGNATURE AND DATE

DEDICATION

This work is dedicated to late Mr. Joseph Ndako Shaba and late Mrs. Victoria Shaba.

My utmost regard goes to my parents Late Mr. Joseph Ndako Shaba and Late Mrs. Victoria Kaka Shaba who both laid the foundation for my education giving it all it takes. It is painful that you both did not live to see this day, but if Henry Long Fellow was right in saying that "Life is real, Life is earnest; and the grave is not his goal. Dust thou art, to dust returned" was not spoken of the soul, then I can feel you around me, not only in flesh but surely in spirit. I love you both but God loves you more, rest on.

My lovely mother Mrs. Comfort Woye Shaba is appreciated. The amount of gratitude I have for all of the sacrifices you have made on my behalf is beyond words, It is only God that can bless you *Nma*. Your prayer for me has kept me going thus far. To my mother-in-law, thank you for accepting me into your family in such a warm and welcoming manner. The fact that you genuinely cared about getting to know the progress of the thesis every time meant a lot to me. You were always there for me in every ramification. I cherish you and appreciate all your prayers, encouragement and financial support during the study. Thank you very much, *Mama.*

 I am and will forever be grateful to my loving wife Mrs. Martha Azara Shaba who has given everything possible and even given up important things to make sure I achieve this feat. I can't find the words that express my gratitude. My wife, you have made me stronger, better and more fulfilled than I could have ever imagined. Without your wonderful support and understanding throughout the study, I would not have been able to complete this study. I love you, *Kube etun*. I also, from the depth of my heart appreciate my children the E. Ys (Ebenezer Yebo-Soko Shaba, Eleazer Yeka-Soko Shaba and Elizabeth Yegun-Soko Shsba) who even at such tender ages have had to endure so much stress and discomfort just for me. This page can't tell it all. I appreciate my siblings and their spouses TPL. Yisapati B. Silas, SP. John Shaba, Mrs Millicent Manmman, Mrs. Lucy shaba and Shaba N Philemon. A Special thanks to Eng. Daniel D. Shaba (big Bros)

in his infinite mercy continue to rest your soul. Rest on my sister. Finally, I want to thank all my students and relatives that I was not able to mention.

ABSTRACT

The wastewater generated from petroleum refinery wastewater contains a variety of organic and inorganic pollutants that must be properly removed before being discharged into the environment. This study evaluates the potential of ZnO, Fe_3O_4, SiO_2, ZnO/Fe_3O_4, ZnO/SiO_2, Fe_3O_4/SiO_2, $Fe_3O_4/SiO_2/ZnO$ (1:1:1), $Fe_3O_4/SiO_2/ZnO$ (1:1:2), $Fe_3O_4/SiO_2/ZnO$ (1:2:1), and $Fe_3O_4/SiO_2/ZnO$ (2:1:1) for the removal of selected heavy metals and other quantity parameters from petroleum refinery wastewater. Fe_3O_4, SiO_2 and ZnO, nanoparticles and their corresponding nanocomposites were synthesized via the sol-gel chemical reduction method. X-ray diffraction (XRD), high-resolution scanning electron microscopy (HRSEM), Energy dispersive X-ray spectroscopy (EDS), Fourier-Transform Infrared spectroscopy (FT-IR), X-ray photoelectron spectroscopy (XPS) and Brunauer-Emmett-Teller (BET) N_2 adsorption-desorption, were used to characterise ZnO, Fe_3O_4, SiO_2 nanoparticles and their corresponding nanocomposites. The HRSEM and XRD analysis of the monometallic oxide nanoparticles indicates the formation of faced-center cubic Fe_3O_4 nanoparticles with a spherical shape. The hexagonal α-quart structure of SiO_2 nanoparticles was synthesised from kaolin while the hexagonal wurtzite phase of ZnO nanoparticles was synthesised at calcination temperature above 100^oC. The bimetallic oxide nanocomposites synthesised (ZnO/Fe_3O_4, ZnO/SiO_2 and Fe_3O_4/SiO_2) showed the formation of rod-like structure as a major shape except for ZnO/Fe_3O_4 nanocomposites which show spherical shape structures. The HRSEM and XRD analysis of $Fe_3O_4/SiO_2/ZnO$ (1:1:1), $Fe_3O_4/SiO_2/ZnO$ (1:1:2), $Fe_3O_4/SiO_2/ZnO$ (1:2:1), and $Fe_3O_4/SiO_2/ZnO$ (2:1:1) show the formation of a mixture of spherical and rod-like structure. The BET adsorption-desorption analysis showed that the surface area of the monometallic oxides was 0.3, 7. and 8 m^2/g for SiO_2, Fe_3O_4 and ZnO nanoparticles respectively. The $Fe_3O_4/SiO_2/ZnO$ (1:2:1) exhibited the highest surface area of 35.469 $m²/g$ compared to 24.918, 30.685 and 5.751 $m²/g$ obtained for $Fe_3O_4/SiO_2/ZnO$ (1:1:1), $Fe_3O_4/SiO_2/ZnO$ (1:1:2), and $Fe_3O_4/SiO_2/ZnO$ (2:1:1) nanocomposites. The effect of contact time, adsorbent dosage and reaction temperature on the removal of selected heavy pollutants based on batch adsorption was studied. The result indicates that the $Fe_3O_4/SiO_2/ZnO$ (1:2:1) nanocomposites have higher adsorption removal efficiency of percentage removal wth 99.03 %, 94.92 %, 90.33 %, 88.99 %, 99.99 %, 99.64 %, 92.50 %, 88.99 % and 90.86 % at time (15 min), adsorbent dosage (0.05g), reaction temperature (35 ^oC) and pH of 6.25 for Pb (II) Cd (II), Ni (II) Cr (VI), Cu (II), total iron, BOD, COD and TOC respectively from petroleum refinery wastewater. The thermodynamic analysis showed a positive value of enthalpy (ΔH) for all the tested samples, indicating the endothermic nature of the adsorption process. The kinetic adsorption data better fitted to the pseudo-second-order kinetic model for all the pollutants, indicating that chemisorption was the rate-determining step. The adsorption isotherm showed that experimental data fitted best to the Langmuir isotherm compared with Freundlich, Temkin, and Dubinin Radushkevich (D-R) isotherms, as demonstrated by higher correlation coefficient values (R^2). The desorption of the $Fe_3O_4/SiO_2/ZnO$ nanocomposites showed that the highest desorption efficiency was at 0.1 $moldm^{-3}$ HNO_3 solution, irrespective of the mixing ratio. The nanoadsorbent was stable after the adsorption process and $Fe_3O_4/SiO_2/ZnO$ nanocomposites can be reused for up to a four-cycles. These findings revealed that $Fe_3O_4/SiO_2/ZnO$ nanocomposites with a mixing ratio of (1:2:1) was a better adsorbent compared with other mixing ratios. $Fe_3O_4/SiO_2/ZnO$ is not a good materials for antimicrobial and antioxidant matrial. The findings from this study demonstrated that $Fe_3O_4/SiO_2/ZnO$ (1:21) nanoadsorbent can effectively be used for the treatment of petroleum wastewater.

TABLE OF CONTENTS

CHAPTER THREE

CHAPTER FIVE

LIST OF FIGURES

xxiv

LIST OF PLATES

ABBREVIATION

ZnO nanoparticles   Zinc Oxide nanoparticles

SiO_2NPs Silicon Oxide nanoparticles

Fe_3O_4NPs Iron Oxides nanoparticles

BET   Brunauer, Emmett and Teller

EDS   Dispersive X-ray analysis

FDA   Food and Drug Administration

FT-IR   Fourier-Transform Infrared spectroscopy

MCL   Maximum contaminated level

PVA   Polyvinyl alcohol

PVP   Polyvinyl pyrrolidone

RS   Raman spectroscopy

SEM   Scanning electron microscopy

UV–vis   Ultraviolet-Visible Spectroscopy

XPS   X-ray photoelectron spectroscopy

XRD   X-ray powder diffraction

DLS   Dynamic Light Scattering

AFM   Atomic Force Microscopy Analysis

$q_e(exp)$ = adsorption capacity determined experimentally (mgg^{-1})

$q_e(cal)$ = adsorption capacity calculated from model (mgg^{-1})

k_1 = pseudo-first-order rate constant (min^{-1})

k_2 = pseudo-second-order rate constant $(g\ mg^{-1}min^{-1})$

q_t = adsorption capacity at time t (mgg^{-1})

k_{id} = intra-particle diffusion rate constant $(mg\ g^{-1}min^{-1/2})$

C = intra-particle constant related to thickness of boundary layer

A and B = Elovich constants (mgg^{-1})

K_c = equilibrium constant

B = Langmuir constant for energy of adsorption (Lmg^{-1})

q_m = theoretical maximum monolayer adsorption capacity ($mg\ g^{-1}$)

K_F = Freundlich isotherm constant (mgg^{-1})

N = Freundlich exponent, dimensionless factor

K_T = Equilibrium binding constant (Lmg^{-1})

B_T = Temkin constant related to heat of adsorption ($Jmol^{-1}$)

B = nconstant related to the adsorption energy (mol^2kJ^{-2})

G = free energy change ($kJmol^{-1}$)

ΔH = nenthalpy change ($kJmol^{-1}$)

ΔS = entropy change ($kJmol^{-1}K^{-1}$)

R = universal gas constant ($J\ mol^{-1}K^{-1}$)

T = absolute temperature (K)

t = time (min)

V = volume of solution (cm^3)

$°C$ = degree celsius

K = kelvin

g = gram

IC_{50} = The free radical scavenging activity at 50 % concentration.

CHAPTER ONE

1.0   **INTRODUCTION**

1.1   Background to the Study

The growing human global population and demand supply chain for petroleum-related products coupled with the expansion of petroleum refinery industries have led to the increasing release of petroleum refinery wastewater into the environment (Rahi *et al*., 2021). The direct discharge of untreated petroleum refinery wastewater contributed to the deterioration of surface and groundwater resources and consequently poses a significant risk to human health and animal life (Mohammadi *et al.*, 2020). Mohanakrishna *et al.* (2020), reported that approximately 3500– 5000 litres of petroleum wastewater are generated per ton of crude oil processed globally.

The petroleum refinery wastewater comprises several organic and inorganic constituents such as toluene, phenols, benzene, ethylbenzene, xylene, vanadium, iron, cadmium, nickel, selenium, chromium, copper, zinc, molybdenum and cyanide, sulfur dioxide, nitrogen oxides and hydrogen sulfate (Briffa *et al*., 2020). Benzene and ethylbenzene exposure have been linked to a higher risk of cancer and leukemia (Zhou *et al*., 2020), xylene and toluene have harmful effects on the reproductive system, especially when exposed for long periods even at low concentrations (Barbara *et al*., 2021).

Exposure to Pb has been linked to nausea, vomiting, abdominal pain, renal failure, hallucinations, mental retardation, birth defects, dyslexia, psychosis, paralysis, muscle weakness, weight loss, brain damage, kidney damage, and even death (Balali-Mood *et al*., 2021 and Wilk *et al*., 2021). Additionally, cadmium is also known to cause stomach irritation,

vomiting, fragile bones, kidney and lung damage (Obasi and Akudinobi, 2020). These pollutants are mobile, sometimes pseudo-persistent, non-biodegradable and highly recalcitrant in the environment and as such difficult to remove by conventional wastewater processes. Thus, the effective removal of these undesirable elements is very necessary for a sustainable ecosystem.

Conventional techniques commonly employed for the treatment of wastewater, include biological processes, flocculation, precipitation, co-precipitation, electrolysis, and membrane processes (Palani *et al.*, 2021), ion exchange, coagulation and adsorption (Qasem *et al.*, 2021) to mention but a few. The performances of these techniques are typically satisfactory, but they have a few limitations. These limitations include maintenance and operation costs, monitoring of pH, formation of intermediates products, use of toxic chemicals, oxidation for complexed metals, large generation and management of sludge (Qasem *et al*., 2021). Additionally, the biological method required maintenance of the microorganisms, inefficient for non-degradable compounds and the slowness of the process (Musa *et al.*, 2021).

Due to the above limitations, the adsorption technique is considered one of the most effective, and economical methods for the removal of heavy metals and organic pollutants from wastewater, due to its excellent advantages of low cost, availability, high efficiency, and easy handling (Sadegh *et al.*, 2017). Due to the aforementioned advantages, extensive research has been done on the development of adsorbents such as activated carbons, polymer materials, zeolites, biofuels and industrial by-products for the removal of heavy metals (Younas *et al*., 2021). However, these adsorbents have significant drawbacks which include limited loading capacities, low selectivity, low metal ion binding sites and economic feasibility (Saleem *et al*., 2019).

2

In light of these setbacks, researchers have focused on the development of adsorbents from nanomaterials for the removal of heavy metals from industrial wastewater. Efforts have been made to produce nonoadsorbent of different sizes, morphologies and shapes, with high compatibility and stability (Andrade *et al*., 2020a), via various synthesis methods including hydrothermal, ball milling method, thermal decomposition, biological methods, coprecipitation, sol-gel, and microemulsion methods (Aragaw *et al*., 2021). Among these methods, the sol-gel method is a versatile and effective approach because of its simplicity and versatility, low temperatures synthesis, cost-effectiveness, and production of a very fine powder. Additionally, in comparison to other synthesis methods, it allows for more control of crystallite size over other processes (Tan *et al*., 2021).

Different nanoadsorbents such as manganese oxides, ferric oxides, titanium oxides, aluminum oxides, selenium oxides, zinc oxides and silicon oxides nanoparticles have been developed for the removal of heavy metals from industrial wastewater (Shaba *et al*., 2021). Metal oxides, such as ZnO have long been recognized as viable nano adsorbents, due to their unique characteristics such as good transparency, high electron mobility and strong room-temperature luminescence. ZnO nanoparticles have drawbacks of stability in the aqueous matrix (Carofiglio *et al*., 2020).

Magnetite (Fe_3O_4) nanoparticles are another type of commonly utilized nanoadsorbents for the treatment of wastewater, due to the advantages which include, ease of separation from aqueous solutions, low-cost, readily available, and environmental friendliness (Zhang *et al*., 2020b). Additionally, Silica (SiO_2) nanoparticles are another metal oxide with several distinct advantages such as a drug delivery vehicle, including great biocompatibility, high

hydrophobicity, thermal stability, high flexibility and pH change resistance, as well as a high degree of multifunctionality (Selvarajan *et al*., 2020).

Recently, attention has been shifted to the synthesis of hybrid nanocomposites with improved properties that the pure nanoparticles could not attain on their own (Sharma *and* Bhattacharya, 2020). Various bimetallic oxides nanocomposites have been used for the removal of heavy metals from wastewater. Nevertheless, many researchers have reported disadvantages associated with the use of bimetallic oxides for the treatment of wastewater including longer contact time to achieve higher adsorption, easily deactivated, a lower surface area that limits the adsorption of pollutants and the presence of less functional groups that reduces adsorption of the pollutants from the wastewater (Shaba *et al*., 2021). Nowadays attention has been shifted to the synthesis of hybrid nanocomposites such as ternary nano composites to solve some of the problems associated with monometallic oxides and bimetallic oxides nanocomposites. However, no work has been performed that specifically studied the adsorptive, antibacterial and antioxidant properties of the ternary hybrid iron oxides/silicon oxides/zinc oxides ($Fe_3O_4/SiO_2/ZnO$) nanocomposites. This study focused on the synthesis, characterisation and the adsorption potential of the $Fe_3O_4/SiO_2/ZnO$ nanocomposites for the removal of selected heavy metals (Pb, Cd, Ni, Cr, Cu and Fe) as well as chemical oxygen demand (COD), biochemical oxygen demand (BOD) and total organic carbon (TOC) in petroleum refinery wastewater. The antibacterial and antioxidant properties of the $Fe_3O_4/SiO_2/ZnO$ nanocomposites were also investigated.

1.2   Statement of the Research Problem

High levels of aromatic compounds and heavy metals in petroleum refinery wastewater constitute a major threat to humans and aquatic life. Environmental issues are caused by the

direct release of petroleum refinery wastewater into the environment. Exposure to petroleum wastewater can cause eye and skin irritation, dizziness, headache, nausea, and cancer. Thus, a need for proper treatment before the discharge into the environment. The available treatment methods namely, biological, flocculation, precipitation, co-precipitation, electrolysis and membrane, ion exchange and coagulation that have been used to remove organic and inorganic pollutants from petroleum wastewater are time-consuming, costly, not environmentally friendly and inefficient for complete removal of the pollutants from the petroleum refinery wastewater. Thus, there is a need for an alternative method that can effectively remove the pollutants generated by the petroleum industries in Nigeria. The use of ZnO nanoparticles as adsorbents usually has some limitations which include aggregation and instability in an aqueous system and poor separation after the adsorption process. Magnetite (Fe_3O_4) nanoparticles are easily oxidized with oxygen and are corroded by acids and bases because of the presence of Fe (II) in their structures.

The commercial source of silicon for the synthesis of silica is commonly found to be tetraethylorthosilicate (TEOS), tetramethyl orthosilicate and sodium silicate. However, these compounds can be harmful to one's health. As a result, new approaches to finding a cleaner, cheaper and more environmentally friendly source of silica are needed.

1.3   Justification for the Study

The use of Fe_3O_4/SiO_2/ZnO nanocomposite as an adsorbent is expected to remove the pollutants that are associated with petroleum refinery wastewater thereby reducing the negative impact of the petroleum refinery wastewater on the environment.

An adsorption technique that is cost-effective and environmentally friendly is expected to serve as a good alternative to solve most of the disadvantages (setbacks) found with the currently used wastewater treatment methods.

The instability of ZnO nanoparticles is expected to be reduced by the incorporation of SiO_2 and Fe_3O_4 nanoparticles to form $Fe_3O_4/SiO_2/ZnO$ nanocomposite.

The oxidation of Magnetite (Fe_3O_4) due to the presence of Fe (II) is expected to be reduced by the incorporation of ZnO and SiO_2 nanoparticles to form $Fe_3O_4/SiO_2/ZnO$ nanocomposite. Locally available Kaolin from Pati Shaba-kolo in Niger State, Nigeria was used for the synthesis of SiO_2 nanoparticles to replace the use of commercial silicon salts and other chemicals as a precursor.

1.4 Aim and Objectives of the Study

1.4.1 Aim

The aim of this study is to prepare, characterise and investigate the adsorption potential of $ZnO/Fe_3O_4/SiO_2$ nanocomposite for the treatment of petroleum refinery wastewater:

1.4.2 Objectives

The aim was achieved through the following specific objectives:

i. Preparation of ZnO, Fe_3O_4 and SiO_2, ZnO/Fe_3O_4, Fe_3O_4/SiO_2 and $Fe_3O_4/SiO_2/ZnO$ nanocomposites via sol-gel chemical reduction methods.

ii. Characterisation of ZnO, Fe_3O_4 and SiO_2, nanoparticles, ZnO/Fe_3O_4, Fe_3O_4/SiO_2 and $Fe_3O_4/SiO_2/ZnO$ nanocomposites using different analytical tools.

iii.   Characterisation of the petroleum refinery wastewater sample; before and after the batch adsorption processes.

iv.   Establishment of the influence of contact time, adsorbents dosage and temperature on the removal efficiency of the adsorbent via batch adsorption method.

v.   Examination of the recyclability/repeated applications of the synthesized $Fe_3O_4/SiO_2/ZnO$ nanocomposite

vi.   Evaluation of the antimicrobial and antioxidant activities of $Fe_3O_4/SiO_2/ZnO$ nanocomposite

CHAPTER TWO

2.0   **LITERATURE REVIEW**

2.1   Nanoparticles

Nanomaterials are materials with particles size from 1-100 nm with unique properties compared to bulk materials (Jeevanandam *et al*., 2018). These nanomaterials have been used in various fields such as biotechnology, medicine, electronics, packaging, cosmetics, coatings and water purification (Mohammad *et al*., 2022). Nanoparticles as advanced materials have been developed for the effective treatment of wastewater through the adsorption process due to their high surface area potential (Pandey *et al*., 2017).

2.1.1 Classification of nanomaterials

Classification of nanoparticles is based on the number of dimensions, which are not confined to the nanoscale range (< 100 nm). The main types based on the dimensions and structures are: zero-dimensional (0D), one-dimensional (1D), two-dimensional (2D), and three-dimensional (3D) nanomaterials (Zhang *et al.,* 2018)

2.1.1.1   Zero dimensional nanoparticles (0D)

In zero-dimensional nanomaterials, all the dimensions (Length, breadth, and heights) are in existence in the nanoscale (< 10 0 nm), 0D nanostructures are the simplest building blocks that can be used to design and create 1D, 2D, and complex 3D nanostructures (Paras *et al.* 2023). Examples of 0D nanomaterials are nanoparticles and nano-Dots.

2.1.1.2   One dimensional nanoparticles (1D)

Two dimensions are in the nanoscale (1–100 nm) and the other one dimensions in the macroscale. Two dimensions nanomaterials have needles shaped such as nanowires, nanofibers, nanorods, nanocapsule, nanowalls and nanotubes (Ghassan *et al.,* 2019).

2.1.1.3   Two dimensional nanoparticles (2D)

In two-dimensional nanomaterial (2D), the two dimensions are outside the nanoscale. The 2D nanomaterials exhibit plate-like shapes such as nanofilms, nanoplates nanolayers, and nanocoatings (Stoller and Ochando-Pulido, 2020).

2.1.1.4   Three dimensional nanoparticles (3D)

In three-dimensional (3D)**,** the three dimensions are not in nanoscale and all dimensions are in macroscale. An example of 3D nanomaterials is nanocomposites (Shehzad *et al.,* 2016).

2.2   Morphologies of Nanoparticles

Different morphologies of nanoparticles have been reported by researchers due to the variation of various process parameters. These include nanorods (Ghannam *et al.,* 2019), nanowires (Li *et al.,* 2020), nanospheres (Li *et al.,* 2022), nanoflowers (Devlekar and Shende, 2022), nanotubes (Norizan *et al*., 2022), nanotetrapods (Aziz *et al.,* 2020), nanoplate and nanotripods (Azhar *et al.,* 2017). The nanosphere nanoparticles are the simplest form of nanoparticles with only one adjustable geometric parameter (radius) exhibiting resonant responses under optical excitation (Ahmadivand *et al.,* 2016). A nanotube is a tube-like structure that belongs to a one-dimensional (1D) nanostructure group (Machín *et al*, 2022). Nanotetrapods have been reported to be nanomaterial with four feet that belong to the dimensional structure (Aziz *et al*., 2020). The advantage of nanotetrapods over other

nanocrystalline geometric shapes of nanomaterials includes alignment of themselves spontaneously to the plane with one standard 'arm' (Shao *et al.,* 2020). Nanotetrapod legs are spatially distributed with an angle of 109.5° (Modi, 2015). A nanowire is a solid rod-like structure having thickness or diameter constrained to tens of nanometers or less (1 nm = 10^{-9} m) that is similar to conventional wires (Li, *et al.,* 2021). Nanowires are known as 1D material due to the large difference between their diameter and length (Nasrollahzadeh *et al.,* 2019). Nanowires have been reported to have fewer structural defects than their bulk counterpart (Machín *et al*., 2022). Nanoflowers are nanostructures similar to plant flowers in a nanoscale range that is usually prepared in extreme conditions like 80–550°C (Shende *et al.,* 2018). Nanoflowers have also been reported to have a high volume-to-surface ratio which improves surface adsorption that can speed up reaction kinetics (Shende *et al*., 2018). Nanoplate is a nanomaterial that has a plate-like structure or has two dimensional nanostructures (2D) (Li *et al.,* 2022). Various metal oxides including ZnO, SiO_2 and Fe_3O_4 nanoparticles exist in different phases and crystal structures.

2.3   Zinc Oxide Nanoparticles

Zinc oxide nanoparticles constitute one of the important metal oxides materials that have been widely applied in materials science due to their unique physical, chemical and biological properties such as biocompatible, environmentally friendly, low cost and non-toxic nature (Ruszkiewicz *et al*., 2017). In each phase, ZnO nanoparticles are a semiconductor material with a direct wide bandgap of ~3.3 eV (Senol *et al*., 2020). The zincblende form can be stabilised by growing ZnO on substrates with cubic lattice structures (Parihar *et al*., 2018). Food and Drug Administration (FDA) include zinc oxide as one of the safest metal oxides that can be used in food industries. Zinc oxide nanoparticles have been synthesised via

different methods including chemical, physical and biological methods (Droepenu *et al*. 2022), using different zinc salts such as zinc acetate

dehydrate($Zn(C_2H_3O_2)_2.2H_2O$), zinc nitrate hexahydrate($Zn(NO_3)_2.6H_2O$) zinc sulphate ($Zn(SO_4)_2.7H_2O$) and zinc chloride ($ZnCl_2$) as a precursor (Sierra *et al.*, 2018).

2.3.1   Crystal structure of zinc oxide nanoparticles

Zinc oxide (ZnO) is a water-insoluble white powder used as an additive in different products, especially foods, paints, sunscreens, lubricants, sealants, and batteries (Perveena *et al.,* 2020). Although ZnO occurs naturally as the mineral zincite, most zinc oxides are chemically produced under different conditions in the laboratory. Zinc oxide nanoparticles can exist in three forms, namely hexagonal-wurtzite, cubic zincblende, and cubic rocksalt (Chandramohan *et al.,* 2017) (see Figure 2.1). The shaded black and gray spheres represent oxygen and zinc atoms. The wurtzite structure is most common and stable at ambient conditions due to its ionicity that resides exactly at the borderline between the covalent and the ionic materials (Chandramohan *et al.,* 2017). The zinc blend ZnO structure can only be stabilized by growing on cubic substrates and the rocksalt structure can be obtained at relatively high pressures, 10 GPa (Shaba *et al.,* 2021). As found with most group II-VI elements, the bonding in ZnO is largely ionic with 0.074 nm for zinc ions (Zn^{2+}) and 0.140 nm for the oxygen ion (O^{2-}) as corresponding radii. This property is responsible for the preferential formation of wurtzite rather than zinc blend structure (Phillips), as well as its high piezoelectricity.
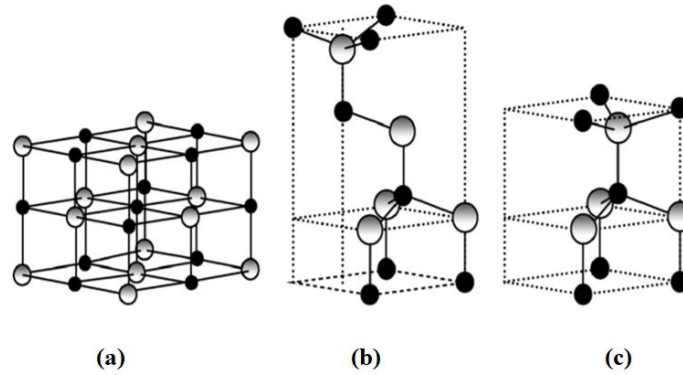
Figure 2.1: Different Phases of ZnO Nanoparticles (a) Cubic Rocksalt, (b) Cubic Zincblende (c) Hexagonal-Wurtzite

2.4   Iron Oxides Nanoparticles

Iron(II) oxide (FeO), Iron(III) oxide   (Fe_2O_3) also known as ferric oxide and iron(II, III) oxide (Fe_3O_4) are the three main types of iron oxide nanoparticles considered to be important materials due to their, low-cost, environmentally friendly nature, biocompatibility, non-toxicity and catalytic activity (Aragaw *et al*., 2021). Among the aforementioned, iron (II, III) oxides nanoparticle (Fe_3O_4), is the most common iron ores. It is ferrimagnetic and one of the iron oxides; attracted to magnets and can be magnetized to become a permanent magnet (Abdel-Maksoud *et al*., 2020). Fe_3O_4 nanoparticles have the highest magnetism of all the transition metal oxides (Ganapathe *et al*., 2020). At room temperature, Fe_3O_4 nanoparticles are ferrimagnetic and have a Curie temperature of 850 K. As compared to other phases of iron oxide, it has a moderately high Curie temperature (Samrot *et al.*, 2020). It is a compound of mixed valence.

2.4.1   Crystal structure of Fe_3O_4 nanoparticle

The crystal structure of magnetite is cubic inverse spinel with a space group of Fd^{3m}, a unit cell consisting of 32 oxygen ions in a face-centered cubic structure, cell parameter of

0.839 nm and regular cubic close-packed along the [110] direction (Zia-ur-Rehman *et al.*, 2018). Generally, Fe_3O_4 crystals are distributed with octahedral and mixed octahedral/tetrahedral layers along the (111) direction (see Figure 2.2). At temperatures above 120 K, Fe^{2+} and half of the Fe^{3+} occupy octahedral sites and the other half of the Fe^{3+} occupies tetrahedral sites. Fe^{2+} occupies octahedral sites to acquire a higher crystal field stabilization energy (CFSE); simultaneously, the trivalent iron atoms remain with a CFSE = 0 in both octahedral and tetrahedral sites.
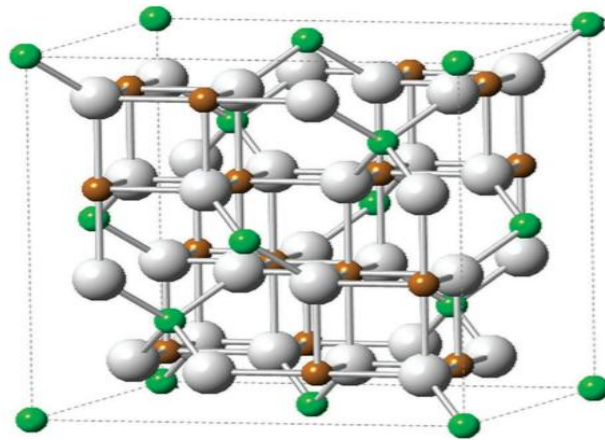
Figure 2.2: **Crystal Structure of Fe_3O_4, Green Atoms are Fe^{2+}, Brown Atoms are Fe^{3+}, Grey Atoms are Oxygen**

2.5   Silicon Oxides Nanoparticles (SiO$_2$)

Silicon oxide (SiO$_2$), also known as silica, is one of the most studied metal oxides second only to water. There are twelve different silica crystal modifications known, the most common being α-quartz (Eder *et al*., 2020). SiO$_2$ nanoparticles have gained growing interest owing to their characteristics such as low toxicity, high stability in aqueous electrolytes and organic solvents and not aggregate (Sabziparvar *et al*., 2018). Silica has been reported to have unique geometric properties that can form improved hybrid nanomaterials without altering or destroying their chemical properties (Gonzalez-Pech and Grassian, 2017). These properties have made silica nanoparticles a unique and interesting metal oxide used for the formation of nanocomposites.

2.5.1   Crystal structure of silicon nanoparticles

SiO$_2$ nanoparticles exist in both crystalline (quartz) and amorphous (fused silica) (see Figure 2.3). Cristobalite, tridymite, and quartz are three polymorphic forms of the crystalline SiO$_2$NPs known **(**Nabata *et al*., 2020**)**. Cristobalite has a cubic zinc-blend structure at high temperatures but can crystallize and persist metastable at lower temperatures, monoclinic tridymite is stable at intermediate temperatures, and quartz is hexagonal at low temperatures (Henderson, 2021). These crystal forms' structural transformations are gradual, and they may all exist at room temperature.
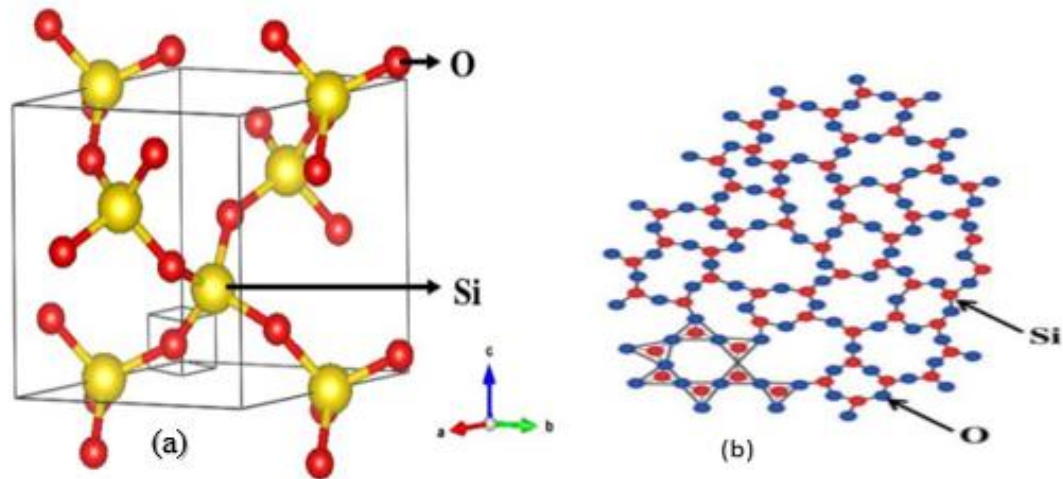
Figure 2.3: Crystal Structure of Crystalline (a) and Amorphous Silica (b)

2.6 Synthesis of Nanoparticles

There are several techniques used to synthesise ZnO nanoparticles, SiO_2 nanoparticles and Fe_3O_4 nanoparticles depending upon various factors which determine the shape, size, and stability (Shaba *et al*., 2021). Nevertheless, the techniques are generally classified into physical, chemical and biological.

2.6.1 Physical methods

The physical synthesis involved the use of a tube furnace at atmospheric pressure; it does not involve the use of any chemical during the synthesis. The physical method has some disadvantages such as the consumption of a high amount of energy, while raising the environmental temperature around the source material, requires a lot of time to achieve thermal stability and required a large space (Khan *et al*., 2019). Some of the important physical approaches are summarised in Table 2.1 with some of the advantages and disadvantages.

Table 2.1: Physical Methods with their Advantages and Disadvantages

Methods	Advantages	Disadvantages
Tube furnace	Occurs at atmospheric pressure (Singh *et al.*, 2017)	Requires large space and time for thermal stability, and heats the environment (Raj *et al.*, 2022)
Phase deposition	Synthesis of particles can be done in bulk quantities along with easy execution	Inability to maintain the size of the nanosize of particles throughout the experiment (Samrot *et al.*, 2020)
Ceramic heater	Use local heat source, prepared in high concentrations, can be used for calibration for nanoparticle measuring devices (Carvalho *et al.*, 2021)	Requires rapid cooling (Xiong *et al.* 2020)
Laser ablation	The absence of chemical reagents in solutions Gives pure and uncontaminated nanoparticles (Galatage *et al.*, 2021).	Can be affected by various factors such as wavelength, timing, and the influence of ablation for perfect nanoparticle structure (Lazar *et al.*, 2022).
Tube furnace	Occurs at atmospheric pressure (Varghese *et al.*, 2019)	Requires large space and time for thermal stability, and heats the environment
Laser ablation	The absence of chemical reagents in solutions gives pure and uncontaminated nanoparticles (Wang *et al.*, 2022).	Can be affected by various factors such as wavelength, timing, and the influence of ablation for perfect nanoparticle structure (Hong *et al.*, 2019).

2.6.2 Chemical/liquid phase techniques

Chemical or liquid phase techniques have been used for the preparation of ZnO, Fe_3O_4 and SiO_2 nanoparticles. Chemical methods include sol-gel, chemical precipitation/co precipitation sonochemical, pyrolysis, hydrothermal/solvothermal, electrochemical method s, and microemulsion techniques (Chen *et al*., 2019, Zaky *et al*., 2021). These methods have been widely used, due to their simplicity, which includes the use of low temperatures, low pressure, good control over size and morphology as well as size distribution and do not require inert gas condensation (Jameel *et al*., 2020).   Nevertheless, the purity of the nanoparticles synthesised by the chemical method remains a major issue (Zahoor *et al*., 2021). Hence, the nanoparticles produced from this method require further purification (Baig *et al*., 2021). Further washing with distilled water, ethanol, or other solvents is required to clean the impurities and to obtain high-purity nanoparticles (Shaba *et al*., 2022). The main advantage of this method is that it allows the synthesis of a large number of nanoparticles. Nevertheless, the control of particle size distribution is limited, because only kinetic factors are controlling the growth of the crystal. In general, important components are used in the chemical synthesis of nanoparticles in solution: (i) metal precursors, (ii) reducing agents, and (iii) stabilizing/capping agents (Javed *et al*., 2020). The advantages and disadvantages of chemical methods are summarized in Table 2.2.

Table 2.2: Chemical Methods with their Advantages and Disadvantages

Methods	Advantages	Remarks
Reduction	Used reducing agents are sodium citrate, Dimethylformamide (DMF), and Sodium borohydride ($NaBH_4$) poly block polymers (Quintero *et al*., 2019)	Requires stabilizing agents for long term stability (Javed *et al*., 2020)
Hydrothermal	Particle size and shapes are easily controllable homogeneities. highly homogeneous crystalline material. It favours a decrease in agglomeration between particles, narrow distributions of particle size, phase homogeneity, and regulated particle morphology (Suvaci and Özel, 2020). DO not involve the use of organic solvent nor required calcination after the synthesis which makes it a simple and environmentally friendly method (Parihar *et al*., 2018).	The reaction required both high temperature (100–400 °C) and pressure (Jang *et al*., 2020)
Solvothermal	High crystallization of the produced products at a low temperature (180 °C), the capacity to control crystal development, the convenience of the handle and its suitability for large-scale sample preparation.	Higher temperature is required and solvent (Marinescu *et al*., 2022)
Sonochemical	A more uniform size distribution, a larger surface area, a shorter reaction time, and better phase purity	mechanism not still understood

Sol-gel	simple synthesis, low cost and low processing temperature	Thermal treatment is required (Kamanina *et al.*, 2022).
Thermal Decomposition	particle size and shapes are controllable	time-consuming synthesis at high temperatures (Hamidreza, 2017)
Chemical Precipitation Method	Simple and effective	Not suitable for the preparation of high-purity accurate stoichiometric phase
Photoinduced reduction	Polymeric compounds as microreactors can convert nanoparticles into nanocrystals of 30- 120 nm in length	Requires stabilizing agents for long-term stability (polymeric compounds, citrate)
Electrochemical synthetic	Homogeneity and various sized nanoparticle can be formed	Polymeric compounds must require for stabilizing and it is difficult to reproduce (Ijaz *et al.*, 2020)
Laser irradiation	Perfect-sized and shaped nanoparticles formed Requires few chemical reagents	

2.6.3   Biological synthesis biological synthesis

The biological methods are similar to chemical methods but the only difference is that the biological products/extracts are used as the reducing agents and the capping agents.

These are primarily green synthesis of the nanoparticle. It has some advantages like less energy consumption and moderate technology without using toxic chemicals (Azmath *et al.*, 2016; Khan *et al.*, 2017). Although these are more environment friendly, the particles produced might be less stable, and non-uniform with less homogeneity and more agglomeration, because of the above-stated reasons. Apart from plants and bacteria, proteins such as ferritin from viruses have been shown to provide a platform for the synthesis of iron oxide nanoparticles (Samrot *et al.*, 2020).

2.7   Factors Influencing the Synthesis of Nanoparticles

The quality and quantity of synthesised nanoparticles, as well as their characterisation and applications, are greatly influenced by several factors such as the pH of the reaction mixture, temperature, calcination temperature, time, precursor concentration and different metal salts.

2.7.1   pH of the reaction mixture

The pH of the reaction mixture determines the types of nanoparticles formed (Aziz and Jassim, 2018). The crystallite size, morphology, phases, and surface areas of the nanoparticles depend largely on the amount of positively and negatively charged ions present in the medium during the preparation (Shaba *et al.*, 2021). This is because solution pH alters the electrical charge of molecules and such alteration will affect their reduction (Hasan *et al.,* 2018). During the synthesis of nanoparticles in an acidic medium (pH < 7), the amount of hydroxyl ions (OH^-) is usually low

in the solution which hinders hydrolysis and condensation processes, leading to the smaller aggregates at the end of the poly-condensation process (Tourné-Péteilh *et al.,* 2018). The decrease in the crystallite size of the nanoparticles in an acidic medium may be attributed to the preferential corrosion of the crystal structure. At the pH of 7 (neutral), the hydrogen ion (H^+) and the hydroxyl ion (OH^-) concentrations are equal, therefore, making the solution have little or no influence at the interfaces of zinc oxide crystals (Mohammadi and Ghasemi, 2018). When the pH of the reaction mixture is greater than 7, the number of OH^- ions is usually high causing a strong attraction between the positively charged Zn^+ and OH ion; subsequently, increasing the rate of crystal formation of the nanoparticles. Under high concentration of the hydroxyl ions in a solution, intermediate products such as zinc hydroxide ($Zn(OH)_2$) (see Eq. 2.1) and salt-containing tetrahydroxozincate ion ($[Zn(OH)_4]^{2-}$) (see Eq. 1.2) are formed. The drying in the oven and calcination of the products in the furnace as shown in Eqs. (2.1) and (2.2) usually lead to the formation of zinc oxide nanoparticles of large crystallite size (Buazar *et al.,* 2016). The reaction mechanism of growth of ZnO nanoparticles for variation of solution pH from acidic to the basic region is shown in Equations 2.1– 2.6

$$Zn^{2+} + 2OH^- \leftrightarrow Zn(OH)_2 \tag{2.1}$$

$$Zn(OH)_2 + 2OH^- \leftrightarrow [Zn(OH)_4]^{2-} \tag{2.2}$$

$$[Zn(OH)_4]^{2-} \leftrightarrow ZnO_2^{2-} + 2H_2O \tag{2.3}$$

$$ZnO_2^{2-} + 2H_2O \leftrightarrow ZnO + 2OH^- \tag{2.4}$$

$$ZnO + OH^- \leftrightarrow Zn\,OOH^- \tag{2.5}$$

$$ZnOH^- + Na^+ \leftrightarrow Zn\,OOH - Na \tag{2.6a}$$

$$ZnO(OH)_2 \rightarrow ZnO + H_2O \tag{2.6b}$$
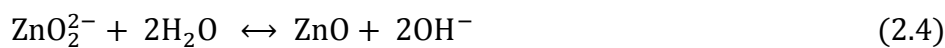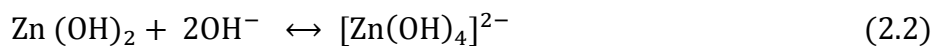
The $[Zn(OH)_4]^{2-}$ formed in Eq. (2.2) can also exist in the form of $Zn(OH)^+$, $Zn(OH)_2$, or $Zn(OH)^{3-}$, depending on the process parameters, such as the concentration of the zinc ion (Zn^{2+}) and hydroxyl ion (OH^-) ion during the chemical reaction (Purwaningsih *et al.,* 2016). When the concentration of Zn^{2+} and OH^- reaches the supersaturation degree, ZnO nuclei are formed based on the reaction (2.4) (Osman and Mustafa, 2015). The previous findings showed that the pH of the reaction mixture influenced the crystallite size and the morphology of zinc oxide nanoparticles. Researchers such as Ogbomida *et al.,* (2018) reported the synthesis of ZnO nanoparticles via sol-gel method using $Zn (CH_3COO)_2 \cdot 2H_2O$ and NaOH as starting materials. The mixture was stirred for 2 h and subsequently dried for 1h. ZnO nanoparticles produced were characterised using XRD, SEM, and UV−visible/diffuse reflectance spectroscopy and the calculated crystallite size of 49.98 nm, 48.31 nm, 38.32 nm, and 36.65 nm ZnO nanoparticles prepared at the solution pH of 8, 9, 10 and 11 were obtained, respectively. The authors found that the ZnO nanoparticles formed were mostly spherical with an optimum solution pH of 9. On the contrary, Purwaningsih *et al*. (2016) employed Zn $(CH_3COOH)_2 \cdot 0.2H_2O$ as a precursor, NH_4OH (precipitating agent) solutions to prepare ZnO nanoparticles via sol-gel method.

The mixture was stirred at 85 °C for 6 h and dried at 100 °C for 5 h after which the precipitates were washed and dried for 15 min at 80 °C and the size of the crystals formed was directly proportional to the solution pH. The crystallite size increases from 10.94, 17.44, and 38.27 to 74.04 nm as pH increases in the solution pH from 7, 8, 10, and 12, respectively. More so, the mineralogical phase of the prepared ZnO nanoparticles was examined using XRD and the authors observed that as the solution pH increases from 7, 8, 10, and 12, the purity of ZnO nanoparticles also increases and the percentage yield increased from 42.9%, 62.2%, 64.7%,

to 100%, respectively. The differences in the crystallite size were linked to the reaction conditions used during the synthesis of the ZnO nanoparticles. In addition, Goryacheva, (2016) demonstrated the green synthesis of ZnO nanoparticles using an aqueous extract of *Citrus aurantifolia* as a stabilizer and zinc nitrate as a zinc salt precursor. The synthesis was carried out at 90 °C at pH 5, 7, and 9, respectively. The precipitates formed were washed, dried and annealed in air at 300 °C yielding nanorods with a crystallite size of 100 nm. XRD and SEM analysis confirmed the formation of pure hexagonal wurtzite ZnO nanostructure of different shapes irrespective of solution pH. The authors reported the formation of ZnO of spherical shape at pH 5 and nanorods at pH of 7 and 9, respectively.

The increase in particle size and change in the morphology of the ZnO nanoparticles synthesised at the pH of 5, 7, and 9 further suggest that solution pH plays an important role in the crystallite size and morphology of ZnO. Similar research conducted by Andrade *et al*. (2020b) confirmed that Fe_3O_4 nanoparticles prepared within the pH values range 9.7 to 10.6 tend to have very pure magnetite with little or no other iron oxide. Other products, such as maghemite and goethite tend to appear when the synthesis was performed in pH values below 8.5. In another research conducted by Faiyas *et al*. (2020), they reported that maintaining a pH value of 6 and 9 in a solution containing iron salts (II) and (III) ions produce Fe_3O_3 nanoparticles. Whereas a pH value of 11 produces a magnetite (Fe_3O_4) phase. Similarly, the effect of solution pH on the synthesis of Fe_3O_4 nanoparticles synthesised via direct co-precipitation method at room temperature using a mixture of iron (II) chloride ($FeCl_2$).$4H_2O$ and 0.02 M iron (III) chloride $FeCl_3$.$6H_2O$ have been studied and the result shows that particle size increases from 10 nm to 13 nm as the solution pH increases from 8 to 12.5. This result indicated that pH has a greater effect on the particle size of the Fe_3O_4 nanoparticles (Qin *et*

al., 2022). Another researcher synthesised Fe_3O_4 nanoparticles at a solution pH of 11.33 to 12.15 via the co-precipitation method. The synthesised Fe_3O_4 nanoparticles were characterised using FESEM, FTIR and XRD. In their analysis, the smaller particle size of Fe_3O_4 nanoparticles was produced when the pH was increased from 11.33 to 12.15. However, a remarkably large size was formed at a pH greater than 12.15 suggesting that synthesis of Fe_3O_4 nanoparticles may depend on pH (Yusoff *et al*., 2020). The research by Malyutin *et al*. (2015) also confirmed that Fe_3O_4 nanoparticles at pH greater than 8, due to lower surface tension of the particles, and at a higher pH, ionic strength would result in smaller particle size and larger distribution size. The result of the analysis by Jamal *et al.,* (2019), who synthesised ZnO nanoparticles from zinc chloride via co-precipitation reported a decrease in the crystallite size from 100, 92.5, 61.8 to 41.9 nm as the pH increases from 10, 11, 12, to 13 respectively.

The decrease in crystallite size as the pH increases were attributed to the fact that at higher pH values, supersaturation during co-precipitation was higher, promoting nucleation overgrowth, thus giving smaller particle sizes. The authors also reported that ZnO nanoparticles had no definite shape for all the pH, except at pH of 13 which exhibited a needle-shaped particle. Additionally, the effect of solution pH on the synthesis of silicon oxides has also been reported by many researchers including (Badanayak and Vastrad, (2021). Who studied the effect of solution pH on synthesis of silicon oxides and reported that the crystallite size increases from 19 to 62 nm as the solution pH increases from 2 to 9. The authors attributed the trend to the fast reaction due to the availability of the hydroxide ion in the solution leading to the solubility of intermediate products formed during the process. Tijani *et al*. (2019) have also studied the synthesis of SiO_2 nanoparticles at different solution

pH (5, 8 and 10). The authors reported that there was no discernible pattern in the crystallite size. For example, the predicted crystallite size at pH 5 was 3.10 nm, which decreased to 2.39 nm at pH 8 and increased slightly to 4.25 nm at pH 10. However, Yee and Fatehah (2017) have also studied the effect of pH on the crystallite size of SiO_2. The authors observed that the particle size increased when the pH was reduced, with the largest particle size being around 5000 nm. Aggregation was proven to occur between pH 5.4 and pH 3.2. The particle size remains below 500 nm when the pH is increased from 5.4 to 11.

2.7.2 Reaction temperature

The physical methods mostly employed to synthesise nanoparticles require a higher temperature above 350°C, while the chemical route used for the synthesis of nanoparticles can be carried out at room temperature (Shaba *et al.,* 2021). The chemical method is the easiest way to synthesise ZnO, Fe_3O_4 and SiO_2 nanoparticles (Ul-Haq *et al.,* 2017). It has been reported that higher temperatures resulted in to increase in reaction rate causing rapid consumption of metal ions and hence the formation of nanoparticles of a smaller size (Saxena *et al.,* 2016). On the contrary, another researcher reported a smaller size of nanoparticles even at a lower temperature (Pelicano *et al.,* 2016). However, a study by Liu *et al.,* (2020) observed that reaction temperature played a critical role in the actual crystallite size of nanoparticles so also the concentration of metal salt precursors. The authors found that a low concentration of the precursors often leads to the formation of smaller crystalline sizes either at a lower or higher temperature, due to the competition between nucleation and growth processes. It has also been reported that the synthesis of nanoparticles carried out at lower temperatures can also lead to the formation of smaller crystallite sizes while at higher temperatures nucleation

was more favoured. Research by Khan *et al.,* (2017) revealed that employing zinc acetate dihydrate, NaOH and cetyltrimethylammonium bromide (CTAB) as precursors produced flowers shaped like ZnO nanoparticle at different reaction temperatures (25 °C, 35 °C, 55 °C, and 75 °C). The synthesised ZnO nanoparticles were examined using XRD, SEM, EDS, and UV–visible spectrophotometer. The authors revealed average crystallite sizes to be 23.7 nm, 82.5 nm, 69.6 nm, and 88.8 nm for ZnO nanoparticles prepared at 25 °C, 35 °C, 55 °C, and 75 °C, respectively. The increase in the crystallite size of the ZnO nanoparticle in a solution as the temperature increases was attributed to two phenomena, namely Oswald ripening and oriented attachment as shown in Figure 2.4.
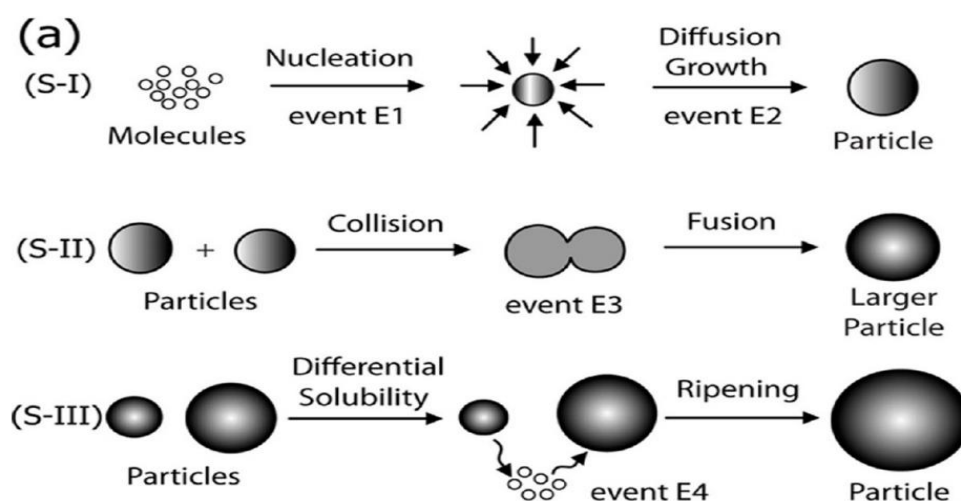
Figure 2.4: Schematic of the Stage Wise-growth of Nanocrystals in Solution Created Based on the Research by Shaba *et al.,* (2021)

The SEM results showed the existence of two types of flower petal morphologies (slender needle-like and wide-arrowlike). The slender needle-like petals were found in excess at lower temperatures compared to the large arrow-like petals in the different flower bunches of the ZnO colonies. These observations suggested that the temperature exerted a great influence

on the crystallite size and morphology of the ZnO nanoparticles. The differences as reported by the previous researchers (Pushpanathan *et al.,* 2021) may be due to the difference in synthesis methods and the nature of the capping agents used. However, Manzoor *et al.,* (2015) reported the synthesis of ZnO nanoparticles via co-precipitation method using zinc acetate with potassium hydroxide and ethanol as precursors. The mixture was stirred for 1.3 h at different synthesis temperatures from 65 °C, 70 °C to 75 °C. The final product was dried in the oven aqt 60 °C for 8 h and characterised using SEM, XRD, FTIR, and UV–visible spectrophotometer. The average crystallite sizes of the ZnO nanoparticle obtained at the three studied temperatures were 98 ± 43, 135 ± 77, and 458 ± 243 nm, respectively. The authors established a direct relationship between the reaction temperature and crystallite sizes.

Furthermore, Pelicano *et al.,* (2016) employed a precipitation method involving mixing zinc acetate dihydrate as the precursor, with ethanol and dimethyl sulfoxide; tetramethyl, ammonium hydroxide as a solvent and precipitating agent to produce ZnO nanoparticles. The prepared ZnO nanoparticles were investigated by TEM, UV–visible spectrophotometer and PL. The TEM result indicated an increase in crystallite size (4.72 nm, 5.24 nm, 6.70 and 7.61 nm) as the reaction temperature increases (26 °C, 40 °C, 60 °C and 80 °C).

Different researchers have also reported the synthesis of Fe_3O_4 nanoparticles at different temperatures including, Khalil (2019) who synthesised Fe_3O_4 nanoparticles with a particle size of nanocrystals 7.84 nm and nanorods with an average particle size of 6.3 nm at room temperature and 70 °C respectively. Another qresearcher synthesised Fe_3O_4 nanoparticles at 200 °C and 260 °C and reported 16 and 21 nm as the particle sizes using a hydrothermal process. Other researchers have also reported the synthesis of SiO_2 nanoparticles at different

synthesis times. For instance, Zainal *et al.* (2021) have reported that by increasing the synthesis temperature (30 °C to 70 °C), the size of silica nanoparticles has been reported to increase from 28.91 nm to 113.22 nm.

The authors attributed the increment in the crystallite size to the increase in the critical particle radius and coalescence of the smaller particles to complement the growth into larger ones based on Ostwald ripening (for more soluble materials) and oriented fixing (for less soluble crystals) as earlier shown in Figure 2.4. From Figure 2.4, the first stage in the synthesis of nanoparticles is the nucleation of a solid crystal (E1); this is made possible via rapid precipitation reaction of the salt by the precipitating agents such as sodium hydroxide, $(NH_4)_2CO_3$ and NH_4OH. The second stage involved the growth of the nucleus by diffusion of nanoparticles molecules from solution onto the surface of the nucleated particle (E2), followed by collision and fusion (E3) of two particles via the oriented attachment (OA) and E4 depicts the Ostwald ripening (OR) which involved inter-particle growth via exchange (dissolution and diffusion) of molecules between various particles. The report by Shaba *et al*., (2021) confirmed that the increase or decrease in the crystallite sizes of nanoparticles did not only depend on the reaction temperature but also the method of synthesis.

2.7.3 Calcination temperature

Calcination involves heat-treating a material at a controlled temperature and in a controlled environment (Hammood *et al*., 2019).

During the calcination process, the particles fuse and enlarge their primary crystallite size (Ruys 2019). This process is called particle coarsening, a phenomenon in solid (or liquid) solutions often used for the growth of larger crystals from those of smaller size and leads to

a reduction in the number of smaller particles while larger particles continue to grow (see Figure 2.5).
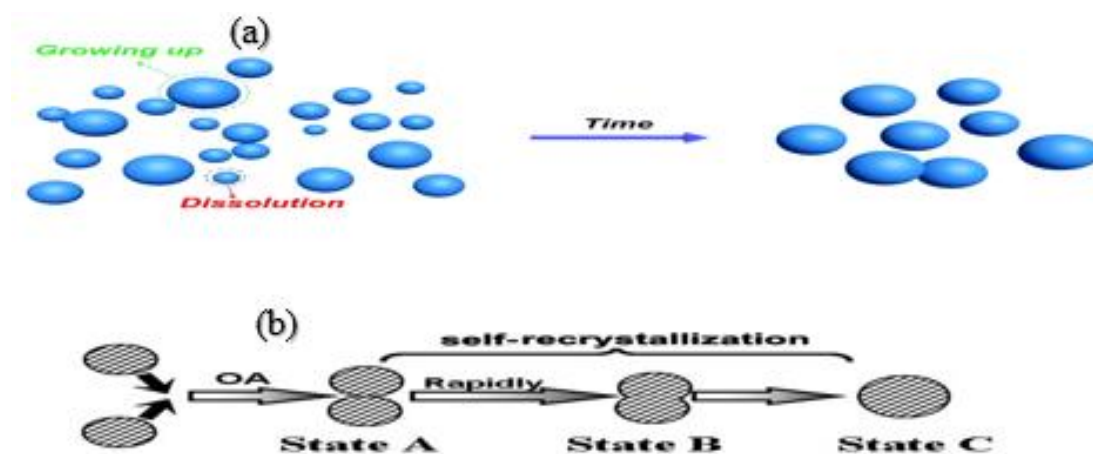
Figure 2.5: Scheme of Nanoparticle Growth Controlled by: (A) Ostwald Ripening Mechanism; (B) Oriented Attachment Mechanism

The particle coarsening phenomenon occurs due to the fact that the smaller nanoparticles are less energetic and unstable compared to the well-packed nanoparticle with a large crystallite size. This process can also take place at room temperature and however can be accelerated during the heating process. Different researchers have studied the effect of calcination temperature on the properties of ZnO nanoparticles and Fe_3O_4 nanoparticles these are reviewed as follows: Ashaf *et al.,* (2015) studied the effect of calcination temperature on the properties of ZnO nanoparticles prepared by sol-gel using zinc acetate as a precursor. The XRD results indicated the formation of pure phase hexagonal wurtzite ZnO; however, the crystallite size decreases from 24 to 17 nm as the calcination temperature increased to 300 °C. Further increase in calcination temperature to 500 °C resulted in to increase in the crystallite size to 19 nm. Moreover, a similar trend was reported by Mallika *et al.,* (2015) that

employed the sol-gel method to prepare zinc oxide nanoparticles using zinc nitric and polyvinyl alcohol (PVA) as a precursor and stabilizing agent respectively.

The authors varied the calcination temperature from 400 °C, 500 °C, and 600 °C to 700 °C at a holding time of 1 h. The synthesised ZnO nanoparticles were characterised using XRD, SEM, EDS, FTIR, and UV−visible Spectrophotometer and the average crystallite sizes were 7, 23, 35, and 35 nm. The authors found that as annealing temperatures increase, grain growth also increases in size. A similar trend was observed when citric acid (CA) was used as a reducing agent under the same calcination temperatures and holding time. They reported an increase in the crystallite size from 13, 23, 30, and 40 nm. ZnO nanoparticles have been synthesised by a sol-gel technique using zinc acetate dihydrate and diethanolamine as the precursor materials. The effects of calcination temperatures 300 °C, 500 °C, 650 °C, 700 °C, and 750 °C were studied. The properties of the ZnO nanoparticles were examined by SEM, XRD, FTIR, and UV−visible Spectrophotometer.

The XRD result according to the Scherer equation indicated that the crystallite size increased with increasing calcination temperature (Kayani *et al.,* 2015). Similarly, Worawong *et al*. (2016) investigated the effect of calcination temperature on Fe_3O_4 nanoparticles at 400°C, 450°C and 500°C. The XRD result shows the formation of nanoparticles at a calcination temperature of 400°C. Pure Fe_3O_4 nanoparticles without any impurity. While as the calcination temperature increases to 450°C, the result indicates the presence of another phase of iron namely γ-Fe_2O_3 while at 500°C Fe_2O_3, γ-Fe_2O_3, Fe_3O_4 nanoparticles.

The average particle size of the Fe_3O_4 nanoparticles synthesised was reported to be 13 nm, 24 nm and 45 nm for Fe_3O_4 nanoparticles calcined at 400°C, 450°C and 500°C, respectively.

Another researcher studied theq effect of temperature on the synthesis of SiO$_2$ nanoparticles and reported that the SiO$_2$ synthesised at calcination temperatures of 600 and 1000°C shows more quartz silica peaks and that calcination increases the crystallinity of the SiO$_2$ produced (Norhasyimi *et al*., 2016). Synthesis of SiO$_2$ nanoparticles has also been reported from natural clay at different temperatures (room temperature and 900°C. The authors reported the synthesised nanoparticles to be amorphous with a crystallite size of 72.85 nm at room temperature. It was reported that the phase shift from amorphous to polycrystalline occurred at 900 °C calcination temperature for 10 hours, with cristobalite tridymite, quartz, and crystal structure dominating. The authors concluded that the temperature treatment had a significant impact on the transition from amorphous to crystallized SiO$_2$ nanoparticles, resulting in larger particle grain sizes and the disappearance of the particle grain boundary (Munasir *et al*., 2018). Generally, from the review above it can be concluded that as the calcination temperature increases, the crystallite sizes of the nanoparticles increase which can also affect their purity and morphology. Furthermore, the growth of nanoparticles usually occurs via two mechanisms, namely oriented attachment (OA) and Ostwald repining (OR). Oriented attachment is a physical process that is important during the crystallization process and involved direct self-organization of the primary nanoparticles and subsequent conversion by interface fusion to single crystals through sharing a common crystallographic, as illustrated in Figure 2.5.

Ostwald ripening (Figure 2.5a) involved the diffusive transfer of the dispersed phase from the smaller to the larger droplets. The Ostwald Ripening occurs because larger particles are thermodynamically stronger than smaller particles. High temperature influences Ostwald ripening due to its effect on interfacial energy, coefficients of growth rate, and solubility (Westen and Groot, 2018). Oriented attachment happens (Figure 1.5b) because the

aggregation decreases the system's interphase boundary and total surface energy (Dalod *et al.,* 2017).

2.7.4   Effect of different salts precursor

The synthesis of ZnO nanoparticles using different zinc salts precursors such as zinc acetate (Zn $(CH_3COO)_2$, zinc nitrate (Zn $(NO_3)_2$, zinc sulfate ($ZnSO_4$) and zinc chloride ($ZnCl_2$) has been widely investigated (Manisalidis *et al.,* 2020). Magnetite nanoparticles are usually synthesised from different salts of different iron salt combinations such as $FeCl_2$, $FeCl_3$, $FeSO_4$ and $Fe(NO_3)_3$ (Rashid *et al*., 2019 and Kobylinska *et al.* 2021). Additionally, SiO_2 is synthesised from metal alkoxides, such as Tetraethyl orthosilicate (TEOS), or inorganic salts like sodium silicate (Ismail *et al*., 2021). The use of different zinc salt precursors also influenced the morphological, textural and optical properties of ZnO nanoparticles (Mayekar *et al.,* 2015). For instance, Yu and Dong (2016) used different zinc salts (Zinc nitrate hexahydrate, zinc acetate dihydrate and zinc sulfate heptahydrate) as precursors to synthesise ZnO nanoparticles. The mixture of zinc salts and potassium hydroxide was autoclaved at 120 °C for 3 h and later the precipitate was washed severally and dried at 70 °C for a few h. The synthesised nanoparticles were characterised using XRD, SEM, TEM, PL. It was noticed that the average crystallite size of ZnO nanorods obtained were 100, 200 nm, 50 nm and 200 nm using zinc nitrate hexahydrate, zinc acetate dihydrate, and zinc sulfate heptahydrate respectively. The SEM result shows the formation of nanoflowers, nanoflakes, nanoprisms for zinc nitrate hexahydrate, zinc acetate dihydrate and zinc sulfate heptahydrate precursors respectively. Also, Gopal and Kamila (2017) utilised zinc nitrate hexahydrate, zinc nitrate hexahydrate, zinc sulfate heptahydrate and sodium hydroxide to prepare ZnO nanoparticles

via the precipitation method. The mixture was maintained at 70 °C for 1 h, and the precipitate was later dried at 65 °C for several h. The properties of ZnO nanoparticles were identified using XRD, SEM and UV-visible spectrophotometer, and it was found that the crystallite size was 23.04 nm, 19 nm and 37 nm for zinc nitrate hexahydrate, zinc nitrate hexahydrate and zinc sulfate heptahydrate respectively.

ZnO nanoparticles synthesised from sulfate precursors were distinct with organized rods and flowers-like morphology before calcination but the morphology changed after calcination at 400°C to only flakes type. However, the morphology did not change even after calcination for the nanoparticles synthesised from other two precursors such as zinc ac etate and zinc nitrate. Moreover, Perillo *et al.,* (2018) employed a precipitation method to s ynthesise ZnO nanoparticles using zinc acetate dihydrate, zinc chloride, zinc nitrate hexahy drate hexamethylenetetramine sodium hydroxide as precipitating agent. The reaction was stirred at 87 °C for 6 h, and later oven-dried at 80 °C for 7 h. The ZnO nanoparticles produced were characterised by XRD, SEM, EDX and BET. All ZnO samples showed a rod-like shape network with different sizes. When zinc acetate dihydrate was used as a precursor short rods were formed and longer nanorods were obtained using zinc chloride. The results showed the successful synthesis of ZnO nanorods with crystallite sizes of 46 nm, 41.3nm and 40.6 nm for zinc acetate dihydrate, zinc chloride and zinc nitrate hexahydrate respectively. This further confirmed that the source of precursor (Zn) from different zinc salts did not have any significant effect on the crystallite size of the ZnO nanoparticles produced.

In another research, Suppiah and Johan, (2018) synthesised Fe_3O_4 nanoparticles at pH 10 using different iron salts such as iron chloride ($FeCl_2$) and sulfate ($FeSO_4$). The result

revealed that the use of Cl⁻ anion, (the slower hydrolysis process-induced) requires more hydroxyl ions to reach pH equilibrium leading to larger maghemite nanoparticles (50–60 nm) and the iron sulfate ($FeSO_4$) shows a smaller average crystalline size (35–45 nm). The synthesised Fe_3O_4 nanoparticles were characterised using FTIR, XRD and BET. Their analysis shows that the use of different iron salt affects particle size. Zinc acetate and zinc nitrate hexahydrate has been used to synthesised ZnO nanoparticles via the green method and the result shows spherical and flower shape of ZnO nanoparticles with an average crystallite size of 21.49 nm and 25.26 nm were produced using Zinc acetate and Zinc nitrate precursors respectively. Different Zinc precursors exerted a slight effect on the crystallite size of the ZnO nanoparticles but do not guarantee the purity of the nanoparticle produced. Vanichvattanadecha *et al*. (2020), have reported the synthesis of silicon oxide from different sources such as tetraethyl orthosilicate (TEOS) and rice husk (RH). The authors found that the highly organized mesoporous structures, narrow pore size distributions, and large surface areas were synthesized from tetraethyl orthosilicate. The disordered properties were observed in the SiO_2 nanoparticles synthesized from rice husk that had been pre-treated with enzyme solutions for 7 days (7D-RH).

2.7.5   Concentration of precursors, precipitating and capping agents

The morphology and crystallite size of nanoparticles often depends on the concentration of metal salt precursors precipitating and capping agents used (Phan & Nguyen, 2020). Thus, these factors play an important role in the synthesis of nanoparticles and other nanostructured materials and are thus very frequently used to avoid the overgrowth of nanomaterial. The capping agent is responsible for the control of growth rate, particle size, and prevention of particle aggregation (Bakshi, 2015). Moreover, it has been reported by Kyomuhimbo and

Brink, (2023) that the nanoparticles can be stabilized by immobilization on a support such as an organic ligand shell, polymers, dendrimers, cyclodextrins, and polysaccharides (See Figure 2.6).
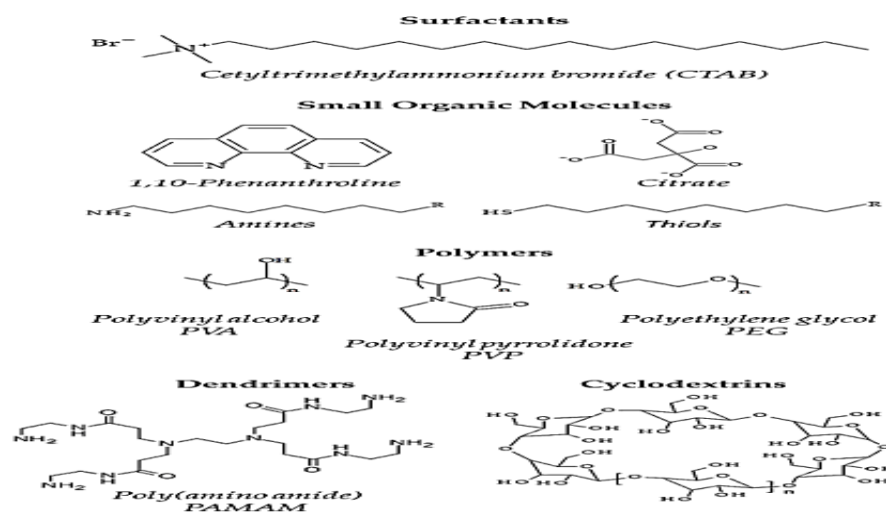
Figure 2.6: Selected Capping Agents Used in Synthesis of NPs, Possible Mechanism of Formation of ZnO Nanoparticles Using Plant Extract

The capping agents must be stable enough and withstand enough heat to prevent aggregation of the nanoparticles at temperatures suitable for synthesis. Many researchers including Alami *et al.,* (2015) have reported the synthesis of ZnO nanoparticles using different concentrations of Zn $(NO_3)_2$, $6H_2O$ (0.08, 0.1, and 0.08 M). The reaction was carried out at solution spray rates of 2 ml/min onto a preheated glass substrate at 500°C for 10 min. The crystallite sizes obtained were 9.95, 27.40, and 32.35 nm for 0.08, 0.1, and 0.08 M concentrations of the Zn salt which confirms the earlier analysis that the concentration of zinc salt greatly affects the crystallite size of the ZnO nanoparticles. The effect of the concentration of potassium hydroxides (0.5 M, 1 M, 1.5 M, and 5 M) on the synthesis of magnetite has been reported. the result indicates there was a shape transformation from cube to octahedron as the

concentration of potassium hydroxides increased from 0.5 M to 5 M (Fatima *et al*., 2018). Synthesis of polyvinyl pyrrolidone (PVP)-coated Fe_3O_4 nanoparticles by chemical co-precipitation method has been reported by Pandey *et al*. (2018) and the result shows that the crystallite size decreases from 35, 32 to 30 nm as the amount of PVP increases from 1 g, 2 g and 3 g respectively. This indicates that the higher the concentration of the PVP, the smaller the particles size. Additionally, the Ex-Situ Synthesis of Polyvinyl alcohol (PVA)-coated Fe_3O_4 Nanoparticles by Coprecipitation-Ultrasonication Method has been reported by Riva'i *et al*. (2018). The result indicates that the longer ultrasonication time results in smaller crystallite size and larger lattice parameters. The formation of mesoporous SiO_2 materials using different concentration of NaOH have been reported by Gosiamemang and Heng, (2023). The authors reported that if anions and cations are carefully balanced, the formation of SiO_2 is determined by the number of ions in the solution.

2.7.6 Reaction time

Reaction time is the time required for the completion of all steps during the synthesis of nanoparticles including the reduction and formation of nanoparticles (Shaba *et al*., 2021) Reports have shown that the formation of nanoparticles starts within minutes after the addition of the metal salt precursors and increases as the reaction time increases (Manzoor *et al.,* 2015). For instance, Manzoor *et al.,* (2015) prepared ZnO nanoparticles via the green route using zinc acetate with *Pichia kudriavze* Yeast Strain as precursors. The final product was dried in the oven at 60ºC for 8 h and characterised using XRD, TEM, PL, FTIR and UV-Visible spectrophotometer. They found the crystallite size of the ZnO nanoparticles to be

11.25 nm, 38.48 nm and 54.27 nm for nucleation times of 12, 24 and 36 h. The authors found the ZnO nanoparticles have a nearly spherical shape.

The effect of reaction time on the synthesis of Fe_3O_4 nanoparticles has also been reported by various researchers, for example, Karade *et al*. (2018) studied the effect of reaction time via the modified green synthesis method. The authors reported an increase in the crystallite size from 7.5, 9.8, 9.9 11.1 to 12 nm as the reaction time increases from 2, 4, 6, 8, and 10 min respectively. Attentionally, Kao *et al*. (2019) have reported the effect of reaction time on the structural properties of the SiO_2 via the sol-gel method. The authors reported that as the reaction time increases from 30 min to 6h the crystallite particle increases from 58 and 684 nm. Additionally, the Synthesis of SiO_2 has been reported at different synthesis times. The authors reported that as the time increases from 80 s, 300 s, to 360 s, the average crystallite sizes increase from 3 nm, 25 nm to 65 nm. The authors also discovered that as the reaction time increased, so did the size and degree of aggregation of the obtained silica nanoparticles (Nikolic *et al*., 2015).

In another research by Engku *et al*. (2017) synthesised SiO_2 nanoparticles and confirms the amorphous form of SiO_2 nanoparticles, with an average particle size of less than 100 nm irrespective of the time (30 to 180 min). The sample with a reaction time of 90 min was reported to have the highest specific surface area and average pore volume, indicating fine porous characteristics. This result may be attributed to the availability of pores as the synthesis time increases. From the result above, it can be deduced that the reaction time is proportional to the crystallite size of nanoparticles. The step-by-step involved in the variation of reaction time during the synthesis of nanoparticles is shown in Figure 2.7.
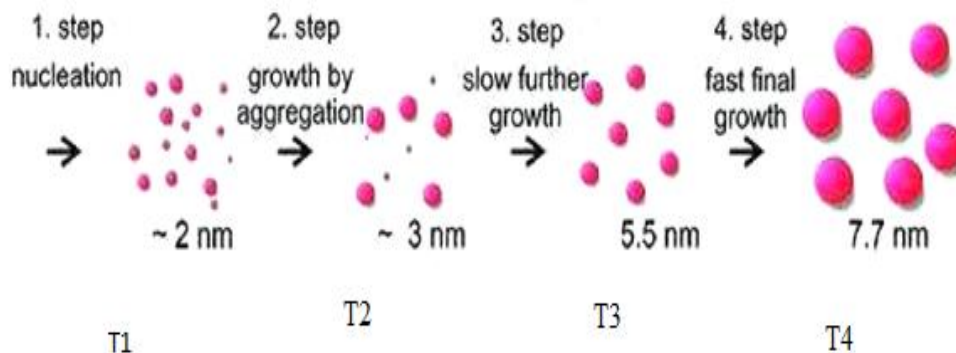
Figure 2.7: Schematic Illustration for Effect of Reaction Time on The Synthesis of Nanoparticles

The first step 1(T_1) in Figure 2.7 depicts the nucleation process (the process whereby nuclei (seeds) act as templates for crystal growth) which is the first step in the formation of metal oxide nanoparticles. This process takes place within a few seconds of the reaction. Step 2 involves the growth of the nanoparticles up to an average crystallite size of 5.2 nm as the time increases from T_1 to T_3. However, it has been reported by Smolkova *et al.,* (2017) that the diffusion mechanism controlled the growth of nanoparticles during the synthesis which only occurs over a few seconds. The fourth stage is a rapid consumption of the metal salt left in the solution where the particle size increases rapidly from 5.2 to 7.7 nm.

2.7.7   Synthesis of SiO$_2$ nanoparticles from natural sources

It has been observed that SiO$_2$ nanoparticles made from chemical sources have fewer properties than those made from natural sources, such as sugarcane bagasse, corn cob, wheat husk, rice husk, and kaolin (Meena *et al.* 2020; Mahajan *et al.* 2021). Among these sources, kaolin calcined at a higher temperature (metakaolin) has been recognized as a very good source of silicon for the synthesis of SiO$_2$ nanoparticles (Tchanang *et al.*, 2021).

In recent years scientists have focused on the synthesis of SiO_2 nanoparticles from natural sources which include the synthesis of SiO_2 nanoparticles from Kankara kaolin by Salahudeen, (2018). Velmurugan *et al*. (2015) have reported the synthesis of nanosilica from corn cob ash via alkaline extraction and acid precipitation method. The synthesised SiO_2 nanoparticles were characterised using XRF, XRD, FTIR and SEM. In another research by Ajayi and Owoeye (2015), the authors obtained a soluble sodium silicate solution from corn cob and used it as a source of silicon for the synthesis of nanosilica. The authors reported sheet-like morphology having irregular structural shapes. Zulfiqar *et al*., (2016) synthesise silicon oxide nanoparticles from bentonite clay at different concentrations (5 M, 10 M and 15 M) of nitric acid in the presence of ethanol as solvent. The result shows that the particle size decreases (95 nm, 86 nm 69 nm) as the concentration of the acid increases. The SEM result indicates the formation of a spherical shape. Nandiyanto *et al*., 2016 reported synthesised silica from rice straw waste and found crystallite size to be 200 nm. Another analysis by Fidai *et al*. (2021) and Athinarayanan *et al*. (2017), both studied the influence of calcination temperature and alkali concentration on the structure of silica. Silica nano-fillers from kaolinite were successfully synthesised by sonochemical and modified sol-gel methods by Goad and Hamad (2017). The crystallite size was confirmed to be 50 nm by XRD results. The authors also found that the optimum conditions for the synthesis of silica from bentonite via a sol-gel method be calcination at 30°C and a stirring time of 2.5 h.

Cassava Periderm calcined at 700°C has been used as a source of silicon for the synthesis of silicon oxide nanoparticles based on the modified sol-gel method. The produced silica nanoparticles were characterised using FT-IR, TEM, Raman, SEM, XRD, EDX, and PSA and the result indicates that the crystallite size ranges from 3.12 to 50.75 nm (Adebisi, *et al*.,

2018). Additionally, Flower-like α-quartz microstructures from kaolin have been reported using the hydrothermal method. The produced quartz was characterised using SEM, XRD and FTIR. In another research by Tijani *et al*. (2019), the authors synthesised SiO_2 at different synthesis conditions such as solution pH (5, 8 and 10) and concentration of NaOH (0.5 M, 1 M and 2 M), calcination temperatures (600ºC, 700ºC and 800ºC) respectively. The prepared SiO_2 nanoparticles were characterised by XRD, HRSEM, and EDS respectively. Akhayere *et al*., (2019) synthesised nanosilica nanoparticles from barley grass waste at 400, 500, 600, and 700ºC. The produced nano-silica was investigated using SEM, TEM, BET and FTIR. The average crystallite size of around 150 nm and the surface area of 323 m^2/g were reported for the synthesised nanosilica. Ruey *et al*., (2020) reported that the silica nanoparticles can be prepared from natural sources. From the review above it can be concluded that the silicon oxides nanoparticles can be synthesised from locally available materials instead of using available chemical compounds for the synthesis of silicon oxides.

2.8   Synthesis of Nanocomposites

Nanostructured materials and hybrid nanocomposites have recently attracted significant attention owing to their exceptional properties and multiple functionalities, which cannot be achieved by single-component materials or just oxide materials. This has encouraged various researchers to prepare different nanocomposites such as SiO_2/Fe_3O_4. Various polymer/Zinc oxide composites have been studied by various researchers; polystyrene/Zinc oxide nanocomposites (Alam *et al.*, 2021). Polyvinyl alcohol (PVA) doped with different concentrations (0, 0.15, 0.5, 1, 2, 2.5, and 3 wt %) of Zinc oxide nanoparticles using the solution casting method had also been reported (Mansour *et al.*, 2015). Similarly, composite compresses of silver (Ag) and Zinc oxide have been reported; Ag-Zinc oxide with a spherical

shape was prepared and their morphological sizes and shapes were characterised by SEM (Ghosh *et al.*, 2015). Ag/Zinc oxide nanocomposite synthesised at 400°C has been reported by Hosseini *et al.* (2015). Zinc oxide nanoparticles with different amounts of silver ions have been used to prepare Zinc oxide/Ag nanocomposite calcinated at 600°C for 8 h (Mosquera *et al.*, 2015). Zelepukin *et al*. (2017) reported the synthesis of Fe_3O_4/SiO_2 nanocomposites with an average crystallite size of 25 nm via the sol-gel method. Zinc oxide/Ag nanowires composite was prepared by electrochemical deposition. The nanocomposite of Zinc oxide/starch with particle size ranging from 40–60 nm as shown by the XRD and confirmed by SEM and TEM results (Ma *et al.*, 2016). Nanocomposites of Zinc oxide and some selected polymers such as polyethylene glycol, polyvinylpyrrolidone, and polyacrylonitrile, were synthesised by a chemical method (Quadri *et al.*, 2017).

Zinc oxide nanoparticle/N-doped reduced graphene oxide nanocomposite with surface areas of 200.55 m^2/g have been prepared by Yang, *et al.* (2017). Restrepo *et al.* (2018), prepare polyvinyl alcohol-stabilized polylactic acid/Zinc oxide nanocomposites via melt processing in a Brabender mixer at 60 rpm for 8 min at 190°C. Iron Oxide/Silica by gel method (Tavassoli *et al.*, 2017), Zinc oxide/Polystyrene (Al-Karam, 2017). Zinc oxide/SiO_2 nanocomposite with particle sizes ranging from 8 ±5 nm to 40 ±5 nm has been reported (Bharati and Suresh, 2017). Similar findings from Indramahalakshmi, (2017) revealed that *Opuntia ficus indica* fruit can be used to synthesis Zinc oxide with an average particle size of 21.75. Pachl *et al.* (2018) prepared Ag: Fe_3O_4 (1:100) with average particle size ranging between 16–17 and 20 nm as revealed by XRD and SEM results respectively. Another analysis by Arévalo-Cid *et al*., (2018) confirmed the synthesis of amino-functionalized Fe_3O_4/SiO_2 and $CoFe_2O_4/SiO_2$ nanocomposites with a core-shell structure has been prepared

by co-precipitation and hydrothermal synthesis for removal of Cu^{2+} cations removal in aqueous media. Fe_3O_4/SiO_2 (10.1 nm, 13.7, and 14.2 nm) nanocomposites have been synthesised by Nikmah *et al*. (2019) and the authors found reported that the higher the composition of the silicon the larger the particle size of the composites. In another research Du *et al*. *(*2019*)*. Synthesised Fe_3O_4/SiO_2 nanofluids. The average crystallite size of Fe_3O_4/SiO_2 nanocomposites ranging from 20-23 nm has been reported by Nadi *et al*. (2019). Additionally, Nikmah *et al*. (2019) reported the synthesis of Fe_3O_4/SiO_2 nanocomposites at different dosages of Fe_3O_4 and SiO_2. They found average crystallite size to increase as the amount of the SiO_2 increases (10.1 nm, 13.7, and 14.2 nm). Synthesis of magnetite/silica nanocomposites from natural sand has been reported and the authors found that the particle size increases from 8.2 to 13.2 nm with increasing silica content (Taufiq *et al*., 2020).

2.9   Characterisation Techniques

Understanding the properties and applications of nanoparticles and nanocomposites generally requires their characterisation. Different characterisation tools such as X-ray diffraction (XRD), high-resolution scanning electron microscopy (HRSEM), Energy Dispersive X-ray analysis (EDS), Brunauer-Emmett-Teller (BET), X-ray photoelectron spectroscopy (XPS), and Fourier transform infrared spectroscopy (FTIR) have been used for characterisation of nanoparticles and their composites.

2.9.1   X-ray diffraction (XRD)

XRD is the most popular and efficient method for determining whether a material is amorphous or crystalline, as well as the average crystallite size of any material (Bunaciu *et al*., 2015; Rajeswari *et al*., 2020). The interplanar distance 'd' values obtained from XRD

data are usually compared with the fundamental data in Joint Committee on Powder Diffraction Standards (JCPBS). The constructive interference of monochromatic X-rays from a crystalline sample is the basis for X-ray diffraction. The X-rays from a cathode ray tube are filtered to create monochromatic radiation, which is collimated and aimed at the sample. X-rays mainly interact with electrons in atoms, colliding and deflecting several photons from the incident beam away from their original location (Civan, 2016). The X-rays collide in a diffraction pattern on the detector, which is both constructive and destructive. If the reflections from the different planes interact constructively, the incident X-ray radiation creates a Bragg peak (see Figure 2.8). When the phase shift is a multiple of 2 λ, the interference is constructive; this condition is expressed by Bragg's law (see equation 2.7)

$$2\ d\sin\theta = n\lambda \qquad\qquad (2.7)$$

Where:

d = inter-plane distance of (ions, atoms, molecules)

$\theta =$ is the angle between the incident ray and the scattering planes

n = integer representing the order of the diffraction peak

$\lambda =$ wavelength of the x-ray.

The nanoparticle crystallite sizes are calculated using Scherrer's equation (See equation 2.8) can be used to estimate the average crystallite size

$$D = \frac{k\lambda}{\beta \cos\theta} \qquad\qquad (2.8)$$

where D is the crystallite size

k = 0.9,

a correction factor to account for particle shape

β = is the full width at half maximum (FWHM) of the most intense diffraction plane

= is the wavelength of Cu target = 1.54 Å

θ = is the Bragg angle.
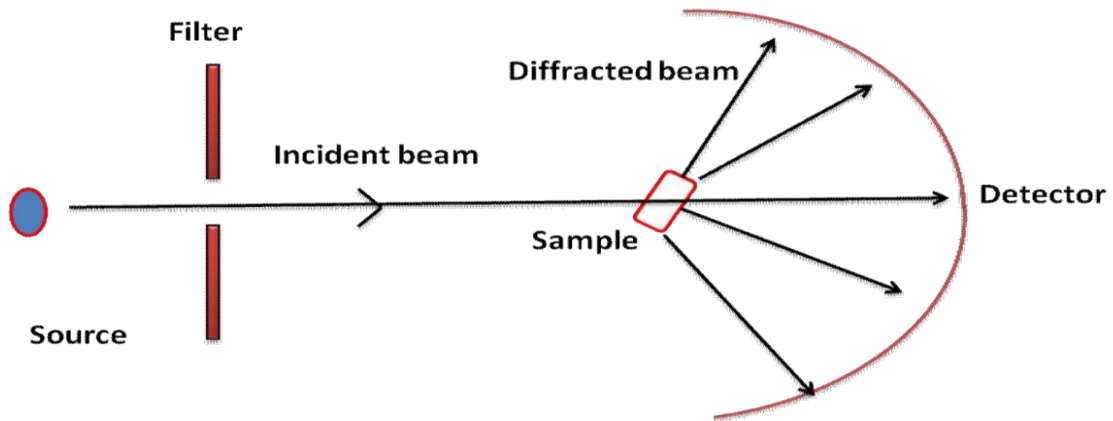
Figure 2.8: Schematic Diagram of X-ray Diffraction

2.9.2 High-resolution scanning electron microscopy (HRSEM)

The High-resolution scanning electron microscope (HRSEM) is an imaging technique that uses an electron beam to obtain high-magnification images of specimens. The signals produced by electron sample interactions reveal information about the sample, such as its surface morphology or texture. Figure 2.9 shows the image of HRSEM.
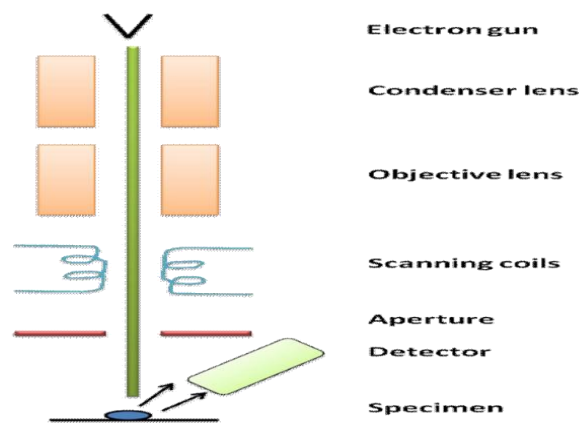
Figure 2.9: Schematic Diagram of a High-resolution Scanning Electron Microscopy

2.9.3   Fourier transform infrared spectroscopy (FTIR)

FTIR is a characterisation technique for identifying compounds by comparing the spectrum of an unknown compound to a reference spectrum, as well as for identifying functional groups in the sample. The FTIR Spectrum, also known as the sample's fingerprint, is a characteristic of each specimen. The IR area of the electromagnetic spectrum is thought to cover a range of approximately 50 to 12,500 cm^{-1} (Whatley *et al*., 2023).   Figure 2.10: Schematic Representation of FTIR spectrometer.
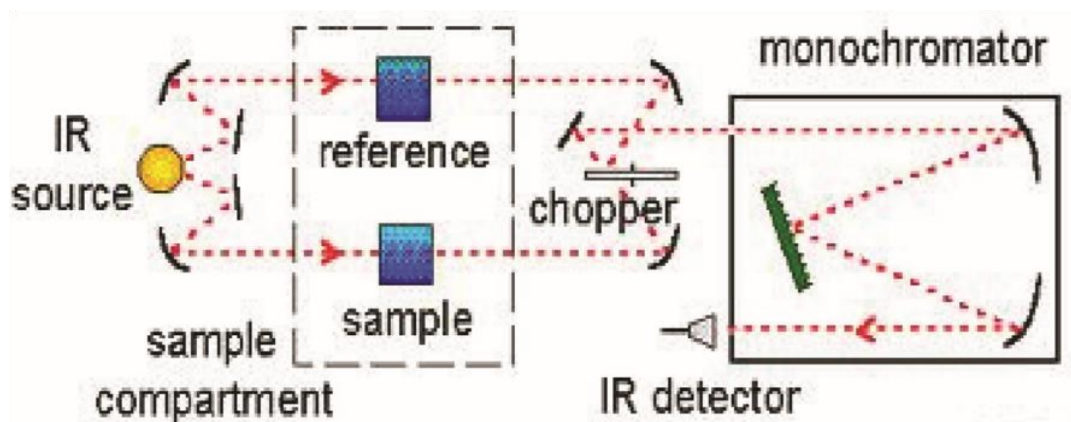
Figure 2.10: Schematic Representation of FTIR Spectrometer

2.9.4   Energy-dispersive X-ray spectroscopy (EDX, EDS, or XEDS)

Energy-dispersive X-ray spectroscopy (EDS) is a surface analytical technique that uses an electron beam to excite an electron in an inner shell, allowing it to eject and form an electron hole in the element's electronic structure (Mallakpour and Azimi, 2020). Its characterisation abilities are primarily due to the basic concept that each element has a unique atomic structure, resulting in a unique collection of peaks on the X-ray spectrum. A high-energy

beam of charged particles such as electrons or protons, or a beam of X-rays, is directed into the sample being examined to induce the emission of characteristic X-rays from it. At rest, an atom in the sample contains ground state (or unexcited) electrons bound to the nucleus in distinct energy levels or electron shells. The incident beam can excite an electron in an inner shell, causing it to be ejected from the shell and leaving an electron hole in its place (Hodoroaba, 2020). The hole is then filled with an electron from an outer, higher-energy shell, and the energy difference between the higher-energy shell and the lower-energy shell may be emitted as an X-ray. An energy-dispersive spectrometer can determine the amount and energy of X-rays emitted by a specimen. Since the energy of the X-rays is related to the difference in energy between the two shells as well as the atomic structure of the material from which they were released, the elemental composition of the specimen can be determined (Shirley and Jarochowska, 2022). The following are some of the drawbacks of the EDS. The sample must be solid and must fit into the microscope chamber. The maximum size in horizontal dimensions is normally about 10 cm, vertical dimensions are much smaller, seldom exceeding 40 mm. Most techniques involve samples being stable in a vacuum at 10-5 to 10-6 torr. The representation of EDX is shown in Figure 2.11
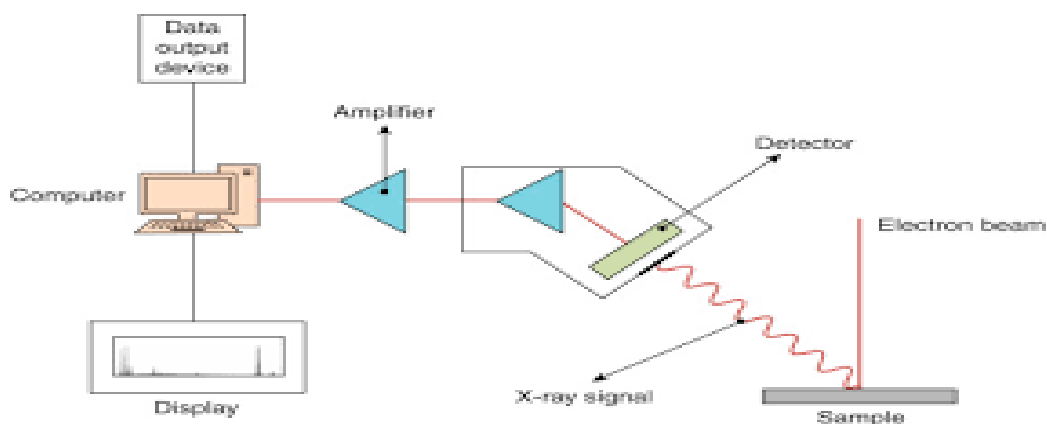
Figure 2.11: Schematic Representation EDX Equipment

2.9.5 Brunauer–emmett–teller (BET)

The surface of a nanomaterial contains a considerable proportion of atoms, and it is these atoms that often determine the particle's qualities (Wu *et al*., 2020). As a result, understanding the behaviour of a nanomaterial generally requires a measurement of the specific surface area (SSA) or the total surface area per unit of mass. A surface area measurement is usually taken of the accessible surface and calculated using gas adsorption techniques (Skripkina *et al*., 2020). The Brunauer-Emmett-Teller (BET) method is usually used to determine the specific surface area of nanoparticles and the composites. The Brunauer, Emmett, and Teller (BET) method are based on the principle of physical adsorption of a gas on a solid surface, and it was named after the researchers' surnames, Brunauer, Emmett, and Teller (Sinha *et al*., 2019). It is extensively used to determine the surface area of nanostructures since it is a generally accurate, quick, and simple method. Figure 2.12 shows a simple BET method.
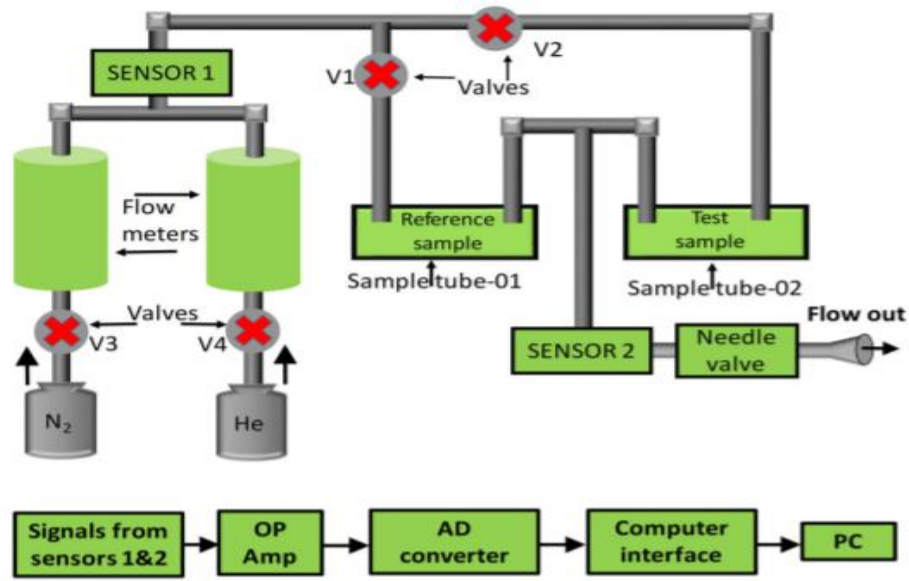
Figure 2.12: Schematic Representation BET Equipment

The following are some characteristics of BET isotherms according to the IUPAC (Ambroz *et al*., 2018):

i.   Type I Isotherm

There are two patterns in the reversible type I isotherm, which is common in microporous materials. Type I(a) refers to materials with micropore widths of less than 1 nm, whereas type I(b) refers to solids with both broader micropores and narrow mesopores.

ii.   Type II Isotherm

Nonporous or macroporous materials correspond to the reversible type II isotherm. The monolayer coverage is connected to point B on the isotherm. The curvature change is sharp if the monolayer coverage is finished, as opposed to a more gradual curvature that marks the start of multilayer adsorption (monolayer coverage overlaps).

49

iii.   Type III Isotherm

When the interactions between the adsorbent and the adsorbate are weak, the Type III isotherm is formed. As a result, information on monolayer coverage and formation is unavailable.

iv.   Type IV Isotherm

Type IV isotherm has two patterns, both of which are connected to pore width. A Type IV(a) is obtained when the width is greater than the critical width, which is determined by the material's adsorption properties and temperature. A type IV (b) isotherm, on the other hand, is observed in materials with smaller mesopore widths and is frequent in mesoporous materials.

v.   Type V Isotherm

 A type V isotherm has a form that is comparable to that of a type III isotherm over low P/P0 ranges. The poor adsorbent–adsorbate interactions are responsible for these phenomena. Hysteresis, as in the case of type IV(a), can be seen at higher relative pressures. The filling of holes occurs after molecular clustering.

vi.   Type VI Isotherm

The Type VI isotherm is indicative of multilayer adsorption on nonporous surfaces with a high degree of uniformity. The isotherm has the form of a stepwise curve that is affected by the material, gas, and temperature.

A linear BET range on the plot with a high regression coefficient must be used to determine the BET specific surface area from a BET plot ((P P/ / 0 0) n P 1 / P as a function of P/P0). Typically, a pressure range of 0.08–0.30 is used. Different types of Isotherms is presented in Figure 2.13
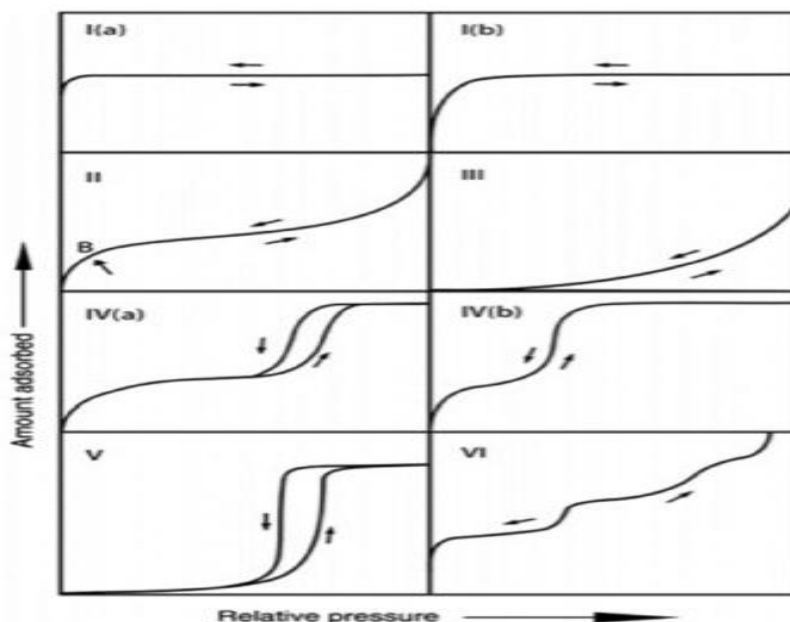
Figure 2.13: IUPAC Classification of BET Isotherms

2.9.6   X-Ray photoelectron spectroscopy (XPS)

XPS is a surface chemical analysis technique that can be used to investigate the surface chemistry of a substance. It is used to estimate the elemental composition or empirical formula, electronic state, and chemical state of the elements on the surface up to 10 nm of a nanomaterial (Yahia and Mireles, 2017). It also detects pollution in the surface of the sample, if any occurs. XPS is also known as electron spectroscopy of chemical analysis (ESCA). When a sample is irradiated with X-rays in an ultra-high vacuum (UHV), electrons are released from the core orbitals of the top 10 nm of the surface elements of the material being

studied. The XPS spectra are generated by measuring the kinetic energy (KE) and the number of electrons escaping from the material's surface.

The oxidation state of the particular surface elements is expressed in the electron binding energy. The proportion of unique elements on the surface is reflected in the number of electrons. The electron binding energy (BE) of each of the released electrons can be estimated using equation 2.3. The XPS equipment is represented in Figure 2.14

$$E_{binding} = E_{photon} - E_{kinetic} - \Phi \qquad\qquad (2.9)$$

Where:

$E_{binding}$ is the energy of the electron emitted from one electron configuration within the atom.

E_{photon} = the energy of the X-ray photons being used.

$E_{kinetic}$ = the kinetic energy of the emitted electron as measured by the instrument

Φ = the work function of the spectrometer (not the material).
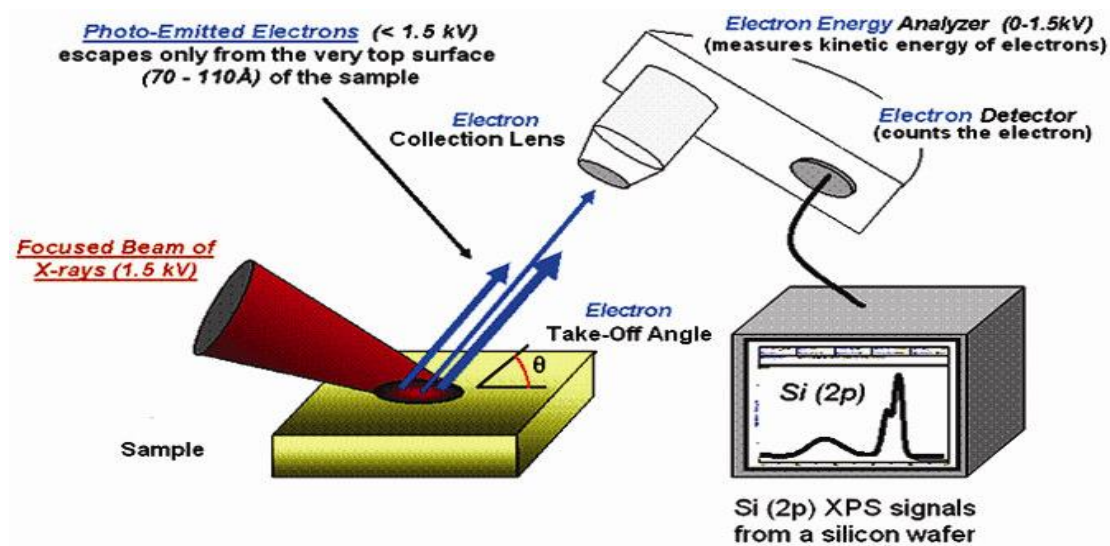
Figure 2.14: **Schematic Representation of XPS**

2.10 Water Pollution

Water pollution occurs when unwanted materials enter into water bodies, change their quality, and later become harmful to the environment and human health (Shaba *et al.,* 2022). Water is an important natural resource that needs to be protected against foreign toxic materials (Subramanian, 2018). Water pollution is the leading worldwide cause of death and diseases (Ladu *et al.,* 2018). The discharge of untreated wastewater into the water bodies has been attributed to the growing number of several diseases such as cholera and typhoid fever among others (Singh *et al.,* 2018). It has been estimated that the world generates more than 5–10 billion tons of industrial waste, much of which is pumped untreated into rivers, oceans, and other waterways.

2.10.1 Petroleum refinery and associated pollutants in the environment

Petroleum products are used widely in a range of industrial applications. The largest quantities find use as fuels for a range of purposes, including gasoline, diesel oil, and aviation fuel and heating oil. There has been an increase in the demand for these products over the years due to a high increase in population growth, which has led to an increase in the discharge of wastewater from petroleum refineries. This wastewater contains hazardous pollutants of hydrocarbons and other organic compounds that pose serious risks to humans, animals and the environment (Honda and Suzuki, 2023).

2.10.2 Organic pollutants

Water pollution due to the presence of active organic pollutants has been reported to be one of the most serious types of environmental pollution attracting increasing attention and leading research studies in recent years, due to their impacts on aquatic organisms (Patel *et al*., 2019). A lot of active organic compounds such as phenols, toluene, benzene, ethylbenzene and xylene have been reported in many water bodies worldwide by various researchers (Bashir *et al*., 2020). This has made surface and groundwater resources more polluted with petroleum refinery products and consequently poses a significant risk to human health as well as animal well-being. Benzene, Toluene, Ethylbenzene, and Xylenes (BTEX) are important industrial waste pollutants and are classified as hazardous substances contaminating groundwater resources (Wongbunmak *et al*., 2020). A considerable amount of these pollutants enter the environment through leakage from underground storage tanks, accidental spills, and improper wastewater disposal (Bashir *et al*., 2020). The BTEX compounds, though present in low percentages in petroleum refinery wastewater is of high

interest as they have been classified as priority pollutants regulated by the Environmental Protection Agency (Ivan *et al*., 2021).

When organic pollutants like phenols and BTEX are released into the environment, the function and structure of the microbial communities are generally affected. The International Agency for Research on Cancer classified benzene as carcinogenic to humans (Muda *et al*., 2023). It has been reported that chronic exposure to benzene can reduce the production of both red and white blood cells from bone marrow in humans, resulting in aplastic anemia (He *et al*., 2020). In a similar view, Justyna and Eugenia, (2018) have also reported that xylene can metabolise in the liver via oxidation of methyl groups, which high concentration can lead to liver damage. The potential hazard of toluene in both humans and animals for short-term and long-term exposure often resulted in the distortion of the central nervous system, causes irritation of the upper respiratory tract and eyes, sore throat, dizziness, headache and sometimes it can affect the kidneys and liver (Davidson *et al*. 2021). Phenol and phenolic compounds are also commonly occurring pollutants in petroleum refinery industries. Phenol is toxic to human beings and the environment; meanwhile, it is difficult to remove from wastewater due to its non-biodegradable nature (Panigrahy *et al*., 2022). Phenol is reported to be highly irritating to the skin, eyes and mucous membranes in humans after acute (short-term) inhalation or dermal exposures as shown (Villegas *et al*., 2016). Exposure to a low or high concentration of phenols can lead to anorexia, progressive weight loss, diarrhea, vertigo, salivation and dark colouration of the urine (Satish *et al*., 2018).

2.10.3 Pollution by heavy metals

Petroleum refinery wastewater is associated with several pollutants such as heavy metals which include lead (Pb), zinc (Zn), nickel (Ni), arsenic (As), copper (Cu), chromium (Cr), iron (Fe), selenium (Se), vanadium (V), cobalt (Co), cadmium (Cd), and mercury (Hg) (Alalwan *et al.,* 2020). These heavy metals are recognised as a major toxic hazardous material to humans and the aquatic system (Honda and Suzuki, 2023). Globally, heavy metals pollution in water has caused serious health effects on humans and the ecosystem since they are non-biodegradable and highly toxic (Ogbomida *et al.,* 2018). These heavy metals are distributed in the environment through natural and anthropogenic activities (Liu *et al.,* 2022). Exposure to metals such Pb, Zn, Ni, As, Cu, Cr, Fe, Se, V, Co, Cd, and Hg can affect growth and development causing mental disorders, cancer, damage to the liver, kidneys, lungs, and in extreme cases, death depending on the exposure dose and time (Balali-Mood *et al.,* 2021). The specific effects of some of the heavy metals have been summarized (see Table 2.3). The possible removal of these pollutants from the wastewater before the discharge to the environment has recently become the focus of many researchers owing to its negative effect on the environment.

Table 2.3: The MCL standards for the most hazardous heavy metals

Heavy metal	Toxicities	MCL (mg/L)
Arsenic	Skin manifestations, visceral cancers, vascular disease	0.08
Cadmium	Kidney damage, renal disorder, human carcinogen	0.01
Chromium	Headache, diarrhea, nausea, vomiting, carcinogenic	0.08
Copper	Liver damage, Wilson disease, insomnia	0.15
Nickel	Dermatitis, nausea, chronic asthma, coughing, human carcinogen	0.2
Lead	Damage the fetal brain, diseases of the kidneys, circulatory system, and nervous system	0.006

2.11 Toxicity of heavy metals

2.11.1 Lead (Pb)

Lead (Pb) is a heavy metal with an atomic number 82 and a silvery bluish look that fades to a dull gray colour when exposed to air (Balali-Mood *et al*., 2021). Lead pollution comes from a variety of sources, including fertilizers, battery waste, vehicle pigment, pesticides, finishing processes, metal plating, ore smelting, exhaust, fuel additives and petroleum wastewater. Because of its extensive use, this heavy poisonous metal is becoming a global environmental and health problem. The Environmental Protection Agency has declared lead (Pb) to be a carcinogenic element (EPA). The word "lead poisoning" refers to the toxicity of lead, which can be chronic or acute. Various health problems such as kidney damage, brain damage, mortality, mental retardation, dyslexia, and birth defects are some of the problems associated with lead poisoning (Obasi and Akudinobi, 2020).

2.11.2 Cadmium (Cd)

Cadmium is a bluish-white soft metal with an atomic number of 48 and chemical properties similar to group 12. The toxicity of Cd has been reported in electroplating, pigments, the nuclear industry, alloys, batteries, cigarettes and plasticizers (Genchi *et al*., 2020). Cadmium is prevalent in the environment at low levels in most cases; nevertheless, industrial wastes have considerably raised those amounts. Cadmium poisoning can harm the kidneys, respiratory systems, and bones, as well as be carcinogenic to humans (Sharma and Bhattacharya, 2020). The Agency for Dangerous Substances and Disease Registry ranks cadmium as the eighth-most toxic element (Rahi *et al*., 2022). Divalent, tetravalent, pentavalent, and hexavalent states of chromium exist; however, trivalent and hexavalent

states are the most stable (Chen *et al*., 2021). Humans and animals both require chromium (III) as a dietary supplement and the chromium (VI) form, on the other hand, is extremely hazardous and carcinogenic (Sharma *et al*., 2022). Chromium is discharged into the environment matrix (air, water, and soil) via a variety of sources, including wastewater and air mostly from metallurgical and chemical industries. Hexavalent chromium Cr (VI) is an industrial contaminant that has been proven to cause cancer in humans (Wise *et al*., 2022).

2.11.3 Copper (Cu)

Copper is a very common metal that occurs naturally in the environment and spreads across it due to natural processes. Cu(I) and Cu (II) are the two kinds of copper that are available (An *et al*., 2022). Copper has become one of the most extensively utilized metals as technology has progressed (Tavares-Dias, 2021). Metal finishing industries, circuit boards, chemical production industries, and mining drainage are the principal sources of copper waste discharged from industries (Malhotra *et al*., 2020). Excess amounts of copper in the body can inhibit the enzyme dihydrophil hydratase, an enzyme involved in hemopoiesis. Wilson's illness is an inherited ailment in which the body retains copper because it is not eliminated by the liver into the bile. If this disease is not addressed, it might cause brain and liver damage. Copper in excess in the water has also been reported to harm marine life (Yap and Al-Mutairi, 2022). Copper poisoning has been documented in fish and other animals, causing damage to the gills, liver, kidneys, and central nervous system (Borobia *et al*., 2022).

2.11.4 Nickel (Ni)

Nickel is widely distributed in the environment and is the twenty-fourth most abundant element in the earth's crust. Nickel usually has two valence electrons, but oxidation states of

+1, +3, or +4 may also exist. Leaching from metals in contact with drinking water, such as pipes and fittings, is the principal source of nickel in drinking water. Nickel, on the other hand, may be present in some groundwaters due to dissolution from nickel ore-bearing rocks (Ullah *et al*., 2022). The various effect such as nausea, vomiting, stomach discomfort, and diarrhea, headache, giddiness, coughing, and shortness of breath, are all common signs of acute nickel toxicity. Nickel salts affect humans' lungs and digestive tracts. If the dose of soluble nickel compounds is too high, it can cause respiratory tract cancer (Rahi *et al*., 2022).

2.11.5 Chromium (Cr)

Chromium is found in petroleum and coal, as well as chromium steel, pigment oxidants, fertilizers, catalyst, oil well drilling, and tanneries for metal plating. Chromium is widely utilized in a variety of industries, including wood preservation, electroplating, metallurgy, paint and pigment manufacturing, chemical manufacturing, tanning, and pulp and paper manufacturing. These businesses contribute significantly to chromium pollution, which harms biological and ecological species (Prasad *et al*., 2021). Industrial and agricultural practices contribute to chromium pollution in the environment. In recent years, chromium pollution has primarily been caused by hexavalent chromium (Georgaki *et al*., 2023).

2.12 Pollution Indicators

Analytical tools used to determine the pollution degree of wastewater are lab-based tools that measure the oxygen demand required to oxidize contaminants (Aniyikaiye *et al*., 2019). Biological Oxygen Demand (BOD), Chemical Oxygen Demand (COD) and Total organic carbons (TOC) are the analytical parameters often utilized to determine the pollution of wastewater. BOD and COD measure the oxygen-depleting effects of waste contaminants.

The exception to this standard is the measurement of Total Organic Carbon (TOC), which directly measures inorganic and organic carbon. Below is a summary of each parameter, what they measure, and general strengths and weaknesses.

2.12.1 Biological oxygen demand (BOD)

BOD is an indicator of the fraction of organic matter that can be degraded by microorganisms, typically expressed as the amount (mg/L) of oxygen consumed over five days at 20°C (Hughes *et al*., 2020). BOD includes readily biodegradable organic carbon (carbonaceous or cBOD) and occasionally ammonia (nitrogenous or nBOD). BOD is the primary driver of BOD and includes soluble, particulate, and colloidal organic carbon compounds (Choi, *et al*., 2017).

2.12.2 Chemical oxygen demand (COD)

COD is the amount of oxygen required for the chemical oxidation of compounds in water. This demand is determined using a strong oxidant, with most standard methods using dichromate and to a lesser extent permanganate (Han *et al*., 2022). Because the chemical can always oxidize more oxygen equivalents than microorganisms, the COD test typically returns greater oxygen-equivalent results than the usual BOD5 test (Syukor *et al*., 2021).

2.12.3 Total organic carbon (TOC)

Organic Carbon in Total (TOC) The TOC test is another indicator parameter for determining the amount of organic matter in water, and it is particularly useful for evaluating low levels of organic matter (Lee *et al*., 2020). The TOC is the amount of carbon bonded in organic molecules in wastewater (total organic carbon). Except for a few carbon species that are

considered inorganic, nearly all carbon compounds are classified as organic (carbon dioxide, hydrogen carbonate, carbonate, cyanide and some further examples which are not commonly found in wastewaters). To detect organic carbon in aqueous samples, the entire sample is oxidized at 900°C with CO_2-free air in the presence of a catalyst.

2.13 Adsorption Technology

Adsorption is a mass transfer process that involves the accumulation of substances at the interface of two phases, such as liquid-solid, liquid-liquid, liquid-gas and solid-gas interface and becomes bound by physical or chemical interaction (Jiang *et al*., 2022). Adsorption is an effective and inexpensive process used for the treatment of wastewater (Lata *et al*., 2019). These processes remove pollutants when an adsorbate in a solution comes into contact with the adsorbent, it concentrates or accumulates on another surface as shown in VIII Adsorption process is often reversible, since the adsorbents can be regenerated by the desorption process (Cai *et al*., 2019). Adsorption can be classified into physical adsorption (physisorption) and chemical adsorption. Adsorption depends on the properties of both the adsorbate and the adsorbent (Ziółkowska *et al*, 2017). An adsorbent material must have certain important properties, such as high surface area, the distribution of pores and the existence of the pores that have a significant influence on the form of the adsorption process, high internal volume accessible to the various target components (Wang *et al*., 2023). If the forces of attraction that exist between adsorbate and adsorbent have a physical nature, the process is called physisorption. This process is characterised by the formation of weak intermolecular forces such as van der Waals forces, reversible process, and formation of multilayer of adsorbate on the adsorbent, decreases with an increase in temperature and has a low enthalpy of adsorption while if the interaction between the adsorbent and adsorbate has a chemical nature, the

process is known as chemisorption. This results in the formation of a strong chemical bond (Moussa *et al*., 2023), chemisorption process is characterised by the formation of a monolayer of adsorbate on the adsorbent, has a high enthalpy of adsorption can take place at all temperatures and in most cases not reversible (see Figure 2.15).
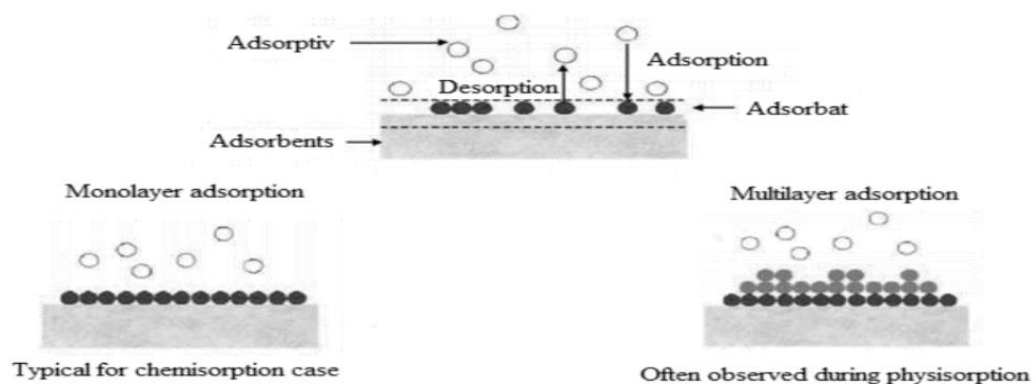
Figure 2.15: Adsorption Process and Adsorption Types

2.14 Mechanisms of Adsorption Techniques

The mechanism of adsorption involves the sorption of adsorbate molecules on the surface of the sorbents through molecular interactions, and the diffusion of adsorbate molecules from the surface into the interior of the sorbent materials, either by monolayer or multilayer (Zhao *et al*., 2022). The adsorption process involves the binding of metal ions by physical (van der Waals forces) or chemical (ion exchange, chelation, precipitation, binding, complexation, and reduction). Various factors such as the nature of adsorbent, temperature, dosage, adsorption time, and reaction temperature and the surface area played an important role in the removal of heavy metals by ZnO nanoparticles (Iftekhar *et al*., 2018). The adsorption of heavy metals from wastewater using ZnO nanoparticle could be complex depending on the nature of capping agents used during the synthesis of ZnO nanoparticles, because the capping

agent may contain different functional groups that may greatly influence the removal of the heavy metals through metal ion exchange, chelation, precipitation, binding, complexation, and reduction (see Figure 2.15).

2.14.1 Physical adsorption

Physical adsorption (physisorption) is the simplest immobilization method, it occurs when the attractive forces present between adsorbate and adsorbent are weak such as van der Waals forces, hydrophobic interactions and hydrogen bonding (Shaba *et al*., 2022). This process occurs readily at low temperatures and decreases with increasing temperatures. Physical adsorption has been reported to have a low enthalpy of adsorption with a multilayer adsorbate on adsorbent (Mathew *et al*., 2016).

2.14.2 Chemical adsorption

Chemical Adsorption is the type of adsorption which involves a chemical reaction between the adsorbent and adsorbate. This process occurs only if there is a chemical bond formation between the adsorbent and adsorbate and have a higher enthalpy of adsorption of about 80 - 240 KJ/mol.
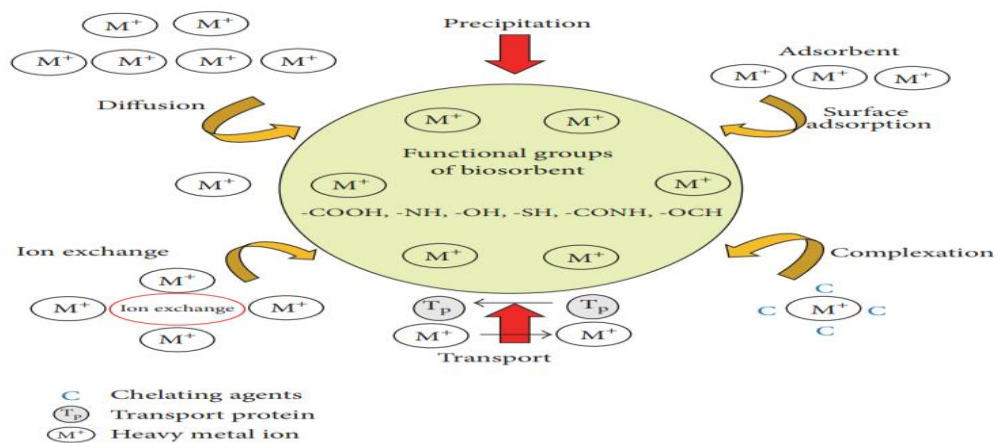
Figure 2.16: Adsorption Mechanisms

63

2.15 Nanoadsorbent

A variety of nanoadsorbents have been developed, modified, and used for the treatment of wastewater. Large surface area, active sites, and reusability of the nanoadsorbents are the most significant properties of an effective adsorbent (Ramos-Guivar *et al*., 2021). ZnO, SiO$_2$ and Fe$_3$O$_4$ nanoparticles and their composite, which are nanoadsorbents made up of two or more types of nanoparticles, such as ZnO, SiO$_2$ and Fe$_3$O$_4$ nanoparticles that have been combined to optimize their morphological properties, specific surface area, and adsorption capacity. Different nanoadsorbent has been studied for the removal of different pollutants in wastewaters as discussed below.

2.15.1 Zinc oxide nanoparticles as nanoadsorbent

Mahdavi *et al*. (2012) investigate the removal of Cd (II), Cu (II), Ni (II), and Pb (II) from aqueous solutions using ZnO nanoparticles as an adsorbent. The XRD result the ZnO nanoparticles revealed a crystallite size of 16.70 nm while SEM analysis confirmed the formation of rod-like shape with a crystallite size of 25 nm. The BET analysis of the ZnO nanoparticles revealed specific surface area, total pore volume and pore size of 31.20 m^2/g, 12.09 and 15.81 nm respectively. The authors found that the adsorption of the metal ions increases as the pH of the solution increases from acidic to alkaline. It was noticed that the pH of the solution played an important role in the adsorption of heavy metals by nanoadsorbent. This is expected, because at lower pH (acidity conditions), the hydrogen ions could strongly compete with heavy metal ions in the solution (Ouyang *et al*., 2019).

In addition, Salmani, *et al*. (2023) reported a removal efficiency of 89.6% for Cd (II)ion using ZnO nanoparticles. The authors reported that the Cd^{2+}ion removal followed pseudo-

second order and Langmuir isotherms model and the efficiency was highly sensitive to the change in pH and ionic strength. They also confirmed that removal efficiency increases as the pH of the solution become higher from 4 to 7, their result showed that the removal of Cd (II) ion low contact times was high and decreases with further increase in the contact time. This shows that the solution pH, contact time, concentration of metal and temperature affect the removal of metal ions using ZnO nanoparticles as an adsorbent. Moreover, the authors also observed that an increase in the absorbent dose (0.5 to 5 g L^{-1}) increased the removal efficiency of Cd (II), Cu (II), Ni (II) and Pb (II) with Pb (II), having the highest percentage removal of 81.5 % at a dosage of 5mg/g and were attributed to the increase in the number of binding sites as the nanoabsorbent increases (Xie *et al*., 2018). The maximum removal efficiency was achieved for all four ions after 180 min and there was no significant increase in the removal efficiency of the metal ions after 180 min to 24 h. The maximum uptake of the metal ions was reported to be 114.5 mgg^{-1}.

Moreover, Angelin *et al*., (2015) have also reported the use of spherical ZnO nanoparticles (8 nm) synthesised via the sol-gel method as an adsorbent for possible removal of Pb^{2+}, Hg^{2+}, Cd^{2+} Bi^{3+} under the reaction condition of time (60 min), dosage (0.250 g), temperature (30°C), and metal ions concentration of 0.01M. Authors reported the percentage removal of 97.1, 86.8, 80.9, 61.2 for Pb (II), Hg (ii), Cd (II), Bi (III) respectively. It was also noted by the authors that the removal of Pb^{2+} ions shows a maximum adsorption capacity of 8.768 mg/g with the highest removal of 97.1%. Ma *et al*. (2016) in another research synthesized Pinecone-like ZnO nanoparticles by thermal method and reported an average crystallite size of 30 nm. The ZnO nanoparticles were used as an adsorbent for the removal of Cr (VI)under the condition of solution pH (5.6) and temperature of 298 K, their result shows the maximum

adsorbed amounts of Cr (VI) adsorbed at 298 K with a high maximum adsorbed amounts of Cr (VI), being 14 256 mg g^{-1}.

The removal of As (III) has been reported using ZnO nanoparticles nanocubes synthesized by the Green route under reaction conditions of 2 g adsorbent dosage a pH (6) contact time (60 min) and an agitation speed of 300 rpm. The authors reported that the percentage removal of As (III) was very significant at 0.03 ppm with a removal efficiency of 79.47 to 96.19% (Yuvaraja *et al*. (2019). Table 2.4 shows the summary of ZnO nanoparticles and the percentage removal of some selected heavy metals.

Table 2.4: Summary of ZnO Nanoparticles as an adsorbent for removal of heavy metals

Method	Characterisation Techniques	Shape	Crystal lite size(nm)	Pollutant	Removal (%)	Other adsorption Conditions	Research Findings	References
Precipitation	FTIR, SEM, FTIR and TGA	Spherical	73	Cu (II), Pb (II), Cd (II)	100, 77.47, 97.85	Stirred at 120 rpm at 30°C for 150 min, adsorbent dosage (0.1 g)	Optimal conditions were observed at solution pH 8. The reaction fit to Pseudo-second order kinetic	Anusa *et al*. (2017)
Green	XRD TEM, and UV–vis	Regular hexagonal surface shape	10.01 2.6	Pb (II)	93.00	pH of 5, temperature of 70°C.	The maximum removal efficiencies were 93% at pH 5. The good efficiency of the as-synthesized ZnO nanoparticles makes it suitable for the removal of heavy metals from aqueous system	Azizi *et al*. (2017)
Precipitation	XRD, TEM and DLS	Spherical	11	Cd(II)	98.71	Dosage (120 mg), volume of aqueous solution (10 ml), pH (5), Contact time (20 min) and initial heavy metal ion concentration (300 mg/l)	The maximum removal was achieved at solutions pH of 5 and an initial heavy metal ion concentration of 300 mg/l. Adsorption isotherm studies indicated that the data fitted well to the Freundlich isotherm model.	Nalwa *et al*., (2017)
Precipitation.	XRD, FT-IR spectroscopy, SEM, and TGA	Nanorods	_____	As(III)	96	pH (7), dosage (0.4 cont act time (105 min), temperature (323 K).	The results revealed that the pseudo-second-order kinetic model provided the best described data. The maximum As(III) sorption capacity of ZnO nanorods was found to be 52.63 mg/g at pH 7, adsorbent dose 0.4 g, contact time 105 min, and temperature 323 K.	Yuvaraja *et al*., (2019)
Precipitation	XRD, SEM and EDX	Nanorods arranged like flower		Cr(VI)	98	40 min with optimum value of pH 3	The amount of chomium adsorption increases with an increase in adsorbent dosage, whereas the adsorption was maximum in the first 40 min with optimum pH of 3. The morphology of ZnO nano rods changes into nano sheets after the adsorption process.	Kamath *et al*. (2019)

2.15.2 Magnetite (Fe_3O_4) nanoadsorbent

Owing to their low cost, ease of use, easy availability, and environmental friendliness, Fe_3O_4 nanoparticles are another type of commonly utilized nanoadsorbent (You *et al*., 2021).

Fe_3O_4 nanoadsorbents are proving to be highly effective functional materials with excellent absorption efficiency (Abdel-Maksoud *et al*. 2020). Fe_3O_4 nanoadsorbents are associated with a high specific surface area, large pore volumes, and intensively interconnected porous networks (Masunga *et al*., 2019 and Pan *et a.l*, 2021).

Various researchers have reported the use of Fe_3O_4 nanoparticles for the treatment of wastewater (Sun *et al*., 2021). For instance, Shirsath and Shirivastava (2019), have synthesised Fe_3O_4 nanoparticles via co-precipitation with an average crystallite size of 13 nm as revealed by the XRD. The authors studied the adsorptive capacity of Fe_3O_4 nanoparticles at pH (5.5), temperature (25ºC), adsorbent dosage (2 g) and contact time (1.5 h), concentration (10 m/L) respectively. They found that Fe_3O_4 nanoadsorbents have the potential of removing 95% of Zn (II) ions from wastewater. Another researcher has reported the use of Fe_3O_4 nanoparticles for the removal of Pb (II), Cd (II) and Cr(III) ions from wastewater and reported the percentage adsorption removal to be 98.8, 89.4, 99.9% for Pb(II), Cd(II) and Cr(III) at pH (7), temperature (55ºC), adsorbent dosage (5 g) and contact time (20 min), concentration (10 mg/L) respectively. The authors found that for the three metal ions studied, the adsorption efficiency increases with temperature (Ali *et al*., 2018).

Other studies on the use of Fe_3O_4 nanoparticles for the treatment of wastewater by various researchers have been summarised in Table 2.4. Despite the high adsorptive capacity of Fe_3O_4 nanoparticles for the treatment of wastewater, there exist some drawbacks including

rapid oxidation and corrosion of Fe_3O_4 nanoparticles due to the presence of Fe (II) ion. As a result, magnetite particles are frequently changed on the surface and easily agglomerated in an aqueous system (Tamjidi *et al*., 2019). It has been reported that the incorporation of Fe_3O_4 into other materials can improve their adsorption stability and efficiency for the treatment of wastewater (Liu *et al*. 2021).

Table 2.5: Summary of Fe₃O₄ Nanoparticles as an Adsorbent for Removal of Heavy Metals

Method	Characterisation Techniques	Size(nm)	Pollutant	Removal (mg/ g) %)	Other adsorption Conditions	Research Findings	References
Co-precipitation	XRD, SEM	___	Cu (II)	4.021 (mg g-1)	pH (4.5), at room temperature (25ºC), adsorbent dosage (2.5 g), contact time (40 min) concentration (10 mg/L)	The authors are found that the removal efficiency of Cu (II) strongly depended on pH.	Kalpaklı, (2015)
Co-precipitation	XRD, SEM, EDS, TEM, FEG and DLS	12.300	As (VI)Cur(II)	99.2% 69.46 %	Adsorbent dosage (0.08 g), contacts time (30 min),	The authors reported that as the crystallite size increases from 12 nm to 300 nm the adsorption efficiency decreases.	Iconaru *et al. (*2016)
Chemical vapor deposition	HRTEM, SEM, EDX	20 n	(As III and V)	87%, 98%	Temperature (60ºC), conctact time (15 min)	The authors observed that the As ions were via a chemical process.	Monárrez-Corderoa *et al.* (2016)
Co-precipitation	SEM, XRD, FTIR	27.68	Cr (VI)	80%	pH (4), at room temperature, adsorbent dosage (25 mg/L), contact time (250 min)	The authors reported that Fe₃O₄ nanoparticles could remove 80%.	Hossain *et al.*, 2018
Electrochemical	TEM	12	Cr (VI)	100 %	pH (3.5), temperature (60ºC), adsorbent dosage (2 g), conctact time (2h) concentration (25 mg/L)	The results showed that the removal of Cr (VI) is strongly dependent on the heating mode, when compared to room temperature, the removal efficiency is about doubled.	Rivera *et al.* (2019)
Coprecipitation	TEM, FT-TIR, XRD,	9.22nm	Ni (II), Co (II)	97.88 and 95.01 %,	pH (7), at room temperature (25ºC), adsorbent dosage (0.4 g), concentration (100 mg/L)	The adsorption method was discovered to be pH-dependent	El-Shamy *et al.* (2019)
Commercial nanoadsorbent		20	Cr (VI), Cu(II)	88.83 % and 96.10 %	pH (4), temperature (25ºC), adsorbent dosage (2.5 g), contact time (90 min) concentration (1 mg/L)	The removal rates for Cr (VI) and Cu(II) were higher when pH was 4.0 and that temperature had no discernible effect on the adsorption process	Zhang *et al.* (2020a)

2.15.3 Silica oxides nanoadsorbent

Silicon oxide nanoparticles are another type of nanoadsorbentss that are commonly utilized for the treatment of wastewater ions due to their hydrophilic surface, non-toxicity, low cost and higher surface area. Different researchers have reported the use of SiO2 nanoparticles for the treatment of wastewater. For example, Najafifi *et al*., (2012) studied the adsorptive potential of SiO_2 nanoparticles for the removal of Cd (II), Ni (II), and Pb (II). The authors reported that for all of the adsorbents, the adsorption capacity decreased in the order of Pb (II) > Cd (II) > Ni (II), which the authors linked to the electronegativity of the metal ions, which led to stronger interactions with the negatively charged adsorbent surface. Other research by different others has been summarized in Table 2.6

Table 2.6: Summary of SiO_2 Nanoparticles as an adsorbent for removal of heavy metal

Method	Characterisation Techniques	Size(nm)	Pollutant	Removal (mg/g and %)	Other adsorption Conditions	Research Findings	References
So- gel	TEM and EDX	50	Fe(II)	9 mg	pH (4.5), temperature (25ºC), adsorbent dosage (0.1 g), contact time (20 min) concentration (1 mg/L)	The authors found that the adsorption efficiency can be enhanced by the modification of SiO_2 with functional groups.	Nguyen et al. (2019)
Sol-gel	FTIR, XRD, TEM, XPS	56	Pb (II), Cu (II), Hg (II), and Cd(II)	341.4, 289.8, 162.9, and 146.7 mg/g	pH (5), at room temperature, adsorbent dosage (1 g), contact time (30 min)	The authors reported that the contact time played an important role in the adsorption process	Kotsyuda *et al.* (2017)
Commercial	FTIR,and SEM	39	Pb (II), Cu(II) and Cd (II)	140.23, 100.75 and 48.03 mg/g	pH (5), temperature, adsorbent (25 °C)	The authors reported high adsorption of the metal's ions at pH of 5 and stability of the adsorbent after 6 recycle period	Huang *et al.* (2020)

2.15.4 Nanocomposites as adsorbents

Researchers have shifted attention from the use of individual nanoparticles as an adsorbent for the removal of different pollutants from wastewater (Younas *et al*., 2021). Researchers have recently focused on the formation of nanocomposites based on ZnO, SiO_2, and Fe_3O_4 with other materials (Elshypany *et al.,* 2021). These nanocomposites have been reported to have a better adsorption performance compared with individual nanoplatelets (Hajjaoui *et al*., 2021).

The use of nanocomposites as an adsorbent has been reported by many researchers for the removal of different pollutants, for example, Najafpoor *et al*., (2020) have studied the elimination of chemical oxygen demand (COD) from wastewater using Fe_3O_4 nanoparticles and Fe_3O_4/silver. Nanocomposites. The authors reported that Fe_3O_4 nanoparticle adsorption efficiency increased from 36.56 % compared with the 43 % recorded for the Fe_3O_4/silver nanocomposites. This result indicates the formation of the composites leads to an increase in the adsorption efficiency of the nanocomposites. Additionally, another researcher has studied the potential of $Co_3O_4@SiO_2$ coated with nylon 6 polymer at 298^oC. The authors reported maximum adsorption of 666.67 mg/g for Pb (II) from wastewater (Mohammadi *et al*., 2020). The efficacy of ZnO/ Polyaniline (PANI) nanocomposites was studied for the removal of Cr (VI). The authors reported that within 120 minutes, the maximum capacity was 139.47 mg/g for pH of 2 at 50°C. Other research by different others has been summarized in Table 2.7

Table 2.7: Summary of Different Nanocomposites used as an adsorbent for removal of heavy metal

Method	Nanocomposites	Characterisation Techniques	Pollutant	Removal (mg/g or %)	Other adsorption Conditions	Research Findings	References
Co-precipitation	DNPH/SDS/Fe_3O_4	EM–EDXS, FTIR	Cr (VI)	99.50%	pH (4.5), temperature (25ºC), adsorbent dosage (0.08 g), contact time (90 min) concentration (50 mg/L)	The Fe_3O_4 nanocomposites before and after the adsorption process can be easily separated from the aqueous solution by the external magnetic field.	Sobhanardakani and Zandipak. (2017)
Co-precipitation	Fe_3O_4/SiO2	SEM, FTIR, XRD	Cd (II) and Ni (II)	81.627 and 63.995m gg−1,	pH (6), temperature (25ºC), adsorbent dosage (40 mg) and contact time (30 min)), concentration (50 m/L)	The adsorption capacities of Fe_3O_4 nanocomposites were enhanced upon the surface modification with malic acid which provides numerous surface carboxyl and hydroxyl groups	Ghafoor *and* Ata (2017)
Green	Hull (Prunus amygdalus-Fascionello)/Fe_3O_4	VSM, SEM	Pb(II)	91.34%	pH (9), room temperature, adsorbent dosage (5 g/L) and contact time (80 min), concentration (10 m/L)	The removal efficiency is enhanced by increasing contact time.	Nasseh *et al*., (2017)

Method	Nanocomposites	Characterisation Techniques	Pollutant	Removal (mg/g or %)	Other adsorption Conditions	Research Findings	References
Precipitation	*Dowex (Mag-Dow)*	BET, XRD, TEM FITR	Cr (VI), Ni(II) Cu (II), Cd (II), Pb (II)	97.5%, 97%, 98%, 97 % , 96%	pH (10), at temperature (80ºC), adsorbent dosage (0.6 g/L) and contact time (30 min)), concentration (20 mg/L)	The adsorption attained equilibrium at 30 min using a volume of 0.5 g/L. The composite adsorbs metals in order Cu (II)>Cr (VI)>Cd (II)> Ni (III)> Pb2+. All metals were poorly adsorbed at pH < 4	Lasheen et al., 2017
Precipitation	Clinoptilolite/ Fe_3O_4	XRD, SEM,	Pb	124.955 mg/g.	pH (5.49), temperature (60ºC), adsorbent dosage (0.48 g), concentration (89.08 mg/L)	The authors reported that chemical adsorption controls the adsorption process	Javanbakht and Ghoreishi (2017)
Chemical precipitation	$NiFe_2O_4$@Salen Si	SEM, XRD, FT-IR, and VSM	Ni(II) w	95%	pH (9), temperature (24ºC), contact time (45 min), concentration (10 mg/L)	The contact time played an important role in the adsorption process	Babadi *et al*. (2018)
Thermal	$Fe_3O_4/SiO_2/PEI$ -NTDA	TEM, SEM , EDX	Pb (II)	285.3 mg g^{-1}	pH (6), temperature (25ºC), adsorbent dosage (0.5 g) and contact time (3h), concentration (200 mg/L)	In the acid leaching treatment with 2 M HCl solution for 144 hours, the magnetic adsorbents demonstrated high stability with a weight loss of less than 0.65%.	Jia *et al*. (2019)
Precipitation	ultrafine mesoporous Fe_3O_4	BET, XRD. TEM	Pb (II), Cd (II), Cu (II), and Ni(II),	98, 87, 90, and 78%,	pH (6), temperature (25ºC), adsorbent dosage (2.5 g), contact time (90 min) concentration (1 mg/L)	The authors reported that Fe_3O_4 was reusable and can be used several times even after five succeeding cycles.	Fato *et a.l* (2019)

Method	Nanocomposites	Characterisation Techniques	Pollutant	Removal (mg/g or %)	Other adsorption Conditions	Research Findings	References
Coprecipitation	Fe₃O₄/Alginate	TEM, FTIR, XRD,	Ni (II),Co (II)	97.88 and 95.0	pH (7), at room temperature (25ºC), adsorbent dosage (0.4 g), concentration (10 0 mg/L)	The adsorption method was discovered to be pH-dependent	El-Shamy *et al*., 2019
thermal	Fe₃O₄/SiO2/PEI-NTDA	TEM, SEM, EDX	Pb (II)	285.3 mg g 1	pH (6), temperature (25ºC), adsorbent dosage (0.5 g) and contact time (3h), concentration (200 mg/L)	In the acid leaching treatment with 2 M HCl solution for 144 hours, the magnetic adsorbents demonstrated high stability with a weight loss of less than 0.65%.	Jia *et al*., 2019
Co-precipitation	Fe₃O₄/ethoxylated para-phenylenediamine	FTIR), (XRD) TEM,	Cd (II), Pb (II), Zn (II)	85 95 95	pH (6.7), at room temperature, adsorbent dosage (0.6 g/L) and contact time (30 min)), concentration (20 mg/L)	Adsorption efficiencies improved steadily from pH of 2 and reached the maximum efficiency of adsorption at pH of 6 for Pb^{2+} and Zn^{2+}, while pH of 7 for Cd^{2+}.reaches equilibrium within four hours and is greatly influenced by the solution's pH and the dosage of the adsorbent.0.6 g	Fawzia *et al*., 2020

Method	Nanocomposites	Characterisation Techniques	Pollutant	Removal (mg/g or %)	Other adsorption Conditions	Research Findings	References
co-precipitation	Fe₃O₄/Al₂O₃/ZrO2	BET, XRD, SEM, EDX FITR	Cd(II), Cr(VI) and Pb(II)	96.65%, 96.55% and 97.2% for	pH (6), at room temperature (80ºC), adsorbent dosage (0.1 g) and contact time (24 h), concentration (30 mg/L)	The sorption property of the mixed oxide adsorbent has also been treated with respect to thermodynamic parameters and the sorption process was found to be spontaneous and endothermic. Cd(II), Cr(VI) and Pb(II) ions adsorption were observed to increase with increasing pH indicating relatively favorable conditions for recycling of the sorbent at higher pH values.	Tsegaye *et al.*,2020
co-precipitation	starch-coated magnetic nanoparticles	FTIR (XRD) , SEM	CR(VI)	98	pH (4), temperature (25ºC), adsorbent dosage (5 g), contact time (20 min), concentration (1 0 mg/L)	It was observed that the removal of Cr (VI) at high pH values decreased in comparison with low pH values, and the optimum removal was obtained at pH 4.0. . the optimum removal was obtained at pH 4.0. Similarly, optimum process conditions such as adsorbent	Şimşek *et al.*, 2020

Method	Nanocomposites	Characterisation Techniques	Pollutant	Removal (mg/g or %)	Other adsorption Conditions	Research Findings	References
						concentration, initial Cr (VI) concentration and contact time were determined as 2.0 g/L, 10 mg/L and 60 min	
One-Pot	ZnO_2/GO		Pb (II)	6.81%	Dosage (0.16 g/L), pH (5), Temperature (30°C) Time (30 min)	The authors reported that the carboxylic moiety included in the functional group was found to alter the adsorption effectiveness of Pb and Cu. The removal efficiency of Pb and Cu ions rose by two folds as the number of carboxylic moieties increased.	Ahmad *et al*. (2020)
Co-precipitation	Amino Propyl-Functionalized Silica	SEM, TEM, XRD	Pb (II), Cu (II)	95%	pH of 9, Temperature (30°C)	The research revealed that carboxylic moiety included in the functional group was found to be responsible for the adsorption effectiveness of Pb and Cu. The removal efficiency of Pb and Cu ions rose by two folds as	Alswieleh *et al*. (2021)

Method	Nanocomposites	Characterisation Techniques	Pollutant	Removal (mg/g or %)	Other adsorption Conditions	Research Findings	References
						the number of carboxylic moieties increased.	
Co-precipitation	Ash/GO/Fe_3O_4	FESEM, TEM, EDX mapping, BET/BJH, XRD, FTIR, and VSM	Pb (II), Cd (II)	99.67% and 98.68%	pH (6), concentration (10 mg/L), dosage (1 g), stirring speed (600 rpm), Temperature (25 °C) and contact time (150 min)	The authors found that the high surface area and the small crystallite size of the produced hybrid nanocomposites were responsible for the high absorption properties of the nanoparticles	Pelalak *et al.* (2021)

2.16 Desorption and Recyclability of the Nanocomposites

Desorption experiments are conducted on adsorbent that has been exhausted for the removal of various pollutants. Desorption is one of the most cost-efficient regeneration processes, it provides a better understanding of the type of adsorption, such as physical or chemical and the feasibility in practical applications (Siddeeg *et al*., 2020).

Desorption is done to determine the performance of the adsorbent for subsequent usage, to lower the cost of the adsorption process. Desorption can be divided into two types: (1) Thermal desorption (solvent-free), in which heat is used to carry out the desorption process. This method is quick and efficient, but have limitations due to the need for pretreatment, the release of hazardous contaminants, cost, degrade the pores of adsorbent, time-consuming, pollution of air and public perception issue (2) Solvents desorption method: This method of desorption is environmentally friendly, inexpensive, quick, promising, and has a lot of potentials (Patel, 2021).

Table 2.8 give a summary of the advantages and disadvantages of various adsorbent regeneration methods. Several researchers have done experiments to determine the nanoparticles' reusability. In a reusability investigation with 0.5 M H_3PO_4 and 1.0 M HNO by Martín *et al.* (2018), ion-selective polyacrylonitrile nanofibers were utilized to remove divalent ions of zinc, lead, and copper with up to four cycles of good efficiency of more than 90%. For the removal of zinc and lead using these nano adsorbents, stable adsorption results were reported, showing the ease of reusability and recyclability, but adsorption results for copper ions decreased with reusability. Fe_3O_4 used to remove divalent lead ions was also

cleaned with 0.1 M HPO$_4$ and H$_2$O to see if it could be reused. During the reusability cycles, the adsorption capacity of this nanosorbent was somewhat reduced.

The adsorption capacity was still greater than 85% after 5 cycles. Even after 5 rounds of lead removal, the findings showed great reusability. Due to the competition between Pb ions and protons for active sites on the nanoadsorbent. The summary of different methods used for the regeneration of adsorbents is given in Table 2.8.

Table 2.8: Advantages and disadvantages of different adsorbent regeneration methods

Methods	Advantages	Disadvantages
Thermal desorption method	Efficient	Extremely costly Degrade the adsorbent's pores, It's time-consuming and courses air pollution
Biological method	Eco-friendly and Efficient	Block the pores of adsorbent, Very slow, Only applicable for biodegradable pollutants
Microwave regeneration	Efficient, Less time-consuming, Eco-friendly	Highly expensive, Degrade the pores of adsorbent, Required further treatment
Ultrasound regeneration	Efficient, Less time-consuming, Eco-friendly	Highly expensive, Degrade the pores
Supercritical fluid extraction method	Efficient and consume less time	Degradation of adsorbent pores, and highly expensive
Advance oxidative method	Efficient	Highly expensive, Degrade the pores of adsorbent, Time-consuming
Ozonation	Efficient	Highly expensive, Degrade the pores of adsorbent, Formation of acidic surface, Required before treatment

2.17 Research Gaps

      i.   Most of the research that has been reported in the literature used simulated wastewater for the removal of heavy metals and organic pollutants. This research uses real industrial petroleum refinery wastewater for the adsorption process.

      ii.   The use of ZnO/Fe_3O_4/SiO_2 nanocomposites for the removal of inorganic and organic pollutants from petroleum refinery wastewater via the the adsorption process is new, there is little or no information on any published research on the use of ZnO/Fe_3O_4/SiO_2 nanocomposite as an adsorbent for the treatment of petroleum refinery wastewater in Nigeria or any other country via adsorption method.

      iii.   As compared to other conventional wastewater treatment techniques, adsorption technology for the treatment of petroleum refinery wastewater is an environmentally friendly cost-effective and simple method. The technology can be used by the refineries in Nigeria and other developing countries in need of environmentally friendly, efficient, low-cost wastewater treatment methods.

      iv. SiO_2 nanoparticles have been synthesised from different natural sources to reduce the usage of available toxic chemicals but no research has been conducted that specifically uses kaolin from Pati Shaba-kolo for the synthesis of SiO_2 nanoparticles**.**

In summary, the effects of different synthesis parameters on the textural, optical and microstructural properties of the nanoparticles have been provided. The adsorptive behaviour of the different nanoparticles for the treatment wastewater especially at different solution pH has also been summarized. Based on the review, the following conclusions were drawn. The

acidic medium favoured the formation of the smaller size of the nanoparticles compared to the alkaline medium. Several reports indicated a decrease in the crystallite size of the nanoparticles as the pH increased from 7 to 12.

Reaction time, reaction temperature and calcination temperatures influenced the crystallite size of the nanoparticles. Different metal salts have little effect on the crystallite size but exert a greater influence on the morphology of the nanoparticle produced. The concentration of the metal precursor shows increases in the crystallite size at a higher concentration of the metal in the solution. These findings indicated that these factors strongly affect the crystallite size and the morphology of the nanoparticles.

The crystallite sizes concerning each parameter also depend on the methods of synthesis of the nanoparticles. There are still divergent views as reported by the researchers on the increase and decrease in the particle size of the nanoparticle. The mechanisms of the increase or decrease in the crystallite size concerning the variations of solution pH, synthesis temperature, different salt precursors, and synthesis time are not clearly understood and still require further investigation. It is indicated that heat treatment played an important role in the purity of the nanoparticles since many of the synthesis methods lead to the formation of metal hydroxides which need to undergo heat treatment to remove the water molecules. These nanoparticles have a lot of potential as an adsorbent for the treatment of wastewater. However, various bottlenecks must be solved before these nanomaterials can be used more effectively in water treatment. To begin with, most nanomaterials are unstable and tend to aggregate, limiting their ability to be removed. Additionally, due to their nanoscale size, it is frequently difficult to quickly and efficiently remove nanomaterials from aqueous solutions.

The use of hybrid nanocomposites appears to be a viable solution to all these issues. Nevertheless, more research into the synthesis process, long-term performance adsorptive, and other concerns linked to nanocomposites is required. Secondly, synthesis of the nanoparticles from natural sources is required to reduce the synthesis of nanomaterials from commercial chemical sources to reduce cost and toxicity.

The use of nanomaterials as adsorbents has given new alternatives to conventional adsorbents used for the treatment of wastewater. However, much of the work studied uses stimulated water with relatively basic components for the adsorption process. Regeneration of the composites should be performed to evaluate the cost-effectiveness of the nanoparticles as an adsorbent. Future research should focus on the immobilization of all the nanoparticles on suitable supports for easy separation after usage.

CHAPTER THREE

3.0 MATERIALS AND METHODS

3.1 Materials

The list of chemicals/reagents and equipment used in the study are given in Table 3.1 and 3.2 respectively; and all chemicals/reagents were used without further purifications.

Table 3.1: List of Chemicals/Reagents

S/No.	Item	Manufacturer	Percentage purity (%)
1	Ammonium iron (II) sulphate	Sigma Aldrich	98
2	Ferrous ammonium sulfate	Sigma Aldrich	99
3	Hydrogen tetraoxosulphate (VI) acid	BDH Chemicals	96
4	Iron (III) chloride tetrahydrate	Sigma Aldrich	98
5	Potassium dichromate	BDH Chemicals	98
6	Manganese (II) tetraoxosulphate	Sigma Aldrich	97
7	Nitric acid	Merck	98
8	Polyvinylpyrrolidone	BDH Chemicals	99
9	Potassium iodide	Merck	98
10	Sodium borohydride	BDH Chemicals	97
11	Sodium thiosulphate	Sigma Aldrich	95
12	Sodium hydroxide	BDH Chemicals	95
13	Zinc nitrate hexahydrate	Merck	98

Table 3.2: List of Apparatus/Equipment

S/No.	Apparatus/Equipments	Model	Manufacturer
1	Mortar and Pestle	Porcelain	SEDI, Minna
2	Electric Weighing	Pro SP 202	Ohaus Corp., Pine
4	Magnetic Stirrer	model 400	Gallenkamp, England
5	Muffle furnace	Size 1 (1000°C)	Gallenkamp, England
6	Sieve (75um)	PHD-4	Rex, Shanghai, China
7	pH Meter	PHB-4	Rex, Shanghai, China
11	Crucibles	Porcelain	SEDI, Minna
12	HRSEM/EDS	Zeiss Auriga	SCO teen, Germany
13	XRD	XRD-60000	Shimadzu Scientific instrument
14	FT-IR	Frontier FTI-R	Perkin Elmer, UK
15	BET	NOVA 4200e	Quantachrome instruments, UK
17	Desiccator	Pyrex	England
18	Filter paper	Whatman	England
19	Funnel	Ok plast	Nigeria
20	XPS	XPSHI 5400	England
21	AAS	PG -90	England

3.2   Methods

3.2.1   Sample collection and preparation

3.2.1.1 Collection of kaolin

The raw kaolin sample was collected from Patishaba-kolo in Lavun local Government area, Niger State. Niger State is located in the North Central region of Nigeria between latitudes 8° 20′N and 11° 20′N and longitude 3° 30′ E and 7° 20′ E. The map of the sampling location is shown in Plate II

Plate I: Map Showing the Location of Patishaba-Kolo, Niger State

3.2.1.2 Collection of petroleum refinery wastewater

The Petroleum refinery wastewater was collected from Kaduna refinery January 8th 2018. The Kaduna refinery has a refining capacity of 110,000 barrels per day and is located in Kaduna, Kaduna State, Nigeria. The refinery is located in the southern part of Kaduna metropolis between latitude 10º North and longitude 7º East.

Plate II: Map of Kaduna Town Showing the Location of Kaduna Refinery
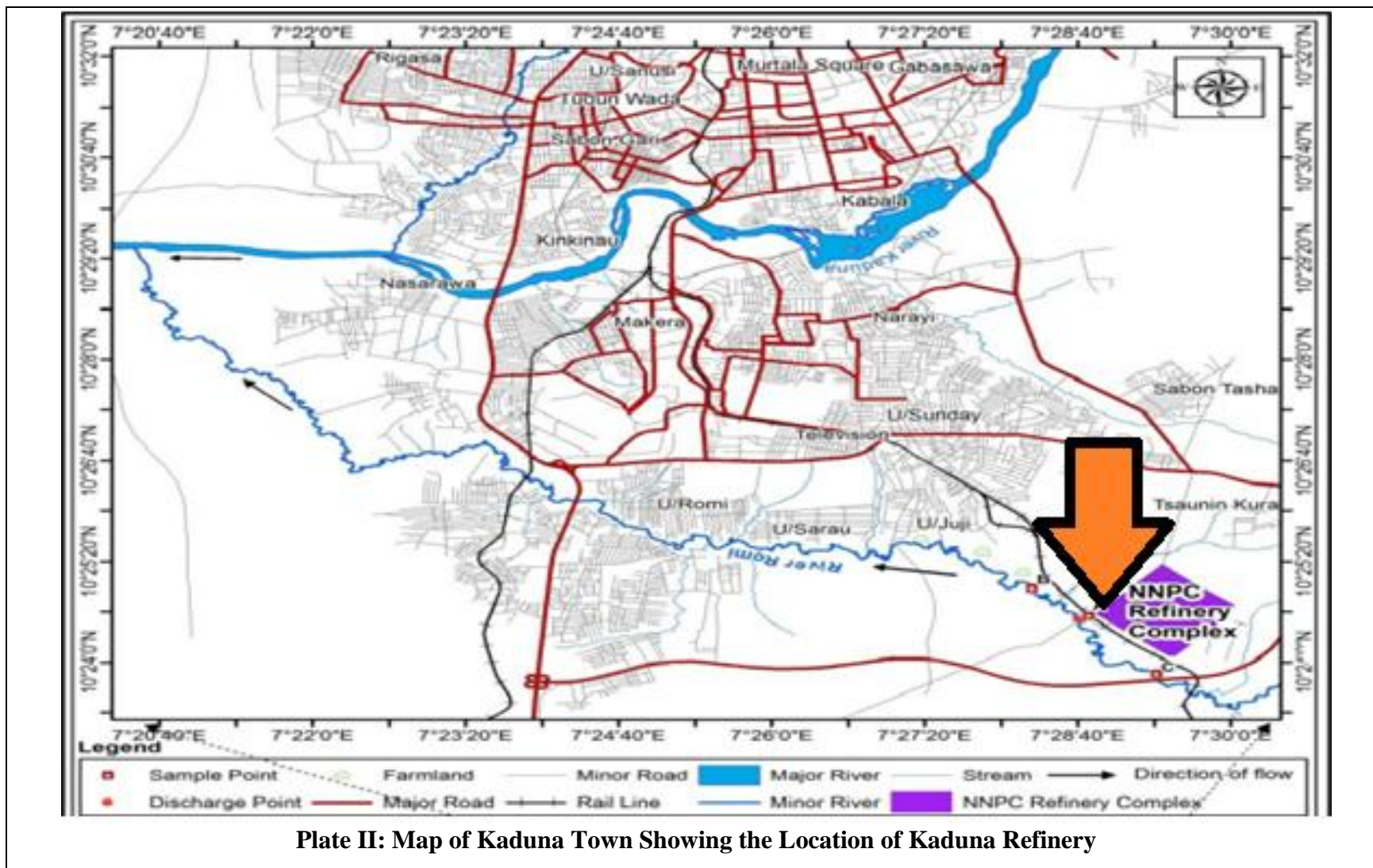
3.2.1.3 Kaolin pre-treatment

With the help of a mortar and pestle, the kaolin collected from Pati Shaba-kolo was disaggregated. A 75-um mesh sieve was used to sieve the crushed kaolin. To make a slurry, 400 g of crushed kaolin was soaked in 1000 cm^3 of distilled water for a week. The supernatant was decanted until distilled water became colourless and the slurry was dried overnight at 100°C (Ibrahim *et al* 2023).

3.2.1.4 Meta kaolinisation

In this case, 20 g Meatakaolinization of the Pati Shabakolo kaolin was carried out by calcination of 20 g of the treated kaolin (800°C) in a Muffle furnace for 2 h Ibrahim *et al* 2023).

3.2.2 Synthesis of selected metal oxides nanoparticles

3.2.2.1 Sol-gel synthesis of Fe$_3$O$_4$ nanoparticles

The Fe$_3$O$_4$ nanoparticles were synthesised using Sodium borohydride and Polyvinylpyrrolidone (PVP) as reducing and stabilizing agents respectively. 0.1 moldm^{-3} of Iron (III) chloride tetrahydrate was prepared and 25 cm^3 was measured into a 250 cm^3 beaker and stirred for 15 min. Then 30 cm^3 of 0.3 moldm^{-3} sodium borohydride was added into the iron chloride solution and stirred continuously at constant temperature (30°C) for 15 mins. 10 cm^3 of the 5 % PVP was added to the mixture and accompanied by the formation of a sol-gel-like solution. The brownish gel-like solution was later dried at 100 °C in the oven overnight. The dried samples were calcined at different temperatures (300-700°C) for 2 h to give Fe$_3$O$_4$ nanoparticles (Farahmandjou and Soflaee, 2015).

3.2.2.2 Sol-gel synthesis of ZnO nanoparticles

0. 1 M of 60 cm^3 zinc nitrate hexahydrate was introduced into a 250 cm^3 beaker and placed on a magnetic stirrer. 25 cm^3 of 1.0 moldm-^{3} sodium hydroxide solution was added to the solution of zinc nitrate solution. After which, 10 cm^3 of 5 % w/v Polyvinylpyrrolidone (PVP) solution was added to the same mixture leading to the formation of a white gel. The gel-like solution mixture was dried at 100°C for 2 h and later calcined at different temperatures (300-700°C) for 2 h (Al-Harbi and El Ghoul, 2021).

3.2.2.3 Sol-gel synthesis of silicon oxide nanoparticles

The Silicon oxide Nanoparticles were synthesised by measuring 100 cm^3 of 2 moldm-^{3} NaOH into 250 cm^3 conical flasks followed by the addition of 1.5 g of metakaolin. Subsequently, 10 cm^3 of 5 % w/v of polyvinyl pyrrolidone was added to the solution containing metakaolin. The mixture was stirred on a magnetic stirrer at 2000 rpm for 2 h to get a homogenous solution, and allowed to age overnight. The hydrothermal process was carried out at 150°C by weighing 3 g into the Teflon at different ageing times (3, 6, 9, 12 h) using an autoclave reactor (Teflon bottle). After the crystallization, the SiO$_2$ nanoparticles produced were washed with distilled water to a neutral pH of 7 (Patel *et al*., 2022).

3.2.3 Preparation of nanocomposite

3.2.3.1 Preparation of bimetallic oxides nanocomposites

Firstly, ZnO nanoparticles were prepared by measuring 60 cm^3 of a known concentration of zinc nitrate (0. 1 M) into a 250 cm^3 beaker and placed on a magnetic stirrer. 25 cm^3 of 1.0 moldm-^{3} sodium hydroxide (NaOH) solution was slowly added. After which, 10 cm^3 of 5 % w/v Polyvinylpyrrolidone (PVP) solution was added to the same mixture. This was

accompanied by the formation of a gel-like solution. The gel solution was aged overnight before being dried in an oven (100°C) for 2 h and then calcined (450°C) for 2 h. Secondly, SiO_2 nanoparticles were prepared by measuring 100 cm^3 of 2 moldm-^{3} NaOH into 250 cm^3 conical flasks followed by the addition of 1.5 g of metakaolin. To achieve a homogeneous solution, the solution was vigorously agitated for 2 h at 2000 rpm on a magnetic stirrer (model 400) and then left to age overnight. The sample was washed thoroughly using distilled water to get a neutral pH after crystallization (7). The obtained sample was calcined at 200°C overnight. Furthermore, the sol-gel method was followed to synthesize the ZnO/SiO_2 nanocomposites by measuring 0. 1 moldm-^{3} of zinc nitrate into a 250 cm^3 beaker and placing on a magnetic stirrer followed by the addition of 1.5 g of metakaolin. To get a homogenous solution, the solution was vigorously stirred at 2000 rpm on a magnetic stirrer for 2 h. The resulting solution was vigorously stirred for 30 min under a mechanical shaker and allowed to age for 24 h. ZnO/SiO_2 nanocomposites were calcined (450°C) for 2 h (Kumaresan and Ramamurthi, 2020). Other binary composites were synyhesized following the same methods as described in section 3.3.1 using different precursors for ZnO/Fe_3O_4, Fe_3O_4/SiO_2. Altogether 13 runs of varying ratios of Fe_3O_4, ZnO, and SiO_2 were prepared as indicated in Table 3.3.

Table 3.3: Experimental Runs for the Synthesis of the Bimetallic Nanocomposites

		Ratio of blending	
S/No	**ZnO**	**Fe_3O_4**	**SiO_2**
1	1	1	-
2	1	2	-
3	2	1	-
4	1	-	1
5	2	-	1
6	1	-	2
7	-	1	1
8	-	2	1
9	-	1	2

3.2.3.2 Preparation of ternary Fe3O4/SiO2/ZnO nanocomposites

The ternary hybrid $Fe_3O_4/SiO_2/ZnO$ metal oxides nanocomposites were synthesised following the procedure reported in 3.3.4.1 with different mixing ratios as shown in Table 3.4.

Table 3.4: Experimental runs for Ternary hybrid ZnO/Fe$_3$O$_4$/ SiO$_2$ Metal Oxides Nanocomposites

S/No	**ZnO**	**Fe_3O_4**	**SiO_2**
1	1	1	1
2	2	1	1
3	1	2	1
4	1	1	2

3.2.4 Characterisation of the various nanoparticles and nanocomposites produced

Characterisation of The ZnO, Fe_3O_4 and SiO_2 nanoparticles, ZnO/SiO_2 ZnO/Fe_3O_4, Fe_3O_4/SiO_2 and $Fe_3O_4/SiO_2/ZnO$ nanocomposites was carried out to determine their mineralogical phases, morphology, elemental compositions, functional groups, chemical states and surface area using High-Resolution Scanning Electron Microscopy (HRSEM) (MEL-300000), X-ray diffraction (XRD) (XRD-60000), Energy Dispersive Spectroscopy, X-ray photoelectron spectroscopy (XPS) (XPSHI 5400), Brunauer, Emmett. and teller (BET) N_2 adsorption-desorption method and Fourier-transform infrared (FTIR) spectroscopy (Frontier FTI-R).

3.2.4.1 Fourier transform infrared (FTIR) spectrometer

The FT-IR instrument was used to analyse the functional groups on ZnO, Fe_3O_4 and SiO_2 nanoparticles, ZnO/SiO_2, ZnO/Fe_3O_4, Fe_3O_4/SiO_2 and $Fe_3O_4/SiO_2/$ ZnO nanocomposites. The FTIR pellets were made by mixing equal masses of KBr salt and the samples and the mixture was admitted to a pressure of several tones in a die, to produce a highly transparent plate or disc which can be inserted into the spectrophotometer. 15 mg of each sample was placed on the Attenuated Total Reflectance (ATR) sample holder of a Perkin Elmer spectrum 100 FT-IR spectrometers. The Infrared spectrum was measured in the range of 400-4000 cm^{-1} with a resolution of 4 cm^{-1} and averaging over 32 scans.

3.2.4.2 High-resolution scanning electronic microscope (HRSEM)

The ZnO, Fe_3O_4 and SiO_2 nanoparticles, ZnO/SiO_2 ZnO/Fe_3O_4, Fe_3O_4/SiO_2 and $Fe_3O_4/$ ZnO $/SiO_2$ nanocomposites samples were analyzed with HRSEM to visualize the micro structures present in each sample. A carbon adhesive tape was placed onto an aluminum stub. A small

amount of each sample was applied to the carbon adhesive tape. ZnO, Fe_3O_4 and SiO_2 nanoparticles, ZnO/SiO_2 ZnO/Fe_3O_4, Fe_3O_4/SiO_2 and $Fe_3O_4/$ ZnO $/SiO_2$ nanocomposites were coated with carbon to prevent charging diving imaging. The analysis was done with a Zeiss Auriga High-Resolution Scanning Electron Micro-analyser equipped with a CDU-lead detector at 25 kV and a tungsten filament.

3.2.4.3 X-Ray diffraction (XRD)

The mineralogical phases of the ZnO, Fe_3O_4 and SiO_2 nanoparticles, ZnO/SiO_2, ZnO/Fe_3O_4, Fe_3O_4/SiO_2 and $Fe_3O_4/$ ZnO $/SiO_2$ nanocomposites were assessed using XRD. Each sample was analyzed using a Bruker AXS D8 advanced diffract meter, coupled with Cu-Kα radiation at 40 kV and anode current of 40 mA with a PSD Lynx-Eye, Si-strip detector. The sample was placed into the instrument sample holder and the diffraction patterns were collected with the measured range of 2Θ angles between 10° and 80°. The mineral identification was done by comparison with available d-spacing data and major peaks from the International Centre for Diffraction Data and EVA software from Bruker. The crystallite size was calculated using equation (2.8).

3.2.4.4 Brunauer emmett teller (BET) N_2 adsorption-desorption analysis

The surface area, pore volume, and pore size (textural properties) of nanoparticles $Fe_3O_4/$ ZnO $/SiO_2$ nanocomposites are assessed using BET. 400 mg of the respective sample was outgassed under vacuum in a suitable measurement burette at 250 ℃ for 4 h. Then the N_2 adsorption/desorption isotherm was obtained at the equilibrium time of 3 min.

3.2.4.5 XPS analysis

The oxidation state of the ZnO, Fe_3O_4 and SiO_2 nanoparticles and Fe_3O_4/ ZnO /SiO_2 nanocomposites were studied using X-ray photoelectron spectroscopy (XPS). The XPS measurements were carried out with a spectrometer using Al Kα radiation (hυ = 1486.7 eV). The instrument vacuum exceeded 5×10^{-8} Torr during the experiments. The spectrometer was calibrated with the photoemission lines of Ag 3d5/2, Au 4f7/2 and Cu 2p3/2. The spectra were recorded in constant analyzer energy mode at pass energy of 143.05 eV for survey spectra and 35.75 eV for high-resolution spectra. The survey spectra were summed over 3 scans, and high-resolution spectra were summed over 15 cycles. All spectra were energy calibrated using the hydrocarbon peak at the binding energy of 285.0 eV. The data was evaluated using the XPS software, and the background subtraction applied to the high-resolution scans followed the method according to Shirley and Jarochowska, (2022). The experimental curves were fit using Gaussian-Lorentzian product functions; 70% Gaussian and 30% Lorentzian.

3.2.5 Determination of heavy metal concentrations of the petroleum refinery wastewater

The chemical wet digestion method was used to digest the petroleum wastewater. About 50 cm^3 of refinery wastewater was digested with 10 cm^3 concentrated HNO_3 at 80°C until the volume reached 20 cm^3, then cooled and filtered. The clear solution was diluted to a mark of 100 cm^3, and blank digestion was performed for HNO_3 at 80°Cin the same manner. Triplicates of each sample were digested and a flame Atomic Absorption spectrophotometer

was then used to analyse the Pb (II) Cd (II), Ni (II), Cr(VI), Cu (II) and total iron metal ions (Igbagara and Ntekim, 2021).

3.2.6 Determination of dissolved oxygen (DO)

Winkler's method was used to determine the level of dissolved oxygen (DO) in refinery Petroleum wastewater. Refinery petroleum wastewater was collected in BOD bottles, which were then treated with 2.0 cm^3 manganese (II) tetraoxosulphate (VI) (MnSO4) and 2.0 cm^3 potassium iodide (KI). They were then filled with refinery petroleum wastewater to a capacity of 250 cm^3 to the mark. This was corked and thoroughly mixed for a while to precipitate, after which the precipitate was allowed to settle. Then, 2.0 cm^3 of concentrated hydrogen tetraoxosulphate (VI) acid (H_2SO_4) was added and well stirred until the precipitate was completely dissolved. 203 cm^3 of wastewater was measured into a conical flask and titrated against 0.025 M sodium thiosulphate starch was used as an indicator. The colour change was observed from blue to colourless (Carvalho *et al*., 2021). The level of DO in refinery petroleum wastewater was calculated using equation 3.1

$$DO \left(\frac{mg}{dm^3}\right) = \frac{0.08 \times 1000 \times (0.025M \times Vol.of \ odium \ thiosulphate}{203} \tag{3.1}$$

3.2.7 Determination of biological oxygen demand

About 50 cm^3 of petroleum wastewater was analyzed for the first day of dissolved oxygen (DO) and then incubated at 20 ℃ for 5 days and the 5th day DO was recorded (APHA, 2017). A blank was made in the same way, and the level of BOD was calculated using equation 3.2.

$$BOD \left(\frac{mg}{dm^3}\right) = \frac{(D_1 - D_2) - (B_1 - B_2) \times 100}{\% \ dilution} \tag{3.2}$$

where D1 is the DO of the sample immediately after preparation (mg/dm^3), D_2 is the DO of the sample after incubation (mg/dm^3), B_1 is the DO of blank (seeded dilution water) before incubation (mg/dm^3), and B_2 is the DO of blank (seeded dilution water) after incubation (mg/dm^3).

3.2.8 Determination of chemical oxygen demand (COD)

The COD level of the petroleum wastewater was determined using the dichromate method developed by the American Public Health Association (APHA, 2017). 25 cm^3 of the wastewater was measured into a 250 cm^3 beaker followed by the addition of two drops of ferrous sulfate indicator. The mixture was then titrated against ferrous ammonium sulfate (FAS). During the titration, the titrant (Fe^{2+}) reacted instantly with hexavalent chromium (Cr^{6+}) in the wastewater forming trivalent chromium (Cr^{3+}) and ferric ion (Fe^{3+}) as shown in equation (3.1):

$$3Fe\,(II) + Cr(VI) \rightarrow 3Fe\,(II) + Cr(III) \tag{3.3}$$

The final hexavalent chromium level was then subtracted from the initial value before titration to determine the amount of hexavalent chromium that was reduced during the digestion. This difference was then used to calculate the COD by the following equation

$$COD\ (mg/L) = \frac{(A - B) \times N \times 8000}{volume\ of\ sample} \tag{3.4}$$

where A is the volume in cm^3 of FAS required for the titration of the blank,

B is the volume in cm^3 of FAS required for the titration of the waste wastewater sample,

N is the normality of FAS (APHA, 2017).

3.2.9 Determination of organic carbon content

25 cm^3 of petroleum wastewater and 10.0 cm^3 of 0.5 M K$_2$Cr$_2$O$_7$ solution were introduced into 250 cm^3 conical flask. After which 20.0 cm^3 of conc. H$_2$SO$_4$ was added to the mixture, shaken vigorously and allowed to settle and cool down for 30 min. 100 cm^3 of distilled water was added to the cold mixture and drops of ferroin indicator were added before titrating with ammonium iron (II) sulfate solution until the colour changed to maroon. The percentage of organic carbon level was obtained using Equation 3.2.

$$\% \ Organic \ Carbon = \frac{(B-S) \ X \ 0.4N \ X \ 0.003 \ X \ 100 \ X \ F}{Mass \ of \ the \ sample} \tag{3.5}$$

Where B (28.1) is a constant called blank, S is the titration value, N is the normality of the solution, F is the correction factor (1.33).

3.2.10 Batch adsorption experiment

3.2.10.1 Effect of contact time

The adsorption of Pb (II), Cd (II), Ni (II), Cr (VI), Cu (II) and total iron ions, COD, BOD, TOC from the refinery wastewater using the nanoparticles and the corresponding nanocomposites as an adsorbent were studied by measuring 50 cm^3 of the petroleum wastewater into separate conical flasks. The conical flasks were corked and the solution was stirred continuously at 250 rpm at various contact times (1, 5, 10, 15, 20 and 25 min) at 30ºC and adsorbent dosage (0.08 g) and pH of 6.25 for ZnO, Fe$_3$O$_4$ and SiO$_2$ nanoparticles, ZnO/SiO$_2$ ZnO/Fe$_3$O$_4$, Fe$_3$O$_4$/SiO$_2$ and Fe$_3$O$_4$/ ZnO /SiO$_2$ nanocomposites. The liquid phases were filtered out of the solution at the end of each mixing interval using Whatman filter paper no 4 and the residual concentrations of Pb (II), Cd (II), Ni (II), Cr (VI), Cu (II) and total iron

ions, COD, BOD and TOC were determined using AAS and standard methods for the determination of BOD, COD and TOC as described in section 3.7-3.9 (Sobhanardakani and Zandipak, 2017).

3.2.10.2 Effect of adsorbent dosage

The adsorption of Pb (II), Cd (II), Ni (II) Cr(VI), Cu (II) and total iron ions, COD, BOD, TOC from the refinery wastewater was studied at different adsorbent dosages ranging from 0.02, 0.04, 0.06, 0.08, 0.1to 0.12 g/50 cm^3 into separate conical flasks. The conical flasks were corked and the mixture was stirred continuously on a magnetic stirrer at 250 rpm. All other parameters such as solution pH and constant time were kept constant at 6.25 and 15 min respectively. The liquid phases were separated from the solution by filtration with Whatman filter paper at the end of each mixing period, and the residual concentrations of Pb (II) Cd (II), Ni (II) Cr(VI), Cu (II) and total iron ions, COD, BOD and TOC were determined using AAS and standard methods for the determination of BOD, COD and TOC as described in section 3.7-3.9 (Sobhanardakani and Zandipak, 2017).

3.2.10.3 Effect of reaction temperature

The adsorption of Pb (II), Cd (II), Ni (II), Cr(VI), Cu (II) and total iron ions, COD, BOD and TOC from the refinery wastewater was studied at different temperatures (30, 40, 50, 60, 70 and 80°C) regulated by a thermostat attached to a shaker. A known volume of the refinery wastewater (50 cm^3) was measured into separate conical flasks. The conical flasks were corked and the mixture was stirred continuously on a magnetic stirrer at 250 rpm. All other parameters such as time, dosage, solution pH and constant time were kept constant at 15 min, 0.08 g and 6.25 respectively. The liquid phases were separated from the solution by filtration with Whatman filter

paper no 4 at the end of each mixing period, and the equilibrium concentrations of Pb (II), Cd (II), Ni (II), Cr (VI), Cu (II) and total iron ions, COD, BOD and TOC were determined using AAS and standard methods for the determination of BOD, COD and TOC as described in section 3.7-3.9 (Sobhanardakani and Zandipak, 2017).

3.2.11 Data analysis

The data obtained in this analysis were subjected to different kinetic models and adsorption isotherms to understand the adsorption efficiency and mechanism of the adsorption process between Pb (II), Cd (II), Ni (II), Cr (VI), Cu (II) and total iron ions, COD, BOD and TOC. Equations (3.6) and (3.7) were used to compute the equilibrium adsorption capacity and percent (%) removal of Pb (II) Cd (II), Ni (II) Cr (VI), Cu (II) and total iron ions, COD, BOD and TOC

$$qe = \frac{(C_i - C_f) \, X \, V}{m} \tag{3.6}$$

$$\% \, Adsorption = \frac{C_i - C_f}{C_i} \, x \, 100 \tag{3.7}$$

Where qe represents the amount of heavy metal adsorbed at equilibrium (mg/L), C_i and C_f represent the initial and final heavy metal concentrations in the petroleum refinery wastewater, V represents the volume of solution (L), and m represents the mass of the adsorbent (g).

3.2.11.1 Pseudo first-order model

The data were subjected to the pseudo-first-order kinetic model which assumes that the rate of adsorption on the available site is proportional to the number of vacant sites and that

adsorption takes place exclusively on isolated sites, and the adsorbed ions did not interact. The equation for the pseudo-first-order kinetic model is as follows: (3.6).

$$\log(q_e - q_t) = \log(q_e) - \frac{K_1}{2.303} \; x \; t \tag{3.6}$$

Where qe (mg/g) is the mass of metal adsorbed at any time (t) and k_1 (min-1) is the pseudo-first-order adsorption equilibrium rate constant. The values of K_1 and q_e are determined by the slope and intercept of the plot of log (q_e - q_t) vs t, respectively.

3.2.11.2 Pseudo second-order model

The pseudo-second-order model for the kinetic process of metal ion adsorption on adsorbent has been described by Revellame *et al.* (2020). The pseudo-second-order model predicts behaviour over the whole range of adsorption by assuming that chemical sorption or chemisorption is the rate-limiting step (Hubbe *et al.*, 2019). In this case, the adsorption rate was determined by the adsorption capacity rather than the adsorbate concentration. The pseudo-second-order equation is written as equation 3.7.

$$\frac{t}{q_t} = \frac{1}{k_2 \, q_e^2} + \frac{t}{q_e} \tag{3.7}$$

3.2.11.3 Intraparticle diffusion model

Weber and Morris developed and suggested the intraparticle diffusion model, which considers pore diffusion. Intraparticle diffusion is assumed to be the slowest stage during the adsorption process, resulting in the rate-controlling step, with instantaneous adsorption in the internal diffusion model (Pholosi *et al.*, 2020). The equation for the adsorption system is given by Weber and Morris in equation 3.8.

$$q_t = k_i t^{0.5} + C \tag{3.8}$$

The pseudo-second-order rate constant (g/mg/min) is denoted by k_2. The slope of the plot of t/qt vs t determines the value of qe.

3.2.11.4 Elovich model

Elovich model is used to predict the nature of adsorption in wastewater processes. The model implies that the rate of adsorption reduces exponentially as the amount of adsorbed solute increases. Equation 3.9 is the Elovich equation:

$$qt = \frac{1}{\beta}\ln\alpha\beta - \frac{1}{\beta}\ln(t) \tag{3.9}$$

Where α is the initial adsorption rate (mg g^{-1} min^{-1}), β is the desorption constant (g mg^{-1}). The value of the reciprocal of β reflects the number of sites available for adsorption, whereas the value of adsorbed quantity when ln t is equal to zero is given by $\frac{1}{\beta}\ln\alpha\beta$.

3.2.12 Adsorption isotherms

Adsorption Isotherms give basic physiochemical data for determining the adsorption process applicability as a unit operation (Benjelloun *et al*., 2021). The Freundlich model deals with heterogeneous adsorption, while the Langmuir model assumes monolayer adsorption. The Temkin isotherm model predicts that the heat of adsorption of the molecules present in the adsorbed layer decreases linearly rather than in a logarithmic pattern with the coverage of the molecules. Dubinin-Radushkevish is another isotherm that assumed adsorption to be homogeneous and heterogeneous (Ahmad *et al*., 2020). The Langmuir, Freundlich, Temkin, and Dubinin-Radushkevish equations are shown in Table 3.5.

Table 3.5: Equation of Adsorption for Langmuir, Freundlich, Temkin and Dubinin-Radushkevish (R-D)   Isotherms

Isotherm	Equation	
Langmuir	$\frac{C_e}{q_e} = \frac{1}{q_{max} K_L} + \frac{C_e}{q_{max}}$	(3.10)
Freundlich isotherm	$\log q = \log K_f + \frac{1}{n}\log C$	(3.11)
Temkin	$q_e = \frac{RT}{b}\ln K_T + \frac{RT}{b}\ln C_e$	(3.12)
R-D	$\ln q_e = \ln q_m - K_{D-R}\varepsilon^2$	(3.13)

Where q_e(mg/g) is the equilibrium adsorption capacity, q_{max} (mg/g) is the maximum adsorption capacity, K_L (L/mg) is the Langmuir constant describing adsorption affinity for the adsorbent, K_F, is the Freundlich constant, 1/n is the Freundlich constant related to the multilayer adsorption capacity, and n is the heterogeneity factor, which represents the extent to which the adsorption depends on the equilibrium concentration. b (g J mol^{-2}) is the Temkin constant, R is the universal gas constant (8.314 J K^{-1}), T is the temperature in K Ce (mg/L) is the equilibrium adsorbate concentration Co (mg/L): initial concentration, k_{D-R} is a constant related to the adsorption energy, and ε is Polanyi potential which is related to the equilibrium concentration, R_L Separation factor. The essential feature of the Langmuir equation can be expressed in terms of a separation factor, R_L (dimensionless), which is defined by the following equation.

3.2.13 Thermodynamics evaluation of adsorption process

The removal of Pb (II), Cd (II), Ni (II), Cr (VI), Cu (II), total iron, BOD, COD and TOC from petroleum refinery wastewater using ZnO, Fe_3O_4, SiO_2, nanoparticles, ZnO/Fe_3O_4, ZnO/SiO_2, Fe_3O_4 /SiO_2 and Fe_3O_4/SiO_2/ZnO nanocomposites nanorods was studied from a thermodynamic perspective to predict the adsorption mechanism.

Standard Gibb's free energy change(ΔG^o), Standard enthalpy change (ΔH^o), and the standa

rd entropy change ΔS^o were used to determine the values of thermodynamic parameters. The slope and intercept of the linear plot of $\ln K_d$ versus $\frac{1}{T}$ was used to calculate (ΔH^o) and $(\Delta S^{o)}$ respectively (see equation 3.14). Standard Gibb's free energy change (ΔG^o) was determined using equation 3.16 and the result is presented in equations 3.14 to 3.16.

$$\Delta G^o = -RT \ln K_d \tag{3.14}$$

$$\ln K_d = \frac{\Delta H^o}{R} - \frac{\Delta S^o}{RT} \tag{3.15}$$

$$\Delta G^o = \Delta H^o - T\Delta S^o \tag{3.16}$$

Where ΔG^o is the standard Gibb's free energy change for the adsorption (J/mol), R is the universal gas constant, T is the temperature (K), K_d is the distribution coefficient of the adsorbate, is the R=8.3149x10^3(ΔH^o)is the s the standard enthalpy change (ΔS^o) is the standard entropy change.

3.2.14 Desorption experiment

Desorption studies were performed using 0.025, 0.08 and 0.1 moldm^{-3} HNO$_3$ solutions respectively. The nanocomposites previously exposed to the petroleum refinery wastewater was pulled up from the solution and mixed with 20 cm^3 of HNO$_3$ solutions. The agitation was performed on the orbiter shaker for 15 min. The concentration of the heavy metals was measured. Desorption efficiency was calculated using the following formula in equation 3.17:

$$\text{Desorption efficiency (\%)} = \frac{\text{Concentration of metal desorbed}}{\text{Concentration of metal adsorbed}} \times 100 \tag{3.17}$$

3.2.15 Reusability

To determine the reusability of $Fe_3O_4/SiO_2/ZnO$ nanocomposites adsorption-desorption cycle was repeated four times on the same sample. Desorption studies were performed using 0.1 moldm^{-3} HNO$_3$ solutions. The $Fe_3O_4/SiO_2/ZnO$ nanocomposites previously exposed to the refinery wastewater were desorbed from the solution and mixed with 20 cm^3 of HNO$_3$ solutions. The agitation was performed on the orbiter shaker for 15 min. The desorbed $Fe_3O_4/SiO_2/ZnO$ nanocomposites were used for the removal of the heavy metals from the refinery wastewater by measuring 0.05g of the desorbed nanocomposites into the conical flasks containing 50 cm^3 of petroleum wastewater. The conical flasks were corked and the mixture was stirred continuously on a magnetic stirrer at 250 rpm at 15 min, 30°C, adsorbent and pH of 6.25. The liquid phases were separated from the solution by filtration with Whatman filter paper no 4 at the end of each mixing period, and the equilibrium concentrations of Pb (II) Cd (II), Ni (II) Cr(VI), Cu (II) and total iron ions, were determined using AAS (Singh *et al*., 2016).

3.2.16 Characterisation of the $Fe_3O_4/SiO_2/ZnO$ nanocomposites after the desorption

The $Fe_3O_4/SiO_2/ZnO$ Nanocomposites prepared at different mixing ratios were characterlised after desorption of the heavy metals using the same procedures as described in sections 3.4.2 and 3.4.3.

3.2.17 Antibacterial activity of the $Fe_3O_4/SiO_2/ZnO$ nanocomposites

3.2.17.1 Bacterial cultures used

The bacterial cultures used in this study are *E. coli, Salmonella typhi* and *Klebsiella pneumoniae*. All the bacteria were collected from General Hospital Minna, Niger state.

3.2.17.2 Preparation of nutrient agar

Seven grams (7g) of agar powder was weighed and dissolved into a 250 cm^3 volumetric flask with distilled water. The mixture was roughly stirred with a rod to fully dissolve all components, the autoclaved for 30 minutes at 120°C. This was allowed to cool under room temperature but not solidify. The agar was poured into each petri dish and left on the sterile surface until the agar solidified.

3.2.17.3 Antimicrobial susceptibility test

The antimicrobial activity of the ternary $Fe_3O_4/SiO_2/ZnO$ (1:1:1), $Fe_3O_4/SiO_2/ZnO$ (1:1:2), $Fe_3O_4/SiO_2/ZnO$ (1:2:1) and $Fe_3O_4/SiO_2/ZnO$ (2:1:1) nanocomposites on the *E.coli, Salmonella typhi and Klebsiella pneumoniae* were determined at different concentrations of the nanocomposites using Agar diffusion method. Each of the microorganisms (*E. coli, Salmonella typhi and Klebsiella pneumoniae*) (Mohamed *et al*., 2020). In this method nutrient, agar medium was prepared and poured into Petri dishes and allowed to solidify and labeled properly. A sterile cork borer (4mm) was used; five holes were bored on the surface of the agar medium equidistant from one another. Various concentrations of the nanocomposites (20 mg/ml, 40 mg/ml, 60 mg/ml, 80 mg/ml and 100mg/ml) were introduced into the holes and allowed to fully diffuse at room temperature, after which were inoculated with *E. coli, Salmonella typhi and Klebsiella pneumoniae* respectively. The plates were incubated at 37°C for 24 h. The nanocomposites of the radial growth were then observed after incubation. The resulting zones of inhibition were measured with a millimeter ruler for each bacterial strain. The experiment was repeated three times and average values were reported.

3.2.18 Antioxidants activity of the ternary Fe₃O₄/SiO₂/ZnO nanocomposites

2,2-diphenyl-1-picrylhydrazyl (DPPH) method was used to determine the free radical scavenging activity ternary $Fe_3O_4/SiO_2/ZnO$ (Cao *et al.*, 2020). An equal volume (1 cm^3) of each of the nanocomposites of various concentrations (6.25 – 500 µg/mL) and 0.4 mM methanolic solution of DPPH were mixed in a test tube. The mixture was left in the dark for 30 mins and the absorbance was recorded at 516 nm. The percentage inhibition of DPPH radical was subsequently calculated for the reference (which contains all the reagents without the test sample) using the equation 3.18:

$$\text{Inhibition (\%)} = \frac{A0 - A1}{A0} \; X \; 100 \tag{3.18}$$

Where A_0 is the absorbance of the control (without sample) and A_1 is the absorbance of the sample and DPPH solution.

CHAPTER FOUR

4.0   **RESULTS AND DISCUSSION**

4.1   Characterisation of Nanoparticles and Nanocomposites

Characterisation of Fe_3O_4, SiO_2, ZnO nanoparticles, ZnO/Fe_3O_4, ZnO/SiO_2, Fe_3O_4/SiO_2 and $Fe_3O_4/SiO_2/ZnO$ nanocomposites were carried out to determine their mineralogical phases, morphology, elemental compositions, chemical states and surface areas using X-ray diffraction (XRD), High-Resolution Scanning Electron Microscopy (HRSEM) coupled with Energy Dispersive Spectroscopy respectively, and X-ray Photoelectron Spectroscopy (XPS), Brunauer, Emmett., and Teller − N_2 adsorption-desorption method (BET). The results of each analysis are presented and discussed in the subsequent section.

4.2   Analysis of Fe_3O_4 Nanoparticles

4.2.1   HRSEM analysis of Fe_3O_4 nanoparticles

The surface morphologies of the Fe_3O_4 nanoparticles synthesised were studied by HRSEM and the results are shown in Plate III.

Plate III: **HRSEM Images of Fe₃O₄ Nanoparticles Calcined at (a) 100 °C (b) 300°C and (c) 500 °C. (d) 700°C**
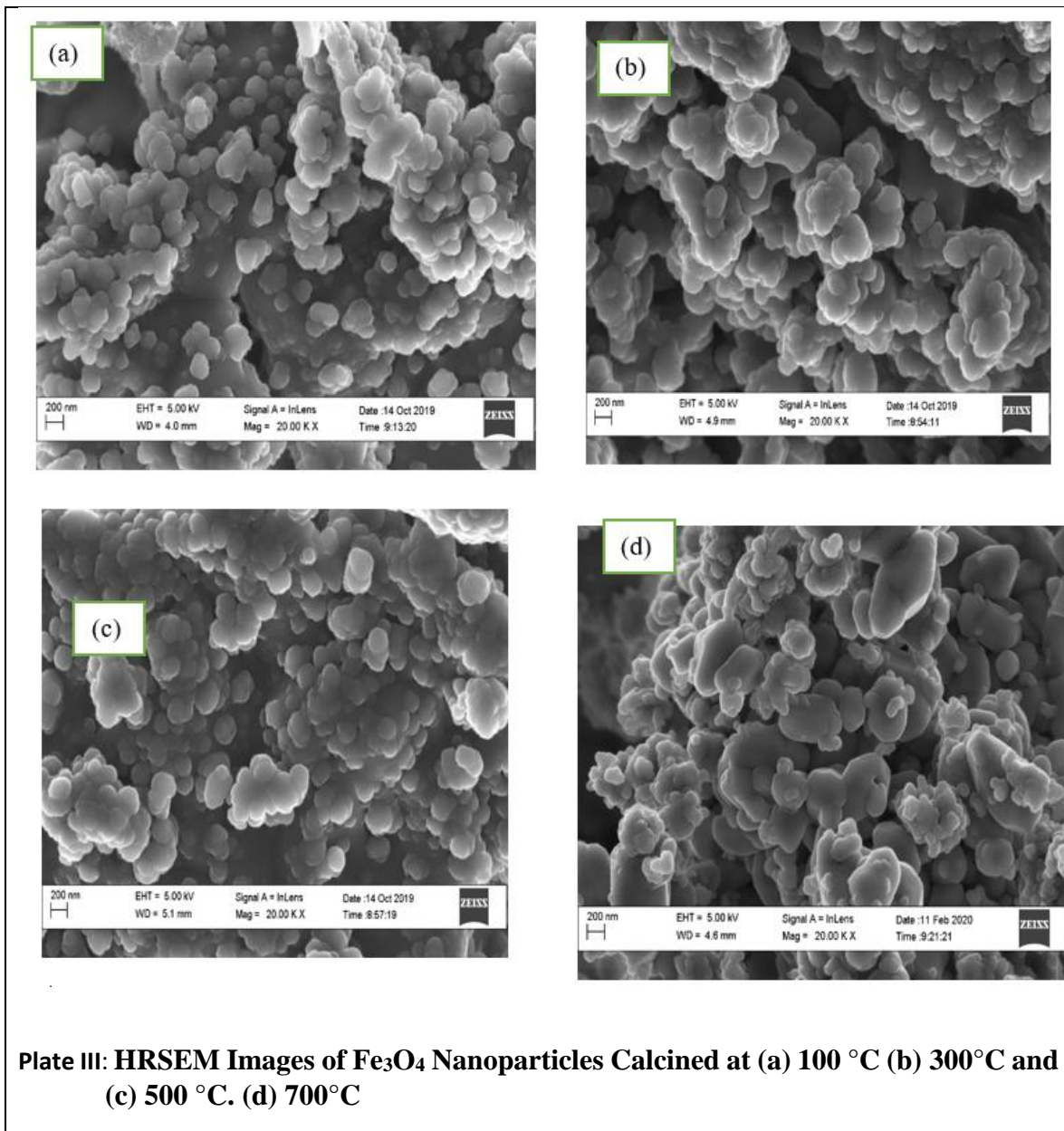
Plate III (a) reveals the formation of widely scattered spherical-shaped particles. The HRSEM in Plate IIII (b) shows the formation of distinct spherical shapes of Fe₃O₄ nanoparticles. From the result, it could be noted that clearer spherical shape of Fe₃O₄ nanoparticles was formed compared with the image in Plate IIII (a). This result agrees with the analysis of the XRD of Fe₃O₄ nanoparticles, where the crystallite size decreases from 16.712 nm (see Figure 4.1 (a))

to 14.170 nm (see Figure 4.1 (b)). This may be due to the increased coalescence or fusion effect of the nanoparticles leading to the reduction of the size of the Fe_3O_4 nanoparticles. The HRSEM in Plate III (c) revealed a more agglomerated spherical shape with a bigger particle size. At 700°C (Plate III (d)) the agglomerated larger spherical shape was observed compared with the Fe_3O_4 calcined at 100 °C 300 °C, 500 °C. This may be due to the effect of high calcination temperature which favoured particle size growth (Akbarzadeh *et al.*, 2018). In addition, agglomeration also occurs at high temperatures because of the sintering effect in which the particles move together during the dehydration process (Toledo *et al.*, 2023). The observation in this study indicates that the temperature rise can induce a change in particle morphology with a more regular crystal shape. The observed trend may also be linked to recrystallization and aggregation of the particles during calcination, in which the small thermodynamically stable Fe_3O_4 nanoparticles fused to form larger nanoparticles (Berent *et al.*, 2019). This analysis shows that temperature rise promoted a change in the particle morphology

4.2.2   XRD analysis of Fe_3O_4 nanoparticles

The mineralogical phases of the Fe_3O_4 nanoparticles prepared via the sol-gel reduction method and calcined at different temperatures were investigated using XRD and the results are shown in Figure 4.1
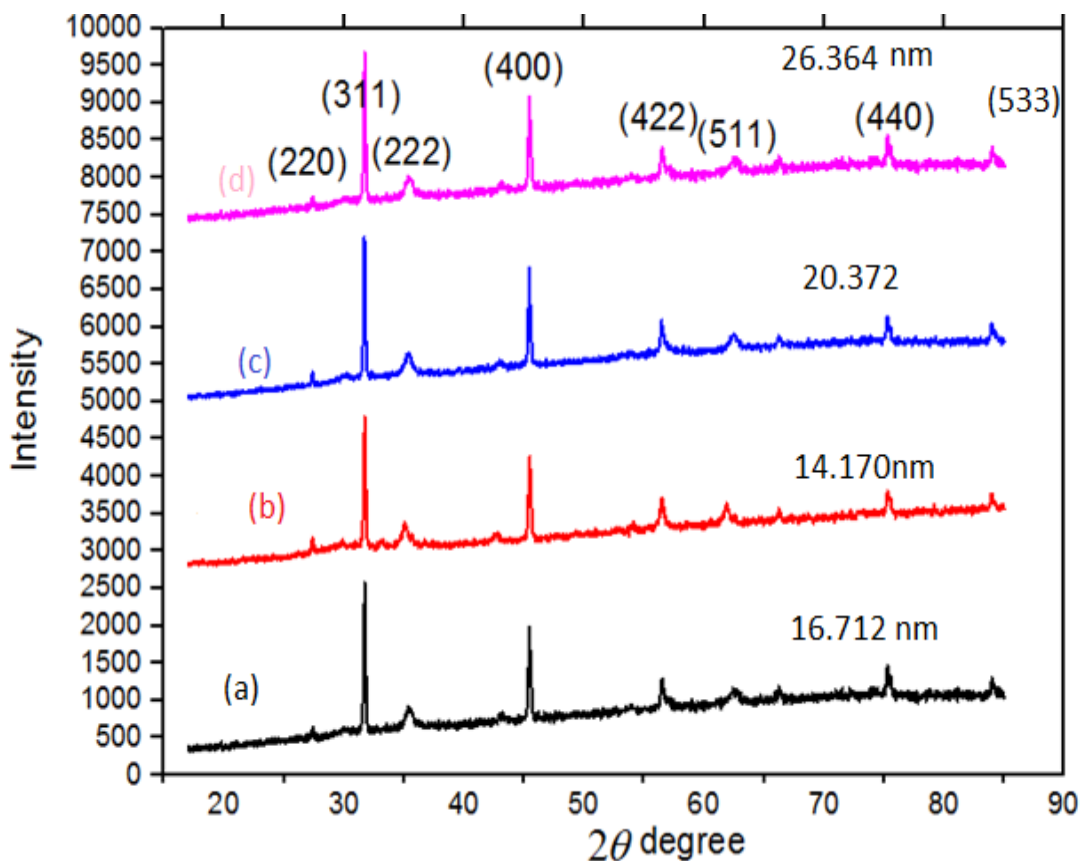
Figure 4.1: XRD Patterns of Pure Fe₃O₄ Nanoparticles Calcined at (a) 100 °C, (b) 300 °C (c) 500 °C and 700 °C

Figure 4.1 reveals the presence of sharp intense and medium diffraction peaks at 2θ values of 27.43°, 31.65°, 35.42°, 45.51°, 54.01°, 56.44°, 62.66 ° and 75.28°, which correspond to the following crystal planes of (220), (311), (222), (400), (422), (511), (440), and (533). The analysed diffraction peaks matched well with the standard magnetite of face-cantered cubic structure with unit cell length of a = 8.396 (JCP2-190629) irrespective of the calcination temperature, which conformed to the crystallographic system of the cubic structure of Fe₃O₄ nanoparticles phase. The crystallite size was estimated using the Debye Scherrer equation and the value ranges from 14.170 – 26.3464 nm as the calcination temperature increases from

300°C to 700°C. This is evidence of increased crystallinity and purity of the synthesised Fe_3O_4 nanoparticles as the calcination temperature increases. Chomchoey *et al*., (2018), found that as the calcination temperatures increase from 80° C, 350° C to 700°C, the crystallite size also increases from 12.7 nm, 18.5 nm, to 27.6 nm respectively. The result also corroborated the work of Hossain *et al.* (2018) who also found that the crystallite size increases from 18.46 nm to 27.68 nm as calcination temperature increased from 250°C to 300°C respectively. This implies that crystallite size is greatly influenced by calcination temperature and most cases directly proportional. In addition, Ruíz-Baltazar *et al.* (2015) studied the effect of PVP on the synthesis of Fe nanoparticles via chemical reduction using $NaBH_4$ as a reducing agent and PVP as a capping agent. The authors reported the existence of Fe, Fe_2O_3, and Fe_3O_4. The existence of Fe, and Fe_2O_3 in their analysis may be due to no thermal treatment during the process of the synthesis of the nanoparticles. The method employed in this work may be an alternative way to synthesise pure Fe_3O_4 nanoparticles without the presence of other forms of iron nanoparticles. The possible reaction mechanisms for the synthesis of Fe_3O_4 using $NaBH_4$ and PVP were proposed (see equation 4.1-4.10). In conclusion, pure Fe_3O_4 cannot be synthesised by sol-gel reduction alone using $NaBH_4$ without thermal treatment.

$$FeCl_3 + 6NaBH_4 + 18H_2O \leftrightarrow Fe^{2+} + 6NaCl + 6B(OH)_3 + 21H_2 \qquad (4.1)$$

$$Fe + 2H_2O \longrightarrow Fe^{2+} + H_2 + 2OH^- \text{ (Slow)} \qquad (4.4)$$

$$Fe^{2+} + O_2 + 2H_2O + 4e^- \longrightarrow 2Fe^{2+} + 4OH^- \text{ (fast)} \qquad (4.5)$$

$$4Fe^{2+} + 3O_{2} + 8e^- \longrightarrow 2Fe_2O_3 \qquad (4.6)$$

$$3Fe + 4H_2O \rightleftharpoons Fe_3O_4 + 4H_2 \qquad\qquad (4.7)$$

$$4Fe_2O_3 + Fe \longrightarrow 3Fe_3O_4 \qquad\qquad (4.8)$$

$$3\ Fe_2O_3 + H_2 \rightleftharpoons 2Fe_3O_4 + H_2O \qquad\qquad (4.9)$$

$$3Fe_2O_3 + CO \longrightarrow 2Fe_3O_4 + CO_2 \qquad\qquad (4.10)$$
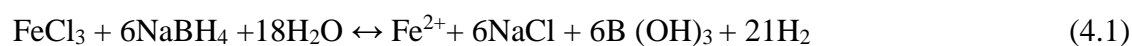
Equation 4.3 is the reaction between the iron (III) chloride ($FeCl_3$) and sodium borohydride $NaBH_4$ in water (H_2O) to form Fe^{2+}. The Fe^{2+} reacts with (H_2O) and oxygen (O_2) to form iron (II) oxide (Fe^{2+}) in solution (see equations 4.4 and 4.5). This reaction is faster in the presence of water. The Fe^{2+} oxide further reacts with O_2 and formed of Fe_2O_3 (see equation 4.6). The Fe^{3+} in the solution that did not completely reduce by the $NaBH_4$ further, react with H_2O to form magnetite under hydrothermal conditions (see equation 4.7). The Fe_2O_3 form could also react with iron metal (Fe) through the hydrothermal process to form Fe_3O_4 under thermal conditions.

4.2.3   EDS analysis of Fe₃O₄ nanoparticles

The Energy-dispersive X-ray spectroscopy (EDS) was used to analyse the chemical composition of the Fe_3O_4 nanoparticles and the result is shown in Figure 4.2.
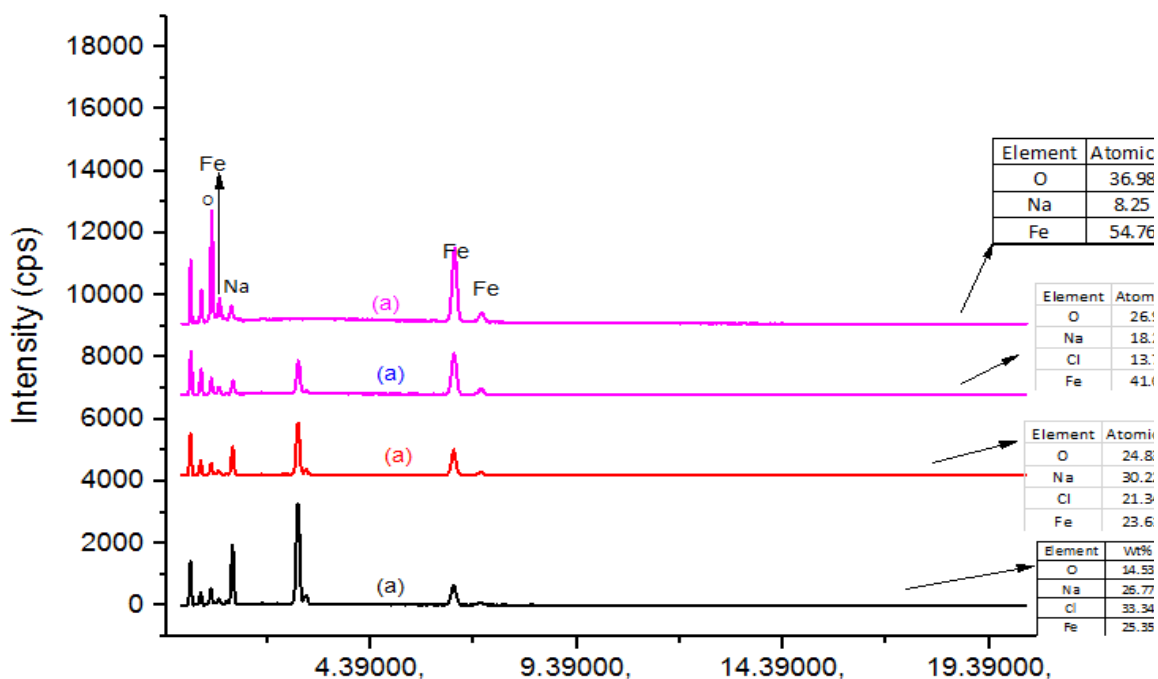
Figure 4.2: X-ray Energy Dispersive Spectrometry Spectra of Pure Fe₃O₄ Nanoparticles Calcined at (a) 100°C (b) 300°C and (c) 500 °C and 700°C

The EDS spectra revealed the presence of Fe, O, Na and Cl elements in all the samples except sample (d) due to the increases in the calcination temperature. The Fe ions concentration (wt. %) was found to be 25.35 %, 23.61 % and 41.03 %, 54.76 % for samples calcined at 100 °C, 300 °C, 500 °C and 700 °C respectively. This implies that calcination temperature plays an important role in the purification and removal of unwanted materials in the nanoparticles. The EDS spectrum indicates that the synthesised nanoparticles contain Fe, Zn, and O as the major elements with Na and Cl detected in minute quantities. The peak of O appears at 0.54 keV, Fe signal appears at 0.72 keV, 6.43 keV, and 7.10 keV while the appearance of Na and Cl at 1.06 keV and 2.62 keV indicate the presence of some contaminants. The results show the removal of chloride ions at a very high temperature in

114

the sample. This promoted the co-precipitation of Fe $(OH)_2$ and α-FeOOH, resulting in the rapid formation of a single Fe_3O_4 nanoparticle phase. The Fe and O contents increase as temperature increases, due to the reduction of other impurities such as sodium, carbon and chlorine that might have formed a complex or precipitated with the Fe^{2+} or Fe^{3+} in the solution.

4.2.4   Fourier transform infrared spectroscopy (FTIR) analysis of Fe_3O_4 nanoparticles

FTIR analysis of Fe_3O_4 nanoparticles was investigated to confirm the presence of the functional groups in Fe_3O_4 nanoparticles and the result is given in Figure 4.3
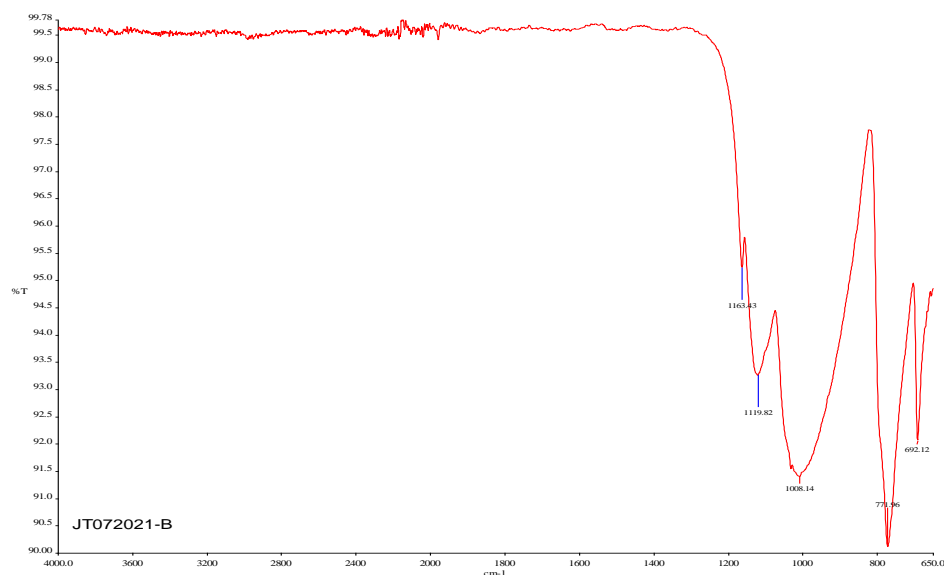
Figure 4.3: FTIR Spectra of Fe_3O_4 Nanoparticles

The absorption bands at 692.12 and 771.96 cm^{-1} in Figure 4.3 correspond to the stretching vibrations and vibration of Fe–O, respectively.   The vibration bond at 1119 cm^{-1} can be linked to the C–O bond, a similar bond has been reported by Abdolmohammad-Zadeh *et al*. (2020). Another adsorption bond appears at a wavelength of 1163 cm^{-1} corresponding to the

C-O-C bond. Additionally, the adsorption bond at 1035 cm^{-1} is due to the N-H stretching and bending vibration of the amine NH$_2$ group in the PVP used as the structure-directing agent (Aboelwafa *et al.*, 2021). The formation of different bonds from the FTIR result is due to bonds resulting from the formation of Fe$_3$O$_4$ nanoparticles with other compounds used during the synthesis of Fe$_3$O$_4$ nanoparticles

4.2.5   Brunauer–Emmett–Teller (BET) analysis of Fe$_3$O$_4$ nanoparticles

The Brunauer–Emmett–Teller (BET) N$_2$ adsorption-desorption method was used to investigate the surface area, pore diameter and pore volume of the Fe$_3$O$_4$ nanoparticles and the result is presented in Figure 4.4.
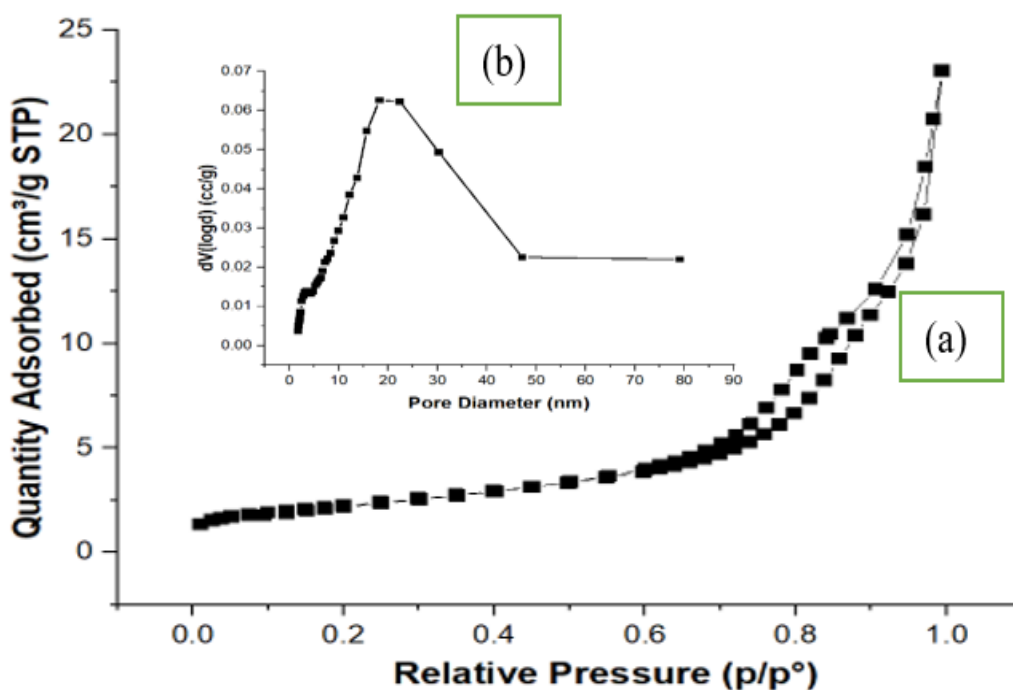
Figure 4.4: (a) Nitrogen Adsorption Desorption Isotherms and (b) Pore Size Diameter Distributions for Fe$_3$O$_4$ Nanoparticles

Figure 4.4 (a) shows a monolayer of nitrogen gas was adsorbed on the surface of the Fe_3O_4 nanoparticles at low relative pressure at the knee of the isotherm curve. When the pressure was raised to a modest level (0.50 p/p^0), a multilayer of adsorbed gas formed, which then condensed at high pressures within pore structures (0.90 p/p^0). The surface area was found to be 7.864 m^2/g. The pore volume of Fe_3O_4 nanoparticles was determined to be 4.2 cm^3/g. The inserted pores diameter in Figure 4.4 (b) is 18.245 nm which is less than 50 nm, suggesting that the prepared material is mesoporous. According to the IUPAC classification, the hysteresis loop indicates a type IV adsorption isotherm. The 7.864 m^2 g^{-2} surface area recorded in this analysis is higher than the 6.8 m^2 g^{-1} reported for Fe_3O_4 nanoparticles (80 nm) synthesised via the co-precipitation method and lower than the 1006.8 m^2 g^{-1} recorded for Fe_3O_4 nanoparticles with a smaller crystallite size (10 nm) as reported by Iconaru *et al.* (2016). This is an indication that the crystallite size of Fe_3O_4 nanoparticles plays an important role in the surface area of the nanoparticles. However, another researcher has also reported the surface area of Fe_3O_4 nanoparticles to be 82.490 m^2 g^{-1}, 110.94 m^2 g^{-1}, 88.142 m^2 g^{-1} for Fe_3O_4 nanoparticles with crystallite sizes of 35, 32 and 30 nm 82.490 nm (Pandey *et al.*, 2018). These values are higher than the surface area recorded in this analysis. This difference may be linked to the method used for the synthesis of the Fe_3O_4 nanoparticles.

4.2.6 XPS analysis of Fe₃O₄ nanoparticles

The XPS analysis of the Fe_3O_4 nanoparticles was studied to determine the oxidation states and the chemical bonding of the elements in Fe_3O_4 nanoparticles and the results of the general XPS survey is presented in figure 4.5
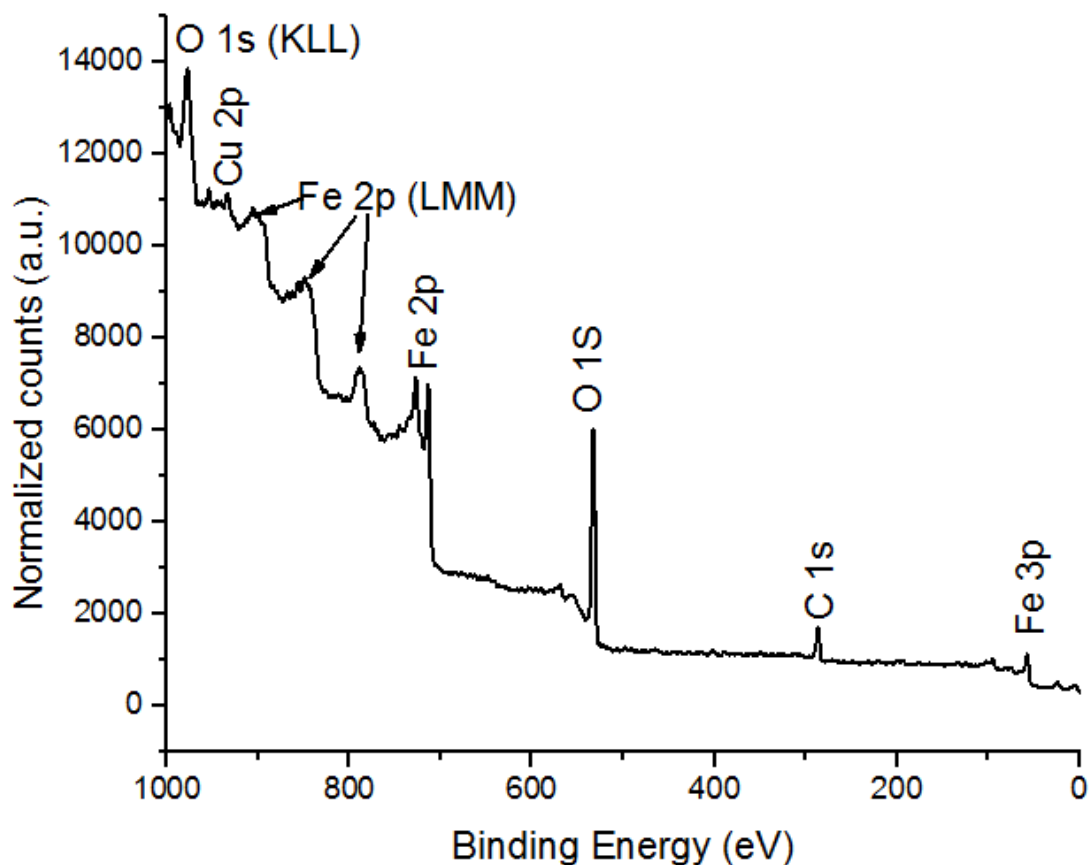
Figure 4.5: General XPS Survey Spectrum of Fe₃O₄ Nanoparticles

The General XPS survey spectra of the Fe_3O_4 nanoparticle presented in Figure 4.5 shows peaks at the binding energies of 288.6 eV, 533.06 eV, 713.5 eV and 727.0 eV belonging to C (1s), O (1s) and double splitting of Fe (2p) in Fe_3O_4 nanoparticles. The Fe (2p) core levels were divided into 2p1/2 and 2p3/2 components with significant split spin-orbit components

(Δmetal) of 14 eV attributed to the existence of Fe in the + 2 and +3 oxidation state. Xie *et al.* (2018) and Huang *et al.* (2019) independently reported similar results with 14.16 eV significant split spin-orbit components. Similar results have also been reported for Fe (2p3/2) and Fe (2p1/2) with 710.4 and 723.2 eV by Shimoshige *et al.* (2017). However, Kac *et al.* (2021) reported peaks at around 710.9 and 724.6 eV for the Fe2p1/2 and 2p3/2. The difference in the reported binding energies may be due to the method of synthesis, precursor, iron salt, reaction and the calcination temperature employed by the authors (Shaba *et al.*, 2021).

The presence of (1s) peak suggests a considerable concentration of carbonaceous material which may be from the PVP used as a capping agent during the synthesis of Fe_3O_4 nanoparticles. The presence of Cu at 934.56 eV may be from the Cu holder used during the XPS analysis. Xie *et al.* (2019); have reported similar observations from their analysis. They attributed the various peaks exhibited at a binding energy of 286.35 eV, 533.02 eV, and 712.01 eV to the presence of C 1s, O 1s, and Fe 2p for the magnetite respectively. In another analysis by Momose *et al.,* (2020), the presence of the Fe 2p3/2 peak at a binding energy of 711.1 eV was attributed to both Fe^{2+} and Fe^{3+} signals in Fe_3O_4. The deconvoluted XPS analysis of Fe was further carried out and the result is shown in the next section.

4.2.7 XPS analysis of the Fe_3O_4 Fe (2p3/2) orbital in nanoparticles

The XPS analysis of the Fe_3O_4 nanoparticles was studied to determine the deconvolution in Fe 2p3/2 peaks and the results are presented in figure 4.6
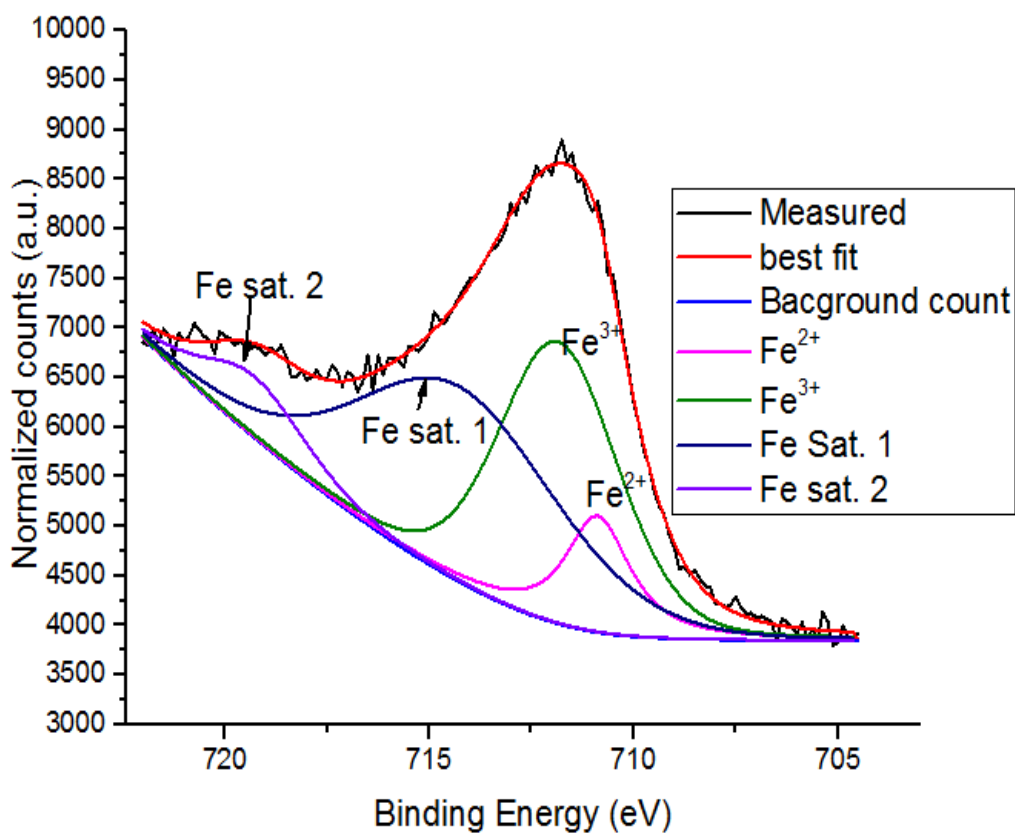
Figure 4.6: High-Resolution XPS Spectrum Fe 2p$_{3/2}$ Peak

As shown in Figure 4.6, two main peaks and two satellite peaks belonging to Fe 2p1/2 and Fe 2p3/2 orbitals were observed. The binding energy of 710.96 eV is a characteristic of Fe^{2+} ions, with a corresponding satellite at 719.30 eV and 714.30 eV and the octahedral Fe^{3+} was found at 711.88 eV binding energy (Momose *et al*., 2020). Similar results have been reported

by Momose *et at*., (2020). The authors ascribed the binding energies (eV) for Fe 2p3/2 for iron metal and iron oxides: to be 708.3 eV of Fe_3O_4

4.2.8 Oxygen 1s peaks of Fe_3O_4 nanoparticles

To understand the nature of the oxygen bonds in Fe_3O_4 nanoparticles synthesised XPS was used and the result is presented in Figure 4.7
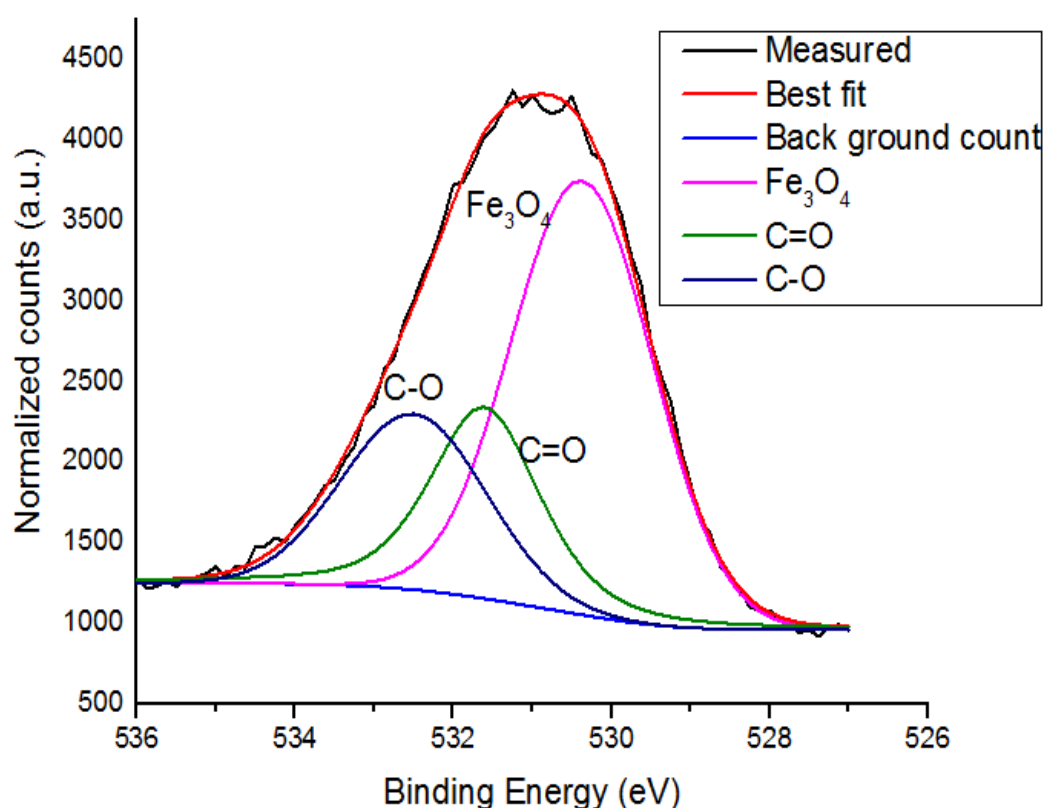
Figure 4.7: The Oxygen 1s Peaks of Fe_3O_4 Nanoparticles

The O (1s) spectrum shown in Figure 4.7 indicates the presence of three peaks at binding energies of 531.6 eV, 532.6 eV, and 530.3 eV, which correspond to carbon double bond to oxygen (C=O), single bond to carbon (C-O) and, lattice oxygen in Fe_3O_4 (Hui *et al*., (2018).

The C=O and C-O bond originated from the polymer (PVP) used during the synthesis of the Fe$_3$O$_4$ nanoparticles. Similarly, the analysis by Hui *et al.* (2018) also confirmed the presence of carbon bonds and oxygen lattice in Fe$_3$O$_4$ at binding energies of 530.5 and 531.7 eV respectively. Furthermore, Hu *et al.* (2019) also observed the binding energies in 529.7, 531.9 and 533.3 eV in O (1s) spectral, which correspond lattice oxygen in Fe$_3$O$_4$, C-O bond and C-H and O-H bonds respectively. Bandara *et al.* (2020) have reported a similar observation and attributed it to the presence of C−C, O−C-O, C−O−C, C−OH and C−O in the poly (acrylic acid) and oil used for the synthesis.

4.2.9   XPS analysis of the C (1s) orbital in Fe$_3$O$_4$

XPS was used to study the nature of the adventitious carbon bonds in Fe$_3$O$_4$ nanoparticles synthesised, and the result is presented in Figure 4.8
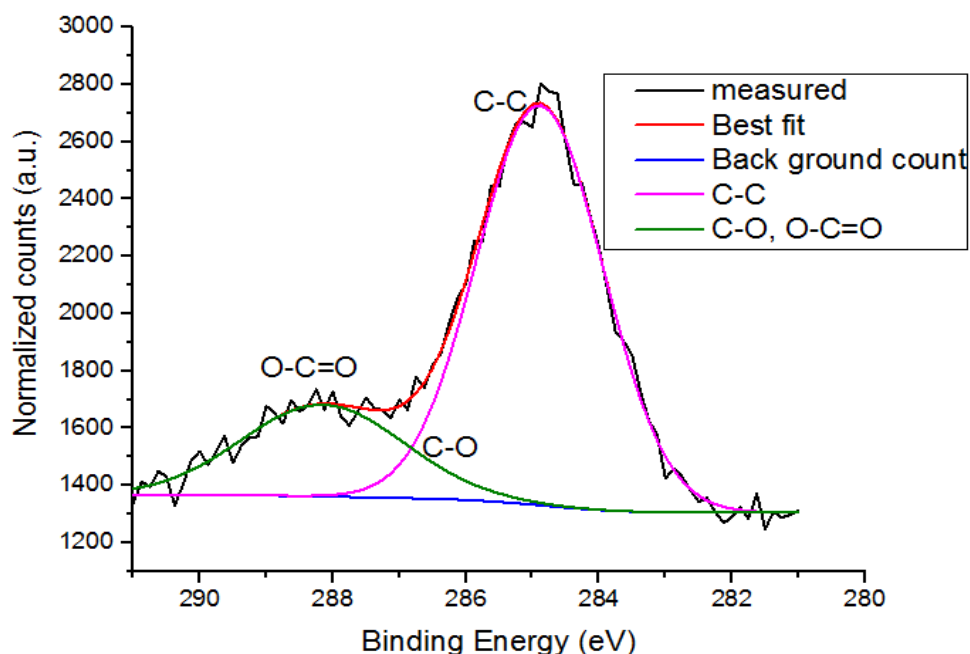
Figure 4.8: XPS Scan for the C (1s) Envelope for Fe3O4 Nanoparticles

Figure 4.8 shows the deconvoluted C 1s spectrum at the binding energies of 284.8 eV, 286.4 eV, and 288.5 eV corresponding to the following carbon frameworks C-C, C-O-C and O-C=O respectively. These three peaks originated from the PVP used as the capping agent. Guo *et al.* (2018) reported similar peaks from Fe_3O_4-graphene composites. Additionally, Abazari *et al.* (2021) also noted the presence of sp^2 (C=C, 284.8 eV), epoxy/hydroxyls (C–O, 286.2 eV), Carbonyl (C=O, 287.8 eV) and carboxylates (O-C=O, 289 eV) in the synthesised of Fe_3O_4 nanoparticles embedded in 3D carbonaceous nanocomposites. The presence of single or double bonds as shown in Figure 4.8 may be due to sp^2 and/or sp^3 hybridizations and sp^2 and/or sp^3 carbon bonded to oxygen groups like hydroxyl (C–OH), carbonyl (C=O), and carboxyl (C–OOH) (Lesiak *et al.*, 2018)

4.4   Analysis of SiO_2 Nanoparticles

4.3.1   HRSEM analysis of SiO_2 nanoparticles

The surface morphologies of the SiO_2 nanoparticles prepared from metakaolin at different aging times were studied using HRSEM and the results are shown in Plate IV.
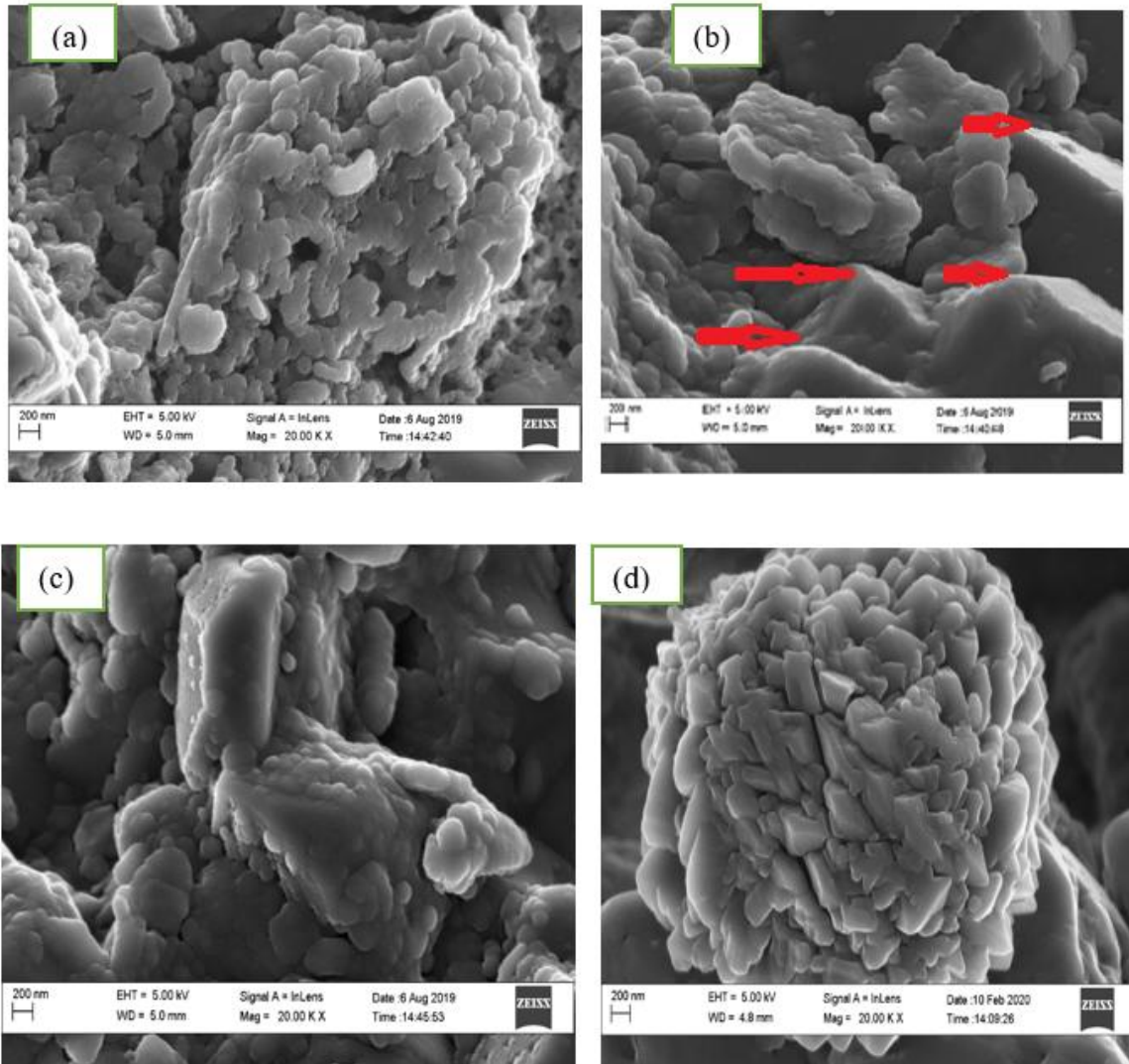
Plate IV: HRSEM Images of SiO₂ Nanoparticles Obtained from Metakaolin at Aging Times of (a) 3 h (b) 6 h and (c) 9 h and (d) 12 h

The HRSEM results show that the morphology of the SiO$_2$ synthesised changes from the agglomerated spherical shape in Plate IV (a) to a mixture of spherical and pyramid-like shapes in Plate IV (b). Also, irregular structural shape and uniform layered component in Plate IV (c) as well as the fused pyramid-like shape shown in Plate IV (d). The structural

transformation could be due to the increase in the aging time from 3 h to 12 h as shown in

Plate IV. A longer aging time increases the condensation of silicon materials, creating more

crystalline solids and a change of structure. The observation may also be attributed to the fact

that longer aging time increases the collision rate between Si particles leading to the

formation of a more homogeneously shaped network of SiO_2 structures (Boles *et al.*,

2016). The trend observed in phase changes result is an indication that aging time influenced

the size and morphology of the SiO_2 nanoparticles from natural Kaolin (metakaolin). The

morphologies of the SiO_2 nanoparticles obtained in the present study are different from the

findings of Slatni *et al*. (2020). They reported platy particle shape using the difference

method. The difference in the morphologies observed could be due to the different methods

of synthesis employed.

4.3.2 XRD analysis of SiO$_2$ nanoparticles prepared at the different aging time

The mineralogical phase of the SiO2 nanoparticles prepared from metakaolin at the different

aging times was investigated using XRD and the results are shown in Figure 4.9
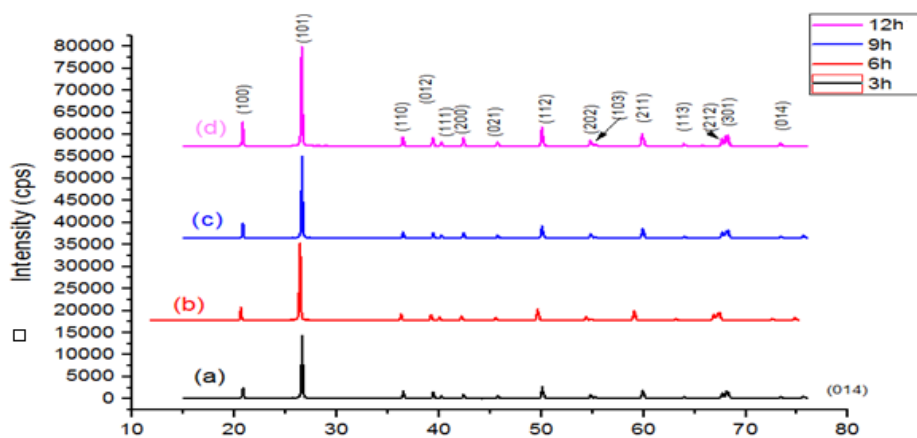
Figure 4.9:   **XRD pattern of the SiO2 Nanoparticles Prepared at (a) 3 h (b) 6 h and (c) 9 h and (d) 12 h**

Figure 4.9 indicates the presence of diffraction peaks at 2θ values of 20.81°, 26.51°, 36.49°, 39.39°, 40.22°, 42.39°, 45.71°, 50.04°, 54.77°, 55.21°, 59.86°, 63.90°, 67.62°, 68.19°, and 73.29° which correspond to crystal planes of (100), (101), (110), (012), (111), (200), (021), (112), (202), (103), (211), (113), (212), (301) and (014) respectively. The diffraction peaks correspond to various SiO_2 nanoparticles with JCP2-83-0539 (Fneich *et al*., 2021). The variation of the aging time between 3 h to 9 h led to the formation of hexagonal structure α-quart phase of SiO_2 nanoparticles with a unit cell of a = 4.92100, c = 5.41630 Z = 3. It was noticed that beyond 9 h tetragonal structure cristobalite phase of SiO_2 nanoparticles was observed with a unit cell of *a*= 4.97320 *c* = 6.92360 and Z = 4 (JCP2-391425). The differences in the unit cell further support the change in phase from quartz to cristobalite. This implies that an increase in aging time at a particular temperature could lead to a change in the phase and crystal size of SiO_2 nanoparticles.

It could be noted in Figure 4.9. that the intensity of the diffraction peak at 2θ value of 20.28 ° increases with increasing aging time from 3 h to 12 h, suggesting an increase in crystallinity of the SiO_2 nanoparticles as the aging time increases. The longer the aging time the better the material characteristics in terms of its purity, rigidity and strength (Ubaid *et al*., 2017); because longer aging results in a greater concentration of primary material, and faster crystallization rates (Phelps *et al*. 2020).

During the aging process, more silicon species were formed which further react with sodium hydroxide to form sodium silicate and at a longer aging duration, the dissolution of the sodium silicate was accelerated, prompting the conversion of quartz phase nanoparticles to the cristobalite phase (Munasir *et al.,* 2018). Previous studies have shown that the conversion

of quartz into other forms of silica such as cristobalite and tridymite is time and temperature-dependent with the formation of cristobalite at a low temperature (250 to 260°C) and tridymite at a temperature above 260°C. On the other hand, Perera *et al*., (2019) established the formation of cristobalite as temperature increased from 650°C, to 750°C, to 850°C. Ratnawulan *et al*. (2018) reported the formation of cristobalite from silica sand at 800 °C, 900 °C, 950 °C, 1000 °C, and 1100 °C for 2 h. This temperature is relatively higher than 100 °C used in this research, the change in the phase from α- quartz to cristobalite may be due to the synthesis at a longer aging time of 12 h. The result showed that aging time and not only temperature influenced the phase types.   The crystallite size was calculated using Debye–Scherrer equation (see equation 3.1). It was observed that the average crystallite size increases from 23.00 nm, 23.59 nm, and 28.60 nm, 62.25 nm as aging time increases from 3, 6, 9 - 12 h respectively. The observed increase in the crystallite size could be because the longer ageing time increases the collision rate between Si particles and results in the formation of larger crystallite sizes (Shaba *et al*., 2021).

4.3.3   EDS analysis of SiO_2 nanoparticles

 The elemental contents of synthesised SiO_2 nanoparticles at different ageing times from metakaolin were analysed using Energy-dispersive X-ray spectroscopy (EDS) and the result is presented in Figure 4.10
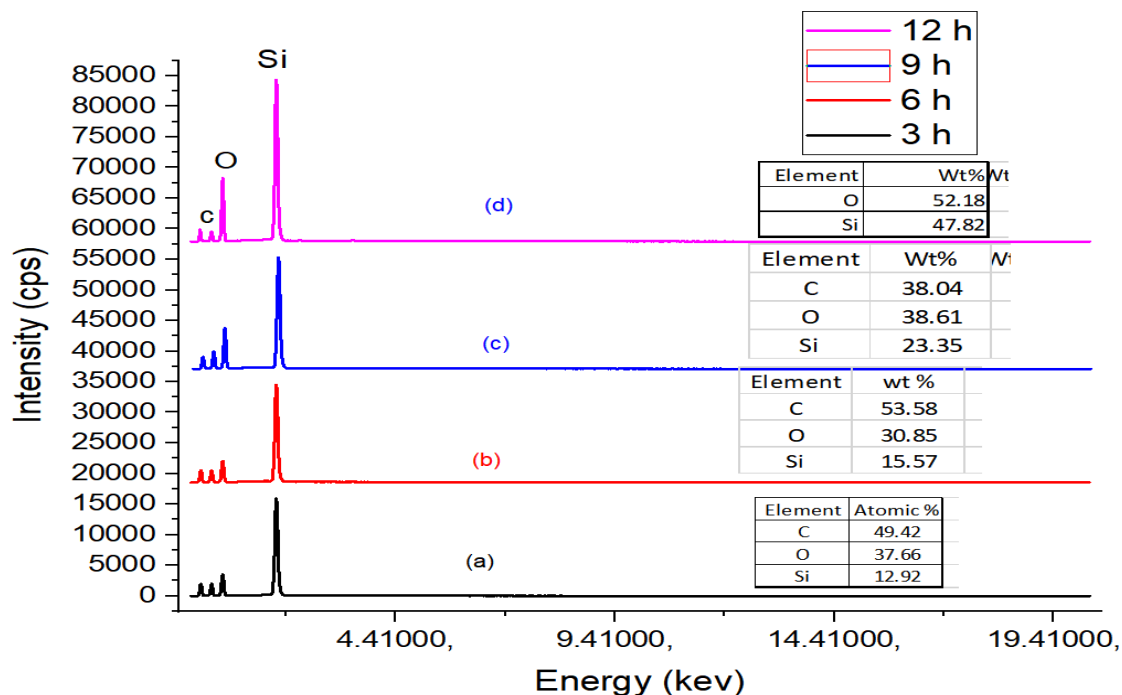
Figure 4.10: EDS of the SiO₂ Nanoparticles at (a) 3 h (b) 6 h (c) 9 h and (d) 12 h

The EDS spectrum of SiO_2 synthesised at 3 h, 6 h, 9 h and 12 h respectively are shown in Figure 4.10. The peaks indicate the weight percentage of major elements present in the samples. Si and O are the dominant elements while C was detected as impurities. The Si, O, and C appear at a binding energy of 1.69 Kev, 0.47 Kev, and 0.250 Kev. The percentage weight (wt %) for the Si^{4+} ion was observed to be 12.9 %, 15.57 % and 23.35 % for Figure 4.10 (a), (b), (c), and (d) respectively. The Si and O contents increase with I increasing ageing time, which is evidence of increased crystallinity. The increase in the percentage composition of oxygen and silicon also suggests the disappearance of the impurities in the samples.

The percentage weights of ion O^{2-} ion in the sample for Figure 4.10 a, b, c, and d were 37.66 %, 30.85 %, 38.61 %, and 52.18 % respectively while the C ion show percentage weight to be 49.42 %, 53.58%, 38.08 % and 0 % for 3 h 6 h 9 h and 12 h respectively. The results agree

with the findings of Singh *et al.* (2017). They synthesised silica using quartz sand as a precursor and confirmed silica as the major component with a very small amount of carbon. The increase in the Si content as a function of aging time suggests an increase in the purity of the prepared sample. The elemental analysis results are similar to the result earlier reported in Plate IV (d) where the SEM image of the SiO_2 nanoparticle synthesised at 2 h shows **a** pyramid-like shape.

The result revealed that the cristobalite phase of SiO_2 was obtained at 12 h which corroborated the XRD result (see Figure 4.9). The observed trend may be explained in terms of longer aging time which accelerated the burning off of carbon atoms from the samples leaving behind only Si and O atoms in the samples.

4.3.4 Fourier transform infrared spectroscopy (FTIR) analysis of SiO_2 nanoparticles

FTIR analysis of the SiO_2 nanoparticles was carried out to determine the functional groups present and the result is presented in Figure 4.11.
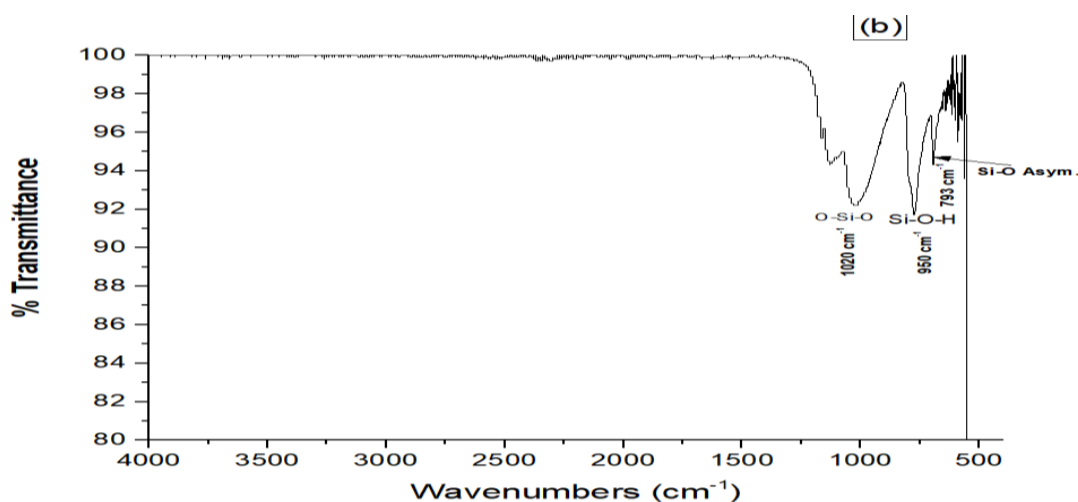
Figure 4.11: FTIR Spectra of SiO_2 Nanoparticles

Figure 4.11 shows a typical FTIR spectrum of O-Si-O nanoparticles in the range 500–4000 cm^{-1} spectral region. The peaks at 793 cm^{-1} and 1020 cm^{-1} correspond to the asymmetric vibration mode and symmetric stretching modes vibration of the SiO_2 groups (O-Si-O) respectively. This result is similar to the adsorption bond reported by Cabello-Ribota *et al.* (2021). The occurrence of asymmetrical Si–H bond vibration is responsible for the peak at 950 cm^{-1}. The appearance of a peak at 1640 cm^{-1} is due to O–H groups of SiO_2 (H bonding) bending of adsorbed water, which is based on water molecular scissor bending vibration. These functional groups may be advantageous in the application of SiO_2 nanoparticles as nanoadsorbent for wastewater treatment.

4.3.5 Brunauer–Emmett–Teller (BET) analysis of SiO₂ nanoparticles

The Brunauer–Emmett–Teller (BET) method was used to determine the surface area, pore diameter and pore volume of SiO_2 nanoparticles and the result is presented in Figure 4.12.
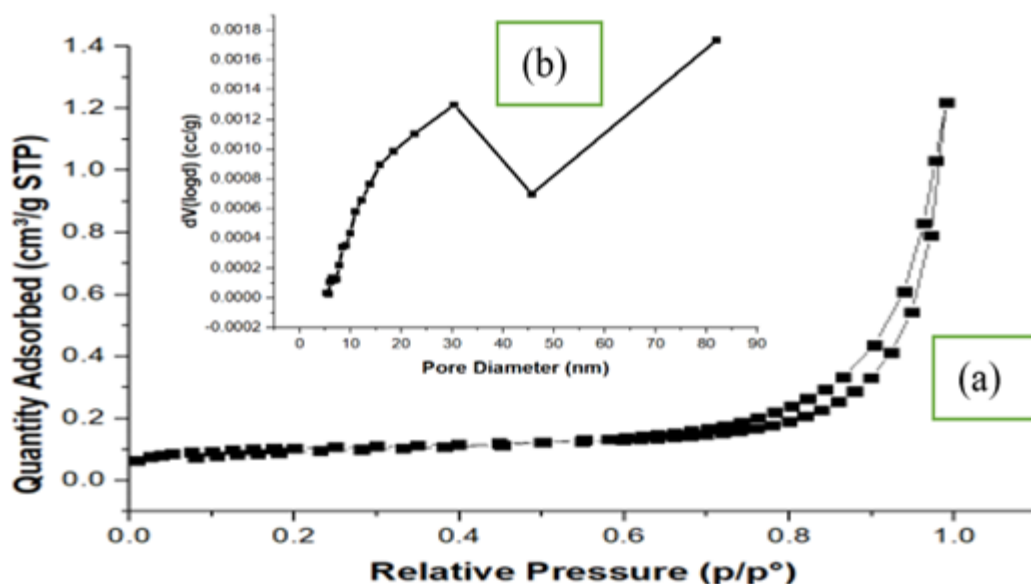
Figure 4.12:   **(a) Nitrogen Adsorption Desorption Isotherms and (b) Pore Size Diameter Distributions for SiO₂ Nanoparticles**

130

Figure 4.12 shows that the adsorption isotherm of SiO_2 nanoparticles exhibited a typical baheaviour similar to that of mesoporous material following the pattern described by IUPAC. Figure 4.12 (a), it can be noticed that SiO_2 nanoparticles exhibited Type IV isotherm of typical mesoporous materials. Figure 4.12 also shows that the hysteresis loops were formed at a relative pressure of 0.57-0.98. The result indicates that SiO_2 nanoparticles have a low surface area of 0.386 m^2/g. with pore volumes and diameters of 0.002 cm^3/g and 32.150 nm, respectively as shown in Figure 4.12 (b). The pore diameter suggests that SiO_2 nanoparticles have mesoporous characteristics in line with the IUPAC classification of pore materials that, the pore diameter between 2 to 50 nm are categorized as mesopores materials. This suggests that the SiO_2 nanoparticles synthesised are mesoporous. Furthermore, Slatni *et al*. (2020) obtained mesoporous silica with a surface area of 161 m^2 /g. contrary to 0.386 m^2 /g obtained in this study. The surface area was obtained in this study. This may be linked to the method of synthesis and the nature of silicon, precursor.

4.3.6 XPS analysis of SiO_2 nanoparticles

The XPS analysis of the SiO_2 nanoparticle was studied to determine the chemical oxidation states of elements. The XPS general survey spectra, deconvoluted spectra of O (1s) and Si (2p) of the SiO_2 nanoparticles are presented in Figure 4.13 (a), (b), and (c) respectively.
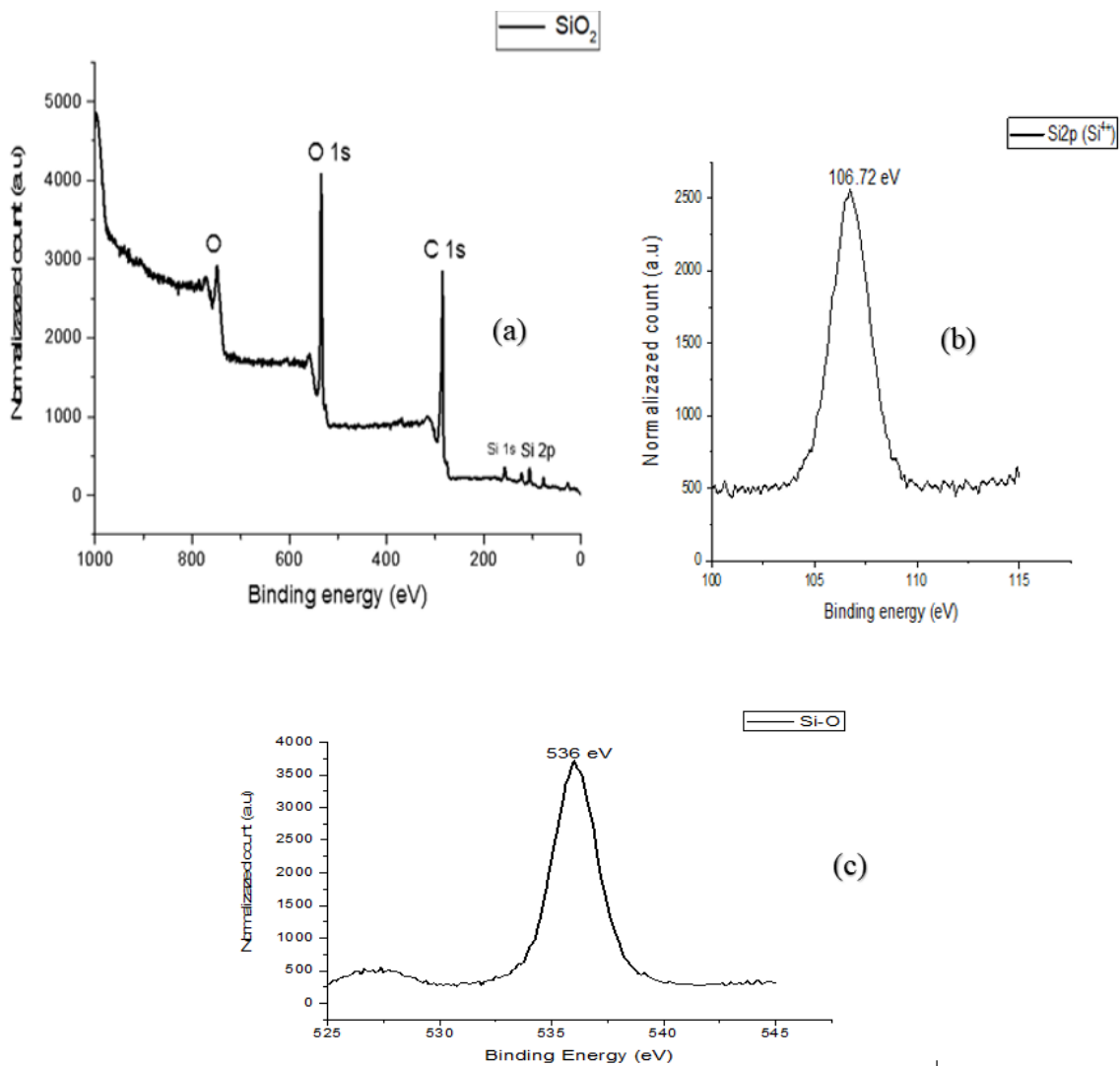
Figure 4.13 (a) XPS Survey Spectrum of the SiO₂ Nanoparticles, XPS Deconvoluted Patterns of the Si (2p) for SiO₂ Nanoparticles and (c) XPS Deconvoluted Patterns of the O 1s for SiO₂ Nanoparticles

Figure 4.13 (a) shows the full XPS survey spectrum of the SiO_2 nanoparticles. The result

indicates the presence of silicon, oxygen and carbon components in the sample with the

electron core level XPS spectra of Si (2p), Si (2s), O (1s), O (2s), and C (1s) respectively.

The result reveals the presence of Si species at 154.2 eV for Si 2s signal peak. The presence

of carbon atoms at the binding energy of 286 eV may be due to the carbon in the quartz sand.

Figure 4.13 (b) shows the presence of a broad peak at the binding energy at 106.72 eV

indicating the presence of Si in +4 oxidation state (Si^{4+}). Figure 4.13 (c) depicts O1s spectra

single sharp peak which appears at the binding energy of 536.3 eV, the presence of a very

high peak clearly shows evidence of more oxygen in the SiO_2 nanoparticles. A similar result

has been reported by Lanco *et al*. (2021). The result obtained from this study is different from

the 532.3 eV reported by Zenkovets *et al*. (2021 or 2020???), due to the difference in the

method, precursors and synthesis processes used for the synthesis of SiO_2 nanoparticles.

4.4   Analysis of ZnO Nanoparticles

4.4.1   HRSEM analysis of ZnO nanoparticles

The surface morphologies of the ZnO nanoparticles calcined at different temperatures were

investigated using HRSEM and the result is shown in Plate V.
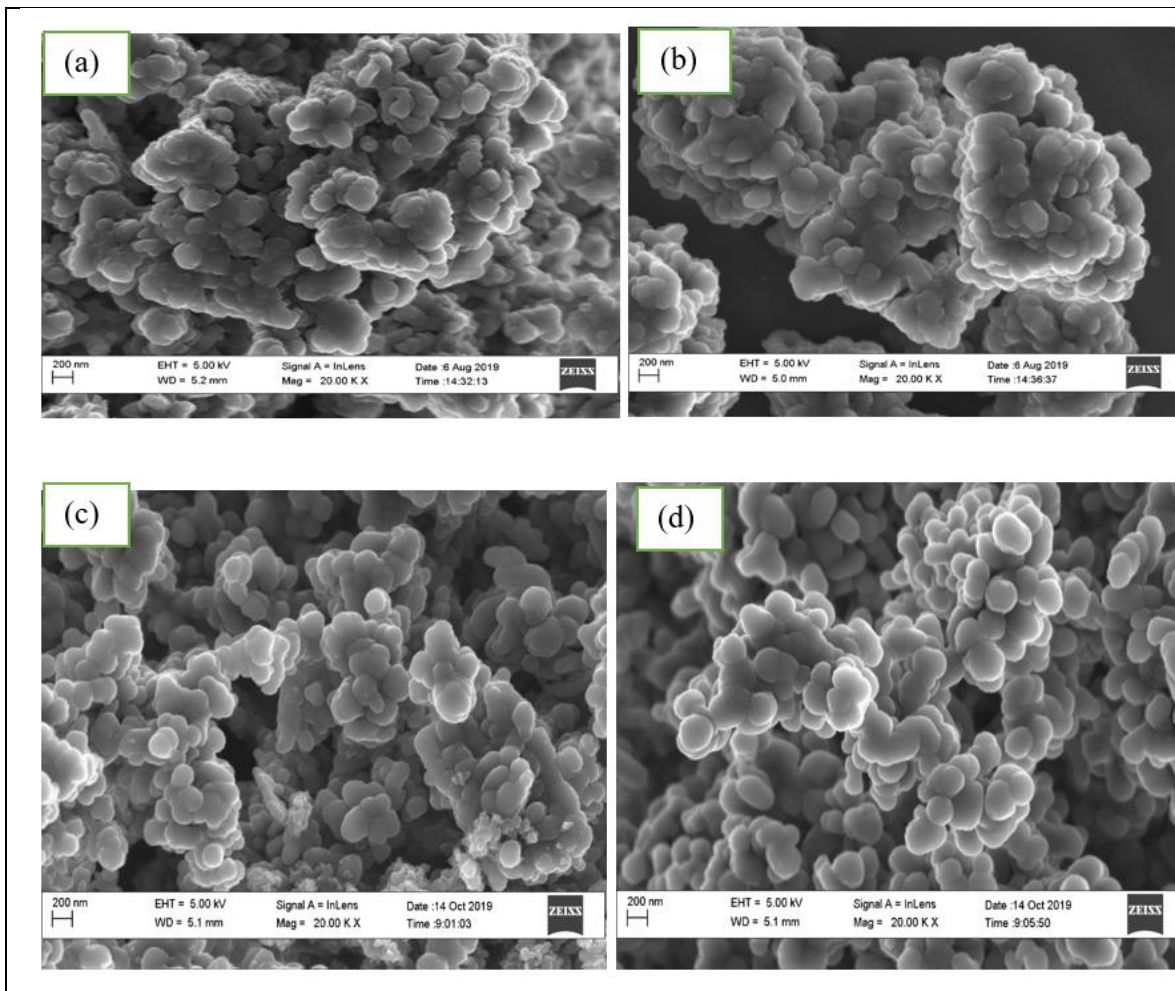
Plate V: **High-Resolution Scanning Electron Microscope (HRSEM) Images of the ZnO Nanocomposites (a) Uncalcined ZnO Nanoparticles at (b) ZnO Calcined at 300 °C (c) 500 °C and (d) 700 °C for 2 h**

Plate V (a) which represents uncalcined ZnO nanoparticles reveals the formation of the densely distributed spherical shape of ZnO nanoparticles while the sample calcined at 300 °C (b) has highly aggregated irregular spherical nanoparticles with a slightly amorphous mixture compared with the HRSEM images in Plate V (c) 500°C and (d) 700°C which indicates well-arranged uniform spherical crystals with the larger sizes. The larger particles were observed as the calcination temperature increased from the ambient to 300° C, 500° C

and 700 ° C respectively. The formation of larger particles as a function of temperature at a specific time (2h) may be attributed to the fast-kinetic energy of the particles resulting in the Ostwald ripening growth mechanism where small zinc oxide nanoparticles that are energetically unstable fused and recrystallize onto larger nanoparticles (Masjedi-Arani *et al.*, 2016; Gharibshahi *et al.*, 2017). The decrease in the agglomeration of nanoparticles during the annealing treatment process may be due to electron transfer between Zn^{2+} and O^{2-} species in the surface energy of the mixture.

4.4.2   XRD analysis of ZnO nanoparticles

The XRD spectra of the ZnO nanoparticles prepared via the sol-gel method and calcined at different temperatures is shown in Figure 4.14.
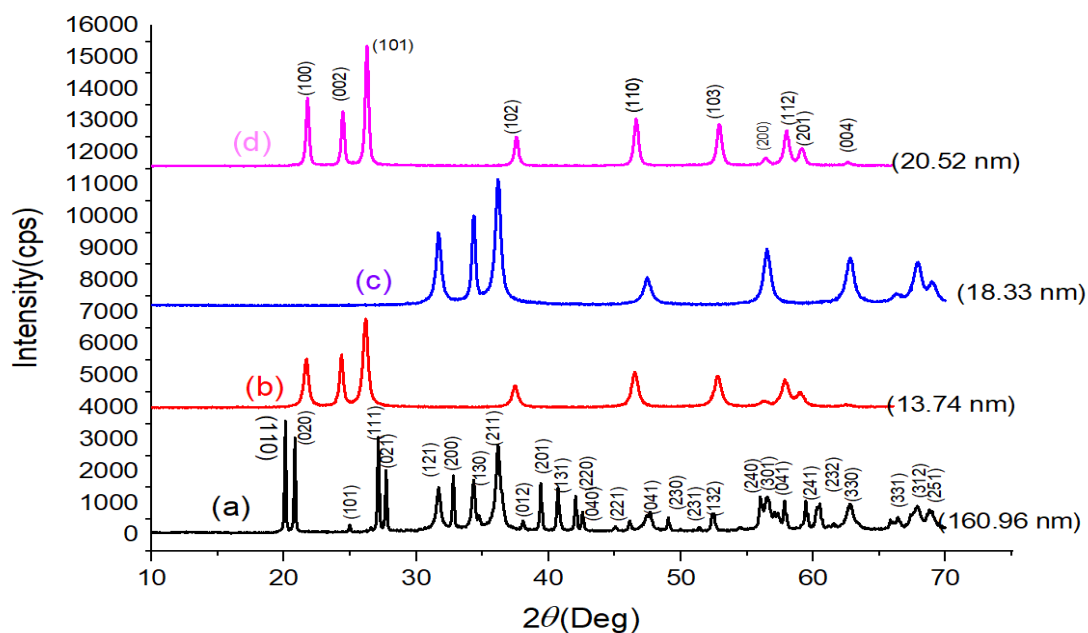
Figure 4.14: XRD Patterns (a) Uncalcined ZnO Nanoparticles and ZnO Nanoparticles   Calcined at (b) 300°C (c) 500°C (d) 700°C

It can be noticed that all the samples exhibited similar XRD diffraction patterns except for the uncalcined (a) with 27 different peaks at 2θ values of 20.1°, 20.81°, 24.9°, 27.1°, 27.7°, 32.7°, 34.7°, 36.0°, 36.4°, 38.0°, 39.4°, 40.6°, 40.9°, 42.4°, 44.9°, 46.2°, 47.6°, 51.2°, 55.9°, 56.6°, 57.1°, 59.4°, 60.4°, 62.1°, 66°, 67.3°, and 68.6°, these diffraction angles were assigned to the following miller indices (111), (020), (101), (111), (021), (121), (200), (130), (211), (012), (201), (131), (220), (040), (221), (041), (230), (240), (301), (041), (241), (232), (330), (311), (312), and (251) respectively with a lattice structure of orthorhombic and lattice constant of a = 5.16 Å, b = 8.53 Å, c = 4.92 Å, a/b = 0.60492, and c/b = 0.57679 .

This matched well with the Joint Committee on Powder Diffraction Standards number (JCP2-76-1778) of zinc hydroxide (Zn (OH)$_2$). The XRD results for the calcined ZnO nanoparticles at 300°C (c) 500°C and (d) 700°C shown in Figure 4.14 indicates nine different peaks at 2θ values of 21.70°, 24.47°, 26.25°, 37.64°, 46.73°, 52.92°, 56.36, 58.02°, 59.12° and 62.77°, these correspond to (100), (002), (101), (102), (110), (103), (200), (112), (201) and (004) crystal planes of the hexagonal wurtzite zincite (ZnO) nanoparticles (Araújo *et al.*, 2017).

 All the diffraction peaks were indexed hexagonal wurtzite structures of ZnO nanoparticles where the oxygen atoms are arranged in a hexagonally closed type packed with zinc atoms occupying half of the tetrahedral sites. The peaks have a lattice constant of a = b = 3.242 Å and c = 5.205 Å which matched well with the Joint Committee on Powder Diffraction Standards number (JCP2-36-1451).

This result corroborated the outcome of Singh *et al.* (2016) who found that the peaks become sharper and more intense as the calcination temperature increases, suggesting an increase in the crystallinity of the ZnO nanoparticles. The disappearance of other peaks in the calcined

136

samples ((b), (c) and (d)) is an indication that calcination temperature plays an important role in the removal of water and other impurities during the transformation of Zn (OH)$_2$ into ZnO nanoparticle (see equation 4.1). This result suggests that the formation of Zn (OH)$_2$ took place at a lower temperature (below 100°C) and later transformed into a crystalline ZnO above 100 °C as shown in Figure 4.14. The average crystallite sizes were estimated using the Debye– Scherrer equation (see equation 2.8). The average crystallite sizes were 160.96 nm for uncalcined and 13.74 nm, 18.33 nm, and 20.52 nm for ZnO nanoparticles calcined at 300, 500, and 700°C for 2 h respectively. The large crystallite size of the uncalcined sample indicates the formation of amorphous ZnO. A Similar trend was observed by Kayani *et al.* (2015), who reported an increase in crystallite size as the calcination temperature increased from 300°C, 500°C, 650, 700, and 750 °C for ZnO nanoparticles prepared using the sol-gel technique with zinc acetate dihydrate and diethanolamine as the precursor materials. Also, Sharma *et al.* (2023), synthesised ZnO nanoparticles via a sol-gel technique and established a direct relationship between calcination temperature and crystallite sizes.

4.4.3   EDS analysis of ZnO nanoparticles

The Energy-dispersive X-ray spectroscopy (EDS) was used to analyse the elemental composition of the ZnO nanoparticles prepared via the sol-gel method and the results are displayed in Figure 4.15.
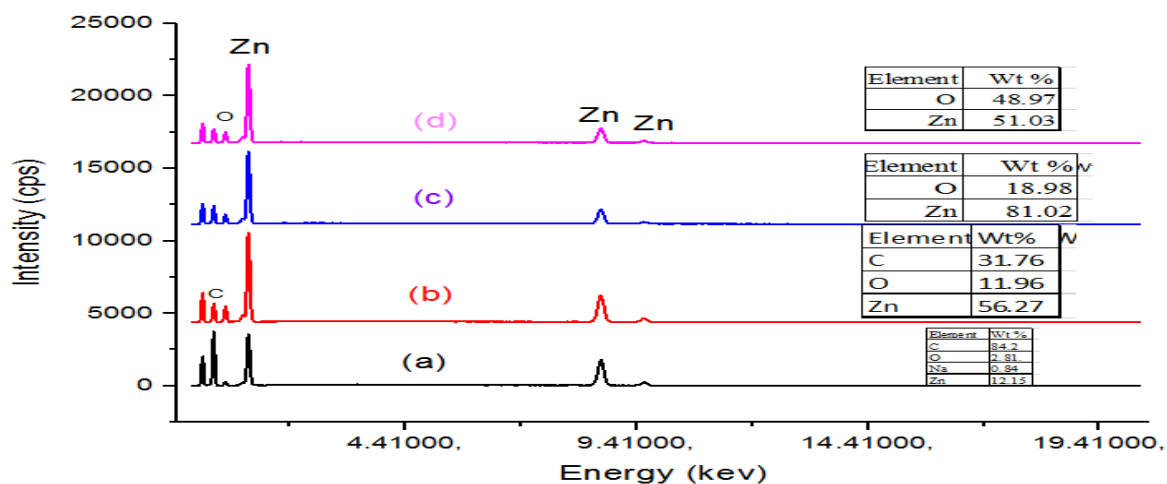
Figure 4.15: EDX Spectra of ZnO (a) Uncalcined, (b) Calcined at 300 °C, (c) 500°C and (d) 700 °C

The results in Figure 4.15 reveal the presence of Zn, O, and C as the dominant elements. In all the samples carbon was present except for ZnO nanoparticles calcined at 700°C where the carbonaceous material was burnt off. This observation indicates that at a higher calcination temperature, there is enough heat that can completely burn off the residual carbon from the polyvinyl pyrrolidone (PVP) used as a stabilizing agent and gives room for the complete formation of pure ZnO nanoparticles. The peak of O appears at 0.50 keV, Zn at 1.01 keV. 8.65 keV and 9.49 keV for Zn with the atomic percentage of 12.15 %, 56.27 %, 81.02 %, 51. 03 % while the O atomic percentage was 2.81 %, 11.96 %, 11.23 %, 32.40 % and atomic percentage of C decrease as the calcination increases from 84.2 %, 31.76, to 0 %. The samples calcined at 300 °C, 500 °C, and 700 °C respectively. The absence of carbon in Figure 4.15 ((c) and (d)) indicates the purity of the ZnO nanoparticles produced.

138

4.4.4 Fourier transform infrared spectroscopy (FTIR) analysis of ZnO nanoparticles

FTIR spectra of the ZnO nanoparticles were carried out to determine the functional groups present and the result is presented in Figure 4.16.
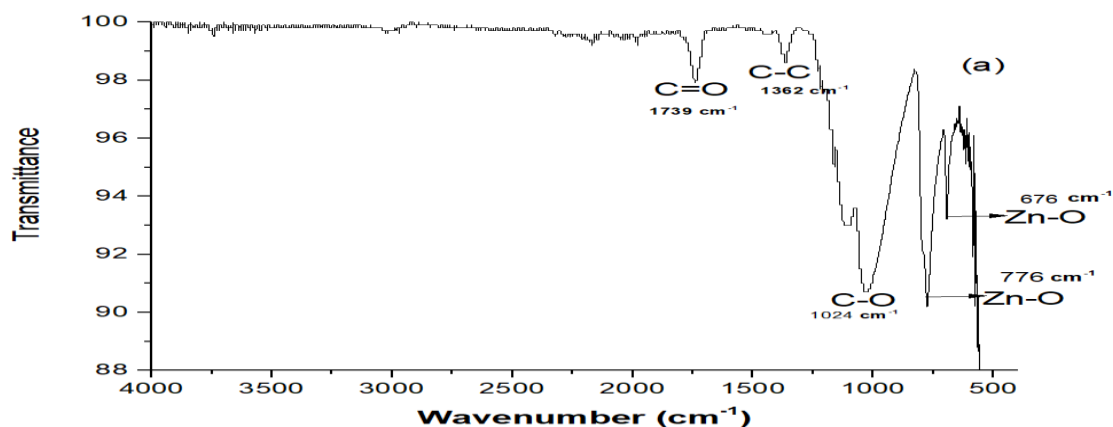
Figure 4.16: FTIR Spectra of ZnO Nanoparticles

Figure 4.16 shows a typical FTIR spectrum of ZnO nanoparticles in the range between 500 to 4000 cm^{-1} spectral region. Figure 4.16 displays a stretching vibration of the C=O at 1735 cm^{-1}, which emanated from the PVP. The presence of the C–H bond is responsible for the adsorption bond at 1358 cm^{-1}. The PVP used as structure-directing is responsible for C–N stretching vibrations at 1110.8 cm^{-1}. The presence of a peak at 1024 cm^{-1} is due to the C-O stretching vibration.

4.4.5 Brunauer–emmett–teller (BET) N_2 adsorption-desorption analysis of ZnO nanoparticles

The Brunauer–Emmett–Teller (BET) method was used to determine the textural properties of ZnO nanoparticles and the result is presented in Figure 4.17
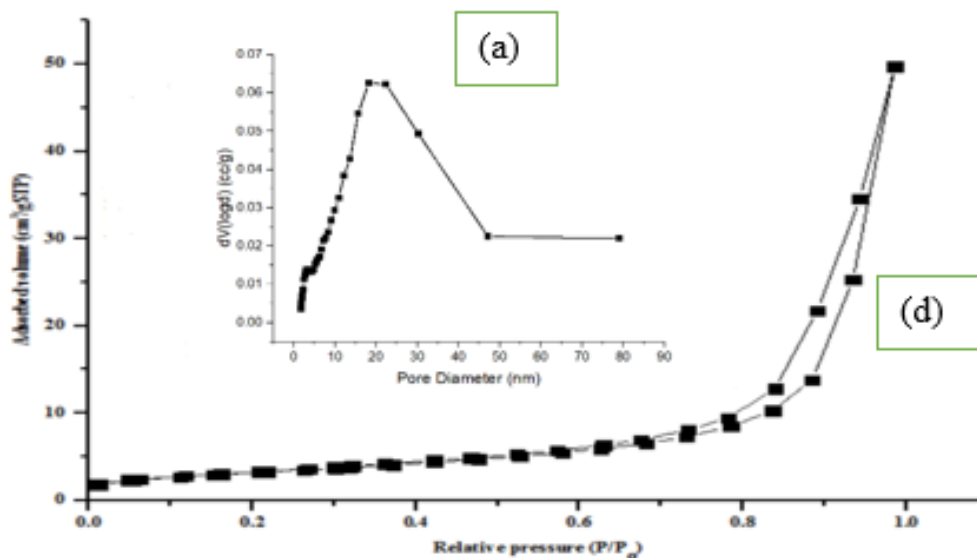
Figure 4.17: (a) Nitrogen Adsorption Desorption Isotherms and (b) Pore Size Diameter Distributions for ZnO Nanoparticles

Based on the classification of adsorption isotherms by IUPAC, the curve in Figure 4.17 (a) exhibited a Type IV isotherm of typical mesoporous materials with relative pressure of 0.7-1.5. The result indicates that the volume of nitrogen adsorption increases with relative pressure until a limit is reached, indicating the availability of pores. The surface area of the ZnO nanoparticles was 8.620 m^2/g with a pore volume of 0.353 cm³/g respectively. The pore size distribution of the ZnO nanoparticles was assessed using the BJH model. Figure 4.17 (b) shows the inserted pore diameter. The pore size distribution of the ZnO nanoparticles was 13 nm. This value is in the range of pore size distribution of 2 to 50 nm range that described type IV isotherm nanoparticles of a mesoporous material. A similar surface area (7.6, 10.7 and 12.3 m^2/g) has been reported by Aljameel and Ali (2021) using different synthesis methods such as sol-gel precipitation and combustion method. The similarity observed in this study may be due to the use of a similar calcination temperature (700 °C) for 3 h.

4.4.6 XPS analysis of ZnO nanoparticles

The general survey of the ZnO nanoparticle was studied using XPS to determine the chemical oxidation states of elements and the corresponding result is presented in Figure 4.18.
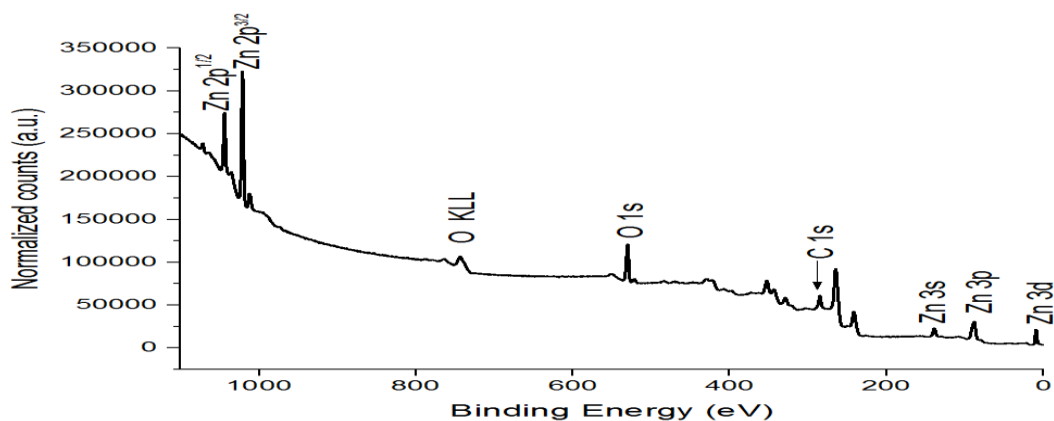
Figure 4.18: XPS General Survey Spectra of ZnO Nanoparticles

Figure 4.18 shows different peaks at binding energies of 1021.80 eV and 1045.07 eV which were related to Zn 2p3/2 and Zn 2p1/2 core levels. The two peaks have narrow linewidth suggesting the dominance of the Zn^{2+} ions in the nanoparticle. The binding energetic difference between the peaks for 2p3/2 and 2p1/2 is 23.27 eV indicating that the Zn2p peak has significantly split spin-orbit components which is not significantly different from 23.00 eV obtained by Al-Gaashania *et al.* (2023) for ZnO nanoparticles despite different synthetic methods. This result confirms that the Zn exists mostly as Zn^{2+} surrounded by the O^{2-} oxidation state in the hexagonal wurtzite ZnO form. The spectra also show a peak at a binding energy of 284.60 eV corresponding to C (1s) which indicates a considerable concentration of adventitious carbonaceous material onto the surface of the nanoparticles, thus may be from

141

the polyvinyl pyrrolidone (PVP) used as a stabilizing agent during the synthesis of the zinc

oxide nanoparticles.

4.4.7   XPS analysis of Zn (2p3/2) orbital of ZnO nanoparticles

The deconvoluted XPS spectrum of Zn2p3/2 (ZnO) is presented in Figure 4.19
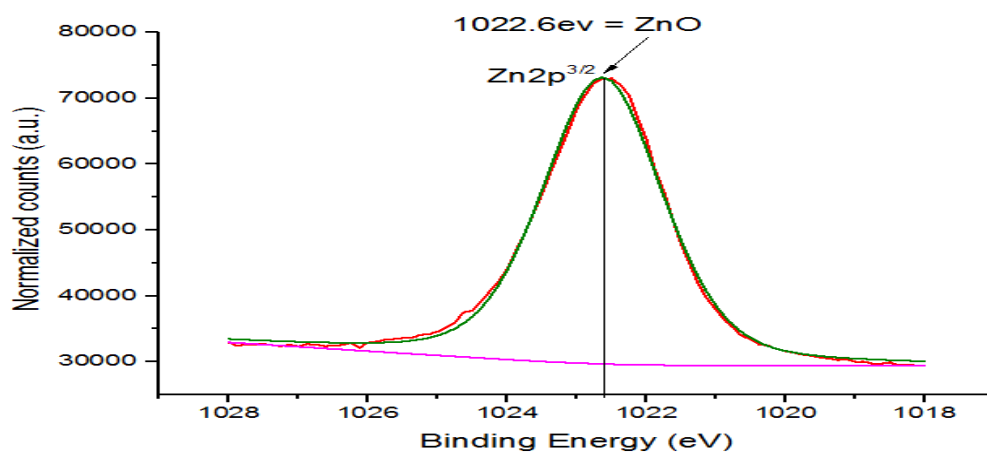
Figure 4.19: XPS Spectrum of Zn 2p3/2 in ZnO Nanoparticles

Wagner plot was used to get the best fit of the different compounds extracted from the NIST

database and the result is shown in Figure 4.20
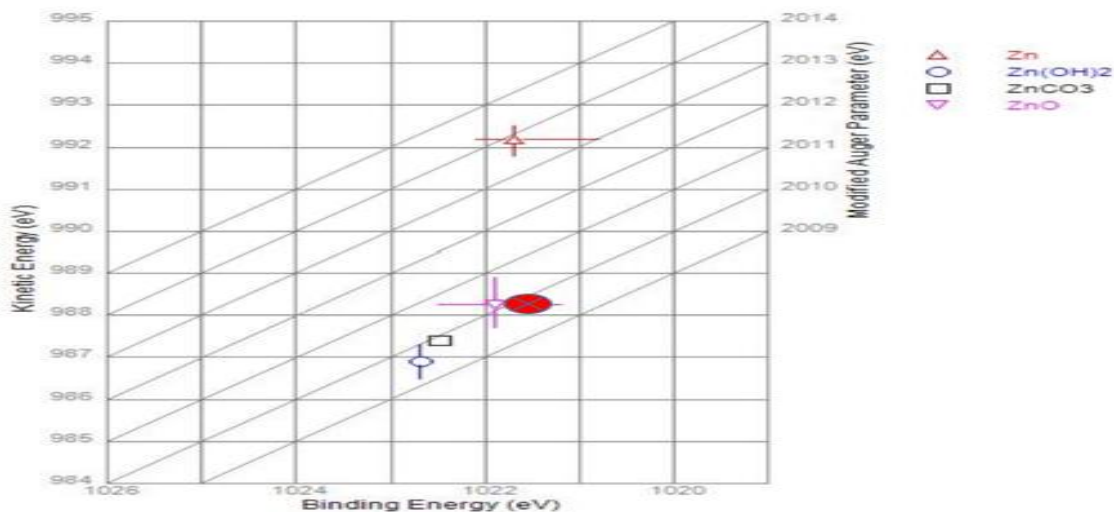
Figure 4.20: Wagner plot of Zn and Different Compounds Extracted from the NIST Database

Figure 4.20 which represents the High-resolution XPS spectrum of Zn $2p^{3/2}$ (ZnO) shows the appearance of a single broad peak at a binding energy of 1021.80 eV. This further indicates the presence of a highly electropositive zinc ion (Zn^{2+}) with two donated electrons in a highly electronegative environment with charged O^{2-} ions in the geometry of a hexagonal Wurtzite structure. Zn $2p^{3/2}$ peak was fitted to only one Gaussian in the samples analysed at a binding energy of 1021.80 eV (Figure 4.20). This result agrees with the findings of Ferreira, *et al.*, (2019), who observed the presence of ZnO at the binding energies of 1022.6 and 1022.15 eV. The binding energies reported in this work are not different from the previous studies reported by Claros *et al.* (2020), who stated the binding energy of the auger parameter of metal at the nanoscale change, especially for Zn photoelectron. Figure 4.20 represents the Wagner plot of Zn and different compounds extracted from the NIST Database. The red circle with a cross represents the current data which corresponds well with the ZnO marker.

4.4.8 XPS deconvoluted spectra of O (1s) analysis of ZnO

XPS was used to study the deconvoluted O (1s) spectral of ZnO nanoparticles and the results are presented in Figure 4.21.
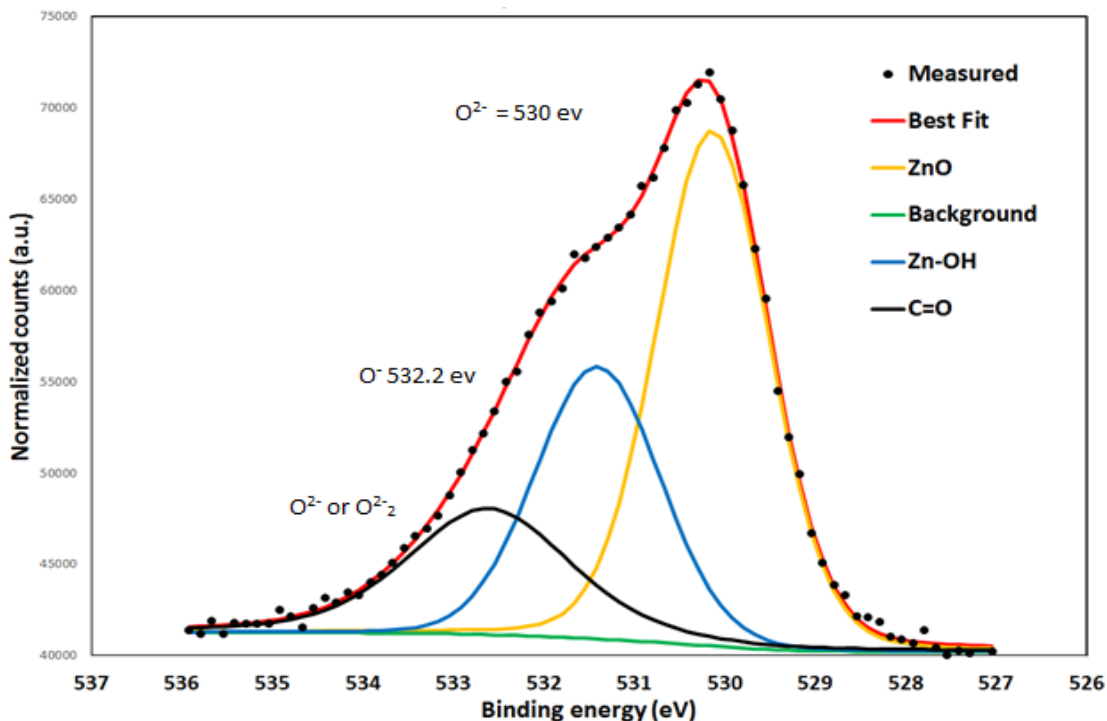
Figure 4.21: The Comparison of Orbital Binding Energy States of High-Resolution XPS Spectra of O (1s) Core-level

Figure 4.21 shows three different peaks at binding energies of 530.6, 532.2, and 533.5 eV corresponding to O^{2-} and O^- ions. The peak located at the binding energy of 530.6 eV is characteristic of zinc oxide (bond between Zn and O) usually called the zinc oxide peak (Geng *et al.*, 2022). The O (1s) atom with a binding energy range of 527– 530 eV is typical of O^{2-} ions in metal oxides (Mohamed *et al*, 2017). While binding energies between 530.6 – 531.1 eV is typical of the species of oxygen incorporated in the matrix of ZnO. The binding energies between 531.1 – 532eV may be due to low coordinated oxygen species described as

O$^-$ ions capable of forming compounds such as C=O, COO$^-$ (Pawlak *et al*., 2020). Another researcher also reported that the binding energies of 530 or 532 eV, which correspond to ZnO and the binding energies around 530.6, 532.2 eV, and 533.2 eV were attributed to O^{2-}, O$^-$ and ions respectively. Additionally, a similar trend was observed by Kamarulzaman *et al.* (2016) with binding energies at 530.6 eV, 532.2 eV for O^{2-} and O$^-$ respectively assigned to O-Zn-O and Zn(OH)$_2$.

4.5   Analysis of Binary ZnO/SiO$_2$ Nanocomposites

4.5.1   HRSEM analysis of ZnO/ SiO$_2$ nanocomposite

The morphologies of the ZnO, SiO$_2$, nanoparticles and ZnO/SiO$_2$ nanocomposite (ratio 1:1, 1:2 and 2:1) were studied using HRSEM and their corresponding micrograph is displayed in Plate VI
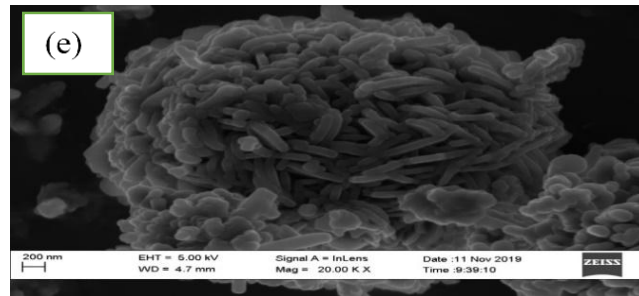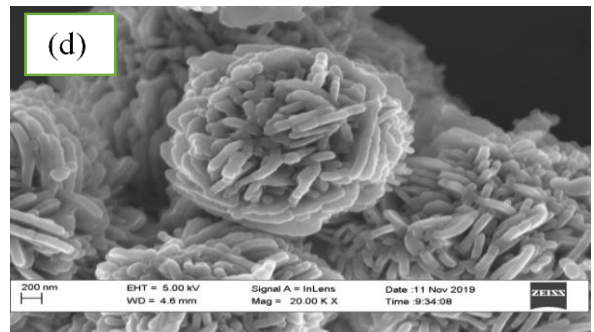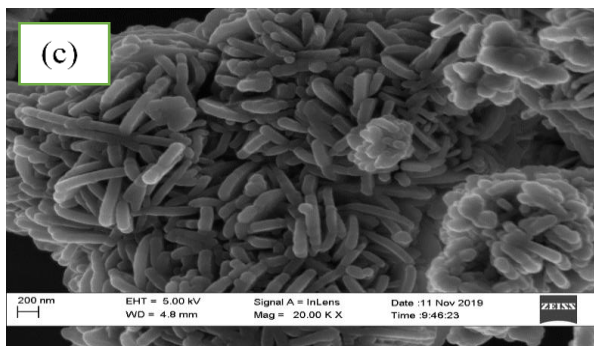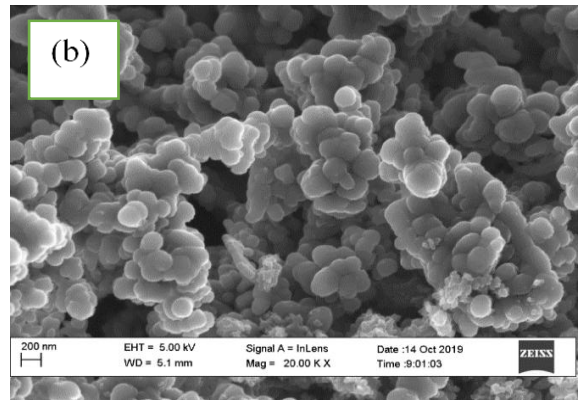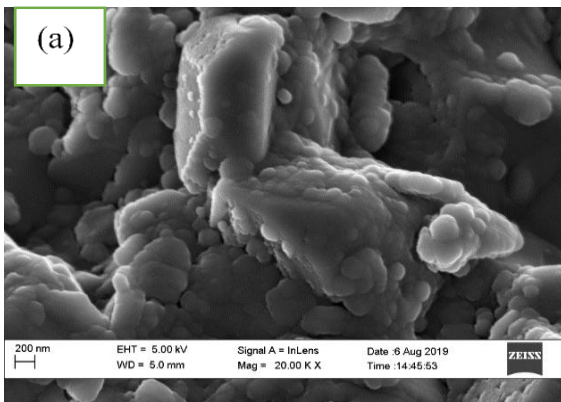
Plate VI: HRSEM images of the ZnO (a), SiO$_2$ (b) ZnO/SiO$_2$ Nanocomposites of Mixing Rario (c) 1:1 (d) (1:2), (e) 2:1

It can be noticed that the morphology of the pure ZnO and SiO_2 completely transformed from the spherical shape and irregular hexagonal shape obtained for ZnO (a) and SiO_2 (b) to rod-like shape in images shown in (c), (d) and (e) respectively. The morphological transformation may be due to the formation of oxide clusters of Si-O-Zn caused by the differences in the atomic radii of SiO_2 (0.4 Å) nanoparticles and ZnO (0.74 Å). Plate VI (c), (d) and (e) suggest there is the formation of new material different from the SiO_2 and ZnO nanoparticles. The result indicates that the agglomeration rate reduces as the amount of SiO_2 nanoparticles increases in the binary composite (see Plate VI (c), (d), and (e). The trend observed in this analysis is an indication that the addition of SiO_2 nanoparticles could reduce the agglomeration of nanoparticles. The highly dispersed agglomerated rod-like morphology observed in Plate VI (c) may also be related to the increases in the concentration of dissolved Si or Zn which promoted electrostatic force of attraction between the particles, thus leading to the formation of fused rod-like morphology in Plate VI (d) and (e) respectively (Shrestha *et al*., 2020).

4.5.2   XRD analysis of ZnO/SiO$_2$ nanocomposites

The mineralogical phase of binary ZnO/SiO_2 nanocomposites prepared by sol-gel chemical reduction method followed by calcination at 450°C was investigated using XRD and the result is given in Figure 4.22
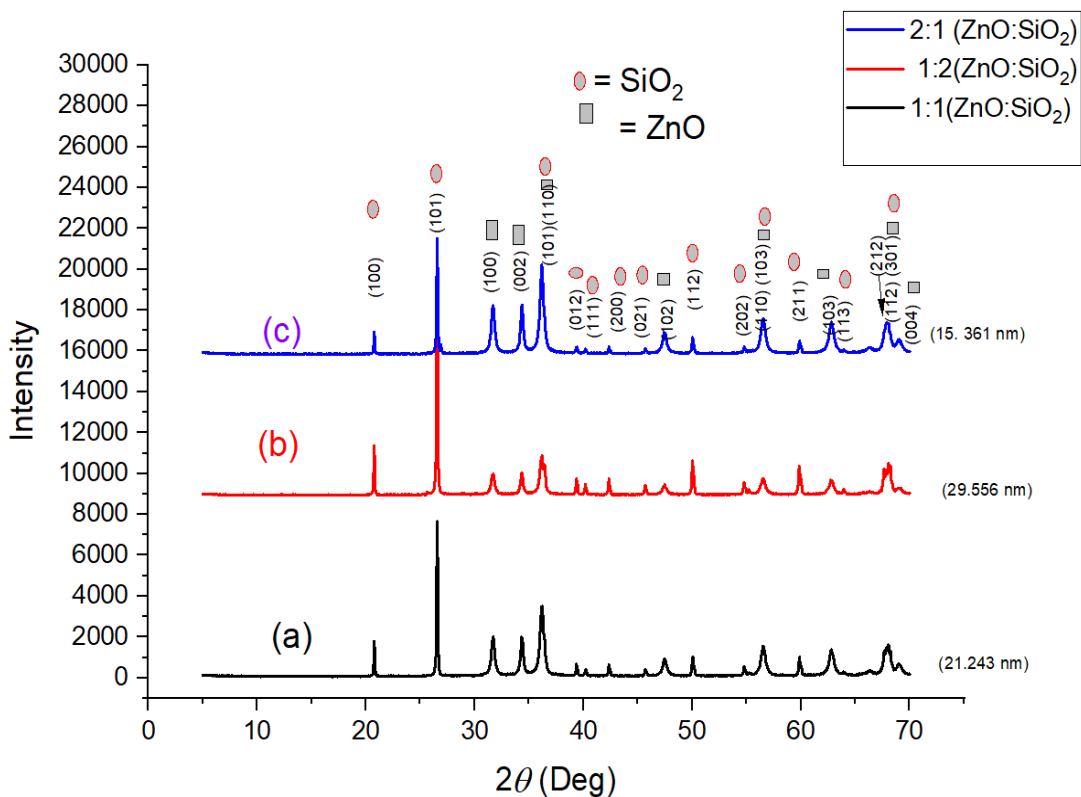
Figure 4.22: **XRD Patterns of the Prepared ZnO/ SiO₂ Nanocomposites with Mixing Ratio (a) 1:1 (b) 2:1 and (c) 1:2**

XRD results for ZnO/SiO₂ nanocomposites (1:2) in Figure 4.22 (b) show prominent diffraction peaks compared to the low intense peaks observed for ZnO/SiO₂ nanocomposites prepared using mixing ratio (1:1) and (2.1) respectively (see Figures 4.22 (a and c). The increased peak intensity in Figure 4.22 (b) may be linked to the increasing amount of SiO₂ in the ZnO/SiO₂ nanocomposite which further enhanced the crystallinity of the ZnO/SiO₂ nanocomposite. This observation could also be attributed to the fact that SiO₂ is more energetically stable in the nanocomposites than ZnO.

The XRD pattern confirmed the presence of ZnO at 2θ values of 31.63°, 34.45°, 36.24°, 47.64°, 56.56°, 62.81°, 67.67, 68.05°and 69.34° corresponding to the following miller indices (100), (002), (101), (102), (110), (103), (200), (112), and (004) respectively. This matches well with those in the Joint Committee on Powder Diffraction Standards (JCPBS 36-1541) with hexagonal wurtzite phase (Al-Ariki *et al*., 2021). The XRD also shows sharp and intense diffraction peaks at 2θ values of 20.81°, 26.53°, 36.38°, 39.44°, 40.32°, 42.38°, 45.83°, 50.04°, 54.77°, 56.56°, 60.13°, 63.90°, 67.62°, and 68.19° with corresponding crystal planes (100), (101), (110), (012), (111), (200), (021), (112), (202), (103), (211), and (212), (301) respectively. This matched well with crystalline SiO_2 nanoparticles with JCP2_83-0539 of the α-quartz phase of silica (Tracy *et al*., 2020).

In comparison with the result presented for SiO_2 and ZnO in Figures 4.9 and 4.14, it is obvious of a quartz-dominating phase of ZnO/SiO_2 nanocomposites was formed. After the formation of the ZnO/SiO_2 nanocomposite, the characteristic peaks of the pure SiO_2 nanoparticle with the ZnO nanoparticle did not change except that ZnO appears at a higher diffraction angle (2θ), suggesting successful immobilization of SiO_2 nanoparticle onto the core-shell of ZnO nanoparticles. The dominant effect of SiO_2 in ZnO/SiO_2 nanocomposites matrix suggests diffusion of silicon (Si) ions onto the core-shell of Zn ion based on ionic radius mechanism, Si^{4+} (0.26 Å) with smaller ionic radius diffused successfully onto and Zn^{2+} (0.74 Å) with higher ionic radius respectively. The analysis of Bahrami and Karami (2018), also confirmed that the addition of SiO_2 did not change the ZnO crystal structure. The crystallite size of the ZnO/SiO_2 nanocomposites was calculated using Debye Scherrer's equation (see equation 3.1).

The average crystallite sizes were found to be 21.24 nm, 29.56 nm, and 15.36 nm for ZnO/SiO$_2$ at 1:1, 1:2 and 2:1 respectively. The result shows the highest increase in crystallite size for sample (b) 1:2 with a high dosage of SiO$_2$ nanoparticles. This is because the incorporation of SiO$_2$ into the ZnO nanoparticles unit cell causes the cell to expand resulting in the formation of oxide clusters of the Si-O-Zn (Chen *et al.*, 2017). This may also be attributed to the electron affinity of Si ion which is positive ($+134.068$ J·mol^{-1}) and that of the Zn^{2+} (**-** 58 J·mol^{-1}), thus Zn^{2+} is more likely to interact with O^{-2} ($+140.976$ J·mol^{-1}) than with Si ion. The combination of the attractive/repulsive interactions improves the diffusivity of the oxygen and zinc ions in the domains and aids the movement of electrons within the molecules that caused the expansion of the unit cells of ZnO.

4.5.3   EDS analysis of ZnO/SiO$_2$ nanocomposites

The (EDS) was used to analyse the chemical composition of the ZnO/SiO2 nanocomposites and the results are shown in Figure 2.23.
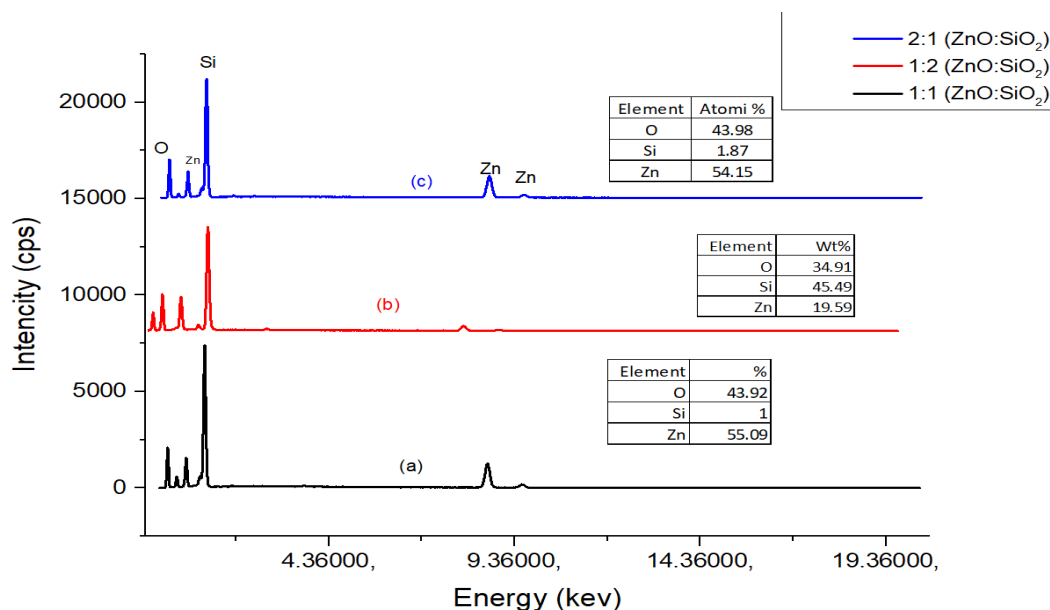
Figure 4.23:   **EDS of the prepared ZnO/SiO2 nanocomposites using (a) 1:1 (b) 1:2 and (c) 2:1**

The EDS spectrum in Figure 4.23 indicates that the synthesised ZnO/SiO_2 nanocomposite primarily contains Si, Zn, and O elements with a small amount of Na. The peak of O appears at 0.57 keV with Zn at 1.08 keV, 8.75 keV and 9.68 keV, while the Si signal appears at 1.75 keV. The values obtained for the ZnO/SiO_2 nanocomposite show increase in the binding energy for C, O, Zn and Si due to the diffusion of SiO_2 nanoparticles into the interstitial spaces between Zn^{2+} and O^{2-} ions. The Zn ions concentration (wt. %) was found to be 55.09 %, 54.15 % and 19.59 % for (a), (b) and (c) respectively. While Si ions concentration (wt. %) was found to be 1 %, 1.87 % and 40.49 % for (a), (b) and (c) respectively. The increase in the atomic weight percentage of Si in the matrix of ZnO/SiO_2 nanocomposites may be responsible for the formation of a highly compacted/fused rod-like network in plate VI (e). Moreover, O ions concentration (wt. %) was found to be 43.92 %, 43.98% and 34.91 % for the sample displayed in Figure 4.23 (a), (b) and (c) respectively. This result corroborated the earlier results of XRD and the HRSEM in Figure 4.22 and Plate VI where the XRD result of the sample with a higher dosage of SiO_2 shows higher intense peaks and larger particle sizes respectively.

4.6   Analysis of Binary ZnO/Fe_3O_4 nanocomposites

4.6.1   HRSEM analysis of ZnO/Fe_3O_4 nanocomposites

The surface morphology of pure ZnO, Fe_3O_4 and ZnO/Fe_3O_4 nanocomposite were investigated by HRSEM and their corresponding images are presented in Plate VII.
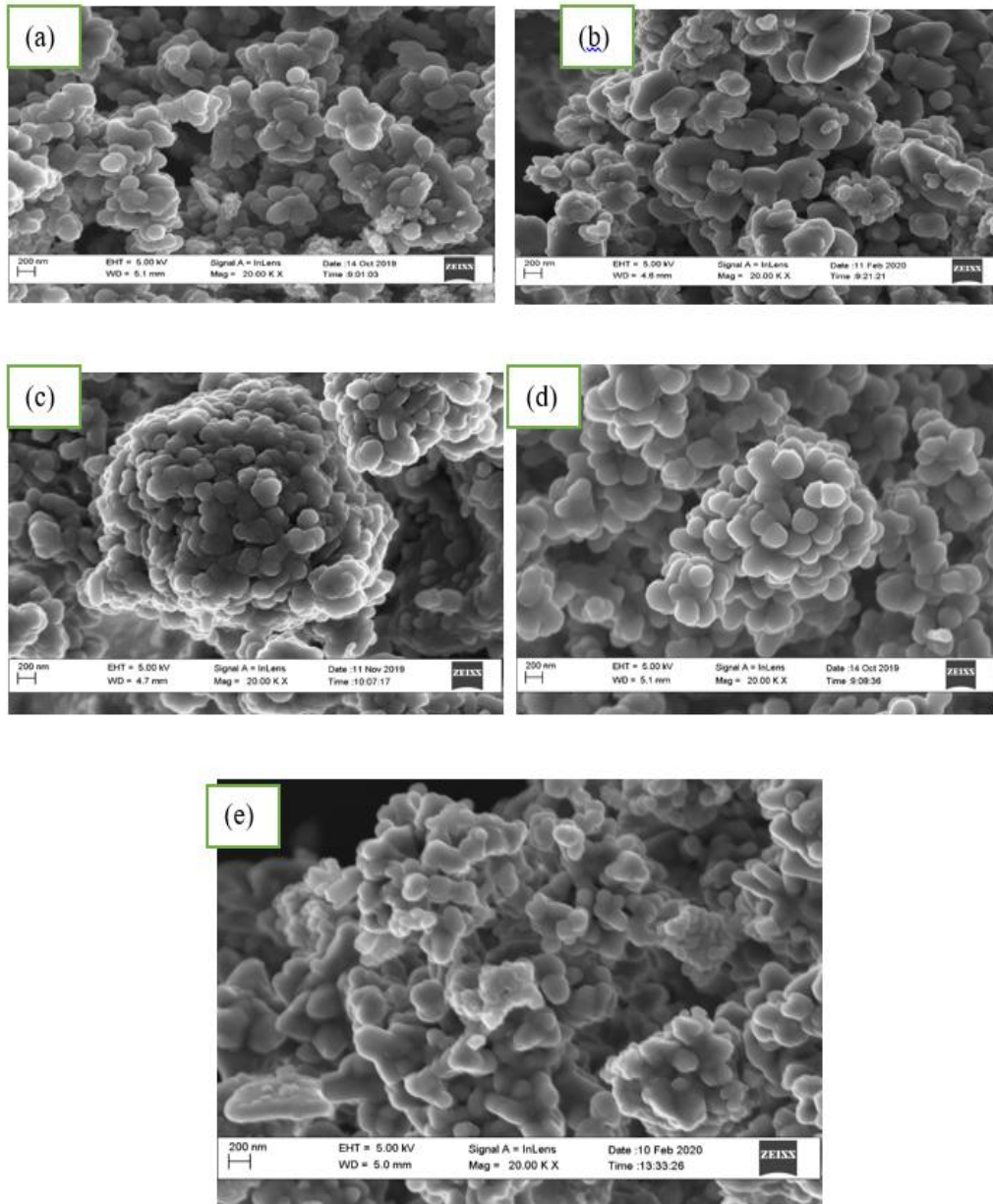
Plate VII: HRSEM Patterns of Pure ZnO (a), Fe₃O₄ (b) and ZnO/Fe₃O₄ Nanocomposites Prepared using different Mixing Ratio c (e) 1:1, (d) 1:2, and e (c) 2:1

The HRSEM images in Plate VII show similar morphology (spherical) for ZnO (a), Fe_3O_4 (b) with that of the nanocomposites in ((c), (d) and (e)), the only difference is that particle size of the composites samples ((c), (d) and (e)) increases relative to the pure ZnO nanoparticles due to the introduction of Fe_3O_4 nanoparticles on the surface of ZnO nanoparticles. The findings support the XRD result in Figure 4.2 which shows the existence of both the Fe_3O_4 and ZnO nanoparticles in the composites. Sample (d) with a mixing ratio of 1:2 shows a very distinct clear and less agglomerated spherical shape with a larger particle size due to the high dosage of Fe_3O_4 nanoparticles in the nanocomposites. The high density of Fe_3O_4 (5.175 g/cm^3) compared to that of ZnO (5.606 g/cm^3), suggest the suppression of ZnO by Fe_3O_4 in the composition. The high particle size can also be linked to the diffusion of Fe into the cell lattice of the ZnO nanoparticles. Sample (e) shows a more agglomerated spherical shape compared to (d) and (c) with a more dispersed spherical shape and void/holes in between the nanoparticles. The aggregation of surface particles could have originated from the high surface energy due to the strong attractive interaction between the ZnO and Fe_3O_4 nanocomposites (Shrestha *et al*., 2020). It can be concluded that the incorporation of Fe_3O_4 onto the ZnO lattice layer did not reduce the agglomeration of the nanocomposites compared with the result of the ZnO/SiO_2 nanocomposites

4.6.2 XRD analysis of binary ZnO/Fe₃O₄ nanocomposites

The mineralogical phase of ZnO/Fe_3O_4 nanocomposite prepared at different mixing ratios was a study using XRD and the result is presented in Figure 4.24
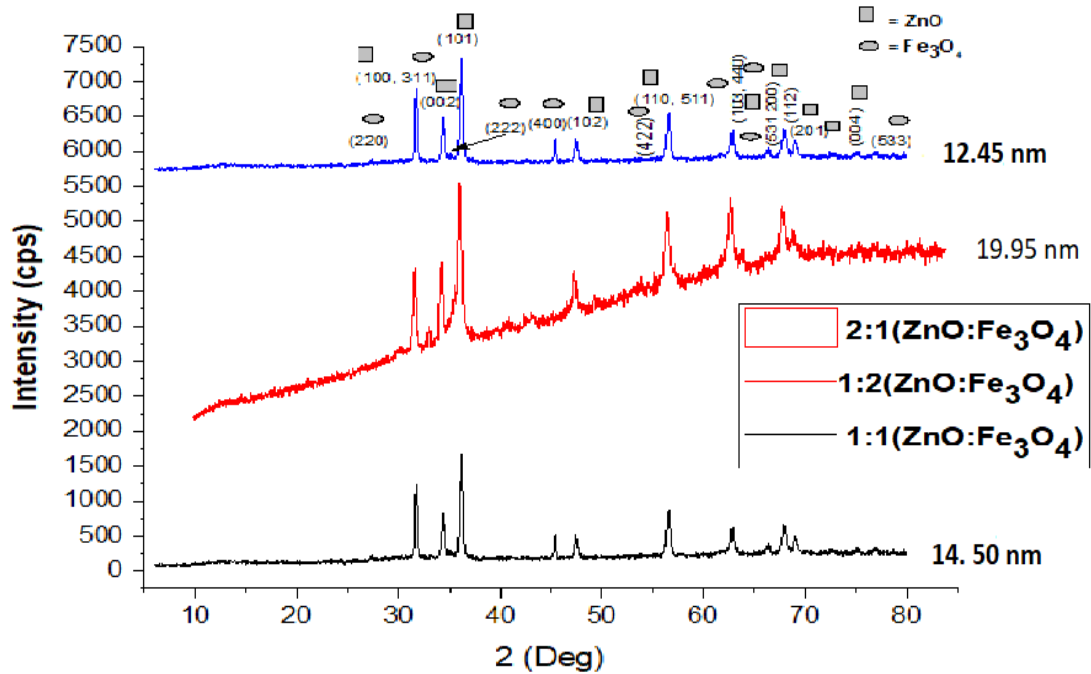
Figure 4.24: XRD Patterns of ZnO/Fe₃O₄ Composites Nanoparticles Calcined at 450°C (a) 1:1, (b) 1:2. (C) 2:1

The result in Figure 4.24 indicates peaks at 2θ values of 31°, 34°, 36°, 47°, 56°, 62, 66, 67° and 72°; corresponding to (100), (002), (101), (102), (110), (103), (200), (112), (201) and (004) planes reflecting ZnO hexagonal wurtzite. While the diffraction peaks at (2θ) values of 27.30°, 31.66°, 34.40°, 53.19°, 56.47°, 62.80°, and 72.82°, were assigned to the crystal planes of (220), (311), (400), (422), (511), (440), and (533), which is an indication of immobilization of ZnO wurtzite lattice onto the core shells of Fe_3O_4 see Figure 4.24 (a). The result indicates that the Fe_3O_4 nanoparticles in the nanocomposite appear at lower 2θ values compared to the pure Fe_3O_4 due to the incorporation of Fe_3O_4 nanoparticles into the ZnO nanoparticles. The phases of ZnO and Fe_3O_4 remained unchanged however ZnO dominated with intense peaks while Fe_3O_4 exhibited a weak diffraction peak with a face-centered cubic phase (JCP2_40-

1141). This may be because some of the Fe^{2+}/Fe^{3+} ions in Fe_3O_4 nanocomposites were substituted and replaced the O^{2-} ions and did not enter the void spaces of ZnO leading to a reduction of the intensity of Fe_3O_4 in the nanocomposites.

The average particle size of the ZnO/Fe_3O_4 nanocomposites was 14.50 nm, 19.95 nm and 12.45 nm of ZnO: Fe_3O_4 for the sample prepared with mixing ratios 1:1, 1:2 and 2:1 respectively. A similar trend has been reported by Ulya *et al*. (2019) for ZnO/ Fe_3O_4 prepared by a combination of sonochemical and sol-gel methods. In their analysis, the authors reported a mixture of Fe_3O_4 and α-Fe_2O_3 nanoparticles after the formation of the nanocomposites.

The final product after calcination was α-$Fe_2O_3/ZnFe_2O_4$ nanocomposite. The differences observed may be due to the method of synthesis of the nanoparticle and its composites, the nature of the metal salt precursors and the calcination temperature employed. Additionally, Długosz *et al*. (2021) have also reported the highly intense diffraction peaks of ZnO to compare with the Fe_3O_4 in composites formation. Also, the XRD result shows that as the amount of the Fe_3O_4 nanoparticles increases in the nanocomposites, the crystallite size of the particles increases. This may be attributed to the higher density and dominance of Fe (7.874 g/cm^3) compared to the density of Zn (7.14 g/cm^3). The observation may also be attributed to the difference in ionic radii of Fe^{2+} (0.76 Å) and Fe^{3+} (0.64 Å) compared to that of Zn^{2+} (0.74 Å). Fe^{2+} (0.76 Å) with a higher ionic radius than Zn^{2+} (0.74 Å) dominated and this resulted in compression strain and an increase in the unit cell of the ZnO nanoparticle. On the other hand, Fe ions in ZnO/Fe_3O_4 matrix may also exist in the form of Fe^{3+} (0.64 Å) with a smaller ionic radius than Zn^{2+} (0.74 Å), and resulted in the tensile strain as well as a decrease in the unit cell of the ZnO/Fe_3O_4 formed. In a similar analysis, Singh *et al.* (2016),

synthesised ZnO/Fe_3O_4 composites and observed a decrease in the crystallite size of the doped nanocomposites compared to the pure ZnO nanoparticles. The trend observed in this study contradicts the result obtained by the previous researchers because previous studies did not study the effect of nanoparticle mixing ratio (ZnO and Fe_3O_4).

4.6.3   EDS analysis of ZnO/Fe_3O_4 nanocomposites

The elemental composition of the ZnO/Fe_3O_4 nanocomposites prepared via variation of mixing ratios (a) 1:1, 1:2 (b) and 2:1 (c) was examined using energy dispersive X-rays spectroscopy (EDS) and the corresponding result is shown in Figure 4.25
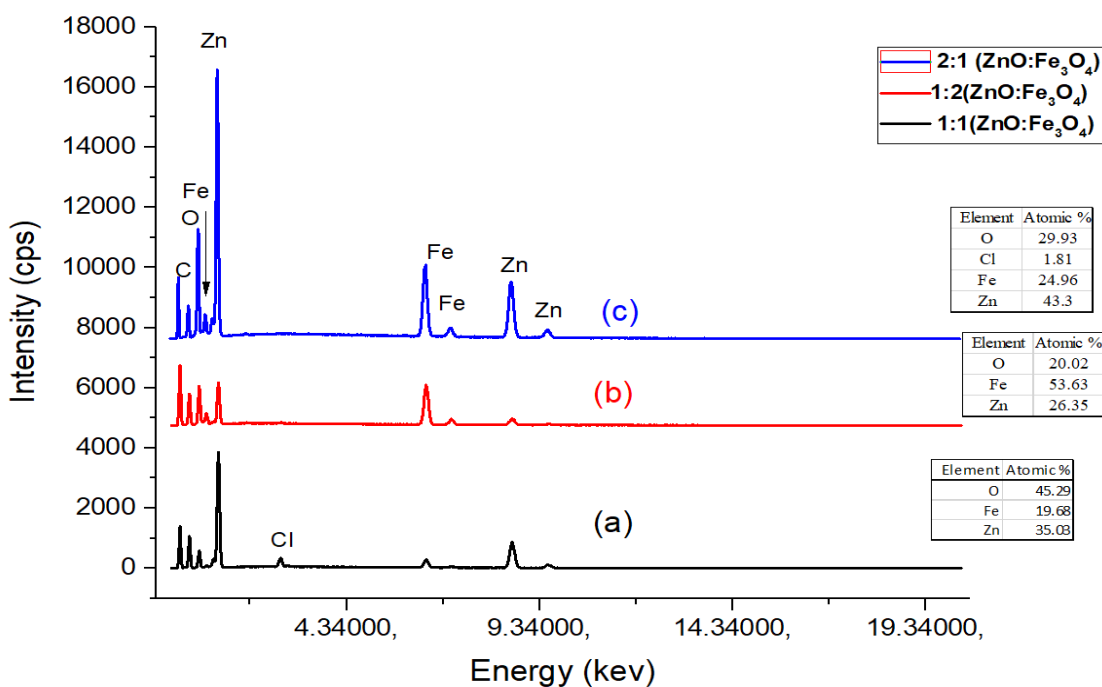
Figure 4.25: EDS Patterns of ZnO/Fe_3O_4 Nanocomposites Prepared using Mixing Ratio of (a) 1:1 (b) 1:2, (c) 2:1

The EDS spectra in Figure 4.25 reveal strong peaks of Zn, Fe and O and weak peaks for Na and Cl in the ZnO/Fe$_3$O$_4$ nanocomposites. The peaks at kα = 6.4 keV and lα= 0.705 keV are related to the binding energies of Fe suggesting the presence of iron in the material. Figure 4.25 (a) indicates a very strong peak for Zn (35.03 %) ion compared to the Fe (19.68 %) due to the higher density of Zn (7.134 g/cm^3) relative to Fe (7.874 g/cm^3). Based on the density differences, Fe may settle at the bottom with Zn deposited at the surface of the Fe during the synthesis. The high peak observed in (b) with 53.6 % concentration of Fe and 26.35 % of Zn ion concentration may be due to the higher dosage of Fe$_3$O$_4$ in the nanocomposites compared to ZnO or due to diffusion of the Fe into the unit cell of ZnO nanoparticles. Figure 4.25 (c) shows that the Zn ion has the highest percentage concentration in the sample compared to Figure 4.25 (a and b), Thus suggesting the dominance of the Zn ion over the Fe ion in the composition. This result agrees with the observation of Ulya *et al*., (2019) who reported the elemental composition of Fe (33.08 %) and Zn (66.91%) in the formation of ZnO/Fe$_3$O$_4$ nanocomposites. Another researcher has reported 70.84 % and 14.79 % for Zn and Fe ions during the formation of ZnO/Fe$_3$O$_4$ nanocomposites (Długosz *et al*., 2021). The percentage of Zn in the sample (c) may be due to the high concentration of ZnO in the composition.

4.7 Analysis of Binary Fe$_3$O$_4$/SiO$_2$ nanocomposites

4.7.1 HRSEM analysis of binary Fe$_3$O$_4$ /SiO$_2$ nanocomposites

The result of the HRSEM analysis of Fe$_3$O$_4$ /SiO$_2$ nanocomposites prepared via variation of mixing ratio is presented in Plate VIII.
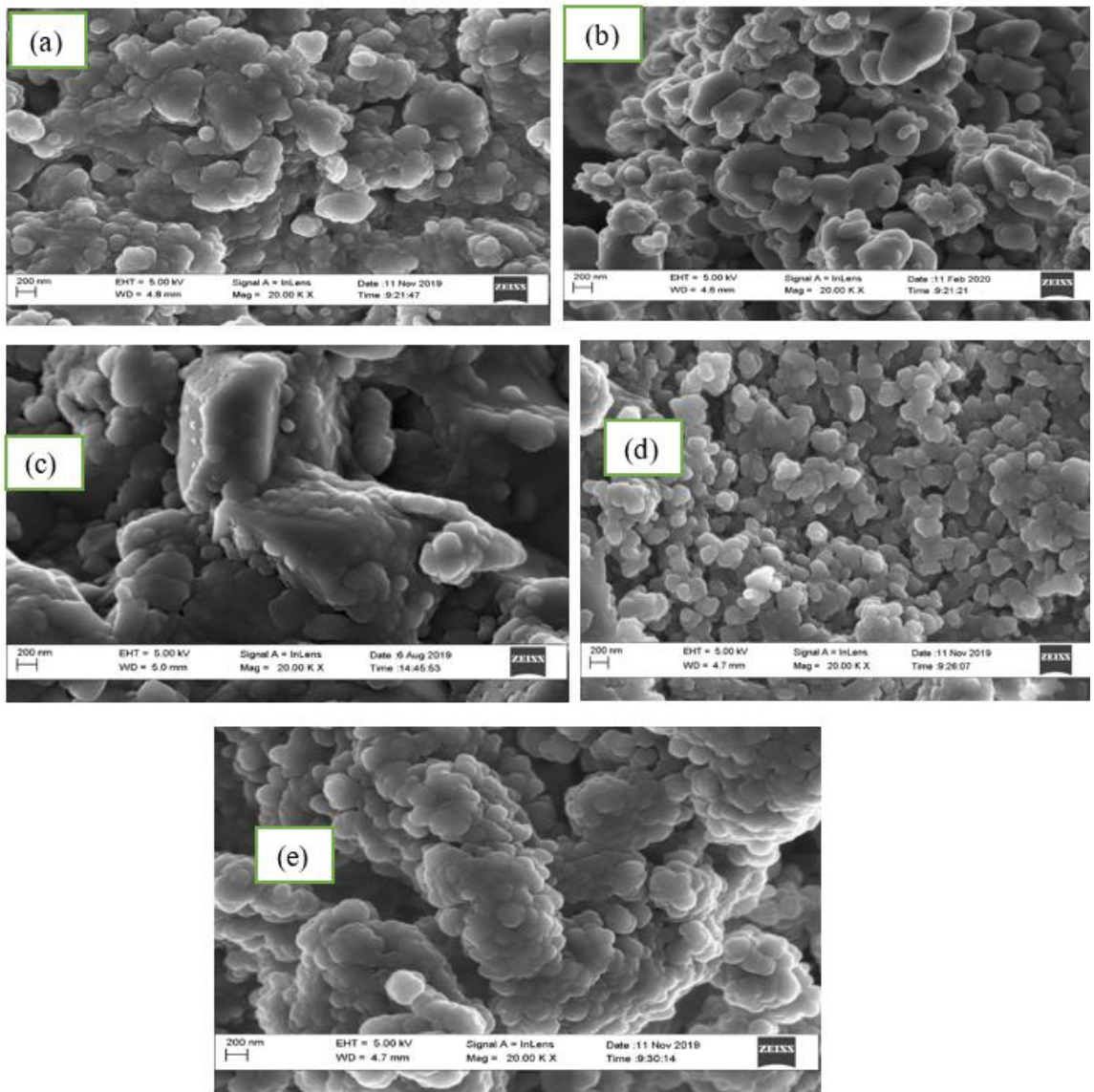
Plate VIII: HRSEM Images of Fe₃O₄/SiO₂ Nanocomposites (a) Fe₃O₄ (b) SiO₂, (c) 1:1, (d) 1:2 and (c) 2:1

158

Plate VIII (c) revealed the formation of highly aggregated spherical particles compared with the structural network of plate VIII (d). The image in Plate VIII (d) with mixing ratio (1:2) shows the particles were less agglomerated and uniform compared with plate VI (e) and (c) respectively. The result also confirmed the higher crystalline nature of Fe_3O_4 /SiO_2 nanocomposites with a mixing ratio of 1:2 and SiO_2 plays important in the reduction of agglomeration of Fe_3O_4 nanoparticles. The image in plate VIII (e) shows a non-uniform agglomerated spherical shape due to the low dose of SiO_2 nanoparticles while image (c) shows less agglomeration spherical shape compared to (e) due to increases in the dose of SiO_2 nanoparticles in the nanocomposite. This result also suggests that SiO_2 nanoparticles shielded Fe_3O_4 nanoparticle core-shell by acting as a capping agent for the growing Fe_3O_4 nanoparticles to form Fe_3O_4/SiO_2 nanocomposites. This observation also corroborated the earlier result from the XRD results (see Figure 4.26 (b)) where the peaks for the (101) plane increase as the dosage of SiO_2 increases in the composition, indicating increases in the crystallinity of the nanocomposites. It can be concluded that an increase in the amount of SiO_2 increases the distribution of Fe_3O_4 leading to the formation of less agglomerated spherical shapes. It has also been reported by Ganapathe *et al*. (2020) that Fe_3O_4 nanoparticles with high surface energy tended to accumulate rapidly with the presence of organic silica.

4.7.2 XRD analysis of binary Fe_3O_4/SiO_2 nanocomposites

XRD pattern of the Fe_3O_4/SiO_2 nanocomposite prepared using different mixing ratios of (a) 2:1 (b) 1:2 and (c) 1:1 is shown in Figure 4.26
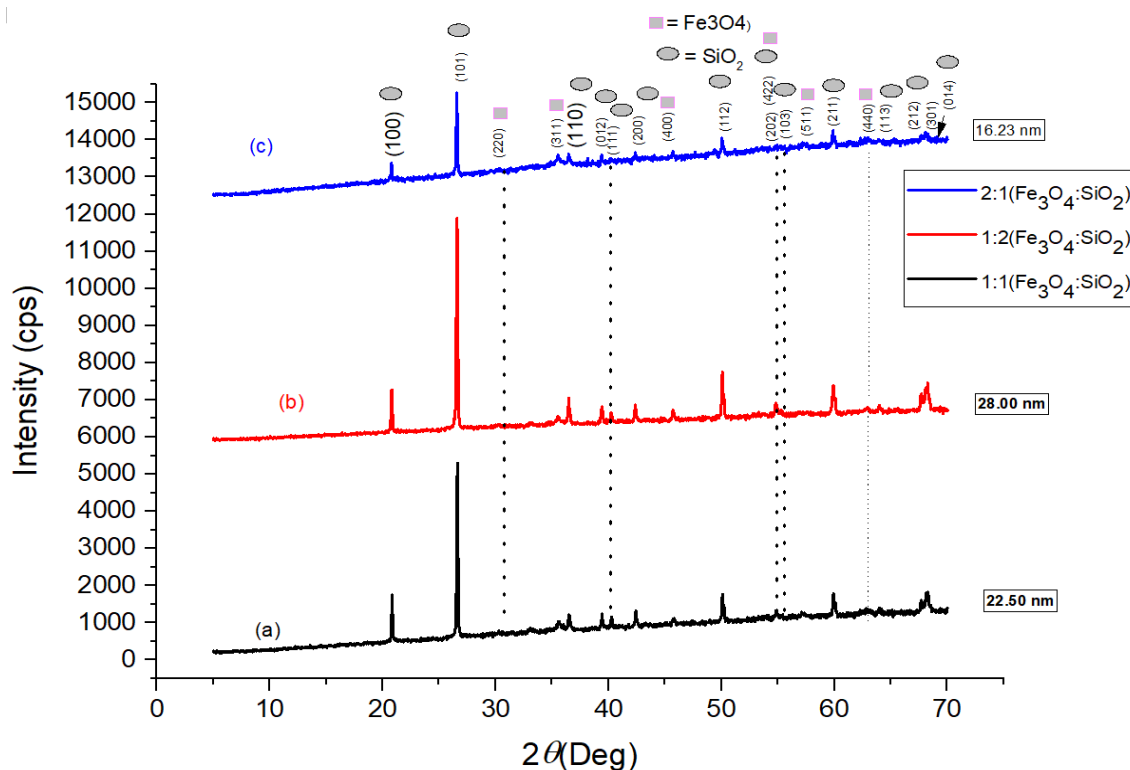
Figure 4.26: XRD patterns of Fe₃O₄ /SiO₂ Nanocomposite (a) 1:1 (b) 1:2 and (c) 2:1

Figure 4.26 revealed the presence of different peaks belonging to Fe_3O_4 and SiO_2. The diffraction peaks for Fe_3O_4 nanoparticles appeared at 2θ values of $30.56°$, $35.86°$, $43.46°$, $54.01°$, $57.38°$, $63.00°$, and $74.46°$, with a corresponding crystal plane of (200), (311), (400), (422), (511), (440), and (533). These matched well with the JCP2_33-0664 standard. The low intensity observed for Fe_3O_4 nanoparticles may be due to the coverage of the core of Fe_3O_4 covered by the shell SiO_2. The diffraction peaks for SiO_2 nanoparticles appeared at 2θ values of $20.91°$, $20.66°$, $26.56°$, $36.50m°$, $39.39°$, $40.22°$, $42.39°$, $45.71°$, $50.04°$, $54.77°$, $55.21°$, $59.86°$, $63.90°$, $67.62°$, $68.19°$, and $73.29°$ with miller indices ((100), (101), (110), (012), (111), (200), (021), (112), (202), (103), (211), (113), (212), (301) and (014). There were no major differences in the intensity of diffraction peaks between Fe_3O_4 /SiO₂ peaks and

that of the SiO$_2$ standard (JCP2830539), which has a quartz crystal structure. This suggests that the addition of SiO$_2$ did not alter the structure of the Fe$_3$O$_4$ crystal phase. The intensity of the peaks decreases from Figure 4.26 (b) 1:2 compared to (a) 2:1 and (c) 1:1; due to the dominant effect of SiO$_2$ in the formation of Fe$_3$O$_4$/SiO$_2$ nanocomposites. Another reason for this observed trend may be linked to the magnetic behaviour of Fe$_3$O$_4$ nanoparticles which may attract particles from the SiO$_2$. This makes it difficult for the XRD instrument to identify the phase of the Fe$_3$O$_4$ covered by the SiO$_2$ Shell. The absence of the peaks corresponding to the Fe$_3$O$_4$ nanoparticles in the XRD of the Fe$_3$O$_4$/SiO$_2$ nanocomposites (15 nm) was reported by Nadi *et al*. (2019). The authors attributed the absence of Fe$_3$O$_4$ peaks to the existence of organic silica, which covers the entire surface of the magnetic nanoparticles. Not only that, the organic silicon act as a shield to avoid X-ray interaction on the sample's crystal phase.

The result also revealed an increase in the crystallite size of the Fe$_3$O$_4$/SiO$_2$ nanocomposites as the dosage of SiO$_2$ increases from 16. 23 nm, 22.50 nm to 28.00 nm for 2:1, 1:1 and 1:2 respectively. This may be due to the confinement of the Fe$_3$O$_4$ nanoparticles inside the SiO$_2$ matrix leading to the expansion of the particle size of the nanocomposites (Fuentes-García *et al*., 2018). The observation could also be attributed to the fact that Fe$_3$O$_4$ has a magnetic property that could attract the SiO$_2$ magnetic core (Kumar and Bhatnagar, 2018). Another researcher has reported that Fe$_3$O$_4$/SiO$_2$ nanocomposites functionalised with 2,6-pyridine dicarboxylic acid have an average particle size of 20 nm (Shokrollahi and Zamani, 2019). However, Shen *et al.* (2019) in their analysis observed the complete disappearance of SiO$_2$ after immobilization of Fe$_3$O$_4$/SiO$_2$ due to the amorphous nature of SiO$_2$. Thus, the presence of SiO$_2$ nanoparticles in the composites of Fe$_3$O$_4$/SiO$_2$ enhanced its degree of crystallinity.

4.7.3   EDS analysis of binary Fe₃O₄ /SiO₂ nanocomposites

The elemental composition of the different ratios of binary Fe_3O_4 /SiO_2 nanocomposites using different mixing ratio was studied and the EDS and the spectral is given in Figure 4.27
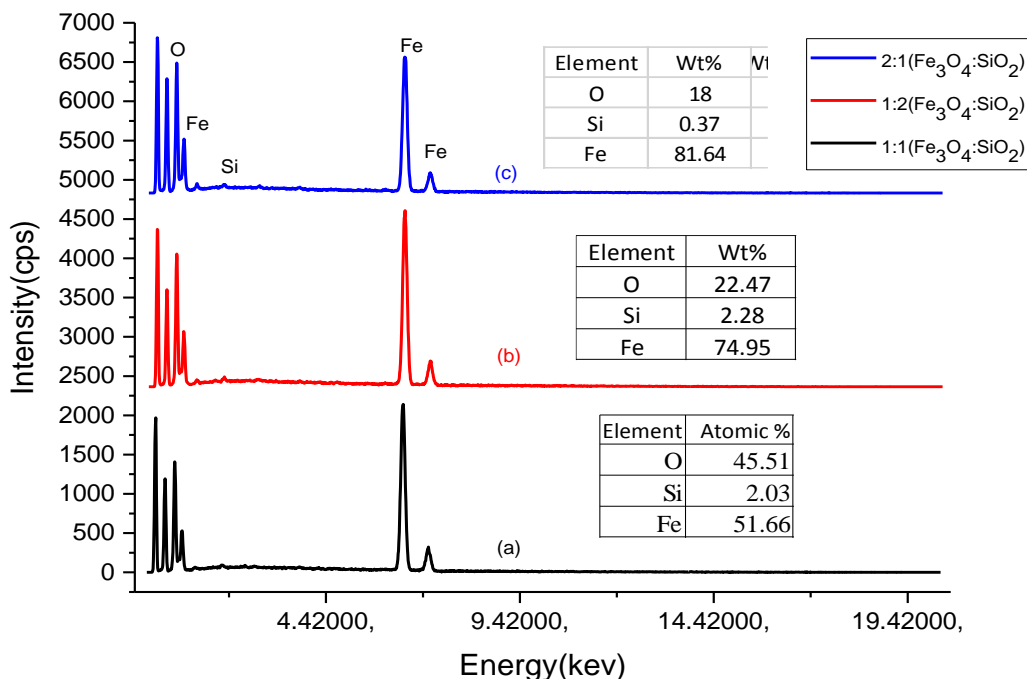
Figure 4.27: EDS of Fe₃O₄ /SiO₂ Nanocomposites (a) 1:1 (b) 1:2 and (c) 1:1

From the EDS spectrum, it can be noticed that the Fe_3O_4 /SiO_2 nanocomposites contained O, Fe and Si, as major elements. The spectral peak of O appears at 0.57 keV, Fe signal appears at 0.77 keV, 6.48 keV, and 7.11 keV, Si ion shows peaks at 1.80 KeV respectively. The Fe ion concentrations appear at a very higher binding energy, indicating the formation of nanocomposites consisting of Fe_3O_4 and SiO_2 nanoparticles. Iron shows a very high percentage concentration irrespective of the dose. This may be attributed to the high weight

162

of iron ions compared to the silicon ion, leading to compression and coverage of Si ion surface.

4.8   Analysis of Ternary Fe₃O₄/ SiO₂/ZnO Nanocomposites

4.8.1 HRSEM analysis of Fe₃O₄/SiO₂/ZnO nanocomposites

The surface morphology of Fe₃O₄/SiO₂/ZnO nanocomposites prepared using different mixing ratios was investigated using HRSEM and their corresponding micrographs are shown in Plate IX.

Plate IX: HRSEM Images of (a) Fe₃O (b) SiO₂ (c) ZnO, and Fe₃O₄/SiO₂ /ZnO Nanocomposites with Mixing Ratio (d) 1:1:1 (e) 1:1:2, (f) 1:2:1 and (g) 2:1:1d)
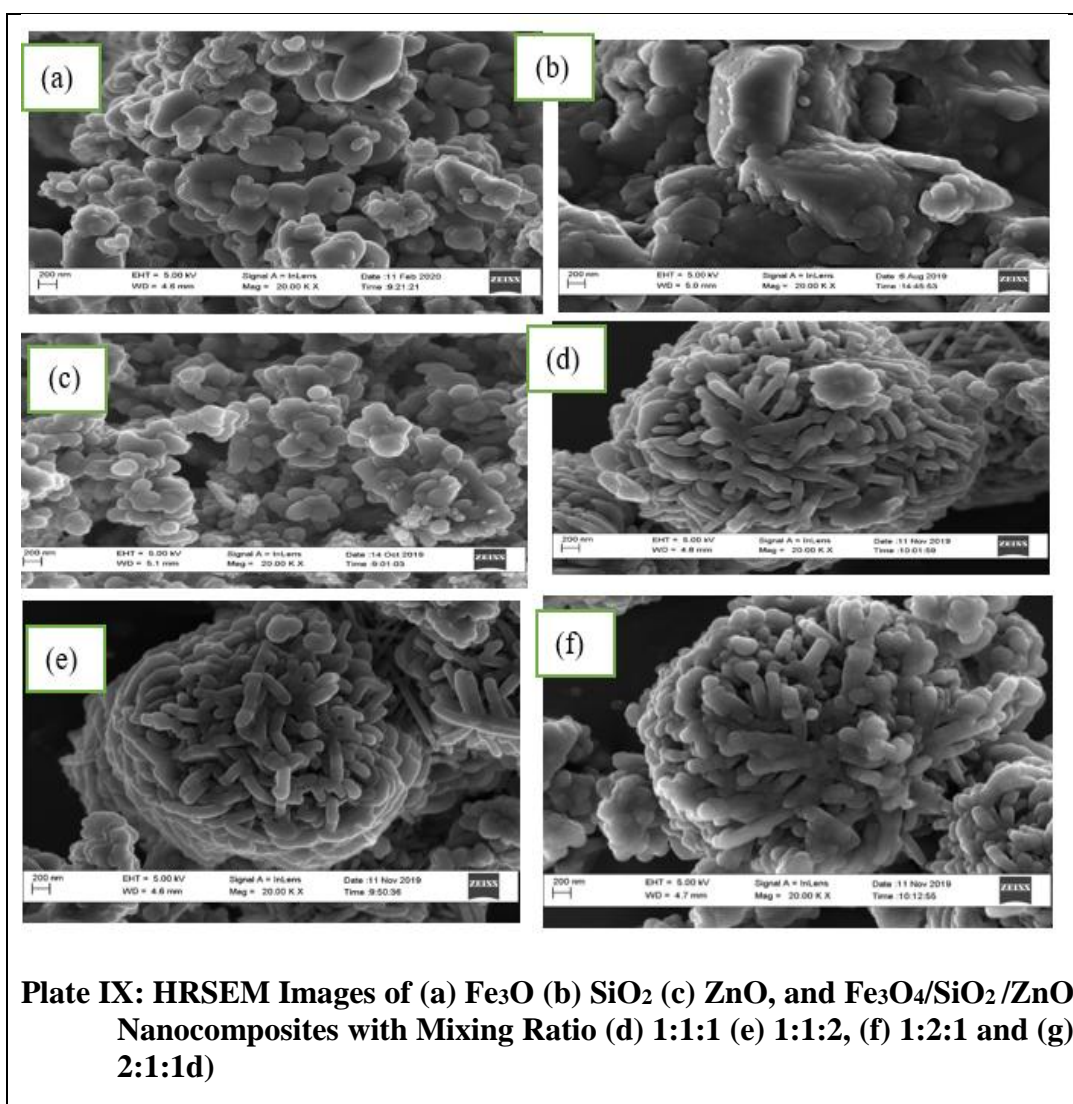
Plate IX (d), (e), (f), and (g) revealed the formation of homogeneously distributed spheroid and spherical particles with less aggregation compared to pure ZnO and Fe_3O_4. After the addition of the SiO_2, the surface morphology becomes rod-like with little spherical shapes on the surfaces irrespective of the dosage of the nanoparticles, indicating the formation of a new material consisting of Fe_3O_4, SiO_2, and ZnO nanoparticles. Plate IX (d), (e), and (f) show less agglomeration compared to nanoparticles with Plate IX (g) which shows a high agglomeration of the nanocomposites due to a smaller amount of SiO_2 earlier noted in the formation of SiO_2/ZnO nanocomposites. Plate IX (f) shows rod-like with increased spherical shapes compared to Plate 4.8 (d), (e), and (g). This may be due to more dosage of Fe_3O_4 in the composites. A homogeneous distributed rod-like structure and less agglomeration were observed in plate IX of (e) due to the higher dosage of SiO_2 in the nanocomposites.

4.8.2   XRD analysis of ternary Fe_3O_4/SiO_2/ZnO nanocomposites

XRD was used to study the crystallographic structure of the ternary Fe_3O_4/SiO_2/ZnO nanocomposites prepared via the sol-gel chemical reduction method at different weight ratios and the corresponding result is given in Figure 4.28
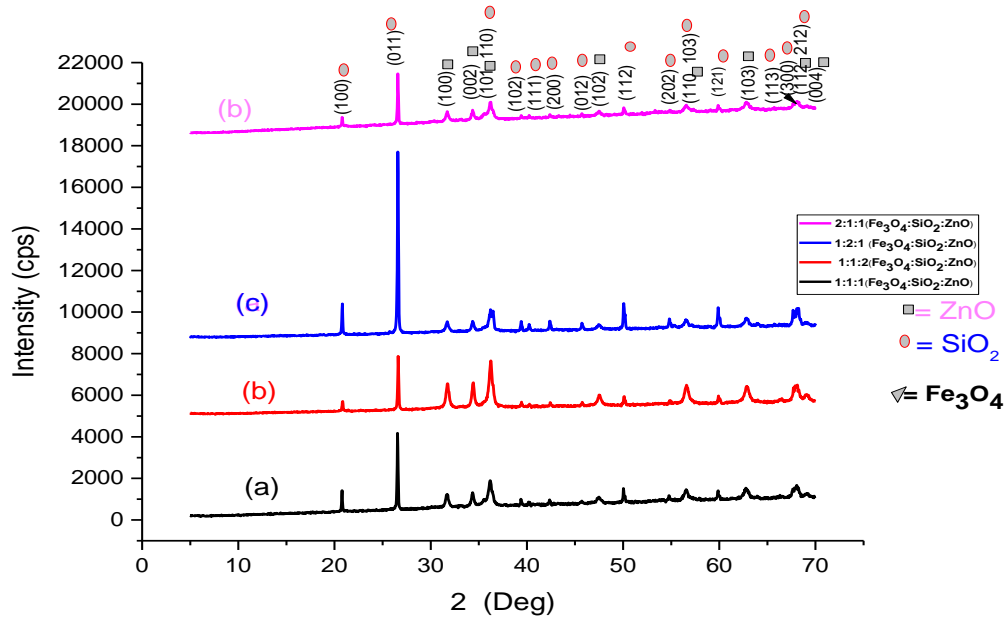
Figure 4.28: **XRD Patterns of Fe₃O₄/SiO₂/ZnO Nanocomposite (a) 1:1:1 (b) 1:1:2, (c) 1:2:1 and (d) 2:1:1**

Figure 4.28 shows the XRD patterns of Fe_3O_4/SiO_2 /ZnO nanocomposite with diffraction peaks at 2θ values of 21.14°, 26.96°, 37.05°, 39.91°, 40.82°, 43.05°, 46.42°, 50.77°, 55.59°, 55.95°, 60.83°, 64.83°, 66.78°, and 68.71°, corresponding to the miller planes of (100), (011), (110), (102), (111), (200), (021), (112), (202), (013), (121), (113), (300), and (212). These match well to the hexagonal α-quartz phase of SiO_2 (JCP278-1255). Comparing the 2θ of the composite with pure SiO_2 nanoparticles (see Figure 4.1), the plane suggests that a slight shift of all diffraction peaks toward the higher 2θ after the incorporation of ZnO and Fe_3O_4 nanoparticles due to the diffusion of SiO_2 onto Fe_3O_4 and ZnO matrix layers (see Figure 4.20). Similar research was conducted by Liu *et al*. (2021) who synthesised graphene-based magnetic at Fe/RGO (1:1) and Fe/RGO (1:4) ratios. They reported the complete disappearance of peaks corresponding to magnetic nanoparticles. Taufiq *et al.* (2020) also reported the disappearance of peaks corresponding to Fe_3O_4 in Silica-magnetite composites.

However, Piranloo *et al*. (2019) reported the synthesis of $Fe_3O_4/SiO_2/ZnO$ nanocomposites material with cubic magnetic cores and reported the disappearance of the peaks corresponding to the SiO_2 nanoparticles. The difference observed in this work may be due to the amorphous nature of SiO_2 nanoparticles used in their study. The authors did not vary the mixing ratio during the formation of the $Fe_3O_4/SiO_2/ZnO$ nanocomposites, which has been reported earlier in this study to have a greater effect on the formation of the nanocomposite.

In addition, the diffraction peaks observed at the 2θ values of 31.77°, 34.42°, 36.25°, 47.53°, 56.60°, 62.86°, 67.96°, and 72.562°; correspond to (100), (002), (101), (102), (110), (103), (112), and (004) crystallographic planes of the hexagonal wurtzite structure of ZnO nanoparticles, suggesting the existence of the ZnO phase after the formation of the nanocomposites (JCP2-36−1451). There are no peaks related to Fe_3O_4 nanoparticles from the XRD results due to the absorption, shielding effects, or because of magnetic properties of Fe_3O_4 (Cheng *et al.,* 2019). Based on the existence of magnetite cores in SiO_2 and ZnO the surface of the Fe_3O_4 nanoparticles was shielded for the XRD instrument, thus responsible for low or weak intensity (Heuer-Jungemann *et al*., 2019).

Figure 4.28 (c) displays diffraction peaks with the highest intensity compared with Figure 4.28 (a) 1:1:1, (c) 1:1:2 and (d) 2:1:1, due to the high dosage of SiO_2 in the composites. Similarly, the higher-intensity peaks observed in Figure 4.28 (b) at 2θ value of 37.05° (101) plane relative to Figure 4.28 (a), (c) and (d) may be ascribed to high dosage of ZnO nanoparticles in the composites of $Fe_3O_4/SiO_2/ZnO$ composites, suggesting an increase in the degree of crystallinity. This phenomenon may be linked to a higher ionic radius of Fe^{2+} (0.76 Å) than the ionic radius of Zn^{2+} (0.74 Å), leading to compression strain and ultimately

increasing the unit cell of the ZnO nanoparticle when compare to the pure ZnO nanoparticle (Carofiglio *et al*., 2020). It also observed that the crystal structure of ZnO nanoparticles in the composites remained hexagonal, irrespective of the mixing ratio.
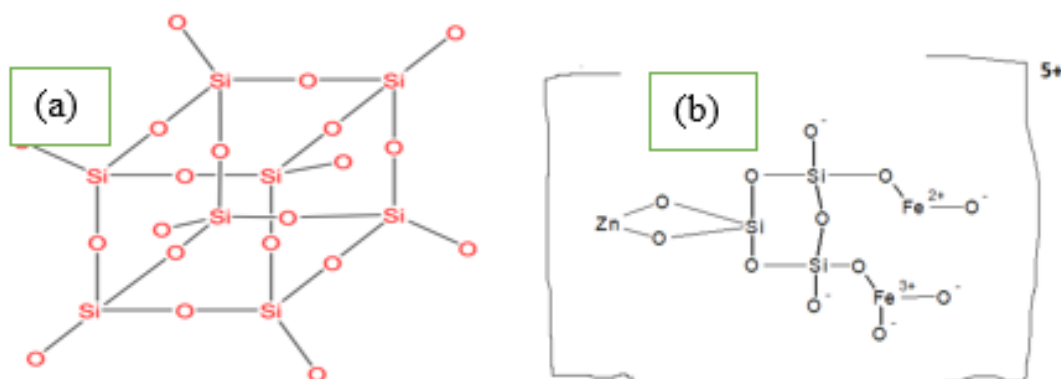
Figure 4.29: **(a) Representation of the Possible Cage-like SiO¬2 Nanoparticles Structure with Four-membered SiO2 Rings on each Face of the Cage (b) Proposed Structure of the Fe3O4/SiO2/ZnO Nanocomposites**

The crystallite sizes of the samples were calculated by Debye Scherrer's equation (see equation 4.2) and the average crystallite size of the $Fe_3O_4/SiO_2/ZnO$ nanocomposites samples was found to be equal to 10.10 nm, 8.84 nm 7.66 nm and 12.40 nm for $Fe_3O_4/SiO_2/ZnO$ nanocomposites with mixing ratios (a) 1:1:1 (b) 1:1:2 (c) 1:2:1, and (d) 2:1:1 respectively. This suggests that the ternary $Fe_3O_4/SiO_2/ZnO$ nanocomposites prepared at 1:2:1 mixing ratio recorded a smaller crystallite size and are expected to be a better nanoadsorbent for the treatment of petroleum wastewater. The increase or decrease in the crystallite size may be attributed primarily to the distortion of the ZnO lattice structure upon the addition of SiO_2 and Fe_3O_4 nanoparticles. From the result of the characterisations, a structure was proposed as seen in Figure 4.29.

Figure 4.29 (a) shows the O atoms linked to the Si on the corners of the cages which is available to form bonds with other cages or terminated as from other nanoparticles.

The Silicon domains create more clustered structures with increasing SiO_2 nanoparticles for the formation of chemical bonds to other elements leading to the formation of more nanoparticles chemically linked to the SiO_2 nanoparticles. As a result, the nanoparticles and interfacial areas become more stable, obstructing the free mobility of the nanocomposites increasing its thermal stability and the resistance to change in pH.

4.8.3   EDS analysis of ternary Fe_3O_4/SiO_2 /ZnO nanocomposites

The elemental composition of the ternary Fe_3O_4/SiO_2 /ZnO nanocomposites was investigated using EDS and the result obtained is displayed in Figure 4.30.
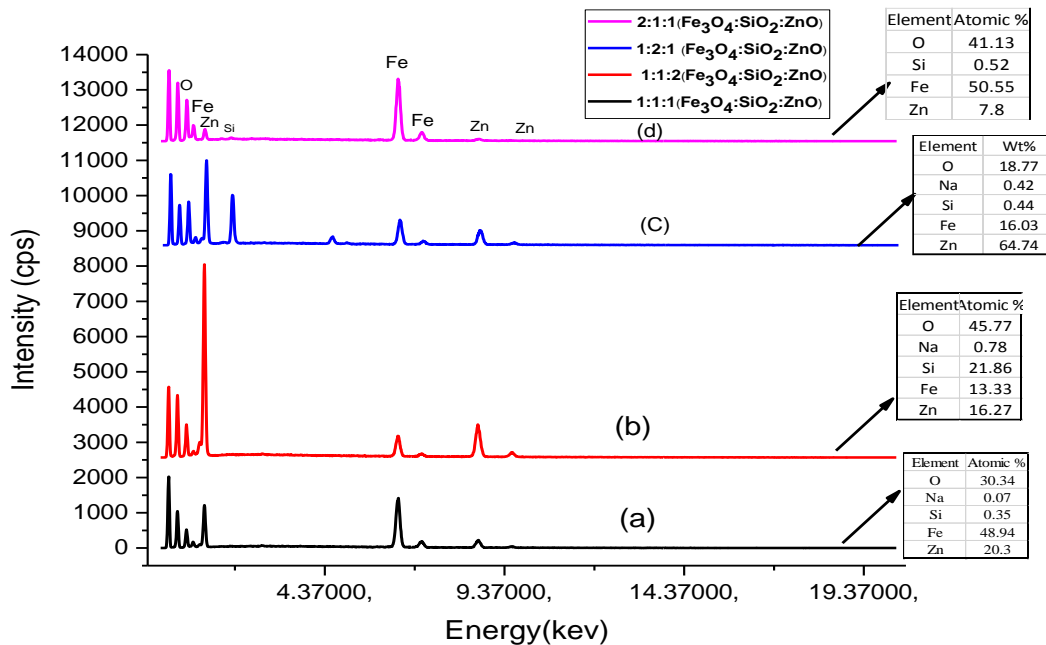
Figure 4.30: EDS Patterns of Fe₃O₄/SiO₂ /ZnO Nanocomposites (a) 1:1:1 (b) 1:1:2, (c) 1:2:1 and (d) 2:1:1

Figure 4.30 reveals that the dominant elements in the ternary metallic oxide composites were Fe, Si, Zn, O while Na was detected as impurities. According to Figure 4.30, the percentage concentration of Fe was 48.94 %, 13.33 %, 16.03 %, 50.55 %, and Si was 0.35 %, 21.86 %, 0.44 %, 0.52 %, Zn was 20.30%, 16.27%, 64.74%, 7.80 % while O was detected to be 30.34 %, 45.77 %, 18.77 %, 41.13 % for (a) 1:1:1 (b) 1:2:1, (c) 1:1:2 and (d) 2:1:1 respectively. The presence of Na may be from the sodium hydroxide or the reducing agent used for the synthesis of the nanoparticles.

4.8.4 BET analysis of ternary Fe_3O_4/SiO_2 /ZnO nanocomposites

The Brunauer–Emmett–Teller (BET) N_2 adsorption-desorption method was used to determine the surface area, pore diameter and pore volume of the Fe_3O_4/SiO_2 /ZnO nanocomposites and the result is presented in Figure 4.31
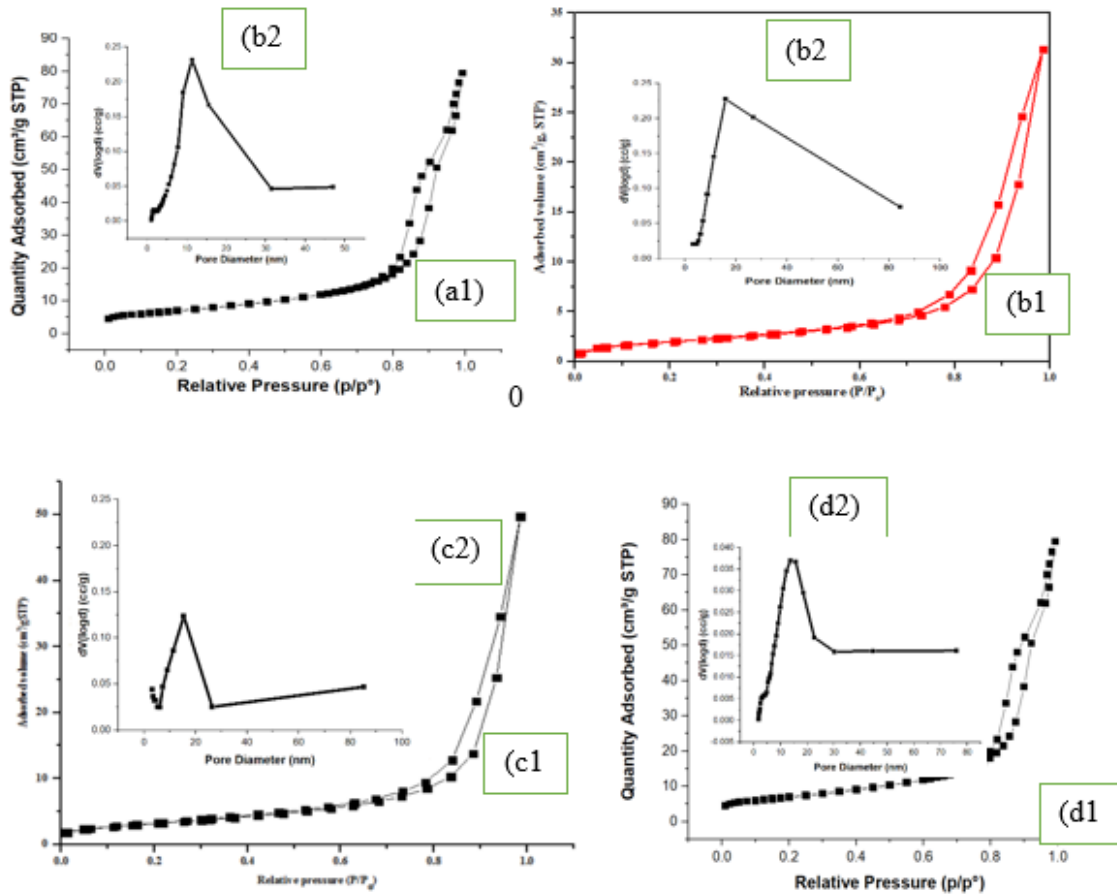
Figure 4.31: (a1) 1:1:1 (b1) 1:2:1, (c1) 1:1:2 and (d1) 2:1:1 Nitrogen Adsorption Desorption Isotherms and (a2) 1:1:1 (b2) 1:2:1, (c2) 1:1:2 and (d2) 2:1:1 Pore Size Diameter Distributions for $Fe_3O_4/SiO_2/ZnO$ Nanocomposite Prepared using mixing ratio (a1) 1:1:1 (b1) 1:2:1, (c1) 1:1:2 and (d1) 2:1:1

According to the International Union of Pure and Applied Chemistry (IUPAC), adsorption isotherm is classified into Type I, Type II, Type III and Type IV. Based on the curve in Figure 4.31 (a1) 1:1:1 (b1) 1:1:2, (c1) 1:2:1 and (d1) 2:1:1, it can be noticed that all four samples exhibited Type IV isotherm of typical mesoporous materials. Figure 4.31 (a) with a mixing ratio of 1:1:1 shows that the hysteresis loops were formed at a relative pressure of 0.8-1.5. Relative pressure of 0.68-1.8 was recorded for (b) 1:1:2 in Figure 4.31(b) 1:1:2.

The hysteresis loops in the relative pressure area 0.5–0.98 were recorded for (c) 1:2:1. The results indicate that the volume of nitrogen adsorption increases with relative pressure until a limit is reached, indicating the availability of pores (Fu *et al.*, 2020). Figure 4.31 (a2) shows the BET plot and the inserted pore diameter plots for $Fe_3O_4/SiO_2/ZnO$ (1:1:1). The result indicates that $Fe_3O_4/SiO_2/ZnO$ (1:1:1) has a surface area, pores diameter and pore volume of ratios 24.918 m²/g, 0.00611 cm³/g and 11.32 nm. Figure 4.31 (b2) with a mixing ratio of 1:1:2 had the surface area, pores diameter and pore volume of 30.685 m²/g, 0.166 cm³/g and 15.00 nm. The surface area, pore diameter and pore volume for $Fe_3O_4/SiO_2/ZnO$ with mixing ratio 1:2:1 were 35.469 m²/g, 0.220 cm³/g and 3.191 nm (Figure 4.32 (c2)).

Additionally, Figure 4.31 (d2) has a surface area, pore diameter and pore volume of 15.751, 0.095 and 3.581 nm respectively (see Table 4.1). Table 4.1 shows the pore diameter for nanocomposites prepared at different mixing ratios $Fe_3O_4/SiO_2/ZnO$ (1:1:1), $Fe_3O_4/SiO_2/ZnO$ (1:1:2), $Fe_3O_4/SiO_2/ZnO$ (1:2:1) and $Fe_3O_4/SiO_2/ZnO$ (2:1:1) and it was found to be less than 50 nm, and according to the IUPAC classification of pore sizes, materials with pore width between 2 to 50 nm are categorized as mesopores materials. It was noticed that $Fe_3O_4/SiO_2/ZnO$ prepared with a mixing ratio 1:2:1 has the highest surface area (35.469 m²/g) followed by 24.918, 30.685, 15.751 m²/g obtained for the $Fe_3O_4/SiO_2/ZnO$ with mixing ratios 1:1:1, 1:1:2, 1:2:1 and 2:1:1 respectively. The increase in surface area may be linked to the increases in the amount of the SiO_2 nanoparticle, suggesting the availability of more binding sites.

The increased surface area of $Fe_3O_4/SiO_2/ZnO$ with a mixing ratio of 1:2:1 also supports the morphological transformation from a spherical shape to a highly compacted rod-like

network. This also corroborated the earlier result presented in Plate IX (f) where the

$Fe_3O_4/SiO_2/ZnO$ nanocomposites show a less agglomerated morphology compared with

other samples in Plate IX (d, e, g and h). The result also suggests that the surface area for all

the nanocomposites prepared at different mixing ratios is higher compared with the

individual metal oxide nanoparticles counterpart with a surface area of 7.864, 0.386, and

8.620 m^2/g as earlier reported in Figure 4.4, 4.12 and 4.17 for Fe_3O_4, SiO_2, and ZnO

respectively. The enhancement in the surface area can be linked to the transformation of the

nanoparticles from spherical to rod-like structure, this results in the creation of more active

sites due to more atoms on the composite's surface and edges. This result suggests that the

$Fe_3O_4/SiO_2/ZnO$ nanocomposites may have higher adsorption capacity compared to the

Fe_3O_4, ZnO and SiO_2 nanoparticles.

Materials with a high surface area are advantageous for the adsorption study because it

provides more active sites for adsorbent adsorption. Additionally, the $Fe_3O_4/SiO_2/ZnO$

nanocomposite produced at a mixing ratio of 1:2:1 compared to the other mixing ratios

recorded a higher surface area as shown in Table 4.1. This observation may be ascribed to

the high density of Fe_3O_4. A similar observation has been reported by Danesh *et al*. (2021),

who reported a decrease in the surface area of GO from 63.647 m^2/g to 3.2897 m^2/g after the

formation of composites with Fe_3O_4. The surface area obtained in this study if higher than

the value obtained by Zohrevand *et al*. (2015) who reported a decrease in the surface area of

polypropylene (PP) and titanium dioxide from 7.1, 1.5 to 0.9 m^2/g as the temperature was

increased from 60 °C, 90 °C to 120 °C. Another researcher has reported a lower surface area

for $Fe_3O_4/CuO/TiO_2$ nanocomposites at different mixing ratios (1:1:1, 1:1:3, 1:1:5). The

authors reported the surface area to be 18.36 and 27.12, 37.64 m^2/g for 1:1:1, 1:1:3 and 1:1:5 respectively.

The values of the internal and external surface obtained during the adsorption-desorption isotherms suggest that the adsorption of the nanocomposites favoured the inter adsorption which is usually related to chemisorption.

Table 4.1: Surface Area, Total Pore Volume and Pore Diameter of Fe$_3$O$_4$/SiO$_2$/ZnO Nanocomposites at different Mixing

Sample Fe$_3$O$_4$/SiO$_2$/ZnO	BET Surface area(m^2/g)	Total Pore Volume (cm^3/g)	BJH pore Diameter (nm)	Internal surface area (m^2/g)	External surface area (m^2/g)
1:1:1	24.918	0.006	11.32	31.7182	25.062
1:1:2	30.685	0.166	15.00	32.439	29.718
1:2:1	35.469	0.220	3.191	39.439	30.08
2:1:1	15.751	0.095	3.581	19.414	17.710

4.8.5   XPS analysis of Fe$_3$O$_4$/SiO$_2$/ZnO nanocomposites

XPS analysis was carried out to determine the chemical states of different elements within the core shell of ternary Fe$_3$O$_4$/SiO$_2$/ZnO nanocomposites and the result of the general XPS survey is displayed in Figure 4.32
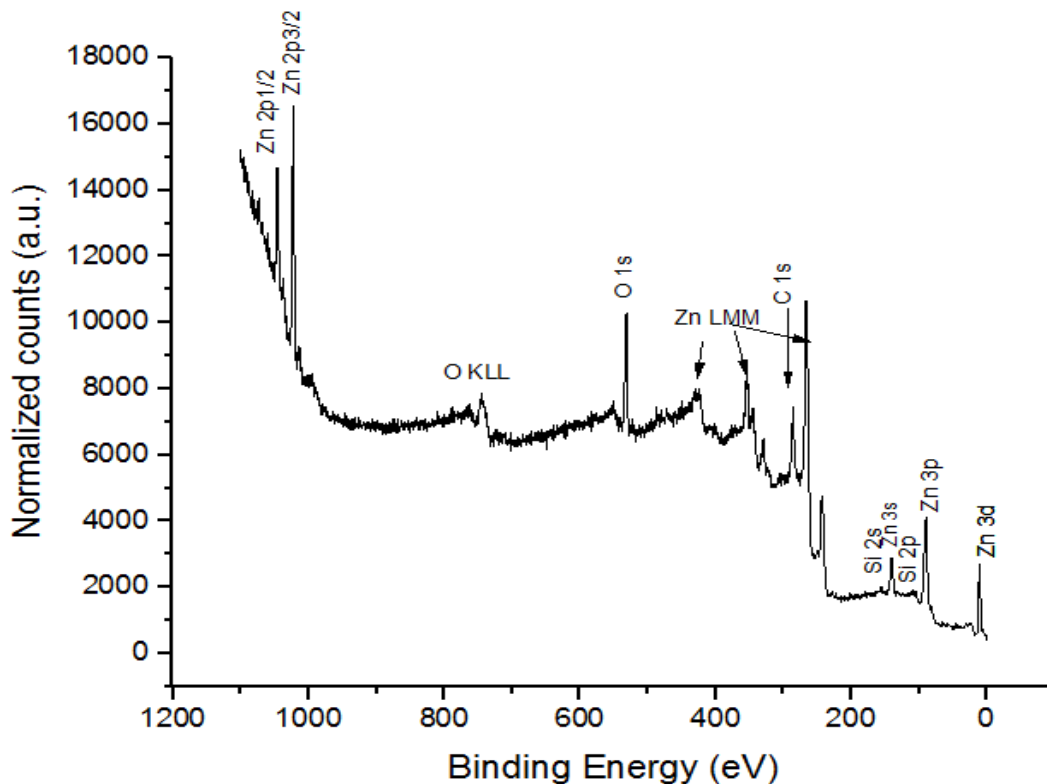
Figure 4.32: General XPS Survey of Fe₃O₄/SiO₂ /ZnO Nanocomposite

Figure 4.32 indicates the presence of peaks at the binding energy of 103.78 eV confirming the existence of Si in SiO_2 nanoparticles. The presence of peaks at 1047 and 1025.1 eV correspond to Zn 2p 1/2 and Zn 2p 3/2 respectively, indicating that the zinc exists in the form of Zn^{2+} chemical state on the sample surfaces. The C (1s) peak at 285.6 eV indicates the presence of an adventitious carbon atom originating from the PVP used as a capping agent for the synthesis of pure Fe₃O₄/ZnO. The absence of peaks belonging to the Fe peak suggests the complete diffusion of Fe onto the internal pores of SiO_2 and ZnO shells. This may also be attributed to the fact that XPS spectra are extremely surface-specific techniques and can cover just about 10 nm of the sample size (Maria and Andreas 2019). XPS results further corroborated XRD results shown in Figure 4.19 where the weak peaks were observed for

174

Fe$_3$O$_4$. The absence of magnetite peaks in the X-ray diffraction patterns depends on the shell thickness. It has been reported that when the shell has a large thickness, the signal from the core is shielded and becomes invisible in the X-ray diffraction pattern (Bakr *et al.*, 2021).

4.8.6   XPS analysis of Zn state in Fe$_3$O$_4$/SiO$_2$/ZnO nanocomposites

XPS was further used to probe the chemical state of the Zn in the Fe$_3$O$_4$/SiO$_2$ /ZnO nanocomposites and the results of the deconvoluted XPS spectral of Zn are presented in Figure 4.33.
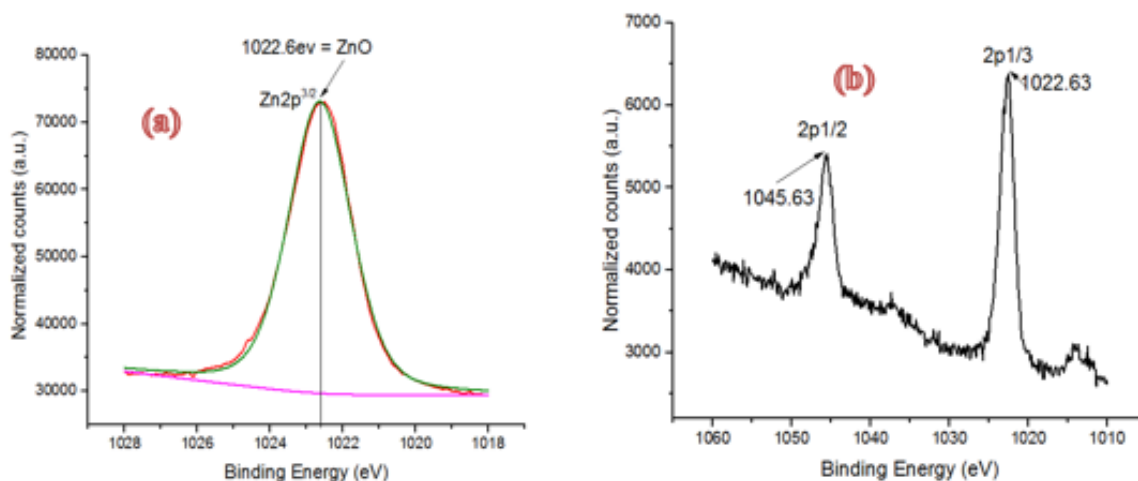
Figure 4.33: XPS Spectrum of Zn 2p3/2 in (a) ZnO Nanoparticles and (b)Fe$_3$O$_4$/SiO$_2$ /ZnO Nanocomposite

Figure 4.33(a) which represents the High-resolution XPS spectrum of Zn 2p3/2 (ZnO) shows the appearance of a single broad peak at a binding energy of 1021.80 eV. This further indicates the presence of a highly electropositive zinc ion (Zn^{2+}) with two donated electrons in a highly electronegative environment with charged O^{2-} ions in the geometry of a hexagonal

Wurtzite structure. Zn 2p3/2 peak was fitted to only one Gaussian in the samples analyzed at a binding energy of 1021.80 eV. Figure 4.33 (b) shows the Zn 2p spectrum, with the peaks at 1045.63 eV and 1022.63 eV which are related to Zn 2p1/2 and Zn 2p3/2 orbitals, suggesting that the Zn element in $Fe_3O_4/SiO_2/ZnO$ nanocomposites exist with only one valence (Zn^+) state as against the Zn^{2+} reported earlier for the pure ZnO nanoparticles in Figure 4.33(a). The presence of Zn with only one valence indicates the formation of a chemical bond with other elements in the Fe_3O_4/SiO_2 leading to the spin-spin splitting of the Zn orbital as observed in Figure 4.33 (b). The result of the in XPS patterns of the Zn 2p for Fe_3O_4/SiO_2 /ZnO nanocomposite shows two peaks compared with the result of the XPS patterns of the Zn 2p for pure ZnO nanoparticles that shows only one peak, indicating that the ZnO nanoparticles have been transformed and incorporated into Fe_3O_4 and SiO_2 to form $Fe_3O_4/SiO_2/ZnO$ nanocomposites via bond formation.

4.8.7   XPS analysis of O state in $Fe_3O_4/SiO_2/ZnO$ nanocomposites

XPS deconvoluted spectra of the O (1s) peak in the Fe_3O_4/SiO_2 /ZnO nanocomposites is presented in Figure 4.34.
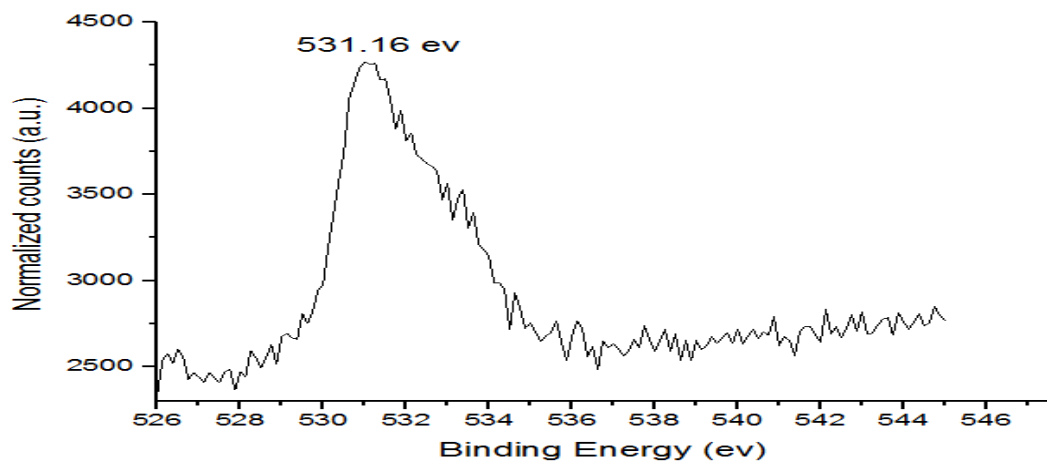
Figure 4.34: XPS of O (1s) Peak of the Fe₃O₄/SiO₂ /ZnO Nanocomposites

The appearance of a peak at the binding energy of 531.16 eV shows that only Si−O−Si or SiO₂ like bonds were present in the composites. This result is different from the analysis by various researchers that have reported peaks corresponding to Si-Si, Si−OH, Al−OH−, C−O bonds (Hajizadeh *et al.*, 2020). The difference observed between this work and previous research may be due to the methods, conditions applied and chemicals used as precursors for the synthesis of the nanocomposites.

4.9   Physicochemical Properties of the Refinery Wastewater

The physicochemical analysis of the petroleum refinery wastewater was studied and the result obtained is presented in Table 4.2.

Table 4.2: Physicochemical Properties Pre and Post treated Petroleum Refinery Wastewater with Various Nanoadsorbents

Pollutants	Concentration Before Adsorption	Concentration after Adsorption Process										WHO Permissible limits (2017)	NSDWQ Permissible limits (2015)
		ZnO	Fe_3O_4	SiO_2	A	B	C	D	E	F	G		
Lead (Pb) mg/L	0.98 ± 0.06	0.192±0.05	0.246±0.10	0.285±0.12	0.090 ±0.30	0.127±0.12	0.166±0.06	0.029±0.20	0.019±0.12	0.009 ±0.10	0.068±0.10	0.003	0.01
Cadmium (Cd) mg/L	1.28 ± 0.10	0.295±0.10	0.338 ±0.05	0.402 ±0.10	0.198 ±0.10	0.230±0.05	0.243±0.12	0.124 ±0.10	0.096±0.20	0.065 ±0.05	0.137±0.10	0.003	0.003
Nikel (Ni) mg/mL	1.34 ± 0.17	0.376±0.10	0.424 ±0.10	0.505±0.05	0.225±0.20	0.291 ±0.30	0.317±0.05	0.139±0.02	0.129 ±0.30	0.092 ±0.12	0.187±0.05	0.1	0.02
Chromium (Cr) mg/mL	0.59 ±0.15	0.263±0.12	0.300 ±0.10	0.322±0.05	0.203±0.01	0.215±0.12	0.241±0.12	0.137±0.05	0.088±0.12	0.065 ±0.10	0.157±0.10	0.08	0.08
Copper (Cu) mg/mL	2.98 ±0.23	0.422±0.10	0.5101±0.12	0.6361±0.11	0.389±0.12	0.4651±0.12	0.571±0.10	0.0333 ±0.30	0.005±0.10	0.00029±0.10	0.120 ±0.15	0.01	1
Iron (Fe) mg/mL	7.07 ±0.14	0.876±0.15	1.076±0.05	1.423 ±0.12	0.517±0.15	0.682±0.03	0.747±0.15	0.0601±0.12	0.0601±0.12	0.026±0.12	0.719±0.10	0.2	0.3
Chemical oxygen demand (COD) mg/L	880.15 ± 0.30	141.7921±0.12	214.3161±0.12	256.123±0.12	138.272±0.20	143.728 ±0.15	167.404±0.5	98.048±0.12	74.724±0.05	66.011±0.05	106.586±0.05	250	500
Biological oxygen demand (BOD) mg/L	190.32 ± 0.20	44.192±0.20	64.899±0.05	76.356±0.20	29.328±0.05	29.328±0.02	38.083 ±0.30	32.39±0.05	29.328 ±0.15	20.954±0.10	44.040 ±0.15	10/5/2007	50
Total organic carbon (TOC) mg/L	560.12 ± 0.03	162.546 ±0.15	180.078±0.20	196.826 ±0.10	103.342±0.20	117.681±0.05	131.348±0.05	74.663±0.04	62.397	51.194±0.05	112.080±0.10	50	40
BOD/COD ratio	0.216 ± 0.40	0.311±0.05	0.302 ±0.15	0.298 ±0.15	0.212±0.05	0.204±0.03	0.227±0.05	0.330±0.05	0.392 ±0.15	0.317±0.20	0.413±0.20		
Conductivity (µS/cm)	483.74 ±0.12	124.03±0.10	130.100±0.08	184.24 ±0.10	96.000 ±0.10	83.01±0.12	99.05±0.06	64.02 ±0.12	54.21±0.11	43.96±0.1	64.04 ±0.1		
pH	6.25 ±0.10	7.02 ±0.11	6.81 ±0.11	6.34 ±0.05	6.25 ±0.10	7.02 ±0.11	6.81 ±0.11	6.34 ±0.05	6.25 ±0.10	7.02 ±0.11	6.81 ±0.11	6.34 ±0.05	

NSDWQ = Nigerian Standard for Drinking Water Quality, WHO = World Health Organization

A= ZnO/Fe$_3$O$_4$, B= ZnO/SiO$_2$, C = Fe$_3$O$_4$/ZnO, D= Fe$_3$O$_4$/SiO$_2$/ZnO (1:1:1), E = Fe$_3$O$_4$/SiO$_2$/ZnO (1:1:2), F= Fe$_3$O$_4$/SiO$_2$/ZnO (1:2:1) and G = Fe$_3$O$_4$/SiO$_2$/ZnO (2:1:1)

Table 4.2 shows the physicochemical parameters of the petroleum refinery wastewater such as pH, conductivity, COD, BOD and Pb (II) and Cadmium Cd (II), Ni (II), Cr (VI) and Fe (II). The pH value obtained was 6.25, which is lower than the 6.51- 8.5 recommended by the WHO and Nigerian Standard for Drinking Water Quality. The low pH could be linked to the dissolved organic carbons in the wastewater and carbon dioxide saturation (Orodu and Alalibo, 2020).

 The value of the electrical conductivity is 483.74 µS/cm, which is greater than the 212.00 µS/cm reported for Port Harcourt refinery wastewater as reported by Osuoha and Nwaichi, (2019). The high electrical conductivity is an indication that the sample contains a significant number of dissolved ions, forming a barrier to organism survival (Meride and Ayenew, 2016). BOD and COD are other frequently used parameters to estimate the amount of organic pollution in wastewater (Tolulope *et al*., 2019).

The refinery wastewater contains a high value of biological oxygen demand (BOD) of 190.32 mg/L compared to the 40 mg/L recommended by the (WHO, 2017). This is an indication that the sample contained a high amount of organic pollutants. Additionally, the higher the BOD, the faster the oxygen in the wastewater is lost, indicating that less oxygen is available to the aquatic life leading to stress, suffocation, and death of the aquatic lives (Xu *et al*., 2020). To determine the overall organic content in the petroleum refinery wastewater, the chemical oxygen demand (COD) index was calculated from the analysis. Table 3.2 also shows that the petroleum refinery wastewater contained 880.15mg/L COD, which is lower than the 2150 mg/L reported by Mohanakrishna *et al*., (2020). The low value of the COD in this study may be linked to the nature of the wastewater. Additionally, this may be due to the less sensitivity

of the inorganic materials present to oxidation by dichromate used as an oxidant. It is important to note that the value of the COD recorded in this study is greater than the BOD shown in Table 4.2. This is because some organic compounds in petroleum refinery wastewater may be resistant to microbial oxidation during the determination of the COD in the wastewater (Abagale, 2021).

The BOD/COD ratio of wastewater is generally used to evaluate the possibility of organic components breakdown in wastewater before treatment. The ratio of the BOD to COD was calculated to determine the biodegradability Index (BI) of the refinery wastewater. The value of the BI (0.216±0.40) was calculated, it has been reported that if the BI value is more than 0.6, the wastewater contained pollutants that can be biologically degraded while if the BI is between 0.3 and 0.6 physiologically methods can be applied for the wastewater treatment. However, if the BI is less than 0.3, hence the wastewater cannot be treated biologically (Dhanke and Wagh, 2020). The value of the BI (0.216±0.40) obtained in this study is less than 0.3 indicating that the petroleum wastewater cannot be treated by biological and physiological methods. This demonstrated that other methods are a better option for the treatment of petroleum refinery wastewater rather than the use of biological or physiological methods. And in this research adsorption method was chosen over biological treatment, due to the low BOD/COD values of 0.216.

 Table 4.2 also shows that the petroleum wastewater contained total organic carbon (TOC) of 560.12 ± 0.03 mg/L, which is above the permissive limit of 50 and 40 mg/L for both Nigerian standards for drinking water quality and world health organization. The high concentration of TOC above the recommended limit has been reported to increases oxidant

demand, lower sterilizing efficacy, and produce hazardous by-products which have negative consequences such as the development of lateral line illness (Pan *et al*., 2020).

Table 4.2 also shows that petroleum refinery wastewater contains different heavy metals. For instance, the concentration of the Pb (II) and Cd (II) was greater than the recommended limits by the WHO. The value of Pb (II) recorded in this study is 0.98±0.06 mg/L, this value is above the 0.003 permissive values by the WHO and NSDWQ. This value is higher than the 0.018 mg/L and 0.47 mg/L reported by Wokoma and Edori (2017) and Olayebi and Adebayo (2017), who independently determined the concentration of Pb (II) in Port Harcourt petroleum refinery wastewater and Warri Refining and Petrochemicals Company respectively. The high concentration of Pb (II) in wastewater has been reported to be poisonous to children resulting in learning and behavioural issues, low intelligence level, growth retardation, anemia, and deafness (Briffa *et al*., 2020). Additionally, it can cause unconsciousness and death at greater levels of toxicity. Pb (II) usually accumulates in the body and is stored in the bones, causing fatal development issues, abortion, and premature birth in pregnant women (Debnath *et al*., 2019). It has cardiovascular effects in adults, raises blood pressure, and causes kidney and reproductive problems (Krishna and Mohan, 2016). The concentration of Cd (II) ion in the petroleum wastewater was 1.28±0.10 mg/L. This value is higher than the concentration of Cd (II) ions (0.001 mg/L) reported by Orodu and Alalibo (2020). Cadmium poisoning hass been reported to harm the kidneys, respiratory systems, and bones, as well as be carcinogenic to humans (Sharma *et al*., 2022).

The concentration of Cr (VI) (0.59±0.15mg/L) is lower than the 1.225 mg/L as reported by Olayebi and Adebayo (2017) from Warri Refining and Petrochemicals Company. This result

is above the WHO permissive limit. Inhalation of Cr (VI) ions is has been linked to nasal ulcer, nasal irritation, lung and skin ulcers (Liu *et al*., 2022). Additionally, it has been reported that the reduction of Cr (VI) to Cr (III) produces reactive intermediates, which contribute to the cytotoxicity, genotoxicity, and carcinogenicity of Cr (VI) containing compounds, along with oxidative stress and oxidative tissue damage (Balali-Mood *et al*., 2021). The concentration of Cu (II) in the petroleum refinery wastewater was recorded to be 2.98 ± 0.23. This value was above the WHO and NSDWQ permissive limits. The presence of Cu (II) ions in the wastewater has been linked to some health challenges such as damage of the liver, brain, kidneys and skin irritation (Moharbi *et al*., 2020).

The concentration of the Fe (II) ions (7.07 ± 0.14 mg/L) compared with the standard permissive limits. Exposure to Fe (II) has been reported to have some effects such as stomach upset, diarrhea, vomiting and nausea. The amount of these heavy metals found in petroleum wastewater is determined by the geological site where the crude is generated (Adeola *et al*., 2021). Most heavy metals that are found in crude oil are due to the type of metals found in the source rock. These metals dissociate in the pore water of these rocks, and the crude oil absorbs them. It is important to note that these pollutants also act as catalysts in the conversion of organic materials to petroleum (Adebiyi *et al*., 2020). As a result, many trace elements identified in crude oil are just a reflection of those picked up during the source of reservoir rock migration (Adeola *et al*., 2021).

The introduction of drilling fluids into the oil during crude oil extraction is another probable source of heavy metals in crude oil (Makeen *et al*., 2021). These compounds are directly introduced to crude oil and eventually end up as pollutants. This helps to explain why drilling

rigs could be a source of heavy metals in wastewater generated by petroleum refinery industries.

4.10 Batch Adsorption Studies

4.10.1 Effect of contact time

Contact time between the adsorbent and adsorbate influences the adsorption process significantly (Virgen *et al*., 2018). This is the most important factor that controls the efficiency of the adsorption process, also determines the economic efficiency of the adsorption process. The effect of contact time on adsorption of Pb (II), Cd (II), Ni (II), Cr(IV), Cu(II) and total iron , as well as BOD, COD and TOC from the petroleum refinery wastewater using ZnO, Fe_3O_4, SiO_2, nanoparticles and ZnO/Fe_3O_4, ZnO/SiO_2, Fe_3O_4/SiO_2, $Fe_3O_4/SiO_2/ZnO$ (1:1:1), $Fe_3O_4/SiO_2/ZnO$ (1:1:2), $Fe_3O_4/SiO_2/ZnO$ (1:2:1), and $Fe_3O_4/SiO_2/ZnO$ (2:1:1) nanocomposites, was studied at different time intervals (1− 25 min) and the results are presented in Figures 4.35-4.43.
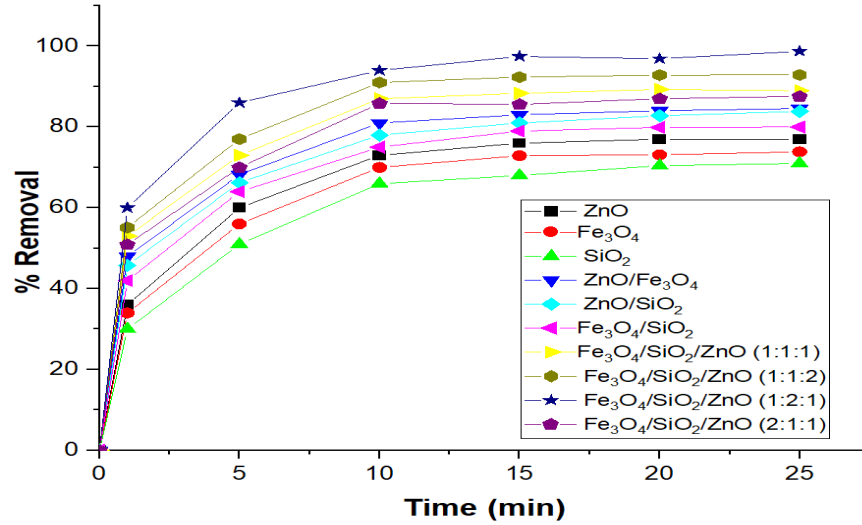
Figure 4.35: Effect of Reaction Time on the Adsorption of Pb (II) **at pH** (6.85), **Dosage (0.05 g), Temperature (30°C) and Volume of the Petroleum Wastewater (50 cm³)**
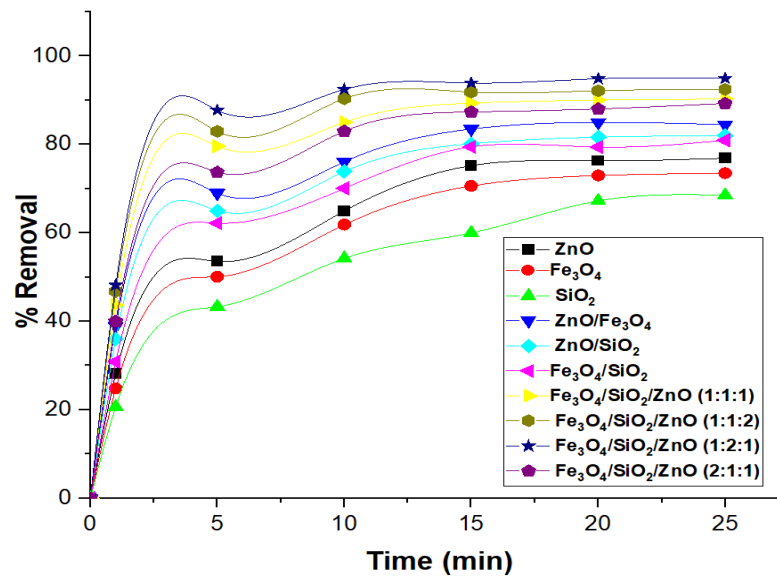
Figure 4.36: Effect of Reaction Time on the Adsorption of Cd (II) **at pH** (6.85), **Dosage (0.05 g), Temperature (30°C) and Volume of the Petroleum Wastewater (50 cm³)**
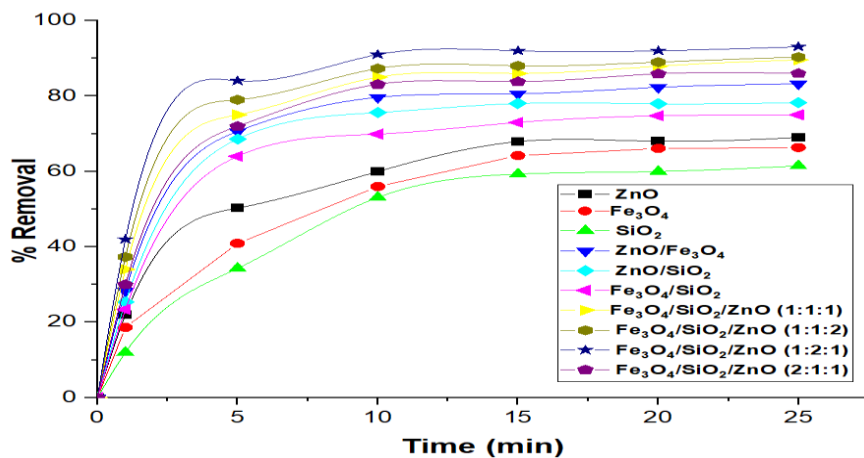
Figure 4.37: Effect of reaction time on the adsorption of Ni (II) at pH (6.85), dosage (0.05 g), temperature (30℃) and volume of the petroleum wastewater (50 cm3)
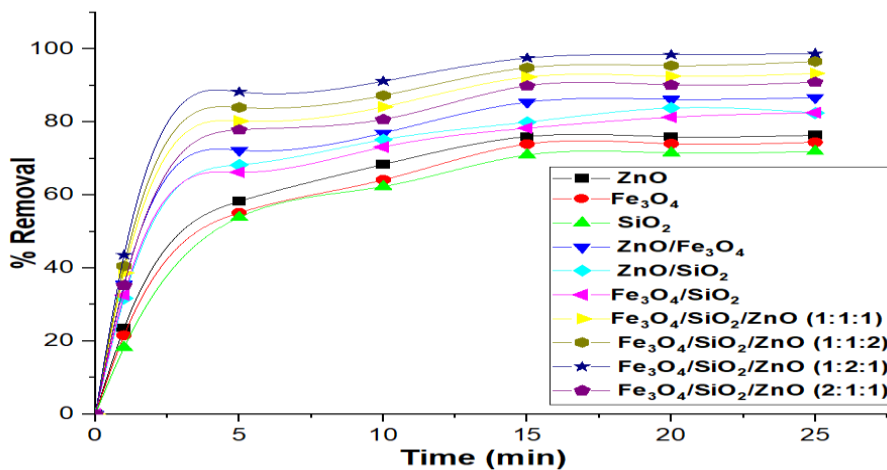
Figure 4.38: Effect of Reaction Time on the Adsorption of Cr (II) at pH (6.85), Dosage (0.05 g), Temperature (30℃) and Volume of the Petroleum Wastewater (50 cm^3)
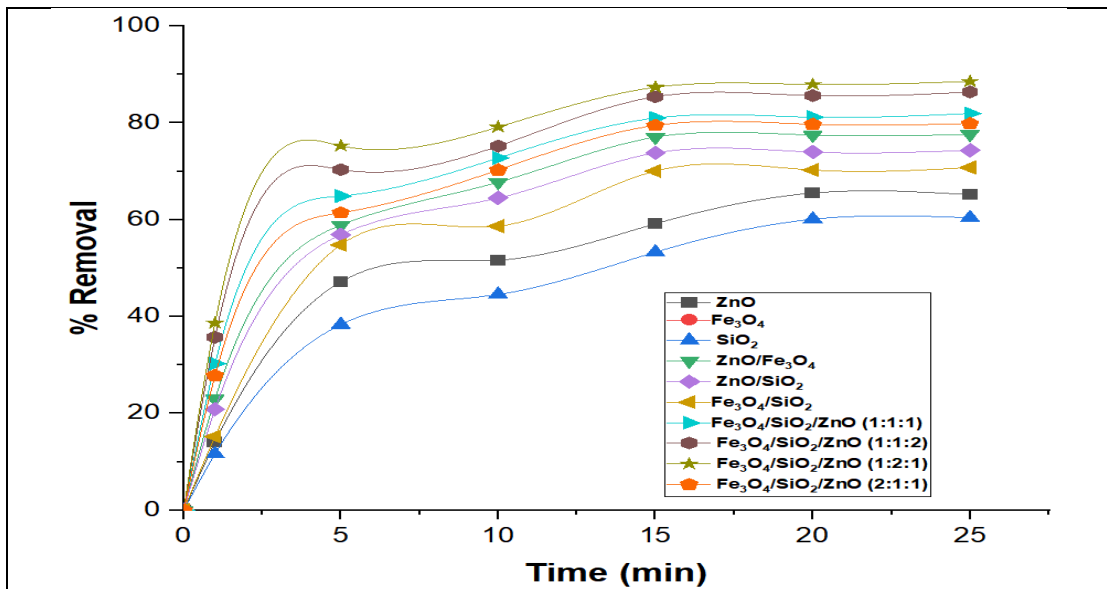
Figure4.39: Effect of Reaction Time on the Adsorption of Cr (VI)at pH (6.85), Dosage (0.05 g), Temperature (30℃) and Volume of the Petroleum Wastewater (50 cm3)
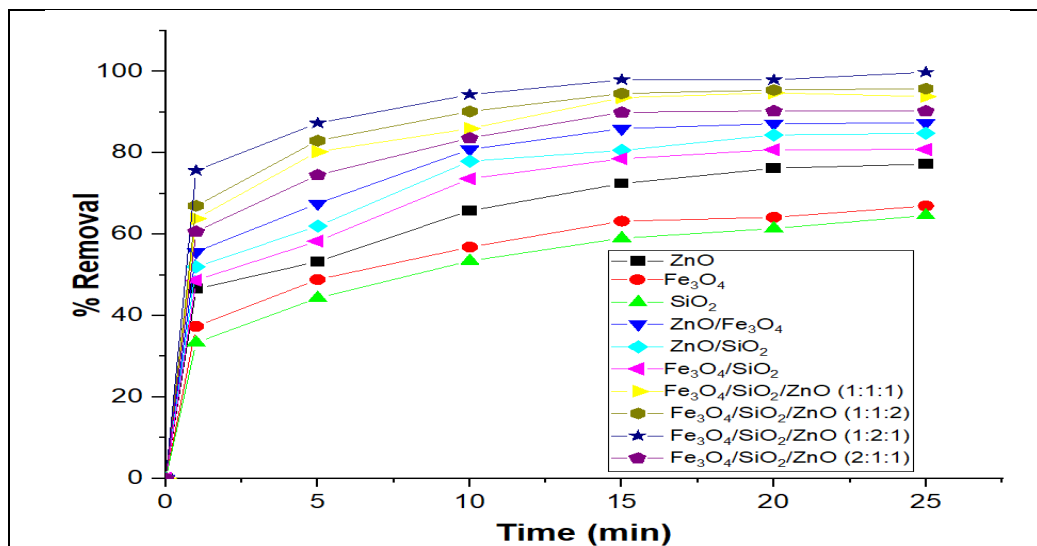
Figure 4.40: Effect of Reaction Time on the Adsorption of Total iron at pH (6.85), Dosage (0.05 g), Temperature (30℃) and volume of the Petroleum Wastewater (50 cm^3)
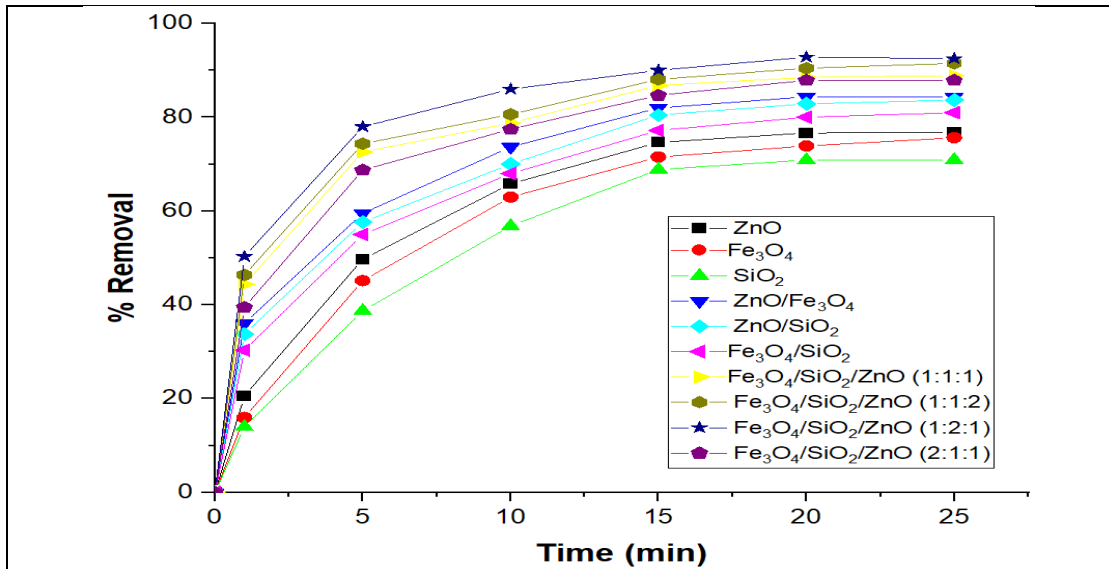
Figure 4.41 Effect of Reaction Time on the Adsorption of BOD at pH (6.85)**, Dosage (0.05 g), Temperature (30℃) and Volume of the Petroleum Wastewater (50 cm³)**
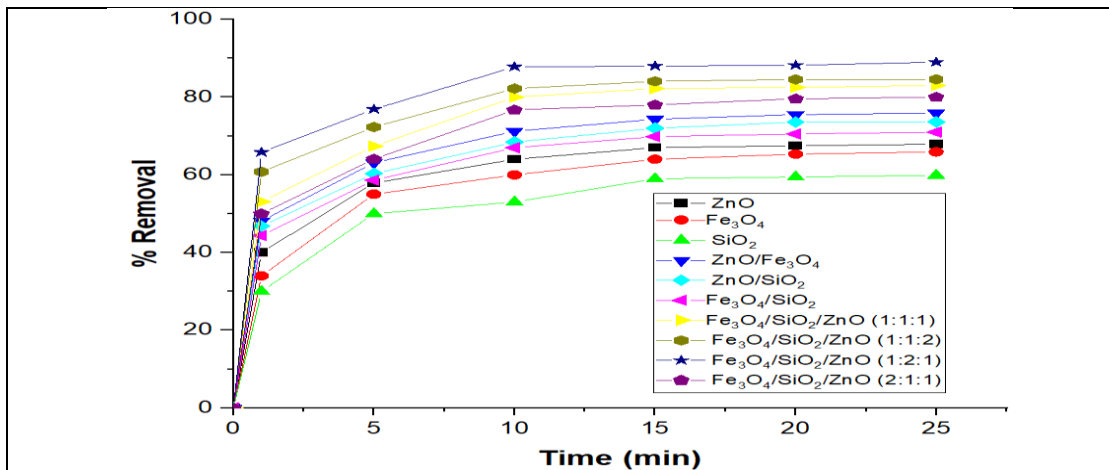
Figure 4.42: Effect of Reaction Time on the Adsorption of COD at pH (6.85), Dosage (0.05 g), Temperature (30℃) and Volume of the Petroleum Wastewater (50 cm³)

Figure 4.43: **Effect of Reaction Time on the Adsorption of TOC at pH** (6.85),
Dosage (0.05 g), Temperature (30℃) and Volume of the Petroleum
Wastewater (50 cm³)
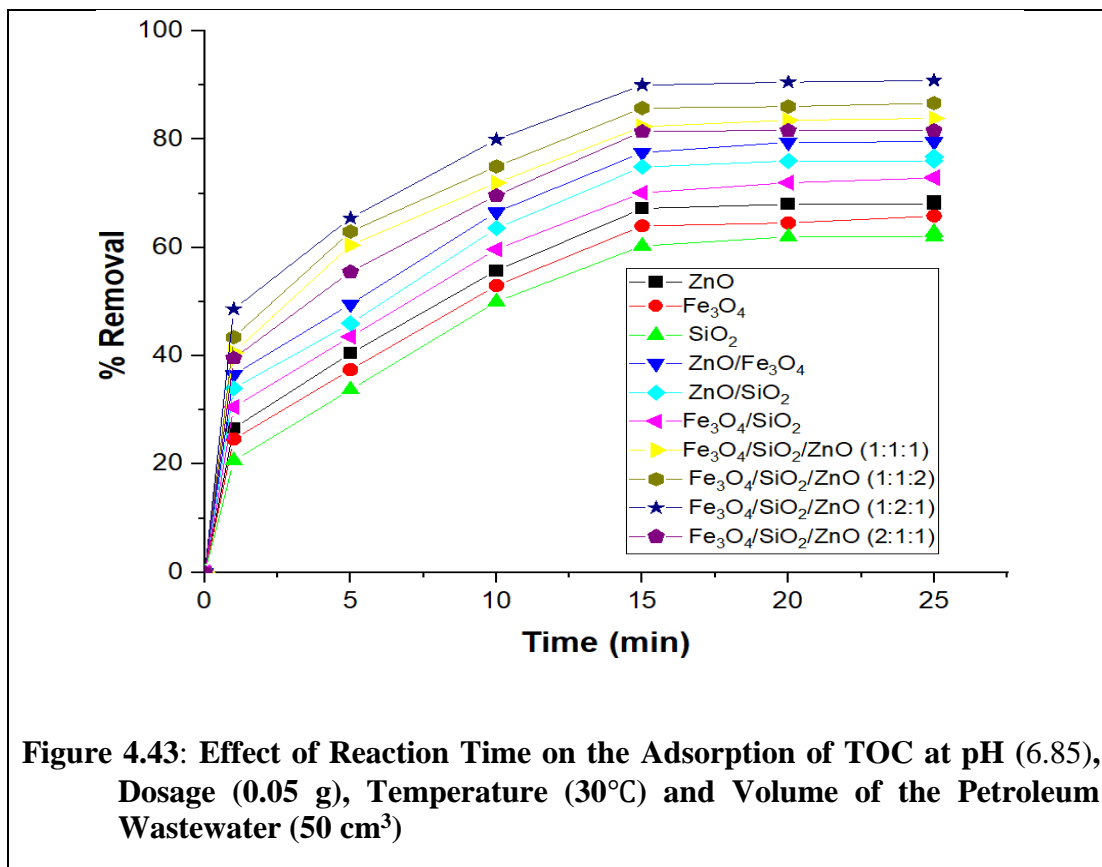
Figure 4.35 demonstrates that the adsorption of Pb (II) by Fe_3O_4, SiO_2, ZnO nanoparticles, ZnO/Fe_3O_4, ZnO/SiO_2, Fe_3O_4/SiO_2, Fe_3O_4/SiO_2/ZnO (1:1:1), Fe_3O_4/SiO_2/ZnO (1:1:2), and Fe_3O_4/SiO_2/ZnO (2:1:1) increase with increase in contact time before equilibrium was reached. The Pb (II) ions removal efficiency was 36.86 %, 34 .03 % and 31.34 % after 1 min of contact time for ZnO, Fe_3O_4 and SiO_2 nanoparticles respectively, then gradually increases to 76.99 %, 73.12 % and 70.44 %, after 20 min of contact time for ZnO, Fe_3O_4 and SiO_2 nanoparticles respectively. After which the removal efficiency was practically constant, indicating that the adsorption was saturated after the 20 min of contact time between the nanoadsorbent and Pb (II). This result revealed that the ZnO nanoparticles recorded the highest percent adsorption removal compared with Fe_3O_4 and SiO_2 nanoparticles. The observed trend may be linked to the average crystallite size and the surface area of the ZnO, Fe_3O_4 and SiO_2 nanoparticles as earlier reported in sections

188

4.2.1, 4.3.1, 4.4.1 and Figure 4.1. A similar trend has been reported by Samad *et al.* (2020), who studied the adsorption characteristics of ZnO nanoparticles for removal of Pb (II) from aqueous solution and reported the increase in the removal efficiency as the contact time increases after 30 min. Similarly, Pb (II) adsorption onto bimetallic oxides nanocomposites (ZnO/Fe_3O_4, ZnO/SiO_2, Fe_3O_4/SiO_2) in Figure 4.35 shows increased dramatically between 1 to 10 min with the highest percentage adsorption of 84.05 %, 80.75 % and 79.80 % for ZnO/Fe_3O_4, ZnO/SiO_2, Fe_3O_4/SiO_2 bimetallic nanocomposites after 15 min of contact time. This result suggests that among the bimetallic nanocomposites, ZnO/Fe_3O_4 recorded the highest percentage removal of Pb (II) with the percentage removal of 84. 05 % compared with $ZnO/SiO_2$and Fe_3O_4, $/SiO_2$. This may be due to the enhanced surface area and synergetic effect between ZnO and Fe_3O_4 nanoparticles and increases in the functional groups present in the nanocomposite leading to higher adsorption of Pb (II) from the petroleum wastewater (Aragaw *et al.*, 2021).

The results of Pb (II) removal by the ternary nanocomposites $Fe_3O_4,/SiO_2/ZnO$ (1:1:1), $Fe_3O_4/SiO_2/ZnO$ (1:1:2), $Fe_3O_4,/SiO_2/ZnO$ (1:2:1), $Fe_3O_4,/SiO_2/ZnO$ (2:1:1) in Figure 4.35 also shows that the contact time has a similar effect on the removal of Pb (II) with $Fe_3O_4,/SiO_2/ZnO$ (1:2:1) having the highest removal efficiency of 98.73 % compared with the 89.07, 92.87 and 87.64 % recoded for $Fe_3O_4,/SiO_2/ZnO$ (1:1:1), $Fe_3O_4,/SiO_2/ZnO$ (1:1:2), $Fe_3O_4,/SiO_2/ZnO$ (2:1:1) nanocomposites after 10 min contact time between the nanoadsorbent and Pb (II), indicating that the ternary nanoadsrbents reached equilibrium faster than the binary and monometallic oxides nanoparticles. Results of Pb (II) removal by the ternary nanocomposites that the adsorption of Pb (II) was for effective using the $Fe_3O_4/SiO_2/ZnO$ (1:2:1) composites compared with the other mixing ratio. The observed trend can be maybe because of the high surface area of the

Fe$_3$O$_4$,/SiO$_2$/ZnO (1:2:1) composites compared with 10.10 nm, 8.84 nm and 12.66 nm for Fe$_3$O$_4$,/SiO$_2$/ZnO (1:1:1), Fe$_3$O$_4$/SiO$_2$/ZnO (1:1:2), Fe$_3$O$_4$,/SiO$_2$/ZnO (1:2:1), Fe$_3$O$_4$,/SiO$_2$/ZnO (2:1:1) as shown in Table 4.1. Additionally, this may be linked to the HRSEM in Plate IX (f) which shows a less agglomerated rod-like structure.

The percentage adsorption removal of Cd (II) for ZnO, Fe$_3$O$_4$ and SiO$_2$ nanoparticles at different times are shown in Figure 4.36. It was discovered that as the contact time between the adsorbent and the petroleum refinery wastewater increased, the adsorption efficiency increases rapidly. The percentage adsorption removal of the Cd (II) increases from 28.14 %, 23.83 % and 20.70 %, to 76.91 %, 73.52 %, 68.54 % respectively when the contact time was increased between 1 min to 15 min for Fe$_3$O$_4$, SiO$_2$ and ZnO nanoparticles. The equilibrium time for the removal of Cd was achieved after 20 min of contact time between the adsorbent and the adsorbate for Fe$_3$O$_4$, SiO$_2$ and ZnO nanoparticles respectively. The result shows that ZnO nanoparticles had the highest removal efficiency compared with Fe$_3$O$_4$ and SiO$_2$ nanoparticles. This may be due to the high surface area and presence of functional groups such as C=O, C-H, C-O and C-N from the PVC used as the structural directing agent.

The result from the bimetallic oxides in Figure 4.36 indicates that the adsorption efficiency is time dependent. The result shows that the ZnO/Fe$_3$O$_4$, ZnO/SiO$_2$, and Fe$_3$O$_4$/SiO$_2$ nanocomposites had the highest adsorption removal of 84.485 %, 81.98 %, and 80.96% for ZnO/Fe$_3$O$_4$, ZnO/SiO$_2$, and Fe$_3$O$_4$/SiO$_2$ respectively at equilibrium time of 15 min. The result revealed that the ZnO/Fe$_3$O$_4$ nanocomposites showed higher percentage adsorption efficiency compared with 81.98 %, 80.96% reported for ZnO/SiO$_2$, and Fe$_3$O$_4$/SiO$_2$ which may be due to the enhanced surface area. The result for the ternary nanocomposites produced at different mixing ratios (Fe$_3$O$_4$/SiO$_2$/ZnO (1:1:1),

$Fe_3O_4/SiO_2/ZnO$ (1:1:2), $Fe_3O_4/SiO_2/ZnO$ (1:2:1), $Fe_3O_4/SiO_2/ZnO$ (2:1:1) are shown in Figure 4.36. The result indicates that the nanocomposites synthesised at 1:2:1 had the highest percentage removal of 96.93% compared to the 90.29%, 92.49 %, and 89.29 % for 1:1:1, 1:1:2, and 2:1:1 respectively. The adsorption removal of the $Fe_3O_4/SiO_2/ZnO$ (1:2:1) nanocomposites may also be a result of the higher surface area and the formation of less agglomerated nanoadsorbent as shown in Plate IX (d, e, f and g).

The results in Figure 4.37 show the effect of contact time on the adsorption of Ni (II). The results reveal that Ni (II) removal increases gradually with contact time. The results for the adsorption of Ni (II) on ZnO, Fe_3O_4 and SiO_2 nanoparticles were 68.99 %, 66.34 % and 61.50 % respectively at an equilibrium time of 20 min. This result suggests that ZnO nanoparticles have higher adsorption for the removal of Ni (II) compared to the Fe_3O_4 and SiO_2 nanoparticles. The high adsorption removal efficiency recorded for ZnO/Fe_3O_4, ZnO/SiO_2, and Fe_3O_4/SiO_2 nanocomposites were 83.23%, 78.24% and 75.00 % respectively. The high adsorption removal efficiency for ZnO/Fe_3O_4 than ZnO/SiO_2, and Fe_3O_4/SiO_2 may be due to the porosity of the ZnO/Fe_3O_4 nanocomposites compared with ZnO/SiO_2, and Fe_3O_4/SiO_2 nanoparticles (Lawtae and Tangsathitkulchai, 2021).

The highest adsorption removal efficiency for the ternary nanocomposites prepared at different mixing ratios were 89.59 %, 90.33 %, 93.07 % and 86 % $Fe_3O_4/SiO_2/ZnO$ (1:1:1), $Fe_3O_4/SiO_2/ZnO$ (1:1:2), $Fe_3O_4/SiO_2/ZnO$ (1:2:1), $Fe_3O_4/SiO_2/ZnO$ (2:1:1) after 15 min of contact time. The high performance of the ternary nanocomposites compared with the bimetallic oxide nanocomposites and the monometallic oxides nanoparticles may be ascribed to the amount of surface charge, availability of active surface sites, increase in surface functionality and less agglomeration of the composites compared with the single nanocomposites (Manyangadze *et al.*, 2020).

The adsorption of Cu (II) presented in Figure 4.38 suggests that ZnO nanoparticles recorded the highest percentage adsorption of 78.40 %, compared with the 74.47 % and 71.99 % recorded for Fe_3O_4 and ZnO nanoparticles respectively. The high adsorption may be linked to the high surface area, porosity and stability of ZnO nanoparticles compared with Fe_3O_4 and SiO_2 nanoparticles (Liosis *et al*., 2021). The adsorption Cu (II) using bimetallic oxides nanocomposites indicates that ZnO/Fe_3O_4 nanocomposite attained a higher adsorption efficiency with a percentage removal efficiency of 86.76 % compared with 83.47 % and 82.57 % for ZnO/SIO_2, and Fe_3O_4/SiO_2 respectively.

The higher adsorption ZnO/Fe_3O_4 nanocomposites than ZnO/SiO_2, and Fe_3O_4/SiO_2 nanocomposites can be explained by the incorporation of ZnO and Fe_3O_4 nanocomposites which have higher surface area compared with the ZnO and Fe_3O_4 nanoparticles that were incorporated into the lattice of SiO_2 which have a lower surface area. The result of the ternary metal oxides nanocomposites presented in Figure 3.38 (d) shows that the highest adsorption removal $Fe_3O_4/SiO_2/ZnO$ (1:2:1) had the highest adsorption removal efficiency (98.78 %) compared with 93.34 %, 96.61 % and 90.94 % for Fe_3O_4/SiO_2, $Fe_3O_4/SiO_2/ZnO$ (1:1:1), $Fe_3O_4/SiO_2/ZnO$ (1:1:2), and $Fe_3O_4/SiO_2/ZnO$ (2:1:1) respectively. The high adsorption of $Fe_3O_4/SiO_2/ZnO$ (1:2:1) may be due to the high porosity of the $Fe_3O_4/SiO_2/ZnO$ (1:2:1) nanocomposites compared with Fe_3O_4/SiO_2, $Fe_3O_4/SiO_2/ZnO$ (1:1:1), $Fe_3O_4/SiO_2/ZnO$ (1:1:2), and $Fe_3O_4/SiO_2/ZnO$ (2:1:1) nanocomposites.

Figure 4.39 shows the adsorption of Cr (VI) using Fe_3O_4, SiO_2, ZnO nanoparticles, ZnO/Fe_3O_4, ZnO/SiO_2, Fe_3O_4/SiO_2, $Fe_3O_4/SiO_2/ZnO$ (1:1:1), $Fe_3O_4/SiO_2/ZnO$ (1:1:2), and $Fe_3O_4/SiO_2/ZnO$ (2:1:1) nanocomposites. The result reveals the adsorption removal of Cr (VI) to be 65.19 %, 62.53 % and 60.41% for ZnO, Fe_3O_4 and SiO_2 nanoparticles

192

respectively. The ZnO nanoparticles adsorbed better than Fe_3O_4 and SiO_2 nanoparticles due to the higher surface area.

The result for the bimetallic oxides and ternary nanocomposites for the removal of Cr (VI) indicates that ZnO/Fe_3O_4, ZnO/SiO_2 and Fe_3O_4/SiO_2 nanocomposites recorded the highest adsorption of 77.65 %, 74.34 % and 70.76 % at equilibrium time of 15 min while the percentage adsorption of $Fe_3O_4/SiO_2/ZnO$ (1:1:1), $Fe_3O_4/SiO_2/ZnO$ (1:1:2), $Fe_3O_4/SiO_2/ZnO$ (1:2:1) and $Fe_3O_4/SiO_2/ZnO$ (2:1:1) nanocomposites were 81.94 %, 86.40 %, 88.57 %, 79.87 % . This result indicates that ZnO nanoparticles performed better than Fe_3O_4 and SiO_2 nanoparticles while ZnO/Fe_3O_4 had the highest adsorption removal efficiency for the removal of Cr (VI) from petroleum refinery wastewater compared to ZnO/SiO_2, Fe_3O_4/SiO_2. The highest among all the nanoadsorbents used for the removal of Cr (VI) from petroleum refinery wastewater was $Fe_3O_4/SiO_2/ZnO$ (1:2:1) with a percentage removal efficiency of 88.57 %. This high removal by ZnO, ZnO/Fe_3O_4 and $Fe_3O_4/SiO_2/ZnO$ (1:2:1) for the monometallic, bimetallic and ternary metallic oxides may be ascribed. This trend may be ascribed to the higher surface area and pore size (Sultana *et al.*, 2022) of ZnO nanoparticles ZnO/Fe_3O_4 and $Fe_3O_4/SiO_2/ZnO$ nanocomposites. The adsorption of Cr(VI) from the petroleum refinery wastewater was accieved within 15 min for all the nanocomposites while the highest adsorption of the single nanoparticles was achieved within 20 min contact time.

The highest adsorption for the removal of total iron from the petroleum refinery wastewater using Fe_3O_4, SiO_2, ZnO nanoparticles, ZnO/Fe_3O_4, ZnO/SiO_2, Fe_3O_4/SiO_2, $Fe_3O_4/SiO_2/ZnO$ (1:1:1), $Fe_3O_4/SiO_2/ZnO$ (1:1:2), and $Fe_3O_4/SiO_2/ZnO$ (2:1:1) nanocomposites as presented in Figure 4.40. The result of the monometallic metal oxides demonstrated that 77.30 %, 66.98 % and 64.65 % of the total iron removal was achieved

for ZnO, Fe_3O_4 and SiO_2 respectively. The high removal of total iron using ZnO nanoparticles compared with Fe_3O_4 and SiO_2 may be ascribed to the high surface area of ZnO nanoparticles compared with Fe_3O_4 and SiO_2 respectively. The result for the bimetallic oxides suggests that ZnO/ Fe_3O_4 recorded the highest removal efficiency of 87.38 % nanoparticles compared with 84.82 % and 80.87 % nanocomposites recorded for ZnO/SiO_2 and Fe_3O_4/SiO_2 respectively.

The result of the ternary nanocomposites shows that the adsorption efficiency was $Fe_3O_4/SiO_2/ZnO$ (1:2:1) > $Fe_3O_4/SiO_2/ZnO$ (1:1:1) > $Fe_3O_4/SiO_2/ZnO$ (2:1:1) > $Fe_3O_4/SiO_2/ZnO$ (1:1:2) for 93.87 % s95.82 %, 99.86 % and 90.32 % respectively. The high performance of the $Fe_3O_4/SiO_2/ZnO$ (1:2:1) nanocomposites may be due to the chemical functionality and stability of the $Fe_3O_4/SiO_2/ZnO$ (1:2:1) than $Fe_3O_4/SiO_2/ZnO$ (1:1:1), $Fe_3O_4/SiO_2/ZnO$ (2:1:1), $Fe_3O_4/SiO_2/ZnO$ (1:1:2) nanocomposites.

Figure 4.38 (g-i) shows the adsorption of BOD, COD and TOC. The BOD, COD and TOC removal efficiency was rapid initially within 1-10 min of the interaction and reached a steady-state at 15 min after which further increases in the contact time did not have a major effect on the adsorption of the adsorbate. Figure 3.38 (g) suggests that the maximum percentage removal efficiency of the BOD was 76.79 %, 75.65 %, 70.90 %, 84.29 %, 83.66 % 80.98 %, 88.86 %, 91.51 %, 92.50 % and 87.89 % for ZnO, Fe_3O_4, SiO_2, and ZnO/Fe_3O_4, ZnO/SiO_2, Fe_3O_4/SiO_2, $Fe_3O_4/SiO_2/ZnO$ (1:1:1), $Fe_3O_4/SiO_2/ZnO$ (1:1:2), $Fe_3O_4/SiO_2/ZnO$ (1:2:1), and $Fe_3O_4/SiO_2/ZnO$ (2:1:1) respectively. Similarly, Figure 4.42 shows that the maximum removal efficiency of COD from petroleum wastewater was 67.89 %, 65.90 %, 59.88 %, 75.90%, 73.59%, 71.00 %, 82.98 %, 84.59 %, 88.99 %, 79.99 % for Fe_3O_4, SiO_2, ZnO, ZnO/Fe_3O_4, ZnO/SIO_2, and Fe_3O_4/SiO_2,

Fe$_3$O$_4$/SiO$_2$/ZnO (1:1:1), Fe$_3$O$_4$/SiO$_2$/ZnO (1:1:2), and Fe$_3$O$_4$/SiO$_2$/ZnO (2:1:1) nanocomposites respectively. Bankole *et al*. (2017) have reported the removal of COD from electroplating wastewater at an optimum contact time of 70 minutes against the 10 to 50 min reported in this study. This finding has both economic and practical implications because the nanocomposites produced in this analysis have a lower contact time for the removal of pollutants from petroleum wastewater. The maximum removal efficiency of TOC from petroleum wastewater was achieved at 68.59%, 65.86 %, 62.86 %, 79.65 %, 76.756 %, 72.99 %, 83.86 %, 86.67 %, 90.86 % and 81.65 % using ZnO, Fe$_3$O$_4$, SiO$_2$, and ZnO/Fe$_3$O$_4$, ZnO/SiO$_2$, Fe$_3$O$_4$/SiO$_2$, Fe$_3$O$_4$/SiO$_2$/ZnO (1:1:1), Fe$_3$O$_4$/SiO$_2$/ZnO (1:1:2), Fe$_3$O$_4$/SiO$_2$/ZnO (1:2:1), and Fe$_3$O$_4$/SiO$_2$/ZnO (2:1:1) as nanoadsorbent as presented in Figure 3.48 (h). The uptake of metal ions and the pollution indicators (BOD, COD and TOC) proceeded in two stages, with the first being rapidly followed by a slower removal. This is because the number of accessible sites is substantially greater thank the number of metal species to be adsoebed, the adsorption process appears to be more rapid (Panda *et al*., 2017). Among the monometallic oxides, the ZnO nanoparticles performed better compared with Fe$_3$O$_4$, SiO$_2$ nanoparticles for the removal of BOD, COD and TOC from the petroleum refinery wastewater.

The result of the bimetallic nanocomposites indicates the order of performance of the nanocomposites were ZnO/Fe$_3$O$_4$ > ZnO/SiO$_2$ > Fe$_3$O$_4$/SiO$_2$ for the removal of all the pollution indicator parameters (BOD, COD and TOC) from the petroleum refinery wastewater.   Among   the   Fe$_3$O$_4$/SiO$_2$/ZnO   (1:1:1),   Fe$_3$O$_4$/SiO$_2$/ZnO   (1:1:2), Fe$_3$O$_4$/SiO$_2$/ZnO (1:2:1), and Fe$_3$O$_4$/SiO$_2$/ZnO (2:1:1) nanocomposites used for the removal of BOD, COD and TOC from petroleum refinery wastewater**,** Fe$_3$O$_4$/SiO$_2$/ZnO (1:2:1) nanocomposites show the highest adsorption removal efficiency. The outstanding

performance of ZnO, ZnO/Fe$_3$O$_4$ and Fe$_3$O$_4$/SiO$_2$/ZnO (1:2:1) nanocomposites may be explained by their higher surface area and small er crystallite size which leads to the availability of a larger number of adsorption active sites during the adsorption process (Sadegh *et al*., 2017).

Generally, it was found that the adsorption of Pb (II), Cd (II), Ni (II) Cr (VI), Cu (II) and total iron was slow between 0-5 min and rapidly increases during the10 minutes, after which, the removal efficiency further increased however at a much slower rate until it reaches equilibrium after between 15 min to 20 min. The fast adsorption rate at the initial stage (10 min) was due to the greater surface adsorption sites at the beginning after which the adsorption then reached a steady-state (Andronic *et al*., 2021). This may also be ascribed to significant interaction between the nanoadsorbent and the adsorbate, leading to higher removal of the heavy metals. As the contact time increases, the heavy metals occupied the active sites leading to the blockage of active sites (El-Saied *et al*., 2017). Accordingly, the percentage adsorption pattern observed for the metal ions was in the order of total iron > Cu (II) > Pb (II) > Cd (II) > Ni (II) > Cr (VI) respectively. The observed trend shows that the ionic radius of the heavy metals ions plays an important role in the removal efficacy of the heavy except for Cu (II) and total iron. Due to their high concentration in the refinery wastewater compared to other elements. The ionic radius is in order of Pb (II) (1.19 Å) Cd (II) (0.97 Å) > Cu (II) (0.73 Å) > Ni (II) (0.72 Å), total iron (0.645 Å) > Cr (VI) (0.62 Å). The larger the ionic radius, the stronger the adsorption of the metal ions due to the lower hydration potential of the heavy metal ions (Fan *et al*., 2021). A similar trend has been reported by Li *et al*. (2018), who obtained higher removal efficiency of 98.0 %, for Pb (II) and 97.3% reported for Cd (II). A similar trend has been observed by Rodríguez, (2020) who studied the potential of

Graphene Oxide–ZnO nanocomposites for the removal of some heavy metal ions from acid mine drainage wastewater. In their analysis, they reported the rapid removal of the heavy metals between 30–60 min. From the result, the ternary nanocomposites perform better than the bimetallic oxides nanoparticles follow by the monometallic metal oxides nanoparticles for all the targeted pollutants. The trend observed may be due to the increase in surface area and the functional groups. Among the monometallic nanoadsorbent ZnO nanoparticle performed better than Fe_3O_4 and SiO_2 nanoparticles while for bimetallic oxides the ZnO/Fe_3O_4 shows a higher adsorption removal efficiency compared follow by ZnO/SiO_2 and Fe_3O_4/SiO_2.

The order of the removal efficiency for the ternary nanocomposites prepared at different mixing ratios was $Fe_3O_4/SiO_2/ZnO$ (1:2:1)> $Fe_3O_4/SiO_2/ZnO$ (1:1:2)> $Fe_3O_4/SiO_2/ZnO$ (1:1:1)> $Fe_3O_4/SiO_2/ZnO$ (2:1:1). Among all the nanoparticles and the nanocomposites studied $Fe_3O_4/SiO_2/ZnO$ (1:2:1) recorded the highest adsorption removal for the selected heavy metals and the organic compounds removed. The high percentage adsorption of the $Fe_3O_4/SiO_2/ZnO$ (1:2:1) nanocomposites could also be related to the high surface area of $Fe_3O_4/SiO_2/ZnO$ (1:2:1) nanocomposites and also enhanced surface area (Table 4.1).

 It is noticed that the monometallic nanoparticles achieve equilibrium at 20 min and both the bimetallic nanocomposites and the ternary nanocomposites attained equilibrium at 15 min for all the targeted pollutants. Therefore the 15 min contact time was used for the experiment.

4.10.2 Effect of adsorbent dosage

The adsorbent dose is one of the significant factors that affect the efficiency of adsorbents in the removal of pollutants from wastewater (Gisi *et al*., 2016). Adsorbent dosage controls the availability of the binding sites during the adsorption (Huang *et al*., 2020). Thus, the effect of adsorbent dosage (0.02, 0.04, 0.06, 0.08, 0.1to 0.12 g) was studied to assess the removal efficiency of Pb (II), Cd (II), Ni (II) Cr(VI), Cu (II), total iron, BOD, COD and TOC from refinery wastewater using ZnO, Fe_3O_4, SiO_2, nanoparticles and ZnO/Fe_3O_4, ZnO/SiO_2, Fe_3O_4/SiO_2, $Fe_3O_4/SiO_2/ZnO$ (1:1:1), $Fe_3O_4/SiO_2/ZnO$ (1:1:2), $Fe_3O_4/SiO_2/ZnO$ (1:2:1), and $Fe_3O_4/SiO_2/ZnO$ (2:1:1) nanocomposites and the results are given in Figures 4.44-52.
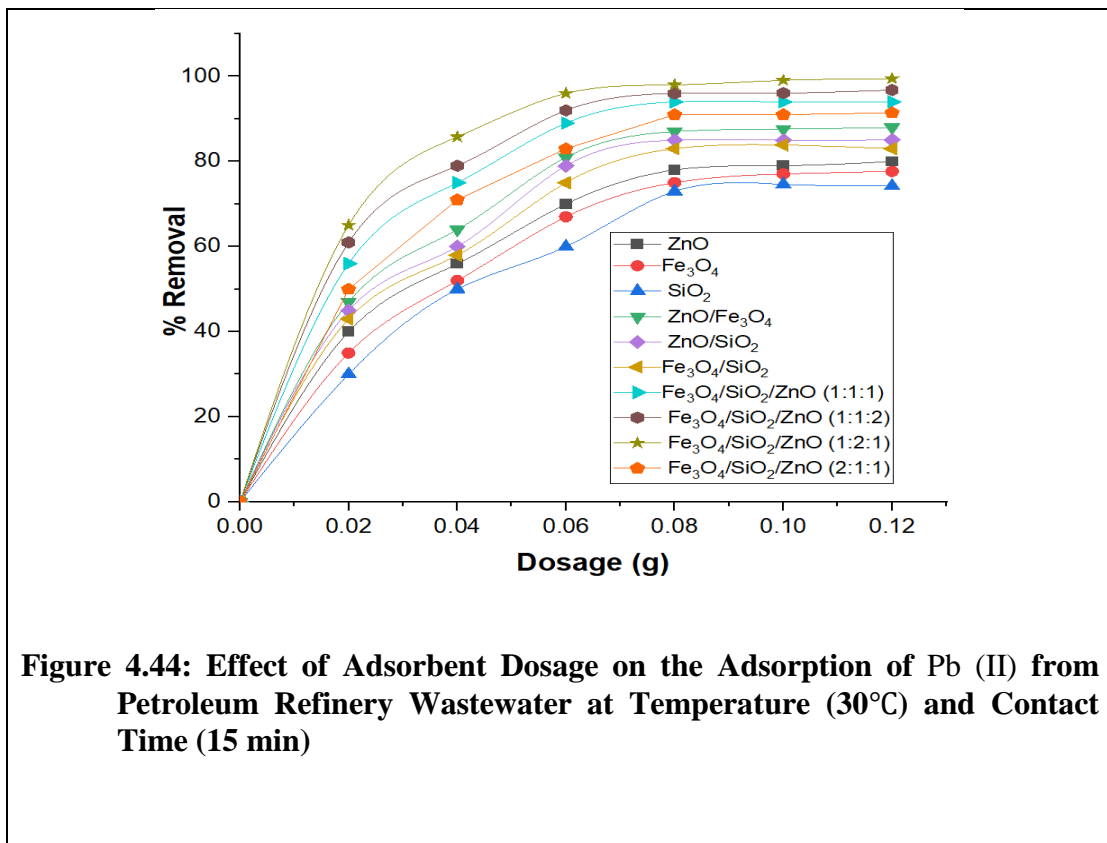
Figure 4.44: Effect of Adsorbent Dosage on the Adsorption of Pb (II) **from Petroleum Refinery Wastewater at Temperature (30°C) and Contact Time (15 min)**
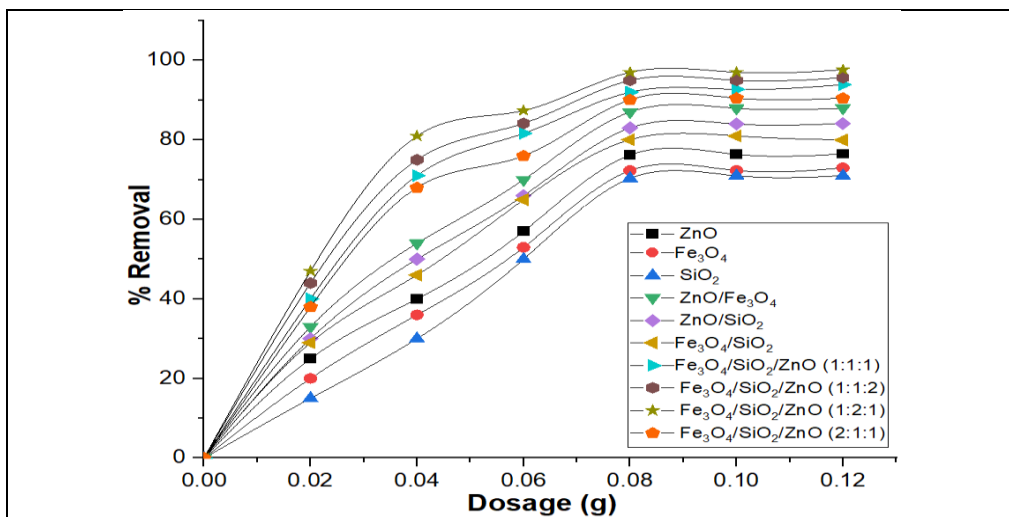
Figure 4.45: Effect of Adsorbent Dosage on the Removal of Cd (II) from Petroleum Refinery Wastewater at Temperature (30°C) and Contact Time (15 min)
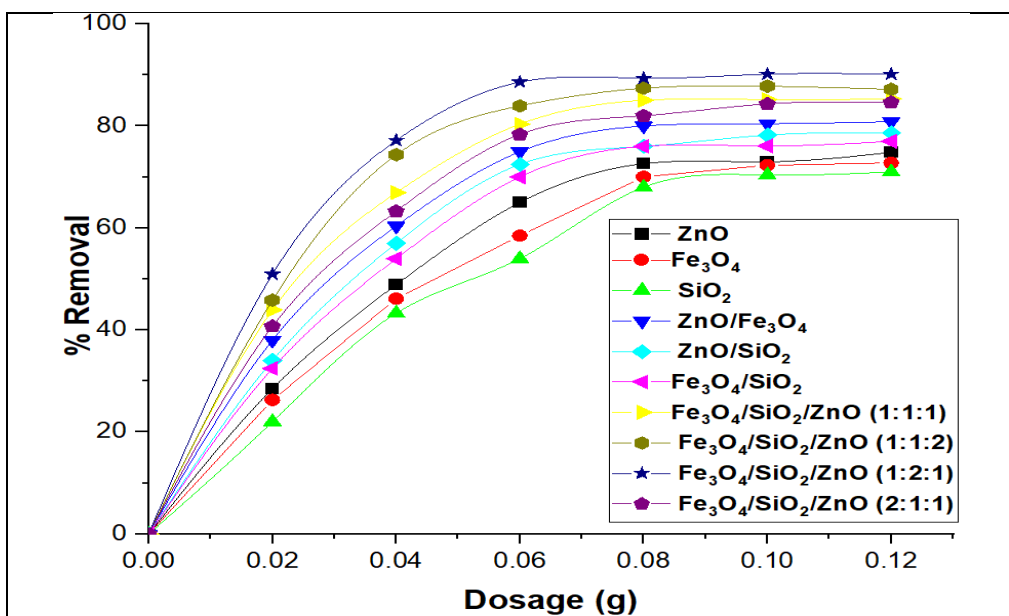
Figure 4.46: Effect of Adsorbent Dosage on the Removal of Ni (II) from Petroleum Refinery Wastewater at Temperature (30°C) and Contact Time (15 min)

Figure 4.47: **Effect of Adsorbent Dosage on the Removal of Cu (II) from Petroleum Refinery Wastewater at Temperature (30°C) and Contact Time (15 min)**

Figure 4.48: Effect of Adsorbent Dosage on the Removal of Cr (VI) from Petroleum Refinery Wastewater at temperature (30°C) and Contact Time (15 min)
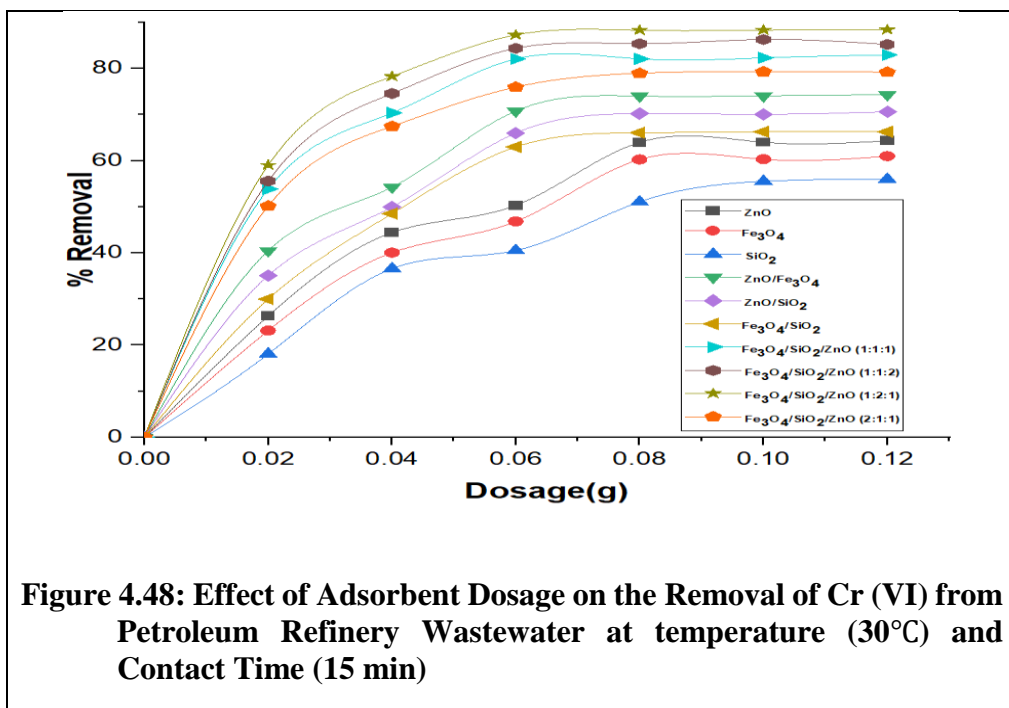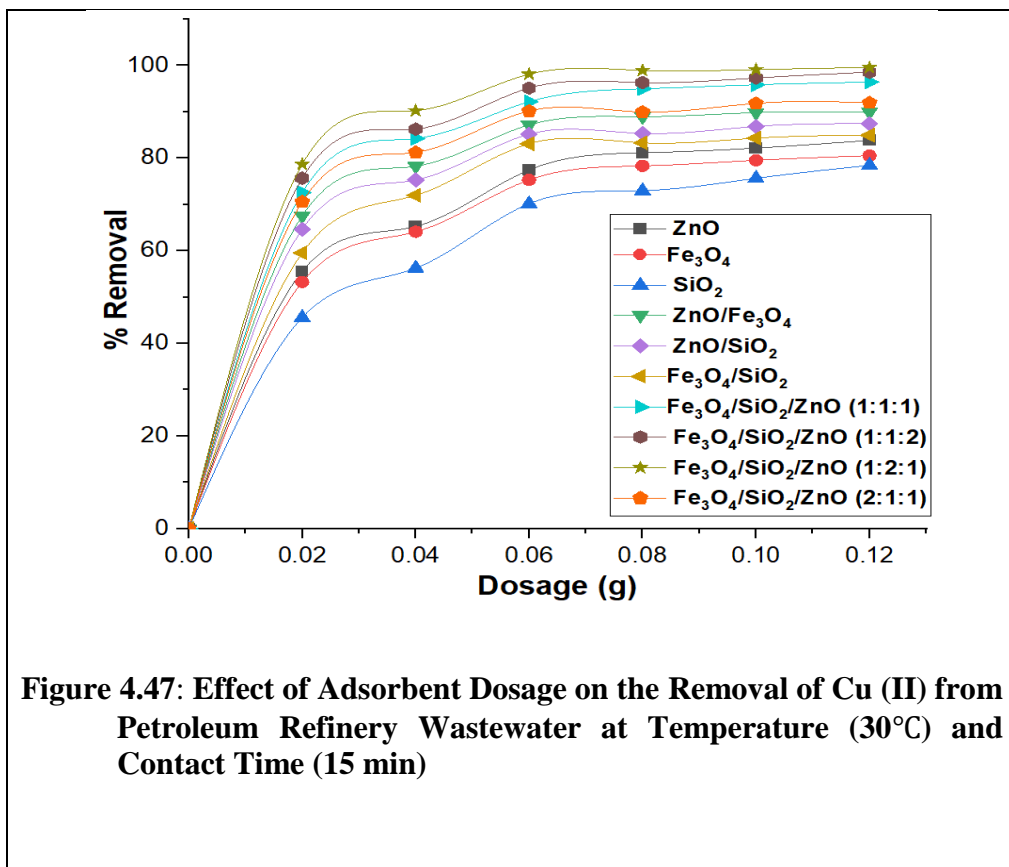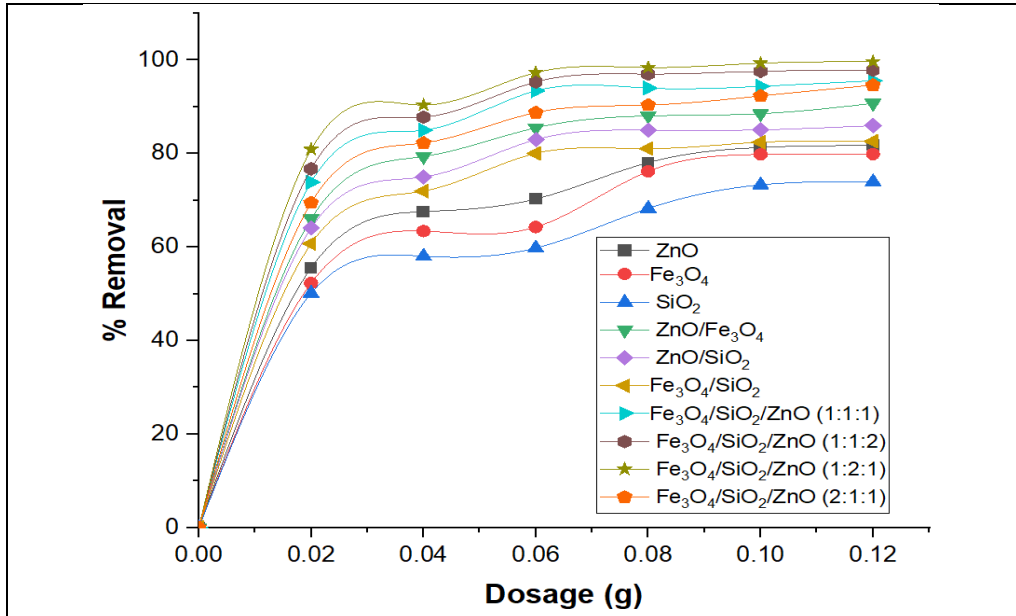
Figure 4.49: Effect of Adsorbent Dosage on the Removal of Total iron from Petroleum Refinery Wastewater at temperature (30℃) and Contact Time (15 min)
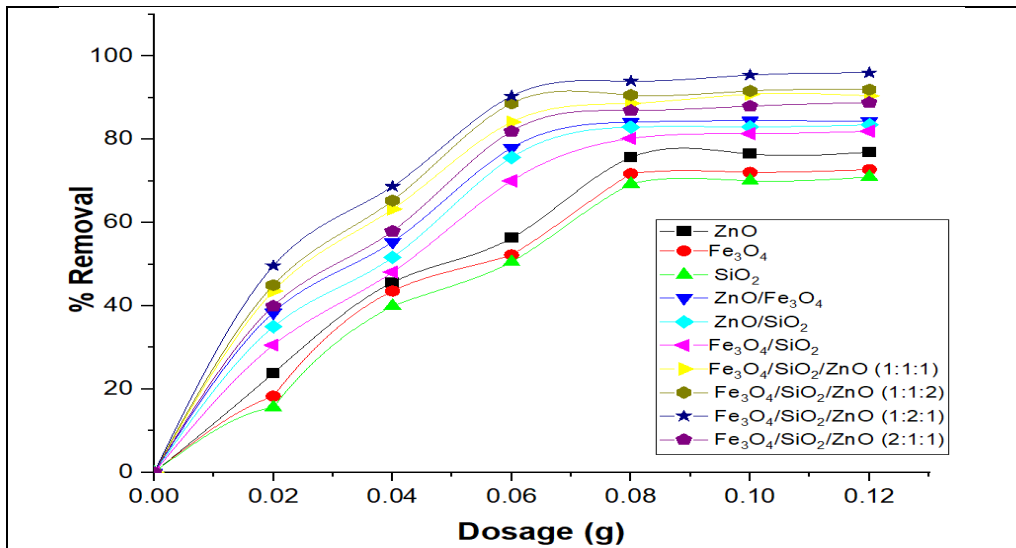
Figure 4.50: Effect of Adsorbent Dosage on the Removal of BOD from Petroleum Refinery Wastewater at Temperature (30℃) and Contact Time (15 min)

Figure 4.51: Effect of Adsorbent Dosage on the Removal of COD from Petroleum Refinery Wastewater at Temperature (30℃) and Contact Time (15 min)

Figure 4.52: Effect of Adsorbent Dosage on the Removal of TOC from Petroleum Refinery Wastewater at Temperature (30℃) and Contact Time (15 min)
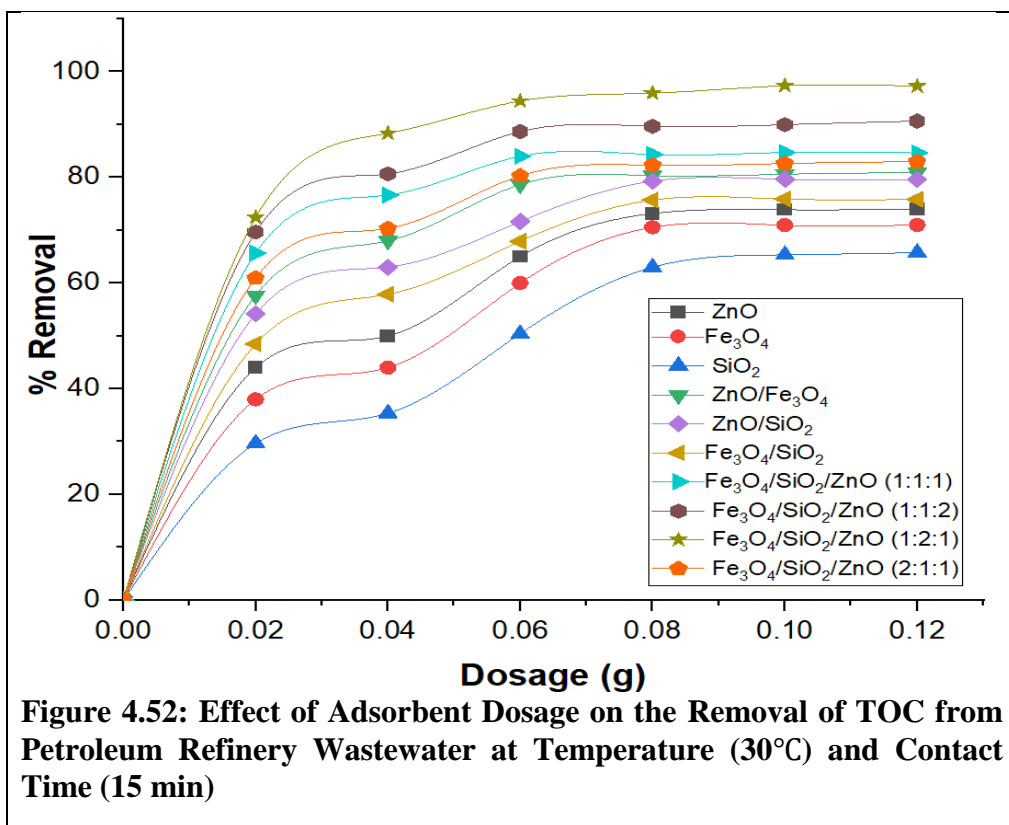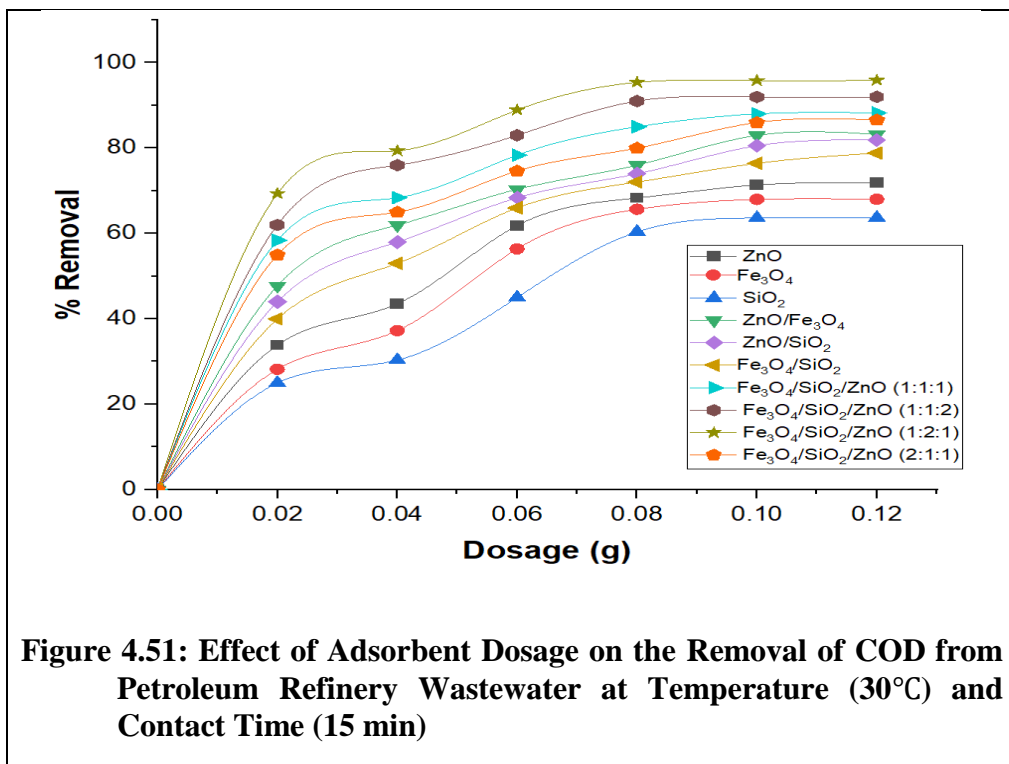
Figure 4.44 shows that ZnO nanoparticles recorded the highest removal efficiency of 80.00 %, compared to 77.65, % and 74.25 % recorded for Fe_3O_4 and SiO_2 respectively, under the conditions of temperature (30℃) and contact time of 15 min.

The high removal of Pb (II) from petroleum refinery wastewater using ZnO nanoparticles may be ascribed to its higher surface area of 8.620 m^2/g compared to the surface area of 7.864 m^2/g and 0.386 m^2/g obtained for Fe_3O_4 and SiO_2 nanoparticles respectively. This is an indication that surface area played an important role in the removal of Pb (II) from petroleum refinery wastewater. The result for the bimetallic oxides suggests that ZnO/Fe_3O_4 recorded the highest removal efficiency of 87.99 %, compared to 85.07 % and 83.02 % recorded for ZnO/SiO_2 and Fe_3O_4/SiO_2 respectively.

This observed trend may be linked to the small crystallite size of ZnO/ Fe_3O_4 (12.45 nm) compared to 16.23 nm and 15.36 nm for Fe_3O_4/SiO_2 and ZnO/SiO_2 nanocomposites as earlier reported in Figure 4.24, 4.26, and 4.22 respectively.

The result of the ternary nanocomposites shows that the removal efficiency of Pb (II) from the petroleum refinery wastewater was in the order of was $Fe_3O_4/SiO_2/ZnO$ (1:2:1) (99.45 %) > $Fe_3O_4/SiO_2/ZnO$ (1:1:2) (96.79 %) > $Fe_3O_4/SiO_2/ZnO$ (1:1:1) (94.01 %) > $Fe_3O_4/SiO_2/ZnO$ (2:1:1) (91.46%) respectively. The outstanding performance of the $Fe_3O_4/SiO_2/ZnO$ (1:2:1) compared to $Fe_3O_4/SiO_2/ZnO$ (1:1:2), $Fe_3O_4/SiO_2/ZnO$ (1:1:1), and $Fe_3O_4/SiO_2/ZnO$ (2:1:1) maybe because of the higher surface area of the $Fe_3O_4/SiO_2/ZnO$ (1:2:1) compared to the surface area obtained for the other ternary composites prepared $Fe_3O_4/SiO_2/ZnO$ (1:1:2), $Fe_3O_4/SiO_2/ZnO$ (1:1:1), and $Fe_3O_4/SiO_2/ZnO$ (2:1:1) as presented in Table 4.1.

Figures 4.45 shows that the removal efficiency of Cd (II) was 78.10 %, 75.97 % and 70.99 % for ZnO, Fe_3O_4 and SiO_2 nanoparticles while the removal efficiency of Cd (II) using bimetallic nanocomposites indicated that ZnO/Fe_3O_4 nanocomposites had the highest removal efficiency of 87.99 % relative to 83.97 % and 80.00 % obtained for ZnO/Fe_3O_4 and Fe_3O_4/SiO_2 respectively. The trend observed may be ascribed to the enhanced surface area of ZnO/Fe_3O_4 compared with ZnO/Fe_3O_4 and Fe_3O_4/SiO_2 nanocomposites. The removal efficiency of the ternary nanocomposites presented in Figures 4.45 shows that $Fe_3O_4/SiO_2/ZnO$ (1:2:1) nanocomposites had removal efficiency of higher 97.63 % against the 93.03 %, 95.65 % and 90.51 % obtained using $Fe_3O_4/SiO_2/ZnO$ (1:1:2), $Fe_3O_4/SiO_2/ZnO$ (2:1:1), $Fe_3O_4/SiO_2/ZnO$ (1:1:1) nanocomposites respectively. The trend observed may be linked to the surface area and the stability of the $Fe_3O_4/SiO_2/ZnO$ (1:2:1) nanocomposites compared to $Fe_3O_4/SiO_2/ZnO$ (1:1:2), $Fe_3O_4/SiO_2/ZnO$ (2:1:1), $Fe_3O_4/SiO_2/ZnO$ (1:1:1) nanocomposites.

In the case of Ni (II) removal from the petroleum refinery wastewater, the highest percentage removal efficiency of Ni (II) were 75.81 %, 72.76 %, 70.98 %, 84.84 %, 78.62%, 76.47 %, 85.31 %, 87.18 %, 90.16% 84.63 % (Figures 4.46) using ZnO, Fe_3O_4 , SiO_2 nanoparticles, ZnO/Fe_3O_4, ZnO/SiO_2, Fe_3O_4/SiO_2, $Fe_3O_4/SiO_2/ZnO$ (1:1:2), $Fe_3O_4/SiO_2/ZnO$ (2:1:1) $Fe_3O_4/SiO_2/ZnO$ (1:2:1), $Fe_3O_4/SiO_2/ZnO$ (1:1:1) nanocomposites respectively as sown in Figures 4.46. The result indicates that ZnO nanoparticles were higher for the monometallic oxides compared to the values recorded for ZnO and Fe_3O_4 nanoparticles respectively. The high removal efficiency recorded for ZnO nanoparticles may be linked to the formation of more bonds such as Vander Waals forces, and electrostatic interactions between the Ni (II) and the functional groups with a

variety of reactive activities compared with the other monometallic metal oxides (Zhang *et al*., 2017).

Figure 4.47 indicates that the removal efficiency of Cu (II) from the petroleum refinery wastewater for monometallic oxides follow order ZnO (86.86%) > Fe_3O_4 (80.57 %) > SiO_2 (78.47 %) nanoparticles while for the bimetallic oxides order was ZnO/SiO_2 (89.99 %) > ZnO/Fe_3O_4 (87.86 %) > Fe_3O_4/SiO_2 (84.97 %). Additionally, the adsorption behaviour of the ternary nanocomposites prepared at different mixing ratios for the adsorption of Cu (II) from the petroleum refinery wastewater shows that the adsorption removal efficiency ranges between 96.47 %, 98.57 %, 99.57 %, 91.99 % for $Fe_3O_4/SiO_2/ZnO$ (1:1:1), $Fe_3O_4/SiO_2/ZnO$ (11:2), $Fe_3O_4/SiO_2/ZnO$ (1:2:1), $Fe_3O_4/SiO_2/ZnO$ (2:1:1) respectively. This result suggests a different trend in the adsorption process compared with the other heavy metals earlier discussed, in that the adoption of Cu (II) from the petroleum wastewater recoded the highest adsorption for $Fe_3O_4/SiO_2/ZnO$ (1:2:1) against $Fe_3O_4/SiO_2/ZnO$ (1:1:1), $Fe_3O_4/SiO_2/ZnO$ (11:2) and $Fe_3O_4/SiO_2/ZnO$ (2:1:1) nanocomposites. The high removal of the nanocomposites compared with the single nanoparticles for the removal of Cu (II) from the petroleum refinery wastewater may be ascribed to the formation of different nanoparticles into a single material leading to the increase in the functional group, surface area and stability (Li *et al*., 2020).

Figures 4.48 demonstrates that the removal of efficiency of Cr (VI) from the petroleum refinery wastewater for the monometallic oxides nano adsorbent follows the order ZnO (64.34 %,) > Fe_3O_4 (61.00 %) > SiO_2 (55.99 %) while the bimetallic oxides nanocomposites were in the order of ZnO/Fe_3O_4 (74.34 %), ZnO/SiO_2 (70.64 %), Fe_3O_4/SiO_2 (66.30 %). The highest removal efficiency for the ternary composites were in

the order of 82.97 %, 85.23 %, 88.42 % and 79.23 % for $Fe_3O_4/SiO_2/ZnO$ (1:1:2), $Fe_3O_4/SiO_2/ZnO$ (2:1:1) $Fe_3O_4/SiO_2/ZnO$ (1:2:1), $Fe_3O_4/SiO_2/ZnO$ (1:1:1) nanocomposites respectively. The trend observed in the removal efficiency shows that the surface area of the nanomaterials used as an adsorbent played an important role in the removal process. This analysis indicates that Cr (VI) has the least adsorption removal among all the selected heavy metals.

The result for the removal of total iron from petroleum refinery wastewater is presented in Figures 4.49. The result shows that the adsorption of total iron was in the order of ZnO (81.76 %) > Fe_3O_4 (79.90 %) > SiO_2 (76.98 %) at adsorbent dosage of 0.05g. The high adsorption removal efficiency of the ZnO nanoparticles relative to Fe_3O_4 and SiO_2 nanoparticles may be explained by the presence of many functional groups such as Zn-O, C=O, C-H, C-O, C-N compared with Fe-O C-O, C-O-C and O-Si-O , Si-H reported for Fe_3O_4 and SiO_2 nanoparticles in Figure 4.4 and 4.11 respectively.

A similar trend was observed for the removal of total iron using bimetallic oxides nanocomposites. The highest removal was achieved at the same adsorbent dosage and the removal efficiency for ZnO/Fe_3O_4, ZnO/SiO_2 and Fe_3O_4/SiO_2 were 90.76, 85.99 %, 82.653 % respectively. From the result, it can be concluded that the removal of total iron was better using ZnO/Fe_3O_4 compared with ZnO/SiO_2 and Fe_3O_4/SiO_2. This trend may be linked to the enhanced surface functionality of ZnO/Fe_3O_4 nanocomposites compared with ZnO/SiO_2 and Fe_3O_4/SiO_2 nanocomposites.

The result of the ternary metallic oxides were 95.59 %, 97.87 %, 99.67 %, and 94.65 % for $Fe_3O_4/SiO_2/ZnO$ (1:1:1), $Fe_3O_4/SiO_2/ZnO$ (1:1:2), $Fe_3O_4/SiO_2/ZnO$ (1:2:1), and $Fe_3O_4/SiO_2/ZnO$ (2:1:1) nanocomposites respectively. This result demonstrated that $Fe_3O_4/SiO_2/ZnO$ (1:2:1) showed higher adsorption for the removal of total iron from

petroleum refinery wastewater and this may be due to its high surface area (35.469 m^2/g) compared with 24.918 m^2/g, 30.685 m^2/g and 15.751 m^2/g obtained for Fe$_3$O$_4$/SiO$_2$/ZnO (1:1:1), Fe$_3$O$_4$/SiO$_2$/ZnO (1:1:2), Fe$_3$O$_4$/SiO$_2$/ZnO (1:2:1), and Fe$_3$O$_4$/SiO$_2$/ZnO (2:1:1) nanocomposites (see Table 4.1).

The results of BOD, COD and TOC removal from petroleum refinery wastewater are shown in Figure 4.50, 4.51 and 4.52 respectively. The results showed that as the adsorbent dosage increases, the removal of the water quantity indicator parameters (BOD, COD and TOC) increases. The rate of removal of the indicator parameters in petroleum refinery wastewater was found to almost double as the adsorbent dosage increases from 0.02 to 0.08 g and after 15 min the removal efficiency become steady due to the interaction between the adsorbent and the adsorbate. The highest removal efficiency of the indicator parameters in petroleum refinery wastewater was 76.97%, 72.78 % and 70.95 % for BOD while that of COD values were 73.99 %, 70.02% and 67.69 %, and TOC removal efficiency was 71.84 %, 68.00% and 65.77% using ZnO, Fe$_3$O$_4$ and SiO$_2$ nanoparticles as adsorbents respectively. The result revealed that ZnO nanoparticles was more effective in the removal of BOD, COD and TOC from the petroleum refinery wastewater compared with the use of Fe$_3$O$_4$ and SiO$_2$ nanoparticles as nanosdsorbent, which may be due to the high surface area of ZnO (8.620 m^2/g) compared with 7.464 m^2/g and 0.386 m^2/g for Fe$_3$O$_4$ and SiO$_2$ nanoparticles. The BOD removal efficiency from petroleum refinery wastewater by the bimetallic oxides nanocomposites was in the order of ZnO/ Fe$_3$O$_4$ (84.37 %) > ZnO/SiO$_2$ (83.55 %) > Fe$_3$O$_4$/SiO$_2$ (81.97 %) for BOD. The COD percentage removal efficiency for COD were in the order of ZnO/ Fe$_3$O$_4$ (83.24 %) > ZnO/SiO$_2$ (81.86 %) > Fe$_3$O$_4$/SiO$_2$ (78.84 %) while the TOC follow the same trend in order of ZnO/ Fe$_3$O$_4$ (80.94 %) > ZnO/SiO$_2$ (79.6 7%,) > Fe$_3$O$_4$/SiO$_2$ (75 .87 %). The trend observed can be explained

by the crystallite size of the nanoparticles. A similar trend has been reported by Nandiyanto *et al*. (2016) and Długosz *et al*., (2021) who independently reported the decrease in removal efficiency as the crystallite size of the nanoparticle increases.

For the ternary nanocomposites the percentage BOD removal was 90.47 %, 91.80 %, 97.28 % and 88.91 %; COD was 84.24 %, 92.01 %, 95.88 % and 86.59 % while the TOC reduction was 80.68, 90.67 %, 93.99% and 82.99 % for $Fe_3O_4/SiO_2/ZnO$ (1:1:1), $Fe_3O_4/SiO_2/ZnO$ (1:1:2) $Fe_3O_4/SiO_2/ZnO$ (1:2:1), $Fe_3O_4/SiO_2/ZnO$ (2:1:1) respectively.

Generally, it was noticed that among the monometallic oxide nanocomposites, ZnO nanoparticles exhibited high removal of pollutants based on its high surface area than others. For the bimetallic oxides nanocomposites, ZnO/Fe_3O_4 demonstrated higher adsorption compared with ZnO/SiO_2 and Fe_3O_4/SiO_2 based on its enhanced surface area. Among the ternary metallic oxides, nanocomposites suggest that $Fe_3O_4/SiO_2/ZnO$ (1:2:1) nanocomposites exhibited the greatest adsorption removal compared to the other nanocomposites prepared at different mixing ratios to the high surface area than others. The effect of adsorbent dosage on the removal of these pollutants also suggests that the crystallite size and the surface area of the adsorbents played an important role in the removal of the pollutants from petroleum refinery wastewater. It was observed that the removal efficiency was slow between 0.02 to 0.06g and become rapid when the adsorbent increased from 0.06 to 0.08 g. This could be explained in terms of increased coverage of the surface as the adsorbent dosage increases leading to an increase in the number of adsorption sites and enhanced removal efficiency (Nistor *et al*., 2021). Additionally, the result shows that the $Fe_3O_4/SiO_2/ZnO$ (1:2:1) nanocomposites was better than other nanoadsorbents due to their improved surface area as presented in Table 4.1 than others. The ternary nanocomposites performed better in terms of the removal of pollutants from

the petroleum refinery wastewater than bimetallic and monometallic oxide nanoparticles under the applied conditions irrespective of the pollutant studied at a lower dosage, this makes the adsorbent better for the treatment of wastewater.

4.10.3 Effect of adsorption temperature

Temperature is one of the important parameters in the adsorption processes (George *et al*., 2023). The effect of different temperatures (30°C, 40°C, 50°C, 60°C, 70°C, and 80°C) on the adsorption of Pb (II) Cd (II), Ni (II) Cr (VI), Cu (II), total iron, COD, BOD and TOC from petroleum refinery wastewater was carried out and the results are presented in Figure 4.53-4.61.
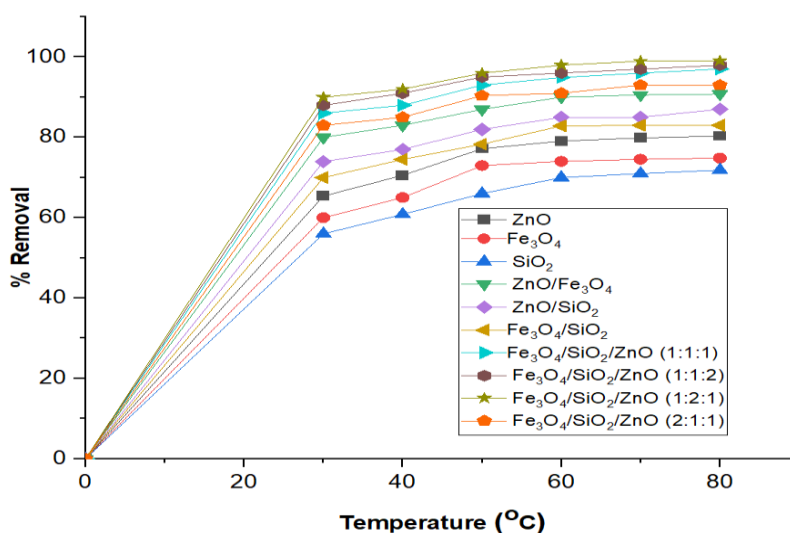
Figure 4.53: Effect of Temperature on the Removal of Pb (II) from Petroleum Refinery Wastewater under the Conditions of Contact Time (15) min and Dosage (0.05 g)
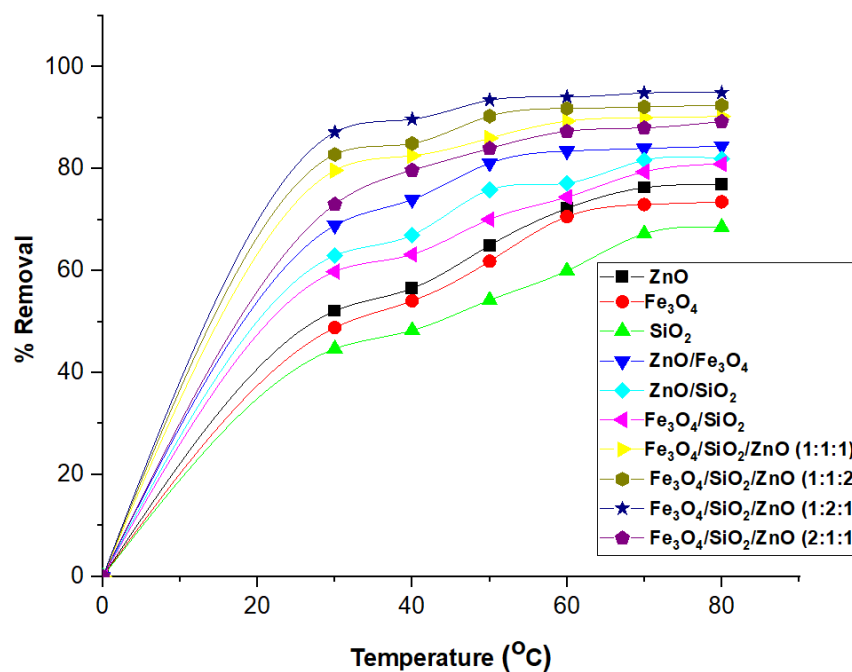
Figure 4.54: Effect of Temperature on the removal of Cd (II) from Petroleum Refinery Wastewater under the Conditions of Contact Time (15) min and Dosage (0.05 g)
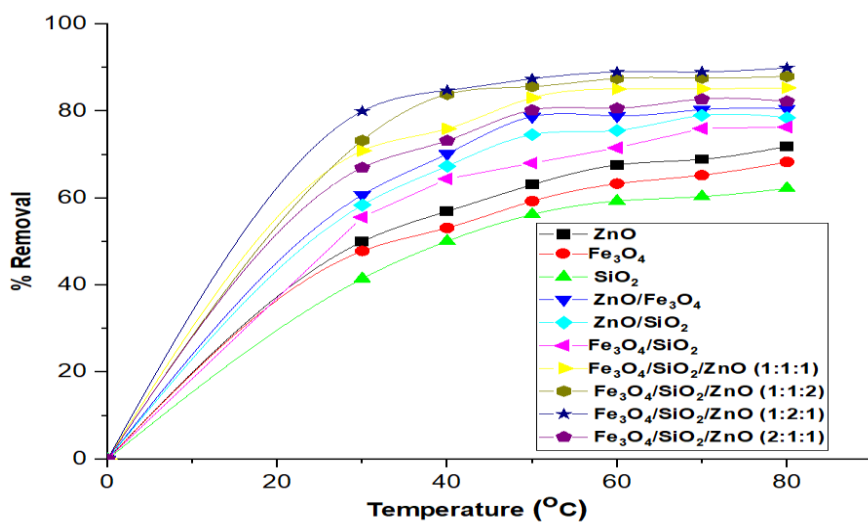
Figure 4.55: Effect of Temperature on the removal of Ni (II) from Petroleum Refinery Wastewater under the Conditions of Contact Time (15) min and Dosage (0.05 g)
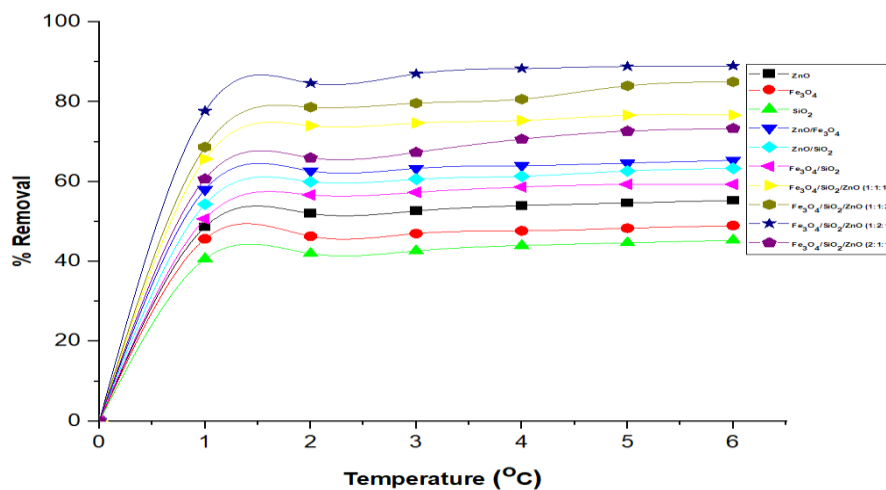
Figure 4.56: Effect of Temperature on the removal of Cr (VI) from Petroleum Refinery Wastewater under the Conditions of Contact Time (15) min and Dosage (0.05 g)
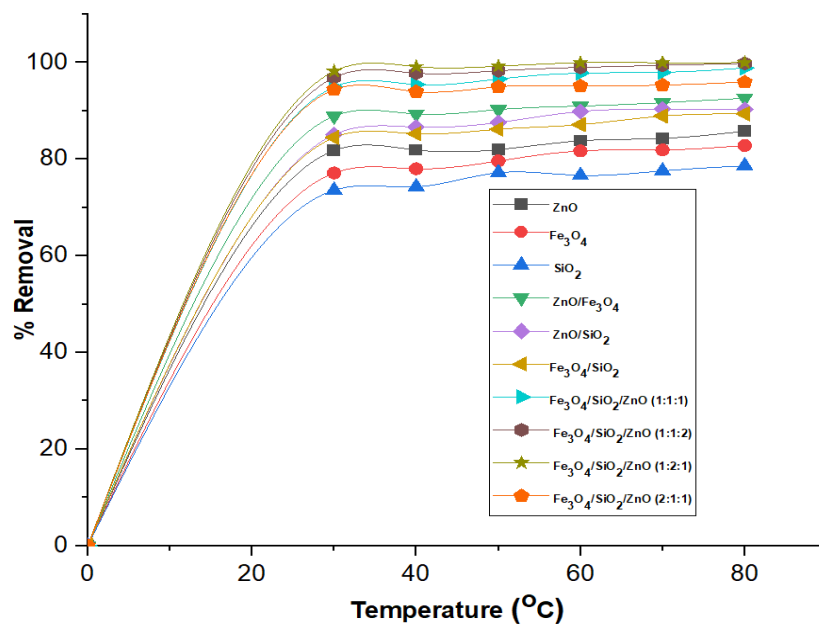
Figure 4.57: Effect of Temperature on the Removal of Cu (II) from Petroleum Refinery Wastewater under the Conditions of Contact Time (15 min) and Dosage (0.05 g)
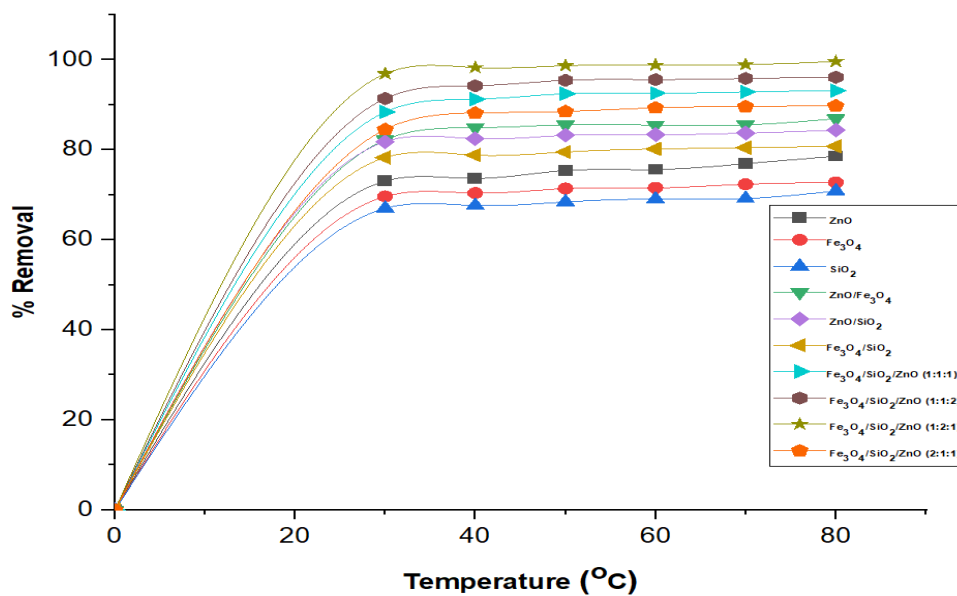
Figure 4.58: Effect of Temperature on the Removal of Total iron from Petroleum Refinery Wastewater under the Conditions of Contact Time (15) min and Dosage (0.05 g)
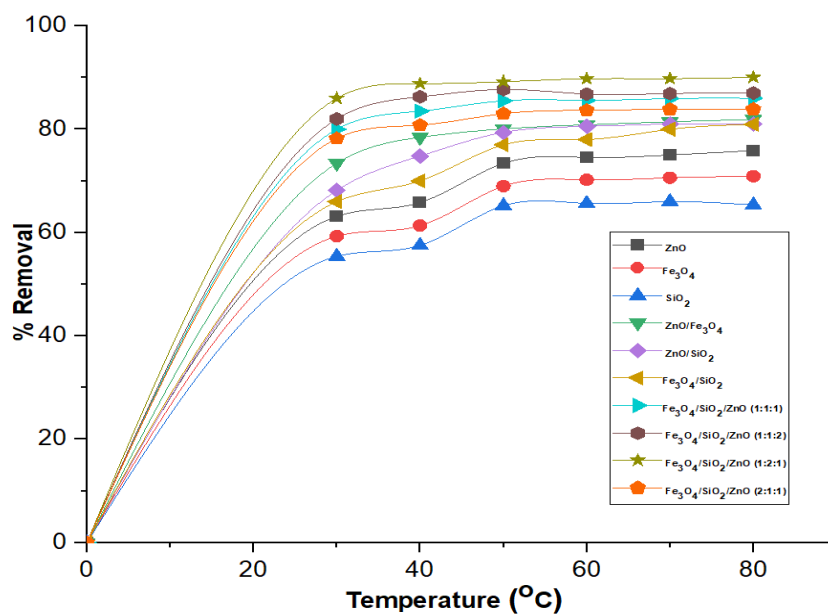
Figure 4.59: Effect of Temperature on the Removal of BOD from Petroleum Refinery Wastewater under the Conditions of Contact Time (15) min and Dosage (0.05 g)
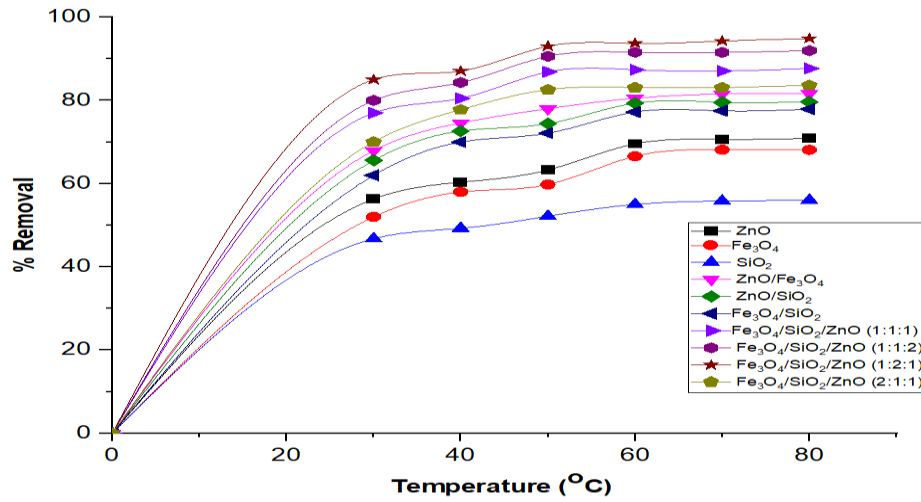
Figure 4.60: Effect of Temperature on the Removal of COD from Petroleum Refinery Wastewater under the Conditions of Contact Time (15) min and Dosage (0.05 g)
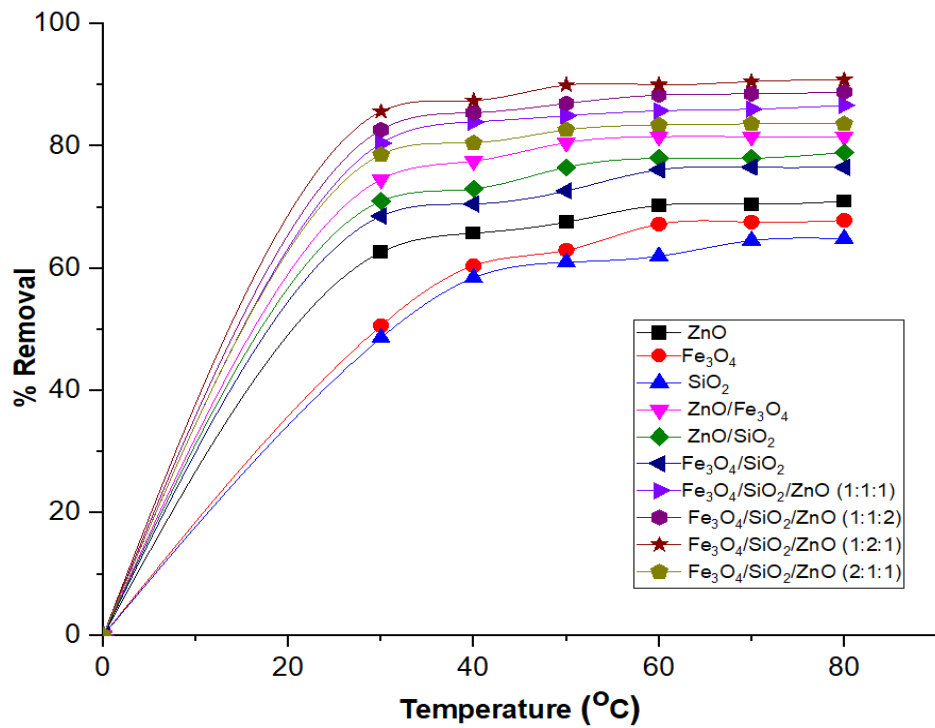
Figure 4.61: Effect of Temperature on the Removal of TOC from Petroleum Refinery Wastewater under the Conditions of Contact Time (15) min and Dosage (0.05 g)

Figure 4.59 depicts the percentage of Pb (II) removed by ZnO, Fe_3O_4, SiO_2 nanoparticles, Fe_3O_4/SiO_2, Fe_3O_4/ZnO, SiO_2/ZnO, Fe_3O_4/SiO_2, $Fe_3O_4/SiO_2/ZnO$ (1:1:1), $Fe_3O_4/SiO_2/ZnO$ (1:1:2), $Fe_3O_4/SiO_2/ZnO$ (1:2:1) and $Fe_3O_4/SiO_2/ZnO$ (2:1:1) nanocomposites. The result suggests that an increase in temperature corresponds to an increase in the percentage of Pb (II) for all the nanoadsorbents. The high adsorptive removal of ZnO nanoparticles than the others may be because of the more functional groups, which act as primary adsorption centers for the removal of heavy metals (Tunega *et al.,* 2020). The highest percentage removal of Pb (II) from the petroleum refinery wastewater was 80.326 %, 74.865 % and 71.865 % using ZnO, Fe_3O_4, SiO_2 nanoparticles as an adsorbent. The observed trend indicates that ZnO nanoparticles exhibited a higher adsorptive potential compoared than Fe_3O_4, SiO_2 nanoparticles. This may be related to the higher surface area and functional groups in ZnO nanoparticles compared to the others.

The highest percentage removal of Pb (II) was recorded to be 90.81 %, 86.99 % and 83.00 % using ZnO/Fe_3O_4, ZnO/SiO_2, $Fe_3O_4/Si O_2$. The result indicates that the ZnO/Fe_3O_4 nanocomposites exhibited higher adsorptive removal compared to ZnO/SiO_2 and Fe_3O_4/SiO_2 nanocomposites which may be due to the enhanced surface are of ZnO/Fe_3O_4 nanocomposites compared to the others. Similarly, the adsorption removal efficiency of the ternary nanocomposites indicated that the highest adsorption removal of Pb (II) was 97.03 %, 98.00%, 99.03 %, 93.00 % for $Fe_3O_4/SiO_2/ZnO$ (1:1:1), $Fe_3O_4/SiO_2/ZnO$ (1:1:2), $Fe_3O_4/SiO_2/ZnO$ (1:2:1), and $Fe_3O_4/SiO_2/ZnO$ (2:1:1) nanocomposites respectively. This indicates that the $Fe_3O_4/SiO_2/ZnO$ (1:2:1) nanocomposites exhibited a high adsorption removal compared to the others, which may be related to the large surface area of $Fe_3O_4/SiO_2/ZnO$ (1:2:1) nanocomposites than others.

Figure 4.54 indicates that the order of the adsorption of Cd (II) by ZnO, Fe_3O_4, SiO_2 nanoparticles; Fe_3O_4/ZnO, ZnO/SiO_2 Fe_3O_4/SiO_2, Fe_3O_4/SiO_2/ZnO (1:1:1), Fe_3O_4/SiO_2/ ZnO (1:1:2), Fe_3O_4/SiO_2/ZnO (1:2:1), and Fe_3O_4/SiO_2/ZnO (2:1:1) nanocomposites from the petroleum refinery wastewater were ZnO (76.91 %) > Fe_3O_4 (73.52 %) SiO_2 > (68.54 %); Fe_3O_4/ZnO (82.48 %) > ZnO/ SiO_2 (81.98 %) > Fe_3O_4/SiO_2 (80.96 %) ;and Fe_3O_4/SiO_2/ZnO (1:2:1) (93.92 %) > Fe_3O_4/SiO_2/ZnO (1:1:2) (92.49 %) > Fe_3O_4/SiO_2/ZnO (1:1:1) (90.29 %) and Fe_3O_4/SiO_2/ZnO (2:1:1) (89.29 %) .

In Figure 4.55, the highest removal of Ni (II) by ZnO, Fe_3O_4, SiO_2 nanoparticles; Fe_3O_4 /ZnO, ZnO/SiO_2 Fe_3O_4/SiO_2, Fe_3O_4/SiO_2/ZnO (1:1:1), Fe_3O_4/SiO_2/ZnO (1:1:2), Fe_3O_4/S iO_2/ZnO (1:2:1), and Fe_3O_4/SiO_2/ZnO (2:1:1) nanocomposites were 71.89 %, 68.31 %, 62.24 %, 84.33 %, 82.56 %, 80.51 %, 85.37 %, 87.96 %, 89.96 %, 82.26 % respectively under the applied conditions.   The result in Figure 4.56 shows also shows that the adsorption removal of Cr (IV) ions increases as the temperature incraeses.

Similarly, the highest removal efficiency of Cu (II) as presented in Figure 4.57 were 76.40 %, 74.47 %, 71.99 %, 89.76 %, 82.47 %, 82.57 %, 98.88 % 99.84%, 99.731%, and 97.28 % by ZnO, Fe_3O_4, SiO_2 nanoparticles; Fe_3O_4/ZnO, ZnO/SiO_2 Fe_3O_4/SiO_2,

 Fe_3O_4/SiO_2/ZnO (1:1:1), Fe_3O_4/SiO_2/ZnO (1:1:2), Fe_3O_4/SiO_2/ZnO (1:2:1), and Fe_3O_4/ SiO_2/ZnO (2:1:1) nanocomposites respectively. Likewise, the highest removal efficiency of the total iron ions was 77.30 %, 66.98 %, 64.65 %, 87.38 %, 84.82 %, 80.87 %, 93.87 %, 95.82 % 99.86 % and 90.32 % using ZnO, Fe_3O_4, SiO_2 nanoparticle; Fe_3O_4/ZnO, ZnO/SiO_2 Fe_3O_4/SiO_2, Fe_3O_4/SiO_2/ZnO (1:1:1), Fe_3O_4/SiO_2/ZnO (1:1:2), F e_3O_4/SiO_2/ZnO (1:2:1), and Fe_3O_4/SiO_2/ZnO (2:1:1) nanocomposites respectivel.

In Figure 4.59, it is clear that the BOD removal efficiency was 67.89 %, 65.9, 59.88 %, 75.90 %, 73.59 %, 71.00 %, 82.98 %, 84.59 %, 88.99 %, 79.99 % was using ZnO, Fe_3O_4, SiO_2 nanoparticles; and Fe_3O_4/ZnO, ZnO/SiO_2 Fe_3O_4/SiO_2, Fe_3O_4/SiO_2/ZnO (1:1:1), Fe_3O_4/SiO_2/ZnO (1:1:2)Fe_3O_4/SiO_2/ZnO (1:2:1), and Fe_3O_4/SiO_2/ZnO (2:1:1) nanocomposites respectively. The highest percentage removal of COD was ZnO (76.79 %) > Fe_3O_4 (75.65 %) > SiO_2 (70.90 %) while that of ZnO/Fe_3O_4, ZnO/SiO_2 and Fe_3O_4/ SiO_2 nanocomposites were 84.29 %, 83.67 %, 80.98 % and 88.86 % respectively. The COD removal efficiency were 88.86 %, 91.51 %, 92.50 % and 87.89 % for Fe_3O_4/SiO_2/ZnO (1:1:1), Fe_3O_4/SiO_2/ZnO (1:1:2), Fe_3O_4/SiO_2/ZnO (1:2:1), and Fe_3O_4/SiO_2/ZnO (2:1:1) as presented in Figure 4.60.

Figure 4.61 depicts that the removal efficiency increases as the temperature increases, the highest removal efficiency of for TOC ZnO, Fe_3O_4, SiO_2 nanoparticles; and ZnO/Fe_3O_4, ZnO/SiO_2 and Fe_3O_4/SiO_2, Fe_3O_4/SiO_2/ZnO (1:1:1), Fe_3O_4/SiO_2/ZnO (1:1:2), Fe_3O_4/SiO_2/ZnO (1:2:1), and Fe_3O_4/SiO_2/ZnO (2:1:1) nanocomposites were 68.59 %, 65.86 %, 62.86 %, 79.65 %, 76.756 %, 72.99 %, 83.86 %, 86.67 %, 90.86 % and 81.65 % respectively. The increase in percentage removal with an increase in reaction temperature for all the nanoasorbent used, suggests that the adsorption process was endothermic. This observation is different from the adsorption principle, which states that adsorption decreases as temperature rises and the amount of adsorbate are adsorbed on a surface desorbed at a higher temperature (Jibril, 2020). This difference may be linked to an increase in the kinetic or thermal energy of the molecules, making the pollutants more mobile and increasing molecular motion, which allowed the adsorbate to enter pores more easily, as well as increased binding site activity as the temperature rises (Xu *et al*., 2017). This increment in the removal efficiency may also be attributed to the adsorption sites

generated due to the breaking or rupture of some internal bonds near the edge of the nanoparticles and composites at high temperatures (Gebretsadik *et al.*, 2020). Additionally, the direct relationship between the reaction temperature and the removal efficiency maybe because the reaction temperature increased, the solubility of the metal ions and the organic pollutants also increased (Mouni *et al.*, 2018). The increase in removal efficiency as the temperature increases is an indication that temperature plays an important role in the adsorption of Pb (II), Cd (II), Ni (II) Cr (VI), Cu (II) and total iron ions, COD, BOD and TOC which suggests that the adsorption process involved chemical reaction as reported by Edet and Ifelebuegu, (2020).

Another observation from the analysis is that the ternary and binary nanocomposites exhibited higher adsorption than the individual ZnO, Fe_3O_4, and SiO_2 nanoparticles respectively, due to the increase in adsorption sites in the former than the latter. The trend observed can also be linked to the increased functional groups on the composites surface making it a potential adsorbent for Pb (II) Cd (II), Ni (II) Cr (VI), Cu (II) and total iron ions, COD, BOD and TOC complexation through both coordinate and electrostatic approaches (Sadegh *et al.*, 2017). Additionally, it was observed that the $Fe_3O_4/SiO_2/ZnO$ with a mixing ratio of 2:1:1 shows a lower adsorption removal compared to the other ternary nanocomposites $Fe_3O_4/SiO_2/ZnO$ (1:1:2), $Fe_3O_4/SiO_2/ZnO$ (1:2:1), and $Fe_3O_4/SiO_2/ZnO$ (1:1:1). This can be linked to the XRD result in Figure 4.28 which revealed that the core-shell of the magnetite was completely covered by the ZnO and SiO_2 this made it difficult for the selected inorganic and organic pollutants to be linked to the available sites/polar group attached on the magnetite phase.

A similar trend was reported by Zhang *et al.* (2020a) where the authors observed an increase in the percentage removal of Cr (VI) and Cu (II) as the temperature increases

using magnetite nanoparticles as an adsorbent. Additionally, zeolite-Fe_3O_4 nanocomposites have been used for the removal of Pb (II) and the result also indicates an increased removal as the temperature increases. However, COD removal from petroleum refinery wastewater using ZnO/SiO_2 nanocomposites has been found to occur 25-30℃. The authors also reported that temperature plays an important role in the removal of COD from wastewater (Rajani and Suresh, 2017). At temperatures of 30 °C and 50 °C, the adsorption of heavy metals increases as temperature rises, demonstrating that elevated temperature was more favourable for the adsorption process. This indicates that heat-absorbing properties are intrinsic to the adsorption mechanism, and further affirm that this reaction is endothermic (Hassan *et al*., 2021). The results obtained in this analysis are compared with other results that have been reported in the literature as presented in Table 4.3, 4.4 and 4.5

Table 4.3: Comparison of the Percentage Removal of Selected heavy metals and other parameters on ZnO, Fe₃O₄ and SiO₂ Nanoparticles

Synthesis Methods	Nanoadsorbent	Characterisation Tools	Crystallite Size (nm)	Pollutants	Removal (%)	Other adsorption Conditions	References
Co-precipitation	Fe_3O_4	XRD, SEM, EDS, TEM, DLS	12.3	Cu (II)	69.46	Adsorbent dosage (0.05 g), contacts time (30 min),	Iconaru *et al.* (2016)
Chemical vapor deposition	Fe_3O_4	HRTEM, SEM, EDX	20	As (III), V	87, 98	Temperature (60℃), contact time (15 min)	Monárrez-Corderoa *et al.* (2016)
Precipitation	ZnO	FTIR, SEM, FTIR and TGA	73	Cu (II), Pb (II), Cd (II)	100, 77.47, 97.85	Stirred at 120rpm at 30℃ for 150 min, adsorbent dosage (0.1 g)	Anusa *et al.* (2017)
Green rout	ZnO	XRD TEM, and UV–vis	10.01 2.6	Pb (II)	93	pH of 5, temperature of 7030℃	Azizi *et al.* (2017)
Precipitation	ZnO	XRD, TEM and DLS	11	Cd (II)	98.71	Dosage (120 mg), volume of aqueous solution (10 ml), pH (5), Contact time (20 min) and initial heavy metal ion concentration (300 mg/l)	Nalwa *et al.*, (2017)
Precipitation	ZnO	XRD, FT-IR spectroscopy, SEM, and TGA	not available	As (III)	96	pH (7), dosage (0.4 contact time (105 min), temperature (323 K).	Yuvaraja *et al.* (2019)
Co-precipitation	Fe_3O_4	SEM, XRD, FTIR	27.68	Cr (VI)	80	pH (4), at room temperature, adsorbent dosage (25 mg/L), contact time (250 min)	Hossain *et al.* (2018)
Precipitation	ZnO	XRD, SEM and EDX	not available	Cr (VI)	98	40 min with optimum value of pH 3	Kamath *et al.* (2019)
Electrochemical	Fe_3O_4	TEM	12	Cr (VI)	100	pH (3.5), temperature (60℃), adsorbent dosage (2 g), conctact time (2h) concentration (25 mg/L)	Rivera *et al.* (2019)

Synthesis Methods	Nanoadsorbent	Characterisation Tools	Crystallite Size (nm)	Pollutants	Removal (%)	Other adsorption Conditions	References
Coprecipitation	Fe_3O_4	TEM, FTIR, XRD,	9.22	Ni (II), Co (II)	97.88 and 95.01	pH (7), at room temperature (25ºC), adsorbent dosage (0.4 g), concentration (10 0 mg/L)	El-Shamy *et al.* (2019)
Precipitation	Ultrafine mesoporous Fe_3O_4	BET, XRD. TEM		Pb (II), Cd (II), Cu (II), Ni(II)	98, 87, 90, 78	pH (6), temperature (25ºC), adsorbent dosage (2.5 g), contact time (90 min) concentration (1 mg/L)	Fato *et al.* (2019)
Commercial nanoadsorbent	Fe_3O_4	SEM, XRD, FTIR	20	Cr (VI), Cu (II)	88.83, 96.10	pH (4), temperature (25ºC), adsorbent dosage (2.5 g), contact time (90 min) concentration (1 mg/L)	Zhang *et al.* (2020a)
Sol-gel	SiO_2	XRD, HRSEM, FTIR, EDX, XPS and BET	28	Pb (II) Cd (II) Ni (II) Cr (VI) Cu (II) Total iron COD BOD, TOC	7.86 68.54 62.24 45.33 78.65 79.87 70.90 59.88 64.86	Temperature (30 °C) Stirring speed (250 rpm), Contact time (15 min) and Dosage (0.05g)	This work
Sol-gel- chemical reduction	Fe_3O_4	XRD, HRSEM FTIR, EDX, XPS and BET	26	Pb (II) Cd (II) Ni (II) Cr (VI) Cu (II) Total iron COD BOD TOC	74.86 73.52 68.31 49.00 82.86 84.77 75.65 65.90 67.85	Temperature (30 °C) Stirring speed (250 rpm), Contact time (15 min) and Dosage (0.05g))	This work
Sol-gel	ZnO		18	Pb (II) Cd (II) Ni (II) Cr (VI) Cu (II)	80.33 76.91 71.88 55.33 85.83	Temperature (30 °C) Stirring speed (250 rpm), Contact time (15 min) and Dosage (0.05)	This work

Synthesis Methods	Nanoadsorbent	Characterisation Tools	Crystallite Size (nm)	Pollutants	Removal (%)	Other adsorption Conditions	References
				Total iron	87.60		
				COD	83.89		
				BOD	76.78		
				TOC	70.98		

It can be observed that the adsorptive removal efficiency of Pb (II), Cd (II), Ni (II), Cr (VI), Cu (II), total iron, COD, BOD and TOC onto ZnO, Fe_3O_4, SiO_2 nanoparticles are lower compared to several other monometallic oxides nanoparticles reported in the literature as shown in Table 4.3. This is not surprising because the authors used stimulated wastewater which has a higher concentration of metal ions compared to real industrial wastewater. Additionally, the lower adsorption removal efficiency compared to the other studies may also be linked to the presence of other pollutants in petrochemical wastewater, which usually competes for the active sites with the heavy metal ions against the use of stimulated wastewater that contained only the heavy metal of interest. The differences in the adsorptive performance of the nanomaterials may also be ascribed to the applied experimental conditions. For instance, in this study maximum removal efficiency occurred within 15 min compared to 30 min − 2 h reported in the literature. Additionally, the adsorbent dosage used in this study is 0.05g compared to the 0.4 -10g reported by the authors. The result from this study when compared with the analysis of Iconaru *et al. (*2016) who used the same adsorbent dosage (0.05g) under the applied condition of 30 min reported lower removal efficiency (69.46) of Cu (II) compared with 85.43 % reported in this study. The lower adsorption efficiency may also be linked to the crystallite size and method of synthesis of the nanoparticles used for the removal of the target pollutant.

Table 4.4: Comparison of the Percentage Removal of Selected heavy metals and other parameters on ZnO/Fe$_3$O$_4$, ZnO/SiO$_2$ and Fe$_3$O$_4$ /SiO$_2$ Nanocomposites

Synthesis Methods	Nanoadsorbent	Characterisation Tools	Crystallite Size (nm)	Pollutants	Removal (%)	Other adsorption Conditions	References
Coprecipitation	ZnO/Polymer	EDX, SEM, XRD, FTIR	8	Pb (II), Cd (II)	97.1, 80.9	Dosage (0.250 g), Contact time (60 min), metal ions concentration at 0.01M and temperature (30°C), Time (10 min)	Angelin *et al.* (2015)
Green	Hull (Prunus amygdalusFascionel lo)/Fe$_3$O$_4$	VSM, SEM	Not available	Pb (II)	98.1	pH (9), room temperature, adsorbent dosage (5 g/L) and contact time (80 min), concentration (10 m/L)	Nasseh *et al.*, (2017)
Precipitation	ZnO/ Montmorillonite	XRD, EDX, SEM	37	Pb (II)	97.20	Initial concentration (100 mg/l), Contact time (40 min), pH 7, (0.2g)	Kamath *et al.* (2019)
Precipitation	Ultrafine mesoporous Fe$_3$O$_4$	BET, XRD. TEM		Pb (II), Cd (II), Cu (II), Ni (II)	98, 87, 90, 78	pH (6), temperature (25°C), adsorbent dosage (2.5 g), contact time (90 min) concentration (1 mg/L)	Fato *et al* (2019)
Coprecipitation	Fe$_3$O$_4$/Alginate	TEM, FTIR, XRD,	9.22	Ni (II), Co (II)	97.88, 95.00	pH (7), at room temperature (25°C), adsorbent dosage (0.4 g), concentration (100 mg/L)	El-Shamy *et al.* (2019)

Synthesis Methods	Nanoadsorbent	Characterisation Tools	Crystallite Size (nm)	Pollutants	Removal (%)	Other adsorption Conditions	References
Precipitation	ZnO2/GO			Pb (II)	56.81	Dosage (0.16 g/L), pH (5), Temperature (30°C) Time (30 min)	Ahmad *et al.* (2020)
Co-precipitation	Fe$_3$O$_4$/Ethoxylated para-phenylenediamine	FTIR), (XRD) TEM,	13.24	Cd (II), Pb (II), Zn (II)	85 95 95	pH (6.7), at room temperature, adsorbent dosage (0.6 g/L) and contact time (30 min), concentration (20 mg/L)	El-Dib *et al.*, (2019)
Co-precipitation	Amino Propyl/SiO$_2$	SEM, TEM, XRD	6	Pb (II),	95	pH of 9, Temperature (30°C)	Alswieleh *et al.* (2021)
Sol-gel	ZnO/Fe$_3$O$_4$	XRD, HRSEM FTIR, EDX, XPS BET	12	Pb (II) Cd (II) Ni (II) Cr (VI) Cu (II) Total iron COD BOD TOC	90.81 84.48 83.23 65.65 86.93 92.68 84.29 84.59 81.55	Temperature (30 °C) Stirring speed (250 rpm), Contact time (15 min) and Dosage (0.05g)	This work
Sol-gel	ZnO/SiO$_2$	XRD, HRSEM FTIR, EDX, XPS and BET	15	Pb (II) Cd (II) Ni (II) Cr (VI) Cu (II) Total iron COD BOD TOC	86.99 81.98 78.24 63.42 84.39 90.34 83.665 84.59 78.99	Temperature (30 °C) Stirring speed (250 rpm), Contact time (15 min) and Dosage (0.05g)	This work
Sol-gel	Fe$_3$O$_4$/SiO$_2$	XRD, HRSEM FTIR, EDX, XPS and BET	16	Pb (II) Cd (II)	83.00 80.96	Temperature (30 °C) Stirring speed	This work

Synthesis Methods	Nanoadsorbent	Characterisation Tools	Crystallite Size (nm)	Pollutants	Removal (%)	Other adsorption Conditions	References
				Ni (II)	76.33	(250 rpm), Contact	
				Cr (VI)	59.04	time (15 min) and	
				Cu (II)	80.81	Dosage (0.05g)	
				Total iron	89.43		
				COD	80.98		
				BOD	79.99		
				TOC	76.55		

The adsorption removal efficiency of Pb (II), Cd (II), Ni (II), Cr (VI), Cu (II), Total iron, COD, BOD and TOC onto ZnO/Fe_3O_4, ZnO/SiO_2 and Fe_3O_4/SiO_2 nanocomposites have comparable percentage adsorption removal compared to several other bimetallic nanocomposites reported in the literature as shown in Table 4.4. The result suggests the crystallites size, morphology and method of synthesis. For instance, the result of El-Shamy *et al*. (2019) reported synthesised $Fe_3O_4/Alginateo$ nanocomposites via precipitation method and reported 9.22 nm with percentage adsorption of 97.88 %. Under condiction of pH (7), at room temperature (25ºC), adsorbent dosage (0.4 g), concentration (100 mg/L).

Amino Propyl-Functionalized Silica with crystallite size recorded 95 % removal efficiency of Cu (II) under the reaction condition of pH of 9, Temperature (30°C) as reported by Alswieleh *et al*. (2021) which is higher than the value of Cu (II) removal for all the bimetallic oxides in this study. The value of COD, TOC were 68.78 %, 47.14 % for $Fe_3O_4/TO_2/carbon$ nanotube which is lower than the value reported in this study. This may be related to the crystallite size of 20-80 nm compared to the lower crystallite size obtained in this study. Another possible explanation of the lower adsorption efficiency of the bimetallic oxides in this study may be ascribed to the use of simulated wastewater by most of the authors which has a higher concentration of metal ions compared to real industrial wastewater.

Additionally, the lower adsorption removal efficiency compared to the other studies may also be linked to the presence of other pollutants in petrochemical wastewater, which usually competes for the active sites with the heavy metal ions against the use of stimulated wastewater that contained only the heavy metal. Other conditions such as time

(15 min) and adsorbent dosage may be responsible for the possible lower efficiency of

ZnO/Fe$_3$O$_4$, ZnO/ SiO$_2$ and Fe$_3$O$_4$/SiO$_2$ nanoparticles compared to the literature.

Table 4.5: Comparison of the Percentage Removal of Selected heavy metals and other parameters on Fe₃O₄/SiO₂/ZnO (1:1:1), Fe₃O₄/SiO₂/ZnO (1:1:2), Fe₃O₄/SiO₂/ZnO (1:2:1) and Fe₃O₄/SiO₂/ZnO (2:1:1)

Synthesis Method	Nanoadsorbent	Characterisation Tools	Crystallite Size (nm)	Pollutants	Removal (%)	Other adsorption Conditions	References
Co-precipitation	DNPH/SDS/Fe₃O₄	EM–EDXS, FTIR	Not available	Cr (VI)	93.65	pH (4.5), temperature (25ºC), adsorbent dosage (0.05 g), contact time (90 min) concentration (50 mg/L)	Sobhanardakani and Zandipak, (2017)
Co-precipitation	Fe₃O₄/Al₂O₃/ZrO₂	BET, XRD, SEM, EDX, FITR	Not available	Cd (II), Cr (VI), Pb (II)	96.65, 96.55, 97.20	pH (6), at room temperature (80ºC), adsorbent dosage (0.1 g) and contact time (24 h), concentration (30 mg/L)	Tsegaye et al. (2020)
Co-precipitation	Ash/GO/Fe₃O₄	FESEM, TEM, EDX mapping, BET/BJH, XRD, FTIR, and VSM	20	Pb (II), Cd (II)	99.67, 98.68	pH (6), concentration (10 mg/L), dosage (1 g), stirring speed (600 rpm), Temperature (25 °C) and contact time (150 min)	Pelalak et al. (2021)
Sol-gel-chemical reduction	Fe₃O₄/SiO₂/ZnO (1:1:1)	XRD, HRSEM FTIR, EDX, XPS and BET	10.10	Pb (II) Cd (II) Ni (II) Cr (VI) Cu (II) Total iron COD BOD TOC	97.03 90.29 89.59 76.66 98.88 99.14 88.86 82.98 86.67	Temperature (30 °C) Stirring speed (250 rpm), Contact time (15 min) and Dosage (0.05 g)	This work

Synthesis Method	Nanoadsorbent	Characterisation Tools	Crystallite Size (nm)	Pollutants	Removal (%)	Other adsorption Conditions	References
Sol-gel-chemical reduction	Fe$_3$O$_4$/SiO$_2$/ZnO (1:1:2)	XRD, HRSEM FTIR, EDX, XPS and BET	8.84	Pb (II)	98.00	Temperature (30 °C) Stirring speed (250 rpm), Contact time (15 min) and Dosage (0.05 g)	This work
				Cd (II)	92.49		
				Ni (II)	90.33		
				Cr (VI)	84.96		
				Cu (II)	99.83		
				Total iron	99.15		
				COD BOD	91.51		
				TOC	84.59		
					88.86		
Sol-gel-chemical reduction	Fe$_3$O$_4$/SiO$_2$/ZnO (1:2:1)	XRD, HRSEMFTIR, EDX, XPS and BET	7.66	Pb (II)	99.03	Temperature (30 °C) Stirring speed (250 rpm), Contact time (15 min) and Dosage (0.05 g)	This work
				Cd (II)	94.92		
				Ni (II)	93.07		
				Cr (VI)	88.91		
				Cu (II)	99.99		
				Total iron	99.63		
				COD	92.50		
				BOD	88.99		
				TOC	90.86		
Sol-gel-chemical reduction	Fe$_3$O$_4$/SiO$_2$/ZnO (2:1:1)	XRD, HRSEM FTIR, EDX, XPS and BET	12.40	Pb (II)	93.00	Temperature (30 °C) Stirring speed (250 rpm), Contact time (15 min) and Dosage (0.05 g)	This work
				Cd (II)	89.29		
				Ni (II)	86.00		
				Cr (VI)	73.33		
				Cu (II)	95.97		
				Total iron	89.83		
				COD	87.89		
				BOD	76.86		
				TOC	79.99		

It can be observed that the adsorption removal efficiency of Pb (II), Cd (II), Ni (II) Cr (VI), Cu (II) and Total iron , COD, BOD and TOC using Fe$_3$O$_4$/SiO$_2$/ZnO (1:1:1), Fe$_3$O$_4$/SiO$_2$/ZnO (1:1:2), Fe$_3$O$_4$/SiO$_2$/ZnO (1:2:1), and Fe$_3$O$_4$/SiO$_2$/ZnO (2:1:1) nanocomposites as nanoadsorbent are higher compared with several other nanocomposites reported in the literature.

The result suggests that the adsorption of the target pollutants using Fe$_3$O$_4$/SiO$_2$/ZnO (1:1:1), Fe$_3$O$_4$/SiO$_2$/ZnO (1:1:2), Fe$_3$O$_4$/SiO$_2$/ZnO (1:2:1), and Fe$_3$O$_4$/SiO$_2$/ZnO (2:1:1) nanocomposites is higher than many of the reported in the literature. This is not surprising because the authors used stimulated wastewater which has a higher concentration of metal ions compared to real industrial wastewater. Additionally, the minima adsorption removal compared to the other studies may also be linked to the presence of other pollutants in petrochemical wastewater, which usually competes for the active sites with the heavy metal ions against the use of stimulated wastewater that contained only the heavy metal of interest. The differences in the adsorptive performance of the nanomaterials may also be ascribed to the applied experimental conditions. For instance, in this study maximum removal efficiency occurred within 15 min compared to 30 min − 2 h reported in the literature (see Table 4.5)

4.11 Adsorption Isotherm

The result of the batch adsorption of Pb (II), Cd (II), Ni (II), Cr (VI), Cu (II), total iron, COD, BOD and TOC from the petroleum refinery wastewater were examined using the Table 4.6, 4.7 and 4.8.

Table 4.6: Adsorption Isotherm Models for the Removal of Selected heavy Metal Ions and Organic pollutants from Petrochemical Refinery wastewater using Monometallic oxides nanoparticles

Target Heavy		Langmuir R²	q_{max} (mg/g)	K_L	R_L	SSE	x^2	Freundlich R²	K_f (mg g⁻¹)	1/n	SSE	x^2	Temkin R²	B T (J/mol)	K_T (L mg⁻¹)	SSE	x^2	D-R R²	qmax (mgg⁻¹)	E kJmol-1	SSE	x^2
Pb (II)	A	0.998	30.772	5.369	0.026	0.058	0.326	0.952	0.079	0.077	0.135	0.267	0.945	328.617	1.098	1.235	15.929	0.895	10.546	954.330	1.160	0.449
	B	0.997	25.623	4.921	0.028	0.055	0.347	0.943	0.039	0.080	0.135	0.252	0.934	306.790	1.072	1.043	13.139	0.892	13.161	912.780	1.161	0.470
	C	0.996	24.860	4.768	0.029	0.053	0.417	0.939	0.060	0.084	0.137	0.269	0.928	262.271	1.044	0.952	12.022	0.890	15.334	322.770	1.167	0.540
Cd (II)	A	0.992	30.328	0.133	0.785	0.054	0.530	0.998	0.719	0.082	0.138	0.270	0.979	222.299	1.312	1.533	19.762	0.891	8.285	1464.150	1.173	0.653
	B	0.990	29.455	0.126	0.794	0.051	0.673	0.982	0.622	0.083	0.140	0.292	0.974	214.278	1.309	1.430	18.061	0.888	9.541	868.260	1.183	0.796
	C	0.988	20.124	0.090	0.844	0.049	0.859	0.978	0.587	0.084	0.143	0.365	0.958	196.548	1.262	1.410	17.762	0.886	10.705	970.530	1.229	0.982
Ni (II)	A	0.991	21.810	0.191	0.718	0.052	0.556	0.970	0.397	0.077	0.135	0.237	0.983	293.781	1.656	0.070	0.267	0.889	3.642	1028.130	1.181	0.679
	B	0.987	23.310	0.120	0.801	0.047	0.571	0.968	0.375	0.079	0.137	0.247	0.982	249.670	1.543	0.070	0.252	0.884	4.808	668.670	1.183	0.694
	C	0.986	20.234	0.084	0.900	0.046	0.774	0.961	0.367	0.079	0.138	0.274	0.979	207.332	1.530	0.073	0.269	0.883	9.029	482.430	1.225	0.897
Cu (II)	A	0.999	44.948	4.921	0.028	0.052	0.432	0.956	1.774	0.343	0.186	0.284	0.941	1972.140	0.795	0.076	0.270	0.896	19.747	988.710	1.274	0.555
	B	0.998	35.024	4.768	0.029	0.053	0.437	0.953	1.487	0.409	0.198	0.295	0.941	1395.420	0.575	0.081	0.292	0.895	20.890	493.530	1.275	0.560
	C	0.997	30.339	2.011	0.931	0.054	0.536	0.899	1.230	0.704	0.218	0.335	0.885	1164.420	0.215	0.104	0.365	0.895	21.486	357.390	1.320	0.659
Cr(VI)	A	0.997	14.539	0.246	0.295	0.057	1.414	0.995	1.673	0.735	0.389	1.101	0.941	805.616	0.795	0.080	0.237	0.894	2.903	3309.480	1.439	1.537
	B	0.995	13.736	0.163	0.357	0.056	1.083	0.994	1.406	0.868	0.407	1.139	0.941	755.076	0.575	0.081	0.247	0.893	3.642	2992.650	1.460	1.206
	C	0.994	13.516	0.010	0.857	0.054	2.226	0.991	1.376	0.888	0.413	1.288	0.885	608.000	0.215	0.102	0.274	0.891	4.650	2721.630	1.600	2.349
Total iron	A	0.998	40.687	5.369	0.026	0.059	0.201	0.984	3.402	0.592	0.011	0.124	0.970	2747.680	0.896	0.127	0.284	0.896	15.056	619.830	1.036	0.324
	B	0.997	33.016	4.921	0.028	0.058	0.223	0.983	2.189	1.067	0.011	0.129	0.967	2305.890	0.853	0.127	0.295	0.895	17.745	564.660	1.037	0.346
	C	0.994	28.432	4.768	0.029	0.055	0.293	0.976	1.680	1.311	0.013	0.146	0.961	1395.420	0.655	0.150	0.335	0.892	19.011	357.060	1.043	0.416
BOD	A	0.999	17.516	0.257	0.028	0.060	0.944	0.990	0.014	0.680	1.651	0.813	0.984	11.514	0.087	0.209	1.101	0.897	3.555	683.040	2.766	1.067
	B	0.997	13.432	0.024	0.029	0.058	1.262	0.987	0.009	0.714	1.692	0.907	0.983	11.181	0.080	0.220	1.139	0.895	3.731	329.610	2.855	1.385
	C	0.994	11.558	0.341	0.029	0.055	1.513	0.983	0.005	0.801	1.780	1.067	0.983	7.302	0.077	0.290	1.288	0.892	4.400	107.880	2.887	1.636
COD	A	0.998	15.687	0.389	0.555	0.059	0.769	0.992	0.050	0.574	1.360	0.389	0.984	6.393	0.087	0.008	0.124	0.896	4.581	668.430	5.425	0.892

		Langmuir						Freundlich					Temkin						D-R			
	B	0.997	14.516	0.322	0.601	0.058	0.769	0.985	0.007	0.601	2.099	0.492	0.979	5.666	0.081	0.008	0.129	0.895	6.626	1172.370	5.954	0.892
	C	0.994	13.432	0.213	0.695	0.055	0.971	0.977	0.001	0.936	3.809	0.766	0.965	4.818	0.022	0.011	0.146	0.892	7.757	1272.090	7.589	1.094
TOC	A	0.993	18.096	0.337	0.298	0.054	1.859	0.988	0.083	0.387	5.518	1.645	0.983	6.393	0.364	0.873	0.813	0.891	2.976	1087.530	7.020	1.982
	B	0.988	17.000	0.244	0.370	0.049	1.811	0.986	0.037	0.481	6.142	1.661	0.978	5.666	0.187	0.917	0.907	0.886	4.287	912.690	7.717	1.934
	C	0.996	15.572	0.212	0.403	0.057	1.949	0.975	0.035	0.498	6.545	1.760	0.965	4.818	0.171	0.933	1.067	0.894	4.603	321.030	7.849	2.072

Table 4.7: Adsorption Isotherm Models for the Removal of Selected heavy Metal Ions and Organic pollutants from Petrochemical Refinery wastewater using bimetallic oxides

Parameters		Langmuir R^2	qmax (mg/g)	KL	RL	SSE	x^2	Freundlich R^2	K_F (mg g−1)	1/n	SSE	x^2	Temkin R^2	B T (J/mol)	K_T (L mg−1)	SSE	x^2	D-R R^2	Qmax (mgg−1)	E kJmol-1	SSE	x^2
Pb	D	0.999	39.052	8.001	0.018	0.070	0.033	0.977	0.210	0.064	0.135	0.267	0.964	625.113	1.312	0.964	0.964	0.965	16.699	1825.680	0.964	0.964
	E	0.998	37.951	5.764	0.024	0.070	0.035	0.959	0.161	0.067	0.135	0.252	0.964	494.881	1.224	0.964	0.964	0.957	18.648	1666.800	0.964	0.964
	F	0.997	36.110	5.420	0.026	0.073	0.042	0.979	0.100	0.074	0.137	0.269	0.950	469.718	1.128	0.950	0.950	0.956	21.905	1919.010	0.950	0.950
Cd	D	0.994	34.922	0.672	0.419	0.076	0.053	0.992	0.622	0.062	0.138	0.270	0.986	384.907	1.458	0.986	0.986	0.957	13.749	1741.830	0.986	0.986
	E	0.993	33.603	0.526	0.480	0.081	0.067	0.975	0.341	0.083	0.140	0.292	0.986	364.649	1.414	0.986	0.986	0.955	14.192	1984.410	0.986	0.986
	F	0.993	33.470	0.394	0.552	0.104	0.086	0.971	0.292	0.090	0.143	0.365	0.984	323.502	1.337	0.984	0.984	0.953	15.463	1301.730	0.984	0.984
Ni (II)	D	0.992	34.950	0.281	0.634	0.080	0.056	0.975	0.479	0.075	0.135	0.237	0.985	290.699	1.694	0.985	0.985	0.956	11.831	1672.410	0.985	0.985
	E	0.991	28.731	0.259	0.652	0.081	0.057	0.974	0.416	0.075	0.137	0.247	0.986	244.529	1.690	0.986	0.986	0.952	13.466	1303.500	0.986	0.986
	F	0.990	27.262	0.198	0.710	0.102	0.077	0.970	0.398	0.076	0.138	0.274	0.989	281.831	1.656	0.989	0.989	0.951	14.584	1129.710	0.989	0.989
Cu (II)	D	0.999	46.955	8.010	0.018	0.127	0.043	0.993	1.929	0.311	0.186	0.284	0.990	14288.700	1.131	0.990	0.990	0.955	22.106	1552.470	0.990	0.990
	E	0.999	44.421	5.420	0.026	0.127	0.044	0.975	1.890	0.342	0.198	0.295	0.961	7871.530	0.897	0.961	0.961	0.953	25.428	1164.000	0.961	0.961
	F	0.998	43.781	5.369	0.026	0.150	0.054	0.969	1.885	0.343	0.218	0.335	0.951	2747.680	0.896	0.951	0.951	0.950	30.195	622.590	0.951	0.951
Cr(VI)	D	0.999	23.766	0.420	0.024	0.209	0.141	0.998	2.097	0.553	0.389	1.101	0.989	951.753	1.131	0.989	0.989	0.957	5.063	3787.410	0.989	0.989
	E	0.999	23.457	0.392	0.026	0.220	0.108	0.998	2.097	0.553	0.407	1.139	0.961	930.937	0.897	0.961	0.961	0.957	5.665	3580.230	0.961	0.961
	F	0.994	23.456	0.369	0.026	0.290	0.223	0.997	1.966	0.602	0.413	1.288	0.950	927.695	0.896	0.950	0.950	0.957	7.199	3127.410	0.950	0.950
Total iron	D	0.999	45.766	8.010	0.018	0.008	0.020	0.995	3.600	0.569	0.011	0.124	0.992	14288.700	2.211	0.992	0.992	0.957	20.336	1136.250	0.992	0.992
	E	0.999	42.456	5.764	0.024	0.008	0.022	0.994	3.449	0.574	0.011	0.129	0.991	7871.530	1.131	0.991	0.991	0.957	23.187	1037.550	0.991	0.991
	F	0.999	37.990	5.420	0.026	0.011	0.029	0.987	3.447	0.585	0.013	0.146	0.970	3237.220	0.897	0.970	0.970	**0.957**	24.895	990.000	0.970	0.970
BOD	D	0.999	27.766	0.513	0.068	0.873	0.094	0.997	0.037	0.402	1.651	0.813	0.995	18.604	0.225	0.995	0.995	0.967	4.557	1056.540	0.995	0.995
	E	0.999	24.990	0.506	0.220	0.917	0.126	0.997	0.030	0.408	1.692	0.907	0.994	18.241	0.216	0.994	0.994	0.957	6.365	867.900	0.994	0.994

233

	F	0.999	21.958	0.430	0.250	0.933	0.151	0.990	0.029	0.593	1.780	1.067	0.990	14.938	0.115	0.990	0.990	0.956	7.153	810.420	0.990	0.990
COD	D	0.999	32.766	1.617	0.231	2.202	0.077	0.996	0.023	0.339	1.360	0.389	0.994	11.453	0.274	0.994	0.994	0.957	8.787	745.440	0.994	0.994
	E	0.999	23.456	1.052	0.316	2.467	0.077	0.994	0.020	0.374	2.099	0.492	0.991	9.878	0.194	0.991	0.991	0.957	12.315	1344.330	0.991	0.991
	F	0.999	21.990	0.938	0.341	3.284	0.097	0.993	0.019	0.381	3.809	0.766	0.989	8.605	0.179	0.989	0.989	0.956	14.906	1351.620	0.989	0.989
TOC	D	0.996	38.102	0.512	0.218	3.000	0.186	0.992	0.078	0.275	5.518	1.645	0.986	11.453	1.341	0.986	0.986	0.958	5.236	1260.540	0.986	0.986
	E	0.995	30.617	0.481	0.229	3.348	0.181	0.990	0.065	0.330	6.142	1.661	0.985	9.878	0.641	0.985	0.985	0.957	6.575	1121.880	0.985	0.985
	F	0.991	25.398	0.410	0.259	0.894	0.894	0.989	0.090	0.353	6.545	1.760	0.983	8.605	0.504	0.983	0.983	0.953	7.665	679.050	0.983	0.983

Table 4.8: Adsorption Isotherm Models for the Removal of Selected heavy Metal Ions and Organic pollutants from Petrochemical Refinery wastewater using Ternary metallic oxides

Parameters		Langmuir						Freundlich					Temkin			D-R		
		R^2	q_{max} (mg g-1)	KL (mg g-1)	RL	SSE	x^2	R^2	K_F (mg g-1)	1/n	SSE	x^2	R^2	B_T (Jmol-1)	K_T (L mg−1)	R^2	q_{max} (mgg−1)	E kJmol-1
Pb	G	0.999	68.388	8.014	0.018	0.012	0.241	0.989	0.352	0.085	0.133	0.241	0.984	1171.000	1.587	0.989	22.842	3688.960
	H	0.999	70.486	8.887	0.015	0.01	0.223	0.993	0.387	0.083	0.131	0.223	0.995	1511.600	1.658	0.983	24.023	4112.720
	I	0.999	75.352	9.200	0.017	0.007	0.206	0.996	0.481	0.062	0.128	0.206	0.998	2309.400	1.848	0.986	28.845	6157.880
	J	0.999	62.052	7.427	0.018	0.013	0.248	0.978	0.226	0.087	0.134	0.248	0.982	944.770	1.340	0.971	30.890	2708.040
Cd	G	0.995	62.494	1.000	0.327	0.016	0.288	0.978	0.213	0.068	0.137	0.288	0.994	464.470	2.007	0.978	22.450	1828.920
	H	0.997	64.200	1.026	0.321	0.014	0.249	0.968	0.212	0.067	0.135	0.249	0.994	469.720	2.085	0.969	25.770	2394.560
	I	0.998	71.538	1.272	0.276	0.013	0.244	0.969	0.228	0.066	0.134	0.244	0.997	536.390	2.235	0.969	27.714	3822.520
	J	0.994	47.384	0.821	0.372	0.017	0.299	0.942	0.184	0.068	0.138	0.299	0.990	442.230	1.551	0.967	29.129	2182.520
Ni (II)	G	0.993	48.554	0.326	0.599	0.012	0.208	0.983	0.629	0.087	0.133	0.208	0.994	250.420	1.892	0.989	15.807	2098.600
	H	0.995	50.296	0.333	0.595	0.011	0.204	0.989	0.714	0.087	0.132	0.204	0.997	158.970	1.985	0.984	17.991	2174.720
	I	0.997	66.696	0.433	0.593	0.011	0.207	0.991	0.946	0.086	0.132	0.207	0.998	171.780	2.201	0.987	18.523	2581.440
	J	0.992	47.860	0.292	0.625	0.012	0.232	0.976	0.490	0.088	0.133	0.232	0.989	136.520	1.829	0.979	19.860	1718.040
Cu (II)	G	0.999	76.328	8.014	0.050	0.013	0.145	0.994	2.201	0.152	0.134	0.145	0.991	20278.000	2.221	0.984	34.567	4172.160
	H	0.999	80.170	8.246	0.022	0.008	0.135	0.996	2.212	0.136	0.129	0.135	0.994	48189.000	2.255	0.986	34.134	4528.840
	I	0.999	98.966	8.394	0.002	0.007	0.134	0.998	2.244	0.094	0.128	0.134	0.997	71785.000	2.409	0.988	37.426	6434.240
	J	0.999	67.960	5.764	0.081	0.022	0.164	0.993	2.078	0.237	0.143	0.164	0.990	14404.000	2.211	0.988	36.792	3946.400
Cr(VI)	G	0.999	24.641	8.246	0.017	0.212	0.810	0.998	2.514	0.351	0.333	0.810	0.992	971.720	2.255	0.988	7.452	4498.480
	H	0.999	26.949	8.392	0.017	0.183	0.690	0.998	2.530	0.336	0.304	0.690	0.995	1164.400	2.221	0.988	8.589	5424.560
	I	0.999	27.637	9.640	0.009	0.081	0.401	0.999	2.538	0.330	0.202	0.401	0.997	1972.100	2.211	0.987	9.157	4833.000
	J	0.999	24.134	4.895	0.018	0.216	0.827	0.997	2.511	0.353	0.337	0.827	0.991	960.780	2.409	0.987	23.549	4322.120
Total iron	G	0.999	84.963	8.246	0.017	0.003	0.118	0.998	3.710	0.509	0.010	0.118	0.995	20278.000	2.255	0.989	25.217	326.440
	H	0.999	91.454	8.392	0.017	0.002	0.1.00	0.999	3.841	0.478	0.008	0.1.00	0.998	48189.000	2.409	0.988	28.102	401.760
	I	1.000	102.709	9.640	0.015	0.001	0.083	0.999	3.917	0.412	0.005	0.083	0.998	71785.000	2.657	0.986	33.668	845.360
	J	0.999	80.201	8.014	0.018	0.005	0.125	0.997	3.675	0.555	0.011	0.125	0.994	14404.000	2.221	0.987	35.525	153.160
BOD	G	0.999	24.134	2.685	0.018	1.41	0.427	0.998	0.048	0.281	1.531	0.427	0.996	30.452	0.850	0.988	9.465	606.360
	H	0.999	24.641	2.724	0.017	1.405	0.389	0.998	0.066	0.275	1.526	0.389	0.997	36.663	0.929	0.988	11.672	802.560
	I	0.999	36.637	6.321	0.017	1.394	0.250	0.999	0.076	0.191	1.515	0.250	0.998	39.632	1.233	0.986	10.095	1215.920
	J	0.999	21.912	1.966	0.024	1.525	0.952	0.997	0.047	0.346	1.646	0.952	0.995	24.785	0.374	0.985	8.238	400.000
COD	G	0.999	24.641	0.764	0.061	2.097	0.311	0.998	0.035	0.237	2.218	0.311	0.996	19.816	1.280	0.987	17.212	522.240
	H	0.999	40.637	0.769	0.039	0.285	0.149	0.999	0.038	0.214	0.406	0.149	0.998	20.937	2.230	0.986	18.812	918.040
	I	0.999	39.806	0.921	0.016	0.257	0.147	0.999	0.042	0.186	0.378	0.147	0.999	39.360	5.035	0.984	19.705	821.640
	J	0.999	24.134	0.741	0.090	1.558	0.340	0.998	0.026	0.303	1.679	0.340	0.995	11.484	0.421	0.983	15.754	429.800

TOC	G	0.997	31.954	1.100	0.115	4.576	1.620	0.992	0.106	0.177	4.697	1.620	0.988	19.816	14.744	0.988	9.452	1541.720
	H	0.998	32.358	1.211	0.106	4.509	1.596	0.993	0.112	0.156	4.630	1.596	0.991	20.937	34.279	0.987	10.808	1623.920
	I	0.998	36.192	1.451	0.090	4.327	1.585	0.996	0.120	0.134	4.448	1.585	0.994	39.360	111.670	0.987	11.711	1772.280
	J	0.996	31.052	0.568	0.201	4.845	1.636	0.990	0.099	0.197	4.966	1.636	0.987	11.484	7.389	0.981	12.002	1292.920

Where G, H, I and J are $Fe_3O_4/SiO_2/ZnO$ (1:1:1), $Fe_3O_4/SiO_2/ZnO$ (1:1:2), $Fe_3O_4/SiO_2/ZnO$ (1:2:1), and $Fe_3O_4/SiO_2/ZnO$ (2:1:1) composites respectively.

Table 4.6 shows the results of experimental data subjected to different isotherm models analysis for the removal of Pb (II), Cd (II), Ni (II), Cr (IV) total iron, Cu (II) ions, COD, BOD and TOC from the refinery wastewater. The results indicate that the adsorption of Pb (II), Cd (II), Ni (II), Cr (IV) total iron, Cu (II) ions, COD, BOD and TOC from petroleum refinery wastewater fit better to Langmuir isotherm model due to its highest correlated coefficient (R^2) values of 0.9967 compared with the 0.9952, 0.9942, 0.9342 recorded for Freundlich, Temkin and D-R isotherm using ZnO nanoparticles as an adsorbent. A similar trend was observed for other nanoparticles (Fe_3O_4 and SiO_2) for the removal of Pb (II), Cd (II), Ni (II), Cr (IV) total iron, Cu(II) ions, COD, BOD and TOC from petroleum refinery wastewater.

The high (R^2) obtained for the Langmuir isotherm compared with the other isotherms suggests that adsorption mechanisms are monolayer in nature. The order of the fittings of the models were Langmuir > Freundlich> Temkin> D-R. The maximum adsorption capacity (q_{max}) values for metal ion binding of Pb (II) were (30.772 mg/g, 25.623 mg/g and 23.860 mg/g); Cd (II) were (30.328 mg/g, 29.455 mg/g and 29.124 mg/g); Ni (II) had the maximal adsorption value of (21.810 mg/g, 23.310 mg/g and 20.234 mg/g); the value for Cu (II) were (40.687 mg/g, 33.016 mg/g and 28.432 mg/g); that of Cr(VI) were (13.736 mg/g, 13.736 mg/g and 13.516 mg/g); that of F (II) were 44.948 mg/g, 35.024 mg/g and 30.339 mg/g using ZnO, Fe_3O_4 and SiO_2 nanoparticles repectively. The value of The maximum adsorption capacity (q_{max}) values for the removal of BOD, COD and TOC were ZnO, Fe_3O_4 and SiO_2 nanoparticles were BOD (17.516 mg/g, 13.432 mg/g and 11.558 mg/g); COD (15.687 mg/g, 14.516 mg/g and 13.432 mg/g); and TOC (18.096 mg/g, 17.000 mg/g and 15.572 mg/g).

This result indicates that among the monometallic oxides nanoparticles ZnO performed better than Fe_3O_4 and SiO_2 nanoparticles due to its high surface area.

The dimensionless (R_L) value from Table 4.6 ranges from 0.026 to 0.901, which is smaller than one (1), indicating that the adsorption process is favourable for ZnO, Fe_3O_4 and SiO_2 nanoparticles. The K_L value is a criterion for determining the affinity of absorbent and adsorbate molecules. The larger the K_L value, the greater the affinity between the absorbent and adsorbate molecules. From the result, the Pb (II) has a greater affinity for ZnO nanoparticles (5.369) compared with the 4.768 and 4.921 obtained for Fe_3O_4, SiO_2 nanoparticles. Additionally, the adsorption of Pb (II) was more favourable using ZnO nanoparticles than Fe_3O_4 and SiO_2 nanoparticles due to its higher surface area than others. It was found that the 1/n value in the case of the Freundlich isotherm model was less than one for all the target pollutants which means that chemisorption played a very vital role in the adsorption of the target pollutants using ZnO nanoparticles Fe_3O_4 and SiO_2 nanoparticles. The higher the adsorption process the smaller the value of 1/n (Lyubchik *et al*., 2018). Also, the D-R isotherm model was used to differentiate between the physical and chemical adsorption of the selected metal ions and organic pollutants.

The adsorption process is considered physical if the free energy of adsorption (E) is between 1 and 16 kJ/mol and chemisorption if E is greater than 16 kJ/mol Ayawei *et al*. (2017). For all nanoadsorbents and the selected heavy metals removed the E value reported in this research is larger than 16 kJ/mol. This shows that the adsorption of Pb (II), Cd (II), Ni (II), Cr (IV) total iron, Cu (II) ions, COD, BOD and TOC using Fe_3O_4, SiO_2 and ZnO as nanoadsorbent is chemisorption in nature. This result corroborated thermodynamic and kinetics data where the adsorption of the heavy metals and the indicator parameters show a positive enthalpy value irrespective of the adsorbent used.

238

Table 4.7 summarizes the correlation coefficients (R^2) values obtained from the four isotherm models for the removal of Pb (II), Cd (II), Ni (II), Cr (VI), Cu (II), total iron, BOD, COD and TOC adsorption from petroleum refinery wastewater using ZnO/Fe_3O_4, ZnO/SiO_2, Fe_3O_4/SiO_2 nanocomposites. Adsorption Langmuir isotherm model had the highest (R^2) values in the range of 0.991-0.999, greater than 0.9589-0.997, 0.9495-0.995 and 0.945-0.958 obtained for Freundlich, Temkin and R-D isotherms indicating that Langmuir isotherm model best described the adsorption of Pb (II), Cd (II), Ni (II), Cr (VI), Cu (II), total iron, BOD, COD and TOC onto ZnO/Fe_3O_4, ZnO/SiO_2, Fe_3O_4/SiO_2 nanocomposites than the other models. It can be noticed from the table that the values of the (R^2) for all the models were higher using ZnO/Fe_3O_4 than ZnO/SiO_2, Fe_3O_4/SiO_2 nanocomposites. This can be ascribed to the high adsorptive efficiency of ZnO/Fe_3O_4 than others due to its higher surface area.

Maximum adsorption capacity (q_{max}), rate of adsorption (K_L) and separation factor (R_L) were calculated from the plot of Ce/qe against Ce (see appendix 1-9) and the result presented in Table 4.7. The q_{max} values for the target pollutants were Pb (II) were (39.052 mg/g , 37.951 and 36.110 mg/g); Cd (II) were (34.922 mg/g, 33.603 mg/g and 33.47 mg/g); Ni (II) had the maximal adsorption value of (34.949 mg/g, 28.731 mg/g and 27.262 mg/g); the value for Cu (II) were (45.766 mg/g, 42.456 mg/g and 37.990 mg/g); Cr (VI) were (23.766 mg/g, 23.457 mg/g and 23.456 mg/g); total iron were (46.955 mg/g, 44.421 mg/g and 43.781 mg/g), BOD were (27.7657 mg/g, 24.990 mg/g and 21.958 mg/g), COD were (32.766 mg/g, 23.456 mg/g and 21.990 mg/g) while the the maximum capacity of TOC were (38.102 mg/g, 30.617 mg/g and 25.398 mg/g) using ZnO/Fe_3O_4, ZnO/SiO_2, Fe_3O_4/SiO_2 nanoadsorbent. The trend of the result reported suggests that the q_{max} value for ZnO/Fe_3O_4 was higher compared to ZnO/SiO_2, Fe_3O_4/SiO_2 for all the target

pollutants. This may be ascribed to the enhanced surface area ZnO/Fe_3O_4 nanocomposites.

Another important parameter from the Langmuir isotherm is the dimensionless constant (R_L). If $R_L > 1$ the adsorption is said to be unfavourable, $R_L = 1$ the adsorption is linear while for $0 < R_L < 1$ favourable and $RL = 0$ the adsorption is said to be irreversible. From the result presented in Table 4.7 the values obtained for the (R_L) values were less than one for all the target pollutants using ZnO/Fe_3O_4, ZnO/SiO_2, Fe_3O_4/SiO_2 nanocomposites as adsorbent suggesting that the adsorption of Pb (II), Cd (II), Ni (II), Cr (VI), Cu (II), total iron, BOD, COD and TOC onto ZnO/Fe_3O_4, ZnO/SiO_2, Fe_3O_4/SiO_2 nanocomposites were favourable irrespective of the adsorbent used. It is important to note that the values of for ZnO/Fe_3O_4 nanocomposites was lower than the values for ZnO/SiO_2, Fe_3O_4/SiO_2 nanocomposites. This indicates that the adsorption of the target pollutants was more favourable using ZnO/Fe_3O_4 nanocomposites as a nanoadsobent. This result justifies the earlier claims that the adsorption of the target pollutants was better using ZnO/Fe_3O_4 than ZnO/SiO_2, Fe_3O_4/SiO_2 nanocomposites.

Table 4.7 shows the result of the Freundlich isotherm models with parameters such as K_F (mg/g (L/mg) which define as the adsorption distribution coefficient, represents the quantity of the pollutant adsorbed onto the nanocomposites and 1/n which is used to identify the favourability, intensity, or surface heterogeneity between adsorbent and the adsorbate. Both K_F and 1/n were calculated from the plot of log qe against log Ce which gave a straight line with a slope of 1/n and intercept of log K_F (see appendix 10-18). The value of (1/n) presented in Table 4.7 is less than one, indicating that the adsorption between the adsorbate and the adsorbent is normal Langmuir isotherm (Lshabanat *et al.*, 2016) since 1/n less than one implies a normal Langmuir isotherm, whereas a value of 1/n

more than one shows cooperative adsorption (Freundlich isotherm). This observed trend supports the earlier result of the (R^2) and R_L that the adsorption of the target pollutants using ZnO/Fe$_3$O$_4$, ZnO/SiO$_2$, Fe$_3$O$_4$/SiO$_2$ nanocomposites is monolayer adsorption (Langmuir isotherm). Additionally, the value of 1/n is an indication that the adsorption is less heterogeneous since the values are closer to zero than its value gets closer to zero (Pudza and Abidin, 2020).

For all the targeted pollutants, the 1/n values derived from the Freundlich model were less than one, indicating that of Pb (II), Cd (II), Ni (II), Cr (VI), Cu (II), total iron, BOD, COD and TOC onto ZnO/Fe$_3$O$_4$, ZnO/SiO$_2$, Fe$_3$O$_4$/SiO$_2$ nanocomposites was favourable. The lower values of ZnO/Fe$_3$O$_4$ than ZnO/SiO$_2$, Fe$_3$O$_4$/SiO$_2$ nanocomposites justify the higher performance of ZnO/Fe$_3$O$_4$ nanocomposites compared to ZnO/SiO$_2$, Fe$_3$O$_4$/SiO$_2$ nanocomposites.

The result of the Temkin isotherm presented in Table 4.7 indicates that the value of is the equilibrium binding constant (K_T (L/g) which corresponds to the highest binding energy was between 0.115-2.211 L/g. The value of Temkin constant B_T (J/mol) which is related to the heat of sorption was in the range of 8.605-14288.700 J/mol using ZnO/Fe$_3$O$_4$, ZnO/SiO$_2$, Fe$_3$O$_4$/SiO$_2$ nanocomposites for the removal of Pb (II), Cd (II), Ni (II), Cr (VI), Cu (II), total iron, BOD, COD and TOC. The presence of a positive value for B_T indicates that the adsorption was endothermic (Yu *et al*. 2021).

The value of E from the Dubinin-Radushkevich (D-R) isotherm model is used to predict the type of adsorption; E values of less more than 8 kJ/mol are often classified as chemisorption and less than 8 kJ/mol are classified as physisorption (Singh *et al*., 2020). The adsorption of Pb (II), Cd (II), Ni (II), Cr (VI), Cu (II), total iron, BOD, COD and

TOC onto ZnO/Fe_3O_4, ZnO/SiO_2, Fe_3O_4/SiO_2 nanocomposites ranges from 1129.71-1919.01 kJ/mol, confirming the earlier reported dominating mechanism of chemisorption.

The values of the q_{max} presented in Table 4.7 the ternary metal oxides nanocomposites shows that $SiO_2/Fe_3O_4/ZnO$ (1:2:1) nanocomposites had highest q_{max} of 75.352 mg g^{-1}, 71.538 mg g^{-1}, 66.696 mg g^{-1}, 98.966 mg g^{-1}, 36.637 mg g^{-1}, 102.709 mg g^{-1}, 30.637 mg g^{-1}, 39.806 mg g^{-1}, 36.192 mg g^{-1} for Pb (II) Cd (II), Ni (II) Cr (VI), Cu (II), total iron, BOD, COD and TOC respectively. Indicate that $SiO_2/Fe_3O_4/ZnO$ (1:2:1) nanocomposites perform better than the others due to its larger surface area.

Table 4.8 present the result of the ternary nanocomposites for Langmuir, Freundlich. Temkin and Dubinin-Radushkevich (D-R) isotherm. The result presented for the removal of Pb (II), Cd (II), Ni (II), Cr (VI), Cu (II), total iron, BOD, COD and TOC onto ZnO/Fe_3O_4, ZnO/SiO_2, Fe_3O_4/SiO_2 nanocomposites follows the same trend, suggesting that the adsorption of the target pollutants follows the order of $Fe_3O_4/SiO_2/ZnO$ (1:2:1) > $Fe_3O_4/SiO_2/ZnO$ (1:1:2) > $Fe_3O_4/SiO_2/ZnO$ (1:1:1) > $Fe_3O_4/SiO_2/ZnO$ (2:1:1) nanocomposites for all the target pollutants in terms of their performance and fitness to the models. The sorption process was better described by Langmuir isotherm model. Generally, among the monometallic oxides ZnO nanoparticles performed better than others, among the bimetallic oxides the Fe_3O_4/ZnO nanocomposite was better than the others while the $Fe_3O_4/SiO_2/ZnO$ (1:2:1) nanocomposites was better followed by $Fe_3O_4/SiO_2/ZnO$ (1:1:2) > $Fe_3O_4/SiO_2/ZnO$ (1:1:1) and $Fe_3O_4/SiO_2/ZnO$ (2:1:1) respectively.

4.12 Adsorption Kinetics

Different kinetic models such as Pseudo-first order, Pseudo second order, intra-particle diffusion model and Elovich kinetic models were used to evaluate the nature of adsorption that occurs during the removal of Pb (II), Cd (II), Ni (II), Cr (VI), Cu (II), total iron, BOD, COD and TOC from the petroleum refinery wastewater using Fe_3O_4, SiO_2 and ZnO nanoparticles and ZnO/Fe_3O_4, ZnO/SiO_2, Fe_3O_4/SiO_2, $Fe_3O_4/SiO_2/ZnO$ (1:1:2), $Fe_3O_4/SiO_2/ZnO$ (2:1:1) $Fe_3O_4/SiO_2/ZnO$ (1:2:1), $Fe_3O_4/SiO_2/ZnO$ (1:1:1) nanocomposites. The parameters for the Pseudo first order, Pseudo second order, elovich and intra-particle diffusion kinetics were calculated from the corresponding slope and intercept of the plots in appendix 28-36 and the results obtained are summarized in Table 4.9, 4.10 and 4.11 respectively.

Table 4.9: Kinetic Parameters for the Adsorption of the Selected Heavy Metals and other COD, BOD and TOC using Fe_3O_4, SiO_2 and ZnO Nanoadsorbents

Parameters		Pseudo First Order					Pseudo Second Order						Intraparticle Diffusion		Elovich		
		R^2	k_1	q_{e1}	SSE	x^2	R^2	K_2	q_{e2}				K_{id}	C	R^2	B	A
			(mg/g·min)	(g/min)				(mg/g·min)	(g/min)	SSE	x^2	R^2	(g/min)			(g/min)	
Pb	A	0.863	0.159	0.087	0.415	4.712	0.990	4.413	0.269	0.016	0.203	0.822	0.031	0.020	0.900	58.309	0.086
	B	0.835	0.156	0.086	0.419	5.292	0.989	3.952	0.255	0.017	0.224	0.810	0.028	0.018	0.898	55.188	0.068
	C	0.753	0.149	0.086	0.457	5.753	0.983	2.936	0.244	0.023	0.294	0.793	0.012	0.012	0.890	51.600	0.083
Cd	A	0.954	0.158	0.103	0.456	6.059	0.987	2.468	0.278	0.029	0.407	0.861	0.013	0.005	0.932	53.908	0.080
	B	0.932	0.156	0.091	0.459	6.358	0.972	1.677	0.282	0.039	0.550	0.844	0.011	0.002	0.917	52.002	0.047
	C	0.921	0.154	0.087	0.486	6.819	0.953	1.271	0.286	0.085	0.736	0.843	0.010	0.001	0.897	45.704	0.034
Ni (II)	A	0.870	0.164	0.108	0.497	5.750	0.972	1.837	0.266	0.037	0.433	0.749	0.013	0.035	0.900	47.985	0.085
	B	0.810	0.163	0.104	0.504	6.310	0.960	1.825	0.262	0.039	0.448	0.669	0.012	0.009	0.879	46.382	0.082
	C	0.780	0.162	0.100	0.539	6.360	0.957	1.369	0.247	0.081	0.651	0.652	0.011	0.001	0.866	45.372	0.036
Cu (II)	A	0.888	0.188	0.441	0.096	5.586	0.999	2.269	0.462	0.130	0.309	0.814	0.024	0.299	0.661	223.435	25.800
	B	0.853	0.182	0.428	0.406	9.66	0.998	2.215	0.396	0.131	0.314	0.811	0.021	0.288	0.659	156.902	23.036
	C	0.812	0.171	0.402	1.469	11.476	0.996	2.003	0.361	0.176	0.413	0.796	0.016	0.257	0.659	143.958	20.894
Cr(VI)	A	0.773	0.175	0.238	4.878	19.275	0.990	2.287	0.361	0.295	1.291	0.727	0.019	0.136	0.659	14.376	32.258
	B	0.721	0.166	0.224	8.266	34.714	0.983	2.046	0.325	0.316	0.960	0.679	0.019	0.127	0.658	1.790	29.560
	C	0.714	0.188	0.240	12.527	42.965	0.958	2.546	0.376	0.456	2.103	0.656	0.016	0.121	0.452	1.615	20.109

Parameters		Pseudo First Order					Pseudo Second Order						Intraparticle Diffusion		Elovich		
		R^2	k_1	q_{e1}	SSE	x^2	R^2	K_2	q_{e2}				K_{id}	C	R^2	B	A
			(mg/g·min)	(g/min)				(mg/g·min)	(g/min)	SSE	x^2	R^2	(g/min)			(g/min)	
BOD	A	0.773	0.244	1.591	6.801	12.437	0.998	4.533	7.440	1.622	0.821	0.924	0.694	5.191	0.905	2026.143	1.468
	B	0.582	0.211	1.181	8.771	13.979	0.996	3.738	6.310	1.711	1.139	0.850	0.684	4.119	0.873	118.134	1.089
	C	0.466	0.116	0.798	9.893	14.115	0.995	1.924	6.294	1.743	1.390	0.840	0.438	3.068	0.818	30.079	1.044
COD	A	0.891	0.293	2.727	1.558	18.195	0.998	10.520	9.911	0.646	6.281	0.803	1.026	4.438	0.944	44.982	0.659
	B	0.885	0.292	2.421	1.604	18.248	0.997	9.783	9.717	0.646	6.810	0.797	1.000	4.412	0.932	37.800	0.635
	C	0.834	0.290	2.543	1.662	20.018	0.995	7.097	8.840	0.848	10.445	0.782	0.818	3.980	0.929	32.901	0.592
TOC	A	0.692	0.136	0.742	1.842	9.977	0.992	0.635	4.554	1.736	7.876	0.797	0.649	0.930	0.954	3.237	0.806
	B	0.681	0.119	0.653	1.890	11.005	0.991	0.545	4.378	1.688	8.573	0.796	0.624	0.902	0.953	3.112	0.727
	C	0.603	0.110	0.511	1.914	11.005	0.990	0.360	4.212	1.826	10.705	0.794	0.602	0.876	0.953	3.073	0.700

KEY: A B, C, are ZnO, Fe_3O_4, SiO_2, nanoparticles respectively.

Appendix 28-36 shows plots of $\log (q_e - q_t)$ against t for the adsorption of Pb (II), Cd (II), Ni (II), Cr (VI), Cu (II), total iron, BOD, COD and TOC from the petroleum refinery wastewater using ZnO, Fe_3O_4 and SiO_2 and nanoparticles. The slope and intercept from the plots were used to calculate the values of the pseudo first order rate constant (k_1) and the amounts of pollutant adsorbed at equilibrium for the pseudo first order kinetics model (q_{e1}). Appendix 37-45 shows plots of t/qt against time for the adsorption of Pb (II), Cd (II), Ni (II), Cr (VI), Cu (II), total iron, BOD, COD and TOC from the refinery wastewater using ZnO, Fe_3O_4 and SiO_2 nanoparticles. The slope and intercept from the plots were used to calculate the values of pseudo-second-order rate constant (k_2) and he amounts of pollutant adsorbed at equilibrium for the pseudo second order kinetics model (q_{e1}). Similarly, appendix 46-54 shows the plot of qt against lnt. The elovich adsorption constant (β) and initial rate of adsorption (α) were calculated from the slope and the intercept respectively.

Table 4.9 shows the coefficient of correlation (R^2) values for the pseudo first-order, pseudo second order, elovich and intraparticle diffusion kinetic models using ZnO, Fe_3O_4 and SiO_2 nanoparticles as nanoadsorbent. The (R^2) values obtained for the pseudo first order kinetic model using ZnO, Fe_3O_4 and SiO_2 nanoparticles for the adsorption of Pb (II) (0.863, 0.835, 0.753); Cd (II) (0.954, 0.932 and 0.921); Ni (II) (0.870, 0.810 and 0.780); Cr (VI) (0.888, 0.853 and 0.812); Cu (II) (0.773, 0.721 and 0.714); BOD (0.773, 0.582 and 0.466); COD (0.891, 0.885 and 0.834); and TOC (0.692, 0.681 and 0.603) from the refinery wastewater was lower than (R^2) of Pb (II) (0.99, 0.989, 0.983); Cd (II) (0.987, 0.972 and 0.953); Ni (II) (0.972, 0.96 and 0.957); Cr (VI) (0.999, 0.998 and 0.996); Cu (II) (0.990, 0.983 and 0.958); BOD (0.998, 0.996 and 0.995); COD (0.998, 0.997 and 0.995); and TOC (0.992, 0.991 and 0.990) for the pseudo second order kinetic model.

Generally, the values obtained for the pseudo second order kinetic model is higher than that of the pseudo-first-order model, showing that the pseudo second order kinetic model best fits the adsorption removal of Pb (II), Cd (II), Ni (II), Cr (VI), Cu (II), total iron, BOD, COD and TOC from the refinery wastewater onto ZnO, Fe_3O_4 and SiO_2 nanoparticles. This is an indication that chemical adsorption dominant the adsorption process and the pseudo second order kinetic model is the rate determining step.

Table 4.9 shows that the values of the pseudo second order rate constant (k_2) using ZnO, Fe_3O_4 and SiO_2 nanoparticles for the removal of Pb (II), Cd (II), Ni (II), Cr (VI), Cu (II), total iron, BOD, COD and TOC were 4.413, 3.952 and 2.936 mg/g·min; 2.468, 1.677 and 1.271 mg/g·min; 1.837,1.825 and 1.369 mg/g·min; 2.269, 2.215 and 2.003 mg/g·min; 2.287, 2.046 and 2.546 mg/g·min; 4.533, 3.738 and1.924 mg/g·min; 10.52, 9.783 and 7.097 mg/g·min; 0.635, 0.545 and 0.360 mg/g·min which is higher than 0.160, 0.156,, 0.149 mg/g·min; 0.087, 0.086 and 0.085 mg/g·min; 0.103, 0.091 and 0.087 mg/g·min; 0.108, 0.104 and 0.100 mg/g·min; 0.441, 0.428 and 0.402 ; 0.238, 0.224 and 0.240 mg/g·min; 1.591, 1.181 and 0.798 mg/g·min; 2.727, 2.421 and 2.543 mg/g·min; 0.742, 0.653 and 0.511 mg/g·min for the pseudo first order rate constant (k_1).

The high values of (k_2) compared to the values of the (k_1) for ZnO, Fe_3O_4 and SiO_2 nanoparticles indicates that the adsorption rate of Pb Pb (II), Cd (II), Ni (II), Cr (VI), Cu (II), total iron, BOD, COD and TOC from the petroleum refinery wastewater was faster for pseudo second order than pseudo first order kinetics, supporting the fact that the reaction fits better to the pseudo second order kinetics model. Similarly, the amount of pollutants adsorbed at equilibrium for the pseudo second order kinetics model (q_{e2}) was higher than amount of pollutants adsorbed at equilibrium for the pseudo first order kinetics model (q_{e1}) using ZnO, Fe_3O_4 and SiO_2 nanoparticles ad an adsorbent.

Generally, the trend observed suggests that the ZnO nanoparticle have higher values of (R^2), $(k_1$ and $k_2)$ and $(q_{e1}$ and $q_{e1})$ followed by Fe_3O_4 nanoparticles while SiO_2 nanoparticles recorded the smallest value of (R^2), $(k_1$ and $k_2)$ and $(q_{e1}$ and $q_{e1})$ for all the pollutants. This suggests that the ZnO nanocomposites was more efficient in the removal of Pb Pb (II), Cd (II), Ni (II), Cr (VI), Cu (II), total iron, BOD, COD and TOC from the petroleum refinery wastewater. This may be due to the higher surface area of ZnO nanoparticles compared to Fe_3O_4 SiO_2 nanoparticles.

To validate the fitness of the adsorption of Pb (II), Cd (II), Ni (II), Cr (VI), Cu (II), total iron, BOD, COD and TOC the data were subjected to different error functions such as chi-square (x^2) and the sum of squared error (SSE). The values presented in Table 4.9 indicate that the x^2 pseudo second order model exhibited a lower value of x^2 for all the metals and indicator parameters irrespective of the adsorbent used. This result supports the fact that the adsorption process was governed purely by a chemical reaction. Similarly, the SSE values for the pseudo second order model exhibited a lower value than that of the pseudo first order model, this also confirms the fact that the adsorption process was chemical adsorption due to the lower value recorded for the pseudo second order compared with the pseudo first order kinetic model irrespective of the adsorbent. It is important to note that the values of chi-square (x^2) and the sum of squared error (SSE) for ZnO nanoparticles was lower than the values obtained for Fe_3O_4 and SiO_2 nanoparticles. This is another confirmation that the ZnO nanoparticles performed better as an adsorbent than Fe_3O_4 and SiO_2 nanoparticles for all the pollutants.

Other kinetic models such as intraparticle diffusion and elovich were used to understand the adsorption mechanisms. Table 4.9 shows that the (R^2) for the intraparticle diffusion ranges from 0.652 to 0.861, comparing these values with the earlier reported values for

the pseudo first order (0.510 – 0.950) and pseudo second order (0.950 to 0.950) kinetic models, it means that the adsorption process of Pb (II), Cd (II), Ni (II), Cr(VI), Cu (II), total iron, BOD, COD and TOC using various nanoadsorbent from the petroleum refinery wastewater was not governed by intraparticle diffusion kinetics model. The k_{id} (g/min) values were found to be higher for ZnO nanoparticles compared with Fe_3O_4 and SiO_2 nanoparticles which was due to the greater driving force between the pollutants and ZnO nanoparticles. This resut justify the high efficiency of ZnO over Fe_3O_4 and SiO_2 nanoparticles.

Additionally, it has been reported that if the rate-controlling step of an adsorption process is governed by intraparticle diffusion kinetic model, the plot of qt against $t^{0.5}$ should be linear and pass through the origin (Byungryul, 2020). As can be seen in appendix 55-63 the plots of qt against $t^{0.5}$ are linear but did not passed through the origin. This deviation strongly suggests that the intraparticle diffusion kinetic model was not the rate-controlling step during the adsorption of terget pollutants from the petroleum refinery wastewater, but other kinetic models may simultaneously control the adsorption rate.

The Elovich kinetics model, is one of the most helpful models for understanding chemisorption. The slope and intercept of the linear plot of qt vs lnt, as shown in appendix 46-542 was used to calculate the initial rate of adsorption (α) and β (g/mg) which is related to the extent of surface coverage and activation energy for chemisorption. The result of the elovich model presented in Table 4.9 indicates that the R^2 ranges between 0.661 to 0.954, this result further supports the earlier claim that the adsorption process is chemisorption (Zand and Abyaneh, 2020). Generally, the pseudo second order kinetic model had a correlation coefficient closer to 1 when compared to pseudo first order, intraparticle diffusion and Elovich kinetics, kinetic models. This suggested that the

removal of Pb (II), Cd (II), Ni (II), Cr (VI), Cu (II), total iron, BOD, COD and TOC from petroleum refinery wastewater irrespective of the nanoadsorbent used was better described by a pseudo second order kinetic model. Additionally, ZnO nanoparticles was a better adsorbent for the removal of all the target pollutants compared with Fe_3O_4 and SiO_2 nanoparticles.

Table 4.10: Kinetic Parameters for the Adsorption of the Selected Heavy Metals and other COD, BOD and TOC using Fe₃O₄/ZnO and Fe₃O₄/SiO₂, , ZnO/ SiO₂ Nanoadsorbents

Parameters	Nanoadsorbent	Pseudo First Order					Pseudo Second Order						Intraparticle Diffusion				Elovich	
		R^2	k_1 (mg/g·min)	q_{e1} (g/min)	SSE	x^2	R^2	K_2 (mg/g·min)	q_{e2} (g/min)	SSE	x^2	R^2	K_{id} (g/min)	C	R^2	β (g/min)	α
Pb	D	0.894	0.187	0.095	0.363	4.216	0.992	5.650	0.273	0.011	0.144	0.842	0.013	0.033	0.928	60.716	0.219
	E	0.881	0.175	0.092	0.364	4.487	0.993	5.425	0.272	0.012	0.129	0.841	0.012	0.031	0.926	60.643	0.181
	F	0.870	0.165	0.090	0.376	4.699	0.993	5.346	0.261	0.014	0.146	0.840	0.011	0.026	0.911	58.858	0.112
Cd	D	0.961	0.168	0.106	0.397	4.608	0.996	4.616	0.318	0.015	0.147	0.883	0.018	0.025	0.953	56.980	0.140
	E	0.954	0.162	0.094	0.399	4.758	0.996	4.427	0.314	0.017	0.169	0.877	0.016	0.019	0.944	56.465	0.134
	F	0.952	0.158	0.093	0.461	5.528	0.992	3.259	0.276	0.020	0.242	0.874	0.014	0.009	0.943	55.897	0.109
Ni (II)	D	0.966	0.182	0.112	0.274	2.879	0.999	6.522	0.293	0.012	0.114	0.780	0.014	0.038	0.947	54.585	0.266
	E	0.923	0.172	0.107	0.301	3.103	0.999	5.921	0.265	0.014	0.124	0.797	0.015	0.041	0.945	49.702	0.237
	F	0.883	0.169	0.104	0.319	3.013	0.998	5.260	0.232	0.015	0.151	0.802	0.015	0.046	0.930	48.780	0.145
Cu (II)	A	0.898	0.196	0.464	0.064	2.462	0.998	2.447	0.490	0.063	0.161	0.918	0.027	0.343	0.898	459.164	34.698
	B	0.884	0.194	0.449	0.374	6.536	0.998	2.321	0.480	0.075	0.172	0.874	0.025	0.303	0.769	315.400	29.949
	C	0.881	0.189	0.442	0.437	8.352	0.993	2.306	0.462	0.095	0.212	0.826	0.024	0.301	0.712	266.770	27.925
C r(VI)	D	0.886	0.193	0.305	4.635	15.205	0.993	2.726	0.426	0.266	0.978	0.821	0.028	0.191	0.819	69.102	45.558
	E	0.863	0.192	0.299	4.821	15.268	0.992	2.567	0.421	0.284	1.016	0.811	0.018	0.173	0.660	22.837	44.484
	F	0.823	0.189	0.292	4.828	16.232	0.991	2.558	0.411	0.290	1.165	0.794	0.019	0.161	0.659	20.112	32.733
BOD	D	0.793	0.258	1.702	5.44	10.998	0.999	5.169	7.890	0.690	1.528	0.873	0.695	4.551	0.926	6789.660	1.500

Parameters	Nanoadsorbent	Pseudo First Order					Pseudo Second Order						Intraparticle Diffusion			Elovich	
		R^2	k_1 (mg/g·min)	q_{e1} (g/min)	SSE	x^2	R^2	K_2 (mg/g·min)	q_{e2} (g/min)	SSE	x^2	R^2	K_{id} (g/min)	C	R^2	β (g/min)	α
	E	0.786	0.258	1.652	5.737	12.029	0.999	4.880	7.876	0.784	1.569	0.813	0.529	4.541	0.915	2652.902	1.495
	F	0.745	0.233	1.459	8.098	13.663	0.997	4.444	7.313	0.944	1.657	0.800	0.403	5.350	0.899	185.909	1.100
COD	D	0.918	0.341	3.021	14.751	1.483	0.999	11.683	11.120	0.266	3.237	0.814	1.088	5.583	0.959	119.443	0.719
	E	0.913	0.298	2.718	15.831	1.489	0.999	11.516	10.785	0.369	3.976	0.813	1.070	5.468	0.951	73.990	0.699
	F	0.895	0.297	2.572	17.127	1.528	0.998	10.562	10.536	0.643	5.686	0.810	1.056	5.059	0.949	70.694	0.672
TOC	D	0.857	0.223	1.039	8.575	1.751	0.998	0.705	5.250	1.522	7.395	0.801	0.751	1.061	0.957	3.506	0.953
	E	0.828	0.172	1.029	9.519	1.771	0.996	0.554	4.958	1.538	8.019	0.800	0.711	1.015	0.955	3.276	0.873
	F	0.814	0.139	0.994	9.596	1.813	0.995	0.490	4.841	1.637	8.422	0.797	0.693	0.962	0.955	3.275	0.825

Where D, E, F are ZnO/Fe_3O_4, ZnO/SiO_2, Fe_3O_4/SiO_2 nanocomposites respective

Table 4.10 shows that the correlation coefficient (R^2) values for the adsorption removal of Pb (II), Cd (II), Ni (II), Cr (VI), Cu (II), total iron, BOD, COD and TOC from petroleum refinery wastewater were in the range of (0.8299 –0.9770) for pseudo first order model kinetics using ZnO/Fe_3O_4, ZnO/SiO_2, Fe_3O_4/SiO_2 nanocomposites as nanoadsorbents. The (R^2) value for the pseudo second order model was higher, ranging from (0.991-0.999). The closeness of the (R^2) value for the pseudo second order kinetics model indicates that the pseudo second order model is more appropriate for describing the adsorption removal of Pb (II), Cd (II), Ni (II), Cr (VI), Cu (II), total iron, BOD, COD and TOC from petroleum refinery wastewater. The values of the (R^2) for both the pseudo first order and pseudo second order models for ZnO/Fe_3O_4, ZnO/SiO_2, Fe_3O_4/SiO_2 nanocomposites were in order of $ZnO/Fe_3O_4 > ZnO/SiO_2 > Fe_3O_4/SiO_2$ nanocomposites for all the target pollutants. The trend observed suggests that the adsorption removal of the target pollutants was more favourable using ZnO/Fe_3O_4 nanocomposites, which may be related to the enhanced surface area of ZnO/Fe_3O_4 nanocomposites compared with ZnO/SiO_2, Fe_3O_4/SiO_2 nanocomposites.

The kinetics rate constants for the pseudo first order model (k_1) range between 0.139 to 0.980 mg/g·min while the kinetics rate constants for the pseudo second order model (k_2) range from 0.490 to 11.683 mg/g·min as presented in Table 4.10. The higher (k_2) value obtained compared to the (k_1) values for the adsorption removal of Pb (II), Cd (II), Ni (II), Cr (VI), Cu (II), total iron, BOD, COD and TOC from petroleum refinery wastewater using ZnO/Fe_3O_4, ZnO/SiO_2, Fe_3O_4/SiO_2 nanocomposites support the fitting of a second-order kinetic model in this adsorption study. The trend as shown in Table 4.10 suggests that the ZnO/Fe_3O_4 nanocomposites recorded the highest values (k_1 and k_2) for all the target pollutants followed by ZnO/SiO_2 and Fe_3O_4/SiO_2 nanocomposites. This trend

supports the outstanding performance of ZnO/Fe$_3$O$_4$ nanocomposites among the bimetallic oxides nanocomposites used for the adsorption removal of Pb (II), Cd (II), Ni (II), Cr (VI), Cu (II), total iron, BOD, COD and TOC from petroleum refinery wastewater. Similarly, the values of qe$_1$ (pseudo first order) were lower than qe$_2$ (pseudo second order) for all the target pollutants using ZnO/Fe$_3$O$_4$, ZnO/SiO$_2$ and Fe$_3$O$_4$/SiO$_2$ nanocomposite as adsorbent. The ZnO/Fe$_3$O$_4$ nanocomposites sh ow a higher value of (qe$_1$) and (qe$_2$) for each of the pollutants compared to ZnO/SiO$_2$ and Fe$_3$O$_4$/SiO$_2$ nanocomposites.

The experimental data obtained from the adsorption of adsorption removal of Pb (II), Cd (II), Ni (II), Cr (VI), Cu (II), total iron, BOD, COD and TOC from the petroleum refinery wastewater using ZnO/Fe$_3$O$_4$, ZnO/SiO$_2$ and Fe$_3$O$_4$/SiO$_2$ nanocomposite as adsorbent were subjected to the error function to validates the fitness of the models. The values of chi-square (x^2) and the sum of squared error (SSE) for ZnO/Fe$_3$O$_4$ nanocomposites was lower than the values obtained for ZnO/SiO$_2$ and Fe$_3$O$_4$/SiO$_2$ nanocomposites for all the target pollutants. This is another confirmation that the ZnO/Fe$_3$O$_4$ nanocomposites performed better as an adsorbent than ZnO/SiO$_2$ and Fe$_3$O$_4$/SiO$_2$ nanocomposites for all the pollutants. This result validates the earlier claims that the ZnO/Fe$_3$O$_4$ nanocomposites performed better as an adsorbent than ZnO/SiO$_2$ and Fe$_3$O$_4$/SiO$_2$ nanocomposites.

The low (R^2) obtained for the intraparticle diffusion implies that the adsorption process did not follow intraparticle diffusion adsorption kinetics. The correlation coefficient, R^2, indicates a poor link between the parameters and also explains why the adsorption process does not suit the diffusion kinetic model. Rodríguez *et al.* (2020); Huang *et al.* (2020) and Pelalak *et al.* (2021) who worked independently had reported that pseudo second order kinetic model was more appropriate in describing adsorption of metal ions using different nanocomposites from wastewater. The values of k$_{id}$ presented in Table 4.10 were

found to be higher for ZnO/Fe_3O_4 nanocomposites compared with the values of k_{id} ZnO/SiO_2 and Fe_3O_4/SiO_2 nanocomposites for all the target pollutants. The trend observed is an indication that there is a greater driving force between the targeted pollutants and ZnO/Fe_3O_4 nanocomposites compared to the use of ZnO/SiO_2 nanocomposites and Fe_3O_4/SiO_2 nanocomposites as nanoadsorbents. This result justifies the high efficiency of ZnO/Fe_3O_4 nanocomposites over ZnO/SiO_2 and Fe_3O_4/SiO_2 nanocomposites.

Additionally, it has been reported that if the rate-controlling step of an adsorption process is governed by intraparticle diffusion kinetic model, the plot of qt against $t^{0.5}$ should be linear and pass through the origin (Manjuladevi *et al*., 2023). As can be seen in appendix 55-63 the plots of qt against $t^{0.5}$ are linear but did not pass through the origin. This deviation strongly suggests that the intraparticle diffusion kinetic model was not the rate-controlling step during the adsorption of target pollutants from the petroleum refinery wastewater, but other kinetic models may simultaneously control the adsorption rate.

The Elovich kinetics model, is one of the most helpful models for understanding chemisorption. The slope and intercept of the linear plot of qt vs lnt, as shown in appendix 46-54 was used to calculate the initial rate of adsorption (α) and β (g/mg) which is related to the extent of surface coverage and activation energy for chemisorption. The result of the elovich model presented in Table 4.10 indicates that the R^2 ranges between 0.660 to 0.959, this result further supports the earlier claim that the adsorption process is chemisorption. Generally, the pseudo second order kinetic model had a correlation coefficient closer to unity when compared to pseudo first order, intraparticle diffusion and Elovich kinetics, kinetic models. This suggested that the removal of Pb (II), Cd (II), Ni (II), Cr (VI), Cu (II), total iron, BOD, COD and TOC from petroleum refinery

wastewater irrespective of the nanoadsorbent used was better described by a pseudo second order kinetic model.

It was found that ZnO/Fe_3O_4 nanocomposites exhibited stronger adsorption of Pb (II), Cd (II), Ni (II), Cr (VI), Cu (II), total iron, BOD, COD and TOC from petroleum refinery wastewater compared to ZnO/SiO_2 and Fe_3O_4/SiO_2 nanocomposites.

Table 4.11: : Kinetic Parameters for the Adsorption of the Selected Heavy Metals and COD, BOD and TOC using Fe$_3$O$_4$/SiO$_2$/ZnO Prepared at different mixing Ratios

Parameters		Pseudo First Order					Pseudo Second Order						Intraparticle Diffusion		Elovich		
		R^2	k_1	q_{e1}	SSE	x^2	R^2	K_2	q_{e2}	SSE	x^2	R^2	K_{id}	C	R^2	β	α
			(mg/g·min)	(g/min)				(mg/g·min)	(g/min)				(g/min)			(g/min)	
Pb	G	0.960	0.187	0.289	0.347	3.643	0.995	5.852	0.095	0.01	0.118	0.861	0.013	0.036	0.929	68.493	0.261
	H	0.970	0.188	0.295	0.304	3.451	0.995	6.979	0.102	0.008	0.1	0.874	0.014	0.039	0.940	68.918	0.274
	I	0.990	0.207	0.308	0.136	1.553	0.996	7.195	0.103	0.005	0.083	0.875	0.015	0.043	0.951	71.327	0.312
	J	0.940	0.179	0.277	0.352	3.829	0.994	5.698	0.093	0.011	0.125	0.853	0.013	0.034	0.929	66.534	0.220
Cd	G	0.976	0.180	0.302	0.371	4.277	0.997	4.983	0.093	0.014	0.165	0.897	0.016	0.033	0.969	60.496	0.208
	H	0.970	0.181	0.307	0.361	3.998	0.998	5.753	0.096	0.012	0.126	0.903	0.017	0.036	0.971	63.816	0.223
	I	0.980	0.188	0.323	0.348	3.481	0.999	5.789	0.098	0.011	0.121	0.917	0.019	0.038	0.974	68.823	0.320
	J	0.973	0.169	0.292	0.418	4.098	0.997	4.674	0.091	0.015	0.176	0.889	0.015	0.027	0.964	58.689	0.169
Ni (II)	H	0.976	0.184	0.247	0.306	2.697	0.999	7.833	0.118	0.01	0.085	0.889	0.019	0.085	0.959	57.208	0.575
	G	0.973	0.185	0.326	0.358	3.148	0.999	7.940	0.121	0.009	0.081	0.903	0.021	0.086	0.963	59.916	0.616
	I	0.988	0.200	0.339	0.262	2.254	0.999	8.194	0.121	0.009	0.084	0.907	0.023	0.088	0.975	60.350	0.752
	J	0.961	0.184	0.355	0.305	2.799	0.999	7.637	0.114	0.01	0.109	0.820	0.017	0.046	0.951	54.735	0.310
Cu (II)	H	0.950	0.209	0.496	0.010	4.445	0.995	2.525	0.485	0.011	0.022	0.937	0.031	0.353	0.938	564.212	36.536
	G	0.960	0.212	0.514	0.003	3.969	0.998	3.687	0.501	0.006	0.012	0.947	0.035	0.356	0.957	565.950	39.417
	I	0.980	0.213	0.514	0.004	3.531	0.999	4.115	0.524	0.005	0.011	0.949	0.038	0.357	0.973	908.076	55.960
	J	0.940	0.197	0.492	0.031	4.63	0.995	2.486	0.473	0.02	0.041	0.934	0.029	0.349	0.930	531.864	36.523
Cr (VI)	G	0.880	0.211	0.445	4.484	14.725	0.996	2.771	0.318	0.21	0.687	0.812	0.025	0.211	0.867	425.360	45.600
	H	0.951	0.194	0.440	3.886	14.706	0.997	4.371	0.332	0.181	0.567	0.813	0.028	0.213	0.914	675.470	45.788
	I	0.955	0.212	0.487	3.642	11.307	0.999	6.555	0.344	0.079	0.278	0.871	0.037	0.227	0.955	742.561	58.173
	J	0.880	0.192	0.433	4.536	15.177	0.995	2.732	0.316	0.214	0.704	0.811	0.022	0.191	0.865	226.825	43.600
BOD	G	0.860	0.278	1.950	1.974	0.251	0.999	6.889	8.407	1.408	10.704	0.665	0.502	5.923	0.944	9908.423	1.565

257

Parameters		Pseudo First Order					Pseudo Second Order						Intraparticle Diffusion			Elovich		
		R^2	k_1	q_{e1}	SSE	x^2	R^2	K_2	q_{e2}				K_{id}	C	R^2	β	α
			(mg/g·min)	(g/min)				(mg/g·min)	(g/min)	SSE	x^2	R^2	(g/min)			(g/min)	
	H	0.900	0.285	2.197	0.398	0.063	0.999	7.039	8.582	1.403	10.066	0.784	0.511	6.159	0.958	10064.887	1.759
	I	0.950	0.325	2.251	0.322	0.043	0.999	7.601	8.684	1.392	8.502	0.799	0.532	6.359	0.974	12588.784	1.766
	J	0.830	0.262	1.807	2.737	0.326	0.999	6.096	8.281	1.523	10.829	0.583	0.489	5.711	0.930	8128.058	1.526
COD	H	0.921	0.290	2.248	14.181	1.491	0.999	12.773	11.798	0.188	2.095	0.856	1.145	6.483	0.964	185.441	0.729
	G	0.935	0.294	2.643	13.011	1.409	0.999	12.858	12.180	0.283	0.026	0.861	1.183	6.776	0.981	217.188	0.755
	I	0.989	0.346	2.587	11.693	1.394	0.999	13.941	12.320	0.255	0.024	0.894	1.272	8.460	0.992	4068.375	0.930
	J	0.920	0.267	2.038	14.579	1.414	0.999	12.167	11.658	0.217	2.556	0.821	1.125	6.481	0.960	164.506	0.726
TOC	H	0.890	0.239	1.198	8.386	1.715	0.999	0.321	5.776	1.497	6.574	0.808	0.827	1.204	0.961	3.806	0.961
	G	0.900	0.244	1.242	7.667	1.699	0.999	0.787	5.824	1.473	6.507	0.811	0.829	1.218	0.962	4.213	0.966
	I	0.910	0.264	1.508	7.155	1.628	0.999	1.096	5.894	1.462	6.325	0.816	0.846	1.262	0.963	4.386	0.981
	J	0.860	0.224	1.059	8.506	1.727	0.999	0.247	5.750	1.513	6.843	0.806	0.816	1.099	0.959	3.767	0.961

Where G, H, I and J are $Fe_3O_4/SiO_2/ZnO$ (1:1:1), $Fe_3O_4/SiO_2/ZnO$ (1:1:2), $Fe_3O_4/SiO_2/ZnO$ (1:2:1), and $Fe_3O_4/SiO_2/ZnO$ (2:1:1) composites respectively

Table 4.11 displays the kinetic parameters for pseudo first, pseudo second order, intraparticle diffusion and elovich models. It can be seen that the pseudo-second order kinetic model fitted better for all the pollutants with the regression (R^2) value ranging from 0.999-0.992 compared with the first-order kinetics (0.460-986) irrespective of the mixing ratio $Fe_3O_4/SiO_2/ZnO$ nanocomposites. The lower (R^2) obtained for pseudo first order model than the pseudo-second order model indicates that the pseudo second order model is better suitable for explaining the Pb (II), Cd (II), Ni (II), Cr (VI), Cu (II), total iron, BOD, COD and TOC adsorption behavior onto $Fe_3O_4/SiO_2/ZnO$ (1:1:1), $Fe_3O_4/SiO_2/ZnO$ (1:1:2), $Fe_3O_4/SiO_2/ZnO$ (1:2:1) and $Fe_3O_4/SiO_2/ZnO$ (2:1:1) nanocomposites. Additionally, it was found that the (R^2) for all the nanoadsorbents was in the order of $Fe_3O_4/SiO_2/ZnO$ (1:2:1) > $Fe_3O_4/SiO_2/ZnO$ (1:1:2) > $Fe_3O_4/SiO_2/ZnO$ (1:1:1) > $Fe_3O_4/SiO_2/ZnO$ (2:1:1) nanocomposites for all the target pollutants.

The results were also subjected to the error function analysis to determine the suitability of the kinetics models. The error function analysis in Table 4.11 shows that the adsorption process primarily followed the pseudo second order kinetic model, as evidenced by lower x^2 and SSE values for the adsorption Pb (II), Cd (II), Ni (II), Cr (VI), Cu (II), total iron, BOD, COD and TOC using various nanoadsorbent compared to the pseudo first-order kinetic. This result confirmed the earlier conclusion from the regression analysis (R^2), that removal of Pb (II), Cd (II), Ni (II), Cr (VI), Cu (II), total iron, BOD, COD and TOC from the petroleum refinery wastewater using $Fe_3O_4/SiO_2/ZnO$ nanocomposites prepared at different mixing ratio followed pseudo second order kinetic model than pseudo first order kinetic. According to the pseudo second order kinetic model, the mechanism of adsorption assumes chemical reaction as the rate-determining step during adsorption process (Hubbe *et al*., 2019). The

result of (k_1) and (k_2) presented in Table 4.11 indiates that for all the target pollutants the value of (k_1) was lower than (k_2), justifying the fitness of the adsorption process to pseudo second order than the pseudo second order model. A similar trend was observed for the qe_1 and qe_2 As shown in Table 4.11. The values of (k_1, k_2) and (qe_1 and qe_2) were in order of $Fe_3O_4/SiO_2/ZnO$ (1:2:1) > $Fe_3O_4/SiO_2/ZnO$ (1:1:2) > $Fe_3O_4/SiO_2/ZnO$ (1:1:1) > $Fe_3O_4/SiO_2/ZnO$ (2:1:1) nanocomposites for all the target pollutants. This trend may be related to the high surface area of $Fe_3O_4/SiO_2/ZnO$ (1:2:1) compared to the other ratios as shown in Table 4.11.

To further understand the nature of the adsorption between the adsorbent and the adsorbate, the experimental data were subjected to the Elovich kinetics models (Table 4. 9). The result also suggests that the adsorption of Pb (II), Cd (II), Ni (II), Cr (VI), Cu (II), total iron, BOD, COD and TOC from the refinery wastewater have a higher value of (R^2) for all the nanoadsorbent. This indicates that the adsorption of Pb (II), Cd (II), Ni (II), Cr (VI), Cu (II), total iron, BOD, COD and TOC on the nanoadsorbents is involved in chemical bonding. The values of α and β presented in Table 4.11 indicates that both α and β values increases in the order of $Fe_3O_4/SiO_2/ZnO$ (1:2:1) > $Fe_3O_4/SiO_2/ZnO$ (1:1:2) > $Fe_3O_4/SiO_2/ZnO$ (1:1:1) > $Fe_3O_4/SiO_2/ZnO$ (2:1:1) nanocomposites for all the target pollutants. This result also justifies the performance of $Fe_3O_4/SiO_2/ZnO$ (1:2:1) nanocomposites compared to $Fe_3O_4/SiO_2/ZnO$ (1:1:2), $Fe_3O_4/SiO_2/ZnO$ (1:1:1) and $Fe_3O_4/SiO_2/ZnO$ (2:1:1) nanocomposites.

The adsorption process was also investigated by subjecting the data to the intraparticle diffusion model. The result of the (R^2) shows that the intraparticle diffusion model plays less role in the adsorption process compared with the pseudo second order, Elovich and pseudo

first order models. From this observation, it can be concluded that process of adsorption of Pb (II), Cd (II), Ni (II), Cr (VI), Cu (II), total iron, BOD, COD and TOC onto the nanoadsorbent used more than one mechanism, with chemical adsorption dominating the adsorption process. It was found that the Pseudo second-order model best describes the experimental kinetic adsorption data for all the nanoadsorbent. This indicates that the rate of occupation of adsorption sites is proportional to the number of empty sites (Uduakobong Augustine, 2020).

The adsorption kinetics of Pb (II), Cd (II), Ni (II), Cr (VI), Cu (II), total iron, BOD, COD and TOC onto $Fe_3O_4/SiO_2/ZnO$ (1:2:1) nanocomposites was faster than $Fe_3O_4/SiO_2/ZnO$ (1:1:1), $Fe_3O_4/SiO_2/ZnO$ (1:1:2) and $Fe_3O_4/SiO_2/ZnO$ (2:1:1) based on the indicated in Table 4.9higher kinetic rate constants values (k_1, k_2, and k_{id}). It is reasonable to conclude that $Fe_3O_4/SiO_2/ZnO$ with a 1:2:1 mixing ratio is a better nonabsorbent compared to monometallic and bimetallic oxide nanocomposites due to its higher (k_1, k_2), (qe_1, qe_2), (β, α) k_{id} as indicated in Table 4.9. This observed trend may be ascribed to the enhanced in the surface area of ternary nanocomposites over mono and bimetallic oxide nanocomposites as earlier reported in Table 4.11.

4.13 Thermodynamics Evaluation of Adsorption Process

The removal of Pb (II), Cd (II), Ni (II) Cr(VI), Cu (II), total iron , BOD, COD and TOC from petroleum refinery wastewater using ZnO, Fe_3O_4, SiO_2, and ZnO/Fe_3O_4, ZnO/SiO_2, F e_3O_4/SiO_2, $Fe_3O_4/SiO_2/ZnO$ (1:1:1), $Fe_3O_4/SiO_2/ZnO$ (1:1:2), $Fe_3O_4/SiO_2/ZnO$ (1:2:1), and $Fe_3O_4/SiO_2/ZnO$ (2:1:1) nanocomposites was studied from a thermodynamic perspective to predict the feasibility of non-feasibility of the adsorption process based on the variation of temperature for the mono, binary and ternary metallic oxide nanocomposites used as nano adsorbent is presented in Table 4.12, 4.13 and 4.14.

Table 4.12: Thermodynamic Parameters for the Adsorption of Heavy Metal, BOD, COD and TOC from Petroleum Refinery Wastewater by Fe_3O_4, SiO_2 and ZnO Nanoparticles

Parameters	Nanomaterials					$\Delta G°$ kJ/mol			
		$\Delta H°$ kJ/mol	$\Delta S°$ J/K.mol	303K	313K	323K	333K	343K	353K
Pb (II)	ZnO	17.595	31.811	6.071	5.767	5.462	5.158	4.854	4.550
	Fe_3O_4	15.29	30.426	6.401	6.293	6.186	6.078	5.971	5.863
	SiO_2	22.747	48.805	7.959	7.471	6.983	6.495	6.007	5.519
Cd (II)	ZnO	16.134	32.351	6.332	6.008	5.685	5.361	5.038	4.714
	Fe_3O_4	15.598	28.942	6.829	6.539	6.250	5.960	5.671	5.381
	SiO_2	9.661	10.759	7.956	7.638	7.320	7.002	6.684	6.366
Ni (II)	ZnO	17.328	34.271	6.944	6.601	6.258	5.916	5.573	5.230
	Fe_3O_4	12.252	16.081	7.547	7.325	7.102	6.879	6.656	6.433
	SiO_2	14.301	22.289	7.379	7.219	7.058	6.897	6.736	6.575
Cu (II)	ZnO	10.015	16.451	5.030	4.866	4.701	4.537	4.372	4.208
	Fe_3O_4	8.521	11.913	4.911	4.792	4.673	4.554	4.435	4.316
	SiO_2	18.866	38.8	7.110	6.722	6.334	5.946	5.558	5.170
Total iron	ZnO	40.316	128.316	1.436	0.153	-1.130	-2.413	-3.696	-4.980

Parameters	Nanomaterials	ΔH° kJ/mol	ΔS° J/K.mol	ΔG° kJ/mol					
				303K	313K	323K	333K	343K	353K
	Fe_3O_4	33.887	105.721	1.854	0.796	-0.261	-1.318	-2.375	-3.433
	SiO_2	39.812	119.341	3.652	2.458	1.265	0.071	-1.122	-2.315
Cr(VI)	ZnO	33	37.875	21.524	21.145	20.766	20.388	20.009	19.630
	Fe_3O_4	36	33	26.001	25.671	25.341	25.011	24.681	24.351
	SiO_2	39.452	34.585	28.973	28.627	28.281	27.935	27.589	27.243
BOD	ZnO	18.428	3.596	17.338	17.302	17.266	17.231	17.195	17.159
	Fe_3O_4	22.622	10.987	19.293	19.183	19.073	18.963	18.853	18.744
	SiO_2	30.042	22.768	23.143	22.916	22.688	22.460	22.233	22.005
COD	ZnO	30.315	22.281	23.564	23.341	23.118	22.895	22.673	22.450
	Fe_3O_4	39.661	45.054	26.010	25.559	25.109	24.658	24.207	23.757
	SiO_2	42.771	44.811	29.193	28.745	28.297	27.849	27.401	26.953
TOC	ZnO	18.577	22.635	11.747	11.443	11.138	10.834	10.530	10.226
	Fe_3O_4	20.965	30.423	11.719	11.492	11.266	11.040	10.813	10.587
	SiO_2	25.775	42.018	13.044	12.623	12.203	11.783	11.363	10.943

Equation 3.15 and 3.16 were used to determine the values of some thermodynamic parameters such as standard Gibb's free energy change (ΔG^o), standard enthalpy (ΔH^o) and entropy changes (ΔS^o) at various temperatures. The slope and intercept of the linear plot of $\ln K_d$ versus $\frac{1}{T}$ in appendix 64-72 were used to calculate (ΔH^o) and ($\Delta S^{o)}$ respectively.

The value of standard enthalpy change (ΔH^o) of adsorption during the adsorption process ranges between18.577 to 44.36 kJ/mol, the ΔH^o values were all positive, as presented in Table 4.17 confirming that the adsorption process for the removal of Pb (II), Cd (II), Ni (II), Cr (VI), Cu (II), total iron, BOD, COD and TOC using Fe_3O_4, SiO_2 and ZnO nanadsorbent was endothermic in nature. Similarly, a positive value ranges in the range of 3.596 to 48.805 J/K.mol was obtained for standard entropy change (ΔS^o) this means that the disorderliness and driving force at the adsorbent-adsorbate interface was positive during the adsorption process. Table 4.12 also reveals that the standard Gibb's free energy change (ΔG^o) of adsorption approaches negative as the temperature increases which indicates an increase in the degree of the spontaneity of the adsorption process at a higher temperature (Wang *et al*., 2022).

The result indicates that Pb (II), Cu (II) and total iron has a lower ΔG^o (negative values) for the nanocomposites suggesting that the removal of Pb (II), Cu (II) and total iron was spontaneous and feasible using the ternary nanocomposites as an adsorbent than the single and bimetallic oxide nanocomposites. This result can be confirmed by the result of the adsorption removal efficiency, isotherm models and the kinetics models earlier reported where the ternary nanocomposites performed better than the bimetallic and monometallic oxide. Other researchers have reported endothermic nature and high disorderliness of the

adsorption process using Fe_3O_4 nanoparticles (Adegoke *et al*., 2017), SiO_2 nanoparticles (Manyangadze *et al*., 2020) and ZnO (Elfeky *et al*., 2019) respectively.

Table 4.13: Thermodynamic Parameters for the Adsorption of Selected Heavy Metal, BOD, COD and TOC using ZnO/Fe₃O₄, ZnO/SiO₂ and Fe₃O₄/SiO₂ Nanocomposites

Parameters	Nanomaterials	ΔH° kJ/mol	ΔS° J/K.mol	ΔG° kJ/mol					
				303K	313K	323K	333K	343K	353K
Pb (II)	ZnO/ Fe₃O₄	23.281	60.856	4.842	4.233	3.625	3.016	2.408	1.799
	ZnO/SiO₂	21.842	55.560	5.008	4.452	3.897	3.341	2.769	2.129
	Fe₃O₄/SiO₂	24.709	63.967	5.328	4.688	4.048	3.409	2.785	2.230
Cd (II)	ZnO/ Fe₃O₄	18.545	43.391	5.397	4.963	4.529	4.095	3.495	2.834
	ZnO/SiO₂	26.184	66.147	6.141	5.48	4.818	4.157	3.661	3.228
	Fe₃O₄/SiO₂	23.863	58.061	6.271	5.69	5.110	4.529	3.949	3.368
Ni (II)	ZnO/ Fe₃O₄	23.515	55.747	6.52	6.067	5.509	4.952	4.394	3.837
	ZnO/SiO₂	19.685	43.45	6.624	6.085	5.651	5.216	4.782	4.347
	Fe₃O₄/SiO₂	18.007	37.657	6.597	6.220	5.844	5.467	5.09	4.714
Cu (II)	ZnO/ Fe₃O₄	20.286	51.749	4.606	4.089	3.571	3.054	2.536	2.019
	ZnO/SiO₂	11.321	20.753	5.033	4.825	4.618	4.410	4.203	3.695
	Fe₃O₄/SiO₂	15.608	32.957	5.622	5.293	4.963	4.633	4.304	3.974
Total iron	ZnO/ Fe₃O₄	37.820	126.247	-0.433	-1.696	-2.958	-4.221	-5.483	-6.746
	ZnO/SiO₂	30.252	104.247	-1.335	-2.377	-3.420	-4.462	-5.505	-6.547
	Fe₃O₄/SiO₂	28.754	99.755	-1.472	-2.469	-3.467	-4.464	-5.462	-6.459
Cr (VI)	ZnO/ Fe₃O₄	18.419	11.902	17.843	17.824	17.805	17.786	17.767	17.748
	ZnO/SiO₂	26.155	20.661	19.895	19.688	19.482	19.275	19.068	18.862
	Fe₃O₄/SiO₂	28.190	18.822	22.487	22.299	22.110	21.922	21.734	21.546
BOD	ZnO/ Fe₃O₄	30.172	27.014	21.986	21.716	21.446	21.176	20.906	20.636
	ZnO/SiO₂	31.692	28.93	22.927	22.637	22.348	22.059	21.769	21.48
	Fe₃O₄/SiO₂	37.876	35.218	27.205	26.853	26.501	26.148	25.796	25.444
COD	ZnO/ Fe₃O₄	28.652	24.848	21.123	20.875	20.626	20.378	20.129	19.881
	ZnO/SiO₂	37.085	39.079	25.244	24.853	24.462	24.071	23.681	23.29
	Fe₃O₄/SiO₂	39.091	42.403	26.243	25.819	25.395	24.971	24.546	24.122
TOC	ZnO/ Fe₃O₄	13.221	10.701	9.979	9.872	9.765	9.658	9.551	9.444
	ZnO/SiO₂	23.283	37.396	11.952	11.578	11.204	10.83	10.456	10.082
	Fe₃O₄/SiO₂	23.022	36.251	12.038	11.675	11.313	10.95	10.588	10.225

The slope and intercept of the linear plot of lnK_d versus $\frac{1}{T}$ in appendix 64-72 was used to calculate the thermodynamic parameters such as standard Gibb's free energy change (ΔG^o) of adsorption, standard enthalpy (ΔH^o) and entropy changes (ΔS^o) at various temperatures. The value of ΔG^o, ΔH^o and ΔS^o is presented in Table 4.13. The values of standard enthalpy (ΔH^o) of adsorption was positive for all the bimetallic oxides used for the removal of Pb (II), Cd (II), Ni (II), Cr (VI), Cu (II), total iron, BOD, COD and TOC from petroleum refinery wastewater using the bimetallic oxides. Table 4.13 shows that the ΔH^o of adsorption ranges between 13.221 to 39.691 kJ/mol suggesting that the removal of Pb (II), Cd (II), Ni (II), Cr (VI), Cu (II), total iron, BOD, COD and TOC from petroleum refinery wastewater using ZnO/Fe_3O_4, ZnO/SiO_2 and Fe_3O_4/SiO_2 nanocomposites were endothermic in nature.

In Table 4.11 it was found that the value of ΔS^o adsorption was positive irrespective of the bimetallic oxide nanocomposites used.

 The values of ΔG^o presented in Table 4.13 indicated that the order of feasibility and spontaneity for the removal of Pb (II), Cd (II), Ni (II), Cr (VI), Cu (II), total iron, BOD, COD and TOC from petroleum refinery wastewater using ZnO/Fe_3O_4, ZnO/SiO_2 and Fe_3O_4/SiO_2 nanocomposites were ZnO/Fe_3O_4, $> ZnO/SiO_2 > Fe_3O_4/SiO_2$. The trend observed in the thermodynamic study is a validation that ZnO/Fe_3O_4 nanocomposites is better nanoadsorbent compared to ZnO/SiO_2 and Fe_3O_4/SiO_2 for the Pb (II), Cd (II), Ni (II), Cr (VI), Cu (II), total iron, BOD, COD and TOC from petroleum refinery wastewater. The higher feasibility of the adsorption process using ZnO/Fe_3O_4 nanocomposites may be related to its smaller crystallites size and enhanced surface area.

Table 4.14: Thermodynamic Parameters for the Adsorption of Selected Heavy Metal, BOD, COD and TOC using Fe₃O₄/SiO₂/ZnO (1:1:1), Fe₃O₄/SiO₂/ZnO (1:1:2), Fe₃O₄/SiO₂/ZnO (1:2:1), and Fe₃O₄/SiO₂/ZnO (2:1:1) Nanocomposites

Parameters	Nanomaterials	ΔH° kJ/mol	ΔS° J/K.mol	ΔG° kJ/mol					
				303K	313K	323K	333K	343K	353K
Pb (II)	Fe₃O₄/SiO₂/ZnO(1:1:1)	31.072	92.224	3.128	2.206	1.284	0.361	-0.561	-1.483
	Fe₃O₄/SiO₂/ZnO(1:1:2)	33.711	102.818	2.558	1.529	0.501	-0.527	-1.555	-2.583
	Fe₃O₄/SiO₂/ZnO(1:2:1)	49.036	153.947	2.390	0.850	-0.689	-2.229	-3.768	-5.308
	Fe₃O₄/SiO₂/ZnO(2:1:1)	23.67	67.701	3.156	2.479	1.802	1.125	0.448	-0.229
Cd (II)	Fe₃O₄/SiO₂/ZnO(1:1:1)	18.735	45.723	5.196	4.597	3.967	3.510	3.015	2.469
	Fe₃O₄/SiO₂/ZnO(1:1:2)	23.334	59.864	5.022	4.424	3.698	3.400	2.801	2.202
	Fe₃O₄/SiO₂/ZnO(1:2:1)	33.977	95.563	4.881	4.066	3.110	2.155	1.199	0.243
	Fe₃O₄/SiO₂/ZnO(2:1:1)	21.730	54.563	5.197	4.652	4.106	3.561	3.052	2.595
Ni (II)	Fe₃O₄/SiO₂/ZnO(1:1:1)	25.934	64.536	6.380	5.735	5.204	4.775	4.236	3.692
	Fe₃O₄/SiO₂/ZnO(1:1:2)	22.100	52.465	6.203	5.678	5.154	4.629	4.104	3.580
	Fe₃O₄/SiO₂/ZnO(1:2:1)	19.078	42.951	6.063	5.634	5.089	4.444	3.799	3.153
	Fe₃O₄/SiO₂/ZnO(2:1:1)	22.884	54.368	6.410	5.867	5.323	4.779	4.345	3.916
Cu (II)	Fe₃O₄/SiO₂/ZnO(1:1:1)	33.249	98.66	3.355	2.369	1.382	0.396	-0.591	-1.578
	Fe₃O₄/SiO₂/ZnO(1:1:2)	35.491	106.221	3.307	2.244	1.182	0.120	-0.942	-2.005
	Fe₃O₄/SiO₂/ZnO(1:2:1)	51.771	160.856	3.032	1.423	-0.185	-1.794	-3.402	-5.011
	Fe₃O₄/SiO₂/ZnO(2:1:1)	35.394	104.304	3.790	2.747	1.704	0.661	-0.382	-1.425
Total iron	Fe₃O₄/SiO₂/ZnO(1:1:1)	38.360	135.614	-2.731	-4.088	-5.444	-6.800	-8.156	-9.512
	Fe₃O₄/SiO₂/ZnO(1:1:2)	29.071	112.462	-5.005	-6.130	-7.254	-8.379	-9.504	-10.628
	Fe₃O₄/SiO₂/ZnO(1:2:1)	25.964	108.053	-6.776	-7.857	-8.937	-10.018	-11.098	-12.179
	Fe₃O₄/SiO₂/ZnO(2:1:1)	35.490	120.825	-1.120	-2.329	-3.537	-4.745	-5.953	-7.162
Cr (VI)	Fe₃O₄/SiO₂/ZnO(1:1:1)	16.619	8.044	14.182	14.101	14.021	13.94	13.86	13.779
	Fe₃O₄/SiO₂/ZnO(1:1:2)	13.422	3.161	12.464	12.432	12.401	12.369	12.337	12.306
	Fe₃O₄/SiO₂/ZnO(1:2:1)	8.152	21.134	3.050	2.838	2.627	2.416	2.204	1.993
	Fe₃O₄/SiO₂/ZnO(2:1:1)	17.580	3.829	16.420	16.381	16.343	16.305	16.267	16.228
BOD	Fe₃O₄/SiO₂/ZnO(1:1:1)	21.016	15.159	16.422	16.271	16.119	15.968	15.816	15.664
	Fe₃O₄/SiO₂/ZnO(1:1:2)	14.127	6.872	12.044	11.976	11.907	11.838	11.77	11.701
	Fe₃O₄/SiO₂/ZnO(1:2:1)	19.235	15.035	9.497	9.498	9.499	9.501	9.502	9.504
	Fe₃O₄/SiO₂/ZnO(2:1:1)	28.371	30.398	19.161	18.857	18.553	18.249	17.945	17.641
COD	Fe₃O₄/SiO₂/ZnO(1:1:1)	24.23	13.056	20.274	20.143	20.013	19.888	19.752	19.621
	Fe₃O₄/SiO₂/ZnO(1:1:2)	26.721	20.541	20.497	20.291	20.086	19.881	19.675	19.470
	Fe₃O₄/SiO₂/ZnO(1:2:1)	15.590	10.745	12.334	12.227	12.119	12.012	11.904	11.797
	Fe₃O₄/SiO₂/ZnO(2:1:1)	27.945	22.951	20.991	20.761	20.532	20.302	20.073	19.843
TOC	Fe₃O₄/SiO₂/ZnO(1:1:1)	23.216	44.307	9.791	9.347	8.904	8.461	8.018	7.575
	Fe₃O₄/SiO₂/ZnO(1:1:2)	19.318	32.323	9.524	9.201	8.878	8.554	8.231	7.908
	Fe₃O₄/SiO₂/ZnO(1:2:1)	21.186	38.543	9.508	9.122	8.737	8.351	7.966	7.580
	Fe₃O₄/SiO₂/ZnO(2:1:1)	22.628	40.598	10.327	9.921	9.515	9.109	8.703	8.297

Appendix 64-72 shows the plots of k_d against $1/T$ for the adsorption of Pb (II), Cd (II), Ni (II), Cr (VI), Cu (II), total iron, BOD, COD and TOC onto $Fe_3O_4/SiO_2/ZnO(1:1:1)$, $Fe_3O_4/SiO_2/ZnO(1:1:2)$, $Fe_3O_4/SiO_2/ZnO(1:2:1)$ and $Fe_3O_4/SiO_2/ZnO(2:1:1)$ from petroleum refinery wastewater. Parameters for thermodynamic studies are listed in Table 4.14. Table 4.14 shows positive values of ΔH^o for all the nanoadsorbents irrespective of the mixing ratio. This confirmed the endothermic nature of the adsorption process. The result in Table 4.12 indicates that the (ΔS^o) is positive irrespective of the adsorbent used. The positive value suggests higher randomness at the solid/solution interface, which could lead to a change in adsorbent and sorbate structure. From the above observation, it can be concluded that the adsorption of Pb (II) Cd (II), Ni (II) Cr(VI), Cu (II), total iron, BOD, COD and TOC onto $Fe_3O_4/SiO_2/ZnO$ (1:1:1), $Fe_3O_4/SiO_2/ZnO$ (1:1:2), $Fe_3O_4/SiO_2/ZnO$ (1:2:1), and $Fe_3O_4/SiO_2/ZnO$ (2:1:1) nanocomposites causes a major change in the surface morphology of the adsorbent due to the positive value of (ΔS^o) obtained for almost the nanoadsorbents.

The Gibbs free energy change (ΔG^o), is a key index for the adsorption process spontaneity. The change in Gibbs free energy (ΔG^o) showed a general decrease as the temperature increased, indicating an increase in the degree of spontaneity during the adsorption process. This implies that the adsorption process becomes more feasible and spontaneous as the temperature increases. Generally, the feasible and spontaneous nature during the adsorption process for the removal of Pb (II), Cd (II), Ni (II), Cr (VI), Cu (II), total iron, BOD, COD and TOC onto $Fe_3O_4/SiO_2/ZnO(1:1:1)$, $Fe_3O_4/SiO_2/ZnO(1:1:2)$, $Fe_3O_4/SiO_2/ZnO(1:2:1)$ and $Fe_3O_4/SiO_2/ZnO(2:1:1)$ from petroleum refinery wastewater using mono metallic, bimetallic and ternary oxides were in order of monometallic oxide > bimetallic oxide > ternary metallic oxides. This suggests that the ternary metallic oxide nanocomposites prepared at different

mixing ratios performed batter than the monometallic and bimetallic oxides. Among the monometallic nanoadsorbents ZnO exhibited better adsorption than Fe_3O_4 and SiO_2 . Similarly among the bimetallic oxides nanocomposites used Fe_3O_4/ZnO nanocomposites performed better than ZnO/ SiO_2 and Fe_3O_4/SiO_2 nanocomposites while the ternary nanocomposites were in order of Fe_3O_4/SiO_2/ZnO (1:2:1) > Fe_3O_4/SiO_2/ZnO (1:1:2) > Fe_3O_4/SiO_2/ZnO (1:1:2 > Fe_3O_4/SiO_2/ZnO(2:1:1). This result is in confirmation of the earlier report from both the isotherm and kinetic models that the best adsorbents among the monometallic, bimetallic and ternary composites were ZnO, Fe_3O_4/ZnO and Fe_3O_4/SiO_2/ZnO (1:2:1) nanocomposites. The observed trend may be linked to the surface area, functionality and crystallite sizes of the nano adsorbents.

4.14 Analysis of Fe_3O_4/SiO_2/ ZnO nanocomposites after the adsorption process

Studies on the stability and regeneration potential of the Fe_3O_4/SiO_2/ ZnO nanocomposites prepared at different mixing ratios (1:1:1, 1:1:2, 1:2:1 and 1:1:2) were carried out to determine their potential usage after four recycle periods for the removal of the targeted pollutants from the petroleum refinery wastewater**.**

4.14.1 HESEM analysis of Fe_3O_4/SiO_2/ZnO nanocomposites after adsorption

The surface morphologies of Fe_3O_4/SiO_2/ZnO nanocomposites utilized for adsorption of selected heavy metals and other parameters were checked after the experiment and the result is presented in Plate X (a- h).
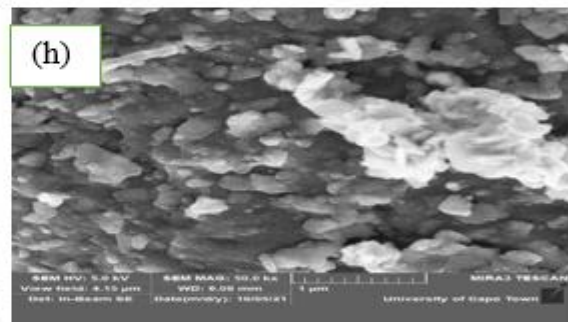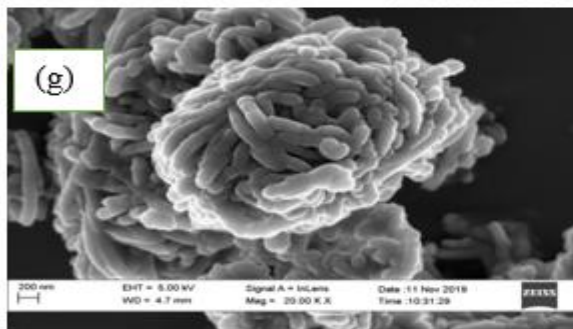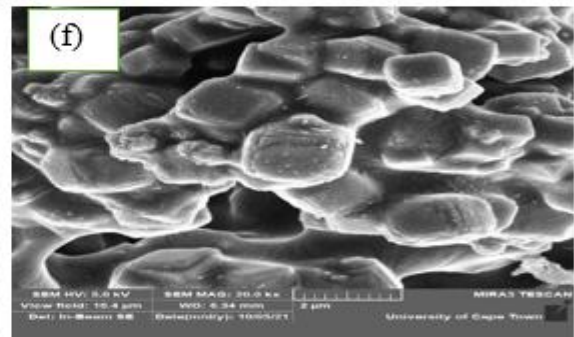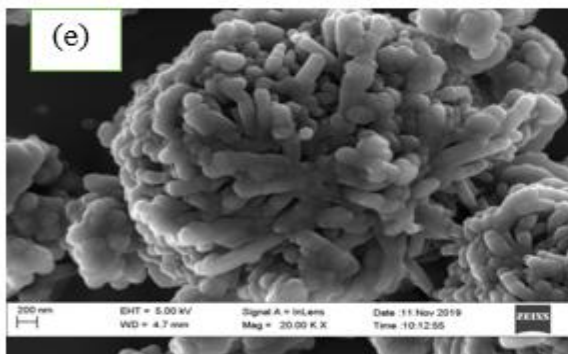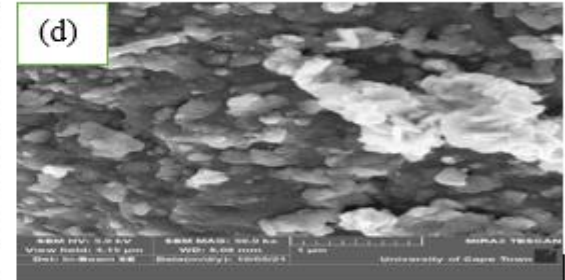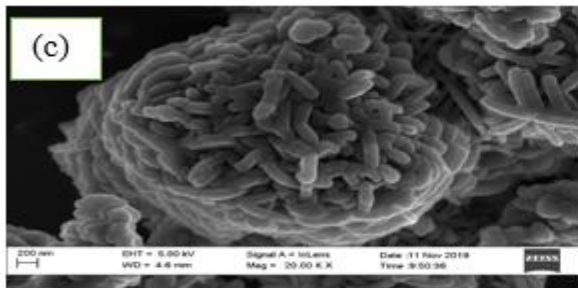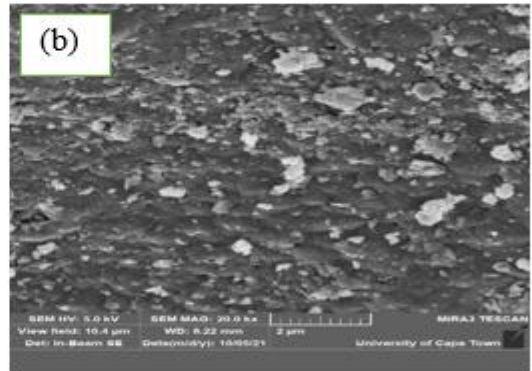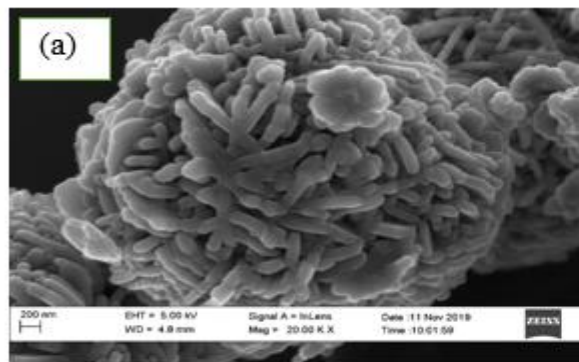
Plate X: HRSEM Images of Fe₃O₄/SiO₂/ZnO Nanocomposites Prepared at different mixing ratios before and after Adsorption (a and b) 1:1:1 (c and d) 1:1:2, (e and f) 1:2:1 and (g and h) 2:1:1

As can be seen in Plate X (a), the surface morphology of prepared $Fe_3O_4/SiO_2/ZnO$ nanocomposites before the adsorption changes from a rod-like structure to a smooth surface (Plate X(b)) indicates that the active sites in the nanocomposites have been completely occupied by the pollutants. Similarly, Plate X (c and d) indicate that the rod-like structure before the adsorption was retained partially, after the adsorption, this may be due to the low adsorption of pollutants on the surface of the adsorbent. It can be concluded that the ratio with a high dosage of Fe_3O_4 nanoparticles transforms completely from rod-like to irregular shape. This may be due to the non-stability of Fe_3O_4 nanoparticles or complexation reactions with other elements.

Plate X (e) shows the complete transformation from a rod-like structure to a cubic-like shape in Plate X (f) with the creation of pores after the adsorption process after the adsorption. This may be due to the fact that the nanocomposites prepared using 1:2:1 adsorbed more pollutants compred to other ratios. This may had resulted to different recation between the nanocomposites and the pollutants leading to the creation of another adsorbent that have more active sites for the removal of the pollutants. This may be due to the high interaction beween the adsorbate and the adsorbent leading to complexation or ion exchange between the nanocomposites and the pollutant. This implies that the ternary nanocomposites prepared at the mixing ratio (1:2:1) exhibited reuseable properties for subsequent applications.

The complete transformation of $Fe_3O_4/SiO_2/ZnO$ (1:2:1) nanocomposites from rod like to cubic structure may be ascribed to the fact that high content of SiO_2 nanoparticles in the $Fe_3O_4/SiO_2/ZnO$ (1:2:1) nanocomposites causes more chemical interactions during the formation of the nanocomposites compared with the chemical bonds formed during the

271

formation of Fe$_3$O$_4$/SiO$_2$/ZnO (1:1:1), Fe$_3$O$_4$/SiO$_2$/ZnO (1:1:2) and Fe$_3$O$_4$/SiO$_2$/ZnO (2:1:1) nanocomposites. The formation of the chemical bonds leads to high hydrophobicity, thermal stability, and pH change resistance, mechanical, as well as a wide range of functional groups without affecting the characteristics of the nanoparticles (Adnan *et al*., 2020). From the HRSEM results presented in Plate X (g), it is evidence that the nanocomposites prepared using a mixing ratio of (2:1:1) transform completely from rod like structure to a smooth surface with spherical shaped on the surface (see Plate X (g)).

Figure 4.62: XRD Patterns of Fe$_3$O$_4$/SiO$_2$/ ZnO Nanocompositea after the Adsorption Process (a) 1:1:1 (b) 1:1:2, (c) 1:2:1 and (d) 2:1:1
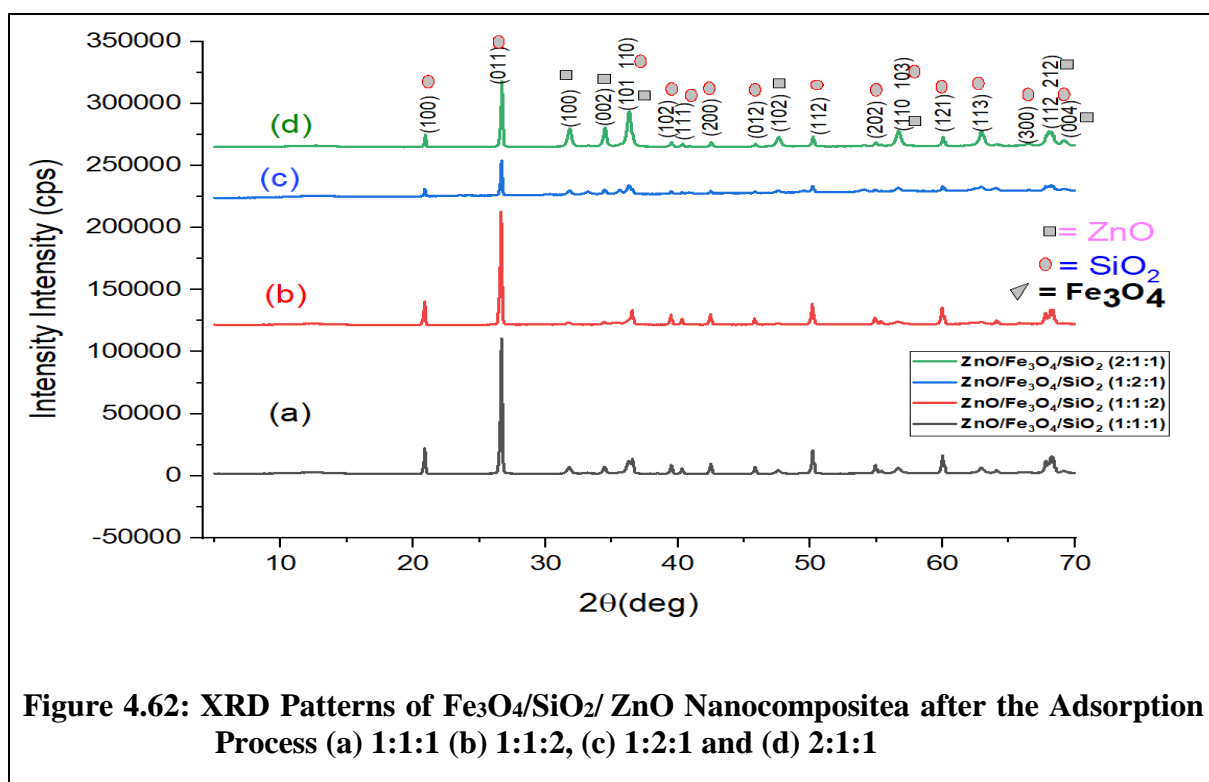
4.14.2 XRD analysis of Fe$_3$O$_4$/SiO$_2$/ ZnO nanocomposites after the adsorption Process

After the adsorption of the metal ions and organic pollutants onto the Fe$_3$O$_4$/SiO$_2$/ ZnO nanocomposites the used Fe$_3$O$_4$/SiO$_2$/ ZnO nanocomposites were raised dried in an oven and

subjected to XRD analysis to confirm their stability and reusability. The results obtained are given in Figure 4.62

Figure 4.62 shows the XRD patterns of Fe_3O_4/SiO_2 /ZnO nanocomposite after the adsorption with diffraction peaks at 2θ values of 20.14°, 25.96°, 36.05°, 38.91°, 39.82°, 42.05°, 45.42°, 49.77°, 54.59°, 54.95°, 59.83°, 63.83°, 65.78°, and 68771°, corresponding to the miller planes of (100), (011), (110), (102), (111), (200), (021), (112), (202), (013), (121), (113), (300), and (212) JCP2_77-001. The XRD preterm in Figure 4.62 revealed a little shift (1.2) in the peak positions and decreases in the intensity of the peaks compared with the XRD pattern of the SiO_2 /Fe_3O_4/ZnO nanocomposites before adsorption as presented in Figure 4.28. This observation can be linked to the distortion of the lattice structure of the nanocomposites after the adsorption process. While the peak reduceses signifies the contraction of the unit cell, indicating loss of crystallinity. The reduction of the peaks may also be attributed to strong chemical interaction during the adsorption process based on the report of ALam *et al*. (2021). The SiO_2 /Fe_3O_4/ZnO nanocomposites (1:2:1) reduces in the diffraction peak compared to the others, this may be due to diffusion ions into the lattice of the ZnO nanoparticles leading to more disordered structure of the nanocomposites after adsorption process. This result coroborate the HRSEM result earlier where the morphology of the nanocomposites completely transforms from rod-like structure (see Plate X (e)) to cubic structure in Plate X (f).

4.14.3 Desorption process of the $Fe_3O_4/SiO_2/ZnO$ naocomposites prepared at different mixing ratio 1:1:1, 1:1:2, 1:2:1 and 2:1:1 respectively

The desorption process was examined to identify the optimal desorbing solution for recovering Pb (II), Cd (II), Ni (II), Cr (IV), Cu (II), total iron ions, BOD, COD, TOC from the used $Fe_3O_4/SiO_2/ZnO$ nanocomposites after the batch adsorption process and the result obtained are presented in Figure 4.63-71.
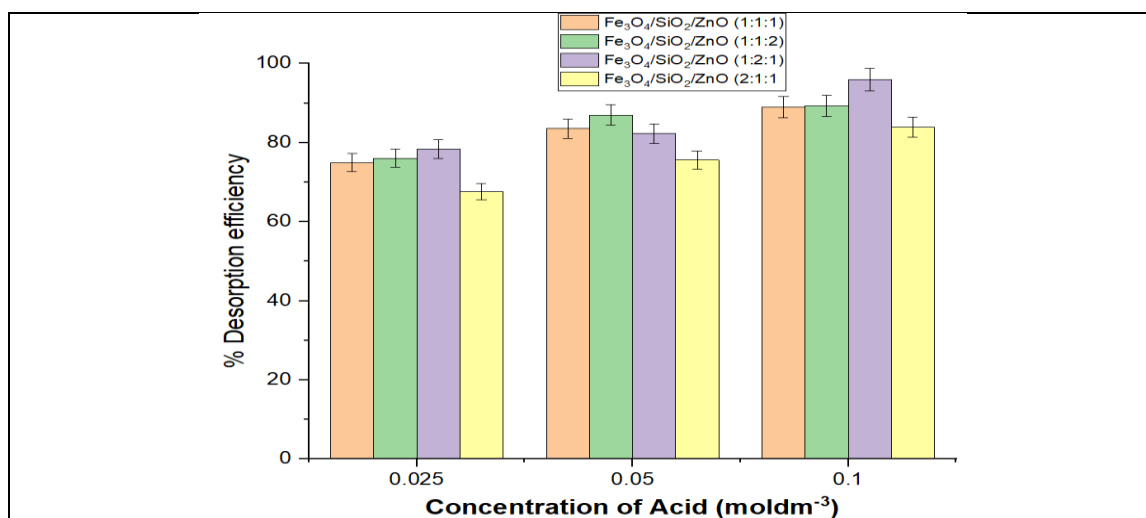
Figure 4.63: Effect of HNO_3 Concentration on the Desorption of Pb (II) Ions Adsorbed onto $Fe_3O_4/SiO_2/ZnO$ Nanocomposites Prepared at Different Mixing Ratio (1:1:1, 1:1:2, 1:2:1 and 2:1:1) at Dosage of (0.05 g), Temperature (30°C), Contact Time (15 min)
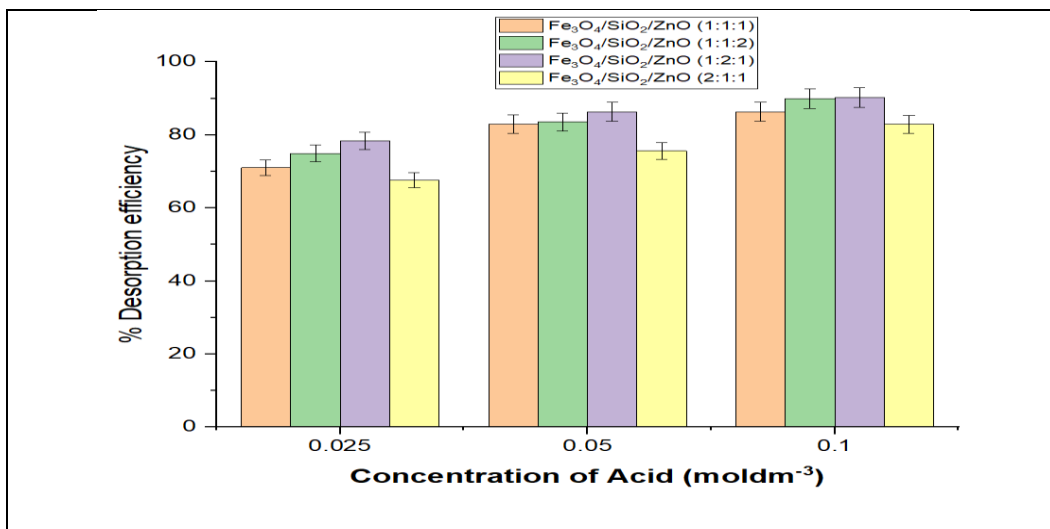
Figure 4.64: Effect of HNO₃ Concentration on the Desorption of Cd (II) Ions Adsorbed onto Fe₃O₄/SiO₂/ZnO Nanocomposites prepared at different mixing ratio (1:1:1, 1:1:2, 1:2:1 and 2:1:1) at Dosage of (0.05 g), Temperature (30℃), Contact Time (15 min)
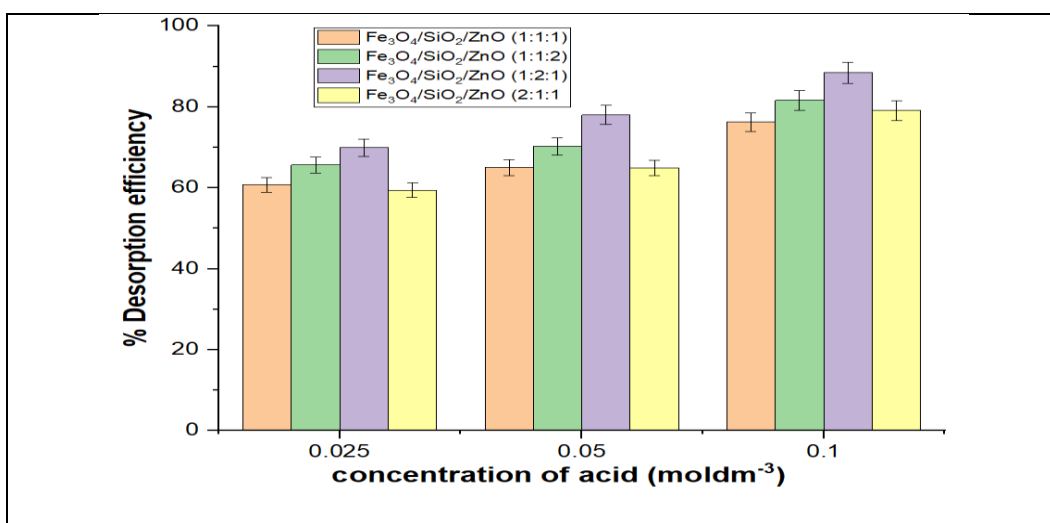
Figure 4.65: Effect of HNO₃ Concentration on the Desorption of Ni (II) Ions Adsorbed onto Fe₃O₄/SiO₂/ZnO Nanocomposites prepared at different mixing ratio (1:1:1, 1:1:2, 1:2:1 and 2:1:1) at Dosage of (0.05 g), Temperature (30℃), Contact Time (15 min)

Figure 4.66: Effect of HNO₃ Concentration on the Desorption of Cr (IV) Ions Adsorbed onto Fe₃O₄/SiO₂/ZnO Nanocomposites prepared at different mixing ratio (1:1:1, 1:1:2, 1:2:1 and 2:1:1) at Dosage of (0.05 g), Temperature (30℃), Contact Time (15 min)

Figure 4.67: (e): Effect of HNO₃ Concentration on the Desorption of Cu (II) Ions Adsorbed onto Fe₃O₄/SiO₂/ZnO Nanocomposites prepared at different mixing ratio (1:1:1, 1:1:2, 1:2:1 and 2:1:1) at Dosage of (0.05 g), Temperature (30℃), Contact Time (15 min)

Figure 4.68: Effect of HNO₃ Concentration onto the Desorption of Total iron Ions Adsorbed on Fe₃O₄/SiO₂/ZnO Nanocomposites Prepared at Different Mixing Ratio (1:1:1, 1:1:2, 1:2:1 and 2:1:1) at Dosage of (0.05 g), Temperature (30℃), Contact Time (15 min)

Figure 4.69: Effect of HNO₃ Concentration onto the Desorption of BOD Adsorbed on Fe₃O₄/SiO₂/ZnO Nanocomposites Prepared at Different Mixing Ratio (1:1:1, 1:1:2, 1:2:1 and 2:1:1) at Dosage of (0.05 g), Temperature (30℃), Contact time (15 min)

Figure 4.70: Effect of HNO₃ Concentration onto the Desorption of COD Adsorbed on Fe₃O₄/SiO₂/ZnO Nanocomposites Prepared at Different Mixing ratio (1:1:1, 1:1:2, 1:2:1 and 2:1:1) at Dosage of (0.05 g), Temperature (30℃), Contact Time (15 min)

Figure 4.71: Effect of HNO₃ Concentration on the Desorption of TOC Adsorbed onto Fe₃O₄/SiO₂/ZnO Nanocomposites prepared at different mixing ratio (1:1:1, 1:1:2, 1:2:1 and 2:1:1) at Dosage of (0.05 g), Temperature (30℃), Contact Time (15 min)

278

Figure 4.63-4.71 shows the desorption of Pb (II), Cd (II), Ni (II), Cr (IV), Cu (II), total iron ions, BOD, COD, TOC adsorbed on the surface of the prepared $Fe_3O_4/SiO_2/ZnO$ nanocomposites of different mixing ratio(1:1:1, 1:1:2, 1:2:1, 2:1:1) at different concentration of nitric acids (HNO_3) ranging from 0.025, 0.08 to 0.1 moldm^{-3}. Figure 4.63 shows that the desorption of the Pb (II) increases from 74.93 %, 83.51 % to 88.92 %; 76.01 %, 86.51 %, to 89.32 %; 78.31%, 86.92 % to 95.94 % and 67.63%, 75.61% to 83.91 % as the concentration of the nitric acid increases from 0.025, 0.08 to 0.1 moldm^{-3} for the $Fe_3O_4/SiO_2/ZnO$ nanocomposites prepared at different mixing ratio (1:11, 1:1:2, 1:2:1, 2:1:1) respectively. This result suggests that 88.92 %, 89.32 %, 95.94 % and 67.88 % of Pb (II) recovery was achieved for the $Fe_3O_4/SiO_2/ZnO$ nanocomposites prepared at different mixing ratio (1:1:1, 1:1:2, 1:2:1, 2:1:1), respectively at contact time (15 min), adsorbent dosage (0.05 g) and temperature of 30°C. From the result the highest recovery was obtanaied using 0.1 moldm^{-3} for the desorption of Pb (II) for all the nanocomposite with $Fe_3O_4/SiO_2/ZnO$ (1:2:1) having the highest desorption of Pb (II) among the other nanocomposites used during the desorption process. Figure 4.64 reveals the highest amount of Cd (II) recovered was 82 .85 %, 86.07 %, 90 .53% and 89.32 % after desorption at 0.1 moldm^{-3}. The amount of Ni (II) that was desorbed under the applied conditions increases from 60.75 % to 76.24 %, 65.63 % to 81.66 %, 69.91 % to 88.45 %, and 59.42 % to 79.08 % as the concentration of HNO_3 increases from 0.025 to 0.1 moldm-3 (see Figure 4.65 and Figure 4.66 indicates increase in the desorption efficiency of Cr (IV) increases from 68.33 % to 39.66 %, 70.63 % to 82.45 %, 80% to 85.00 %, 69.78 to 77.27 % as the concentration of the HNO_3 increase from 0.025 to 0.1 moldm^{-3} respectively. The maximum desorption efficiency obtained for Cu (II) using $Fe_3O_4/SiO_2/ZnO$ prepared at different mixing ratio of (1:11, 1:1:2, 1:2:1, 2:1:1) as

nanoadsorbent was at 0.1 moldm^{-3} with percentage desorption of 80.84 %, 87.00 %, 96.35%, 85.56 % respectively.

In the case of total iron, the highest desorption efficiency was 87.35 %, 89.92 %, 97.24 % to and 82.90 % for the $Fe_3O_4/SiO_2/ZnO$ nanocomposites prepared at different mixing ratio (1:11, 1:1:2, 1:2:1, 2:1:1), respectively as (see Figure 4.68).

Also, it can be observed from Figure 4.69-4.71, that as the concentration of the HNO_3 increases from 0.025 to 0.1 moldm^{-3}, the highest desorption efficiency was 81.98 %, 81.34 %, 86.91 % and 79.6 % for BOD, 87.54 %, 82.56 %, 91.00 %, 81.20 % for COD, and 84.45 %, 85.76 %, 88.64 %, 86.34 % for TOC. These findings also revealed that desorption was more favorable at higher concentration of HNO_3 solution.

Generally, the result suggests that the highest desorption was achieved when the concentration of HNO_3 was at 0.1 moldm^{-3}. This may be ascribed to the fact that an increase in the concentration of the HNO_3 caused increases in the number of H^+ in the solution, which increase the concentration gradient of the metal ions and H^+ and therefore increases the driving force for ion exchange, which favoured of metal ion during the desorption process (Wu *et al*., 2020). Several researchers have reported that acid desorption is more favourable compared to the use of other desorbing agents (Arun *et al*., (2022) and Wang *et al*., 2022). However, Samson *et al*. (2016) who reported studied the desorption of   Cr (VI) using 0.01, 0.1, 1.0 and 1.20 M HCl solutions on modified groundnut hull reported desorption efficiency of 68 % at 0.3 moldm^{-3} for Cr (VI).

The difference in the report may be due to differences in the acid and the material used during the desorption process. It is important to note both their research and the current study showed that an increase in the acid concentration resulted in higher desorption of adsorbed pollutants. The order of the desorption efficiency of the metal ions and the pollution indicator parameters were total iron (97.24 %) > Cu (II) (96.35 %) > Pb (II) (95.94%) > Cd (II) (90.53 5) > Ni (II) (88.45 %)> Cr (VI) (84.00 %) respectively.

The highest desorption efficiency was obtained for $Fe_3O_4/SiO_2/ZnO$ (1:2:1) nanocomposite using when the concentration of HNO_3 was at 0.1 $moldm^{-3}$ after 15 min of contact time for all the heavy metals. Similarly, the result of the desorption efficiency of BOD, COD and TOC were in the order COD (91.00 %) > TOC (88.64 %) > BOD (86.00 %) which was also higher for $Fe_3O_4/SiO_2/ZnO$ (1:2:1) nanocomposites.

This may be corroborated by the fact that Cd (II), total iron, Pb (II) were easily desorbed compared with the other elements (Zhang *et al*. 2020b), this may also be due to the ionic radius of the pollutants. The maximum desorption efficiency occurred at 0.1 $moldm^{-3}$ of HNO_3 irrespective of the pollutant and nanoadsorbent used

4.15 Recyclability potential of $Fe_3O_4/SiO_2/ZnO$ Nanocomposites

The recyclability potential of the $Fe_3O_4/SiO_2/ZnO$ nanocomposites Prepared at different mixing ratios (1:1:1, 1:1:2, 1:2:1 and 2:1:1) was studied to determine the cost-effectiveness and stability of the nanocomposites after the batched adsorption studies. The four $Fe_3O_4/SiO_2/ZnO$ nanocomposites produced were recycled four times under the same conditions to study the reusability of $Fe_3O_4/SiO_2/ZnO$ nanocomposite material and the results obtained are presented in Figure 4.72-4.80.
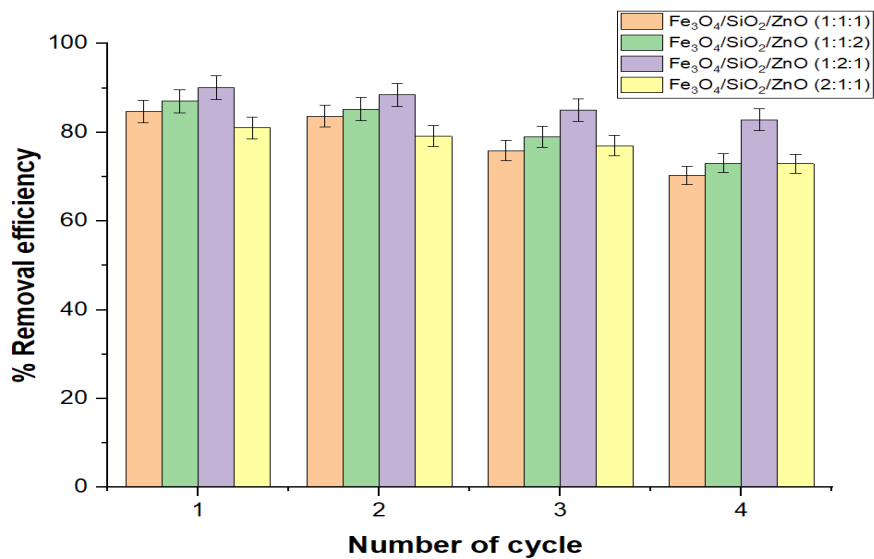
Figure 4.72: Fe₃O₄/SiO₂/ZnO Nanocomposite Reusability for Pb (II) after Four Cycles using 0.1 moldm⁻³ HNO₃ Solution as the Desorption Agent
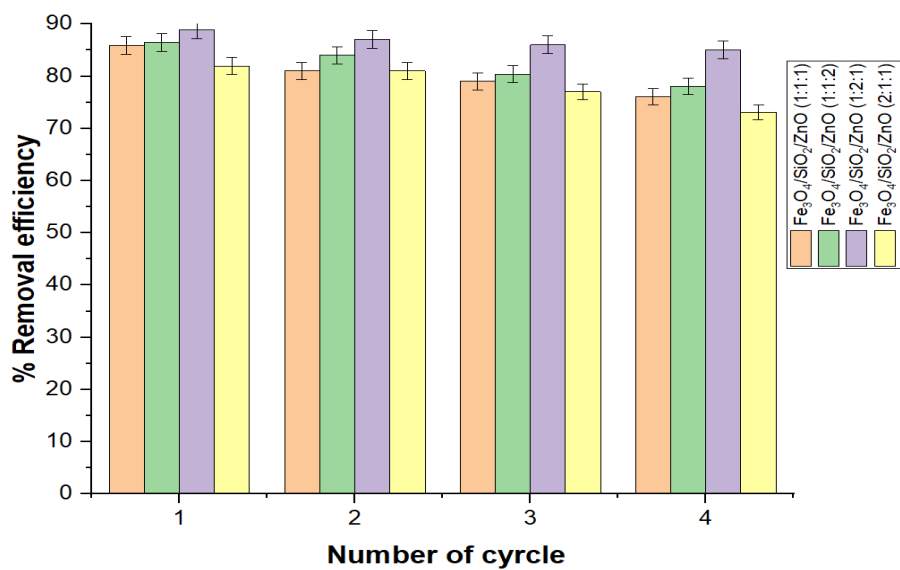
Figure 4.73: Fe₃O₄/SiO₂/ZnO Nanocomposite Reusability for Adsorption of Cd (II) after Four Cycles using 0.1 moldm⁻³ HNO₃ Solution as the Desorption Agent
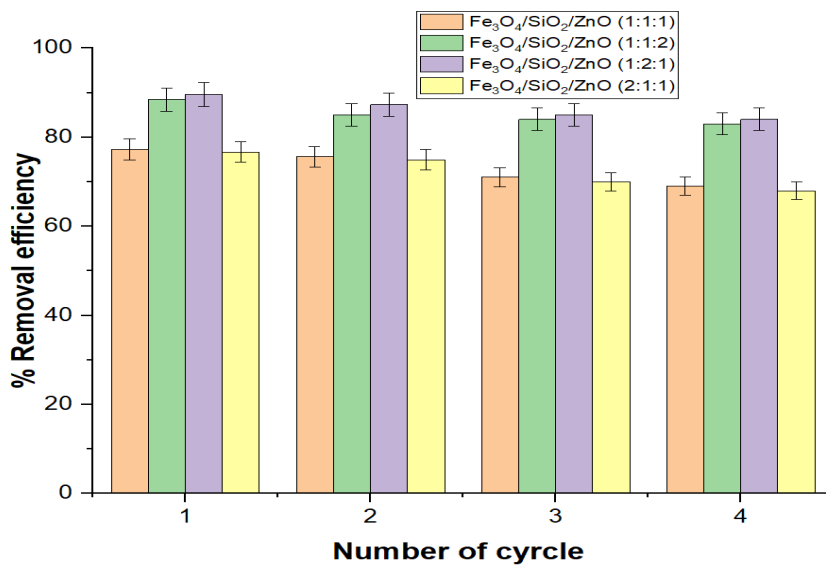
Figure 4.74: Fe₃O₄/SiO₂/ZnO Nanocomposite Reusability for Adsorption of Ni (II) after Four Cycles using 0.1 moldm⁻³ HNO₃ Solution as the Desorption Agent
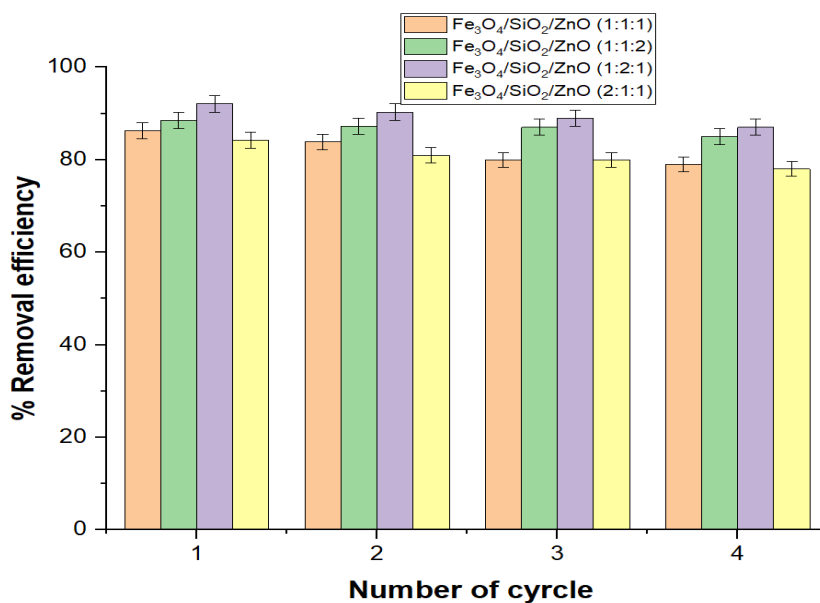
Figure 4.75: Fe₃O₄/SiO₂/ZnO Nanocomposite Reusability for Adsorption of Cu (II) after Four Cycles using 0.1 moldm⁻³ HNO₃ Solution as the Desorption Agent
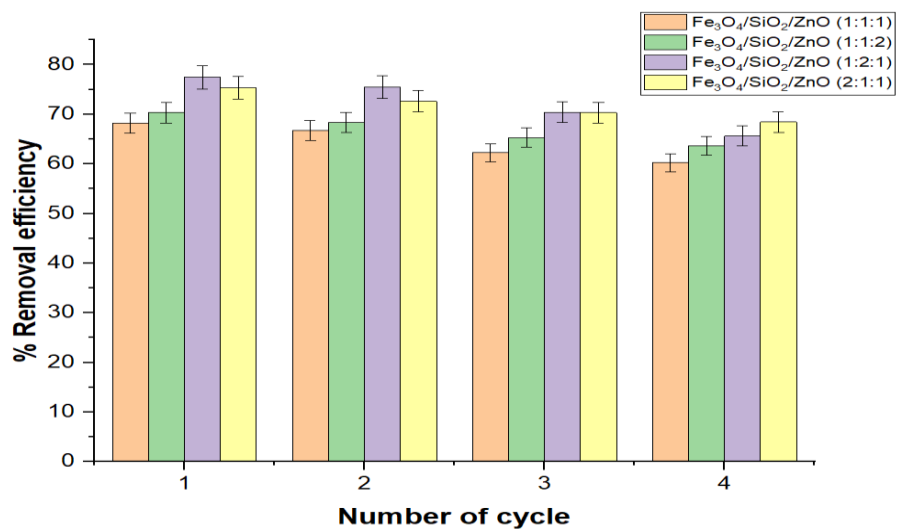
Figure 4.76: Fe₃O₄/SiO₂/ZnO Nanocomposite Reusability for Adsorption of Cr (II) after Four Cycles using 0.1 moldm⁻³ HNO₃ Solution as the Desorption Agent
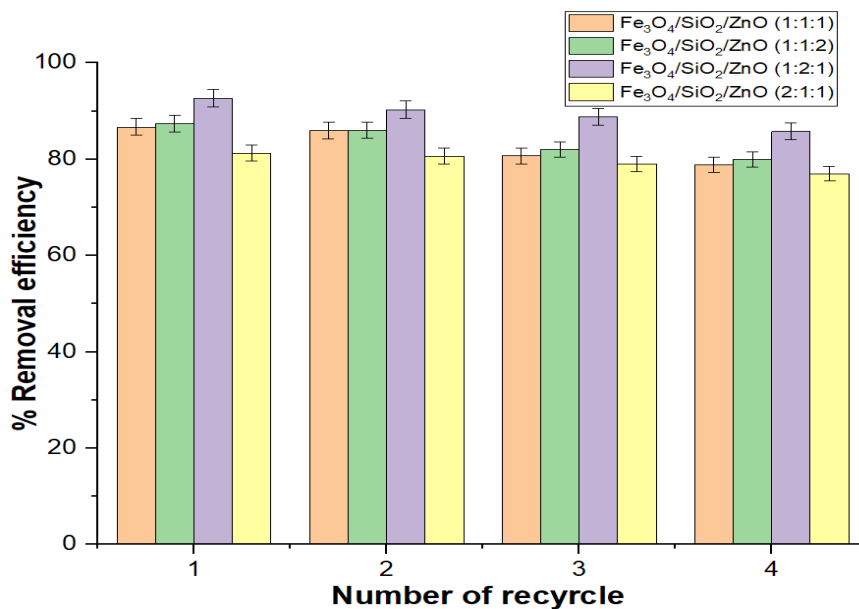
Figure 4.77: Fe₃O₄/SiO₂/ZnO Nanocomposite Reusability for Adsorption of Total iron after Four Cycles using 0.1 moldm-³ HNO₃ Solution as the Desorption Agent
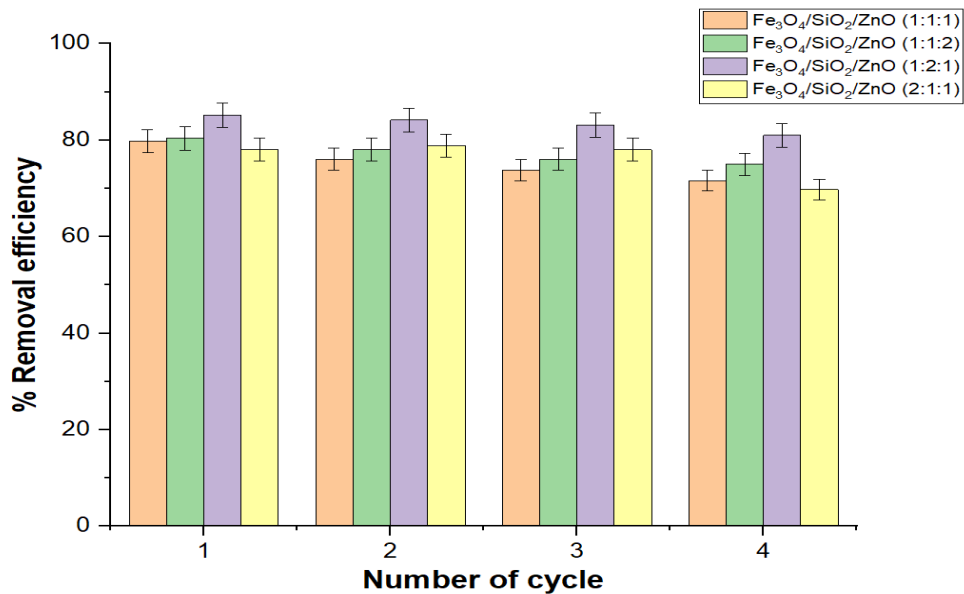
Figure 4.78: Fe₃O₄/SiO₂/ZnO Nanocomposite Reusability for Adsorption of BOD after Four Cycles using 0.1 moldm⁻³ HNO₃ Solution as the Desorption Agent
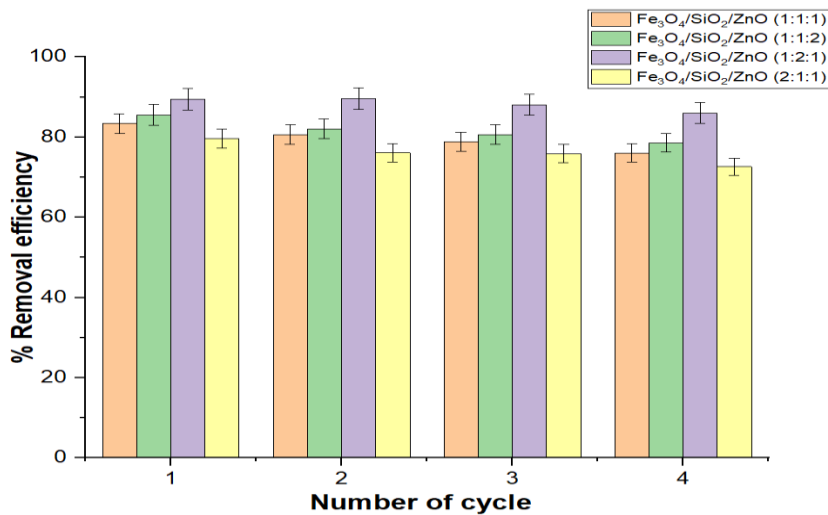
Figure 4.79: Fe₃O₄/SiO₂/ZnO Nanocomposite Reusability for Adsorption of COD after Four Cycles using 0.1 moldm⁻³ HNO₃ Solution as the Desorption Agent
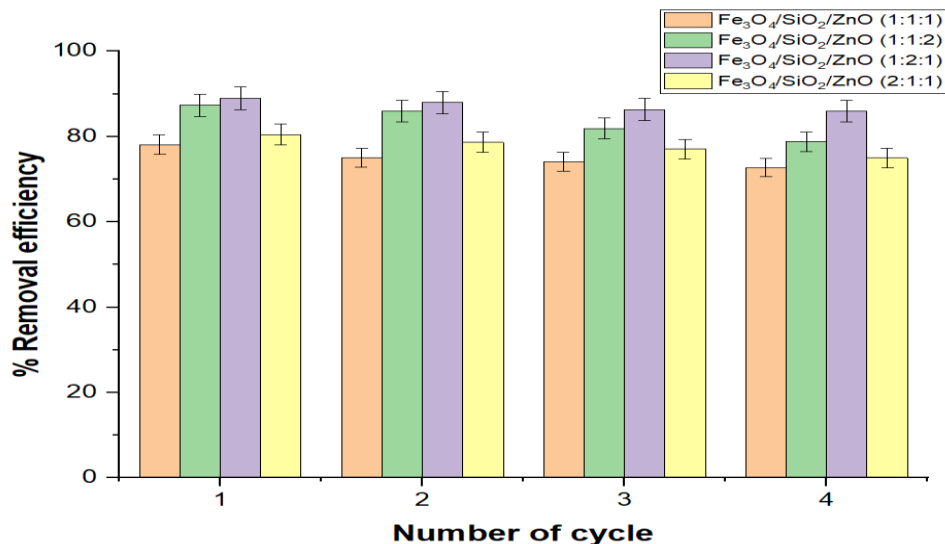
Figure 4.80: Fe₃O₄/SiO₂/ZnO Nanocomposite Reusability for Adsorption of TOC after Four after Four Cycles using 0.1 moldm⁻³ HNO₃ Solution as the Desorption Agent

Figure 4.72 shows the regeneration efficiency of the Pb (II) by $Fe_3O_4/SiO_2/ZnO$ (1:1:1) $Fe_3O_4/SiO_2/ZnO$ (1:1:2), $Fe_3O_4/SiO_2/ZnO$ (1:2:1) and $Fe_3O_4/SiO_2/ZnO$ (2:1:1) nanocomposites and it was noticed that the regeneration efficiency of Pb (II) from petroleum refinery wastewater for the first cycle was 84.66 %, second cycle was 83.66 % the third cycle was 76.86 % while the percentage removal efficiency for the fourth cycles was 74.27 % for $Fe_3O_4/SiO_2/ZnO$ (1:1:1) nanocomposites. For $Fe_3O_4/SiO_2/ZnO$ (1:1:2) nanocomposites, the removal efficiency for the first cycle was 86.99 %, the second cycle was 85.24 % the third cycle was 78.99 % while the percentage removal efficiency for the fourth cycle was 76.02 %. The values obtained for the first, second, third and fourth cycles were 90.01 %, 88.45 %, 87.01 %, and 85.85 % using $Fe_3O_4/SiO_2/ZnO$ (2:1:1) nanoparticles. For $Fe_3O_4/SiO_2/ZnO$ (1:2:1) nanoparticles, the regeneration efficiency for the first cycle was 80.99 %, the second cycle was 79.08 %, the third cycle was 75.99 % fourth cycle was %, 73.91 $Fe_3O_4/SiO_2/ZnO$

(2:1:1) nanocomposites. The result suggests that $Fe_3O_4/SiO_2/ZnO$ (2:1:1) nanocomposites show the lowest regeneration efficiency after the fourth cycle to be 85.85 %.

Similar trends were observed for other target pollutants shown in Figure 4.73-4.80.

Generally, the regeneration efficiency of the nanocomposites followed the order of $Fe_3O_4/SiO_2/ZnO$ (1:2:1) > $Fe_3O_4/SiO_2/ZnO$ (1:1:2) > $Fe_3O_4/SiO_2/ZnO$ (1:1:1) > $Fe_3O_4/SiO_2/ZnO$ (2:1:1) for all the target pollutants. This is an indication that $Fe_3O_4/SiO_2/ZnO$ (1:2:1) nanocomposites were more stable than the other nanocomposites. This observation corroborated the XRD and HRSEM results shown in Figure 4.41 and Plate IX. It's worth noting that as the regeneration process progressed from the first to the fourth adsorption cycle, the saturation time decreased, resulting in lower adsorption removal efficiency of less than 5% from one cycle to another. The observed trend may be linked to the adsorbent structure or functional group deterioration during the desorption process (Bayuo *et al*. 2020). Another possible explanation for the decrease in adsorption efficiency maybe that the desorbing agent acid could not completely remove the adsorbed pollutants from the surface of the adsorbent throughout each cycle period, as a result reducing the number of available sites for the adsorption (Patel, 2021). As a result, the produced nanocomposites can be used as adsorbents for wastewater treatment that are stable, environmentally being, efficient, and reusable.

Table 4.15: Comparison of the Desorbing Agents and Percentage Removal at Different Recycled Periods with the Literature

Adsorbent	Pollutants	Number of Cycles	Concentration/Desorbing agents	Percentage adsorption Removal after the regeneration (%)	Reference
PS/Fe3O₄@PANI	Cu (II)	8	0.1 M HCl	83	Li *et al*. (2017)
GO/PANI Zn	Zn	4	pH = 7	50	Ramezanzadeh *et al*. (2017)
Xanthan gum/ZnO/polyaniline	Cr (VI)	5	0.2 M NaOH	51.67	Ahmad *et al*., (2021)
Fe_3O_4/SiO_2	Total iron	3	HCl	70.81	Meng *et al*. (2018)
CL-PANI/Fe₃O₄	Cr (VI)	10	0.1 M NaOH	80	Lyu *et al*. (2019)
GO/NiO	Cr	5	0.1 M HCl	83	Zhang *et al*. (2018)
pTSA–Pani@CNT	Cr (VI)	3	0.1 M NaOH, 0.1 M HCl, Acetone	98	Kumar and Bhatnagar, (2018)
Sulfhydryl/TiO₂	Pb (II) Cd (II)	5	0.01 M HCl	96	Chen *et al*. (2023)
$Fe_3O_4/SiO_2/ZnO$ (1:1:1)	Pb (II)			88.86	
	Cd (II)			76.11	
	Ni (II)			69.01	
	Cr (VI)	4	0.1 moldm^{-3} HNO₃	60.266	This work
	Cu (II)			79.58	
	Total iron			78.76	
	COD			75.25	

Adsorbent	Pollutants	Number of Cycles	Concentration/Desorbing agents	Percentage adsorption Removal after the regeneration (%)	Reference
Fe$_3$O$_4$/SiO$_2$/ZnO (1:1:2)	BOD			78.34	
	TOC			78.97	
	Pb (II)			88.99	
	Cd (II)			78	
	Ni (II)			83	
	Cr (VI)			63.66	
	Cu (II)	4	0.1 moldm^{-3} HNO$_3$	85.7	This work
	Total iron			80.15	
	COD			73.19	
	BOD			76.28	
Fe$_3$O$_4$/SiO$_2$/ZnO (1:2:1)	TOC			83.45	
	Pb (II)			94.01	
	Cd (II)			85.11	
	Ni (II)			84.48	
	Cr (VI)			65.65	
	Cu (II)	4	0.1 moldm^{-3} HNO$_3$	87.34	This work
	Total iron			85.76	
	COD			78.34	
	BOD			81.43	
	TOC			86.45	
Fe$_3$O$_4$/SiO$_2$/ZnO (2:1:1)	Pb (II)	4	**0.1 moldm^{-3}** HNO$_3$	84.99	This work

Adsorbent	Pollutants	Number of Cycles	Concentration/Desorbing agents	Percentage adsorption Removal after the regeneration (%)	Reference
	Cd (II)			73.11	
	Ni (II)			68.52	
	Cr (VI)			68.45	
	Cu (II)			78	
	Total iron			77.45	
	COD			70.2	
	BOD			74	
	TOC			74.54	

Table 4.15 shows that the nanoadorbent competes favourably with the result reported in the literature. This is an indication that the nanocomposites produced in this research can be used many times as anadsorbent for the treatment of petroleum refinery wastewater and other related industries. Many of the researchers that utilize acid as a desorbing agent recoded higher desorption of the metal ions at 0.1 M. Nevertheless, many of the researcher utilised sulfuric (H_2SO_4) acid during the desorption process. This may be because H_2SO_4 is a very strong oxidizing agent and may destroy the active sites on the nanoadsorbents. Additionally, this may be ascribed to the formation and precipitation of lead sulfate, which is insoluble in water. The percentage of desorption using an alkali solution was lower compared to the use of acid solutions. It can be concluded that acid had a higher desorption potential for the metal ions.

4.16 Antibacterial Activity of Fe_3O_4/SiO_2/ZnO Nanocomposites

The antibacterial properties of the Fe_3O_4/SiO_2/ZnO nanocomposites prepared at different mixing ratios were studied and the result is presented in Table 4.12 and Plate XI, XII, XIII and XIV showing the images of the bacteria activities for *Escherichia coli*, *Klebsiella pneumonia*, and *Salmonella typhi.*

Plate XI: Antibacterial activity of Fe₃O₄/SiO₂/ZnO (1:1:1) Nanocomposites at different concentrations for (a) *Escherichia coli***, (b)** *Klebsiella pneumoniae***, and (c)** *Salmonella typhi*

Plate XII: : Antibacterial activity of Fe3O4/SiO2/ZnO (1:1:2) Nanocomposites at difeent concentration for (a) *Escherichia coli***, (b)** *Klebsiella pneumoniae***, and (c)** *Salmonella typhi*

Plate XIII: Antibacterial activity of Fe₃O₄/SiO₂/ZnO (1:2:1) Nanocomposites at different concentration for (a) *Escherichia coli*, (b) *Klebsiella pneumoniae*, (c) *Styphi*

Plate XIV: Antibacterial activity of Fe₃O₄/SiO₂/ZnO (2:1:1) Nanocomposites at the different concentrations for (a) *Escherichia coli*, (b) *Klebsiella pneumonia*, and (c) *Salmonella typhi*

The antibacterial activity of Fe₃O₄/SiO₂/ZnO nanocomposites on the *Escherichia coli, Salmonella typhi* and *Klebsiella pneumoniae* were determined at different concentrations of the nanocomposites using the Agar diffusion method and the result presented in Table 4.16.

Table 4.16: Antibacterial Activity of Fe$_3$O$_4$/SiO$_2$/ZnO Nanocomposites (mm)

Samples	Bacterium	Concentration				
		20 mg/cm3	40 mg/cm^3	60 mg/cm^3	80 mg/cm^3	100 mg/cm^3
Fe$_3$O$_4$/SiO$_2$/ZnO (1:1:1)	*Escherichia coli*	6.42 ±0.04	8.00±0.12	11.34±0.06	11.00±,013	15.00±0.07
	Salmonella typhi	3.45±0.11	6.00±0.08	7.50±0.14	9.20±0.04	13.00±0.07
	Klebsiella pneumoniae	4.40±0.09	12.00±0.10	15.50±0.02	18.00±0.01	25.00±0.03
Fe$_3$O$_4$/SiO$_2$/ZnO (1:1:2)	*Escherichia coli*	11.50 ± 0.14	12.00±0.10	15.00±0.08	16.34±0.08	18.00±0.12
	Salmonella typhi	6.05±0.09	7.05±0.03	9.500 ±0.06	11.00±0.08	17.00±0.03
	Klebsiella pneumoniae	10.15±0.11	13.00±0.09	17.50±0.08	23.00±0.23	28.50±0.08
Fe$_3$O$_4$/SiO$_2$/ZnO (1:2:1)	*Escherichia coli*	14.50±0.01	13.00±0.07	17.80±0.01	20.34±0.13	25.00±0.06
	Salmonella typhi	10.00±0.07	14.50±0.08	16.40±0.10	19.00±0.15	26.00±0.06
	Klebsiella pneumoniae	10.42±0.03	16.38±0.04	20.00±0.09	26.36±0.03	29.50±0.16
Fe$_3$O$_4$/SiO$_2$/ZnO (2:1:1)	*Escherichia coli*	4.32±0.17	6.00±0.012	8.45 ±0.06	12.00±0.13	15.00±0.04
	Salmonella typhi	5.00±0.08	6.50±0.01	8.00±0.03	10.350±0.15	13.00±0.02
	Klebsiella pneumoniae	9.00±0.15	7.50±0.08	9.00±0.04	11.32±0.03	12.00±0.01
Ciprofloxacin	*Escherichia coli*	6.42 ±0.04	8.00±0.12	11.34±0.06	11.00±,013	15.00±0.07
	Salmonella typhi	3.45±0.11	6.00±0.08	7.50±0.14	9.20±0.04	13.00±0.07
	Klebsiella pneumoniae	4.40±0.09	12.00±0.10	15.50±0.02	18.00±0.01	25.00±0.03

The antibacterial activity of $Fe_3O_4/SiO_2/ZnO$ (1:1:1), $Fe_3O_4/SiO_2/ZnO$ (1:1:2), $Fe_3O_4/SiO_2/ZnO$ (1:2:1), and $Fe_3O_4/SiO_2/ZnO$ (2:1:1) nanocomposites against the Gram-negative bacteria (*Escherichia coli*, *Klebsiella pneumonia*, and *Salmonella typhi*) at different concentrations (20, 40, 60, 80, and 100 mg/cm^3) revealed the bacterial activity is concentration-dependent as presented in Table 4.16.

The highest zone of inhibition observed for $Fe_3O_4/SiO_2/ZnO$ (1:1:1) against the *Escherichia coli, Salmonella typhi* and *Klebsiella pneumonia* were 15.00±0.07 mm, 13.00±0.02 mm, and 25.00±0.03 mm respectively. The highest zone of inhibition observed for $Fe_3O_4/SiO_2/ZnO$ (1:1:2) against Escherichia coli, *Salmonella typhi* and *Klebsiella pneumonia* were 18.00±0.12 mm, 17.00±0.03 mm and 28.50±0.08 mm while the $Fe_3O_4/SiO_2/ZnO$ (1:2:1) zone of inhibition at 100/cm^3 against *Escherichia coli, Salmonella typhi* and *Klebsiella pneumonia* were estimated to be 25.00±0.06 mm, 26.00±0.06 mm and 29.50±0.16 mm. Similarly, the $Fe_3O_4/SiO_2/ZnO$ (1:1:2) zone of inhibition at 100/cm^3 against *Escherichia coli, Salmonella typhi* and *Klebsiella pneumonia* were estimated to be 15.00±0.06 mm, 13.00±0.06 mm and 12.00 ± 0.16 mm using $Fe_3O_4/SiO_2/ZnO$ (1:1:2) nanocomposites.

The order of antibacterial activity of the $Fe_3O_4/SiO_2/ZnO$ nanocomposites respective to the mixing ratio were 1:2:1>; 1:1:2>; 1:1:1> 2:1:1 for *Escherichia coli, Salmonella typhi* and *Klebsiella pneumonia* respectively. This suggests that $Fe_3O_4/SiO_2/ZnO$ (1:2:1) has the highest antibacterial activity against all the tested bacterial. This is an indication that the antibacterial potentials of the ternary nanocomposites are a function of crystallite size and surface area. The smaller the crystallite size of the nanocomposites the more the materials penetrate the bacterial cell wall and disrupt organelles, disrupting biochemical pathways and

295

ultimately leading to bacterial death (Singh *et al*., 2020). All the Fe$_3$O$_4$/SiO$_2$/ZnO nanocomposites prepared at different mixing ratio shows activity against the tested organism thereby validating the report by Khan *et al*. (2019) that the effectiveness of nanomaterials against microorganisms is a function of the crystallite size, which must be less than 50 nm. The crystallite size estimated in this analysis was 10. 10 nm, 8.84 nm, 7.66 nm and 12.40 nm for material with mixing ratios 1:1:1, 1:1:2, 1:2:1 and 2:1:1 respectively.

Yin *et al*. (2020) concluded that the lower the crystallite sizes of nanomaterial the higher the antibacterial activity of nanomaterials. In addition, the high activity of the Fe$_3$O$_4$/SiO$_2$/ZnO nanocomposites with a mixing ratio of 1:2:1 is an indication that it generates more oxidative stress, which is caused by reactive oxygen species (ROS) leading to a higher activity compared with the Fe$_3$O$_4$/SiO$_2$/ZnO nanocomposites prepared at other ratios (Jamshidi and Sazegar, 2020). The high activity may also be linked to the colloidal stability and less agglomeration of Fe$_3$O$_4$/SiO$_2$/ZnO **(**1:2:1**)** nanocomposites compared to the other mixing ratios (Asamoah *et al*., 2020). The highest value of zone of inhibition was observed at a concentration (100 mg/ cm^3) for Fe$_3$O$_4$/SiO$_2$/ZnO (1:2:1)**.**

The zone of inhibition was also observed to be higher in the standard antibiotics (Ciprofloxacin) at a higher concentration (100 mg/ cm^3). However, the highest zone of inhibition was observed at a concentration (60 mg/ cm^3) with a value (of 44.40 mm) against *Klebsiella pneumonia*, while *Escherichia coli and Salmonella typhi* have values: of 37.00 and 35.40 mm respectively. The highest zone of inhibition obtained at low concentrations (60 mg/ cm^3) suggests that lower concentrations of the tested sample displayed potent activity against *Klebsiella pneumonia*. This also indicates that as the concentration increases, the zone

of inhibition increases against *Klebsiella pneumonia* (35.40 mm) indicating better activity at higher concentrations. From the result presented in Table 4.15, the control (Ciprofloxacin) shows a higher activity compared with the four nanocomposites. This may be because ciprofloxacin is a pure compound isolated for the treatment of these bacteria. The ability of $Fe_3O_4/SiO_2/ZnO$ nanocomposites to inhibit bacterial growth is primarily due to irreversible damage to the bacterial cell membrane caused by interactions between the bacteria's surface and these oxides and metals (Abudula *et al*., 2020). The obtained antibacterial activity of $Fe_3O_4/SiO_2/ZnO$ nanocomposites prepared at different mixing ratios against *Escherichia coli, Klebsiella pneumonia* and *Salmonella typhi* has been compared with the bacterial activity of other nanocomposites available in the literature as shown in Table 4.17.

Table 4.17: Comparison of the Bacterial Activity of Fe₃O₄/SiO₂/ZnO Nanocomposites Prepared at different Mixing Ratios with the Previous Works

Sample	Bacterium	Zone of inhibition (mm)	Shape	Crystallite size (nm)	References
SiO₂/ZnO	*Escherichia coli, Klebsiella pneumonia*, *Staphylococcus aureus*	20.08 to 22.8	Flouwer like	8	Kiran *et al*. (2019)
ZnO/Fe₃O₄	*Escherichia coli* and *S. aureus*	15 and 11	spherical	10	Arunima *et al.,* (2020)
ZnO/Montmorillonite	*Escherichia coli, Staphylococcus, Pseudomonas and Enterobacter*	20, 25, 31, and 19	Flaky - like	25	Arthi *et la.* (2020)
Chitosan/Graphite/Zn-MSN	*S. aureus* and *Escherichia coli*.	21 and 24	spherical	70	Jamshidi and Sazegar (2020)
SiO₂/Ag	*Escherichia coli (Escherichia coli)* and	20.3 and 18.8	Spherical	15	Gankhuyag *et al*., (2021)

	Bacillus subtilis (B. subtil				
Fe$_3$O$_4$/SiO$_2$/ZnO (1:1:1)	*Escherichia coli*, *Klebsiella pneumoniae*, and *Salmonella typhi*	15.00,13.00, 25.00	Spherical and rod-like	10. 10	This work
Fe$_3$O$_4$/SiO$_2$/ZnO (1:1:2)	*Escherichia coli*, *Klebsiella pneumonia*, and *Salmonella typhi*	18.00, 17.00 28.50	Spherical and rod-like	8.84	This work
Fe$_3$O$_4$/SiO$_2$/ZnO (1:2:1)	*Escherichia coli*, *Klebsiella pneumoniae*, and *Salmonella typhi*	25.00, 26.00, 29.50	Spherical and rod-like	7.66	This work
Fe$_3$O$_4$/SiO$_2$/ZnO (2:1:1)	*Escherichia coli*, *Klebsiella pneumonia*, and *Salmonella typhi*	15.00, 13.00, 12.00	Spherical and rod-like	12.40	This work

Table 4.16 shows that Fe$_3$O$_4$/SiO$_2$/ZnO (1:2:1) has higher activity compared to other nanocomposites, which suggests Fe$_3$O$_4$/SiO$_2$/ZnO (1:2:1) nanocomposites as a good antibacterial agent. Table 4.16 suggests that the nanocomposites performed exhibited higher antibacterial activities compared to the previous report in the literature. This may be related to the smaller crystallite size of the nanocomposites in this study. This result also justifies the claim that the crystallite size played an important role in the antibacterial activities of the nanoparticles.

4.17 Antioxidant Activity of Fe$_3$O$_4$/SiO$_2$/ ZnO Nanocomposites

The antioxidant potentials of Fe$_3$O$_4$/SiO$_2$/ZnO nanocomposites were evaluated by DPPH radical scavenging assay and the result is presented in Table 4.18.

Table 4.18: Antioxidant Activity of Fe_3O_4/SiO_2/ ZnO Nanocomposites

Sample	Concentration ($\mu g/cm^3$)			
	500	250	125	62.50
Fe_3O_4/SiO_2/ZnO (1:1:1)	33.73±0.60	15.01±0.46	12.10±0.59	9.60±0.49
Fe_3O_4/SiO_2/ZnO (1:1:2)	38.60±0.10	18.68±0.58	14.40±0.34	10.53±0.33
Fe_3O_4/SiO_2/ZnO (1:2:1)	39.54±0.28	20.31±0.34	18.26±0.60	12.57±0.34
Fe_3O_4/SiO_2/ZnO (2:1:1)	24.63±0.50	9.19±0.50	6.97±0.38	5.63±0.23
Ascorbic acid	93.73±0.50	87.83±0.15	79.92±0.20	63.29±0.10

The results obtained from DPPH free radical scavenging activities of the ZnO /SiO_2/ Fe_3O_4 (1:1:1), Fe_3O_4/SiO_2/ ZnO (1:1:2), Fe_3O_4/SiO_2/ ZnO (1:2:1), and Fe_3O_4/SiO_2/ ZnO (2:1:1) standard ascorbic acid at different concentrations (500, 250, 125, and 62.5 $\mu g/cm^3$) are presented in Table 4.18. It was found that all the tested samples and the standard ascorbic acid exhibited free radical scavenging activities in a dose-dependent manner. Fe_3O_4/SiO_2/ ZnO (1:1:1) have scavenging activities with the values 33.73±0.60, 15.01±0.46, 12.10±0.59, 9.60±0.49 $\mu g/cm^3$ Fe_3O_4/SiO_2/ ZnO (1:1:2) have DPPH free radical scavenging activities of 38.60±0.10, 18.68±0.58, 14.40±0.34 and 10.53±0.33 $\mu g/cm^3$, Fe_3O_4/SiO_2/ZnO (1:2:1) exhibited DPPH free radical scavenging activities of 39.54±0.28, 20.31±0.34, 18.26±0.60 and 12.57±0.34 $\mu g/cm^3$ while 24.63±0.50, 9.19±0.50, 6.97±0.38, and 5.63±0.23 $\mu g/cm^3$ were obtained for Fe_3O_4/SiO_2/ZnO (2:1:1) and standard ascorbic acid (93.40, 87.53, 80.08, and 63.63 $\mu g/cm^3$) at different concentrations (500, 250, 125, and 62.5 $\mu g/cm^3$ respectively)

against the radical DPPH. The higher scavenging activity was observed in sample $Fe_3O_4/SiO_2/ZnO$ (1:2:1) with the highest value of 39.00 $\mu g/cm^3$ followed by sample (38.00 $\mu g/cm^3$). $Fe_3O_4/SiO_2/ZnO$ (1:1:1) had the lowest free radical scavenging activity with a value (25 $\mu g/cm^3$). This may be due to its low active principles, especially phenolic compounds (Yu *et al*., 2021). The higher activities obtained from $Fe_3O_4/SiO_2/ZnO$ (1:2:1) may be attributed to the existence of synergy amongst the metal oxides present in the sample. A similar report was established by Hitesh *et al*. (2020) for the in-vitro Antiglycation Activity of Zinc Oxide Nanoparticles Synthesised.

IC_{50} obtained from the regression plot of percentage inhibition against concentration in appendix 73-77 was used to define the free radical scavenging activities of each of the nanoparticles. The free radical scavenging activity at 50 % concentrations (IC_{50}) of the ZnO /SiO_2/ Fe_3O_4 nanocomposite samples showed that there was a significant difference amongst the tested sample with IC_{50} values of 758.09, 806.77, 688.79, 1092.96 and 25.00 $\mu g/cm^3$ for samples $Fe_3O_4/SiO_2/ZnO$ (1:1:1), $Fe_3O_4/SiO_2/ZnO$ (1:1:2), $Fe_3O_4/SiO_2/ZnO$ (1:2:1), and $Fe_3O_4/SiO_2/ZnO$ (2:1:1) and standard ascorbic acid respectively. This indicates that sample $Fe_3O_4/SiO_2/ZnO$ (1:2:1) have the highest radical scavenging activity with the lowest IC_{50} value (688.79 ug/cm^3), followed by $Fe_3O_4/SiO_2/ZnO$ (1:1:1), with IC_{50} of 758.09ug/cm^3; while $Fe_3O_4/SiO_2/ZnO$ (2:1:1) have the lowest activity with the higher IC_{50} value (1092.96 ug/cm^3). Yusoff *et al*. (2020) reported that low IC_{50} values may be a result of high contents of active principles in the sample. The results obtained from this study suggest that all the samples possess active compounds which transferred an electron to free radical, hence displaying antioxidant activities (Rehana *et al*. 2017).

Table 4.19: Comparison of the Antioxidant Activity of Fe₃O₄/SiO₂/ZnO Nanocomposites Prepared at different Mixing Ratios with the Previous Works

Nanomaterial (nm)	Characterisation Tools	Method of synthesis of nanoparticle	Shape	Crystallite size	Evaluation Assays	IC50 Value (µg/mL)	Antioxidant Activity (%)	References
CuO	XRD, EDX, HRTEM, SEM, UV/Vis	Green route	A mixture of rod-like, rectangular and hexagonal shapes	45–65	DPPH	40.81	91.37	Velsankar *et al*. (2020)
MgO	EDX, TEM, XRD, UV/Vis, FT-IR	Green route	Spherical	<100	DPPH, FRAP	—	65, 69.3	Sharmila *et al*. (2019)
ZnO	XRD, UV/Vis, TEM and FT-IR	Green route	Spherical	70–75	DPPH	—	56.11	Sharmila *et al*. (2019)
CuO	XRD, TEM, and EDS	Green route	Spherical	32.3	DPPH	45.29	86.78	Thakar *et al*., (2021)
TiO₂	UV/Vis, FTIR, TEM, EDX, XRD, FESEM	Green route	Spherical	25–191	DPPH	—	62.06	Akinola *et al*. (2021)
Cu/ZnO /polymer	XRD, UV, HRTEM, FTIR	Coprecipitation	Spherical	60	DPPH	91.16	79.9	Al-Rajhi *et al*. (2022)
Fe₃O₄/SiO₂/ZnO (1:1:1)	XRD, SEM, EDX, FT-IR, BET, XPS	Sol-gel chemical reduction	Rod-like	10.1	DPPH	758.09	33.73	This work
Fe₃O₄/SiO₂/ZnO (1:1:2)	XRD, SEM, EDX, FT-IR, BET, XPS	Sol-gel chemical reduction	Rod-like	8.84	DPPH	806.77	38.6	This work

Nanomaterial (nm)	Characterisation Tools	Method of synthesis of nanoparticle	Shape	Crystallite size	Evaluation Assays	IC50 Value (μg/mL)	Antioxidant Activity (%)	References
$Fe_3O_4/SiO_2/ZnO$ (1:2:1)	XRD, SEM, EDX, FT-IR, BET, XPS	Sol-gel chemical reduction	Rod-like		DPPH	688.79	39.54	This work
$Fe_3O_4/SiO_2/ZnO$ (2:1:1)	XRD, SEM, EDX, FT-IR, BET, XPS	Sol-gel chemical reduction	Rod-like	7.66 12.4	DPPH	1092.96	24.63	This work

Table 4.19 shows that the antioxidant activities of the nanocomposites produced in this research are lower compared with various values reported in the literature. This may be because many of the researchers that have reported the antioxidants of the nanoparticles and their corresponding nanocomposites use a green method to synthesise the nanoparticles used for the antioxidant activities. It can be concluded that many of the plant extracts used for the synthesis may contain a compound that has antioxidant properties and the nanoparticles act as drug delivery vehicles that help the active compound to get to the cell wall of the organism.

5.0   **CONCLUSION AND RECOMMENDATIONS**

5.1   **Conclusion**

In summary ZnO, Fe_3O_4 and SiO_2, ZnO/Fe_3O_4, Fe_3O_4/SiO_2, $Fe_3O_4/SiO_2/ZnO$ nanocomposites were synthesized via sol-gel chemical reduction. The synthesised nanoparticles and the composites were characterised using XRD, HRSEM, EDX, BET and XPS. The removal of the pollutantsfrom the petroleum refinery wastewater was done via batch adsorption processes. The petroleum refinery wastewater was collected and analysed for different physicochemical parameters. The suitability of ZnO, Fe_3O_4 and SiO_2, ZnO/Fe_3O_4, Fe_3O_4/SiO_2, $Fe_3O_4/SiO_2/ZnO$ $Fe_3O_4/SiO_2/ZnO$ (1:1:1), $Fe_3O_4/SiO_2/ZnO$ (1:1:2), $Fe_3O_4/SiO_2/ZnO$ (1:2:1), and $Fe_3O_4/SiO_2/ZnO$ (2:1:1) nanocomposites as nanoadsorbent for the removal of Pb (II) Cd (II), Ni (II) Cr (VI), Cu (II), total iron, BOD, COD and TOC from petroleum refinery wastewater was studied. The desorption process was investigated to identify the optimal condition for the recovering Pb (II), Cd (II), Ni (II), Cr (IV), Cu (II), total iron ions, BOD, COD, TOC from the used $Fe_3O_4/SiO_2/ZnO$ nanocomposites after batch adsorption process. Additionally, the recyclability of the $Fe_3O_4/SiO_2/ZnO$ nanocomposites prepared at different mixing ratios (1:1:1, 1:1:2, 1:2:1 and 2:1:1) was studied for four recycles to determine the cost-effectiveness and stability of the nanocomposites. The antimicrobial and antioxidant activities of $Fe_3O_4/SiO_2/ZnO$ nanocomposite were also evaluated. From the results obtained the following conclusions were drawn:

    i.   The face-centered cubic structure of Fe_3O_4 nanoparticles was synthesized via sol-gel chemical reduction method with an average crystallite size between 14.170 to 26.364 nm at calcination temperature between 300 ℃ to 700 ℃. Hexagonal structure SiO_2

nanoparticles was synthesized via the sol-gel method with α-quart phase (3 h – 9h) which transform to cristobalite phase at a longer synthesis period (12 h) was synthesised with average crystallite sizes of 23. 00 nm - 62.25 nm. ZnO nanoparticles hexagonal wurtzite structure was obtained at a calcination temperature of above $100^{\circ}C$ with crystallite size ranging between 13.74 to 20.52. The bimetallic oxide nanocomposites synthesised (ZnO/Fe3O4, ZnO/SiO_2 and Fe_3O_4/SiO_2) showed the formation of rod-like structure as a major shape except for ZnO/Fe_3O_4 nanocomposites which shows spherical shape structure. The tannery metallic oxides ($Fe_3O_4/SiO_2/ZnO$) nanocomposites prepared at different mixing ratios of 1:1:1, 1:1:2, 1:2:1 and 2:1:1 showed the formation of rod-like structure irrespective of the mixing ratio.

ii. The $Fe_3O_4/SiO_2/ZnO$ (1:2:1) nanocomposites had the highest surface area of 35.469 m^2/g compared with 24.918, 30.685 and 15.751 m^2/g reported for the nanocomposites prepared at mixing ratio of 1:1:1, 1:1:2 and 2:1:1 respectively. The oxidation number of Zn^{2+} in ZnO nanoparticles change from +2 oxidation number to +1 after the formation of the composites with Fe_3O_4 and SiO_2 while Fe and Si were +5 (+2 and +3) and +4 remained unchange. Functional groups such as C-O, C-N, C=O, Si-O, Fe-O, Zn-O, Si-Zn were identified in the nanocomposites.

iii. The petroleum wastewater contained some heavy metals and indicator parameters such as Pb (II) Cd (II), Ni (II) Cr (VI), Cu (II), total iron, BOD, COD and TOC with values above the permissive limit of WHO and NQWS.

iv. The diffraction peaks for ZnO shift to a higher 2θ after the formation of the $^{\circ}$ nanocomposites indicating change inthe lattice structure of.the ZnO nanoparticles

v. The batch adsorption studies showed that the adsorption removal efficiency for the removal of Pb (II) Cd (II), Ni (II) Cr (VI), Cu (II), total iron, BOD, COD and TOC onto the monometallic oxides was better using ZnO nanoparticles as an adsorbent compared to other Fe_3O_4 and SiO_2 nanoparticles for all the target pollutants. Among the bimetallic oxides nanocomposites ZnO/Fe_3O_4 nanocomposites exhibited a higher adsorption efficiency for all the target pollutants than Fe_3O_4/SiO_2, ZnO/SiO_2 nanocomposites while for the ternary nanocomposites $Fe_3O_4/SiO_2/ZnO$ (1:2:1) nanocomposites exhibited excellent adsorptive properties on the removal of Pb (II) Cd (II), Ni (II) Cr (VI), Cu (II), total iron, BOD, COD and TOC from petroleum refinery wastewater with percentage removal of 99.03 %, 94.92 %, 90.33 %, 88.99 %, 99.99 %, 99.64 %, 92.50 %, 88.99 % and 90.86 % under the following applied conditions time (15 min), adsorbent dosage (0.05g), reaction temperature (35 °C) and pH of 6.25.

The extent of adsorption is directly proportional to the adsorbent's surface area and the crystallite size of the nanoadsorbent. The adsorption kinetics models and the isotherm models used to describe the adsorption process suggests that the adsorption process fits better to pseudo second order kinetics than pseudo first order, elovich and intraparticle diffusion kinetic models while the experimental data subjected to different isotherm models fitted best to Langmuir isotherm than Freundlich, Temkin and Dubinin-Radushkevich isotherms models for all the adsorbents with maximum adsorptive capacity (q_{max}) of 75.352 mg g^{-1}, 71.538 mg g^{-1}, 66.696 mg g^{-1}, 98.966 mg g^{-1}, 36.637 mg g^{-1}, 102.709 mg g^{-1}, 30.637 mg g^{-1}, 39.806 mg g^{-1}, 36.192 mg g^{-1} for Pb (II) Cd (II), Ni (II) Cr (VI), Cu (II), total iron, BOD, COD and TOC

respectively. Additionally, the thermodynamics parameters showed that the adsorption process for all the pollutants was endothermic in nature and chemisorption dominated the adsorption process compared with the physical adsorption process. The maximum desorption of all the target pollutants 95.94%, 90.24 %, 88.45 %, 85.00 %, 96.45 %, 97.24 %, 83 %, 91.00 % and 87. 04 % for Pb (II) Cd (II), Ni (II) Cr (VI), Cu (II), total iron, BOD, COD and TOC at contact time (15 min), adsorbent dosage (0.05 g) and temperature of 30℃. Notably, even after the four adsorption cycles, the target pollutants percentage removal efficiency was remained over 82 %, according to the batch reusability study. The stability study suggests that ZnO /SiO_2/ Fe_3O_4 (1:2:1) nanocomposites was more stable with a reduction in the percentage removal of the target pollutant ranging from 1-3 % compared with 5 % recorded for most of the other composites prepared at 1:1:1, 1:12, 1:2:1and 2:1:1. Therefore, this research shows the great potential of ZnO/SiO_2/Fe_3O_4 nanocomposites for industrial wastewater treatment operations, and it may pave the way for new approaches to improving sustainable nanoadsorbents for wastewater treatment and other purposes.

vi. Fe_3O_4/SiO_2/ZnO (1:2:1) nanocomposites exhibited the highest antibacterial activity against *Escherichia coli (*25.00±0.06 nm)*, Salmonella typhi (*26.00±0.06 nm)*, Klebsiella pneumoniae* (29.50±0.16 nm) at 100 mg/cm^3

vii. Fe_3O_4/SiO_2/ZnO (1:2:1) nanocomposites exhibited the highest antioxidant activity (39.54±0.28 µg/cm^3) at 500 µg/cm^3.

viii. The Fe_3O_4/SiO_2/ZnO (1:2:1) nanocomposites have an excellent adsorptive potential to reduce the number of toxic pollutants in petroleum refinery wastewater into the

environment, and hence reduce health issues and diseases linked to the release of untreated wastewater from petroleum refineries and related industries.

5.2   Recommendations

The following recommendations are suggested:

i. Fixed bed column studies and pilot scale models should be carried out to study the efficiency of the adsorbent in an industrial setting, where conditions aren't always as ideal as they are in the laboratory.

ii. Other factors, such as precursor salt, the concentration of stabilizing agent (PVC), stirring rate and time, pH, and calcination time should be studied for the synthesis of ZnO, Fe_3O_4, and SiO_2 nanoparticles.

iii. Other optimization conditions, such as concentration of activating agents, and precursor dosage for the preparation of the silicon oxides from kaolin should be investigated

iv. It is important to research efficient methods for removing used nano adsorbents from aqueous solutions.

v. Comparative toxicity of the pure and the nanocomposites should be studied

5.3   Contribution to Knowledge

The novelty of this work lies in the preparation of ternary $Fe_3O_4/SiO_2/ZnO$ nanocomposite for the simultaneous removal of selected heavy metals and total organic carbon from petroleum refinery wastewater.

2. Optimisation of the mixing ratio and establishment of relationship between mixing ratio and physico-chemical properties of binary (ZnO/Fe_3O_4, Fe_3O_4/SiO_2, ZnO/SiO_2), and ternary $Fe_3O_4/SiO_2/ZnO$ nanocomposites was carried out.

3. In this research only 0.08 g of $Fe_3O_4/SiO_2/ZnO$ nanocomposites was used to achieve 99.03 %, 94.92 %, 93.07 %, 88.91 %, 99.99 %, 99.63 %, 92.50 %, 88.99 % and 90.86 % adsorptive removal of Pb (II), Cd (II), Ni (II), Cr (VI), Cu (II), total iron, COD, BOD and TOC from real petroleum refinery wastewater within the contact time of 15 min, stirring speed of 250 rpm and temperature of 30 °C respectively and even after the four adsorption/desorption cycles, the target pollutants percentage removal efficiency remained above 82 %.

The removal of these toxic pollutants before their discharge into the environment will reduce the pollutants associated with the wastewater from the petroleum industries in the environment. Additionally, after four adsorption-desorption cycles, the adsorbents can be effectively regenerated with minimal adsorption capacity losses, reducing cost and solving the problem of disposal of the exhausted adsorbent. The findings from this research work will enlighten the research community, petroleum refineries and other related industries on the alternate method for the treatment of their wastewater.

REFERENCES

Abagale, F. K. (2021). Seasonal variation and removal of organic pollutants in wastewater using low-cost treatment technologies in Tamale metropolis, Ghana. *Journal of Water Resource and Protection*, 13(4), 21-30.

Abazari, S., Shamsipur, A., & Bakhsheshi-Rad, H. R. (2021). Reduced graphene oxide (RGO) reinforced Mg biocomposites for use as orthopedic applications: Mechanical properties, cytocompatibility and antibacterial activity. *Journal of Magnesium and Alloys*, 10(12), 3612-3627.

Abdel-Maksoud, M. I. A., Elgarahy, A. M, Farrell, C., Al-Muhtaseb, A. H., Rooney, D. W. & Osman, A. I. (2020). Insight on water remediation application using magnetic nanomaterials and biosorbents. *Coordination Chemistry Reviews*, 403, 1-33.

Abdolmohammad-Zadeh, H., Zamani, A. & Shamsi, Z. (2020). A simple magnetic solid-phase extraction method based on magnetite/graphene oxide nanocomposite for pre-concentration and determination of melamine by high-performance liquid chromatography. *Environmental Science and Pollution Research*, 27(9), 1–9.

Aboelwafa, M. A., Abdelghany, A. M. & Meikhail, M. S. (2021). Preparation, characterisation, and antibacterial activity of ZnS-NP's filled polyvinylpyrrolidone/chitosan thin films. *Biointerface Research in Applied Chemistry,* 11 (6), 14336 – 14343.

Abudula, T., Qurban, R. O., Bolarinwa, S O., Mirza, A. A., Pasovic, M. & Memic, A. (2020). 3D printing of metal/metal oxide incorporated thermoplastic nanocomposites with antimicrobial properties. *Frontiers in Bioengineering and Biotechnology,* 8, 1-8.

Adebisi, J. A., Agunsoye, J. O., Bello, S. A., Haris, M., Ramakokovhu, M. M., Daramola, M. O., & Hassan, S. B. (2018). Extraction of silica from cassava periderm using modified sol-gel method. *Nigerian Journal of Technological Development,* 15(2), 57-65.

Adebiyi, F. M., Ore, O. T., Akhigbe, G. E. & Adegunwa, A. O. (2020). Metal fractionation in the soils around a refined petroleum products depot. *Environmental Forensics,* 12, 1-13.

Adegoke, H. I., Adekola, F. A., Olowookere, I. T., & Yaqub, A. L. (2017). Thermodynamic studies on adsorption of lead (II) ion from aqueous solution using magnetite, activated carbon and composites. *Journal of Applied Sciences and Environmental Management*, *21*(3), 440-452.

Adeola, A. O., Akingboye, A. S., Ore, O. T., Oluwajana, O. A., Adewole, A. H., Olawade, D. B., & Ogunyele, A. C. (2021). Crude oil exploration in Africa: socio-economic implications, environmental impacts, and mitigation strategies. *Environment Systems and Decisions,* 42, 26–50.

Adnan, M. M., Tveten, E. G., Miranti, R., Hvidsten, S., Ese, M. H. G., Glaum, J. & Einarsrud, M. A. (2020). In situ synthesis of epoxy nanocomposites with hierarchical surface-modified SiO$_2$ clusters. *Journal of Sol-Gel Science and Technology*, 95, 783–794.

Ahmad, S. Z. N., Norharyat W., Salleh W., Yusof, N., Yusop, M. Z. M., Hamdan, R., Awang, N. A., Ismail, N. H., Rosman, N., Sazali, N. & Ismail, A. F. (2021). Pb (II) removal and its adsorption from aqueous solution using zinc oxide/graphene oxide composite. *Chemical Engineering Communications*, 208(5), 646–660.

Ahmad, S. Z. N., Salleh, W. N. W., Yusof, N., Mohd Yusop, M. Z., Hamdan, R., Awang, N. A., Ismail, A. F. (2020). Pb(II) removal and its adsorption from aqueous solution using zinc oxide/graphene oxide composite. *Chemical Engineering Communications,* 208(5), 646–660.

Ahmadivand, A., Karabiyik, M. & Pala, N. (2016). Plasmonic photodetectors. Photodetectors. M*aterials, Devices and Applications*, 1, 157-193.

Ajayi, B. A. & Owoeye, S. S. (2015). Extraction of soluble sodium silicate using corn cob ash as a silica source. *American Journal of Engineering Research (AJER)*, 4(9), 4-56.

Akbarzadeh, O., Mohd, Z. N., Abdulwahab, Y., Hamizi, N., Chowdhury, Z., Aljunid M. Z., Ab Rahman, M., Akhter, S., Shalauddin, M., Johan, M. (2018). Effects of cobalt loading, particle size, and calcination condition on Co/CNT catalyst performance in fischer–tropsch reactions. *Symmetry,* 11(7), 1-18.

Akhayere, E., Kavaz, D. & Vaseashta, A. (2019). Synthesizing nano silica nanoparticles from barley grain waste: effect of temperature on mechanical properties. *Polish Journal of Environmental Studies*, *28*(4), 2513-2521.

Akinola, P. O., Lateef, A., Asafa, T. B., Beukes, L. S., Hakeem, A. S. & Irsha, H. M. (2021). Multifunctional titanium dioxide nanoparticles biofabricated via phytosynthetic route using extracts of *Cola nitida*: antimicrobial, dye degradation, antioxidant and anticoagulant activities. *Heliyon* 6 (8), 1-9.

Alalwan, H. A., Kadhom, M. A. & Alminshid, A. A. (2020). Removal of heavy metals from wastewater using agricultural by products. *Journal of Water Supply: Research and Technology—AQUA,* 69(2), 99–112.

Alam, S., Ullah, B., Khan, M. S., Khan, L., Shah, L. A., Zekker, I., Burlakovs, J., Kallistova, A., Pimenov, N., Yandri, E. & Setyobudi, R. H. (2021). Adsorption kinetics and isotherm study of basic red 5 on synthesized silica monolith particles. *Water*, 13, 1-13

Alami, Z. Y., Salem, M., Gaidi, M. & Elkhamkhami, J. (2015) Effect of Zn concentration on structural and optical proprieties of ZnO thin films deposited by spray pyrolysis. *Advanced Energy: An International Journal (AEIJ)* 2(4), 11–24.

Al-Ariki, S., Yahya, N. A. A., Al-A'nsi, S. A., Jumali, M. H. H., Jannah, A. N., & Abd-Shukor, R. (2021). Synthesis and comparative study on the structural and optical properties of ZnO doped with Ni and Ag nanopowders fabricated by sol-gel technique. *Scientific Reports,* 11(1), 1-11.

Al-Gaashania, R., Radimana, S., Aminu, D., Tabetc, N. & Al-Dourid, Y. (2023). XPS and optical studies of different morphologies of ZnO nanostructures prepared by microwave methods. *Materials Science*, 2(2), 1-16.

Al-Harbi, F. F. & El Ghoul, J. M. (2021). Sol–Gel synthesis of Dy co-doped ZnO:V nanoparticles for optoelectronic applications. *Condens. Matter*, 6(35), 1-11.

Ali, Fayaz, Khan, Sher Bahadar, Kamal, Taheen, Alamry, Khalid A., Asiri, Abdullah M. (2018). Chitosan-titanium oxide fibers supported zero-valent nanoparticles: highly efficient and easily retrievable catalyst for the removal of organic pollutants. *Scientific Reports,* 8(1), 1-18.

Aljameel, A. I. & Ali, M. K. M. (2021). Zinc oxide thin films preparation by chemical methods onto Si substrate for solar cell application. *Journal of Non-Oxide Glasses*, 13(2), 21 – 29.

Al-Karam, L. Q. (2017). Mechanical tribology and antibacterial activity of ZnO/polystyrene nanocomposite. *Journal of Biotechnology &Biomaterials*, 7(3), 1-5.

Al-Rajhi, A.M.H., Yahya, R. & Bakri, M.M. (2022). In situ green synthesis of Cu-doped ZnO based polymers nanocomposite with studying antimicrobial, antioxidant and anti-inflammatory activities. *Appl Biol Chem,* 65, 35-42.

Alswieleh, A. M., Albahar, H. Y., Alfawaz, A. M., Alsilme, A. S., Beagan, A. M., Alsalme, A. M., Almeataq, M. S. & Alshah, A. (2021) Evaluation of the adsorption efficiency of glycine- iminodiacetic acid - and amino propyl-functionalized silica nanoparticles for the removal of potentially toxic elements from contaminated water solution. *Journal of Nanomaterial*, 1-12.

Ambroz, F., Macdonald, T. J., Martis, V. & Parkin, I. P. (2018). Evaluation of the BET theory for the characterisation of meso and microporous MOFs. *Small Methods,* 2(11), 1-17.

An, Y., Li, S., Huang, X., Chen, X., Shan, H. & Zhang, M. (2022). The Role of Copper Homeostasis in Brain Disease. *International Journal of Molecular Sciences*, 23, 1-23

Andrade, A. L., Diana, M., Souza, M. C., Pereira, J. D., Fabrise, R. & Domingues, Z. (2020a). pH effect on the synthesis of magnetite nanoparticles by the chemical reductionprecipitation method. *Quím. Nova.,* 33(3), 524-527.

Andrade, R. G. D., Veloso, S. R., Castanheira, S. & Elisabete, M. S. (2020b). Shape anisotropic iron oxide-based magnetic nanoparticles: synthesis and biomedical applications. *International Journal of Molecular Sciences.* 21(7), 2455–5433.

Andronic, L., Perniu, D. & Duta, A. (2021). Synergistic effect between TiO_2 sol–gel and degussa P25 in dye photodegradation. *Sol-Gel Sci Technol*, 66, 472–480.

Angelin, K. B., Siva, S. & Kannan, R. S. (2015). Zinc oxide nanoparticles impregnated polymer hybrids for efcient extraction of heavy metals from polluted aqueous solution. *Asian Journal of Science Technology.* 6(12), 2139–2150.

Aniyikaiye, T. E., Oluseyi, T., Odiyo, J. O. & Edokpayi, J. N. (2019). Physico-chemical analysis of wastewater discharge from selected paint industries in Lagos, Nigeria. *International Journal of Environmental Research and Public Health*, 16 (7), 1-17.

Anusa, R., Ravichandran, C. & Sivakumar, E. K. T. (2017). Removal of heavy metal ions from industrial waste water by nano-ZnO in presence of electrogenerated fenton's reagent. *International Journal of ChemTech Research*, 10(7), 501–508.

APHA (2017). *Standard methods for the examination of water and wastewater*. 21st edition, American public health association/american water works association/water environment federation, Washington DC. Pg. 1-297.

Aragaw, T. A., Bogale, F. M. & Aragaw, B. A. (2021). Iron-based nanoparticles in wastewater treatment: A review on synthesis methods, applications, and removal mechanisms. *Journal of Saudi Chemical Society,* 25(8), 1-24.

Araújo, J., Edgar, A., Nobre, F. X., Sousa, G. S., Cavalcante, L. S., Rita, M. C. S. M., Souza, F. L., Elias M. J. M. (2017). Synthesis, growth mechanism, optical properties and catalytic activity of ZnO microcrystals obtained via hydrothermal processing. *RSC. Adv.,* 7(39), 24263–24281.

Arévalo-Cid, P., Isasi, J. & Martín-Hernández, F. (2018). Comparative study of core-shell nanostructures based on amino-functionalized $Fe_3O_4@SiO_2$ and $CoFe_2O_4@SiO_2$ nanocomposites, *Journal of Alloys and Compounds*, 10, 10-16.

Arthi, F. T., Sabeena, G., Sakthi, B. M., Pushpalaksmi, E., Jenson, S. J. & Annadurai, G. (2020). Synthesis and characterisation of ZnO-MMT nanocomposite for antibacterial activity. *Journal of Applied Sciences and Environmental Management*, 24 (6), 1079-1084

Arun, V. B., Nanthi, B., Son, A., Hoang., Prasanthi, S., Manish, K., Lal S., Tahereh, J., Lokesh, P. P., Gurwinder, S., Ajayan, V., Binoy, S. M. B., Kirkham, J. R., Shengsen, W., Hailong, W., Rajasekhar, B. & Kadambot, H. M. S. (2022).Recovery, regeneration and sustainable management of spent adsorbents from wastewater treatment streams: *A review. Science of the total environment*, 822, 153555

Arunima, R. S., Khan, A., Asrar, S., Raza, H., Das, R. K. & Sahu, N. K. (2020). Synthesis of $ZnO/Fe_3O_4/rGO$ nanocomposites and evaluation of antibacterial activities towards E. coli and S. aureus. *IET nanobiotechnology*, *13*(7), 682–687.

Asamoah, R. B., Annan, E., Mensah, B., Nbelayim, P., Apalangya, V., Onwona-Agyeman, B. & Yaya, A. (2020). A Comparative study of antibacterial activity of CuO/Ag and ZnO/Ag nanocomposites. *Advances in Materials Science and Engineering,* 7814324, 1–18

Ashaf, R., Riaz, S., Kayani, Z. N. & Naseem, S. (2015). Effect of calcination on properties of ZnONPs. *Mater Today Proc Part B.,* 2(10), 5468–5472.

Athinarayanan, J., Subbarayan, P. V., Alhazmi, M. & Alshatwi, A. A. (2017). Synthesis and biocompatibility assessment of sugarcane bagasse-derived biogenic silica nanoparticles for biomedical applications. *J Biomed Mater Res Part*, 10,1-10.

Ayawei, N., Ebelegi, A. N. & Wankasi, D. (2017). Modelling and interpretation of adsorption isotherms. *Journal of Chemistry,* 1-11.

Azhar, N. E. Z., Shariffudin, S. S., Salman, M. R., Alrokayan, A. H. & Haseeb, A. K. (2017). Investigation of ZnO nanotetrapods at different evaporation temperatures by thermal-CVD method for OLED applications. *Journal of Mechanical Engineering,* 1(1), 19-29

Aziz, A., Majid, I., G. & Aziz, I. (2020). Photoluminescence effect on phosphorous irradiated zinc oxide (ZnO) nanotetrapods synthesized by simple thermal oxidation method. *Journal of Physics and Its Applications*, 3(1), 107-112.

Aziz, W. J. & Jassim, H. A. (2018). A novel study of pH influence on Ag nanoparticles size with antibacterial and antifungal activity using green synthesis. *World Sci News*, 97, 139–152.

Azizi, S., Shahi, M. M. & Mohamad, R. (2017). Green synthesis of zinc oxide nanoparticles for enhanced adsorption of lead ions from aqueous solutions: equilibrium, kinetic and thermodynamic studies. *Molecules,* 22(6), 1-14.

Azmath, P., Baker, S., Rakshith, D. & Satish, S. (2016). Mycosynthesis of silver nanoparticles bearing antibacterial activity. *Saudi Pharmaceutical Journal,* 24(2), 140–146.

Babadi, N., Tavakkoli, H., Afshari, M. (2018). *Synthesis and* characterisation of nanocomposite $NiFe_2O_4$@SalenSi and its application in efficient removal of Ni (II) from aqueous solution. *Bulletin of the Chemical Society of Ethiopia,* 32(1), 77–. 88.

Badanayak, P. & Vastrad, J. (2021). Impact of pH and Calcination Temperature on Synthesis, Characterization, and Cytotoxicity of Silicon Oxide Nanoparticles. *Silicon*, 14(14),1-1.

Bahrami, K. & Karami, Z. (2018). Core/shell structured $ZnO@SiO_2$ TTIP composite nanoparticles as an effective catalyst for the synthesis of 2-substituted benzimidazoles and benzothiazoles. *Journal of Experimental Nanoscience,* 13(1), 272–283.

Baig, N., Kammakakam, I. & Falath, W. (2021). Nanomaterials: a review of synthesis methods, properties, recent progress, and challenges. *Materials Advances,* 2(6), 1821–1871.

Bakr, E. A., El-Nahass, M. N., Hamada, W. M. & Fayed, T. A. (2021). Facile synthesis of superparamagnetic Fe_3O_4@noble metal core–shell nanoparticles by thermal decomposition and hydrothermal methods: comparative study and catalytic applications. *RSC Adv.,* 11(781), 1-17.

Bakshi, M. S (2015). How surfactants control crystal growth of nanomaterials. *Cryst Growth Des.,* 16(2), 1104–1133.

Balali-Mood, M., Naseri, K., Tahergorabi, Z., Khazdair, M. R. & Sadeghi. M. (2021). Toxic mechanisms of five heavy metals: mercury lead chromium cadmium and arsenic. *Front. Pharmacol,* 12, 1-19.

Bandara, P. C., Peña-Bahamonde, J. & Rodrigues, D. F. (2020) Redox mechanisms of conversion of Cr(VI) to Cr(III) by graphene oxide-polymer composite. *Sci Rep.* 10(1), 1-8.

Bankole, M. T., Abdulkareem, A. S., Tijani, J. O., Ochigbo, S. S., Afolabi, A. S. & Roos, W.D. (2017). Chemical oxygen demand removal from electroplating wastewater by purified and polymer functionalized carbon nanotubes Adsorbents. *Water Resources and Industry* ,18,33–50.

Barbara, R. G., Rafaella, F. N., Nunes, Juliana, B. G., Katia, S., Poça, I. G., Paula, V. B., Silva, H. P. S., Ubirani, B., O. & Marcia, S. (2021). Evaluation of exposure to toluene and xylene in gasoline station workers. *Advances in Preventive Medicine,* 1-10.

Bashir, I., Lone, F. A., Bhat, R. A., Mir, S. A., Dar, Z. A., & Dar, S. A. (2020). Concerns and threats of contamination on aquatic ecosystems. *Bioremediation and Biotechnology: Sustainable Approaches to Pollution Degradation*, 1–26.

Bayuo, J., Abukari, M. A. & Pelig-Ba, K. B. (2020) Desorption of chromium (VI) and lead (II) ions and regeneration of the exhausted adsorbent. *Applied Water Science,* 10(**7**), 1-6.

Benjelloun, M., Miyah, Y., Akdemir Evrendilek, G., Zerrouq, F., & Lairini, S. (2021). Recent advances in adsorption kinetic models: their application to dye types. *Arabian Journal of Chemistry,* 14(4), 1-24.

Berent, K., Komarek, S. Lach, R. Pyda, W. (2019). The effect of calcination temperature on the structure and performance of nanocrystalline mayenite powders. *Materials,* 12(21), 1-11.

Bharati, R. & Suresh, S. (2017). Biosynthesis of ZnO/SiO_2 nanocatalyst with palash leaves' powder for treatment of petroleum refinery effluent. *Resource-Efficient Technologies*, 3, 528–541.

Boles, M. A., Engel, M., & Talapin, D. V. (2016). Self-assembly of colloidal nanocrystals: from intricate structures to functional materials. *Chemical Reviews*, 116(18), 11220–11289.

Borobia, M., Villanueva-Saz, S., Arcaute, M., Fernández, A., Verde, M. T., González, J. M., Navarro, T., Benito, A. A., Arnal, J. L., De las Heras, M. & Ortín, A. (2022). Copper Poisoning, a Deadly Hazard for Sheep. *Animals*, 12, 1-16.

Briffa, J., Sinagra, E. & Blundell, R. (2020). Heavy metal pollution in the environment and their toxicological effects on humans. *Heliyon*, 6(9), 1-20.

Buazar, F, Bavi, M., Kroushawi, F., Halvani, M., Khaledi-Nasab, A., Hossieni, S. A. (2016). Potato extract as reducing agent and stabiliser in a facile green one-step synthesis of ZnONPs. *Journal of Experimental Nanoscience*, 11(3), 175–184.

Bunaciu, A. A., Udriştioiu, E. G. & Aboul-Enein, H. Y. (2015). X-Ray diffraction: Instrumentation and applications. *Critical Reviews in Analytical Chemistry,* 45(4), 289–299.

Byungryul, A. (2020). Cu (II) and As(V) adsorption kinetic characteristic of the multifunctional amino groups in chitosan. *Processes*, 8, 1-15.

Cabello-Ribota, B. S, Farías, R. & Reyes-López, S. Y. (2021). Surface enhanced infrared absorption studies of SiO_2–TiO_2–Ag nanofibers: effect of silver electrodeposition time on the amplification of signals. *Crystals,* 11, 563, 1-19

Cai, Y., Liu, L., Tian., H., Yang, Z. & Luo, Z. (2019). Adsorption and desorption performance and mechanism of tetracycline hydrochloride by activated carbon-based adsorbents derived from sugar cane bagasse activated with $ZnCl_2$. *Molecules,* 24(24), 1-17.

Cao, X., Yang, L., Xue, Q., Fuyu, Y., FanYao, Yang, Y. & Liu, Y. (2020). Antioxidant evaluation-guided chemical profiling and structure-activity analysis of leaf extracts from five trees in *Broussonetia* and *Morus* (Moraceae). *Scientific Report*, 10, 1-14.

Carofiglio, M., Barui, S., Cauda, V. & Laurenti, M. (2020). Doped zinc oxide nanoparticles: synthesis, characterisation and potential use in nanomedicine. *Applied Sciences,* 10(15), 1-43.

Carvalho, A., Costa, R., Neves, S., Oliveira, C. M. & Silva, R. J. N. (2021). Determination of dissolved oxygen in water by the Winkler method: Performance modelling and optimisation for environmental analysis. *Microchemical Journal, 165, 1-9*

Chandramohan, K., Valli, R. & Mageswari, B. (2017). Synthesis and characterisation of zinc nanopartical from luffa acutangula. *International Journal of Scientific Research,* 6(11), 339–340.

Chen, B., Li, L., Liu, L. & Cao J. (2023). Effective adsorption of heavy metal ions in water by sulfhydryl modified nano titanium dioxide. *Front Chem*, 1-10

Chen, G., Liu, F., Ling, Z., Zhang, P., Wei, B. & Zhu, W. (2019). Efficient organic light emitting diodes using solution-processed alkali metal carbonate doped ZnO as electron injection layer. *Front. Chem.* 7, 1-9.

Chen, W., Zhang, Y., Shi, W., Cui, Y., Zhang, Q., Shi, Y. & Liang, Z. (2021). Analysis of Hydrogeochemical Characteristics and Origins of Chromium Contamination in Groundwater at a Site in Xinxiang City, Henan Province. *Applied. Sciences*, 11, 1-15

Chen, Y., Ding, H. & Sun, S. (2017). Preparation and characterisation of ZnO nanoparticles supported on amorphous SiO_2. *Nanomaterials,* 7(8), 1-12.

Cheng, H., Wei, S., Ji, Y., Zhai, J., Zhang, X., Chen, J. & Shen, C. (2019). Synergetic effect of Fe_3O_4 nanoparticles and carbon on flexible poly (vinylidene fluoride) based films with higher heat dissipation to improve electromagnetic shielding. *Composites Part A: Applied Science and Manufacturing.* 121,139–148.

Choi, Y., Baek, S., Kim, J., Choi, J., Hur, J. T., Park, C. & Lee, B. (2017). Characteristics and biodegradability of wastewater organic matter in municipal wastewater treatment plants collecting domestic wastewater and industrial discharge. *Water,* 9(6), 1-11.

Chomchoey, N., Bhongsuwan, D. & Tripob, B. (2018). Effect of calcination temperature on the magnetic characteristics of synthetic iron oxide magnetic nanoparticles for arsenic adsorption. *Chiang Mai J. Sci*, 45(1), 528-539.

Civan, F. (2016). Instrumental and laboratory techniques for characterisation of reservoir rock. *Reservoir Formation Damage,* 593–611.

Claros, M., Setka, M., Jimenez, Y. P. & Vallejos, S. (2020). AACVD Synthesis and Characterisation of Iron and Copper Oxides Modified ZnO Structured Films. *Nanomaterials,* 10(3), 1-16.

Dalod. A. R. M., Grendal, O. G., Skjærvø, S. L., Inzani, K., Selbach, S. M., Henriksen, L., Beek, W. V., Grande, T. & Einarsrud, M. (2017) Controlling oriented attachment and in situ functionalization of TiO2 nanoparticles during hydrothermal synthesis with APTES. *J Phys Chem* 121(21), 11897–11906.

Danesh, N., Mohsen, G. & Azam, M. (2021). Separation of copper ions by nanocomposites using adsorption process. *Scientific Reports,* 11, 1-23

Davidson, C. J., Hannigan, J. H., & Bowen, S. E. (2021). Effects of inhaled combined Benzene, Toluene, Ethylbenzene, and Xylenes (BTEX): Toward an environmental exposure model. *Environmental Toxicology and Pharmacology,* 81, 1-4.

Debnath, B., Waikhom S. S. & Kuntal, M. (2019). Sources and toxicological effects of lead on human health, *Indian Journal of Medical Specialities* ,10(2), 1-7.

Devlekar, B. & Shende, N. P. (2022). Green synthesis of adsorbent nanoflowers for efficient removal of toxins. *Chem. Pap.,* 12, 1-19.

Dhanke, P. & Wagh, S. (2020), Treatment of vegetable oil refinery wastewater with biodegradability index improvement. *Materials Today: Proceedings,* 13, 12-21.

Długosz, O., Szostak, K., Krupiński, M. & Banach, M. (2021). Synthesis of Fe_3O_4/ZnO nanoparticles and their application for the photodegradation of anionic and cationic dyes. *International Journal of Environmental Science and Technology*, 18, 561–574

Droepenu, R. K., Wee, B. S., Chin., S. F., Kok, K. F. Maligan, M. F. (2022). Zinc oxide nanoparticles synthesis methods and its effect on morphology: A review. *Biointerface Research in Applied Chemistry*, 12 (3), 4261 – 4292.

Du, B., Shi, Y. & Liu, Q. (2019). Fabrication of $Fe_3O_4@SiO_2$ nanofluids with high breakdown voltage and low dielectric loss. *Coatings*, 9(11), 716.

Eder, S., Fladischer, K., Yeandel, S. S. R., Yeandel, A., Lelarge, S. C., Parker, E. S. & Holst, B. (2020). A Giant reconstruction of α-quartz (0001) interpreted as three domains of nano dauphine twins. *Scientific Report,* 5, 35-45.

Edet, U. A. & Ifelebuegu, A. O. (2020). Kinetics, isotherms, and thermodynamic modeling of the adsorption of phosphates from model wastewater using recycled brick waste. *Processes, 8*(6), 1-15.

El-Dib, F. I., Mohamed, D. E., El-Shamy, O. A. A., & Mishrif, M. R. (2019). Study the adsorption properties of magnetite nanoparticles in the presence of different synthesized surfactants for heavy metal ions removal. *Egyptian Journal of Petroleum. 29, 1-7.*

Elfeky, A. S., Youssef, H. F. & Elzaref, A. S. (2019). Adsorption of dye from wastewater onto ZnO nanoparticles-loaded zeolite: kinetic, thermodynamic and isotherm studies. *Zeitschrift für Physikalische Chemie*, 234(2), 1-24.

El-Saied, F. A., Abo-Elenan, S. A. & El-shinawy, F. H. (2017). Removal of lead and copper ions from polluted aqueous solutions using nano sawdust particles. *International Journal of Waste Resources*, 7(4), 1-7.

El-Shamy, O. A. A. El-Azabawy, R. E. & El-Azabawy, O. E. (2019). Synthesis and characterisation of magnetite-alginate nanoparticles for enhancement of nickel and cobalt ion adsorption from wastewater. *Journal of Nanomaterials*, 1-8.

Elshypany, R., Selim, H., Zakaria, K., Moustafa, A. H., Sadeek, S. A., Sharaa, S. I. & Nada, A. A. (2021). Elaboration of Fe_3O_4/ZnO nanocomposite with highly performance photocatalytic activity for degradation methylene blue under visible light irradiation. *Environmental Technology & Innovation,* 23, 1-13.

Engku, E. A. G., Matoria, K. A., Saionc, E., Sidek, H. A. A., Zaida, M. H. M. & Alibe, I. M. (2017). Effect of reaction time on structural and optical properties of porous SiO_2 nanoparticle**s**. *Digest Journal of Nanomaterials and Biostructures,* 12(2), 441 – 447.

Faiyas, A.P.A., Vinod, E.M., Joseph, J., Ganesan, R. & Pandey, R. K. (2020). Dependence of pH and surfactant effect in the synthesis of magnetite (Fe_3O_4) nanoparticles and its properties. *Journal of Magnetism and Magnetic Materials,* 322(4), 400–404.

Fan, X., Liu, H., Anang, E. & Ren, D. (2021). Effects of electronegativity and hydration energy on the selective adsorption of heavy metal ions by synthetic NaX zeolite. *Materials* 14, 40-66.

Farahmandjou, M. & Soflaee, F. (2015**).** Synthesis of iron oxide nanoparticles using borohydride reduction. *International Journal of Bio-Inorganic Hybrid Nanomater*ials, 3(4), 203-206.

Fatima, H., Lee, D. W., Yun, H. J. & Kim, K. S. (2018). Shape-controlled synthesis of magnetic Fe_3O_4 nanoparticles with different iron precursors and capping agents. *RSC Advances,* 8(41), 22917–22923.

Fato, F. P., Li, D. Z., Zhao, L., Qiu, K. & Long, Y. (2019). Simultaneous removal of multiple heavy metal ions from river water using ultrafine mesoporous magnetite nanoparticle*s. ACS Omega,* 4(4), 7543–7549.

Fawzia, I. E., Dalia, E., Mohamed, O. E., Marwa, A. A. & Mishrif, R. (2020). Study the adsorption properties of magnetite nanoparticles in the presence of different synthesized surfactants for heavy metal ions removal. *Egyptian Journal of Petroleum*, 29(1), 1-7.

Ferreira, F. V., Franceschi, W., Menezes, B. R. C., Biagioni, A. F., Coutinho, A. R. & Cividanes, L. S. (2019). Synthesis, characterisation, and applications of carbon nanotubes. carbon-based nanofillers and their rubber. *Nanocomposites,* 1–45.

Fidai, R., F., Fen, Y. W., Anuar, M. F., Omar, N. A. S., Zaid, M. H. M., Matori, K. A. & Khaidir, R. E. M. (2021). Synthesis and characterisation of ZnO-SiO_2 composite using oil palm empty fruit bunch as a potential silica source. *Molecules,* 26, 1061.

Fneich, H., Nathalie, G., Stéphane, C., Ahmad, M., & Wilfried, B. (2021). The effect of size and thermal treatment on the photoluminescent properties of europium-doped SiO2 nanoparticles prepared in One Pot by Sol-Gel. *Materials*,14 (7), 1-15

Fu, S., Fang, Q., Li, A., Li, Z., Han, J., Dang, X., & Han, W. (2020). Accurate characterisation of full pore size distribution of tight sandstones by low- temperature nitrogen gas adsorption and high pressure mercury intrusion combination method. *Energy Science & Engineering,* 9(1), 80–100.

Fuentes-García, J. A., Diaz-Cano1, A. I., Guillen-Cervantes, A. & Santoyo-Salazar, J. (2018). Magnetic domain interactions of Fe_3O_4 nanoparticles embedded in a SiO_2 matrix. *Scientific Reports*, 8, 1-10.

Galatage, S. T., Hebalkar, A. S., Dhobale, S. V., Mali, O. R., Kumbhar, P. S., Nikade, S. V., & Killedar, S. G. (2021). *Silver Nanoparticles: Properties, Synthesis,*

Characterisation, Applications and Future Trends. In S. Kumar, P. Kumar, & C. S. Pathak (Eds.), Silver Micro-Nanoparticles - Properties, Synthesis, Characterisation, and Applications. IntechOpen. Vienna, Austria, Pg, 1-50.

Ganapathe, L. S., Mohamed, M. A., Yunus, R. M. & Berhanuddin, D. D. (2020). Magnetite (Fe_3O_4) nanoparticles in biomedical application: from synthesis to surface functionalisation. *Magnetochemistry*, 6, (68), 1-35.

Gankhuyag, S., Bae, D.S., Lee, K. & Lee, S. (2021). One-Pot synthesis of SiO_2@Ag mesoporous nanoparticle coating for inhibition of *escherichia coli* bacteria on various surfaces. *Nanomaterials*, 11(2), 1-10.

Gebretsadik, H., Gebrekidan, A. & Demlie, L. (2020) Removal of heavy metals from aqueous solutions using *Eucalyptus Camaldulensis*: An alternate low-cost adsorbent. *Cogent Chemistry* 6(1), 25-32.

Genchi, G., Sinicropi, M. S., Lauria, G., Carocci, A., & Catalano, A. (2020). The Effects of Cadmium Toxicity. *International Journal of Environmental Research and Public Health,* 17(11),1-24

Geng, X. P., Hsu, C. H., Zhao, M. J. Wu, W. Y., Chiu, Y. J. Lien, S. Y. &Zhu, W. Z. (2022). Effect of water flow rate on properties of zinc oxide thin films prepared using spatial atomic layer deposition. *Thin Solid Films*, 751, 139-229.

Georgaki, M. N., Charalambous, M., Kazakis, N., Talias, M. A., Georgakis, C., Papamitsou, T. & Mytiglaki, C. (2023). Chromium in Water and Carcinogenic Human Health Risk. *Environments*, *10*(2), 1-33.

George, L. Y., Ma, L., Zhang, W. & Yao, G. (2023). Parametric modelling and analysis to optimize adsorption of Atrazine by MgO/Fe_3O_4-synthesized porous carbons in water environment. *Environ Sci Eur* 35 (21) 1-16.

Ghafoor, S. & Ata, S. (2017). Synthesis of carboxyl-modified Fe_3O_4@SiO_2 nanoparticles and their utilization for the remediation of cadmium and nickel from aqueous solution. *Journal of the Chilean Chemical Society,* 62(3), 1-5.

Ghannam, H., Chahboun, A. & Turmine, M. (2019). Wettability of zinc oxide nanorod surfaces. *R Soc Chem Adv.,* 9, 38289–38297.

Gharibshahi, L., Saion, E., Gharibshahi, E., Shaari, A., & Matori, K. (2017). Structural and optical properties of ag nanoparticles synthesized by thermal treatment method. *Materials,* 10(4), 402.

Ghassan, A. A., Mijan, N. & Taufiq-Yap, Y. H. (2019). *Nanomaterials: An Overview of Nanorods Synthesis and Optimization*. In M. S. Ghamsari, & S. Dhara (Eds.), Nanorods and Nanocomposites. IntechOpen. Vienna, Austria, Pg, 1-103.

Ghosh, T. Das, A. B., Jena, B. & Pradhan, C. (2015). Antimicrobial effect of silver zinc oxide (Ag-ZnO) nanocomposite particles, *Frontiers in Life Science*, 8(1), 47-54.

Gisi, S., Lofrano, G., Grassi, M. & Notarnicola, M. (2016) Characteristics and adsorption capacities of low-cost sorbents for wastewater treatment: A review. *Sustainable Materials and Technologies,* 9, 10-40.

Goad, M. A. & Hamad, R. (2017). Synthesis of nano-fillers from local materials by two different methods. *International Journal of Engineering and Information Systems (IJEAIS)*, 1 (5), 14 - 21.

Gonzalez-Pech, N. I. & Grassian, V. H. (2017). Surface chemical functionalities of environmental nanomaterials. Reference module in chemistry. *Molecular Sciences and Chemical Engineering.* 10, 10-16.

Gopal, V. R. V. & Kamila, S. (2017). Effect of temperature on the morphology of ZnONPs: a comparative study. *Appl Nanosci* 7, 75–82.

Goryacheva, I. Y. (2016). Labels for optical immunotests. *In comprehensive analytical chemistry*, 72, 79–131.

Gosiamemang, T. & Heng, J.Y. (2023). Sodium hydroxide catalysed silica sol-gel synthesis: Physicochemical properties of silica nanoparticles and their post-grafting using C8 and C18 alkyl-organosilanes. *Powder Technology*, 417, 1-8.

Guo, T., Bulin, C., Li, B., Zhao, Z., Yu, H., Sun, H., Ge, X., Xing, R., & Zhang, B. (2018). Efficient removal of aqueous Pb (II) using partially reduced graphene oxide-Fe$_3$O$_4$. *Adsorption Science & Technology*, 36(3–4), 1031–1048.

Hajizadeh, Z., Hassanzadeh-Afruzi, F., Jelodar, D. F., Ahghari, M. R. & Maleki, A. (2020). Cu (ii) immobilized on Fe$_3$O$_4$@HNTs–tetrazole (CFHT) nanocomposite: synthesis, characterisation, investigation of its catalytic role for the 1,3 dipolar cycloaddition reaction, and antibacterial activity. *RSC Advances,* 10(44), 26467–26478.

Hajjaoui, H., Soufifi, A., Boumya, W., Abdennouri, M and Barka, N. (2021). polyaniline/nanomaterial composites for the removal of heavy metals by adsorption: A Review. *J. Compos. Sci,* 5(233), 1-22

Hamidreza, S. (2017). Synthesis of nanocomposition of poly acrylic acid/chitosan coated-magnetite nanoparticles to investigation of interaction with BSA and IGG proteins. *International Journal of Nanomaterials, Nanotechnology and Nanomedicine*, 3, 27–33.

Hammood, A. S., Hassan, S. S., Alkhafagy, M. T. & Jaber, H. L. (2019). Effect of calcination temperature on characterisation of natural hydroxyapatite prepared from carp fish bones. *SN Applied Sciences,* 1(5), 1-12.

Han, X., Chen, X., Ma, J., Chen, J., Xie, B., Yin, W., Yang, Y., Jia, W., Xie, D., Huang, F. (2022). Discrimination of Chemical Oxygen Demand Pollution in Surface Water Based on Visible Near-Infrared Spectroscopy. *Water*. 14(19),1-14.

Hasan, M., Ullah, I., Zulfiqar, H., Naeem, K., Iqbal, A., Gul, H., Ashfaq, M. & Mahmood, N. (2018). Biological entities as chemical reactors for synthesis of nanomaterials: progress, challenges and future perspective. *Mater Today Chem* 8, 13–28.

Hassan, M., Liu, Y., Naidu, R., Du, J., Qi, F., Donne, S. W. & Islam, M. M. (2021). Mesoporous biopolymer architecture enhanced the adsorption and selectivity of aqueous heavy-metal ions. *ACS Omega, 6(23), 15316–15331.*

He, J., Han, R., Yu, G., Lavin, M. F., Jia, Q., Cui, P. & Peng, C. (2020). Epimedium Polysaccharide Ameliorates Benzene-Induced Aplastic Anemia in Mice. *Evid Based Complement Alternat Med.* 1-12.

Henderson, C. M. B. (2021). Composition, thermal expansion and phase transitions in framework silicates: revisitation and review of natural and synthetic analogues of nepheline-, feldspar- and leucite-mineral groups". *Solids,* 2(1), 1-49.

Heuer-Jungemann, A., Feliu, N., Bakaimi, I., Hamaly, M., Alkilany, A., Chakraborty, I., Masood, A., Casula, M.F., Kostopoulou, A. & Oh, E. (2019). The role of ligands in the chemical synthesis and applications of inorganic nanoparticles. *Chem. Rev*, 119, 4819–4880.

Hitesh, V. P., Dipeksha, M., Devang, B. K. & Himanshu, S. B. (2020). In-vitro antiglycation activity of zinc oxide nanoparticles synthesized from the bioactive fraction of bambusa arundinacea leaf extract. *Research Journal of Pharmaceutical, Biological and Chemical Sciences*, 11(5), 48-59.

Hodoroaba, V. D. (2020). Energy-dispersive X-ray spectroscopy (EDS). *Characterisation of Nanoparticles,* 397–417.

Honda, M. & Suzuki, N. (2023). Toxicities of polycyclic aromatic hydrocarbons for aquatic animals. *Int J Environ Res Public Health*, 17(4), 1-23.

Hong, J., Kim, M. & Cha, C. (2019). Multimodal carbon dots as biosensors. *Theranostic Bionanomaterials,* 377–400.

Hossain, M. T., Hossain, M. M., Begum, M. H. A., Shahjahan, M., Islam, M. M. & Saha, B. (2018). Magnetite (Fe_3O_4) nanoparticles for chromium removal. *Bangladesh J. Sci. Ind. Res.* 53(3), 219-224.

Hosseini, S. M., Sarsari, I. A., Kameli, P. & Salamati, H. (2015). Effect of Ag doping on structural, optical, and photocatalytic properties of ZnO nanoparticles, *J. Alloys ComPb,* 640, 408-415.

Hu, P., Chang, T., Chen, W., Deng, J., Li, S., Zuo, Y., Kang, L. Yang, F., Hostetter, M. & Volinsky, A. A. (2019). Temperature effects on magnetic properties of Fe_3O_4 nanoparticles synthesized by the sol-gel explosion-assisted method. *Journal of Alloys and Compounds*, 773, 605-611.

Huang, H., Wang, Y., Zhang, Y., Niu, Z. & Li, X. (2020). Amino-functionalized graphene oxide for Cr (VI), Cu (II), Pb (II) and Cd (II) removal from industrial wastewater. *Open Chem*., 18, 97–107.

Huang, X. J., Zeng, X. F., Wang, J. X., Zhang, L. L. & Chen, J. F. (2019). Synthesis of monodispersed ZnO@SiO$_2$ nanoparticles for anti-UV aging application in highly transparent polymer-based nanocomposites. *Journal of Materials Science,* 54(11), 8581–8590.

Hubbe, M. A., Azizian, S. & Douven, S. (2019). Implications of apparent pseudo-second-order adsorption kinetics onto cellulosic materials: A review. *BioRes*., 14(3), 7582-7626.

Hughes, C. B., Brown, D. M. & Camenzuli, L. (2020). Can a chemical be both readily biodegradable AND very persistent Weight-of-evidence determination demonstrates that phenanthrene is not persistent in the environment. *Environ Sci Eur*., 32(14). 1-20.

Hui, C., Shen, C., Yang, T., Bao, L., Tian, J., Ding, H., Li, C. & Gao, H. J. (2018). Large-scale Fe$_3$O$_4$ nanoparticles soluble in water synthesized by a facile method. *J. Phys. Chem. C.* 112:11336–1133.

Ibrahim, A. H., Lyu, X. & ElDeeb, A. B. (2023). Synthesized zeolite based on Egyptian boiler ash residue and kaolin for the effective removal of heavy metal ions from industrial wastewater. *Nanomaterials*, 13, 1-26

Iconaru, S. L., Guégan, R., Popa, C. L., Motelica-Heino, M., Ciobanu, C. S. & Predoi, D. (2016). Magnetite (Fe$_3$O$_4$) nanoparticles as adsorbents for as and Cu removal. *Applied Clay Science,* 134(2), 128-135.

Iftekhar, S., Ramasamy, D. L, Srivastava, V., Asif, M. B. & Sillanpa, M. (2018). Understanding the factors affecting the adsorption of Lanthanum using different adsorbents: a critical review. *Chemosphere* 204, 413–430.

Igbagara, P. W. & Ntekim, J. (2021) Determination of heavy metals concentration in waste water of warri refining and petrochemicals company (WRPC). *Tropical Journal of Science and Technology*, 2(1), 29-37.

Ijaz, I., Gilani, E., Nazir, A. & Bukhari, A. (2020). Detail review on chemical, physical and green synthesis, classification, characterisations and applications of nanoparticles. *Green Chemistry Letters and Reviews*, 13(3), 59–81.

Indramahalakshmi, G. (2017) Characterisation and antibacterial activity of zinc oxide nanoparticles synthesized using *Opuntia ficus indica* fruit aqueous extract. *Asian J Phys Chem Sci,* 3(2), 1–7.

Ismail, A., Saputri, L. N. M. Z., Dwiatmoko, A. A., Susanto, B. H. & Nasikin, M. (2021). A facile approach to synthesis of silica nanoparticles from silica sand and their

application as superhydrophobic material. *Journal of Asian Ceramic Societies,* 9(2), 665–672.

Ivan, R., Kamshat, T., Jiří, J. K. & Kenneth, M. P. (2021). Oil refinery and water pollution in the context of sustainable development: Developing and developed countries. *Journal of Cleaner Production,* 302, 1-13.

Jamal, A., Awad, R. & Yusef, H. (2019) Evaluation of antimicrobial activity of ZnONPs against foodborne pathogens. *Int J Curr Microbiol Appl Sci,* 8(11), 2000–2025.

Jameel, M. S., Azlan, A. & Mohammed, A. (2020) Dheyab green synthesis: proposed mechanism and factors influencing the synthesis of platinum nanoparticles. *Green Processing and Synthesis,* 9(1), 386-398.

Jamshidi, D. & Sazegar, M. R. (2020). Antibacterial activity of a novel biocomposite chitosan/graphite based on zinc-grafted mesoporous silica nanoparticles. *International Journal of Nanomedicine*, 15, 1-8.

Jang, J. N. G., Leong, K. H., Sim, L. C., Oh, W. D., Dai, C. & Saravanan, P. (2020). Environmental remediation using nano-photocatalyst under visible light irradiation: the case of bismuth phosphate. *Nanomaterials for Air Remediation,* 193–207.

Javanbakht, V. & Ghoreishi, S. M. (2017). Application of response surface methodology for optimization of lead removal from an aqueous solution by a novel superparamagnetic nanocomposite. *Adsorption Science & Technology,* 35(1-2), 1-20.

Javed, R. Zia, M. & Naz, S. (2020). Role of capping agents in the application of nanoparticles in biomedicine and environmental remediation: recent trends and future prospects. *J Nanobiotechnol,* 18, 172.

Jeevanandam, J., Barhoum, A., Chan, Y. S., Dufresne, A. & Danquah, M. K. (2018). Review on nanoparticles and nanostructured materials: history, sources, toxicity and regulations. *Beilstein journal of nanotechnology*, 9, 1050–1074.

Jia, C., Zhao, J., Lei, L., Kang, X., Lu, R., Chen, C., Li, S., Zhao, Y., Yang, Q. & Chen, Z. (2019). Novel magnetically separable anhydride-functionalized Fe_3O_4@SiO_2@PEI-NTDA nanoparticles as effective adsorbents: synthesis, stability and recyclable adsorption performance for heavy metal ions. *RSC Advances,* 9(17), 9533–9545.

Jiang, H., Ruihao, L., Yimin, L. & Wei, C. (2022). Recent advances in solid–liquid–gas three-phase interfaces in electrocatalysis for energy conversion and storage. *Wiley Online Library,* 4(4), 1-9

Jibril, A., Jean, M., Bada, S. W. & Oboirien, B. (2020). Equilibria and isosteric heat of adsorption of methane on activated carbons derived from south african coal discards. *ACS Omega* 5, 32530−32539.

Justyna, M. & Eugenia, T. (2018). Toxicity of insecticide carrier solvent: effect of xylene on hemolymph biochemical parameters in blaberus giganteus L. *Polish Journal of Environmental Studies*, 27(5), 2385–2390.

Kac, M, Mis, A., Dubiel, B., Kowalski, K., Zarzycki, A.; Dobosz, I. (2021). Template-assisted iron nanowire formation at different electrolyte temperatures. *Materials*, 14, 1-19

Kalpaklı, Y. K. (2015). Removal of Cu (II) from aqueous solutions using magnetite: A kinetic, equilibrium study. *Advances in Environmental Research,* 4(2), 119-133.

Kamanina, O. A., Saverina, E. A., Rybochkin, P. V., Arlyapov, V. A., Vereshchagin, A. N. & Ananikov, V. P. (2022). Preparation of hybrid sol-gel materials based on living cells of microorganisms and their application in nanotechnology. *Nanomaterials*, 12, 1-34

Kamarulzaman, N., Kasim, M. F. & Chayed, N. F. (2016). Elucidation of the highest valence band and lowest conduction band shifts using XPS for ZnO and Zn0.99Cu0.01O band gap changes. *Results in Physics*, 6, 217-230.

Kamath, S., Gopal, V,, Ramanjaneyalu, V. & Kamila, S. (2019) Application of ZnO nano rods for the batch adsorption of Cr (VI): a study of kinetics and isotherms. *Am J Appl Sci*, 16 (3),1-12.

Kao, M. J., Hsu, F. C. & Peng, D. X. (2019). Synthesis and characterisation of SiO_2 nanoparticles and their efficacy in chemical mechanical polishing steel substrate. *Advances in Materials Science and Engineering*, 1–8.

Karade, V. C., Dongale, T. D., Sahoo, S. C., Kollu, P., Chougale, A. D., Patil, P. S. & Patil, P. B. (2018). Effect of reaction time on structural and magnetic properties of green-synthesized magnetic nanoparticles. *Journal of Physics and Chemistry of Solids,* 120, 161–166.

Kayani, Z. N., Saleemi, F. & Batool, I. (2015). Effect of calcination temperature on the properties of ZnONPs. *Appl Phys*, 119(2), 1-9

Khalil, M. I. (2019). Co-precipitation in aqueous solution synthesis of magnetite nanoparticles using iron (III) salts as precursors. *Arabian Journal of Chemistry,* 8(2), 279–284.

Khan, J. S., Radhakrishnan, A. & Beena, B. (2019). Polyaniline/zinc oxide nanocomposite as a remarkable antimicrobial agent in contrast with PANI and ZnO. *Indian Journal of Advances in Chemical Science*, 6(2), 71-76.

Khan, N. T., Khan, M. J., Jameel, J., Jameel, N. & Rheman, S. U. A. (2017). An overview: biological organisms that serves as nanofactories for metallic nanoparticles synthesis and fungi being the most appropriate. *Bioceram Dev. Appl,* 7, 101.

Kiran, B. L., Seshagiri, R. H., Kishore, P. N. R. & Rami, R. Y. V. (2019). Hydrothermal synthesis of flower-like ZnO-SiO nanocomposites for solar light–induced photocatalysis and anti-bacterial applications. *Materials Research Express,* 1-28.

Kobylinska, N., Klymchuk, D., Shakhovsky, A., Khainakova, O., Ratushnyak, Y., Duplij, V. & Matvieieva, N. (2021). Biosynthesis of magnetite and cobalt ferrite nanoparticles using extracts of "hairy" roots: preparation, characterisation, estimation for environmental remediation and biological application. *RSC Advances,* 11(43), 26974–26987.

Kotsyuda, S. S., Tomina, V. V., Zub, Y. L., Furtat, I. M., Lebed, A. P., Vaclavikova, M. & Melnyk, I. V. (2017). Bifunctional silica nanospheres with 3-aminopropyl and phenyl groups. Synthesis approach and prospects of their applications. *Appl. Surf. Sci*, 420, 782–791.

Krishna, K. A., & Mohan, R. K. (2016). Distribution, correlation, ecological and health risk assessment of heavy metal contamination in surface soils around an industrial area, Hyderabad, India. *Environmental Earth Sciences*, *75*, 1-17.

Kumar, A. S. & Bhatnagar, A. K. (2018). Magnetism from Fe_2O_3 nanoparticles embedded in amorphous SiO_2 matrix. *Applied Nanoscience*, 8, 79–87.

Kumaresan, N. & Ramamurthi, K. (2020). Synthesis of ZnO/rGO nanocomposites by wet impregnation method for photocatalytic performance against RHB Dye and 4-chlorophenol under UV light irradiation. *Journal of Materials Science: Materials in Electronics,* 31(20), 30-39.

Kyomuhimbo, H. D. & Brink, H. G. (2023). Applications and immobilization strategies of the copper-centred *Technol*, 12, 1461–1478.

Ladu, J. L. C., Athiba, A. L., Lako, S. T. V., & Alfred, M. L. (2018). Investigation on the impact of water pollution on human health in Juba County, Republic of South Sudan. *Journal of Environment Pollution and Human Health*, *6*(3), 89-95.

Lanco, H. S., Asadi, M., Zahedi, S. M., Hamzehpour, N., Rasouli, F., Helvacı, M., & Alas, T. (2021). Silicon dioxide-nanoparticle nutrition mitigates salinity in gerbera by modulating ion accumulation and antioxidants. *Folia Horticulturae*, *33*(1), 91-105.

Lasheen, M.R., Ammar, N.S., & Ibrahim, H.S. (2017). Adsorption/desorption of Cd(II), Cu(II) and Pb(II) using chemically modified orange peel: Equilibrium and kinetic studies. *Solid State Sci.,* 14, 202–210.

Lata, S., Prabhakar, R., Adak, A., & Samadder, S. R. (2019). As (V) removal using biochar produced from an agricultural waste and prediction of removal efficiency using multiple regression analysis. *Environmental Science and Pollution Research*, *26*, 32175-32188.

Lawtae, P. & Tangsathitkulchai, C. (2021). The Use of high surface area mesoporous-activated carbon from longan seed biomass for increasing capacity and kinetics of methylene blue adsorption from aqueous solution. *Molecules,* 2, 1-22.

Lazar, O. A., Moise, C. C., Nikolov, A. S., Enache, L. B., Mihai, G. V. & Enachescu, M. (2022). The water-based synthesis of platinum nanoparticles using krf excimer laser ablation. *Nanomaterialsm*, 12, 1-18.

Lee, H. S., Hur, Jin, Hwang, Y. & Shin, H. (2020). A novel procedure of total organic carbon analysis for water samples containing suspended solids with alkaline extraction and homogeneity evaluation by turbidity. *International Journal of Environmental Research and Public Health,* 17(11), 1-13.

Lesiak, B., Kövér, L., Tóth, J., Zemek, J., Jiricek, P., Kromka, A. & Rangam, N. (2018). C sp2 /sp3 hybridisations in carbon nanomaterials − XPS and (X) AES study. *Applied Surface Science,* 452, 223–231.

Li, C., Liu, S., Xu, Y., Ren, T., Guo, Y., Wang, Z., Li, X., Wang, L. & Wang, H. (2022). Controllable reconstruction of copper nanowires into nanotubes for efficient electrocatalytic nitrate conversion into ammonia. *Nanoscale*, 34, 1-18.

Li, T., Yu, Z., Yang, T., Xu, G., Guan, Y. & Guo, C. (2021). Modified Fe3O4 magnetic nanoparticles for COD removal in oil field produced water and regeneration. *Environmental Technology & Innovation,* 23(10), 16-30.

Li, X., He, S., Feng, C., Zhu, Y., Pang, Y., Hou, J., Luo, K. & Liao, X. (2018). Non-competitive and competitive adsorption of Pb^{2+}, Cd^{2+} and Zn^{2+} Ions onto SDS in process of micellar-enhanced ultrafiltration. *Sustainability*, 10, 1-12.

Li, X., Wang, Y., Yin, C. & Yin, Z. (2020). Copper nanowires in recent electronic applications: progress and perspectives. *Journal of Materials Chemistry C*, 8, 849-872.

Li, Y., Qiu, J., Ye, S., Wang, L., Yang, C., Sun, P., & Wang, C. (2017). Facile fabrication of PS/Fe$_3$O$_4$@PANi nanocomposite particles and their application for the effective removal of Cu^{2+}. *New Journal of Chemistry,* 41(23), 14137–14144.

Liosis, C., Papadopoulou, A., Karvelas, E., Karakasidis, T. E. & Sarris, I. E. (2021). Heavy metal adsorption using magnetic nanoparticles for water purifification: A critical review. *Materials*, 14, 1-45.

Liu H, Zhang H, Wang J, & Wei, J. (2020). Effect of temperature on the size of biosynthesized silver nanoparticle: deep insight into microscopic kinetics analysis. *Arab J Chem,* 13(1), 1011–1019.

Liu, J., Zhang, J., Xing, L., Wang, D., Wang, L., Xiao, H., & Ke, J. (2021). Magnetic Fe$_3$O$_4$/attapulgite hybrids for Cd(II) adsorption: Performance, mechanism and recovery. *Journal of Hazardous Materials,* 412, 125-237.

Liu, X., Zhang, J., Huang, X., Zhang, L., Yang, C., Li, E. & Wang, Z. (2022). Heavy metal distribution and bioaccumulation combined with ecological and human health risk evaluation in a typical urban plateau lake, southwest china. *Front. Environ. Sci*., 10, 1-10.

Lshabanat, M., Al-Mufarij, R. S. & Al-Senani, G. M**.** (2016). Study on Adsorption of malachite green by date palm fiber. *Oriental Journal of Chemistry*, 32 (6), 1-6.

Lyu, W., Wu, J., Zhang, W., Liu, Y., Yu, M., Zhao, Y. & Yan, W. (2019). Easy separated 3D hierarchical coral-like magnetic polyaniline adsorbent with enhanced performance in adsorption and reduction of Cr(VI) and immobilization of Cr(III). *Chemical Engineering Journal,* 363, 107-119.

Lyubchik. S., Lyubchik, A., Lygina, O., Lyubchik, S. & Fonsec, I. (2018). Comparison of the thermodynamic parameter's estimation for the adsorption process of the metals from liquid phase on activated carbons. *Thermodynamics - Interaction Studies - Solids Liquids and Gases,* 10, 5772-19514.

Ma, J., Zhu, W., Tian, Y. & Wang, Z. (2016). Preparation of zinc oxide-starch nanocomposite and its application on coating. *Nanoscale Research Letters*, 11, 1-9.

Machín, A., Fontánez, K., Arango, J. C., Ortiz, D., De León, J., Pinilla, S., Nicolosi, V., Petrescu, F.I., Morant, C. & Márquez, F. (2022). One-Dimensional (1D) Nanostructured Materials for Energy Applications. *Materials*, *14* (10), 1-16.

Mahajan, R., Suriyanarayanan, S. & Nicholls, I. A. (2021). Improved solvothermal synthesis of γ-Fe$_2$O$_3$ magnetic nanoparticles for SiO$_2$ coating. *Nanomaterials*, 11, 1-13.

Mahdavi, S., Jalali, M. & Afkhami, A. (2012). Removal of heavy metals from aqueous solutions using F e$_3$O$_4$, ZnO, and CuO nanoparticles. *J Nanopart Res,* 14, 1-18.

Makeen, Y. M., Shan, X., Lawal, M., Ayinla, H. A., Su, S., Yelwa, N. A., Liang, Y., Ayuk, N. E. & Du, X. (2021). Reservoir quality and its controlling diagenetic factors in the Bentiu Formation, Northeastern Muglad Basin, Sudan. *Sci Rep,* 11, 1-13**.**

Malhotra, N, Ger, T. R, Uapipatanaku, B, Huang, J. C, Chen, K. H. & Hsiao, C. D. (2020). Review of Copper and Copper Nanoparticle Toxicity in Fish. *Nanomaterials*. 10(6), 1-28.

Mallakpour, S. & Azimi, F. (2020). Spectroscopic characterisation techniques for layered double hydroxide polymer nanocomposites. *Layered Double Hydroxide Polymer Nanocomposites,* 231–280.

Mallika, N. A., Reddy, A. R. & Reddy, K. V. (2015). Annealing effects on the structural and optical properties of ZnONPs with PVA and CA as chelating agents. *J Adv Ceram.,* 4(2), 123–129.

Malyutin, A. G., Cheng, H., Sanchez-Felix, O. R., Carlson, K., Stein, B. D., Konarev, P. V., Svergun, D. I., Dragnea, B. & Bronstein, L. M. (2015). Coat protein-dependent

behavior of poly (ethylene glycol) tails in iron oxide core virus-like nanoparticles. *ACS Appl Mater Interfaces*. 10, 7(22), 89-98.

Manisalidis, I., Stavropoulou, E., Stavropoulos, A. & Bezirtzoglou, E. (2020). Environmental and health impacts of air pollution: a review. *Frontiers in Public Health*, 8, 2296-2565.

Manjuladevi, M., Anitha, R. & Manonmani, S. (2023). Kinetic study on adsorption of Cr(VI), Ni(II), Cd(II) and Pb(II) ions from aqueous solutions using activated carbon prepared from Cucumis melo peel. *Applied Water Science*, 8, (36), 1-8.

Mansour, A. F., Mansour, S. F. & Abdo, M.A. (2015). Improvement structural and optical properties of ZnO/PVA nanocomposites. *Journal of Applied Physics (IOSR-JAP).*7(2), 60-69.

Manyangadze, M., Chikuruwo, N. M. H., Narsaiah, T. B., Chakra, C. S., Charis, G., Danha, G., & Mamvura, T. A. (2020). *Adsorption of lead ions from wastewater using nano silica spheres synthesized on calcium carbonate templates. Heliyon, 6(11),1-13.*

Manzoor, U., Zaha, F. T., Rafique, S., Moin, M. T. & Mujahid, M. (2015) Effect of synthesis temperature, nucleation time, and postsynthesis heat treatment of ZnONPs and its sensing properties. *J Nanomater*, 11, 48-56.

Maria B., & Andreas, E. (2019). Chapter 1 - Nanostructured thin films–background, preparation and relation to the technological revolution of the 21st century, Editor(s): Maria Benelmekki, Andreas Erbe, *Frontiers of Nanoscience, Elsevier*, 14, 1-34.

Marinescu, L., Ficai, D., Ficai, A., Oprea, O., Nicoara, A.I., Vasile, B. S., Boanta, L., Marin, A., Andronescu, E., Holban, A.-M. (2022). Comparative Antimicrobial Activity of Silver Nanoparticles Obtained by Wet Chemical Reduction and Solvothermal Methods. *Int. J. Mol. Sci. 23*, 1-24.

Martín, D. M., Faccini, M., García, M. & Amantia, D. (2018). Highly efficient removal of heavy metal ions from polluted water using ion-selective polyacrylonitrile nanofibers. *J. Environ. Chem. Eng*, 6, 236–245.

Masjedi-Arani, M., & Salavati-Niasari, M. (2016). *A simple sonochemical approach for synthesis and characterisation of Zn2SiO4 nanostructures. Ultrasonics Sonochemistry, 29, 226–235.*

Masunga, N., Mmelesi, O. K., Kefeni, K. K. & Mamba, B. B. (2019). Recent advances in copper ferrite nanoparticles and nanocomposites synthesis, magnetic properties and application in water treatment: Review. *J Environ Chem Eng*, 7, 103-179

Mathew, B. B., Jaishankar, M., Biju, V. G. & Beeregowda, K. N. (2016) Role of bioadsorbents in reducing toxic metals. *J Toxicol*, 11(1), 20-33.

Mayekar, J., Dhar, V. & Radha, S. (2015). Role of salt precursor in the synthesis of zinc oxide nanoparticles. *Int J Res Eng Technol,* 3(3), 43–45.

Meena, J., Gupta, A., Ahuja, R., Singh, M., Bhaskar, S. & Panda, A. K. (2020). Inorganic nanoparticles for natural product delivery: a review. *Environmental Chemistry Letters,* 1-12.

Meng, C., Zhikun, W., Qiang, L., Chunling, L., Shuangqing, S. & Songqing, H. (2018). Preparation of amino-functionalized $Fe_3O_4@SiO_2$ core-shell magnetic nanoparticles and their application for aqueous Fe^{3+} removal. *Journal of Hazardous Materials*, 341, 198–206.

Meride, Y. & Ayenew, B. (2016). Drinking water quality assessment and its effects on residents health in Wondo genet campus, Ethiopia. *Environ Syst Res,* 5(1), 1-7.

Modi, G. (2015). Zinc oxide tetrapod: a morphology with multifunctional applications advances in natural sciences. *Nanosci Nanotechnol,* 6, 1–8.

Mohamed, E. A. A., Muddathir, A. M. & Osman, M. A. (2020). Antimicrobial activity, phytochemical screening of crude extracts, and essential oils constituents of two *Pulicaria spp.* growing in Sudan. *Sci Rep,* 10**,** 1-8.

Mohamed, E. H., Salah, F. & Shawky, M. H. (2017). Preparation of modified nanoparticles of zinc oxide for removal of organic and inorganic pollutant. *Trends in Applied Sciences Research,* 12, 1-9.

Mohammad, Z.H., Ahmad, F., Ibrahim, S.A. & Zaidi, S. (2022). Application of nanotechnology in different aspects of the food industry. *Discov Food*, 2(12), 1-22.

Mohammadi, F. M. & Ghasemi, N. (2018). Influence of temperature and concentration on biosynthesis and characterisation of zinc oxide nanoparticles using cherry extract. *J Nanostruct Chem*, 8, 93–102.

Mohammadi, L., Rahdar, A., Bazrafshan, E., Dahmardeh, H., Susan, M. A. B. & Kyzas, G.Z. (2020). Petroleum hydrocarbon removal from wastewaters: a review. *Processes*. 8(4), 447.

Mohanakrishna, G., Abu-Reesh, I.M. & Pant, D. (2020). Enhanced bioelectrochemical treatment of petroleum refinery wastewater with Labaneh whey as co-substrate. *Scientific Reports,* 10(1), 1-11.

Moharbi, S. S., Geetha, M., Devi, B. M. & Sangeetha, S. J. (2020). Studies on the removal of copper ions from industrial efuent by Azadirachta indica powder. *Applied Water Science* 10(23), 1-10

Momose, Y., Sakurai, T. & Nakayama, K. (2020). Thermal analysis of photoelectron emission (PE) and x-ray photoelectron spectroscopy (XPS) data for iron surfaces scratched in air, water, and liquid organics. *Applied Sciences,* 10(6), 1-29.

Monárrez-Cordero, B. E., Amézaga-Madrid, P., Leyva-Porras, C. C., Pizá-Ruiz, P. & Miki-Yoshida, M. (2016). Study of the adsorption of arsenic (III and V) by magnetite nanoparticles synthetized via AACVD. *Materials Research,* 19, 103–112.

Mosquera, E., Rojas-Michea, C., Morel, M. Gracia, F., Fuenzalida, V. & Zarate R. A. (2015). Zinc oxide nanoparticles with incorporated silver: structural, morphological, optical and vibrational properties. *Appl. Surf. Sci*. 347, 561-568.

Mouni, L., Belkhiri, L., Bollinger, J. C., Bouzaza, A., Assadi, A., Tirri, A., Dahmoune, F., Madani, K. & Reminie, H. (2018) Removal of methylene blue from aqueous solutions by adsorption on kaolin: kinetic and equilibrium studies. *Appl. Clay Sci*, 153, 38–45.

Moussa, R. S., Mamane, S. O, Habou, I., Alma, M. M. & Natatou, I. (2023). Kinetic, isothermal and thermodynamic modeling of fluoride ion adsorption by raw and activated clays. *GSC Advanced Research and Reviews*, 14(02), 160–173.

Muda, I., Mohammad J. M., Arefeh S., Ali F., Rasha F. O., Masoume T., Najeh A., Shakhawat C. & Majid, F. (2023). Associated health risk assessment due to exposure to BTEX compounds in fuel station workers. *Reviews on Environmental Health*, 9, 1-10.

Munasir, D. A S., Kusumawati, D. H., Putri, N. P., Yulianingsih, A., Sa'adah, I. K. F., Taufiq, A., Hidayat, N., Sunaryono, S. & Supardi, Z. A. I. (2018). Structure analysis of $Fe_3O_4@SiO_2$ core shells prepared from amorphous and crystalline SiO_2 particles IOP conference series, *Materials Science and Engineering,* 367, 1-10.

Musa, M. A. & Idrus, S. (2021). Physical and biological treatment technologies of slaughterhouse wastewater: a review. *Sustainability,* 13(9), 1-20.

Nabata, H., Takagi, M., Saita, K. & Maeda, S. (2020). Computational searches for crystal structures of dioxides of group 14 elements (CO_2, SiO_2, GeO_2) under ultrahigh pressure. *RSC Advances,* 10 (37), 22156–22163.

Nadi, A., Melloul, M., Boukhriss, A., El-Fahime, E., Boyer, D., Hannache, H. & Gmouh, S. (2019). Immobilization of bacillus licheniformis using $Fe_3O_4@SiO_2$ nanoparticles for the development of bacterial bioreactor. *Oriental Journal of Chemistry,* 35(2), 854–862.

Najafifi, M., Yousefifi, Y. & Rafati, A. A. (2012). Synthesis, characterisation and adsorption studies of several heavy metal ions on aminofunctionalized silica nano hollow sphere and silica gel. *Sep. Purif. Technol*, 85, 193–205.

Najafpoor, A., Norouzian-Ostad, R., Alidadi, H., Rohani-Bastami, T., Davoudi, M., Barjasteh-Askari, F. & Zanganeh, J. (2020). Effect of magnetic nanoparticles and silver-loaded magnetic nanoparticles on advanced wastewater treatment and disinfection. *Journal of Molecular Liquids,* 303, 1-7.

Nalwa, K, Thakur A. & Sharma, N. (2017). Synthesis of ZnONPs and its application in adsorption. *Adv Mater Proc.*, 2(11), 697–703.

Nandiyanto, B. D., Risti, R., Rosi, O., Ajeng, S. & Meli, F. (2016). Crystallite sizes on the photocatalytic performance of submicron WO_3 particles asep. *Journal of Engineering Science and Technology*, 15(3), 1506 – 1519.

Nasrollahzadeh, M., Issaabadi, Z., Sajjadi, M., Sajadi, M. & Atarod, M. (2019). Types of nanostructure. *Interface Sci Technol,* 28, 29–80

Nasseh, N., Nasseh, I., Khodadadi, M., Beirami, A. & Kamranifar, M. (2017). The removal of lead from aqueous solution using almond green hull (prunus amygdalus-fascionello) waste material magnetized with Fe_3O_4. *Annals of Military and Health Sciences Research* 5(3), 1-10.

Nguyen, T. T., Ma, H. T., Avti, P., Bashir, M. J. K., Ng, C. A., Wong, L. Y. & Tran, N. Q. (2019). Adsorptive removal of iron using SiO_2 nanoparticles extracted from rice husk ash. *Journal of Analytical Methods in Chemistry,* 1–8.

Nikmah, A., Taufiq, A. & Hidayat, A. (2019). Synthesis and characterisation of Fe_3O_4/SiO_2 nanocomposites. International conference on life sciences and technology. *IOP Conf. Series: Earth and Environmental Science*, 276, 1-10.

Nikolic, M. P., Filipovic, R. & Nikoli, S. S. (2015). Effect of reaction time on formation of silica core/shell particles. *Processing and Application of Ceramics,* 9(4), 209–214.

Nistor, M. A., Muntean, S. G., Ianos, R., Racoviceanu, R., Ianas, C. & Cseh, L. (2021). Adsorption of anionic dyes from wastewater onto magnetic nanocomposite powders synthesized by combustion method. *Appl. Sci.* 11, 1-20.

Norhasyimi, R., Mohd, A. S., Andrei, V. S., Norsuraya, S. I. & Gabriel, S. (2016). Study of calcination temperature and concentration of naoh effect on crystallinity of silica from sugarcane bagasse ash (SCBA). *Rev.Chim*, 67(9), 1-5

Norizan, M. N., Moklis, M. H., Ngah, D., Siti Z., Halim, N. A., Samsuri, A., Mohamad, I. S., Knight, V. F. & Abdullah, N. (2022). Carbon nanotubes: functionalisation and their application in chemical sensors. *RSC Advances,* 10(71), 43704–43732.

NSDWQ (2015). Nigerian Industrial Standard https://rivwamis.riversstate.gov.ng/assets/files/Nigerian-Standard-for-Drinking-Water-Quality-NIS-554-2015.Pbf., 1-28.

Obasi, P. N. & Akudinobi, B. B. (2020). Potential health risk and levels of heavy metals in water resources of lead–zinc mining communities of Abakaliki southeast Nigeria. *Applied Water Science,* 10(184), 1-23.

Ogbomida, E. T., Nakayama, S., Bortey-Sam, N., Oroszlany, B., Tongo, I., Enuneku, A. A., Ogbeide, O., Ainerua, M. O., Fasipe, I. P., Ezemonye, L. I., Mizukawa, H., Ikenaka, Y. & Ishizuka, I. M. (2018). Accumulation patterns and risk assessment of metals and metalloid in muscle and official of free-range chickens, cattle and goat in Benin City, Nigeria. *Ecotoxicol Environ Saf,* 151, 98–108.

Olayebi, O. O. &Adebayo, A. T. (2017). Removal of heavy metals from petroleum refinery effluents using coconut shell-based activated carbon", *Int. J. of Engg. and emerging Scientific Discovery*, 2(2). 2536-7269.

Orodu, V. E. & Alalibo, M. E. (2020). Physicochemical and heavy metal analysis of effluent water from Port Harcourt refinery depot, Nigeria. *Int Aca. J App Biomed Sci.* 1(1), 6-17.

Osman, D. A. M. & Mustafa, M. A. (2015) Synthesis and characterisation of zinc oxide nanoparticles using zinc acetate dihydrate and sodium hydroxide. *J Nanosci Nanoeng*, 1(4), 248–251

Osuoha, J. O. & Nwaichi, E. O. (2019). Physicochemical characterisation of a liquid effluent from a refinery. *J. Appl. Sci. Environ. Manage*, 23(10), 1779-1782.

Ouyang, T. D., Zhuo, Y. Z., Hu, L., Zeng, Q., Hu, Y. & He, Z. (2019). Research on the adsorption behavior of heavy metal ions by porous material prepared with silicate. *Minerals,* 9 (291), 1–16.

Pachl, A., Lendzion-Bieluń, Z., Moszyński, D., Markowska-Szczupak, A., Narkiewicz, U., Wróbel, R. J. Guskos, N. & Żołnierkiewicz, G. (2018). Synthesis and antibacterial properties of Fe_3O_4-Ag nanostructures. *Polish Journal of chemical technology,* 18(4), 110-116.

Palani, G., Arputhalatha, A., Kannan, K., Lakkaboyana, S. K., Hanafiah, M. M., Kumar, V. & Marella, R. K. (2021). Current trends in the application of nanomaterials for the removal of pollutants from industrial wastewater treatment—a review. *Molecules*, 26, 1-16.

Pan, B., Li, Y., Zhang, M., Wang, X., & Iglauer, S. (2020). Effect of total organic carbon (TOC) content on shale wettability at high pressure and high temperature conditions. *Journal of Petroleum Science and Engineering*, 193, 1-8.

Pan. Y., Ding, Q. & Li, B. (2021). Self-adjusted bimetallic zeolitic-imidazolate framework-derived hierarchical magnetic carbon composites as efficient adsorbent for optimizing drug contaminant removal. *Chemosphere,* 263, 1-12.

Panda, H., Tiadi, N., Mohanty, M. & Mohanty, C. R. (2017). Studies on adsorption behavior of an industrial waste for removal of chromium from aqueous solution. *South African Journal of Chemical Engineering,* 23, 132–138.

Pandey, G., Sandhya. S. S. & Hitkari, G. (2018). Synthesis and characterisation of polyvinyl pyrrolidone (PVP)-coated Fe_3O_4 nanoparticles by chemical co-precipitation method and removal of Congo red dye by adsorption process. *International Nano Letters*, 8, 111–121.

Pandey, N., Shukla, S. K. & Singh, N. B. (2017). Water purification by polymer nanocomposites: an overview. *Nanocomposites,* 3(2), 47-66.

Panigrahy, P. N. Priyadarshini, A., Sahoo, M. M., Verma, A. K. Daverey, A. & Sahoo, N. K. (2022). Petroleum Hydrocarbon Catabolic Pathways as Targets for Metabolic Engineering Strategies for Enhanced Bioremediation of Crude-Oil-Contaminated Environments *Environmental Technology & Innovation*, 27, 1-32

Paras, K. Y., Prashant, K., Dharmasanam, R. T., Sudipto, C., Monojit C., Soumya, S. M., Abanti S., Mitch, M. C., C., Chi-Te, L. & Da-Ren, H. (2023). A Review on Low-Dimensional Nanomaterials: Nanofabrication, Characterisation and Applications, *Nanomaterials,* 13(1), 54-63.

Parihar, V., Raja, M. & Paulose, R. (2018). A brief review of structural, electrical and electrochemical properties of zinc oxide nanoparticles. *Rev Adv Mater Sci,* 53, 119–130.

Patel, H. (2021). Review on solvent desorption study from exhausted adsorbent. *Journal of Saudi Chemical Society,* 25(8), 1-11.

Patel, M., Kumar, R., Kishor, K., Mlsna, T., Pittman, C. U. & Mohan, D. (2019). Pharmaceuticals of emerging concern in aquatic systems: chemistry, occurrence, effects, and removal methods. *Chemical Reviews.* 119(6), 3510–3673.

Patel, M., Mishra, S., Verma, R. & Shikha, D. (2022). Synthesis of ZnO and CuO nanoparticles via sol-gel method and its characterisation by using various technique. *Discov Mater.* 2(1), 1-11.

Pawlak, D. A., Ito, M, Oku, M., Shimamura, K. & Fukuda, T. (2020). Interpretation of XPS O (1s) in mixed oxides proved on mixed perovskite crystals. *The Journal of Physical Chemistry B,* 106(2), 504–507.

Pelalak, R., Heidari, Z., Khatami, S. M., Kurniawan, T. A., Marjani, A. & Shirazian, S. (2021). Oak wood ash/GO/Fe_3O_4 adsorption efficiencies for cadmium and lead removal from aqueous solution: Kinetics equilibrium and thermodynamic evaluation. *Arabian Journal of Chemistry* 14(3), 1-17.

Pelicano, C. M., Magdaluyo, E. & Ishizumi, A. (2016). Temperature dependence of structural and optical properties of ZnONPs formed by simple precipitation method. In: *MATEC Web of conferences, published by EDP sciences*, 43, 1–4.

Perera, A. S., Cockcroft, J. K., Trogadas, P., Yu, H., Kapil, N., & Coppens, M. O. (2019). Titanium (IV)-induced cristobalite formation in titanosilicates and its potential impact on catalysis. *Journal of Materials Science. J Mater Sci,* 54**,** 335–345.

Perillo, P. M., Atia, M. N. & Rodríguez, D. F. (2018). Studies on the growth control of ZnO nanostructures synthesized by the chemical method. *Revista Matér*, 23(2), 1–7.

Perveena, R., Shujaat, S., Qureshi, Z., Nawaz, S., Khand, M. I. & Iqbal, M. (2020). Green versus sol−gel synthesis of ZnONPs and antimicrobial activity evaluation against panel of pathogens. *J Mater Res Technol,* 9, 7817–7827.

Phan, C. M. & Nguyen, H. M. (2020). Role of capping agent in wet synthesis of nanoparticles. *Phys Chem A,* 121(17), 3213–3219.

Phelps, P. R., Lee, C. T. A. & Morton, D. M. (2020). Episodes of fast crystal growth in pegmatites. *Nature Communications,* 11(1), 1-10.

Pholosi, A., Naidoo, E. B. & Ofomaja, A. E. (2020). Intraparticle diffusion of Cr(VI) through biomass and magnetite coated biomass: A comparative kinetic and diffusion study. *South African Journal of Chemical Engineering,* 32, 1-17.

Piranloo, F., Bavarsiha, F., Dadashian, S. & Rajabi, M. (2019). Synthesis of core/shell/shell $Fe_3O_4/SiO_2/ZnO$ nanostructure composite material with cubic magnetic cores and study of the photo-degradation ability of methylene blue. *Journal of the Australian Ceramic Society,* 1779.

Prasad, S., Yadav, K. K., Kumar, S., Gupta, N., Cabral-Pinto, M. M. S., Rezania, S. & Alam, J. (2021). Chromium contamination and effect on environmental health and its remediation: A sustainable approaches. *Journal of Environmental Management*, 285, 1-22.

Pudza, M. Y. & Abidin, Z. Z. (2020). A sustainable and eco-friendly technique for dye adsorption from aqueous media using waste from Jatropha curcas (isotherm and kinetic model). *Desalination and Water Treatment*, 182, 365–374.

Purwaningsih, S. Y., Pratapa, S. & Darminto, T. (2016). Synthesis of nanosized ZnO particles by co-precipitation method with variation of heating time. In: *AIP conference proceedings*, 17(1), 1-10.

Pushpanathan, K., Sathya, M., Chitha, M. J., Gowthami, S. & Santhi, R. (2021). Influence of reaction temperature on crystal structure and band gap of ZnONPs. *Mater Manuf Process* 27(12), 1–10.

Qasem, N. A. A., Mohammed, R. H. & Lawal, D. U. (2021). Removal of heavy metal ions from wastewater: a comprehensive and critical review. *NPJ Clean Water,* 4, 1-36.

Qin, Y., Qin, J., Wang, X., Xiao, K., Qi, T., Gao, Y., Zhou, X., Shi, S., Li, J., Gao, J., Zhang, Z., Tan, J., Zhang, Y. & Chen, R. (2022). Measurement report: Investigation of pH- and particle-size-dependent chemical and optical properties of water-soluble organic carbon: implications for its sources and aging processes, Atmos. *Chem. Phys*., 22, 13845–13859.

Quadri, T. W., Olasunkanmi, L. O., Fayemi, O. E., Solomon, M. M. & Ebenso, E. E. (2017). Zinc Oxide Nanocomposites of Selected Polymers: Synthesis, Characterisation, and Corrosion Inhibition Studies on Mild Steel in HCl Solution. *ACS Omega*, 2, 8421−8437

Quintero, Q. C., Acevedo, N., Zapata-Giraldo, J., Botero, L. E., Quintero, J., Zárate-Triviño, D., Saldarriaga, J. & Pérez, V. Z. (2019). Optimization of silver nanoparticle

synthesis by chemical reduction and evaluation of its antimicrobial and toxic activity. *Biomaterials Research,* 23(1), 1-15.

Rahi, A. A., Younis, U., Ahmed, N., Ali, M. A., Fahad., S., Sultan, H., Zarei, T., Danish, S., Taban, S. E., Enshasy, H. A., Tamunaidu, P., Alotaibi, J. M., Alharbi, S. A & Datta, R. (2022). Toxicity of Cadmium and nickel in the context of applied activated carbon biochar for improvement in soil fertility. *Saudi J Biol Sci*. 29(2): 743–750.

Rahi, M. N., Jaeel, A. J. & Abbas, A. J. (2021). Treatment of petroleum refinery effluents and wastewater in Iraq: A mini review. IOP Conference Series: *Materials Science and Engineering,* 1058(1), 1-16.

Raj, S., Trivedi, R. & Soni, V. (2022). Biogenic synthesis of silver nanoparticles, characterisation and their applications a review. *Surfaces*. 5(1), 67-90.

Rajani, B. & Suresh, S. (2017). COD reduction from refi nery wastewater using SiO2 photocatalyst synthesized by wheat husk. *Biosci. Biotech. Res. Comm*. 10(1): 1-5.

Rajeswari, A., Jackcina Stobel Christy, E., Gopi, S., Jayaraj, K. & Pius, A. (2020). Characterisation studies of polymer based composites related to functionalized filler-matrix interface. *Interfaces in Particle and Fibre Reinforced Composites,* 219–250.

Ramezanzadeh, B., Mohamadzadeh Moghadam, M. H., Shohani, N., & Mahdavian, M. (2017). Effects of highly crystalline and conductive polyaniline/graphene oxide composites on the corrosion protection performance of a zinc-rich epoxy coating. *Chemical Engineering Journal, 320, 363–375.*

Ramos-Guivar, J. A., Flores-Cano, D. A. & Caetano P. E. (2021). Differentiating nanomaghemite and nanomagnetite and discussing their importance in arsenic and lead removal from contaminated effluents: A critical review. *Nanomaterials*, 11, 1-31.

Rashid, H., Mansoor, M. A., Haider, B., Nasir, R., Abd, S. B. & Abdulrahman, A. (2019). Synthesis and characterisation of magnetite nano particles with high selectivity using in-situ precipitation method. *Separation Science and Technology,* 1–9.

Ratnawulan, R., Fauzi, A. & Hayati, A. E. S. (2018). Characterisation of silica sand due to the influence of calcination temperature. *IOP Conference Series: Materials Science and Engineering,* 335, 1-6.

Rehana, D., Mahendiran, D., Kumar, R. S. & Rahiman, A. K. (2017). Evaluation of antioxidant and anticancer activity of copper oxide nanoparticles synthesized using medicinally important plant extracts. *Biomed Pharmacother*. 89, 1067-1077.

Restrepo, I., Flores, P., & Rodríguez-Llamazares, S. (2018). Antibacterial nanocomposite of poly (lactic acid) and ZnO nanoparticles stabilized with poly (vinyl alcohol): thermal and morphological characterization. *Polymer-Plastics Technology and Materials*, *58*(1), 105-112.

Revellame, E. D., Fortela, D. L., Sharp, W., Hernandez, R. & Zappi, M. E. (2020). Adsorption kinetic modeling using pseudo-first order and pseudo-second order rate laws: A review. *Cleaner Engineering and Technology,* 1, 1-13.

Riva'i, I., Wulandari, I. O., Sulistyarti, H. & Sabarudin, A. (2018). Ex-Situ Synthesis of Polyvinyl alcohol (PVA)-coated Fe_3O_4 Nanoparticles by Coprecipitation-Ultrasonication Method. *IOP Conference Series: Materials Science and Engineering,* 299, 012065.

Rivera, F. L., Palomares, F. J, H. & Pilar. M, E. (2019). Improvement in heavy metal removal from wastewater using an external magnetic inductor. *Nanomaterials,* 9(11), 1-15.

Rodríguez, C., Tapia, C., Leiva-Aravena, E. & Leiva, E. (2020). Graphene oxide–ZnO nanocomposites for removal of aluminum and copper ions from acid mine drainage wastewater. *International Journal of Environmental Research and Public Health,* 17(18), 6-11.

Ruey, O., H., Iskandar, W. R. E., & Khan, M. R. (2020). Rice Husk Nanosilica Preparation and Its Potential Application as Nanofluids. *Engineered Nanomaterials - Health and Safety*. 1-15.

Ruíz-Baltazar, A., Reyes-López, S. Y., Esparza, R., Estévez, M., Hernández-Martínez, Á., Rosas, G., & Pérez, R. (2015). Synthesis and Characterisation of Bifunctionalα-Fe_2O_3-Ag Nanoparticles. *Advances in Condensed Matter Physics, 1–7.*

Ruszkiewicz, J. A., Pinkas, A., Ferrer, B., Peres, T. V., Tsatsakis, A. & Aschner, M. (2017). Neurotoxic effect of active ingredients in sunscreen products, a contemporary review. *Toxicol Rep*, 4, 245–259.

Ruys, A. (2019). 15-Refractory and other specialist industrial applications of alumina. *Biomed Clin, Appl*, 118, 1-15.

Sabziparvar, N., Saeedi, Y., Nouri, M., Najafi Bozorgi, A. S., Alizadeh, E., Attar, F. & Falahati, M. (2018). Investigating the interaction of silicon dioxide nanoparticles with human hemoglobin and lymphocyte cells by biophysical, computational, and cellular studies. *The Journal of Physical Chemistry B,* 122(15), 4278–4288.

Sadegh, H., Ali, G. A. M., Gupta, V. K., Makhlouf, A. S. H., Shahryari-ghoshekandi, R., Nadagouda, M. N., Sillanpää, M. & Megiel, E. (2017). The role of nanomaterials as effective adsorbents and their applications in wastewater treatment. *J Nanostruct Chem,* 7, 1–14.

Salahudeen, N. (2018). Metakaolinization effect on the thermal and physiochemical propperties of Kankara kaolin," *KMUTNB Int J Appl Sci Technol*, 11(2), 127–135.

Saleem, J., Shahid, U., Hijab, M., Mackey, H. & McKay, G. (2019). Production and applications of activated carbons as adsorbents from olive stones. *Biomass Conv. Bioref*, 9, 775–802.

Salmani, M. H., Zarei, S., Ehrampoush, M. H. & Danaie, S. (2023). Evaluations of pH and high ionic strength solution effect in cadmium removal by zinc oxide nanoparticles. *J Appl Sci Environ Manag* 17(4), 583–593.

Samad, A. U., Alam, M. A., Anis, A., Sherif, E.-S. M., Al-Mayman, S. I., & Al-Zahrani, S. M. (2020). Effect of Incorporated ZnO Nanoparticles on the Corrosion Performance of SiO_2 Nanoparticle-Based Mechanically Robust Epoxy Coatings. *Materials, 13(17), 1-17.*

Samrot, A. V., Sahithya, C. S., Selvarani, A, J., Purayil, S. K. & Ponnaiah, P. (2020). A review on synthesis, characterisation and potential biological applications of superparamagnetic iron oxide nanoparticles. *Current Research in Green and Sustainable Chemistry,* 4, 1-44.

Samson, O., Owalude A. & Tella, C. (2016). Removal of hexavalent chromium from aqueous solutions by adsorption on modified groundnut hull. *Beni-Suef University Journal of Basic and Applied Sciences,* 5, 377–388.

Satish, K., Neeraj, V., Krishna, M. & Santosh, K. K. (2018). Biodegradation of phenol by free and immobilized Candida tropicalis NPB1401. *African Journal of Biotechnology,* 17(3), 1-8.

Saxena, J., Sharma, P. K., Sharma, M. M., Singh, A. & Fu, Y. (2016). Process optimization for green synthesis of silver nanoparticles by *Sclerotinia sclerotiorum* MTCC 8785 and evaluation of its antibacterial properties. *SpringerPlus*, 5(861), 1–10.

Selvarajan, V., Obuobi, S., & Ee, P. L. R. (2020). Silica Nanoparticles—A Versatile Tool for the Treatment of Bacterial Infections. *Frontiers in Chemistry, 8, 1-16.*

Senol, S. D., Yalcin, B., Ozugurlu, E. & Arda, E. L. (2020). Structure, microstructure, optical and photocatalytic properties of Mn doped ZnONPs. *Mater Res Express*, 1(1), 1–18.

Shaba, E. Y., Jacob, J. O., Tijani, J. O. & Suleiman, M. A. T. (2021). A critical review of synthesis parameters affecting the properties of zinc oxide nanoparticle and its application in wastewater treatment. *Applied Water Science,* 11, 1-48.

Shaba, E. Y., Tijani, J. O., Jacob, J. O. & Suleiman, M.A.T. (2022). Simultaneous removal of Cu (II) and Cr (VI) ions from petroleum refinery wastewater using ZnO/Fe3O4 nanocomposite. *J Environ Sci Health A Tox Hazard Subst Environ Eng*. 57(2022), 1146-1167, doi: 10.1080/10934529.2022.2162794.

Shao, X., Wu, Y., Jiang, S., Li, B., Zhang, T., & Yan, Y. (2020). Chiral 3D cdse nanotetrapods. *Inorganic Chemistry. 22, 1-7.*

Sharma , V., Sharma, J.K., Kansay, V., Sharma,D. V., Sharma, A. Kumar, S., Sharma, A.K. & Bera, M.K (2023).The effect of calcination temperatures on the structural and optical properties of zinc oxide nanoparticles and their influence on the photocatalytic degradation of leather dye. *Chemical Physics Impact*, 6, 10096.

Sharma, P., Singh, S. P., Parakh, S. K & Tong, Y. W. (2022). Health hazards of hexavalent chromium (Cr (VI)) and its microbial reduction. *Bioengineered.* 13(3), 4923–4938.

Sharma, S. & Bhattacharya, A. (2020). Drinking water contamination and treatment techniques. *Appl Water Sci,* **7,** 1043–1067

Sharmila, G., Muthukumaran, C., Sangeetha, E., Saraswathi, H., Soundarya, S., & Kumar, N. M. (2019). Green fabrication, characterisation of Pisonia alba leaf extract derived MgO nanoparticles and its biological applications. *Nano-Structures & Nano-Objects, 20, 1-10.*

Shehzad, K., Xu, Y., Gao, C. & Duan, X. (2016). Three-dimensional macro-structures of two-dimensional nanomaterials. *Chemical Soc. Rev,* 20, 1-48.

Shen, L, Li B, Qiao, Y. & Song, J. (2019). Monodisperse Fe_3O_4/SiO_2 and $Fe_3O_4/SiO_2/PPy$ Core-shell composite nanospheres for IBU loading and release. *Materials.* 1-15.

Shende, P., Kasture, P. & Gaud, R. S. (2018). Nanoflowers: the future trend of nanotechnology for multi-applications, artificial cells. *Nanomed Biotechnol.,* 46, 413–422.

Shimoshige, H., Nakajima, Y., Kobayashi, H., Yanagisawa, K., Nagaoka, Y. & Shimamura, S. (2017). Formation of core-shell nanoparticles composed of magnetite and samarium oxide in magnetospirillum magneticum strain RSS-1. *PLoS ONE*, 12(1), e0170932.

Shirley, B. & Jarochowska, E. (2022). Chemical characterisation is rough: the impact of topography and measurement parameters on energy-dispersive X-ray spectroscopy in biominerals. *Facies* 68, 1-15.

Shirsath, D. S., & Shirivastava, V. S. (2019). Adsorptive removal of heavy metals by magnetic nanoadsorbent: an equilibrium and thermodynamic study. *Applied Nanoscience,* 5(8), 927–935.

Shokrollahi, A., & Zamani, R. (2019). Synthesis of $Fe_3O_4@SiO_2$ magnetic nanoparticle, functionalized with 2,6-pyridine dicarboxylic acid. *Inorganic and Nano-Metal Chemistry,* 49:5, *1–5.*

Shrestha, B., Wang, L., Zhang, H., Hung, C. Y. & Tang, L. (2020). Gold nanoparticles mediated drug-gene combinational therapy for breast cancer treatment. *International Journal of Nanomedicine,* 15, 8109–8119.

Siddeeg, S. M., Tahoon, M. A., Mnif, W. & Ben, R. F. (2020). Iron oxide/chitosan magnetic nanocomposite immobilized manganese peroxidase for decolorization of textile wastewater. *Processes*, 8, 5-10.

Sierra, M. J., Herrera, A. P. & Ojeda, K. A. (2018). Synthesis of zinc oxide nanoparticles from mango and soursop leaf extracts. *Contemp Eng Sci,* 11(8), 395–403.

Şimşek, R., Çiftci, B. & Uysal, Y. (2020). An experimental study on the efficiency of chromium (vi) removal with starch-magnetite nanocomposite (Starch@MNPs). *Eskişehir Technical University Journal of Science and Technology A - Applied Sciences and Engineering*, 21 (2), 322-334.

Singh, J., Yadav, P., Pal, A. K. & Mishra, V. (2018). Water pollutants: origin and status. *Sens Water Pollut Monit Role Mater*, 671, 1-15.

Singh, P. K., Gautam, A., Verma, V., Singh, P. M., Shivapriya, S., Shivalkar, A. K., Sahoo, S. & Kumar, A. (2020). Green synthesis of metallic nanoparticles as effective alternatives to treat antibiotics resistant bacterial infections: A review. *Biotechnology Reports*, 25, 1-11.

Singh, R. P., Hudiara, I. S. & Rana, S. B. (2016). Effect of calcination temperature on the structural, optical and magnetic properties of pure and Fe-doped ZnO nanoparticles. *Materials Science-Poland*, 34(2), 451-459.

Singh, Y. P., Abhishek, S. & Pawar, J. (2017). Characterisation of silica nano-particles synthesized by thermo-mechanical route. *International Journal of Advanced Research in Sciences and Engineering*, 6(5), 267-272.

Sinha, P., Datar, A., Jeong, C., Deng, X., Chung, Y. G. & Lin, L. (2019). Surface area determination of porous materials using the brunauer-emmett-teller (BET) method: limitations and improvements. *The Journal of Physical Chemistry,* 1-39

Skripkina, T., Podgorbunskikh, E., Bychkov, A. & Lomovsky, O. (2020). Sorption of methylene blue for studying the specific surface properties of biomass carbohydrates. *Coatings,* 10(11), 1-10

Slatni, I., Elberrichi, F. Z., Duplay, J., Fardjaoui, N. E., Guendouzi, A., Guendouzi, O., Gasmi, B., Akbal, F. & Rekkab, L. (2020). Mesoporous silica synthesized from natural local kaolin as an effective adsorbent for removing of Acid Red 337 and its application in the treatment of real industrial textile effluent. *Environmental Science and Pollution Research*, 205, 1-16.

Smolkova, I. S., Kazantseva, N. E., Babayan, V., Pizurova, N. J. V. & Saha, P. (2017). The role of diffusion-controlled growth in the formation of uniform iron oxide nanoparticles with a link to magnetic hyperthermia. *Cryst Growth Des,* 17(5), 2323–2332

Sobhanardakani, S. & Zandipak, R. (2017). Synthesis and application of TiO2/SiO2/Fe3O4 nanoparticles as novel adsorbent for removal of Cd(II), Hg(II) and Ni(II) ions from water samples. *Clean Technologies and Environmental Policy,* 19(7), 1913–1925.

Stoller, M. & Ochando-Pulido, J. M. (2020). ZnO nano-particles production intensification by means of a spinning disk reactor. *Nanomaterials,* 10(7), 1-15.

Subramanian, K. R. (2018). The crisis of consumption of natural resources. *Int J Recent Innov Acad Res,* 2(4), 8–19.

Sultana, S., Islam, K., Hasan, M. A., Khan, H. J., Khan, M. A. R., Deb, A. & Rahman, M. W. (2022). Adsorption of crystal violet dye by coconut husk powder: isotherm, kinetics and thermodynamics perspectives. *Environmental Nanotechnology, Monitoring & Management*, *17*, 100651.

Sun, Y., Yu, Y. & Zheng, X. (2021). Magnetic focculation of Cu(II) wastewater by chitosan-based magnetic composite focculants with recyclable properties. *Carbohydr Polym* 261, 117891.

Suppiah, D. D., & Johan, M. R. (2018). Influence of solution pH on the formation of iron oxide nanoparticles. *Materials Research Express,* 53-64.

Suvaci, E. & Özel, E. (2020). Hydrothermal Synthesis. *Reference Module in Materials Science and Materials Engineering*, 2, 67-72.

Syukor, A. R., Sulaiman, S., Chandrakant, J. P., Mishra, P., Nasrullah, M., Singh, L. & Zularism, A. W. (2021). Energy generation from fish-processing waste using microbial fuel cells. *Delivering Low-Carbon Biofuels with Bioproduct Recovery,* 101–121.

Tamjidi, S., Esmaeili, H. & Kamyab, M. B. (2019). Application of magnetic adsorbents for removal of heavy metals from wastewater: a review study. *Mater Res Express,* 6, 1-14.

Tan, W. K., Muto, H., Kawamura, G., Lockman, Z. & Matsuda, A. (2021). Nanomaterial fabrication through the modification of sol–gel derived coatings. *Nanomaterials,* 11(1), 181.

Taufiq, A., Nikmah, A., Hidayat, A., Sunaryono, S., Mufti, N., Hidayat, N. & Susanto, H. (2020). Synthesis of magnetite/silica nanocomposites from natural sand to create a drug delivery vehicle. *Heliyon,* 6(4), 3784.

Tavares-Dias, M. (2021). Toxic, physiological, histomorphological, growth performance and antiparasitic effects of copper sulphate in fish aquaculture. *Aquaculture, 535, 1-29*

Tavassoli, N., Ansari, R. & Mosayebzadeh, Z. (2017). Synthesis and application of iron oxide/silica gel nanocomposite for removal of sulfur dyes from aqueous solutions. *Arch Hyg Sci*, 6(2), 214-220.

Tchanang, G., Djangang, C. N., Abi, C. F., Moukouri, D. L. M., & Blanchart, P. (2021). Synthesis of reactive silica from kaolinitic clay: Effect of process parameters. *Applied Clay Science, 207, 106087.*

Thakar, M. A., Saurabh, S., Phasinam, K. Manne, R., Qureshi, Y. & Babu V.V.H. (2021). Materials Today: Proceedings X ray diffraction (XRD) analysis and evaluation of

antioxidant activity of copper oxide nanoparticles synthesized from leaf extract of Cissus vitiginea. *Mater. Today Proc*, 1-6.

Tijani, J. O., Aminu1, U. A., Bankole, M. T., Ndamitso, M. M. & Abdulkareem, A. S. (2019). Adsorptive and photocatalytic properties of green synthesized ZnO and ZnO/NiFe$_2$O$_4$ nanocomposites for tannery wastewater treatment. *Nigerian Journal of Technological Development,* 17(4), 312-322.

Toledo, R.C., Arce, G.L.A.F., Carvalho, J. A., Jr. & Ávila, I. (2023). Experimental development of calcium looping carbon capture processes: an overview of opportunities and challenges. *Energies*, 16, 1-16.

Tolulope, E., Aniyikaiye, T. O., John, O. O. & Joshua, N. E. (2019). Physico-chemical analysis of wastewater discharge from selected paint industries in Lagos, Nigeria. *International journal of environmental research and public health*, 16(7), 1-17.

Tourné-Péteilh, C., Robin, B., Lions, M., Martinez, J., Mehdi, A., Subra, G. & Devoisselle, J. M. (2018) Combining sol–gel and microfluidics processes for the synthesis of protein-containing hybrid microgels. *Chem Commun,* 55, 13112–13115.

Tracy, S. J., Turneaure, Stefan J., Duffy, Thomas S. (2020). Structural response of ±-quartz under plate-impact shock compression. *Science Advances,* 6(35), 1-9.

Tsegaye, F., Taddesse, A. M., Teju, E. & Aschalew, M. (2020). Preparation and sorption property study of Fe$_3$O$_4$/Al$_2$O$_3$/ZrO$_2$ composite for the removal of cadmium, lead and chromium ions from aqueous solutions. *Bulletin of the Chemical Society of Ethiopia,* 34(1), 1-17.

Tunega, D., Gerzabek, M. H., Haberhauer, G., Lischka, H. S., Roland, A. & Adelia, J. A. (2020). Adsorption process of polar and nonpolar compounds in a nanopore model of humic substances. *European Journal of Soil Science,* 71, 845–855.

Ubaid, A., Hidayat, N. & Munasir. (2017). Aging time effect on porous characteristics of natural mud-based silica prepared by hydrothermal-coprecipitation route. *IOP Conference Series: Materials Science and Engineering,* 202, 1-7

Uduakobong, A. E. & Augustine O. I. (2020). Kinetics, isotherms, and thermodynamic modeling of the adsorption of phosphates from model wastewater using recycled brick waste. *Processes*, 8, 1-15.

Ul-Haq, A. N., Nadhman, A., Ullah, I., Mustafa, G., Yasinzai, M, & Khan, I. (2017) Synthesis approaches of zinc oxide nanoparticles: the dilemma of ecotoxicity. *J Nanomater*, 42, 1–14.

Ullah, Z., Rashid, A., Ghani, J., Nawab, J., Zeng, X. C., Shah, M., Alrefaei, A. F., Kamel, M., Aleya, L., Abdel-Daim, M. M. & Iqbal, J. (2022). Groundwater contamination through potentially harmful metals and its implications in groundwater management. *Front. Environ. Sci*. 10, 1-13

Ulya, N. H., Taufiq, A. & Sunaryono. (2019). Comparative structural properties of nanosized ZnO/Fe3O4 composites prepared by sonochemical and sol-gel methods. *IOP Conference Series: Earth and Environmental Science,* 276, 1-10

Vanichvattanadecha, C., Singhapong, W. & Jaroenworaluck, A. (2020). Different sources of silicon precursors influencing on surface characteristics and pore morphologies of mesoporous silica nanoparticles. *Applied Surface Science,* 513, 1-14.

Varghese, J. R., Sakho, E., Hadji M., Parani, S., Thomas, S., Oluwafemi, O. S. & Wu, J. (2019). Introduction to nanomaterials: synthesis and applications. *Nanomaterials for Solar Cell Applications,* 75–95.

Velmurugan, P., Shim, J., Lee, K. J., Cho, M., Lim, S. S., Seo, S. K., Cho, K. M., Bang, K. S. & Oh, B. T. (2015). Extraction, characterisation, and catalytic potential of amorphous silica from corn cobs by sol-gel method. *Journal of Industrial and Engineering Chemistry,* 29, 1-6.

Velsankar, K., RM, A. K., Preethi, R., Muthulakshmi, V., & Sudhahar, S. (2020). Green synthesis of CuO nanoparticles via Allium sativum extract and its characterizations on antimicrobial, antioxidant, antilarvicidal activities. *Journal of Environmental Chemical Engineering*, *8*(5), 104123.

Villegas, L. G. C., Mashhadi, N., Chen, M., Mukherjee, D., Taylor, K E. & Biswas, N. (2016). A short review of techniques for phenol removal from wastewater. *Current Pollution Reports,* 2(3), 157–167.

Virgen, M. R. M., Vázquez, O. F. A., Hernández, V., Montoya, H. V. & Gómez, R. T. (2018). Removal of heavy metals using adsorption processes subject to an external magnetic field intechopen doi: 10.5772/intechopen.74050. retriceived from: https://www.intechopen.com/books/heavy-metals/removal-of-heavy-metals-using-adsorption-processes-subject-to-an-external-magnetic-field

Wang, B., Jingming Lan, Chunmiao Bo, Bolin Gong and Junjie Ou (2023). Adsorption of heavy metal onto biomass-derived activated carbon: review. *RSC Advances*,13, 4275-4302.

Wang, Q., Zhu, S., Xi, C. & Zhang, F. (2022). A review: adsorption and removal of heavy metals based on polyamide-amines composites. *Frontiers in chemistry*, 10, 814643.

Westen, T. V. & Groot, R. D. (2018). Effect of temperature cycling on ostwald ripening. *Cryst Growth Des* 8(9), 4952–4962.

Whatley, C.R., Wijewardane, N.K., Bheemanahalli, R. Bheemanahalli, R., Reddy K. R. & Lu, Y. (2023). Effects of fine grinding on mid-infrared spectroscopic analysis of plant leaf nutrient content. *Sci Rep.* 13, 1-12.

WHO (2017). Guidelines for drinking-water quality 4th edition incorporating the 1st addendum. https://www.who.int/publications/i/item/9789241549950.

Wilk, A., Romanowski, M. & Wiszniewska, B. (2021). Analysis of cadmium mercury and lead concentrations in erythrocytes of renal transplant recipients from Northwestern Poland. *Biology* 10(1), 1-62.

Wise, J. P. J., Young, J. L., Cai, J. & Cai, L. (2022). Current understanding of hexavalent chromium (Cr(VI)) neurotoxicity and new perspectives. *Environ Int*. 4, 1-42.

Wokoma, O. A. F. & Edori, O. S. (2017). Heavy metals content of an oily wastewater effluent from an oil firm at the point of discharge. *International Journal of Chemistry, Pharmacy & Technology,* 2(4), 154-161.

Wongbunmak, A., Khiawjan, S., Suphantharika, M., Pongtharangkul, T. (2020). BTEX biodegradation by *Bacillus amyloliquefaciens* subsp. *plantarum* W1 and its proposed BTEX biodegradation pathways. *Sci Rep,* 10, 17408

Worawong, A., Jutarosaga, T. & Onreabroy, W., (2016). Influence of calcination temperature on synthesis of magnetite (Fe_3O_4) nanoparticles by sol-gel method. *Advanced Materials Research*, 979, 208-211.

Wu, Q., Miao, W., Zhang, Y., Gao, H. & Hui, D (2020). "Mechanical properties of nanomaterials: A review" Nanotechnology Reviews, 9(1), 259-273

Xie, J., Lin, Y., Li, C., Wu, D. & Kong, H. (2019). Removal and recovery of phosphate from water by activated aluminum oxide and lanthanum oxide. *Powder Technol*, 269, 351–357.

Xie, S., Wen, Z., Zhan, H. & Jin, M. (2018). An experimental study on the adsorption and desorption of Cu(II) in silty clay. *Geofluids,* 1-12

Xiong, G., Jia, J., Zhao, L., Liu, X., Zhang, X., Liu, H. & Zhou, W. (2020). Non-thermal radiation heating synthesis of nanomaterials. *Science Bulletin*. 10, 22-30.

Xu, J., Jin, G., Mo, Y., Tang, H. & Li, L. (2020). Assessing anthropogenic impacts on chemical and biochemical oxygen demand in different spatial scales with bayesian networks. *Water* 12(1), 1-19.

Xu, P., Zeng, G. M., Huang, D. L., Yan, M., Chen, M., Lai, C. & Wan, J. (2017). Fabrication of reduced glutathione functionalized iron oxide nanoparticles for magnetic removal of Pb (II) from wastewater. *Journal of the Taiwan Institute of Chemical Engineers*, 71, 165-173.

Yahia, L., & Mireles, L. K. (2017). *X-ray photoelectron spectroscopy (XPS) and time-of-flight secondary ion mass spectrometry (ToF SIMS). Characterisation of Polymeric Biomaterials, 83–97.*

Yang, S., Li, G., Qu, C., Wanga, G. & Wanga, D. (2017). Simple synthesis of ZnO nanoparticles on N-doped reduced graphene oxide for the electrocatalytic sensing of L-cysteine. *Royal Society of Chemistry Advance*. 7, 35004–35011.

Yap, C.K., Al-Mutairi, K.A. (2022). Copper and Zinc Levels in Commercial Marine Fish from Setiu, East Coast of Peninsular Malaysia. *Toxics*, 10(52), 1-20.

Yee, T. Y. & Fatehah, M. O. (2017). Characterization and Transformation of Silicon Dioxide Nanoparticles in Aqueous Suspensions: Influence of pH. *Iranian Journal of Energy and Environment* 8(4), 262-268.

Yin, I. X., Z. J., Zhao, I. S., Mei, M. L., Li, Q. & Chu, C. H. (2020). The antibacterial mechanism of silver nanoparticles and its application in dentistry. *International journal of nanomedicine*, 15, 2555–2562.

You, J., Wang, L., Zhao, Y. & Bao W (2021). A review of amino-functionalized magnetic nanoparticles for water treatment: Features and prospects. *J. Clean Prod,* 281, 124-668.

Younas, F., Mustafa, A., Farooqi, Z. U. R., Wang, X., Younas, S., Mohy-Ud-Din, W., Ashir Hameed, M., Mohsin Abrar, M., Maitlo, A. A. & Noreen, S. (2021). Current and emerging adsorbent technologies for wastewater treatment: trends limitations and environmental implications. *Water,* 13, 215.

Yu, H., & Dong, Y. (2016). Investigation of ZnO nanostructures synthesized from different zinc salts. *ChemXpress*, *9*(1), 091-097.

Yu, X. P., X. P., Zhang, Z., Pu, L, Tang, T, & Guo, F., (2021). Breast cancer overall-survival can be predicted with a 19 lncrna tissue signature. *Eur. J. Gynaecol. Oncol.* 42 (5), 838–843.

Yusoff, N., Ho, L., Ong, S., Wong, Y., Khalik, W. & Ridzwan, M. F. (2020). Enhanced photodegradation of phenol by ZnO nanoparticles synthesized through sol-gel method. *Sains Malaysiana*, 46(12), 2507–2514.

Yuvaraja, G., Prasad, C., Vijaya, Y. & Subbaiah, M. V. (2019). Application of ZnO nanorods as an adsorbent material for the removal of As(III) from aqueous solution: kinetics, isotherms and thermodynamic studies. *Int J Ind Chem* 9, 17–25.

Zahoor, M., Nazir, N., Iftikhar, M., Naz, S., Zekker, I., Burlakovs, J., Uddin, F., Kamran, A.W., Kallistova, A. & Pimenov, N., (2021). A review on silver nanoparticles: classifification, various methods of synthesis, and their potential roles in biomedical applications and water treatment. *Water*, 13, 2216, 1-28

Zainal, N. A., Shukor, S. R. B., Azwana, H. &Wab, K. A. R. (2021). Study on the effect of synthesis parameters of silica nanoparticles entrapped withrifampicin. *Chemical Engeering Transactions*, 32, 2245 - 2250**.**

Zaky, M. G., Elbeih, A. & Elshenawy, T. (2021). Review of nano-thermites: a pathway to enhanced energetic materials central. *European Journal of Energetic Materials*. 18(1), 63-85.

Zand, A.D. & Abyaneh, M.R. (2020). Adsorption of lead, manganese, and copper onto biochar in landfill leachate: implication of non-linear regression analysis. *Sustain Environ Res* 30**,** 18, 1-13

Zelepukin, I. V., Shipunova, V. O., Mirkasymov, A. B., Nikitin, P. I., Nikitin, M. P. & Deyev, S. M. (2017). Synthesis and characterisation of hybrid core-shell Fe3 O4 /SiO2 nanoparticles for biomedical applications. *Acta naturae*, 9 (43), 1-8.

Zenkovets, G. A., Shutilov, A. A., Bondareva, V. M., Sobolev, V. I., Marchuk, A., Tsybulya, S. V., Prosvirin, I. P., Ishchenko, A. & Gavrilov, V. Y. (2020). New multicomponent MoVSbNbCeOx/SiO$_2$ catalyst with enhanced catalytic activity for oxidative dehydrogenation of ethane to ethylene. *ChemCatChem,* 1-16.

Zhang, C., Xie B., Zou, Y., Zhu, D., Lei, L., Zhao, D., Nie, H. (2018). Zerodimensional, one-dimensional, two-dimensional and threedimensional biomaterials for cell fate regulation. *Adv Drug Deliv Rev,* 132:33–56.

Zhang, G., Xiao, X., Li, B., Gu, P., Xue, H., & Pang, H. (2017). Transition metal oxides with one-dimensional/one-dimensional-analogue nanostructures for advanced supercapacitors. *Journal of Materials Chemistry A, 5(18), 8155–8186.*

Zhang, J., Lin, S., Han, M., Su, Q., Xia, L., & Hui, Z. (2020a). Adsorption properties of magnetic magnetite nanoparticle for coexistent Cr (VI) and Cu (II) in mixed solution. *Water*, *12*(2), 1-46.

Zhang, M., Yin, Q., Ji, X., Wang, F., Gao, X. & Zhao, M. (2020b). High and fast adsorption of Cd(II) and Pb(II) ions from aqueous solutions by a waste biomass based hydrogel. *Scientific Reports,* 10(1), 1-13.

Zhao, M., Huang, L., Arulmani, S.R.B., Yan, J., Wu, L., Wu, T., Zhang, H. & Xiao, T. (2022). Adsorption of Different Pollutants by Using Microplastic with Different Influencing Factors and Mechanisms in Wastewater: A Review. *Nanomaterials,* 12, (13), 1-22.

Zhou, Y. Wang, K. Wang, B. Pu, Y. & Zhang, J. (2020). Occupational benzene exposure and the risk of genetic damage: a systematic review and meta-analysis. *BMC Public Health*, 20(1), 1-11.

Zia-ur-Rehman, M., Naeem, A., Khalid, H., Rizwan, M., Ali, S., & Azhar, M. (2018). Responses of plants to iron oxide nanoparticles. *Nanomaterials in Plants, Algae, and Microorganisms*, 221–238.

Ziółkowska, M., Milewska-Duda, J. & Duda, J. T. (2017). Effect of adsorbate properties on adsorption mechanisms: computational study. Adsorption 22, 589–597.

Zohrevand, A., Ajji, A. & Mighri, F. (2015). Microstructure and properties of porous nanocomposite films: effects of composition and process parameters. *Polymer International,* 63(12), 2052–2060.

Zulfiqar, U., Subhani, T., & Husain, S. W. (2016). Synthesis and characterisation of silica nanoparticles from clay. *Journal of Asian Ceramic Societies*, 4(1), 91–96.

Appendix
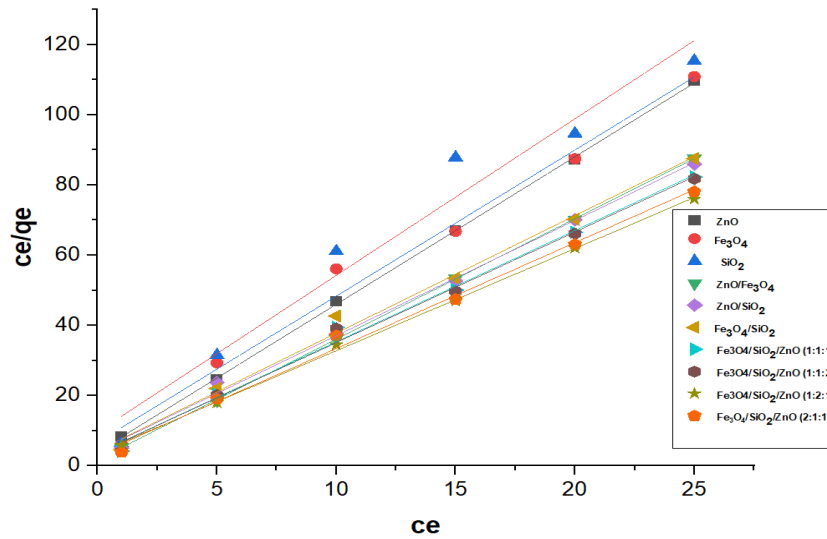
Appendix 1: Plot of log (q$_e$/C$_e$) against C$_e$ for Pb (II)
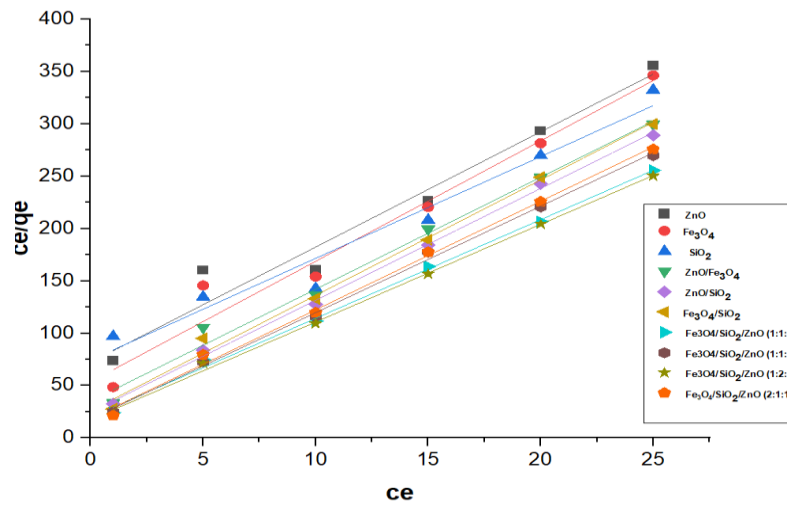
Appendix 2: Plot of log (q$_e$/C$_e$) against C$_e$ for Cd (II)
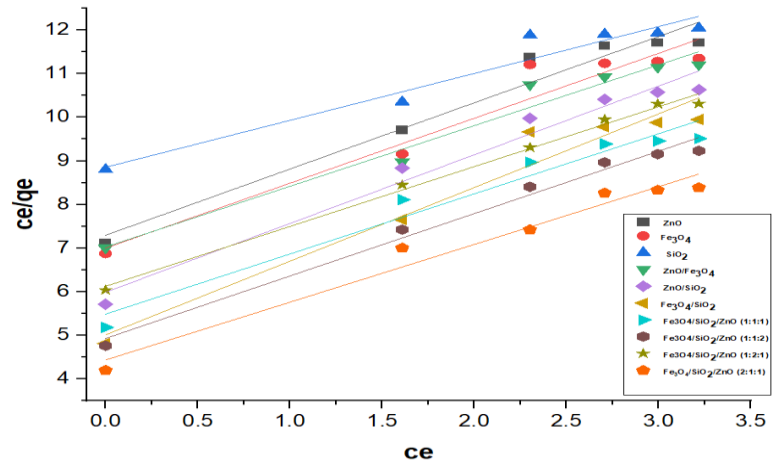
Appendix 3: Plot of log (q$_e$/C$_e$) against C$_e$ for Ni (II)
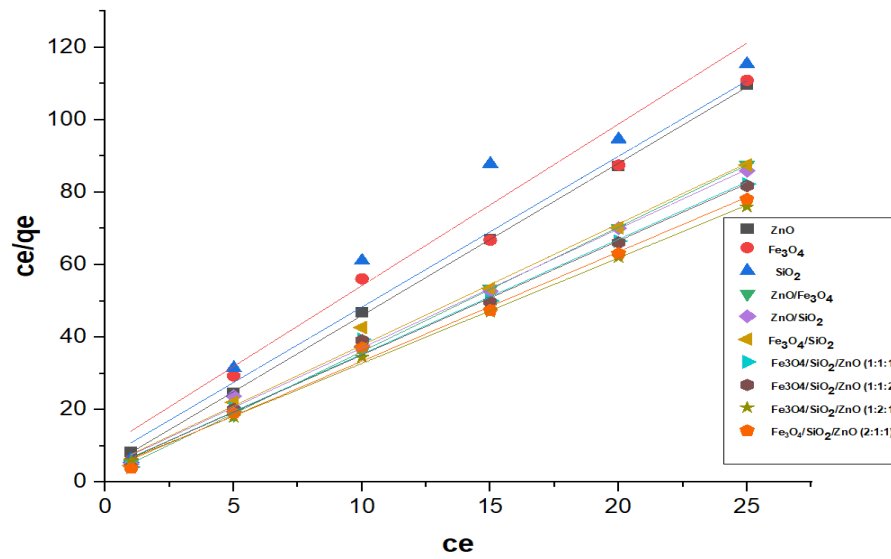
Appendix 4: Plot of log (q$_e$/C$_e$) against C$_e$ for Cr (VI)
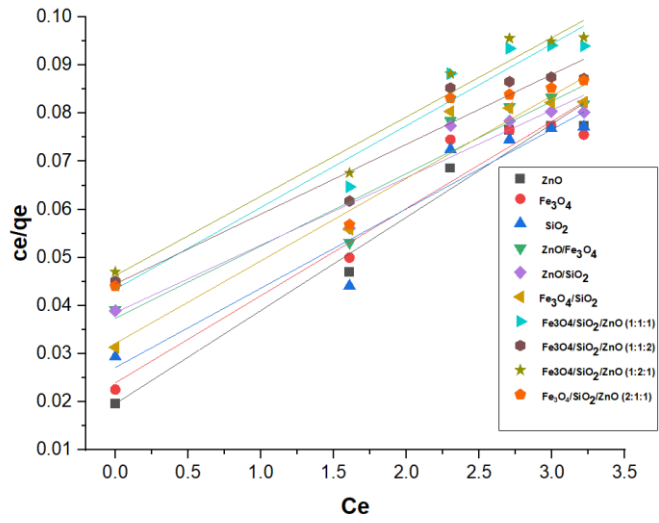
Appendix 5: Plot of log (q$_e$/C$_e$) against C$_e$ for Cu (II)
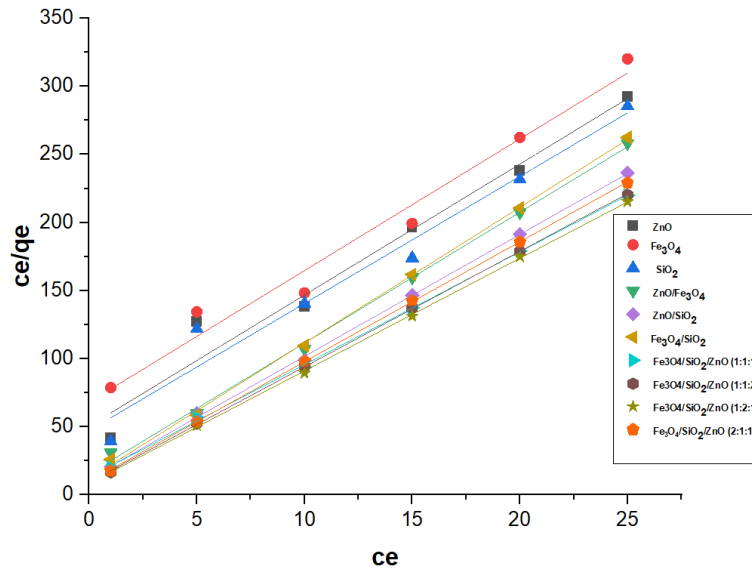
Appendix 6: Plot of log (q$_e$/C$_e$) against C$_e$ for Total iron
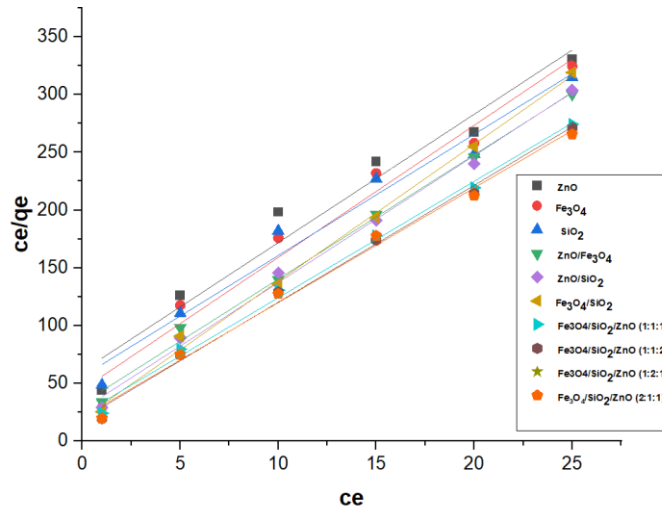
Appendix 7: Plot of log (q$_e$/C$_e$) against C$_e$ for BOD
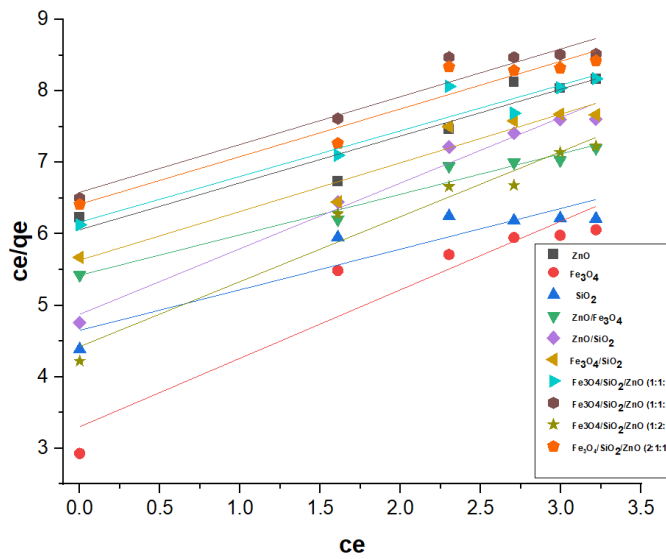
Appendix 8: Plot of log (q$_e$/C$_e$) against C$_e$ for COD
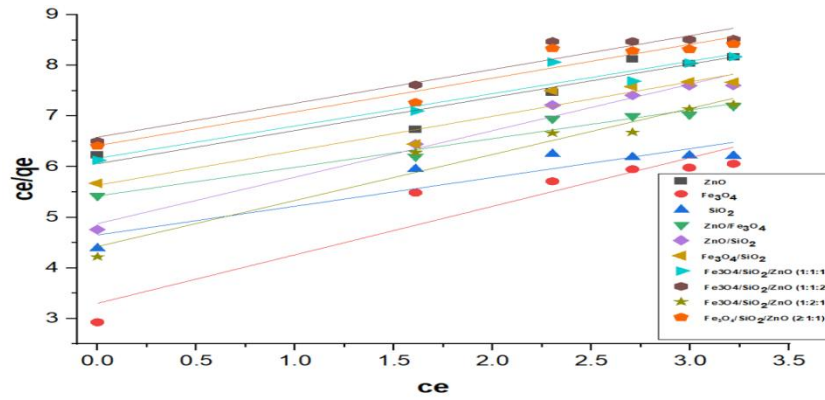
Appendix 9: Plot of log (q$_e$/C$_e$) against C$_e$ for TOC
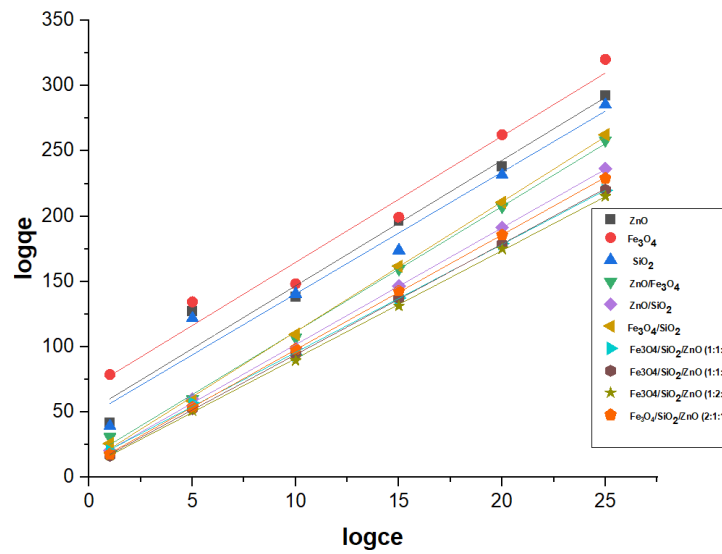
Appendix 10: Plot of log q$_e$ against log C$_e$ for Pb (II)
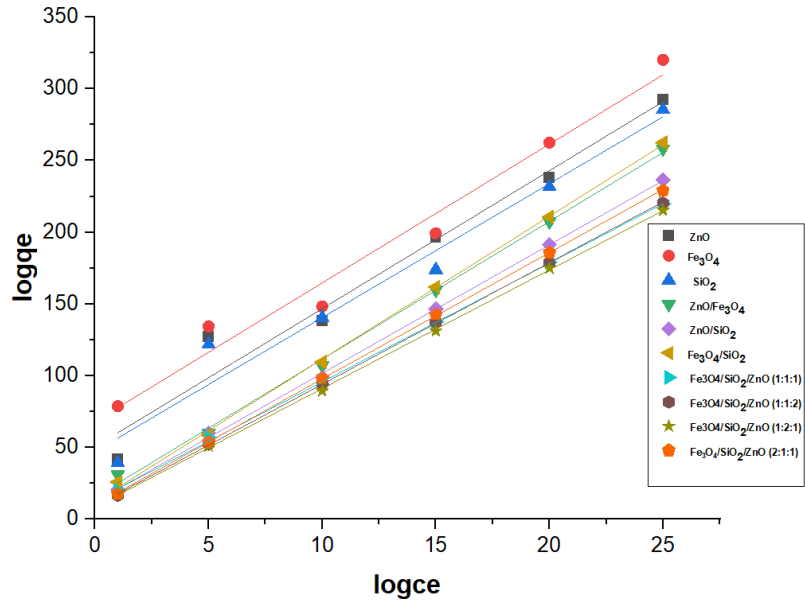
Appendix 11: Plot of log q_e against log C_e for Cd (II)

Appendix 12: Plot of log q_e against log C_e for Ni (II)

Appendix 13: Plot of log q_e against log C_e for Cr (VI)

Appendix 14: Plot of log q_e against log C_e for Cu (II)

353

Appendix 15: Plot of log q_e against log C_e for Total iron

Appendix 16: Plot of log q_e against log C_e for BOD

Appendix 17: Plot of log q$_e$ against log C$_e$ for COD

Appendix 18: Plot of log q$_e$ against log C$_e$ for TOC

Appendix 19: Plot of $\ln q_e$ against E^2 for Pb (II)
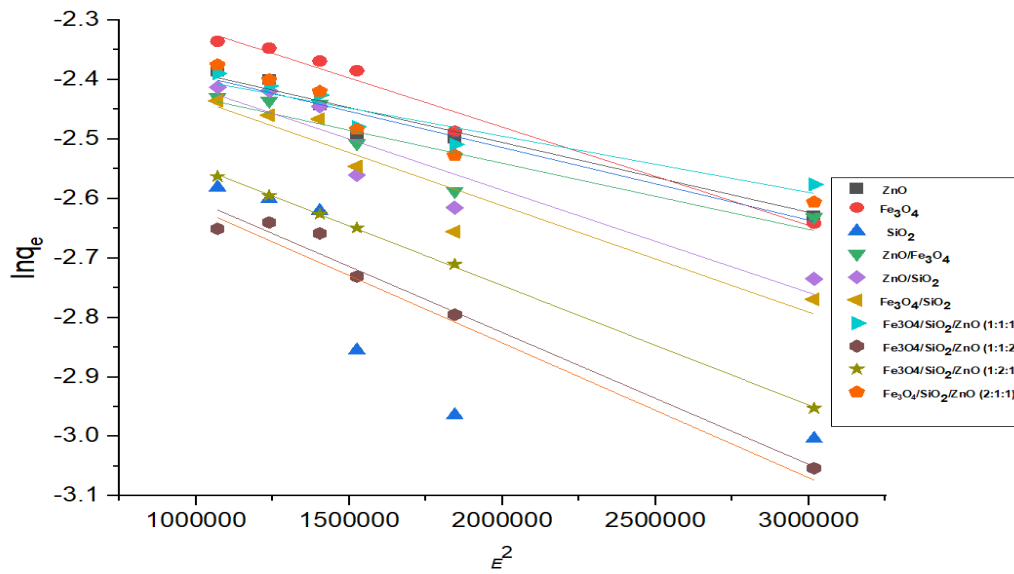
Appendix 20: Plot of $\ln q_e$ against E^2 for Cd (II)
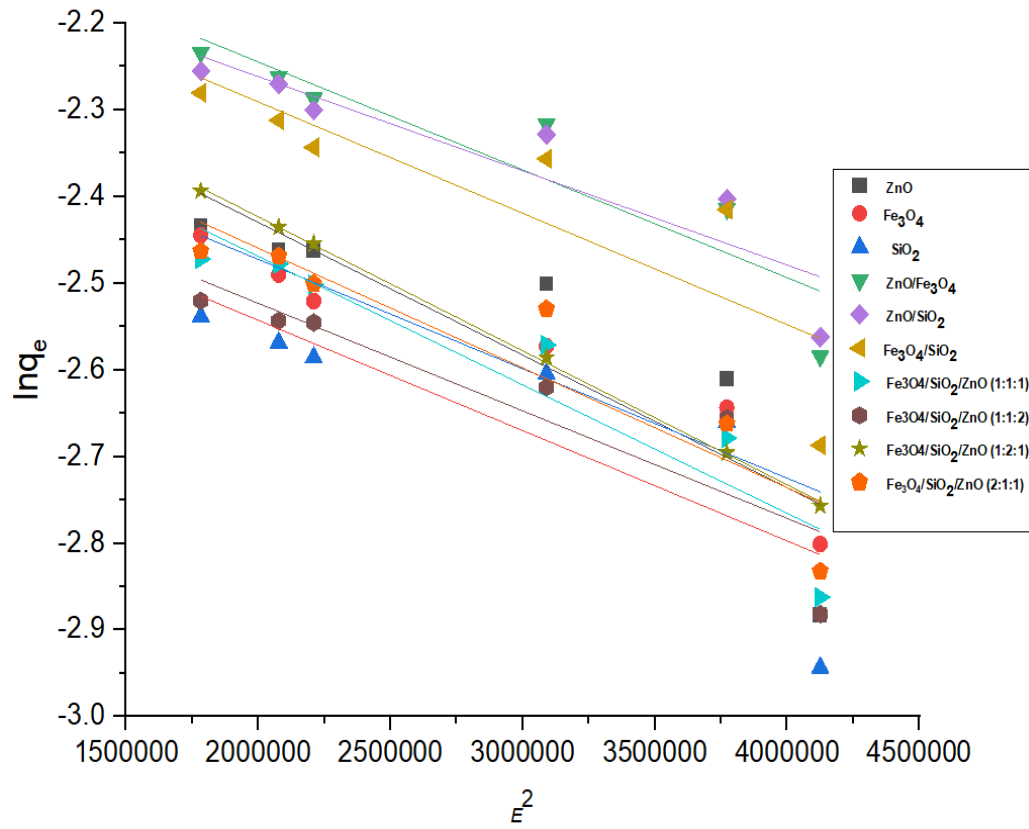
Appendix 21: Plot of lnq$_e$ against E^2 for Ni (II)
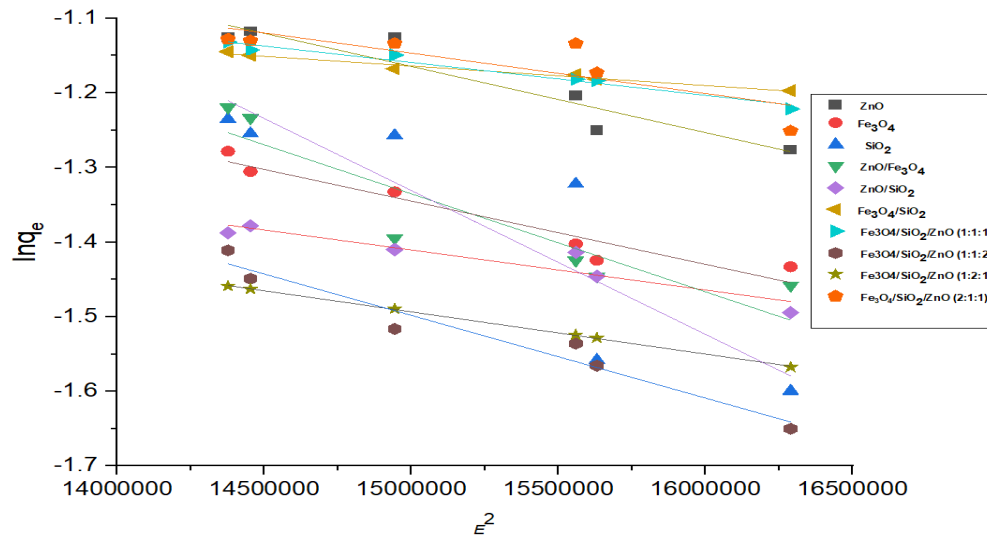
Appendix 22: Plot of lnq$_e$ against E^2 for Cr (VI)
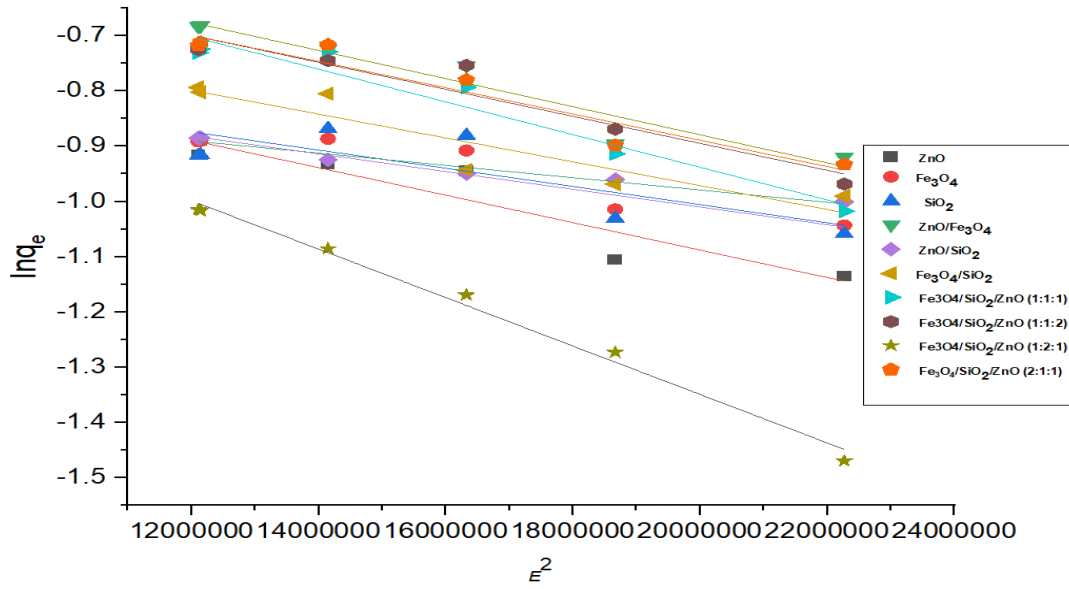
Appendix 23: Plot of lnq_e against E^2 for Cu (II)
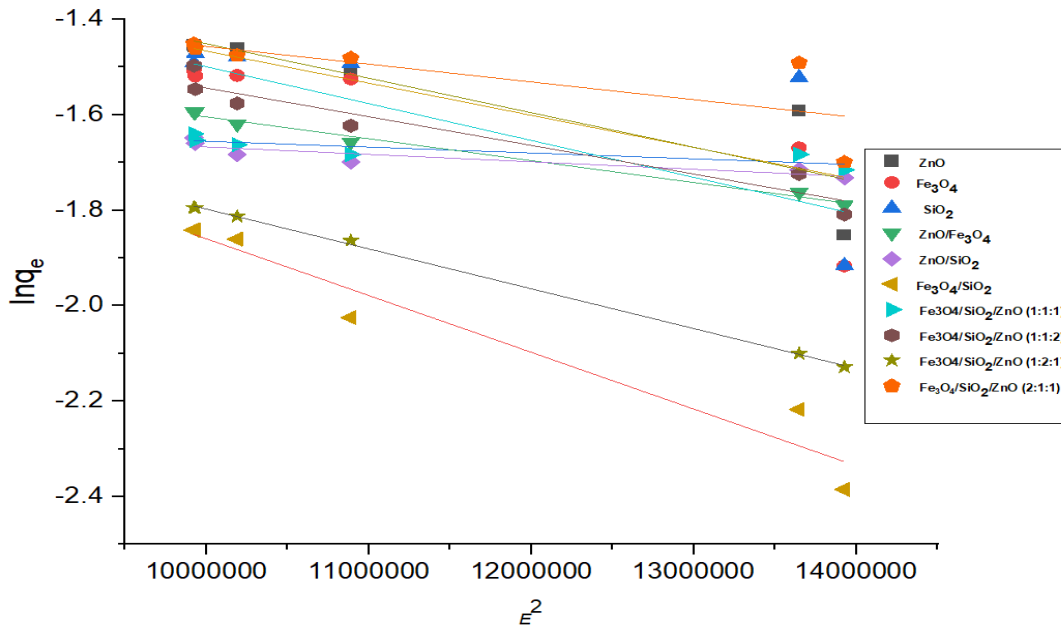
Appendix 24: **Plot of lnq_e against E^2 for Total iron**
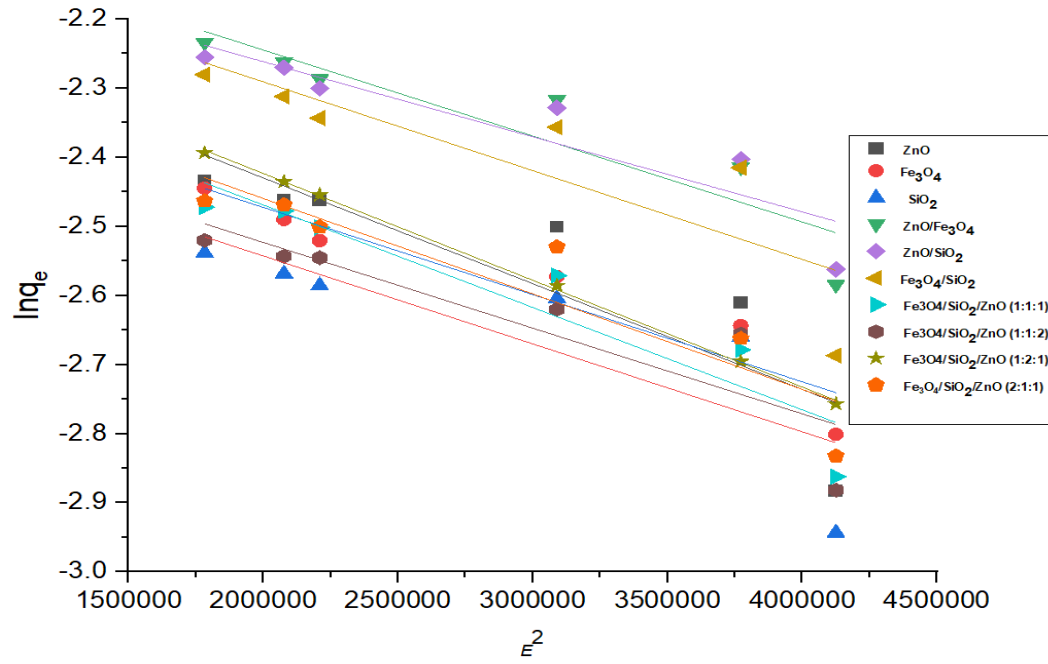
Appendix 25: Plot of lnq$_e$ against E^2 for BOD
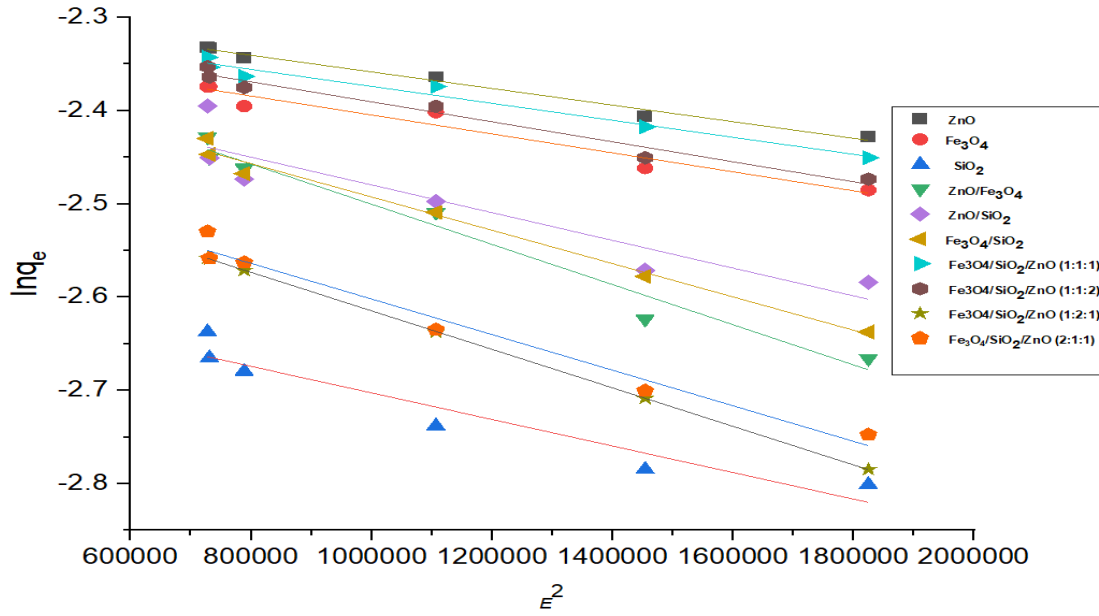
Appendix 26: Plot of lnq$_e$ against E^2 for COD
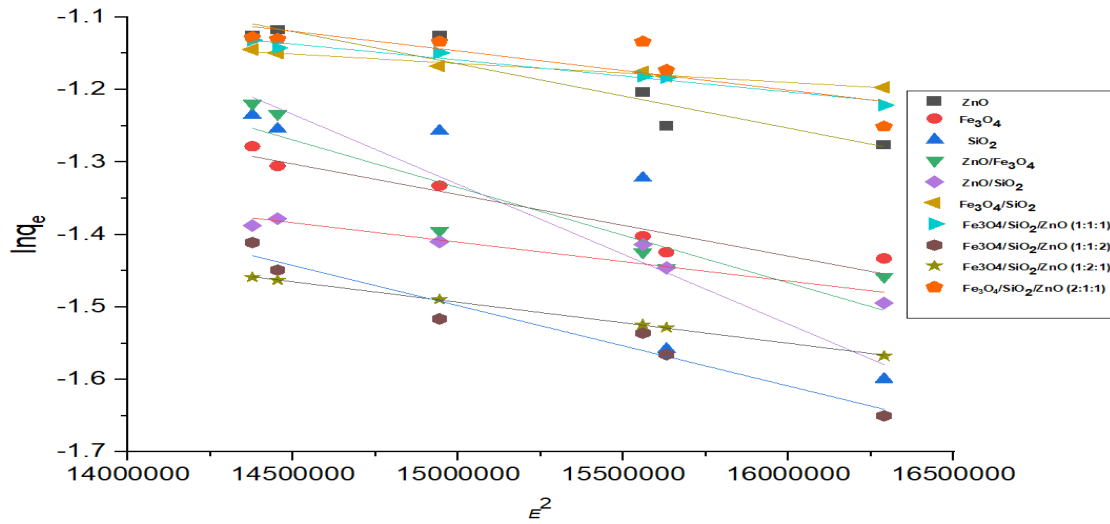
Appendix 27: Plot of lnq$_e$ against E^2 for TOC
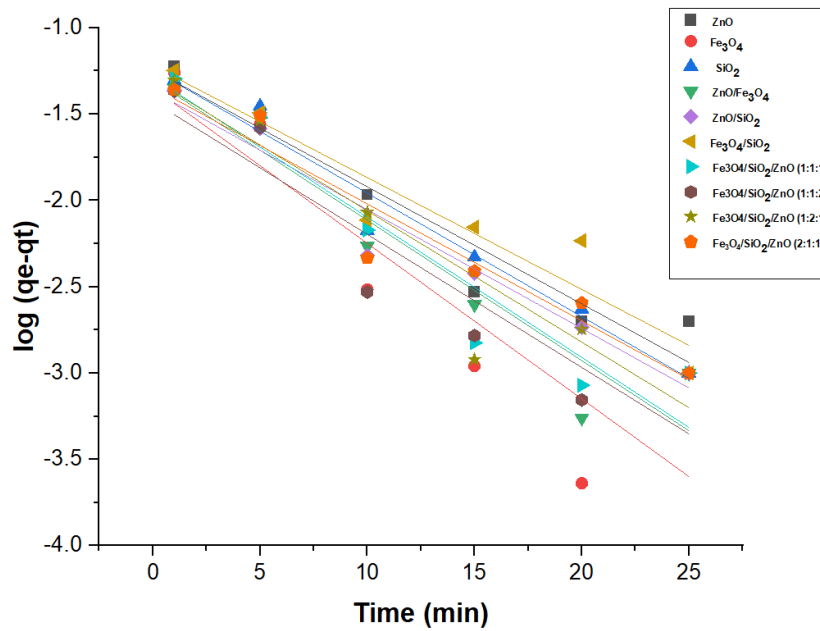
Appendix 28: Plot of log (qe-qt) against Time for Pb (II)
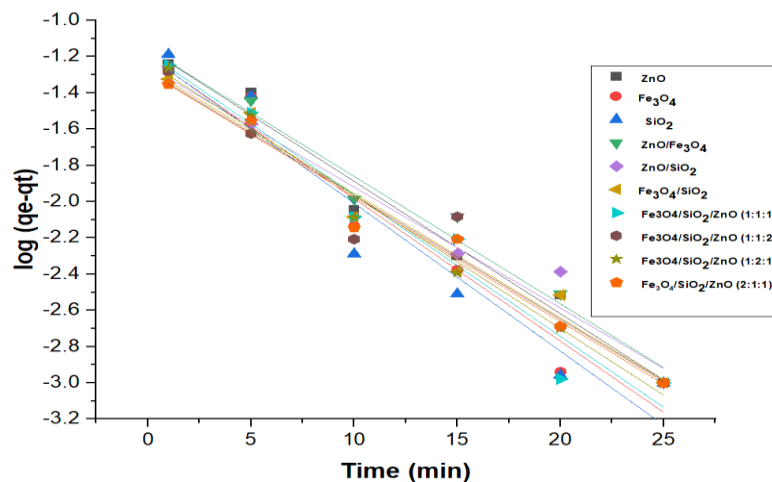
Appendix 29: Plot of log (qe-qt) against Time (min) for Cd (IV)
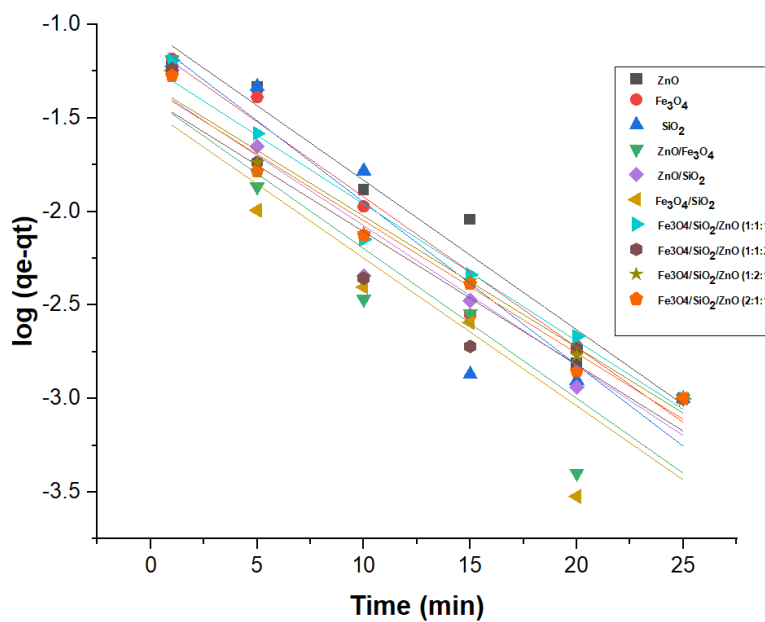
Appendix 30: Plot of log (qe-qt) against Time (min) for Ni (II)
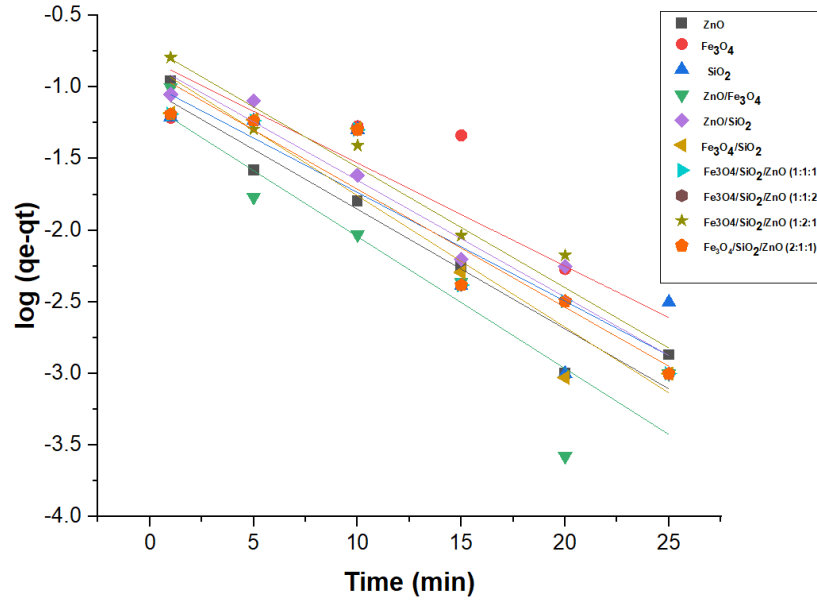
Appendix 31: Plot of log (qe-qt) against Time (min) for Cr (II)
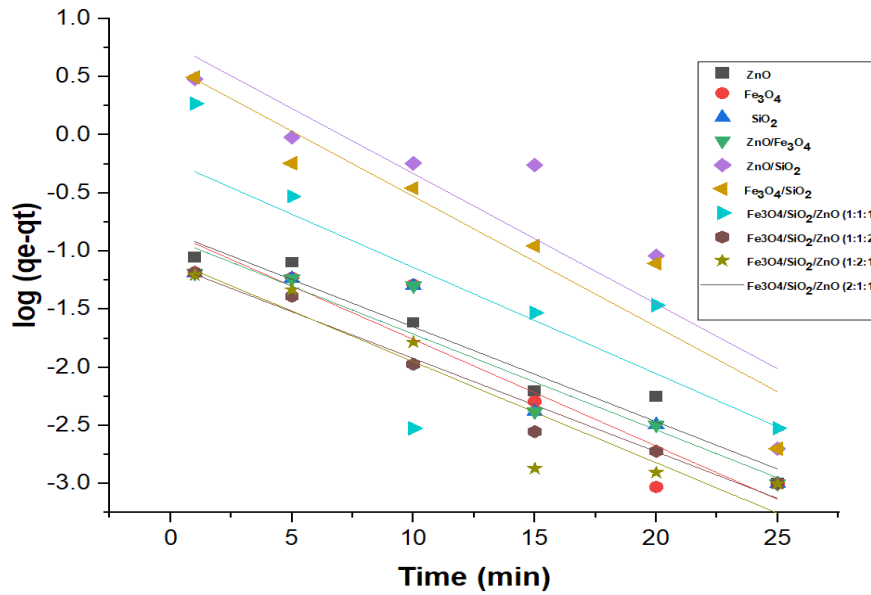
Appendix 32: Plot of log (qe-qt) against Time for Cu (II)
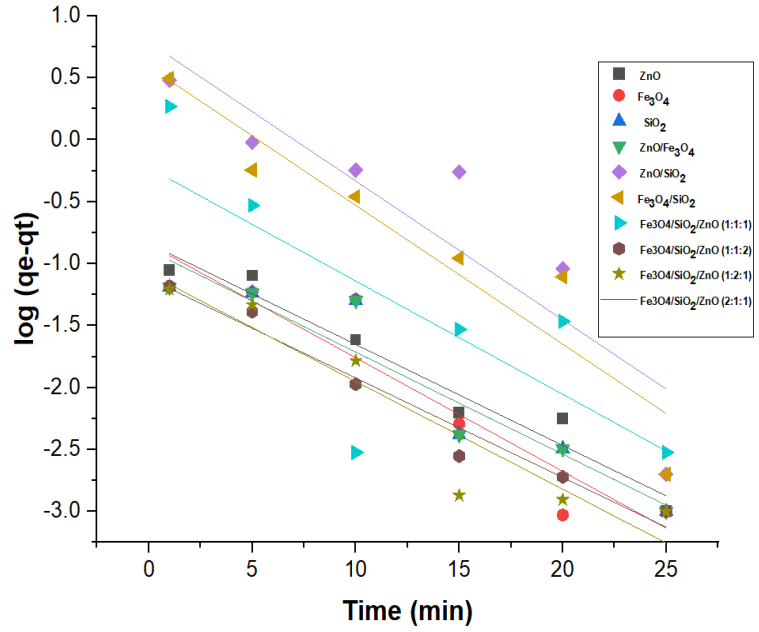
Appendix 33: Plot of log (qe-qt) against Time (min) for Total iron
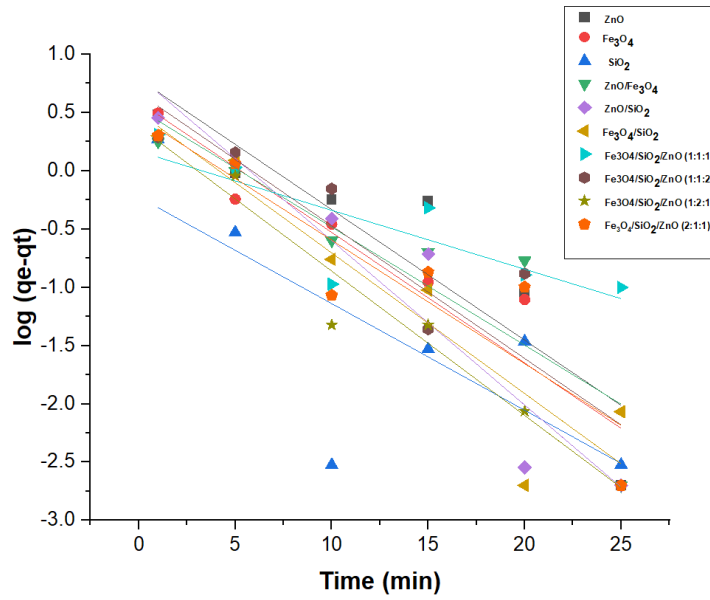
Appendix 34: Plot of log (qe-qt) against Time (min) for BOD
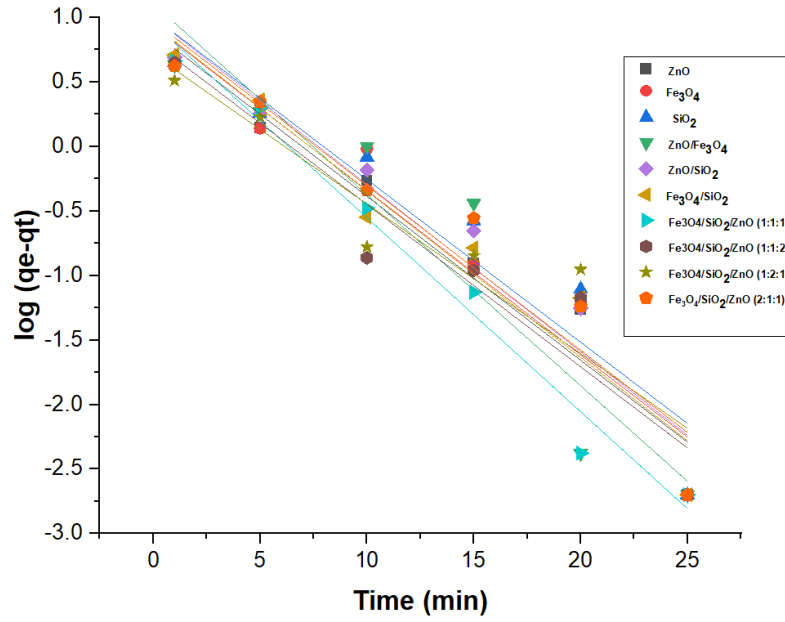
Appendix 35: Plot of log (qe-qt) against Time (min) for COD
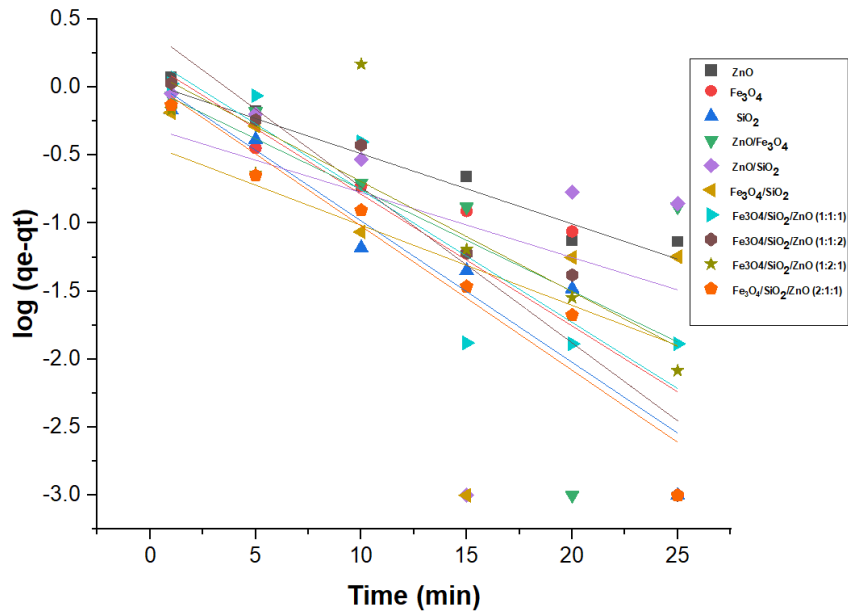
Appendix 36: Plot of log (qe-qt) against Time (min) for TOC
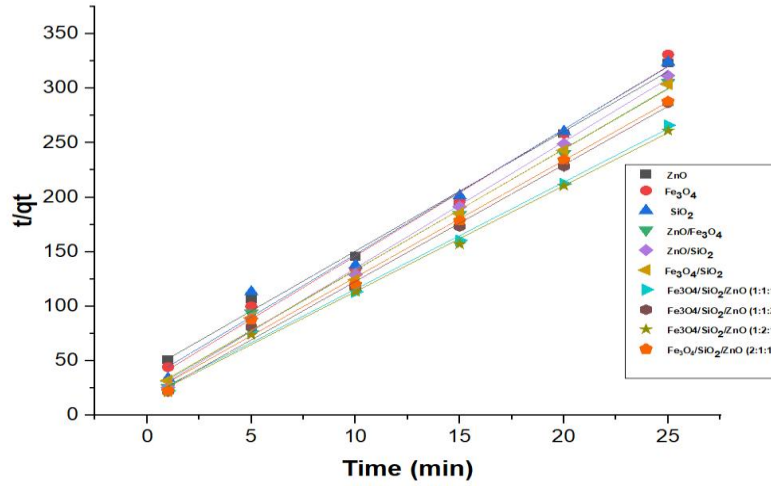
Appendix 37: Plot of t/qt against Time (min) for Pb (II)
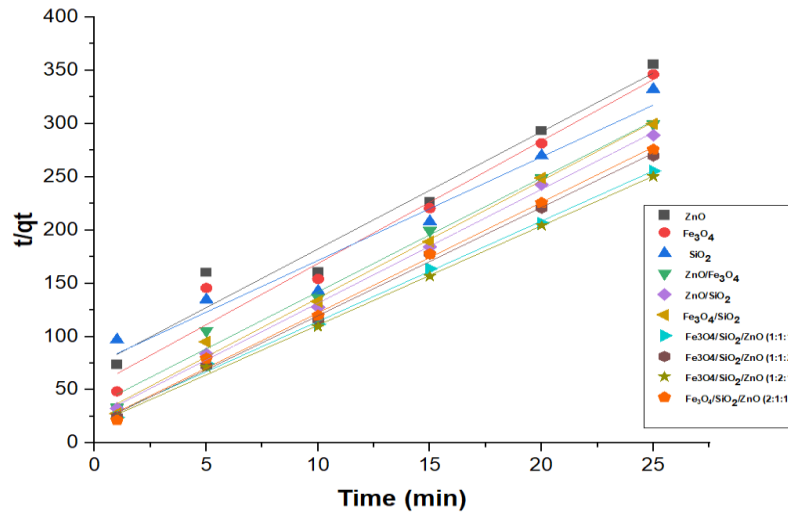
Appendix 38: Plot of t/qt against Time for Cd (II)
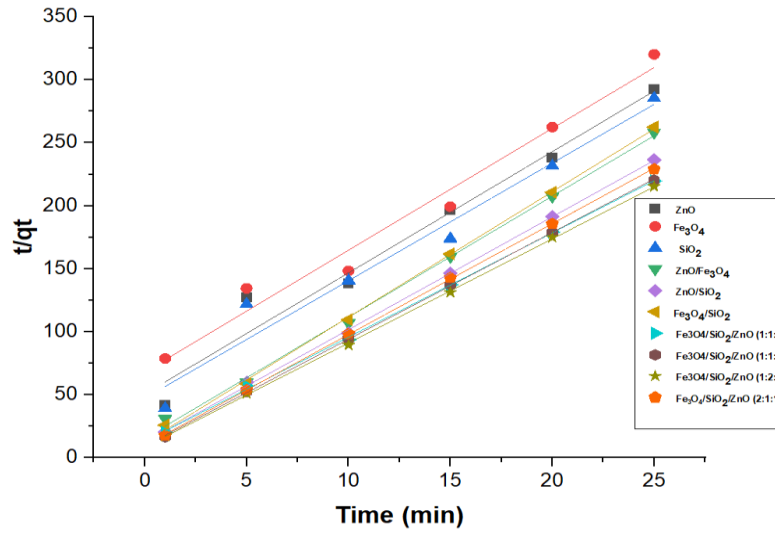
Appendix 39: Plot of t/qt against Time (min) for Ni(II)
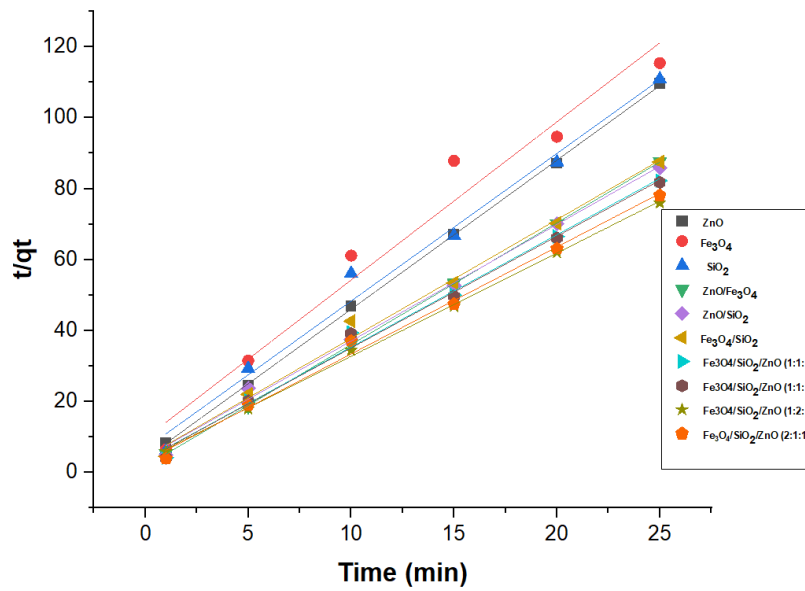
Appendix 40: Plot of t/qt against Time for Cr(VI)
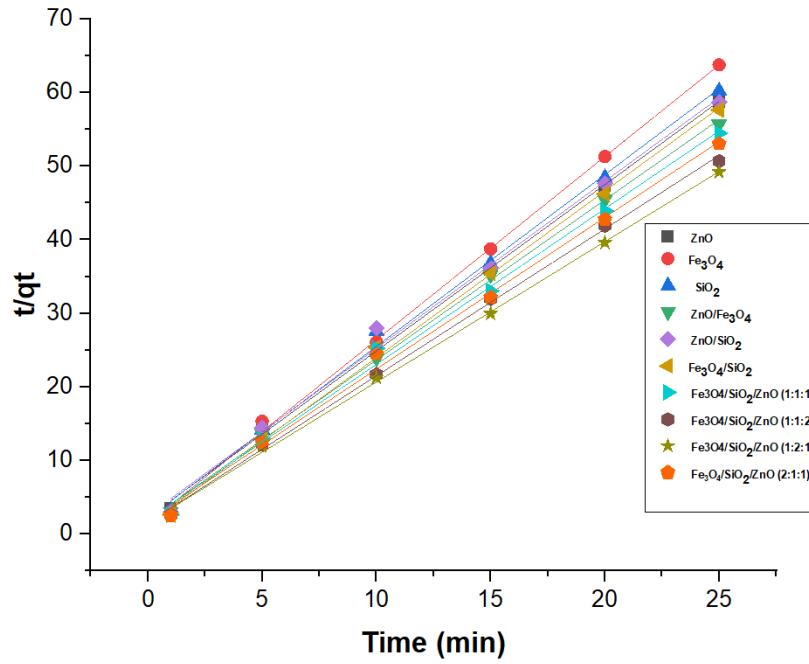
Appendix 41: Plot of t/qt against Time for Cu (II)
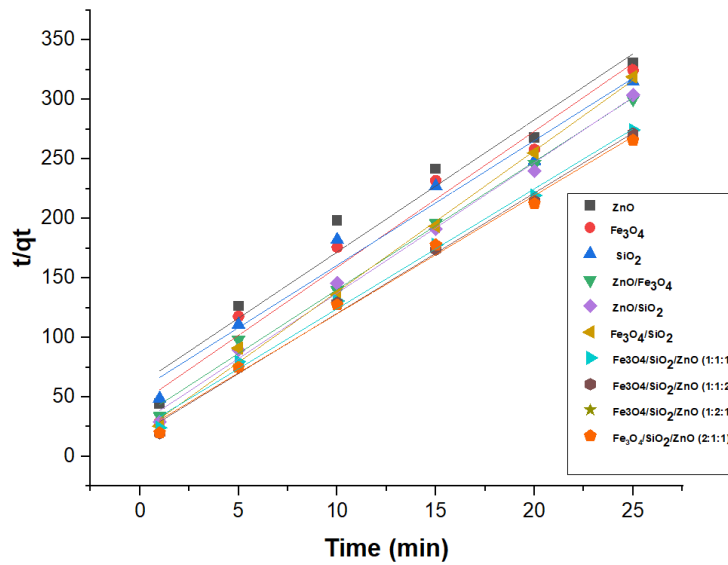
Appendix 42: Plot of t/qt against Time for the Adsorption of Total iron
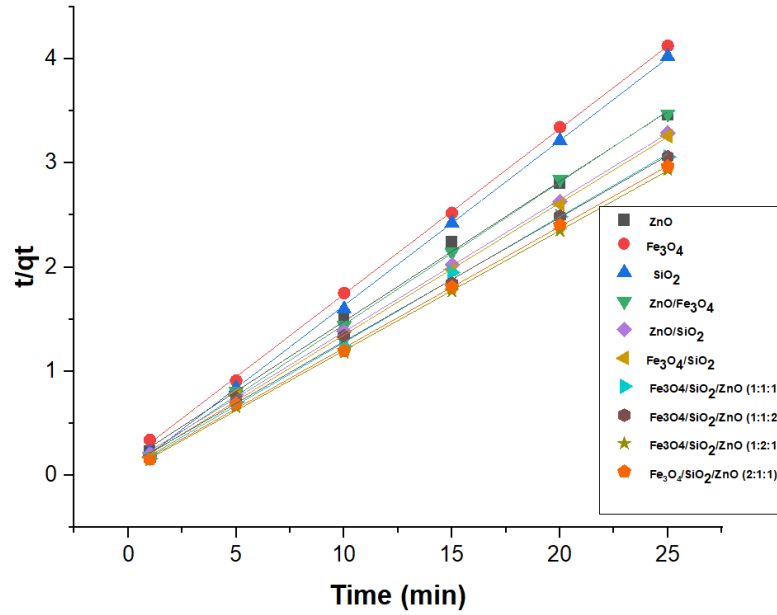
Appendix 43: Plot of t/qt against Time for BOD
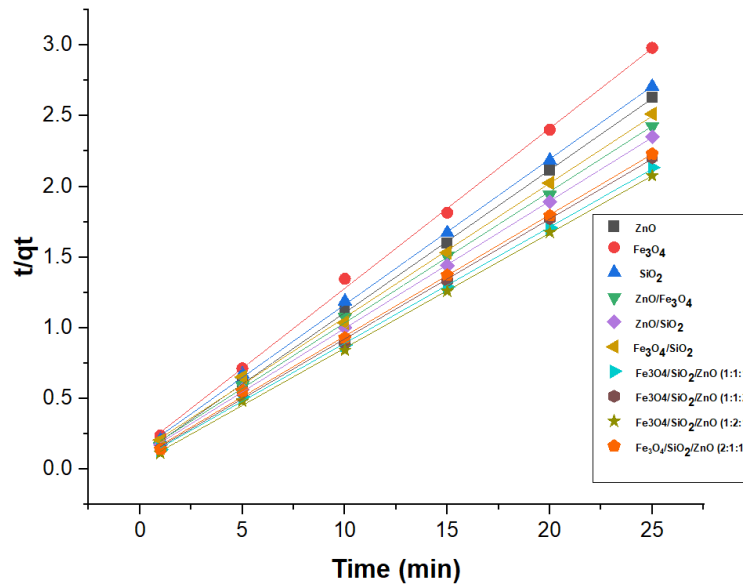
Appendix 44: Plot of t/qt against Time for COD
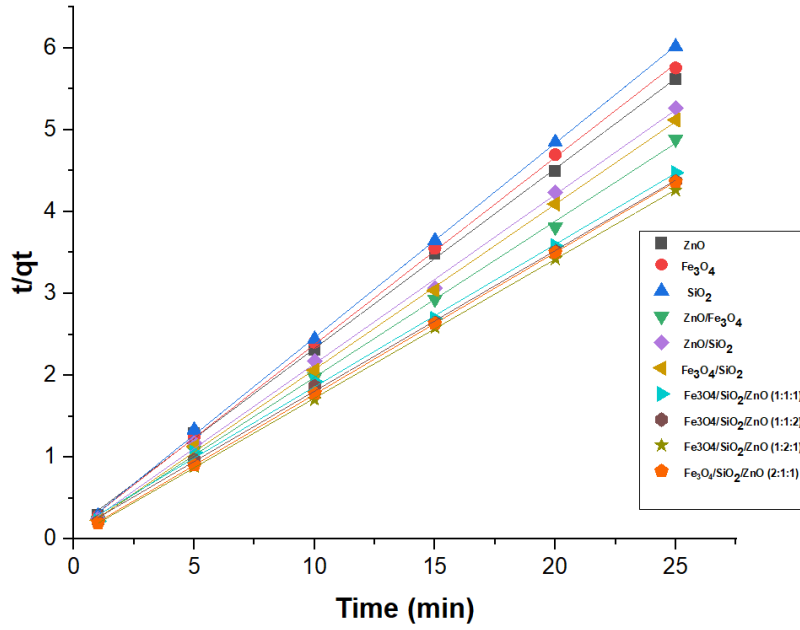
Appendix 45: Plot of t/qt against Time for TOC
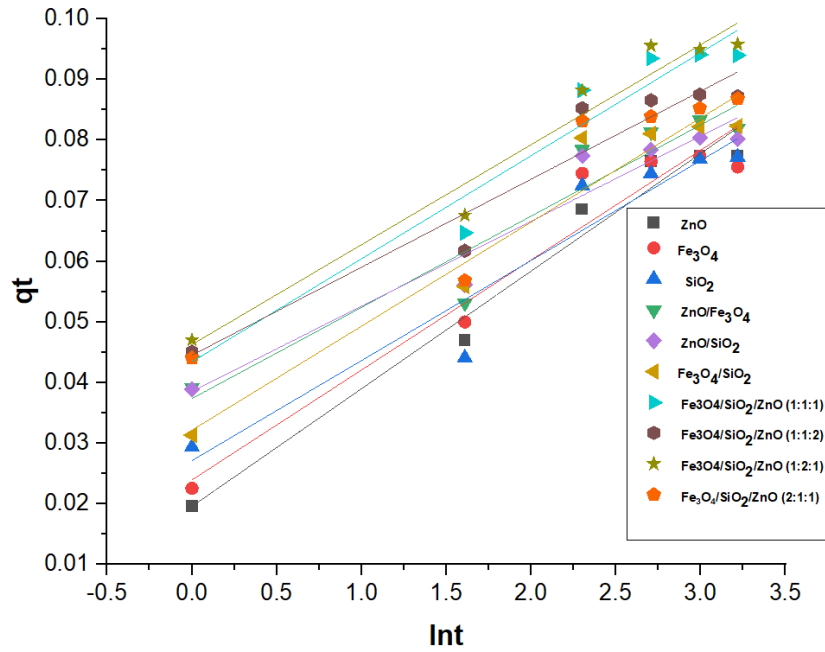
Appendix 46: Plot of qt against lnt for Pb (II)
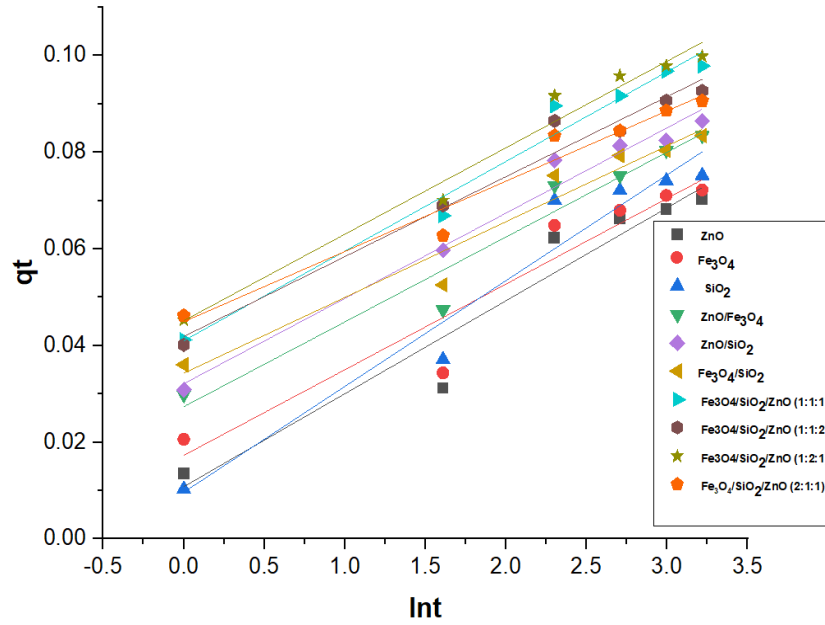
Appendix 47: Plot of qt against lnt for Cd (II)
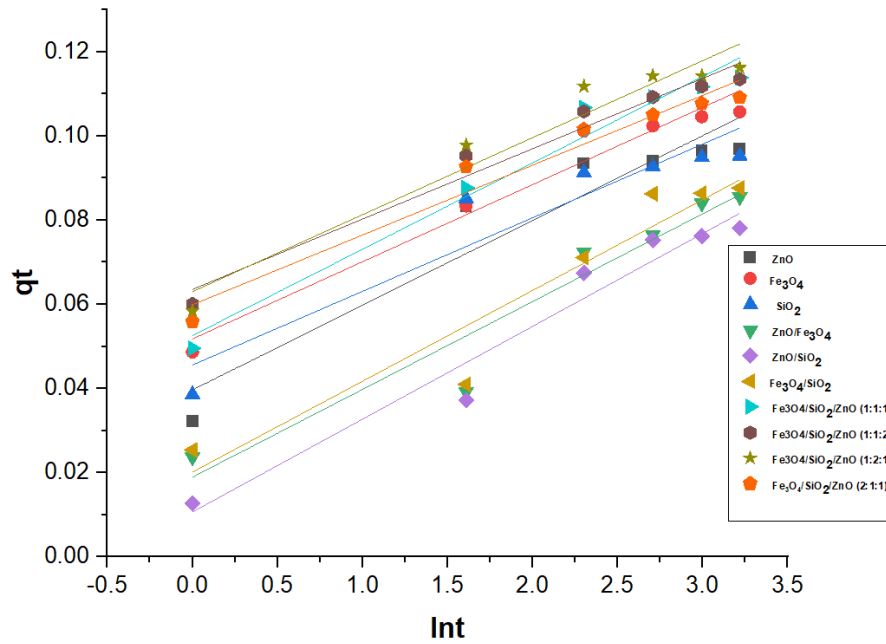
Appendix 48: Plot of qt against lnt for Ni (II)
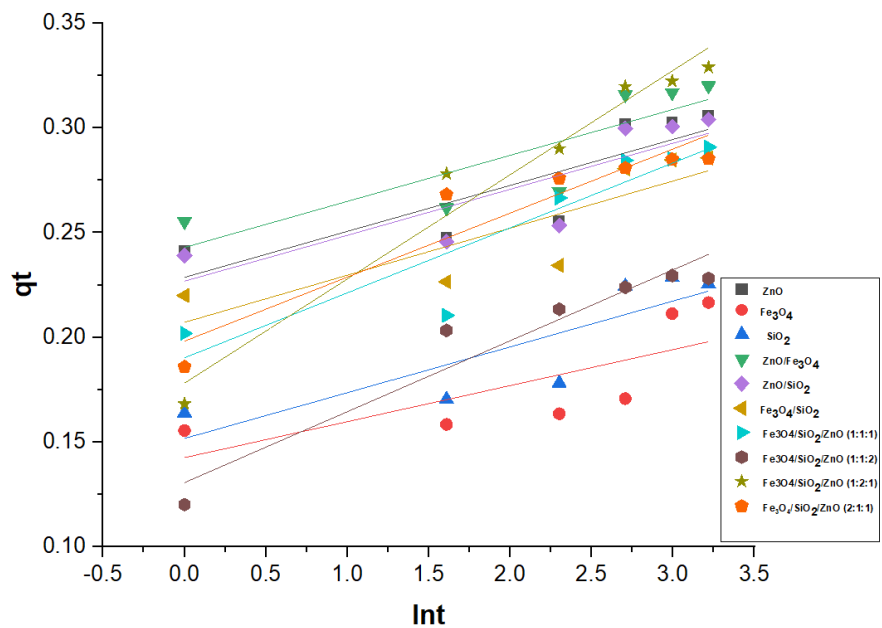
Appendix 49: Plot of qt against lnt for Cr (II)
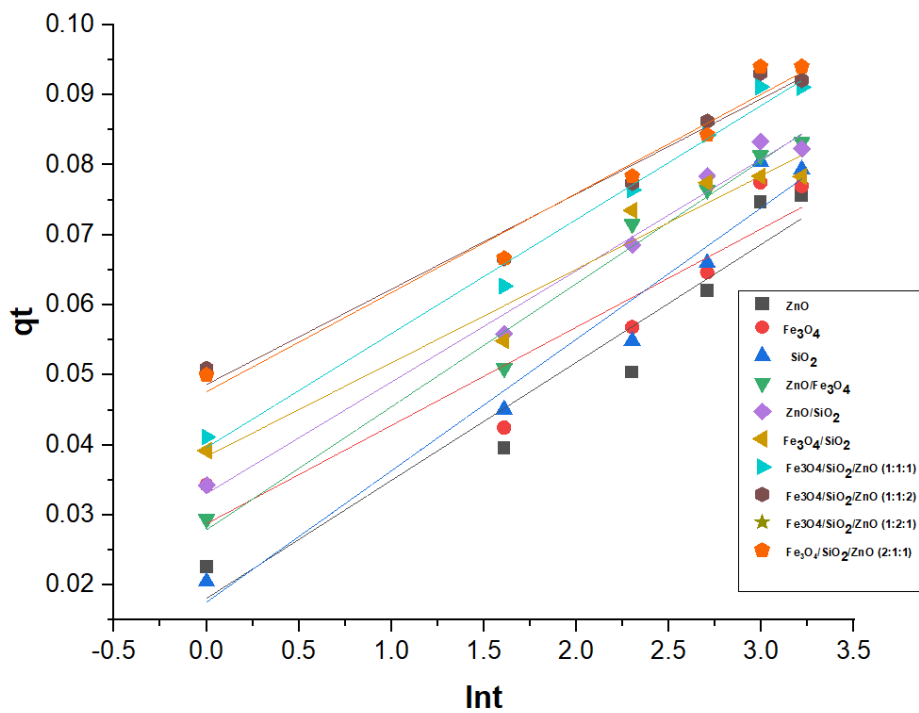
Appendix 50: Plot of qt against lnt for Cu (II)
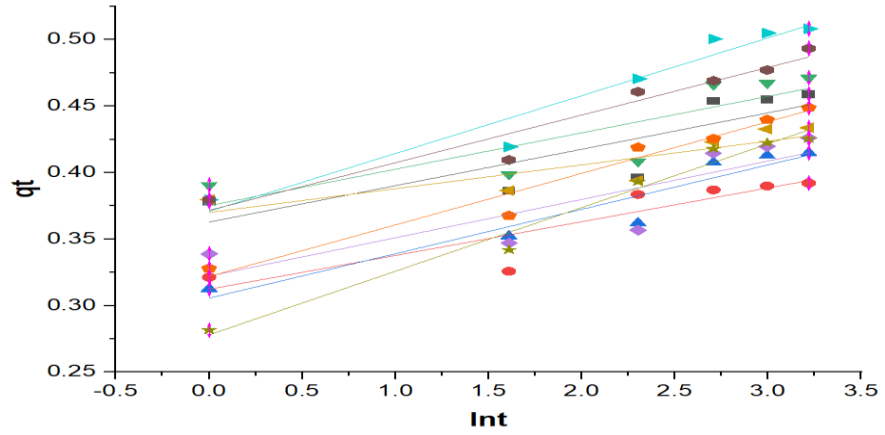
Appendix 51: Plot of qt against lnt for Total iron
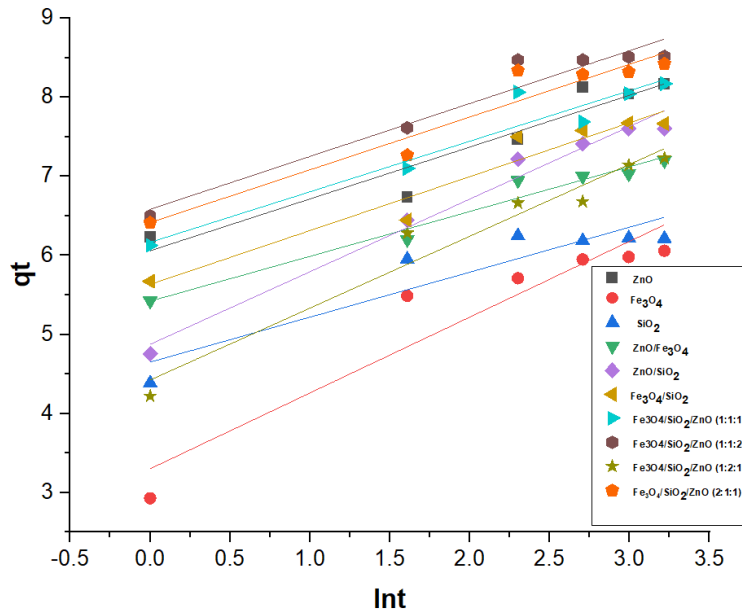
Appendix 52: Plot of qt against lnt for BOD
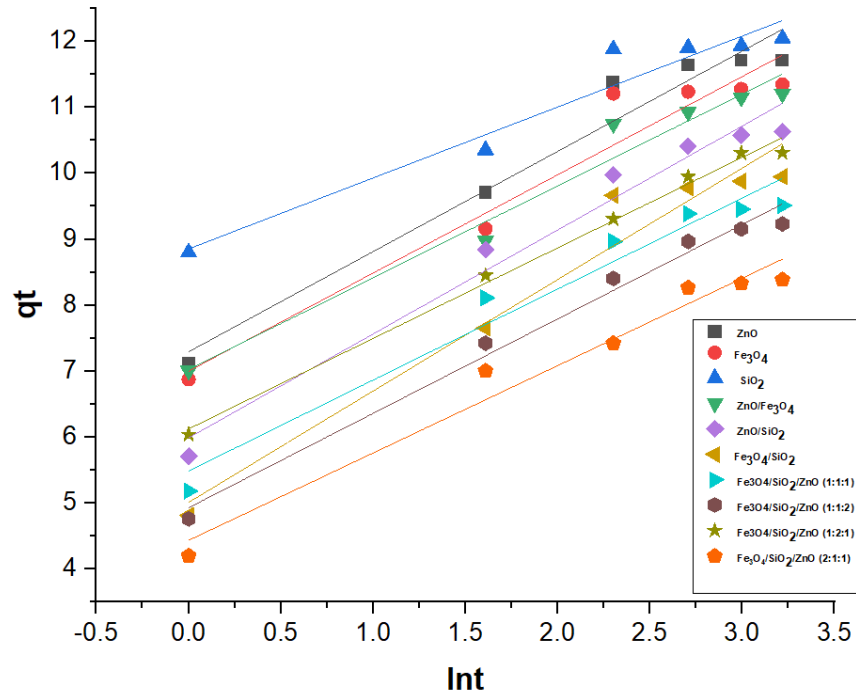
Appendix 53: Plot of qt against lnt for COD
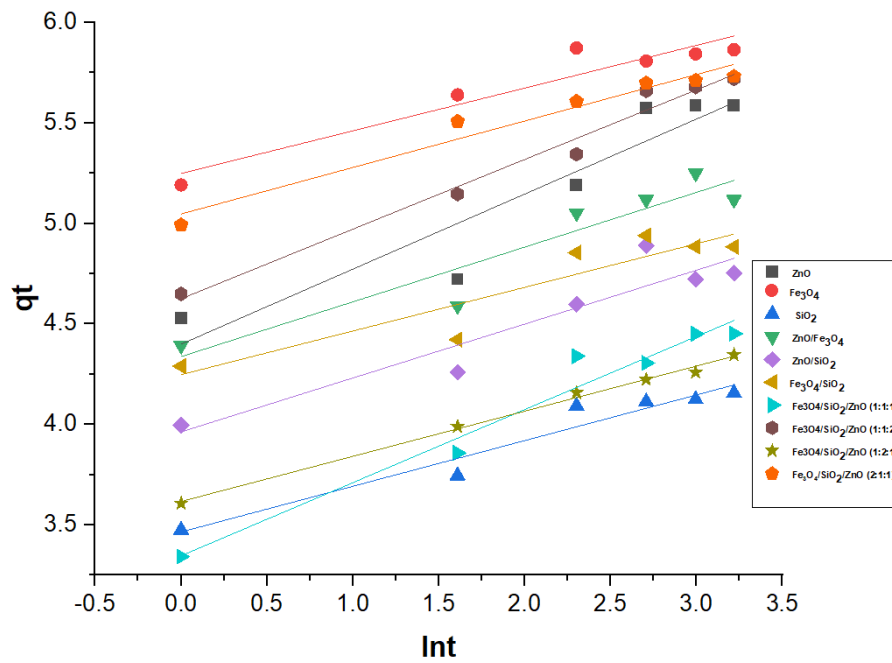
Appendix 54: Plot of qt against lnt for TOC
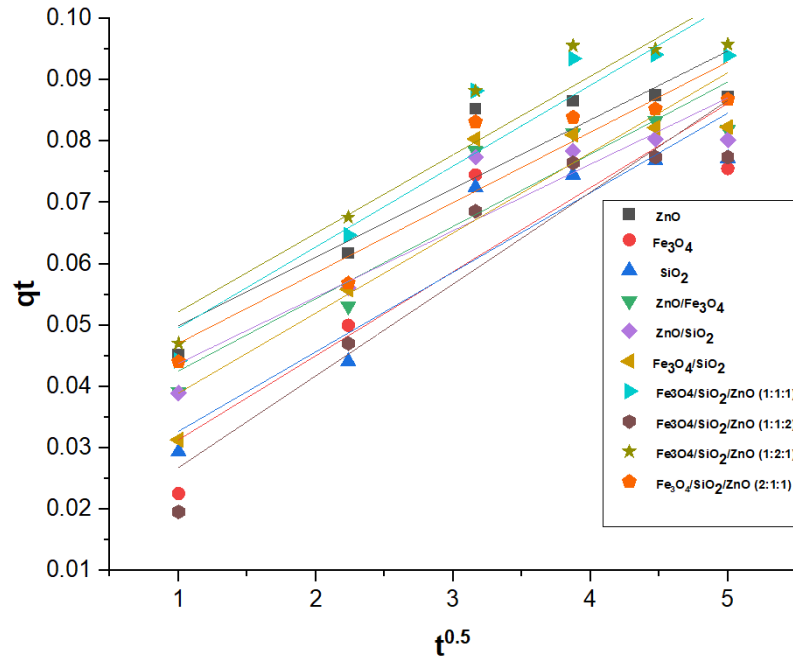
Appendix 55: Plot of qt against $t^{0.5}$ for Pb (II)
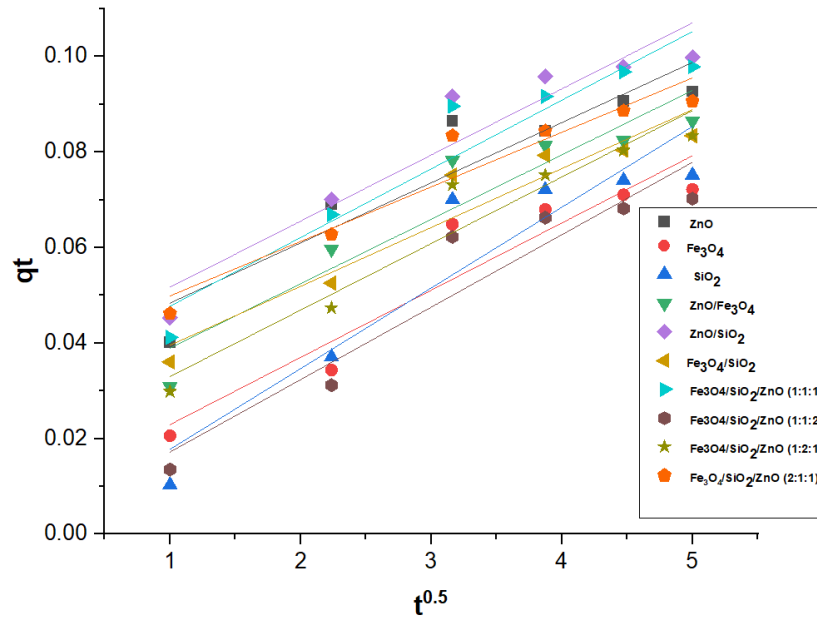
Appendix 56: Plot of qt against $t^{0.5}$ for Cd (II)
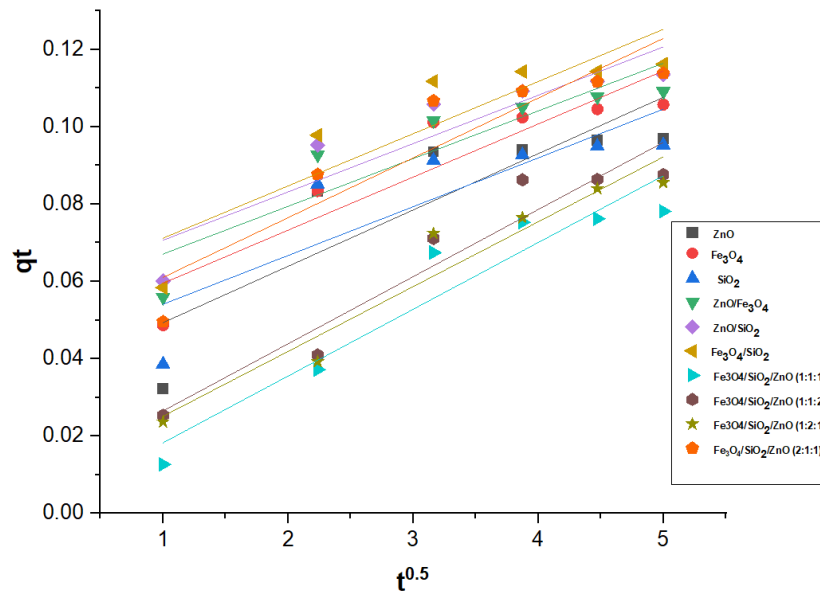
Appendix 57: Plot of qt against t$^{0.5}$ for Ni (II)
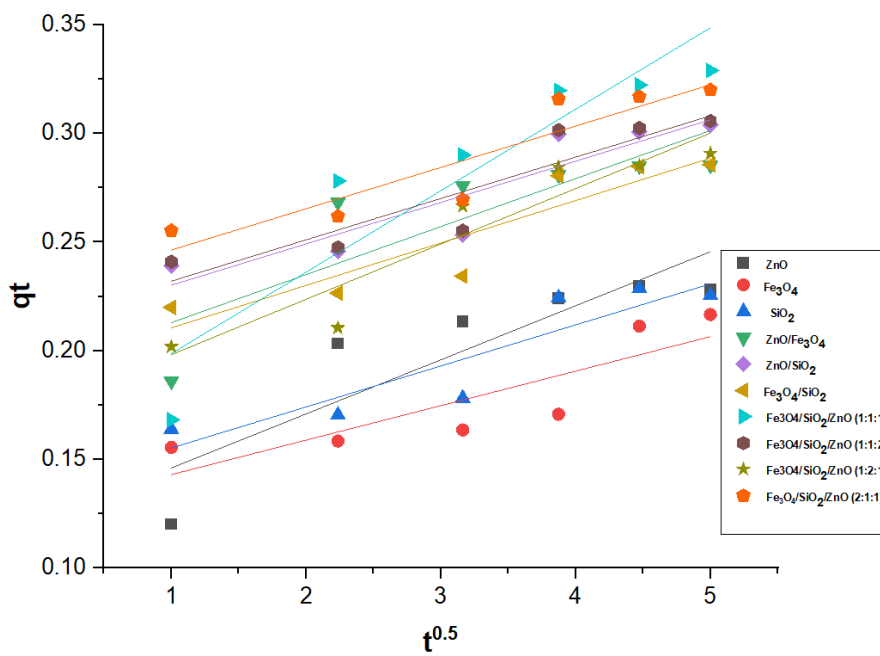
Appendix 58: Plot of qt against t$^{0.5}$ for Cr (II)
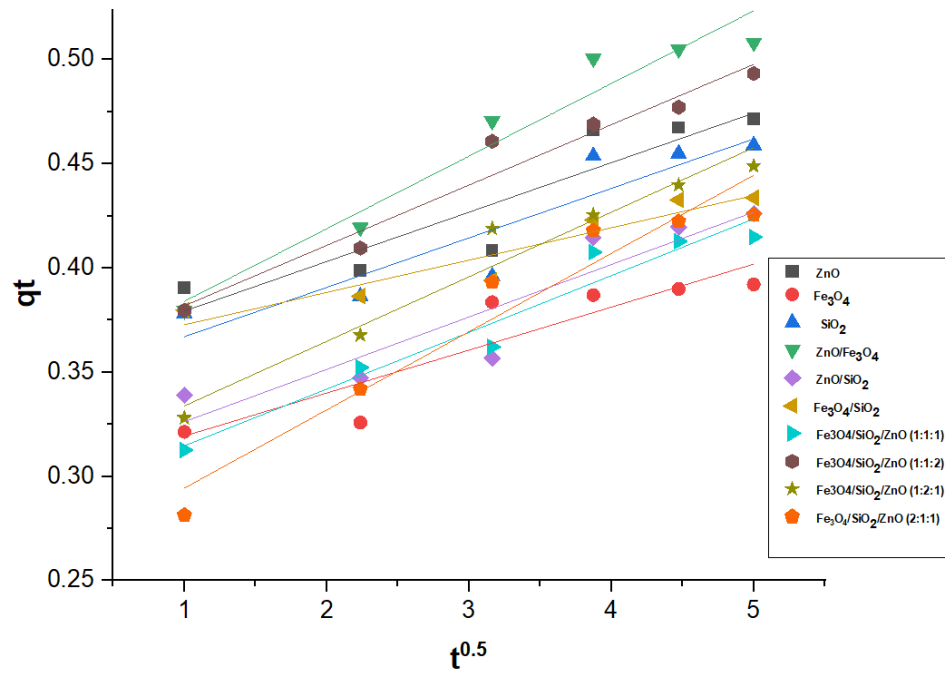
Appendix 59: Plot of qt against $t^{0.5}$ for Cu (II)
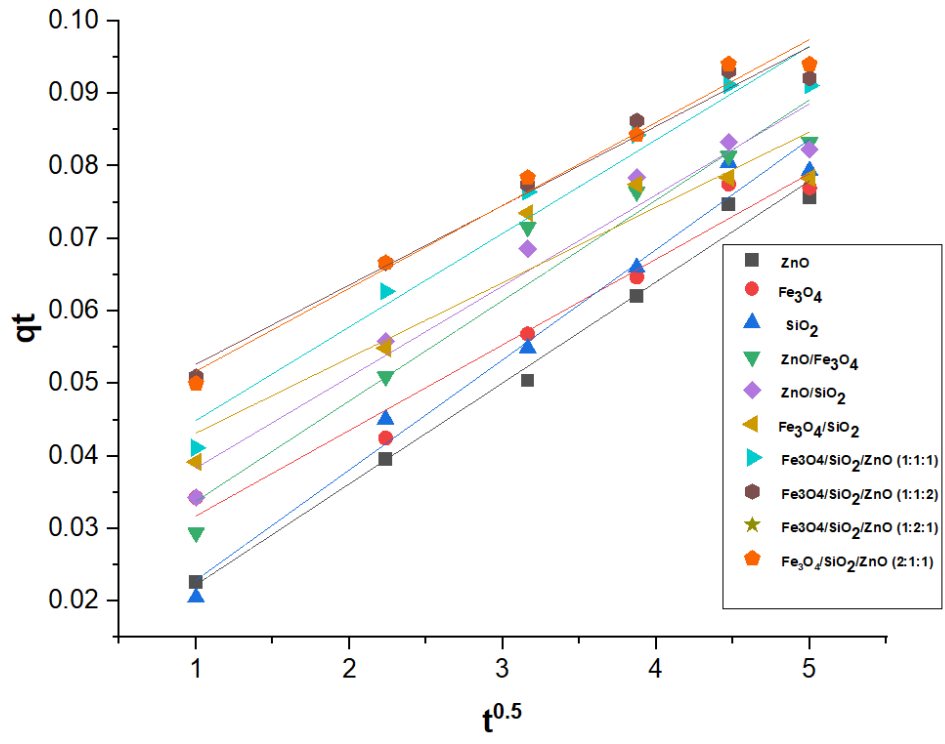
Appendix 60: Plot of qt against $t^{0.5}$ for Total Iron
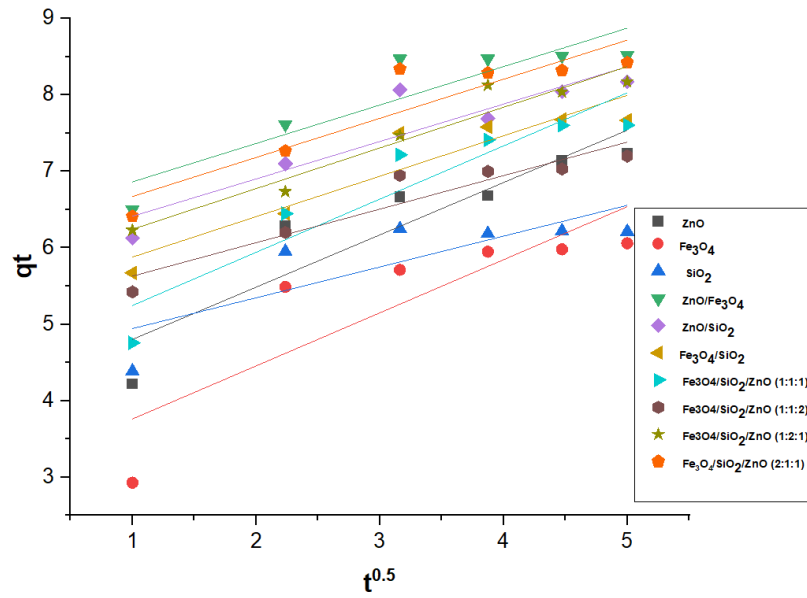
Appendix 61: Plot of qt against $t^{0.5}$ for BOD
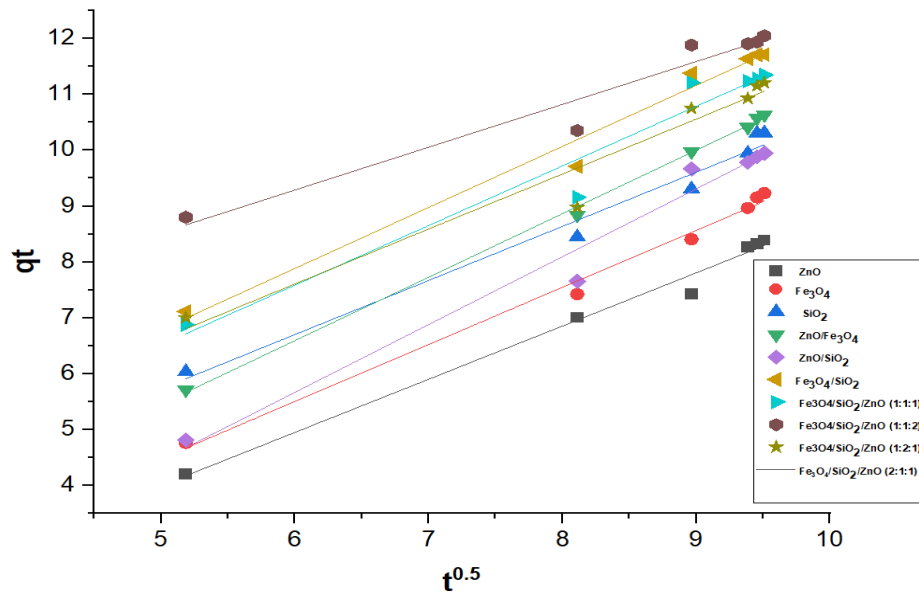
Appendix 62: Plot of qt against $t^{0.5}$ for COD
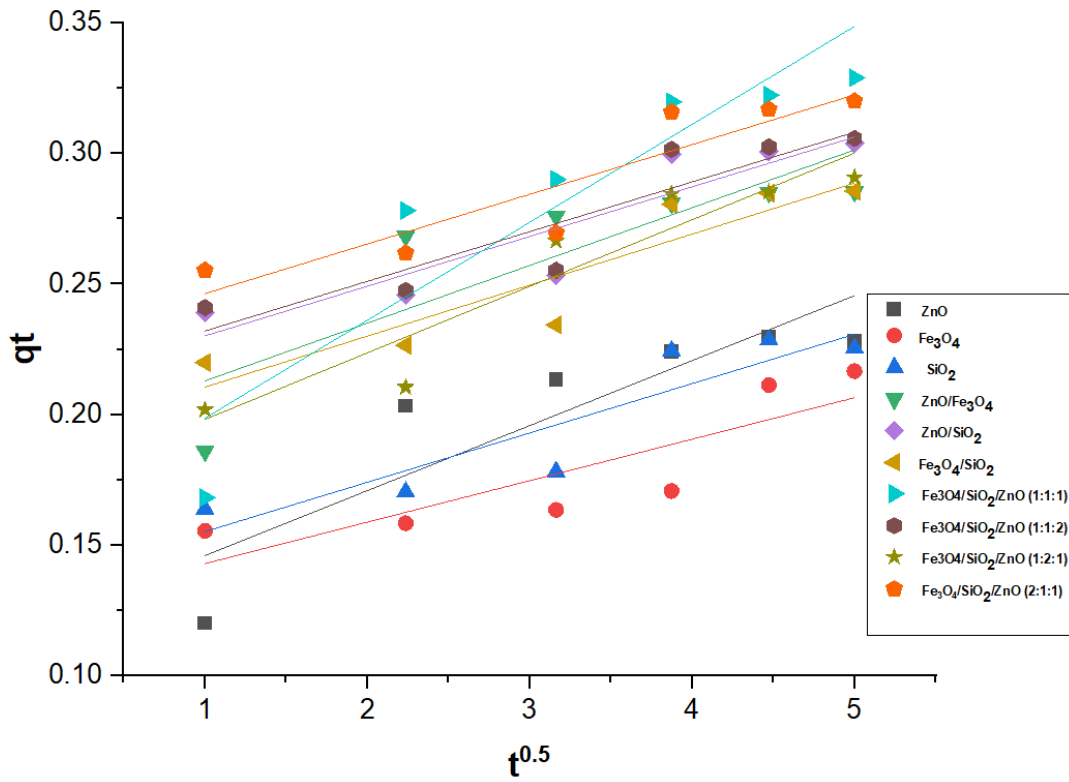
Appendix 63: Plot of qt against t$^{0.5}$ for TOC
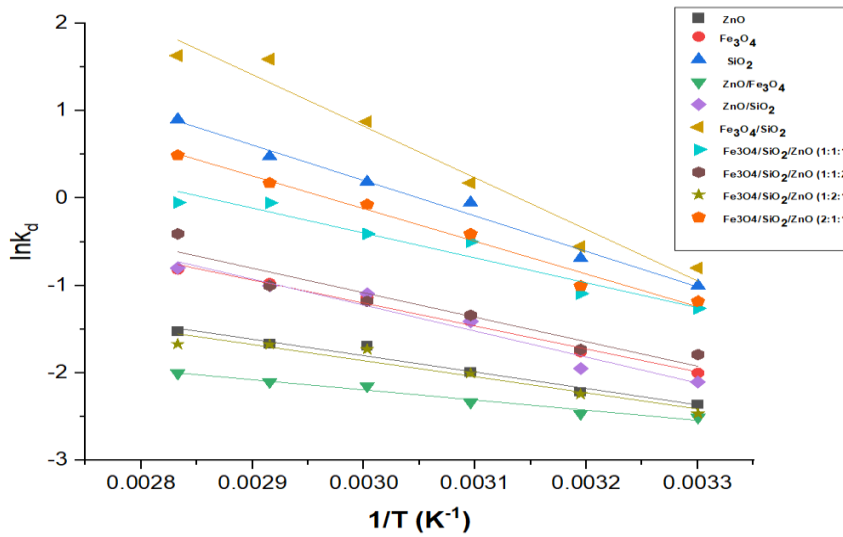
Appendix 64: Plot of qt against t$^{0.5}$ for TOC
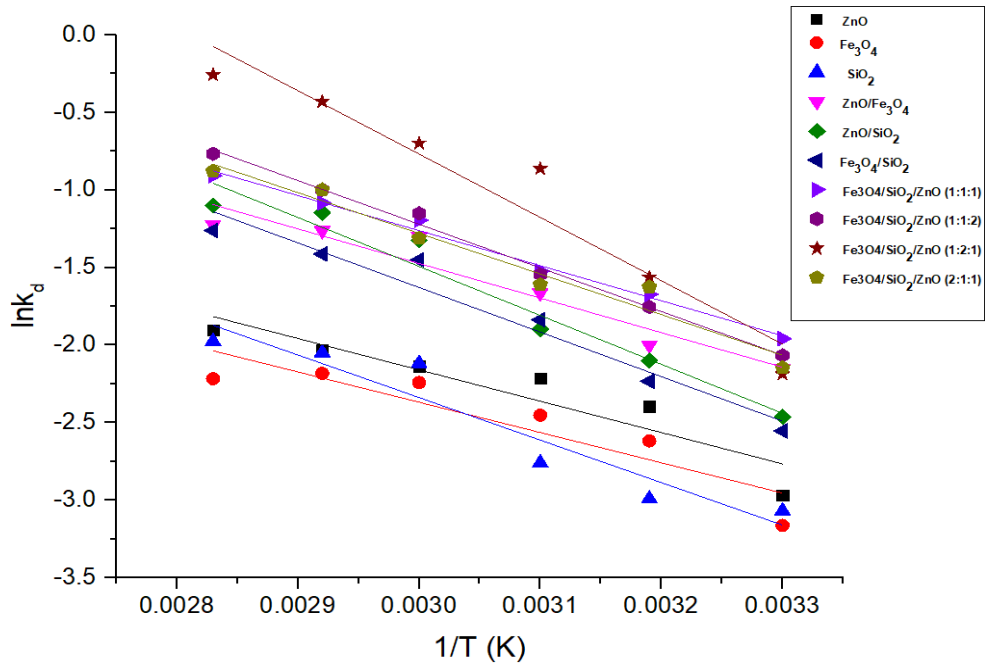
Appendix 65: Plot of InK$_d$ against 1/T (K^{-1}) for Cd (II)
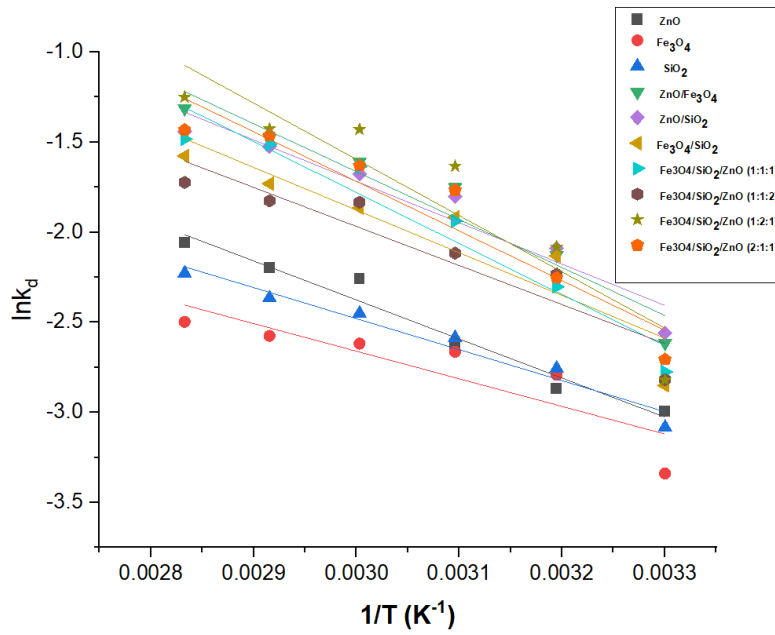
Appendix 66: Plot of InK$_d$ against 1/T (K^{-1}) for Ni (II)
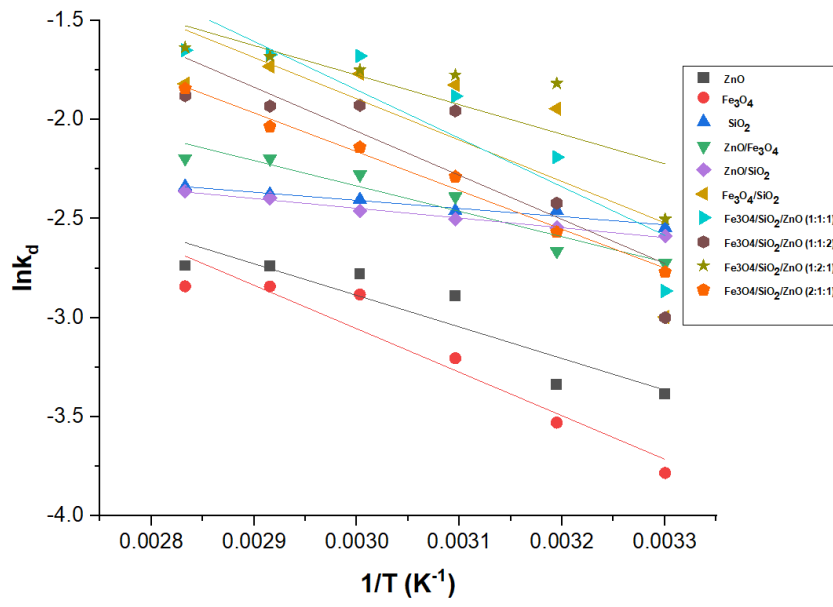
Appendix 67: Plot of InK$_d$ against 1/T (K^{-1}) for Cr (VI)
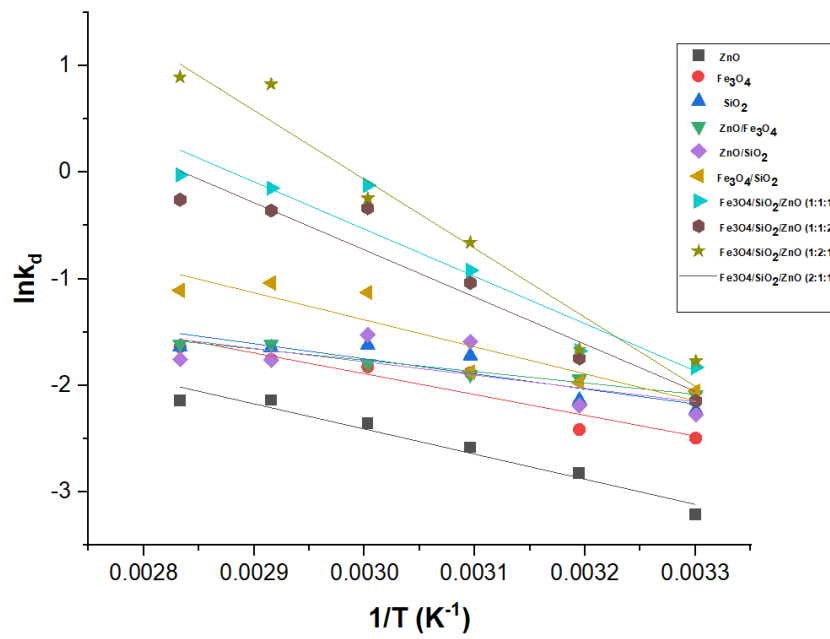
Appendix 68: Plot of lnK$_d$ against 1/T (K^{-1}) for Cu (II)
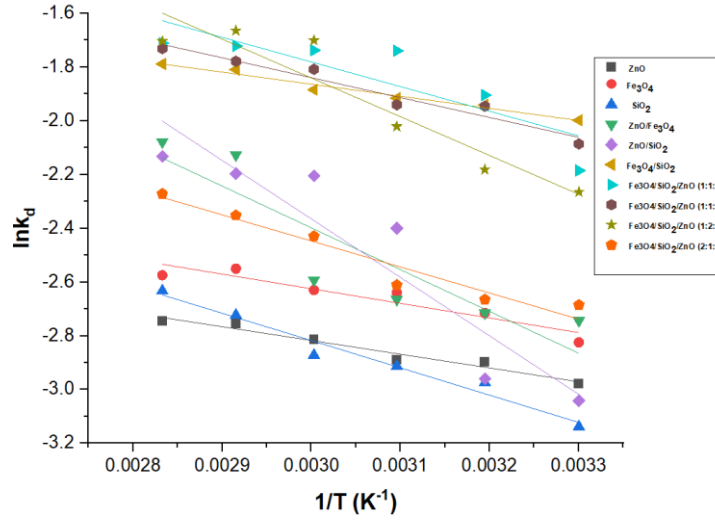
Appendix 69: Plot of lnK$_d$ against 1/T (K^{-1}) for Total Iron
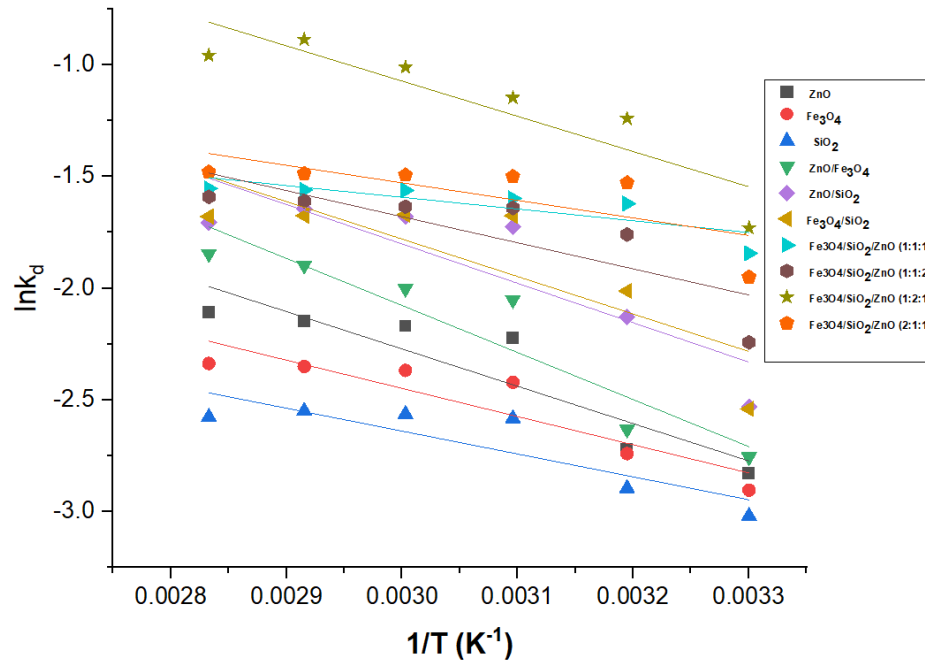
Appendix 70: Plot of lnK$_d$ against 1/T (K^{-1}) for BOD
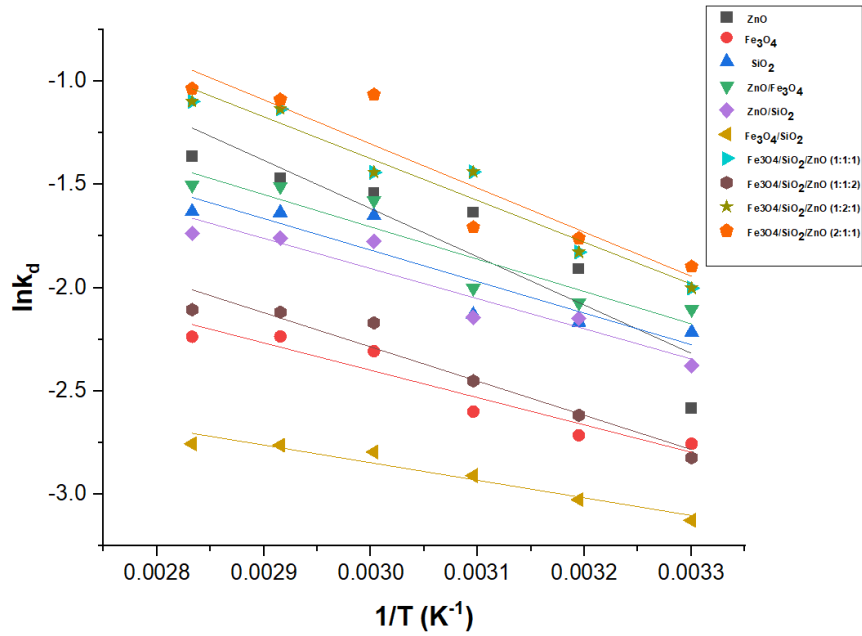
Appendix 71: Plot of lnK$_d$ against 1/T (K^{-1}) BOD
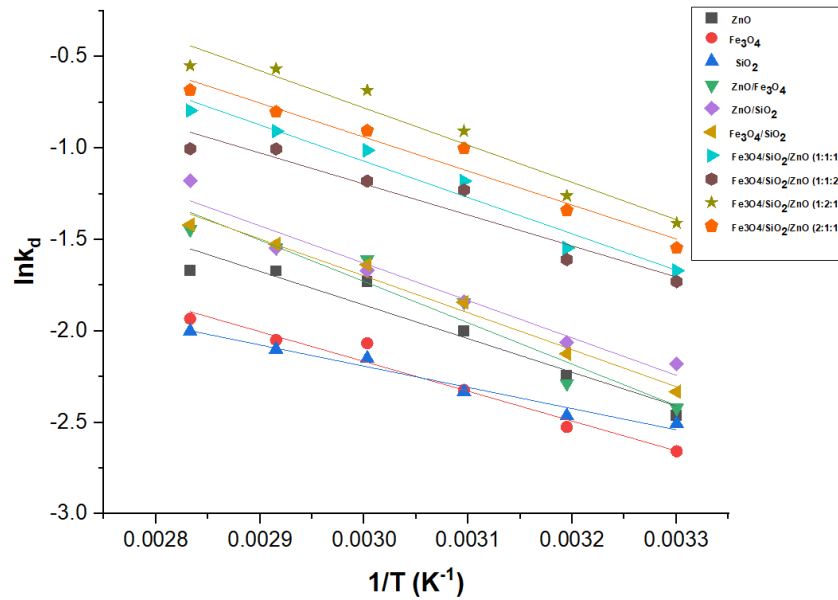
Appendix 72: Plot of lnK$_d$ against 1/T (K^{-1}) TOC
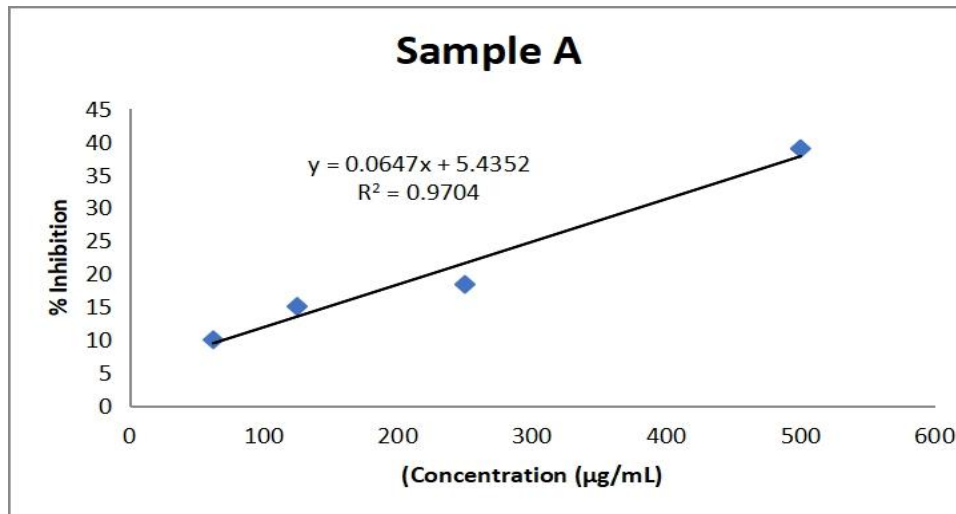
Appendix 73: Plot of % Inhibition against Concentration
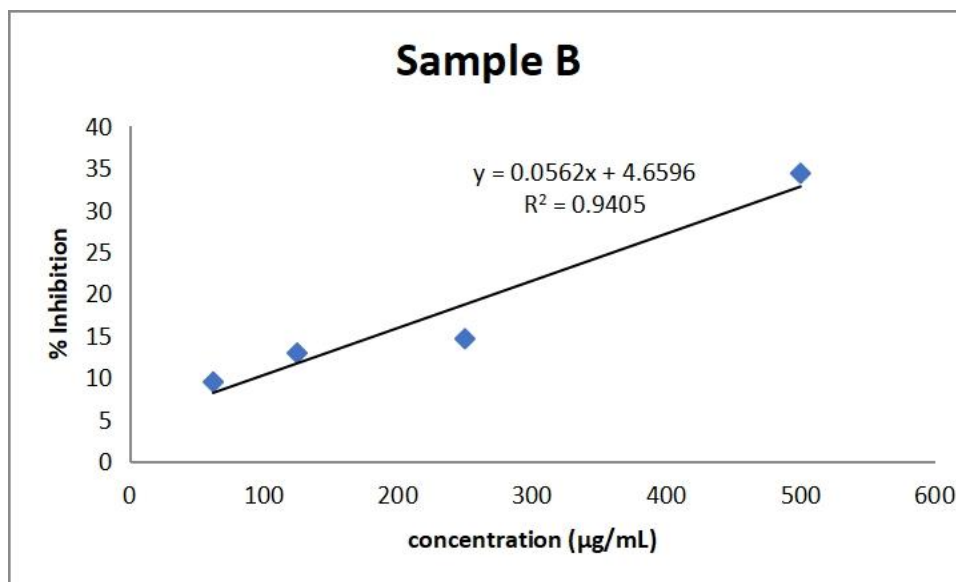
Appendix 74: Plot of % Inhibition against Concentration
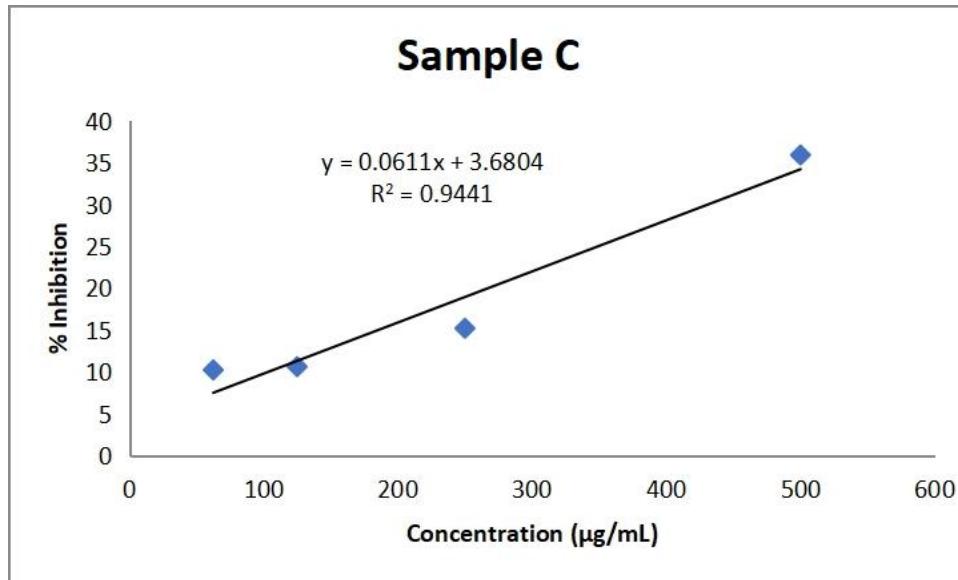
Appendix 75: Plot of % Inhibition against Concentration
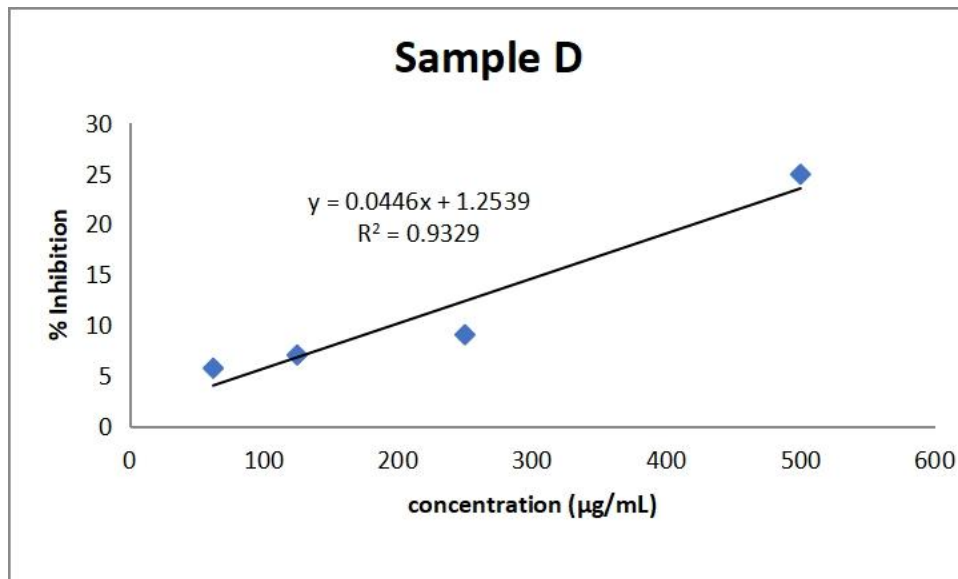
Appendix 76: Plot of % Inhibition against Concentration
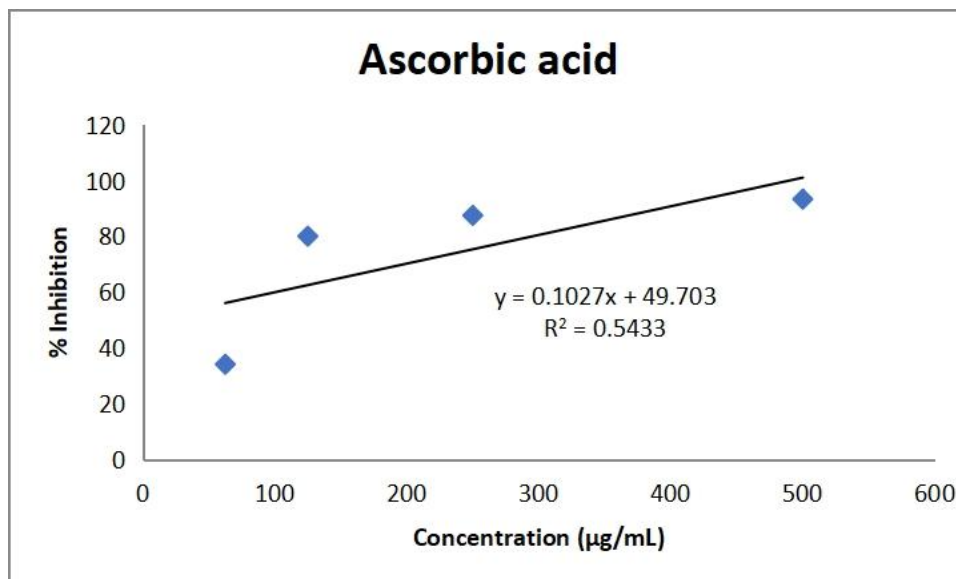
Appendix 77: Plot of % Inhibition against Concentration for Ascob ic Acid

RESEARCH OUTPUT

JOURNALS
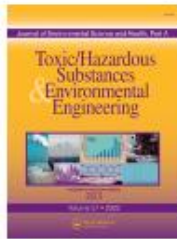
Simultaneous removal of Cu (II) and Cr (VI) ions from petroleum refinery wastewater using ZnO/Fe$_3$O$_4$ nanocomposite

E. Y. Shaba, J. O. Tijani, J. O. Jacob & M. A. T. Suleiman

388

Taylor & Francis
Taylor & Francis Group

Check for updates

Simultaneous removal of Cu (II) and Cr (VI) ions from petroleum refinery wastewater using ZnO/Fe$_3$O$_4$ nanocomposite

E. Y. Shaba (iD), J. O. Tijani, J. O. Jacob and M. A. T. Suleiman

Department of Chemistry, Federal University of Technology, Minna, Niger, Nigeria

ABSTRACT

The presence and removal of heavy metals such as Cu(II) as well as Cr(VI) in petroleum refinery wastewater calls for concerted efforts due to their mobility, toxicity, bioaccumulation, and non-bio-degradability in the environment. In this present work, zinc oxide (ZnO), iron oxide (Fe$_3$O$_4$) nanoparticles and ZnO/Fe$_3$O$_4$ nanocomposites were synthesized via simple sol-gel and chemical reduction methods; characterized using different analytical tools and then applied as nanoadsorbent to sequester Cu(II) and Cr(VI) ions from Petroleum Refinery wastewater via batch adsorption process. Cu(II) and Cr(VI) adsorption processes were examined with respect to contact time (kinetic effect), nanoadsorbent dosage, isotherm equilibrium, and thermodynamic parameters. ZnO/Fe$_3$O$_4$ nanocomposites with higher surface area (39.450 m^2/g) have a mixture of rod-like and spherical shapes as compared to ZnO and Fe$_3$O$_4$ nanoparticles with spherical shape only and surface areas of 8.62 m^2/g and 7.86 m^2/g) according to the high-resolution scanning electron microscopy (HRSEM) and Brunauer–Emmett–Teller (BET) analysis. The X-ray diffractometer (XRD) results revealed the formation of hexagonal wurtzite structure of ZnO and the face-centered cubic structure phase of Fe$_3$O$_4$ nanoparticles, after the formation of the ZnO/Fe$_3$O$_4$ nanocomposites the phases of the nanoparticles were not affected but the diffraction peaks shifted to higher 2θ degree. The average crystallite size of ZnO and Fe$_3$O$_4$ nanoparticles and ZnO/Fe$_3$O$_4$ nanocomposites were 20.12, 26.36 and 14.50 nm respectively. The maximum removal efficiency of Cu (II) (92.99%) and Cr (VI) (77.60%) by ZnO/Fe$_3$O$_4$ nanocomposites was higher than 85.83%; 65.19% for Cu (II) and 80.57%; 62.53 for Cr (VI) using ZnO and Fe$_3$O$_4$ nanoadsorbents individually under the following conditions: contact time (15), dosage (0.08 g) and temperature (30 °C). The experimental data for Cu (II) and Cr (VI) ion removal fitted well to the pseudo-second-order kinetic and Langmuir isotherm models. The thermodynamic study suggested that the removal of the two metal ions from petroleum wastewater was endothermic. The reusability study after the fourth adsorption-desorption cycle indicated the stability of ZnO/Fe$_3$O$_4$ nanocomposites with 85.51% and 69.42% removal efficiency of Cu (II) and Cr (VI). The results showed that ZnO/Fe$_3$O$_4$ nanocomposite achieves higher performance than ZnO and Fe$_3$O$_4$ alone in the removal of Cu (II) and Cr (VI) ions from the petroleum refinery wastewater.

ABBREVIATIONS: 1/n: the intensity adsorption; B (J/mol): the Temkin constant; β: the extent of surface coverage (g/mg); Ce: Final concentration of the metal ions after the interaction with the adsorbent (mg/L); Co: Initial concentration of the metal ions after the interaction with the adsorbent (mg/L); D: crystallite size; EDS: Energy Dispersive Spectroscopy; ε: Polanyi potential; HRSEM: High-Resolution Scanning Electron Microscopy; K1: is a pseudo-first-order rate constant (min − 1); K2: is pseudo-second order the rate constant (min − 1); Kd: is the adsorbate distribution coefficient; kD-R: is the adsorption energy constant; KL: Langmuir constant; KF: Freundlich adsorption capacity; KT: Equilibrium binding constant (L/g); k 0.9 is a constant; m(g): is the mass of the ZnO, Fe3O4 and the ZnO/Fe3O4 nanocomposites (g); qmax: Maximum adsorption capacity (mg/g); qe: Amounts of heavy metals at time t (min); qt: the amounts of heavy metals at equilibrium (mg/g); R: Universal gas constant; T: Absolute solution temperature (K); V: Volume of the petroleum wastewater (mL); X-ray: diffraction (XRD); ΔS°: Standard entropy change (J/mol.K); ΔH°: Standard enthalpy change (kJ/mol); ΔG°: Gibbs free energy (kJ/mol); β: Full width at half maximum (FWHM); α: Adsorption rate (mg/g min),; θ: Angle of Bragg; λ: Wavelength (1.54 Å)

Introductions

Water is essential for healthy ecosystems, socioeconomic development, food and energy production as well as human growth.[1] However, the problem of water scarcity has emerged as a major obstacle to human development due to rapid industrial and urban expansion.[2] It has been reported that by 2025 developing countries will be most affected by water pollution, and half of humanity will reside in water-scarce regions.[3] The pollution of water bodies through the exploration and refining of crude oil results in the production of petroleum-related products such as wastewater.[4] The wastewater generated by the petroleum refinery

Research Article

Adsorptive potential of ZnO/SiO$_2$ nanorods prepared via the sol–gel method for the removal of Pb(II) and Cd(II) from petroleum refinery wastewater

Elijah Yanda Shaba,[*] Jimoh Oladejo Tijani, John Olusanya Jacob and Mohammed Abubakar Tanko Suleiman

Abstract

BACKGROUND: The adsorption technique is considered one of the most effective and economical methods for the removal of heavy metals, due to its excellent advantages of low cost, high efficiency and easy handling. This research looks into the possibility of using ZnO/SiO$_2$ nanorods to remove Cd(II) and Pb(II) from refinery wastewater and their reusability.

RESULTS: ZnO/SiO$_2$ nanorods were synthesized via the sol–gel method. The analysis of ZnO/SiO$_2$ shows the formation of a rod-like structure and surface area of 33 m^2 g^{-1} compared with the 0.3 and 8.620 m^2 g^{-1} for ZnO and SiO$_2$, respectively. Effects of adsorption contact time, adsorbent dosage and temperature were examined via batch adsorption. The result indicates that the ZnO/SiO$_2$ rods exhibited higher adsorption removal efficiency of 85.06% and 84.12% for Pb(II) and Cd(II), respectively, compared to Pb(II) (80.00% and 74.25%) and Cd(II) (76.48% and 70.99%) using ZnO and SiO$_2$ nanoparticles. A thermodynamic study indicates that the adsorption process was endothermic. The data from the adsorption isotherm were well fitted to the Langmuir isotherm. The pseudo-second-order kinetic model best described the adsorption process. An adsorption–desorption study indicated the adsorption to be concentration-dependent and maintained up to 80.65% and 76.90% for Pb(II) and Cd(II) after the fourth regeneration cycle.

CONCLUSIONS: These findings demonstrated that ZnO/SiO$_2$ nanorods are a better nanoadsorbent for the removal of Pb(II) and Cd(II) than ZnO and SiO$_2$ nanoparticles due to their high adsorptive potential and stability.
© 2022 Society of Chemical Industry.
Supporting information may be found in the online version of this article.

Keywords: adsorption; environmental remediation; environmental chemistry; industrial effluents; kinetics; metals; ZnO/SiO$_2$ nanorods

ABBREVIATIONS

$\triangle G^\circ$	Standard Gibbs free energy change of adsorption
$\triangle H^\circ$	Standard enthalpy change of adsorption
$\triangle S^\circ$	Standard entropy change of adsorption
$1/n$	Unit of measurement for intensity
b	Constant for Temkin isotherm (g J mol^{-2})
C	Surface adsorption or boundary layer effect
C_e	Equilibrium metal concentration (mg L^{-1})
C_f	Final concentration of heavy metal in refinery wastewater (mg L^{-1})
C_i	Initial concentration of the heavy metal in refinery wastewater (mg L^{-1})
C_o	thesame (mg/L)
k_1	Pseudo-first-order rate constant (min^{-1})
k_2	Pseudo-second-order rate constant (g mg^{-1} min^{-1})
K_d	Distribution coefficient of adsorbate
k_{O-a}	Constant related to adsorption energy
K_F	Constant for Freundlich isotherm
k_{id}	Intraparticle diffusion rate constant (g mg^{-1} min^{-1})
K_L	Constant for Langmuir isotherm (L mg^{-1})

M	Mass of the nanoadsorbent (g)
q_e	Mass of metal adsorbed at equilibrium
q_{max}	Maximum adsorption capacity (mg g^{-1})
q_t	Mass of metal adsorbed at any time t
R	Gas constant (8.314 J K^{-1})
T	Temperature (K)
V	Volume of refinery wastewater (L)
α	Initial adsorption rate (mg g^{-1} min^{-1})
β	Constant for desorption (g mg^{-1})
ε	Polanyi potential

[*] Correspondence to: EY Shaba, Department of Chemistry, Federal University of Technology, PMB 65, Minna, Niger State, Nigeria. E-mail: elijah.shaba@futminna.edu.ng

Department of Chemistry, Federal University of Technology, Minna, Niger State, Nigeria

Effect of mixing ratios of SiO$_2$ nanoparticles synthesized from metakaolin on the physicochemical properties of ZnO/SiO$_2$ nanocomposites

Elijah Yanda Shaba, Jimoh Oladejo Tijani, John Olusanya Jacob, Mohammed Abubakar Tanko Suleiman

Show more ∨

≪ Share   🗩 Cite

Abstract

Nanomaterials have distinguished themselves as an outstanding class of materials due to their unique physical and chemical characteristics compared to bulk materials. The physicochemical properties of nanomaterials can be improved by forming nanocomposites and manipulating different nanoparticles by varying their mixing ratios. In this study, ZnO and SiO$_2$ nanoparticles and ZnO/SiO$_2$ nanocomposites were produced using a sol–gel method based on the variation of mixing ratios (1:1, 1:2 and 2:1). The monometallic oxide nanoparticles (ZnO, SiO$_2$) and the corresponding nanocomposites (ZnO/SiO$_2$) were characterized using HRSEM, EDX, XRD, FTIR, BET and XPS. Regardless of the mixing ratio of ZnO and SiO$_2$ nanoparticles used, the HRSEM pictures demonstrated a morphological change from the irregular and spherical forms produced for SiO$_2$ and ZnO nanoparticles to rod-like shapes for the ZnO/SiO$_2$ nanocomposite. The quartz phase of SiO$_2$ nanoparticles, with a crystallite size of 43.67 nm, and the hexagonal wurtzite phase of ZnO nanoparticles, with a crystallite size of 31.52 nm, were both synthesized, as revealed by the XRD results. As opposed to this, the XRD patterns of the ZnO/SiO$_2$ nanocomposites synthesized with 1:1, 1:2 and 2:1 mixing ratios showed a mixture of α-quartz (SiO$_2$) and hexagonal wurtzite (ZnO) with crystallite sizes of 21.24, 29.56 and 15.36 nm, respectively. The EDS results confirmed the existence of Zn and O for ZnO; Si and O for SiO$_2$ nanoparticles and Zn, Si and O in the prepared ZnO/SiO$_2$ nanocomposite, irrespective of the mixing ratios. The XPS results showed the existence of Zn in the +1 oxidation state in ZnO/SiO$_2$ compared to single ZnO with the Zn^{2+} valence. The BET surface area indicates that the ZnO/SiO$_2$ nanocomposites had a higher surface area (1:1 (39.042 m^2/g), 1:2 (55.602 m^2/g) and 2:1 (82.243 m^2/g)), irrespective of the mixing ratios, compared to the surface area for the ZnO (8.620 m^2/g) and SiO$_2$ (0.386 m^2/g) nanoparticles. The mixing ratio of the ZnO and SiO$_2$ nanoparticles influenced the crystallite sizes, surface elements oxidation states and morphology of the ZnO/SiO$_2$ nanocomposite formed and the optima mixing ratio for the formation of ZnO/SiO$_2$ nanocomposite was found to be 2:1 of ZnO:SiO$_2$ nanoparticles.

Graphical abstract

REVIEW ARTICLE

A critical review of synthesis parameters affecting the properties of zinc oxide nanoparticle and its application in wastewater treatment

E. Y. Shaba[1] · J. O. Jacob[1] · J. O. Tijani[1] · M. A. T. Suleiman[1]

Abstract

In this era, nanotechnology is gaining enormous popularity due to its ability to reduce metals, metalloids and metal oxides into their nanosize, which essentially alter their physical, chemical, and optical properties. Zinc oxide nanoparticle is one of the most important semiconductor metal oxides with diverse applications in the field of material science. However, several factors, such as pH of the reaction mixture, calcination temperature, reaction time, stirring speed, nature of capping agents, and concentration of metal precursors, greatly affect the properties of the zinc oxide nanoparticles and their applications. This review focuses on the influence of the synthesis parameters on the morphology, mineralogical phase, textural properties, microstructures, and size of the zinc oxide nanoparticles. In addition, the review also examined the application of zinc oxides as nanoadsorbent for the removal of heavy metals from wastewater.

Keywords Zinc oxide · Synthesis parameters · Nanoadsorbent · Heavy metals

Introduction

Zinc oxide nanoparticles constitute one of the important metal oxides materials that have been widely applied in materials science due to its unique physical, chemical, and biological properties such as biocompatible, environmentally friendly, low cost and non-toxic nature (Alwan et al. 2015; Salahuddin et al. 2015; Ruszkiewicz et al. 2017). Owing to its exceptional properties, ZnO nanoparticles have been applied as a functional advanced material to solve different societal problems especially in the field of catalysis for wastewater treatment and also as cosmetics and antimicrobial additives (Ruszkiewicz et al. 2017). ZnO nanoparticles have several advantages which include unique chemical and thermal stability, robustness, and long shelf life over other metal oxides such as TiO_2, WO_3, SiO_2, and Fe_2O_3. Zinc oxide exists in the following phases: hexagonal quartzite, cubic zinc blende, and cubic rock salt (Belver et al. 2019). The wurtzite structure is the most common due to its stability at ambient conditions, where every zinc atom is tetrahedrally coordinated with four oxygen atoms (Barhoum et al.

2019). In each phase, zinc oxide nanoparticles (ZnONPs) are a semiconductor material with a direct wide bandgap of ~ 3.3 eV (Senol et al. 2020). It has advantages such as stabilization on substrate especially the zinc blende form with a cubic lattice structure (Parihar et al. 2018). Food and Drug Administration (FDA) includes also zinc oxide as one of the safest metal oxides that can be used in food industries (Bettini et al. 2016).

Zinc oxide nanoparticles have been synthesized via different chemical and physical methods, namely sol–gel, hydrothermal, precipitation and co-precipitation, chemical vapour deposition, spray pyrolysis, magnetic sputtering, microwave-assisted technique, solvothermal, biological routes amongst others (Ul-Haq et al. 2017). Each of the listed methods has advantages and disadvantages and as such different morphologies of ZnO nanoparticles according to characterization tools ranging from nanoplates, nanostars, nanobelts, nanotubes have been reported (Ambika and Sundararajan 2015). Different zinc salts such as zinc acetate dehydrate ($ZN(C_2H_3O_2)_2 \cdot 2H_2O$)), zinc nitrate hexahydrate ($Zn(NO_3)_2 \cdot 6H_2O$) zinc sulfate ($Zn(SO_4)_2 \cdot 7H_2O$) and zinc chloride ($ZnCl_2$) as precursor have been used to prepare ZnO nanoparticles (Ambika and Sundararajan 2015; Ezhilarasi et al. 2016; Sierra et al. 2018).

However, the problems of stability, dispersion and crystalline structures control of ZnO nanoparticles in aqueous

✉ E. Y. Shaba
elijah.shaba@futminna.edu.ng

[1] Department of Chemistry, Federal University of Technology, P. M. B. 65, Minna, Niger State, Nigeria

Springer

CONFERENCES

FST

FACULTÉ DES SCIENCES ET TECHNIQUES
DE MOHAMMEDIA
UNIVERSITÉ HASSAN II DE CASABLANCA

AMCADD

Association Marocaine de Chimie Analytique
pour un Développement Durable

The Fourth International Symposium on "Analytical Chemistry for a Sustainable Development"- ACSD 2021

March 9- 11, 2021
Mohammedia-
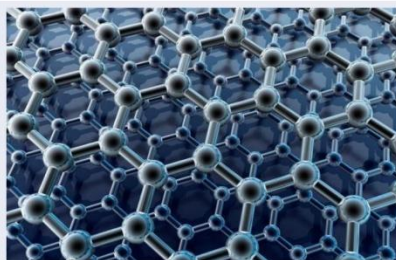
Conference Program ACSD2021
Faculty of Sciences and Technologies of Mohammedia*

*We would like to express our gratitude to all our participants for accepting to attend the Hybrid Conference. Please Note that the health barriers and social distancing should be respected.

Tuesday 9 March 2021

Tuesday 9 March 2021: ACSD 2021- FSTM		
9:00 - 9:40	Opening ceremony	
Chairs : M. EL RHAZI / M. DE LA GUARDIA		
9:40 - 10: 15	**MOHAMED EDDAOUDI,** Reticular Chemistry in Action: MOF Design Strategies to Applications, **Saudi Arabia.**	PL1
10:15 – 10:50	**ABDELHAMID ERRACHID** , Field-Deployable of the future analytical micro-tools based on Lab-on-a-Chip Platforms, **France**	PL2
10:50- 11:20	**Coffee Break - Poster Session (P1-P12)**	
Topic: Emerging techniques in analytical science and materials analysis		
Chairs: S. ALAMI YOUNSSI / B. HAMMOUTI		
11:20 - 11:55	**MOHAMMED ZOUGAGH,** Analytical nanometrology towards solving real analytical problems, **Spain.**	PL3
11:55 – 12:10	**B. JABER,** L'expérience du CNRST en sciences analytiques et en caractérisation des matériaux, **Morocco.**	O1
12:10 - 12:25	**R. A. ODHIAMBO**, Ruthenium(II) Oxathiacrown Ether-based Sensing Probe for Mercury(II) Ions, **Kenya.**	O2
12:25 - 12:40	**I. AJAI,** Impacts of Artisanal Mining Activities on Heavy Metal contents in Soil, Water and Selected Food Crops, **Nigeria.**	O3
12:40- 12:50	**G. IDRISSI SERHROUCHNI,** Investigation of illuminated Moroccan manuscripts by EDXRF, SEM-EDS, XRD, and Raman and FTIR-ATR spectroscopy, **Morocco.**	O4
13:00 - 14:30	**Lunch**	
Topic: New materials and nanomaterials application: water treatment, fuel cell		
Chairs : R. TOUZANI / M. HAFSI		
14:30 - 15:05	**MOHAMED K. AROUA ,** Science and Technology Contribution to Sustainable Development Goals - Membrane Processes for Clean Water Supply to Remote Areas (SDG 6)**, Malaysia.**	PL4
15:05 - 15:20	**R. BEN AMAR,** Synthesis and characterization of clay/zeolite composite ultrafiltration membranes for removal of heavy metals from wastewater, **Tunisia.**	O5
15:20 – 15:30	**F. CHARIK,** Preparation and characterization of low-cost NaA zeolite membrane on Kaolinite support for dehydration of alcohols, **Morocco.**	O6
15:30 - 15:40	**A. BELGADA,** Pretreatment of seawater prior to Desalination using new flat Phosphate membrane, **Morocco.**	O7
15:40 - 15:50	**F. HAMOUCHE,** Behavior and Characterization of Lead-Free Brass and Lead-rich Brass in tap water at different temperatures, **Morocco.**	O8
15:50 - 16:00	**A. KARIM ,** Elaboration of flat ultrafiltration membrane made from natural nano-pozzolan using sonochemical method, **Morocco.**	O9
16:00 - 16:10	**F. LARGO,** Removal anionic dyes of waste water using the natural clay, **Morocco.**	O10
16:10- 16:40	**Coffee break - Poster Session (P13/P26)**	
Chairs : M. K. AROUA / J. BENAZHA		
16:40 – 17:00	**A. ELGAMOUZ,** Effect of AgNPs Internal Solution on the Detection of Mecrury(II) by an Ion-Selective Electrode based on a Thiol Coordination From Cysteine as Ionophore, **United Arab Emirates.**	O11
17:00 - 17:10	**A. EL ATTAR,** Effect of Copper particles regeneration in acidic medium on the electrocatalytic oxidation of ethanol in alkaline media, **Morocco.**	O12
17:10 - 17:20	**G. ACHAGRI,** Super-hydrophobic textile fabric functionalized Organophilc cellulose nanocrystal: Application in water/oil separation, **Morocco.**	O13
17:20 - 17:30	**H. WAKRIM,** Development of a new composite membrane electrolyte for direct methanol fuel cell application, **Morocco.**	O14
17:30 - 17:40	**E.Y. SHABA,** Synthesis and Characterization of Novel Ternary Fe3O4/ZnO/SiO2 Nanocomposites prepared by combination of sol-gel and wet impregnation method, **Nigeria.**	O15
17:40 - 17:50	**M. LAURA SORIANO,** Evaluation of graphene quantum dots as sensing platforms for food and environmental analytical applications, **Spain.**	O16
17:50-18:20	**M. MAJDOUB,** Biosourced tough elastomeric polyurethane/organophilic graphene nanocomposites films as advanced high performance materials, **Morocco.**	O17

CHEMICAL SOCIETY OF NIGERIA (CSN)
ZARIA CHAPTER

14th
ChemClass
Conference

Theme:
The Roles of Chemical Sciences
and Technology in Accomplishing SDG 3:
GOOD HEALTH AND WELL BEING

DATE: THURSDAY 17TH JUNE, 2021

BOOK OF PROCEEDINGS

EFFECT OF CALCINATION TEMPERATURE ON THE CRYSTALLITE SIZE AND MORPHOLOGY OF ZINC OXIDE/POLIVYNL NANO-COMPOSITE SYNTHESIZED VIA SOL-GEL METHOD

E.Y. Shaba[1], J. O., Jacob[1], J. O., Tijani[1] and M.A.T., Suleiman[1]

Department of Chemistry, Federal University of Technology, P. M. B. 65, Minna, Niger State, Nigeria
Corresponding Authors email: 1* elijah.shaba@futminna.edu.ng

ABSTRACT

ZnO/ polyvinyl pyrrolidone nanocomposites were synthesized from zinc nitrite (as a precursor) and polyvinyl pyrrolidone as a stabilizing by sol-gel method at pH of 11 and ambient synthetic temperature. The synthesized ZnO/polyvinyl pyrrolidone (ZnO/PVP) nanocomposites were subjected to different calcination temperature (ambient 300°C, 500 °C, and 700 °C). The synthesized ZnO/ polyvinyl pyrrolidone nanocomposites were characterized by X-ray diffraction (XRD), High resolution Scanning electron microscopy (HRSEM), Energy dispersive X-ray spectroscopy (EDS), and X-Ray Photoelectron Spectroscopy (XPS). The XRD results revealed the crystallite size calculated using the Scherrer equation was 160.96 nm, 10.74 nm, 13.33 nm, and 16.52 for the ambient, 300°C, 500 °C, and 700 °C respectively. The result indicates the synthesis of the hexagonal wurtzite structure of ZnO. The HRSEM shows spherical structures of the nanocomposites. It is observed that at a low temperature, the stoichiometric ratio between Zn and O atoms has a significant deviation from the perfect ratio of 1:1 and becomes optimized as the temperature increases as sown by the EDS result.

Key words: ZnO/ polyvinyl pyrrolidone, nanocomposites, sol-gel, and calcination.

INTRODUCTION

Zinc oxide (ZnO) is one of the most important semiconductor materials with a wide band gap of 3.37 eV (Haque et al., 2020). This semiconductor has several properties, including good transparency, high electron mobility, wide band gap, and strong room temperature luminescence (Ouhaibi et al., 2018). These properties have made ZnO attractive among other metal oxides nanoparticles (Turky et al., 2017). ZnO nanoparticles have been synthesized by different methods including co-precipitation, hydrothermal sol-gel, wet chemical, pulsed vapour deposition and laser ablation, just to mention but a few (Gonçalves, et al., 2021). Among the aforementioned methods, the sol-gel method of synthesis is known to be the most versatile because it provides better homogeneity, high chemical stability, structural control, a wide range of radiation absorption, long shelf life and uses less energy (Aslinjensipriya et al., 2020). However, the activity and toxicity of the ZnO nanoparticle is generally affected due to the stability of the ZnO nanoparticles (Siddiqi et al., 2018). In this paper, the effect of calcination temperature on the synthesis of ZnO/polyvinyl pyrrolidone nanocomposites via sol-gel method were studied.

MATERIALS AND METHODS

Zinc nitrate, Polyvinylpyrrolidone (PVP), sodium hydroxide (NaOH) were purchased from Merck (INDIA). All chemicals were used without further purifications.

Synthesis of ZnO/ Polyvinyl pyrrolidone nanocomposites (ZnO/PVP)

A known concentration of zinc nitrate (0. 1 M) was prepared and 25 cm³ was measured into 250 cm³ beaker and place on a magnetic stirrer. 7cm³ of 1.0 M sodium hydroxide (NaOH) solution was slowly added into the zinc nitrate solution. After which, 10 cm³ of 5 % w/v Polyvinylpyrrolidone (PVP) solution was added to the same mixture, where precipitate was formed. The precipitate was separated from the reaction solution by centrifugation at 5000 rpm at 60°C for 15 min and residue was collected. The residue was dried using a hot air oven operating at 100°C for 2 h. The dried precursor was calcined at different temperature (300-700°C) and holding time of 2 h.

Characterization of nanoparticles

ZnO/polyvinyl pyrrolidone nanocomposites were investigated using X-ray diffraction analysis (XRD), High resolution emission scanning electron microscopy (HRSEM), Energy dispersive spectroscopy (EDS), X-ray photoelectron spectroscopy (XPS)